

Hans Bjerkaas

Characterisation and Plasticity in Extruded Al-Mg-Si Profiles engaging In-situ EBSD

Thesis for the degree philosophiae doctor

Trondheim, June 2007

Norwegian University of Science and Technology
Faculty of Natural Sciences and Technology
Department of Materials Science and Engineering



NTNU

Norwegian University of Science and Technology

Thesis for the degree philosophiae doctor

Faculty of Natural Sciences and Technology
Department of Materials Science and Engineering

© Hans Bjerkaas

ISBN 978-82-471-3375-0 (printed version)
ISBN 978-82-471-3389-7 (electronic version)
ISSN 1503-8181

Doctoral theses at NTNU, 2007:154

IMT-Report 2007:94

Printed by NTNU-trykk

Preface

The experimental research presented in this thesis has been carried out at the Norwegian University of Science and Technology (NTNU), Department of Materials Science and Engineering in the period from August 2002 to March 2006. The thesis reached its final form by end of June 2007.

The work was part of the project FREMAT, sub-project “Microstructure and Shape” and has been financed by the Norwegian Research Council and Hydro Aluminium AS. It has allowed the author to work within both development of new experimental techniques and detailed crystal plasticity of extruded Al-Mg-Si profiles, something that certainly has been appreciated. Hopefully, this work will result in new insight into crystal plasticity, but also initiation of new works within the field of in-situ EBSD.

The close collaboration with Hydro Aluminium AS allowed for introducing the author to various in-depth aspects related to aluminium extrusion technology. This in turn, has opened up for a better understanding of current industrial challenges and hopefully improved the relevance and quality of the work presented herein.

Abstract

A comprehensive characterisation and study of plasticity in two extruded Al-Mg-Si profiles has been carried out. The primary objective of the experimental work has been directed towards obtaining an improved understanding of the operating deformation mechanisms and mechanical anisotropy observed on all length scales during plastic deformation. In-situ deformation in the SEM combined with EBSD investigations has been an important tool in order to obtain this objective. The experimental results have been divided into two separate parts. Part A covers the characterisation and mechanical anisotropy investigations, while Part B covers the more detailed in-situ investigations.

Two alloys, one with a recrystallized microstructure and the other with a non-recrystallized (fibrous) microstructure, have been subjected to a detailed characterisation concerned with mechanical anisotropy, through-thickness variations and effects of various heat-treatments. The experimental investigations showed that both alloys possess highly anisotropic properties. The effects of temper designation, directional dependency and position through the thickness were studied.

The in-situ deformation studies gave new insights into the fundamental reasons for the observed mechanical anisotropy and the related deformation mechanisms. Detailed investigations of the slip traces in combination with calculated Schmid value distributions provided information on potential slip activity for the various slip systems. It was found that the number of slip systems activated was very heterogeneous and this number can even vary from region to region within one individual grain. In other words, the strain distribution seemed very heterogeneous. Further, the actual number of activated slip systems was in general less than predicted by the widely used Taylor model. Consequently, if the accuracy of texture-based calculations should be improved, more advanced models like the GIA (Grain Inter-Action) and the LAMEL models should be applied.

It was also found that crystallographic orientations having a [100] or a [111] parallel to the deformation direction (DD) were more stable during simple tension deformation. Moreover, crystallographic orientations not having this configuration rotated in order to

align the DD to one of the above directions. Also the rotation of individual grains seemed to have a strong relationship to the actual activation of slip systems.

The mechanical anisotropy and shape tolerances could be explained in terms of crystallographic texture, i.e. variations in the actual activation of slip. As a result, the macroscopic properties (e.g. mechanical anisotropy) were to a large extent controlled by the mechanisms operating at the microscopic length scale. A full understanding of the operating mechanisms should therefore involve exact information from all length scales.

Acknowledgments and contributions

The Norwegian Research Council and Hydro Aluminium are gratefully acknowledged for the founding through the FREMAT project. Hydro Aluminium is further acknowledged for giving me the opportunity to gain industrial experience through several internships at different facilities. Special thanks to my supervisors, Professor Hans Jørgen Roven and Professor Jarle Hjelen. They have fully supplemented each other, and their encouragement and enthusiasm has stimulated me to complete this work. I would also like to give a special thanks to Dr. Trond Furu for his motivating interest.

My good friend Dr. Stéphane Dumoulin is gratefully acknowledged for his involvement in strain measurements, mathematical and continuum mechanical calculations. This work could not have been completed without his help. The thorough introduction to in-situ deformation in the SEM provided by Rémi Chiron at the CNRS – PMTM laboratory in Paris has been crucial for this work and is very well acknowledged. I would also like to acknowledge all my colleagues in the department, in particular Dr. Stian Tangen, Dr. Knut Sjølstad, Dr. Jens Christofer Werenskiold, Dr. Bjørn Holmedal, Dr. Håkon Hallem, Mr. Tomas Erlie, Mr. Przemyslaw Szczygiel and Mr. Anders Lilleby, who all assisted me both professionally and socially during this work.

Further, I have been fortunate to supervise three master degree students during my PhD work. I would like to thank Mr. Snorre Kjørstad Fjeldbo, Mrs. Randi Mørkrid and Mr. Peter Bråten for their thorough work performed during their master works.

I would like to acknowledge my colleagues at the scanning electron microscopy laboratory, not only for providing high performance equipment and knowledge that allows state-of-the-art research within this field, but also for the close friendship during my time at NTNU. Also my current colleagues at Hydro Aluminium Holmestrand should be acknowledged for their support this last year.

Finally, I would like to thank the two most important women in my life, my fiancée Margrethe and my new-born daughter Oda, that both have been extremely patient during my time as a PhD-student.

Table of contents

<u>PREFACE</u>	<u>I</u>
<u>ABSTRACT</u>	<u>III</u>
<u>ACKNOWLEDGMENTS AND CONTRIBUTIONS</u>	<u>V</u>
<u>TABLE OF CONTENTS</u>	<u>VII</u>
<u>1 INTRODUCTION</u>	<u>1</u>
<u>2 THEORETICAL BACKGROUND</u>	<u>3</u>
2.1 ALUMINIUM ALLOYS	3
2.1.1 NON-HEAT-TREATABLE ALUMINIUM ALLOYS	3
2.1.2 HEAT-TREATABLE ALUMINIUM ALLOYS	4
2.2 POLYCRYSTALLINE PLASTICITY THEORY	5
2.2.1 BASIC PLASTICITY	5
2.2.2 SCHMID'S LAW – GEOMETRY OF SLIP	9
2.2.3 ROTATION OF THE CRYSTAL LATTICE	11
2.2.4 THE SACHS MODEL	16
2.2.5 THE TAYLOR MODEL	17
2.2.6 THE SELF-CONSISTENT MODEL	20
2.2.7 ADVANCED POLYCRYSTALLINE PLASTICITY MODELS	21
2.3 TEXTURE	23
2.3.1 ORIENTATION OF INDIVIDUAL CRYSTALLITES	24
2.3.2 ORIENTATION DISTRIBUTION	25
2.3.3 ELECTRON BACKSCATTER DIFFRACTION (EBSD)	26

2.3.4	EBSD MEASUREMENTS	28
2.3.5	TEXTURE COMPONENTS IN FCC MATERIALS	33
2.4	ANISOTROPY AND FORMABILITY	36
2.4.1	MECHANICAL ANISOTROPY	36
2.4.2	TEXTURE-BASED CALCULATIONS	37
2.5	MICROSTRUCTURAL EVOLUTION	38
2.5.1	SLIP TRACES	38
2.5.2	TRANSITION AND KINK BANDS	40
2.5.3	SHEAR BANDING	40
2.6	STRAIN MEASUREMENTS	41
2.6.1	DIGITAL SPECKLE CORRELATION ANALYSIS	43
2.7	EARLIER WORK – STATE-OF-THE-ART	45
2.7.1	CRYSTAL PLASTICITY	46
2.7.2	MECHANICAL ANISOTROPY AND FORMING BEHAVIOUR	47
2.7.3	DEFORMATION MECHANISMS	48
2.7.4	AGE-HARDENING	49
2.7.5	AVAILABLE IN-SITU TECHNIQUES	52
3	<u>MATERIALS AND MATERIAL PROCESSING</u>	<u>56</u>
3.1	MATERIALS	56
3.2	MATERIAL PROCESSING	57
3.2.1	EXTRUSION	57
3.2.2	HEAT-TREATMENTS	58
3.2.3	ADDITIONAL PROCESSING	59
4	<u>EXPERIMENTAL TECHNIQUES</u>	<u>61</u>
4.1	SPECIMEN SAMPLING AND PREPARATION	61
4.1.1	SPECIMEN SAMPLING	61

4.1.2	METALLOGRAPHIC PREPARATION AND SURFACE GRIDS	67
4.2	TENSILE TESTING	69
4.3	SCANNING ELECTRON MICROSCOPY (SEM)	69
4.3.1	ELECTRON BACKSCATTER DIFFRACTION (EBSD)	70
4.3.2	IN-SITU DEFORMATION INVESTIGATIONS	73
4.3.3	OPTIMISATION OF IN-SITU SYSTEMS	74
4.4	LOCAL STRAIN MEASUREMENTS	80
<u>5</u>	<u>EXPERIMENTAL RESULTS</u>	<u>81</u>
<u>PART A: CHARACTERISATION OF MATERIALS – EFFECTS OF HEAT-TREATMENT, TEXTURE AND THROUGH-THICKNESS VARIATIONS</u>		<u>82</u>
5.1	CHARACTERISATION OF AS-RECEIVED MATERIALS	82
5.1.1	MICROSTRUCTURE	82
5.1.2	CRYSTALLOGRAPHIC TEXTURE	85
5.1.3	THROUGH-THICKNESS VARIATIONS	87
5.2	MECHANICAL PROPERTIES AND ANISOTROPY	95
5.2.1	MECHANICAL PROPERTIES	95
5.2.2	FURTHER DETAILS REGARDING AGE-HARDENING EFFECTS	102
5.2.3	AGE-HARDENING VS. ANISOTROPY AND SHAPE	111
<u>PART B: SEM IN-SITU INVESTIGATIONS OF PLASTICITY – SLIP ACTIVITY, GRAIN ROTATION AND TEXTURE EVOLUTION</u>		<u>114</u>
5.3	INITIAL INVESTIGATIONS	114
5.4	GLOBAL TEXTURE EVOLUTION WITH INCREASING STRAIN	116
5.5	GRAIN ROTATION WITH INCREASING STRAIN	122
5.5.1	ROTATION PATHS – HEAVILY TEXTURED MATERIAL	122

5.5.2	ROTATION PATHS – RANDOM TEXTURED MATERIAL	126
5.5.3	AMOUNT OF ROTATION	129
5.5.4	ORIENTATION GRADIENTS	132
5.6	PLASTICITY	134
5.6.1	SLIP TRACE EVOLUTION	134
5.6.2	SLIP SYSTEM ACTIVITY	146
5.7	LOCAL STRAIN DISTRIBUTION	153
5.7.1	MICRO SCALE	154
5.7.2	MESO SCALE	159
6	DISCUSSION	166
<hr/>		
6.1	MECHANICAL ANISOTROPY	166
6.1.1	CRYSTALLOGRAPHIC TEXTURE	166
6.1.2	TEXTURE VS. MECHANICAL OBSERVATIONS (MAINLY AA6063)	170
6.2	OBSERVATIONS AND TAYLOR ANALYSES REGARDING THROUGH-THICKNESS VARIATIONS	177
6.2.1	TAYLOR ANALYSES	177
6.2.2	EVALUATION OF THE VOCE-TYPE MODEL	180
6.2.3	EXPERIMENTAL EFFECTS	183
6.2.4	FINAL COMMENTS ON THE VOCE-TYPE MODELLING	186
6.2.5	INTERNAL STRESSES	187
6.2.6	PLASTIC STRAIN RATIOS	188
6.2.7	FINAL COMMENTS ON PROFILE THICKNESS STRAIN DISTRIBUTION	194
6.3	DEFORMATION MECHANISMS AND CRYSTAL PLASTICITY	195
6.3.1	THE NATURE OF SLIP TRACES	195
6.3.2	CRYSTALLOGRAPHIC ROTATIONS DURING DEFORMATION	201
6.3.3	SELECTION OF SLIP SYSTEMS	207
6.3.4	ACTIVATION OF SLIP SYSTEMS – EXPERIMENTAL OBSERVATIONS VS. TEXTURE-BASED CALCULATIONS	211

6.3.5	STRAIN HETEROGENEITIES	215
6.3.6	HARD VS. SOFT ORIENTATIONS	218
6.3.7	EFFECTS OF NEAREST NEIGHBOURS	220
6.4	IMPACT AND RELEVANCE TO SHAPE OF EXTRUSIONS	222
6.5	IN-SITU DEFORMATION IN THE SEM – STATUS AND CHALLENGES	224
6.5.1	IN-SITU DEFORMATION UNIT	224
6.5.2	CHALLENGES (RELATED TO IN-SITU DEFORMATION IN THE SEM)	225
6.5.3	FOCUSED ION BEAM (FIB)	226
<u>7</u>	<u>CONCLUSION</u>	<u>228</u>
	<u>REFERENCES</u>	<u>230</u>
	<u>APPENDIX A – HEATING UNIT</u>	<u>239</u>
	<u>APPENDIX B – CALCULATED ODFS</u>	<u>241</u>
	<u>APPENDIX C – THROUGH-THICKNESS VARIATIONS</u>	<u>242</u>
	<u>APPENDIX D – EFFECT OF AGE-HARDENING</u>	<u>246</u>
	<u>APPENDIX E – THROUGH-SPECIMEN-THICKNESS-CURVATURES</u>	<u>249</u>

1 Introduction

Modern production processes demands a high degree of automation involving tight geometrical tolerances of the various components. The new requirements on profile shape control are the most critical and come from various product areas like the heat transfer business, general extrusion and, of course, production for the automotive industry. The most prominent example is from the automotive industry. Future requirements from down stream processing of profiles challenges the extrusion industry, since extruded profiles often have strong microstructure- and texture gradients through the thickness which clearly affect the mechanical properties.

The strategy of Hydro Aluminium is to be world leading within aluminium extrusion. The “FREMAT – Understanding and Controlling Variations in Extrusion of Aluminium” research program was initiated by Hydro Aluminium in close collaboration with the Norwegian Research Council in order to attain such a position. The very challenging vision of this project is to improve shape tolerances on extruded products by a factor of ~10. To fulfil this vision, it is essential to understand, quantify and control effects from material flow balance, development of residual stresses, microstructural evolution and thermo-mechanical coupling of die and extruded material on a completely new level of accuracy.

This work is part of the “Microstructure and shape” subproject that addresses metallurgical effects and microstructural evolution. The primary objective is directed towards obtaining an improved understanding of the operating deformation mechanisms, and by that obtaining a better understanding of how shape tolerances, i.e. mechanical anisotropy can be controlled. This can only be obtained if the connections between the different deformation mechanisms operating on all length scales are fully understood. Figure 1.1 illustrates the importance of studying individual mechanisms in order to find the net effect.

Introduction

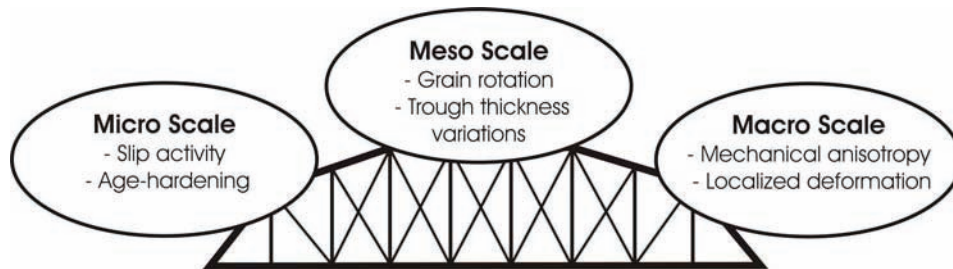


Figure 1.1 – Illustration presenting the different features operating at different length scales that have to be fully understood in order to comprehend how to improve the shape tolerances of extruded profiles with a factor 10.

In this work, special attention has been paid to the effect of heterogeneities in slip activation on the macroscopic mechanical anisotropy. This has been obtained by initially performing a detailed characterisation of two extruded Al-Mg-Si profiles. Further, in-situ EBSD investigations have been applied to better understand the macroscopic properties.

2 Theoretical background

The main objective of this theoretical part is to give a summary of previous work done concerning room temperature plastic deformation behaviour in face-centred cubic (FCC) materials. A good understanding of crystal plasticity and the mathematical models used to describe crystal plasticity is of prime importance in order to provide a physical basis for microstructure- and alloy design. On the other hand, experimental observations are critical to the developers of plasticity modelling and for understanding the real phenomena taking place in nature. Hence, a two-fold understanding is a key factor in reaching the main objectives of this investigation. Further, this part summarises the main findings reported in the literature concerning in-situ deformation and electron backscatter diffraction (EBSD) observations on aluminium alloys. The theoretical background for the most important experimental techniques applied is also given in this chapter.

2.1 Aluminium alloys

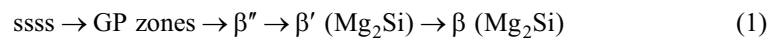
Aluminium is an important material for the transportation industry due to its low density, high specific strength and competitive crash performance (Hirsch 2004). Also, the ability to easily recycle aluminium alloys is very advantageous from an environmentally point of view (Hirsch 2004). The properties of aluminium have made this material become an even more important material for the future. Wrought aluminium alloys are divided in two groups based on their age-hardenability.

2.1.1 Non-heat-treatable aluminium alloys

Non-heat-treatable aluminium alloys constitute a class of alloys that owe their strength mainly to elements in solid solution. However, also some types of particles will give rise to additional strength increase, mostly due to Orowan hardening (Orowan 1948, Verhoeven 1975). A heat-treatment will generally not produce any strengthening precipitates as in the heat-treatable alloys. The alloy systems belonging to this class are the AA1xxx, AA3xxx, AA5xxx and the AA8xxx alloy systems. A description of the different alloying systems and their main alloying elements are given in Table 2.1.

2.1.2 Heat-treatable aluminium alloys

The heat-treatable aluminium alloys achieve their strength mainly from precipitates, and belong to the AA2xxx, AA6xxx and AA7xxx alloy systems (see Table 2.1) (AAUS 1970). These alloys are usually first solution-heat-treated, i.e. heated into the single-phase area of the phase diagram where alloying elements are dissolved in solid solution. A rapid quench freezes the atoms in a supersaturated solid solution (ssss) from where the precipitation sequence starts (Martin 1968). Alloys investigated in the solution-heat-treated condition are often denoted the “W-condition” (ISO 2004). As an example, the precipitation sequence in the AA6xxx system is generally given by:



Precipitation after solution heat-treatment can take place at room temperature (natural age-hardening), in which the stabilised material condition is referred to as the “T4-condition” (ISO 2004). However, artificial age-hardening are normally used in order to achieve a more stabilised material with as high strength as possible. Following the above sequence from left to right, the size of the precipitates increases and the coherency between the matrix and the precipitates is gradually lost. The maximum strength (T6-condition) generally occurs when there is a mixture of coherent and semi-coherent precipitates. Over-ageing to the T7-condition produces stable incoherent particles which results in a lower strengthening effect (Martin 1968). Material cooled from the fabrication temperature (natural solution heat-treatment) and then naturally aged is referred to as the T1-condition (ISO 2004). For a more comprehensive review of heat-treatable aluminium alloys see e.g. Polmear (2004).

Theoretical background

Table 2.1 – IADS (International Alloy Designation System) for wrought aluminium alloys. (X) indicates that only a fraction of the AA8xxx alloys are heat-treatable (AAUS 1970).

Alloy system	Heat-treatable	Description
AA1xxx	-	Commercially pure Al (>99% Al)
AA2xxx	X	Al-Cu and Al-Cu-Li
AA3xxx	-	Al-Mn
AA5xxx	-	Al-Mg
AA6xxx	X	Al-Mg-Si
AA7xxx	X	Al-Mg-Zn
AA8xxx	(X)	Al-Li, Sn, Zr, B, Fe or Cr

2.2 Polycrystalline plasticity theory

The primary task of a polycrystalline plasticity theory is to formulate the relations between the macromechanical behaviour of the polycrystal and the fundamental mechanisms of single crystal deformation. Several objectives can be achieved from investigations concerned with polycrystalline plasticity. First, it allows for identification of the believed micro mechanisms that are responsible for observed macroscopic phenomena. Secondly, the increased understanding on the fundamental level may in turn provide a basis for improved predictions of the macroscopic plastic deformation.

2.2.1 Basic plasticity

The mechanical properties of a material may be represented by a stress-strain diagram. If the applied stress is less than the elastic limit, the deformation is said to be elastic. The material deforms plastically if the stress level is equal to or greater than the yield stress, and any stress level above the yield stress is referred to as the flow stress. Hence, elastic deformation is completely recoverable while plastic deformation is not recoverable upon release of stress. Only the plasticity theory is presented in this section since just the plastic part of the deformation is treated in this work.

Plastic deformation of metals can take place by use of four primary mechanisms (Verhoeven 1975): slip, twinning, grain boundary sliding and diffusional creep. In

Theoretical background

general, grain boundary sliding and diffusional creep become significant only at high temperatures but they must also be considered at very low strain rates. Twinning, on the other hand generally becomes operative at low temperatures in materials having HCP structure. However, twinning in aluminium has been observed but then at very low temperatures or very high strains (see e.g. Gray III 1988 and Werenskiold 2004). Slip is by far the most important deformation mechanism in aluminium and only this mechanism will be treated in the following.

The slip mechanism has been described by Verhoeven (1975) as the parallel movement of two adjacent regions relative to each other across some plane (or planes). The early work of Ewin and Rosenheim (1900) showed that slip takes place along well-defined crystallographic planes. Such crystallographic planes are referred to as the slip plane, while the direction of shear in the plane is called a slip direction. The combination of a slip plane and a direction in that plane is referred to as a slip system. The slip planes in FCC metals are usually those with the closest atomic packing, while the slip direction is always the closest packed direction in the slip plane. Figure 2.1 presents the atomic arrangement of the closest packed planes in a FCC metal.

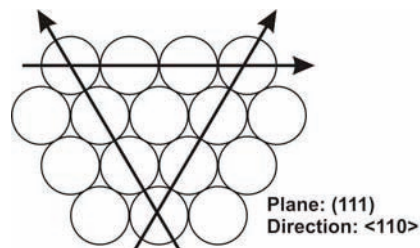


Figure 2.1 – The atomic arrangement in the plane with closest atomic packing in aluminium. The three closest packed directions are also indicated.

The FCC metals deform primarily on the close-packed octahedral {111} planes in the <110> close packed directions. In special cases non-octahedral slip in aluminium alloys has been observed on both the {110} and the {100} planes (see e.g. Perocheau and Driver 2002). However, for all practical considerations only octahedral slip is activated during deformation of aluminium at room temperature. A crystallite consists of four different {111} planes and each plane has three equivalent closest packed directions as indicated in Figure 2.1. Hence, face-centred cubic metals have a total of twelve possible slip systems which can take part in the deformation. Schmid and Boas (1935) developed

Theoretical background

a notation used to distinguish the twelve possible slip systems in an individual crystal as shown in Figure 2.2. The notation is based on a letter A-D which defines the slip plane and a number 1-6 which defines the slip direction. Table 2.2 presents the twelve possible slip systems based on the Schmid and Boas notation.

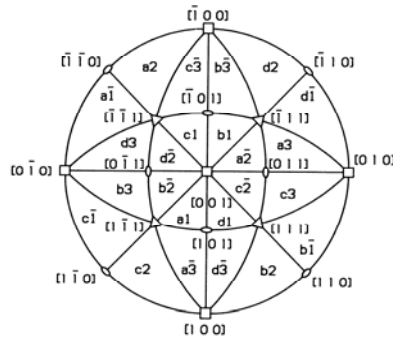


Figure 2.2 – Standard [001] stereographic projection of FCC crystals (Kahn and Huang 1995).

Table 2.2 – Schmid and Boas notation for slip systems in FCC crystals (Schmid and Boas 1935).

Slip System	Slip plane	Slip direction
A2	$(\bar{1}11)$	$[0\bar{1}1]$
A3	$(\bar{1}11)$	$[101]$
A6	$(\bar{1}11)$	$[110]$
B2	(111)	$[0\bar{1}1]$
B4	(111)	$[\bar{1}01]$
B5	(111)	$[1\bar{1}0]$
C1	$(\bar{1}\bar{1}1)$	$[011]$
C3	$(\bar{1}\bar{1}1)$	$[101]$
C5	$(\bar{1}\bar{1}1)$	$[1\bar{1}0]$
D1	$(1\bar{1}1)$	$[011]$
D4	$(1\bar{1}1)$	$[\bar{1}01]$
D6	$(1\bar{1}1)$	$[110]$

Theoretical background

Theoretically, any of the 12 different $\{111\}\langle 110\rangle$ slip systems can be activated during deformation but the strain is often distributed among a limited number of these slip systems. The required number of slip systems activated has been discussed heavily since the introduction of the well known Sachs (Sachs 1928) and Taylor (Taylor 1938) models in the first half of last century. The process of slip activation during deformation is still under debate and the arguments for selection of slip systems will most likely be debated for a long time.

Moreover, from a crystal plasticity point of view, the probability for slip is the same for all slip systems with equal Schmid value. This means that activation of slip system A2 (Schmid and Boas notation) on a given A-plane within a particular grain means that the same slip system also should be activated on all other parallel A-planes within that grain. The slip (deformation) should in other words be homogeneously distributed among all A2 slip systems in that particular grain. However, this is normally not the case for aluminium alloys, and the slip tends to localise to small regions separated by regions without or very limited plastic deformation (see e.g. Honeycombe 1984 and Yau and Wagoner 1993). It is this localisation of slip which makes the slip traces visible at the specimen surface, i.e. the traces are an area with localised deformation. The reason for this localisation is not fully understood, but it is believed that the origin lies within the material itself. The condition for initiating localised deformation after any amount of pre-straining is usually related to a situation taking place in the material where the next increment of strain-induced hardening is cancelled out by an accompanying strain-induced softening. Then further straining tends to concentrate in the locations where resistance to continued deformation is first lost, i.e. the deformation is localised to a limited number of slip planes (Backofen 1972, Sørensen 1997). As a consequence, the microstructure often develop slip traces when the dislocations move along activated slip planes and intersect the specimen surface. Hence, the activation of slip plane, and by that the activation of slip systems, can be investigated by studying the appearance of the slip traces.

Predictions of the mechanical properties, i.e. how the material deforms, is often performed by computerised modelling in order to simulate the production of new components. The deformation behaviour is for simplicity often with satisfying results

Theoretical background

described by continuum mechanics (see e.g. Liu et al. 1997 and Wilkinson et al. 1997) even though the material deforms by slip, which clearly is a non-continuous deformation process (Verhoeven 1975 and Honeycombe 1984).

2.2.2 Schmid's law – geometry of slip

Slip will occur upon the $\{111\}$ planes when a single crystal of an FCC metal is deformed in tension. The force causing slip is not the tensile force but rather the decomposed shear force in one of the $\{111\}$ planes along one of the slip directions. Hence, the tensile force must be decomposed into the individual slip systems. This was first postulated by Schmid in 1924, where he states that yield would begin on a slip system when the resolved shear stress on this system reached a critical value, independent of the axial tensile stress and other normal stresses on the lattice plane. This statement is now commonly referred to as Schmid's law.

Consider a crystal of cross-sectional area A having a tensile load L imposed giving a tensile stress σ_t . Figure 2.3 shows this crystal and its slip plane in which OX is the slip direction and λ is the angle between the axis and the slip direction. The tensile axis makes an angle χ with the slip plane, so that the area of the slip plane is $A/\sin\chi$. Therefore, the tensile stress on the slip plane is

$$\frac{L}{A} \sin \chi = \sigma_t \sin \chi \quad (2)$$

and the shear stress on the slip plane resolved in the slip direction is

$$\tau = \sigma_t \sin \chi \cdot \cos \lambda = \sigma_t \cos \phi \cdot \cos \lambda = \sigma_t \cdot m \quad (3)$$

where ϕ is the angle between the tension axis and the normal ON of the slip plane, and σ_t is the tensile stress (Honeycombe 1984). The geometrical part of this equation is often referred to as the Schmid value, m . The general Schmid tensor of the slip system s is computed in the crystal coordinate system using

$$m_{ij}^s = \frac{1}{2} (s_i^s n_j^s + s_j^s n_i^s) \quad (4)$$

Theoretical background

where \mathbf{n}^s is the slip plane normal and the \mathbf{s}^s is the unit vector in the Burgers vector (slip) direction of slip system s .

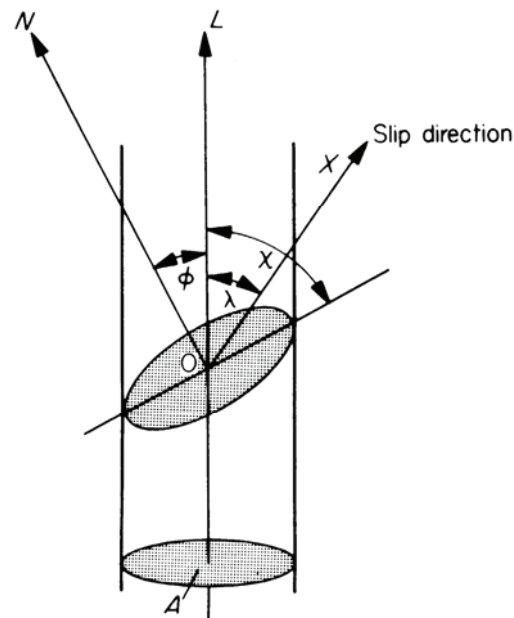


Figure 2.3 – Schematic illustration of the resolved shear stress on a slip system during simple tension deformation (Honeycombe 1984).

It is also worth noticing that in some special circumstances the equation above will become zero. τ becomes zero if the tension axis is normal to the slip plane ($\lambda=90^\circ$), or if the tension axis is parallel to the slip plane ($\chi=0^\circ$). Deformation by slip will not be expected in these two extreme orientations. The reason is that the shear stress in the slip direction would be zero. On the other hand, the maximum shear stress is obtained when $m=0.5$, that is when ϕ and λ are both 45° , hence $\tau_{\max}=0.5\sigma_t$. Here, it is evident that single crystals will give rise to a plastically anisotropic behaviour due to a discrete distribution of slip systems.

Furthermore, the Schmid value of the individual slip systems is controlled by the orientation of the crystallite in relation to the tensile stress. The primary slip systems (highest Schmid value) of the different standard stereographic triangles are included in the standard stereographic projection presented in Figure 2.2. For some orientations, the

Theoretical background

Schmid values of several slip systems are equivalent, and these crystallites are assumed to have more than one operative slip system (Figure 2.4).

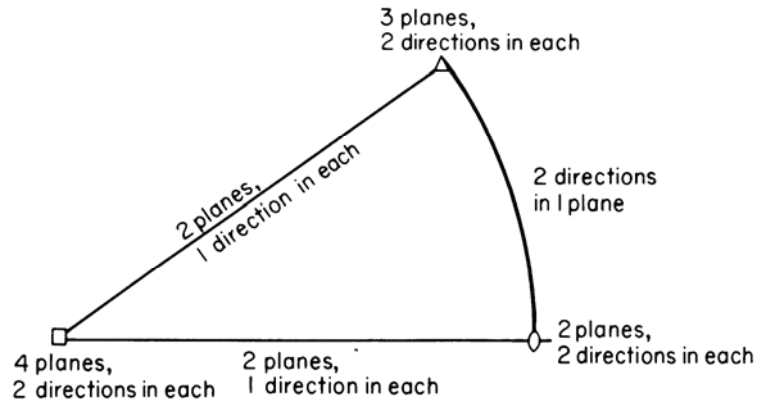


Figure 2.4 – Number of equivalent slip systems at special orientations in the inverse pole figure. The squares, triangles and circles indicate eight, six and four equivalent slip systems respectively (Honeycombe 1984).

2.2.3 Rotation of the crystal lattice

A very important phenomenon in plastic deformation is that the crystal lattice will rotate relative to a fixed coordinate frame (e.g. the tensile machine and the loading axis which are fixed to the ground) during significant plastic deformations. To illustrate lattice rotation, simple tension of a single crystal will be presented as shown in Figure 2.5. If the grips of the tensile machine could move freely without friction in the lateral direction, the specimen would deform as shown in Figure 2.5 (b). However, the tensile grips allow no lateral movement of the specimen ends. As a consequence, the lack of motion in the lateral direction must be accomplished by a simple rotation of the lattice, i.e. the slip direction s would rotate toward the tensile axis. Close to the grips some additional bending and appurtenant distortion has to be included in order to obey the constraint enforced from the fixed grips.

Theoretical background

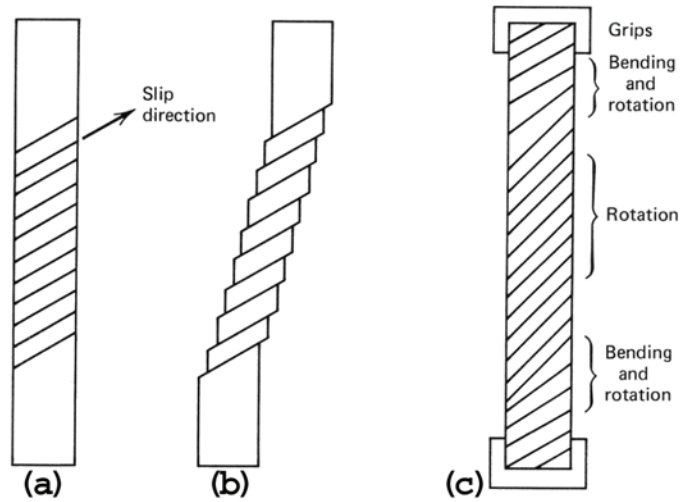


Figure 2.5 – Physical changes in a single crystal deformed in a tensile machine. (a) Undeformed single crystal. (b) Deformed single crystal without friction in the lateral direction. (c) The lateral movement accomplished by simple rotation of the lattice in the centre and combined rotation and bending near the grips (Verhoeven 1975).

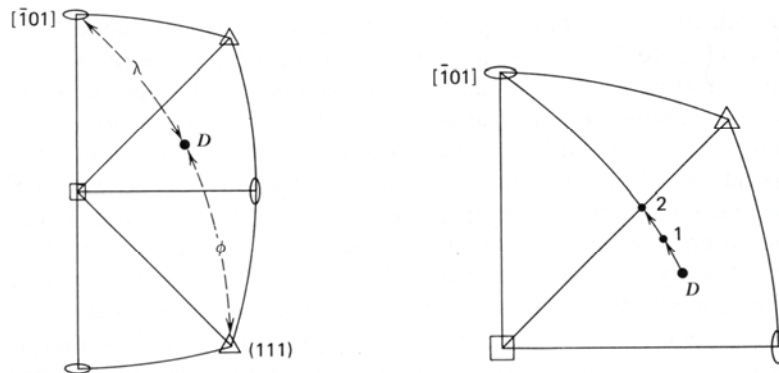


Figure 2.6 – Representation on a stereographic projection of a deformation induced crystal rotation (Verhoeven 1975).

The slip direction of a single crystal with initial orientation D will during large tensile plastic deformation rotate toward the tensile axis so that $\lambda < \lambda_0$, where λ_0 and λ are the initial and current angle between the tensile axis and slip direction respectively. This rotation can be represented by moving the point D toward the $[\bar{1}01]$ direction along the great circle through D and $[\bar{1}01]$ as shown in Figure 2.6. At any instant of the deformation, using the current relative orientation of the loading axis (deformation

Theoretical background

direction) to the crystal lattice, one point can be found in the standard triangle that represents the loading axis. Therefore the loading axis during deformation can be traced by a series of points in this triangle as shown in the same figure. After a rotation from D to point 2, the specimen has become orientated so that two slip systems have the same maximum Schmid value. Normally at this point, deformation proceeds on both slip systems simultaneously to produce duplex or multiple slip. The additional slip system is often referred to as the conjugate slip system. The duplex slip causes further movement of the specimen axis along the $[001]-[\bar{1}11]$ boundary toward the $[\bar{1}12]$ pole which is the mid way between the two operative slip directions. When the stress axis reaches this orientation, it is assumed that this orientation is maintained until localised necking take place, followed by fracture.

If the movement of individual dislocations are omitted, slip on a slip system can be modelled by homogeneous shear (\mathbf{F}^P) as illustrated in Figure 2.7. The shape change occurring during shear of the considered volume element is generally accompanied by a rigid rotation (\mathbf{F}^*). This rotation changes the orientation of the crystal axes whereas slip (by itself) does not. In fact both slip and rotation take place simultaneously ($\mathbf{F} = \mathbf{F}^* \cdot \mathbf{F}^P$), hence the volume element changes its shape and rotates at the same time as shown in Figure 2.7 (Kahn and Huang 1995).

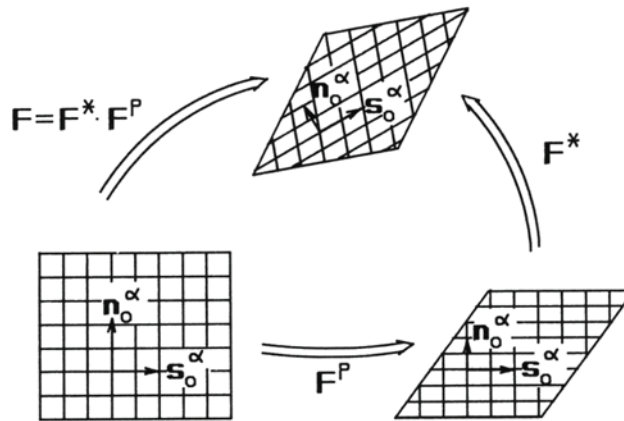


Figure 2.7 – Illustration of the kinematics of single-crystal deformation. The mutually perpendicular grids represent the crystal lattice. \mathbf{s}_0^α and \mathbf{n}_0^α are the initial unit vector in the slip direction and the initial unit normal vector to the slip plane of the α slip system, respectively (Kahn and Huang 1995).

Theoretical background

Plastic deformation of single crystals often proceeds by slip in only one slip system as illustrated in Figure 2.7. However, in polycrystalline material (Figure 2.8) each crystallite is surrounded by its neighbours. This requires continuity of plastic deformation across the grain boundaries. The enforced shape change introduces usually slip (and thus rotation) on several slip systems simultaneously. Therefore, the lattice rotations in the polycrystalline metal are not uniform within each individual grain. The orientation rotation behaviour of each grain during deformation is not easy to interpret. It has been found that the rotations of the crystallites show a very broad spread, which may be attributed to the individual environment of each crystallite. However, the average rotation paths of the grains are usually quite well described by the Taylor model (see e.g. Bunge and Fuchs 1969, Han et al. 2003 and Winther et al. 2004). This means that grains having an initial orientation with a $[100]$ or $[111]$ parallel to the deformation direction (DD) are relatively stable during deformation, while grains having a $[110]$ parallel to the DD tend to rotate towards a more stable orientation.

It has also been shown that different parts of a crystallite may rotate in different directions such that they become distinguishable crystallites themselves (see e.g. Wert 2002). In this sense a polycrystalline material is composed of crystallites, each of which has its particular crystal orientation \mathbf{g} and each of which rotates in its own way as is illustrated schematically in Figure 2.8. The rotations lead to texture changes, i.e. the development of deformation textures. This process has been studied in great detail (see e.g. Dillamore and Roberts 1965). Texture changes resulting from plastic deformation are often accompanied by changes of the plastic properties. Hence, the orientation changes of the crystallites must be taken into account in any comprehensive theory of polycrystal plasticity. This can be done particularly on two different length scales (Bunge and Nielsen 1997):

Theoretical background

1. Small single-crystalline volume elements (Figure 2.8 a) which are characterised by their crystallographic orientation \mathbf{g} and the rotation $\Delta\mathbf{g}$ after a small deformation step.
2. Big polycrystalline volume elements (Figure 2.8 b) which are characterised by their orientation distribution function $f(\mathbf{g})$, i.e. the texture, and the texture change $\Delta f(\mathbf{g})$ after a small deformation step. In this latter case, the total texture change $\Delta f(\mathbf{g})$ may be divided into two parts:
 - i. An average rotation $\Delta\bar{\mathbf{g}}$ as indicated by the big circular arrow in Figure 2.8 (b). This part can be interpreted qualitatively as the rotation of some common reference axis system characteristic of the whole volume element (b).
 - ii. A "spreading" of the individual crystal orientations away from this common (rotated) reference system indicated by the small individual arrows in volume element (b).

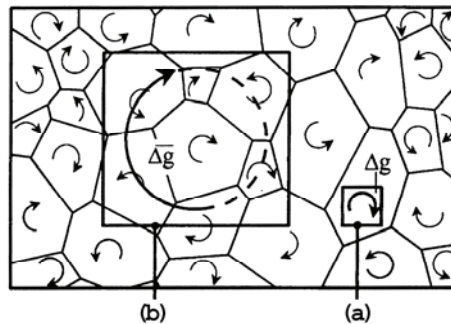


Figure 2.8 – Schematic illustration of lattice rotation in a polycrystalline material. (a) Small single-crystalline volume element with unique lattice rotation ($\Delta\mathbf{g}$). (b) Large polycrystalline volume element with individual rotations ($\Delta\mathbf{g}$) and the average rotation ($\Delta\bar{\mathbf{g}}$) (Bunge and Nielsen 1997).

Crystal rotations can be modelled using different assumptions for the individual single crystalline volume elements (Figure 2.8 a) as well as for the interaction of the differently oriented crystallites (inside the volume element of Figure 2.8 b). The basis of some classical crystal plasticity models will be presented in the following.

Theoretical background

2.2.4 The Sachs model

The oldest plasticity model is the one proposed by Sachs in 1928 and later proposed by Cox and Sopwith (1937) and Kochendörfer and Swanson (1960) in a slightly different form. Sachs assumed that each grain only deforms by one activated slip system, namely that with the highest resolved shear stress. He further assumed that a polycrystal is an aggregate of independently deforming single crystals, and the principle axes of stress are the same in all grains of a homogeneously stressed polycrystal. Hence, the Sachs model is based on the Schmid value of each crystallite. Please notice, according to the Sachs model, single slip in a grain leads to a misfit of its shape with respect to the surroundings. It would lead to large interaction stresses between grains and it would quickly lead to material separation at the grain boundaries. This is schematically illustrated in Figure 2.9.

However, the arguments used in favour of the Sachs model are nevertheless based on metallographic observations. A single set of slip traces is often observed on the surface of deformed polycrystalline materials, except near grain boundaries (see e.g. Zankl 1963, Schwink 1965 and Schwink and Vorbrugg 1967). There are a number of objections to such observations (Kocks 1970). Firstly, the surface grains are not under the full constraint of the compatibility conditions caused by the interaction of grains across grain boundaries. Secondly, one observed slip trace can correspond to several independent slip systems. Thirdly, even under the condition of several slip systems activated, it is rarely expected that an equal amount of slip on all activated slip systems occurs. In general, it seems that the Sachs model is quite satisfactory at the very beginning of plastic yielding of crystal aggregates. However, for higher plastic strains, the Taylor model is assumed to give a better description of reality.

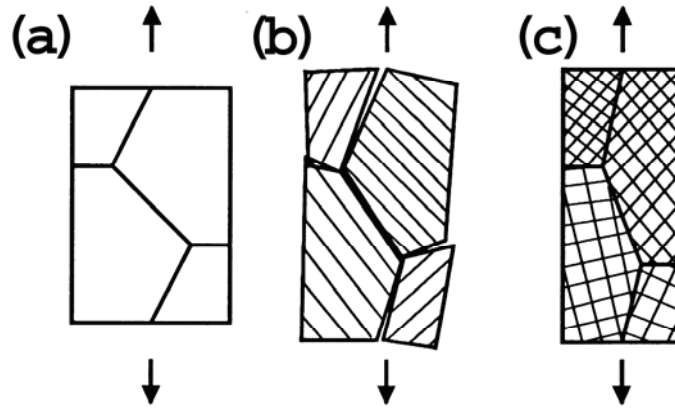


Figure 2.9 – Tension of a polycrystal (a) Before plastic deformation. (b) Large plastic deformation according to the Sachs model (single slip). (c) Large plastic deformation according to the Taylor model (polyslip) (Gambin 2001).

2.2.5 The Taylor model

The Taylor model (Taylor 1938) states that the plastic strain of all crystallites within a polycrystal is the same and hence equal to the macroscopic plastic strain. The idea behind the Taylor model can also be formulated as follows: The neighbourhood of a grain embedded in a polycrystalline material introduces very strong constraints on the individual grains; it must have exactly the same strain as its surroundings; no misfit strains are allowed. The elastic strains are also neglected. The original version of the Taylor model is normally referred to as the Full Constraint (FC) Taylor model, as it maximises the influence of the geometrical constraints (Van Houtte et al. 2005).

In order to develop this model, Taylor made use of a local constitutive law based on crystal plasticity which establishes the relation between the local stress, strain and rigid body rotation inside a RVE (representative volume element). The local constitutive law consists of a kinematical equation and an energetic assumption.

The kinematical equation relates the microscopic velocity gradient l_{ij} which describes the local deformation (per unit time) with the slip rates of all active slip systems:

$$l_{ij} = \dot{\Omega}_{ij}^L + \sum_{s=1}^{12} b_i^s n_j^s \dot{\gamma}^s \quad (5)$$

Theoretical background

In this equation; $\dot{\Omega}_{ij}^L$ is the spin of the crystal lattice, $\dot{\gamma}^s$ is the shear slip rate of slip system s , b_i^s is the slip direction of slip system s , and n_j^s is the normal of the slip plane of this slip system. The kinematical equation is based on the assumption that the macroscopic velocity gradient tensor L_{ij} is known and equal to the microscopic velocity gradient:

$$L_{ij} = l_{ij} \quad (6)$$

The macroscopic velocity gradient for simple tension deformation is given by:

$$L_{ij} = \begin{bmatrix} 1 & 0 & 0 \\ 0 & -\frac{r}{1+r} & 0 \\ 0 & 0 & -\frac{r}{1+r} \end{bmatrix} \cdot \dot{\epsilon} \quad (7)$$

where $\dot{\epsilon}$ is the strain rate and r is the r -value or Lankford coefficient ($r = \frac{\epsilon_w}{\epsilon_t}$). Further,

the kinematical equation also states that the slip rates, $\dot{\gamma}^s$ of all slip systems must be calculated and the combination of all slip processes active at a given moment determines what happens to the crystal. Hence, the symmetric part of l_{ij} becomes the strain rate tensor:

$$d_{ij} = \frac{1}{2} \sum_{s=1}^{12} (b_i^s n_j^s + b_j^s n_i^s) \dot{\gamma}^s \quad (8)$$

This equation gives a set of five independent equations with twelve unknown $\dot{\gamma}^s$. Hence, an additional set of requirements is needed in order to solve the equation.

The energetic assumption of Taylor fulfils this requirement. This assumption suggests that the slip systems are chosen so that the internally dissipated friction work per unit time \dot{W} is minimised:

Theoretical background

$$\dot{W} = \sum_{s=1}^{12} \tau_c^s \cdot |\dot{\gamma}^s| = \min \quad (9)$$

where τ_c^s is the critical resolved shear stress on slip system s .

A slip system is activated when the shear stress, τ^s reaches the critical value, τ_c^s . This requirement gives a stress relation when considering the active slip systems:

$$\frac{1}{2} \sum_{s=1}^{12} (b_i^s n_j^s + b_j^s n_i^s) \sigma'_{ij} = \tau_c^s \quad (10)$$

from which the deviatoric stress, σ'_{ij} in each grain can be obtained. However, no unique solution is obtained for the stress when the critical resolved shear stress is set to be identical in all slip systems (common assumption for FCC materials). The equation will give several equal solutions of five non-zero $\dot{\gamma}^s$ -values all giving a \dot{W} minimum (five activated slip systems). This problem is often referred to as the Taylor ambiguity, and there exist several different methods of solving this ambiguity. The simplest method is to simply pick one of the solutions by random.

For this approach even to be viable, each of the individual crystals must be able to accommodate an arbitrary deformation, requiring five independent slip systems. While the Taylor assumption is reasonable for materials comprising crystals with many slip systems of comparable strength, using the model in other situations can lead to prediction of excessively high stresses, incorrect texture components, or both (Wenk and Van Houtte 2004).

The Taylor FC model offers a solution for the strain rates and stresses in every grain of a polycrystal used during a simulation. If, considering such a solution for a grain with a particular lattice orientation, it can hardly be interpreted as the stress occurring in a grain of a real polycrystal with the same lattice orientation. Indeed a real grain has boundaries with other grains, each with particular lattice orientations. As a result, the solution offered by the FC model will not achieve stress equilibrium at these grain boundaries (Van Houtte et al. 2005).

Theoretical background

It has been argued that the Taylor FC model is too strict and the results could have been improved by somewhat “relaxing” the geometrical constraints. The idea of relaxation was conceived approximately 20 years ago (see e.g. Honneff and Mecking 1981, Kocks and Chandra 1982 and Van Houtte 1982) and was based on the observation that grains tend to become flattened and elongated during rolling. The misfit caused by a difference between for example l_{13} and L_{13} could perhaps be tolerated, and such a relaxation is the basis behind the relaxed constraint (RC) Taylor model. Relaxation of the longitudinal shear (l_{13}) is often referred to as the “lath” type Taylor RC model. Four slip systems would be active according to this model. The “pancake” type model also adopts this relaxation, but this model also relaxes the transverse shear (l_{23}), hence only three slip systems will be activated. Figure 2.10 presents a schematic illustration of the relaxation in the lath and pancake type Taylor RC model.

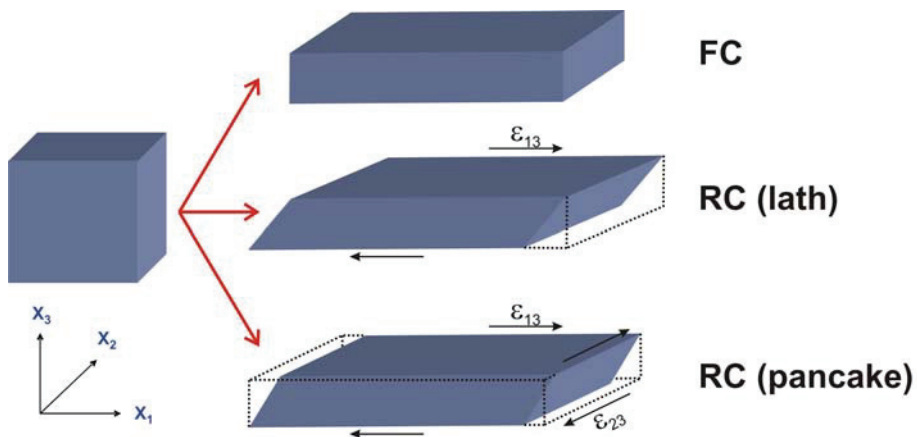


Figure 2.10 – Schematic illustration of the full constraint (FC) and the relaxation in the lath and pancake type relaxed constraint (RC) Taylor models.

2.2.6 The Self-Consistent model

In the Taylor model, the strain compatibility is achieved at the expense of the stress continuity and equilibrium at the grain boundaries. In the Sachs model, on the other hand, the stress continuity and equilibrium are chosen over the strain compatibility. Neither of these models gives a satisfying description of the material during deformation. However, it is possible to satisfy both strain compatibility and stress equilibrium for simplified grain shapes by employing a self-consistent model. These

Theoretical background

models try to obtain better average stresses and strains than the Taylor and the Sachs models. The self-consistent models may be regarded as generalised RC models, in which the relaxation is determined on the basis of a mathematical model for the interaction between a grain and its surroundings. The latter is then treated as a homogenous medium. Self-consistent models are much more complicated than the Taylor models (relaxed or not). A more comprehensive review of the self-consistent model may be found in e.g. Lebensohn and Tomé (1993).

2.2.7 Advanced polycrystalline plasticity models

Neither of the models presented above provide satisfying deformation texture predictions, especially not if quantitative methods are used for the comparison with experimental results. One reason could be that the local interaction between grains is insufficiently taken into account. Therefore, some new and more advanced plasticity models have been proposed. The Crystal Plasticity Finite Element Method (CPFEM) model (Kalidindi et al. 1992, Bate 1999, Mika and Dawson 1999) is a more recent plasticity model. The CPFEM model is based on finite element mesh placed over the microstructure (each element represents a single grain, or part of a single grain), and the crystallographic texture is represented by statistical distribution of orientations representing a few thousand grains. The orientations are chosen such that they offer a suitable representation of a macroscopic RVE, i.e. a volume element large enough to have the average properties of the polycrystalline material. This means that both lattice orientations, locations of grains with given orientations, grain shapes and sizes and orientation of grain boundaries are all chosen at random from a real microstructure in a representative way. Usually all this is done in a rather rudimentary way and much progress can still be made in this field, for example by incorporating topological data obtained by using orientation imaging microscopy. However, the CPFEM model requires two orders of magnitude more calculation time than other advanced polycrystalline plasticity models. Therefore, this model is practically impossible to use for industrial forming simulations (Van Houtte et al. 2005).

However, newer polycrystalline plasticity models which are much faster than the CPFEM models but still reach a comparable quantitative accuracy have been developed. In these so-called “multi-grain” models, the Taylor condition is no longer enforced on

Theoretical background

each individual grain; it is only required that the average deformation of all grains belonging to a cluster is equal to the macroscopic deformation. The Taylor condition is then maintained at the boundary of the cluster. It is clear that this boundary is artificial, since in a real microstructure this boundary usually does not have a different character than the grain boundaries inside the cluster. It is also clear that the choice of N , the number of grains in the cluster, size and shape of the cluster are very important. It is possible to obtain a FC Taylor model ($N=1$), Sachs model ($N=\text{very large}$) and anything in between. The most widely known multi-grain models are the LAMEL model (Van Houtte et al. 2002) and its new “brother”, the advanced LAMEL (ALMAEL) model (Van Houtte et al. 2005) both with $N=2$, together with the Grain Inter-Action (GIA) model (Crumbach et al. 2001 and Engler et al. 2005) having $N=8$. Figure 2.11 presents an illustration of the two most common types of grain clusters in the LAMEL model as well as the grain cluster arrangement used in the GIA model. It is much more complicated to investigate the selection of activated slip systems for these more advanced models. The number of activated slip systems in the individual grains is dynamic and depends on the orientations’ composition within the cluster. It is therefore difficult to determine the number of activated slip systems for the individual grains (orientations) and it is reasonable to assume that the number of activated slip systems for one orientation can vary from one to five.

It should be noted that LAMEL and ALAMEL model simulations do not need significantly more calculation time than a standard FC Taylor calculation. The GIA model does need more time, but not so much as the CPFEM model (Van Houtte et al. 2005).

It has been shown that these new and more advanced polycrystalline plasticity models give far better predictions of deformation texture than the more standard models presented above (see e.g. Li and Van Houtte 2002 and Van Houtte et al. 2005).

Theoretical background

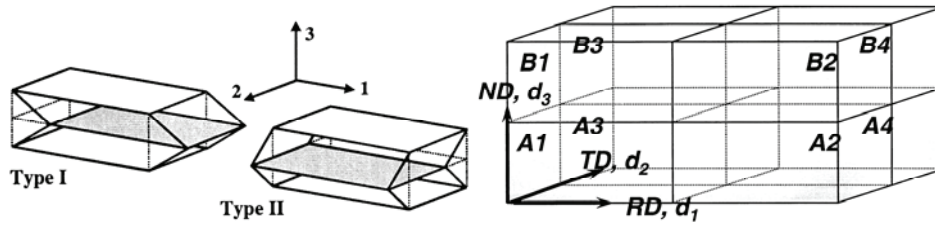


Figure 2.11 – Schematic illustration of the two most common types of grain clusters in the LAMEL model (left, Van Houtte et al. 2005) as well as the grain cluster arrangement used for the eight grains in the GIA model (right, Crumbach et al. 2004).

2.3 Texture

Most polycrystalline materials contain grains with crystallographic orientations that are not randomly distributed but instead are clustered to some degree around a particular orientation or set of orientations. Materials in which the grains are oriented non-randomly are said to have a preferred orientation or texture. The mechanical and thermal history of a specimen determines the nature of the texture that is developed. This section is concerned with the basic features of texture and texture measurements. Texture development in aluminium alloys and the effect of crystallographic texture are also treated to some extent.

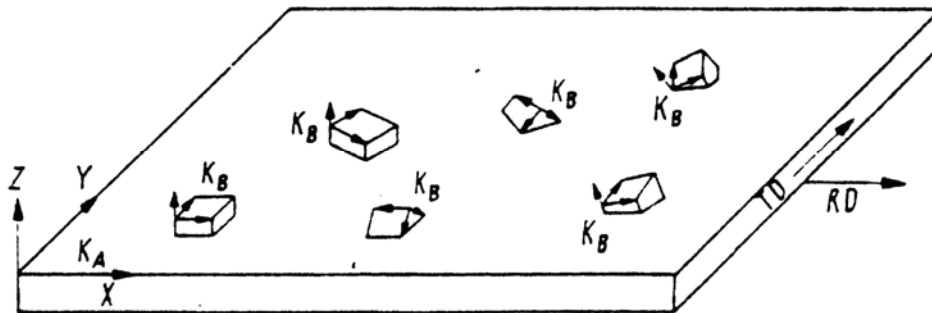


Figure 2.12 – The sample fixed coordinate system K_A and the crystal fixed coordinate system K_B in a sheet (Bunge 1983).

Theoretical background

2.3.1 Orientation of individual crystallites

The texture of a polycrystalline material is often defined as the orientation distribution function (ODF) of all the crystallites. A sample coordinate system K_A is defined in order to describe the orientation of the individual crystallites. In the same way, each crystallite is given a crystal coordinate system K_B , and the rotation \mathbf{g} (crystallographic orientation) which is specified with respect to the sample-fixed coordinate system K_A .

$$K_B = \mathbf{g} \cdot K_A \quad (11)$$

The crystal coordinate system may conveniently be adapted to crystal symmetry, e.g. the cubic axes $[100]$, $[010]$, $[001]$ of the unit cell. Also the sample coordinate system will usually be adapted to sample symmetry, e.g. RD (ED in extruded profiles), TD, ND in sheet metals as shown in Figure 2.12.

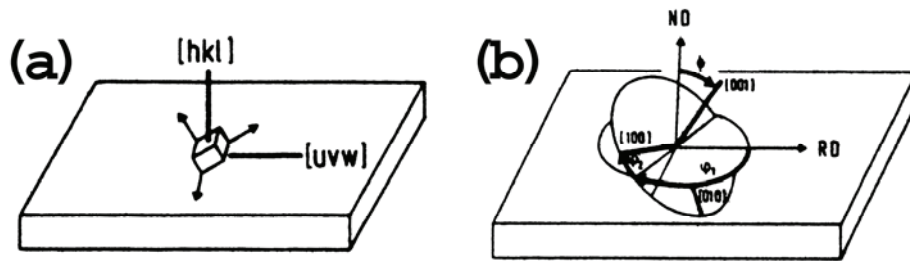


Figure 2.13 – Two representations of the orientation \mathbf{g} (a) Miller indices $(hkl)[uvw]$ (b) Euler angles $\{\varphi_1, \Phi, \varphi_2\}$ (Bunge 1983)

The two most common ways to represent the orientation \mathbf{g} which describes the crystallographic orientation of the individual crystallites are Miller indices and Euler angles as shown in Figure 2.13. The Miller indices represent the orientation given by the plane (hkl) parallel to the rolling plane (extrusion plane in extruded profiles) and the direction $[uvw]$ parallel to the rolling (extrusion) direction:

$$\mathbf{g} = (hkl)[uvw] \quad (12)$$

Euler angles are by far the most widely used representation of crystallographic orientations. Here the orientation is described by a set of three dependent Euler angles. The Euler angles are obtained by initially putting the crystal coordinate system parallel

Theoretical background

to K_A (the red orientation in Figure 2.14) and then rotating the variable coordinate system until it reaches the orientation \mathbf{g} (the green orientation in Figure 2.14). First, the crystal is rotated about the ND-axis through the angle φ_1 . Then it is rotated about the new RD'-axis through the angle Φ . Finally the variable frame is again rotated about the new ND''-axis (001) through the angle φ_2 . The definition of the Euler angles is presented in Figure 2.14. This representation is often referred to as Bunge notation:

$$\mathbf{g} = \{\varphi_1, \Phi, \varphi_2\} \quad (13)$$

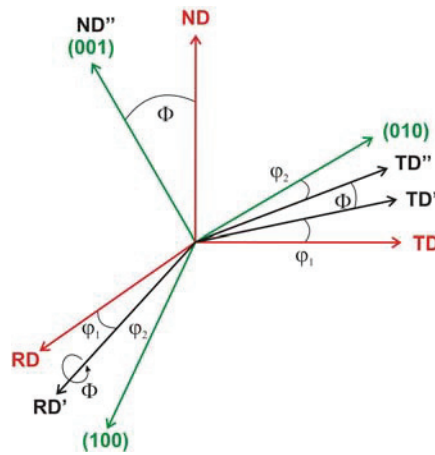


Figure 2.14 – Definition of the Euler angles by use of the Bunge notation (after Engler 2004).

2.3.2 Orientation distribution

In polycrystalline materials, crystallites of different shape, size and orientation are generally present. It can thus also occur that regions of different orientation are not separated from each other by clearly defined grain boundaries. On the contrary, continuous orientation changes are often observed through the microstructure. Variations within the specimen make it necessary to specify the orientation \mathbf{g} of each position through the specimen volume in order to completely describe the crystal orientation of a polycrystalline material. Such a representation of the crystal orientation is very complicated, and its mathematical treatment so advanced that it is not practically applicable. However, a good approximation is obtained by considering only the orientations and not the position coordinates of the individual crystallites within a

Theoretical background

volume element of the sample. If the totality of all volume elements in the sample which possess the orientation $d\mathbf{g}$ is denoted $d\mathbf{V}$, and the total sample volume is denoted \mathbf{V} , then an orientation distribution function can be defined by (Bunge 1983):

$$\frac{d\mathbf{V}}{\mathbf{V}} = f(\mathbf{g})d\mathbf{g} \quad (14)$$

This is the orientation distribution of the volume and $f(\mathbf{g})$ the orientation distribution function which is a description of the crystallographic texture of the material. A material without any crystallographic texture has $f(\mathbf{g})=1$. The crystallographic texture of a material is often presented by an orientation distribution function (ODF) plot but also different kinds of pole figures are widely used to represent the texture. The orientation distribution function of a material can, for example, be calculated from the EBSD measurements obtained in the SEM.

2.3.3 Electron backscatter diffraction (EBSD)

Electron backscatter diffraction (EBSD) has become a common technique used in the characterisation of polycrystalline materials. EBSD in the scanning electron microscope (SEM) is a technique that can provide a vast amount of information about crystalline materials. Orientation imaging mapping (OIM) performed on a grain-by-grain basis provides information about the crystallographic orientation of the individual grains in a material (microtexture) and the relation of these orientations to significant microstructural features (Randle and Engler 2000). Since the very beginning of this technique has the Norwegian University of Science and Technology been a pioneer within EBSD (Hjelen 1990). In fact, the 3rd commercial EBSD system available was in 1985 installed at SINTEF/Norwegian Institute of Technology (NTH) by David Dingley (1984), another pioneer within EBSD. (NTH is now known as the Norwegian University of Science and Technology, NTNU.) In the very beginning EBSD measurements were used to manually determine the crystallographic orientation of individual grains. Hjelen et al. (1991) used this technique to study the origin of recrystallization textures in aluminium. The technique has since then been used as a powerful tool within both the metallurgical and geological communities. The crystallographic aspects of plastic deformation together with the recrystallization behaviour of aluminium alloys have been

Theoretical background

the main focus at NTNU. This work was initiated by Hjelen (1990) and has since then been continued by several PhD works at NTNU. Skjervold (1993) used the technique to investigate the orientation gradient evolution in grains during deformation. This was the first attempt to investigate the microstructure evolution during deformation. In more recent times investigations of deformation behaviour and microstructure evolution of large strains have become possible. The deformation and softening behaviour of heavily cold rolled AA3xxx series alloys have been investigated by Sjølstad (2003) and Tangen (2004). They used the technique to study both the deformation structure and the recrystallized microstructure after annealing. The average grain size and the grain size distribution were also determined by use of EBSD techniques (Tangen et al. 2002). Material processed by severe plastic deformation (SPD) develops very small grain sizes ($\sim 4\mu\text{m}$) (Iwahashi et al. 1997), and are therefore very difficult to characterise by EBSD. Also this problem has been overcome by using field emission scanning electron microscopes with improved spatial resolution (Tangen et al. 2003). Aluminium alloys deformed by Equal channel angular pressing (ECAP) has been characterised by Werenskiold (2004), and the EBSD technique made it possible to perform a detailed study of the deformation mechanisms operating in the ECAP process. At NTNU there has also been considerable interest given to characterisation of the microstructure and through-thickness variations of extruded aluminium profiles, and EBSD has also been used for this purpose (see e.g. Ryen 2003, Fjeldbo et al. 2005 and Hallem 2005). The state-of-the-art EBSD work performed at NTNU has led to a continuous improvement of this powerful technique.

In-situ EBSD applications have been a new field of great interest for the last few years. Also here, the SEM laboratory at NTNU has been a pioneer with regard to development and application of new experimental techniques. The work by Kobberrød et al. (1998) was the initiation of in-situ EBSD investigations in SEM. Kobberrød et al. performed heating experiments where they studied the grain boundary migration in aluminium. Subsequent heating experiments combined with EBSD investigations have been performed to study the recrystallization behaviour of aluminium alloys (see e.g. Tangen et al. 2001, Karlsen et al. 2004 and Korsnes et al. 2004). In the last decade, some in-situ deformation investigations have been performed in order to study the rotation and deformation behaviour of the individual grains within a polycrystalline material (see e.g.

Theoretical background

Cizek et al. 1996, Tong et al. 1997, Tatschl and Kolednik 2003, Poulsen et al. 2003 and Han et al. 2003). For the last couple of years there has been major progress in this type of work at NTNU.

The EBSD technique can also be used for identification of micrometer or submicrometer crystalline phases through determination of the characteristic crystallographic parameters such as crystal plane spacing, angles between planes, and crystal symmetry elements (Schwartz et al. 2000). This is especially important for characterisation of geological materials (see e.g. Moen et al. 2004 and Leinum et al. 2004).

2.3.4 EBSD measurements

EBSD patterns are obtained in the SEM by illuminating a highly tilted specimen with a stationary electron beam. The electrons will be subjected to scattering in all directions when the electron beam enters a crystalline sample. Some of the electrons will have an angle of incidence with the different atomic planes that fulfils the Bragg law:

$$\lambda = 2d_{hkl} \cdot \sin \theta_B \quad (15)$$

where θ_B is the Bragg angle, λ is the electron wavelength and d_{hkl} is the interplanar spacing for the crystal plane with the Miller indices (hkl). The electrons that fulfil the Bragg law will be elastically scattered and will result in two cones as illustrated in Figure 2.15. The two diffraction cones are positioned symmetrically around the diffracting crystal plane and separated by twice the Bragg angle ($2\theta_B$). The two cones will be recorded on a two-dimensional phosphor screen as hyperbolas. However, since diffraction of the electrons through the Bragg angle is occurring in all directions, the locus of the diffracted radiation is the surface of a cone which extends about the normal of the reflecting atomic planes with half apex angle $90 - \theta_B$. Hence, the hyperbolas appear as two almost straight parallel lines on the phosphor screen. These lines are the backscattered Kikuchi lines, and each pair of these lines corresponds to the diffraction from a particular crystal plane which produces an electron backscattered pattern (EBSP) as shown in Figure 2.16. The Kikuchi lines are used to determine the crystallographic orientation of the material volume generating the EBSP. The formation of the EBSP is described in great detail by e.g. Reimer (1998) and Wells (1999).

Theoretical background

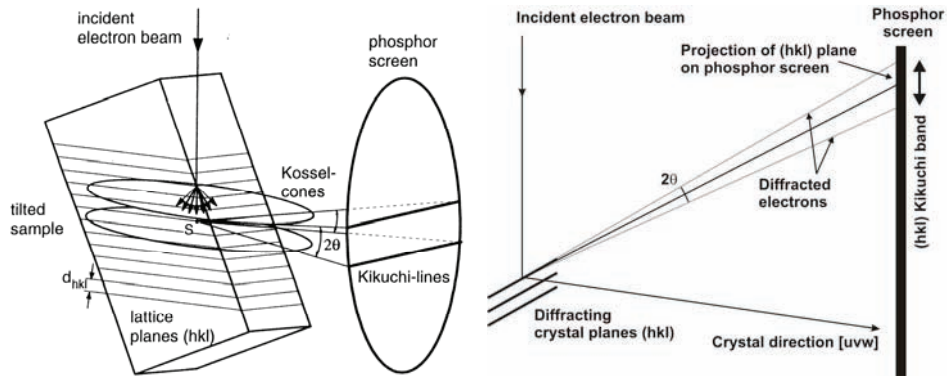


Figure 2.15 – Schematic illustration of the formation of one set of Kikuchi lines from diffraction of the electron beam with one family of lattice planes. Left 3D-view (Randle and Engler 2000) and right 2D-view.

The phosphor screen converts the electrons to light, which makes it possible to acquire the EBSP by a low-light-level CCD camera (Hjelen et al. 1993). The locations of the Kikuchi lines are identified by performing a Hough transformation of the digital images (Krieger Lassen et al. 1992). The Hough transformation

$$r = x \cdot \cos \delta + y \cdot \sin \delta \quad (16)$$

makes it possible to describe the Kikuchi lines by their distance r from the origin and the rotation δ of its normal vector as illustrated in Figure 2.16. The position of the pixel transformed from the EBSP is given by the x and y values. The Kikuchi lines are transformed to spots in the (δ, r) space (Hough transformation space) and the positions of the peaks can be determined by standard peak findings techniques. The positions of the spots correspond to the diffracting planes in the sample, and the crystal orientation can be identified when a sufficient number of planes are determined (Krieger Lassen et al. 1992).

Theoretical background

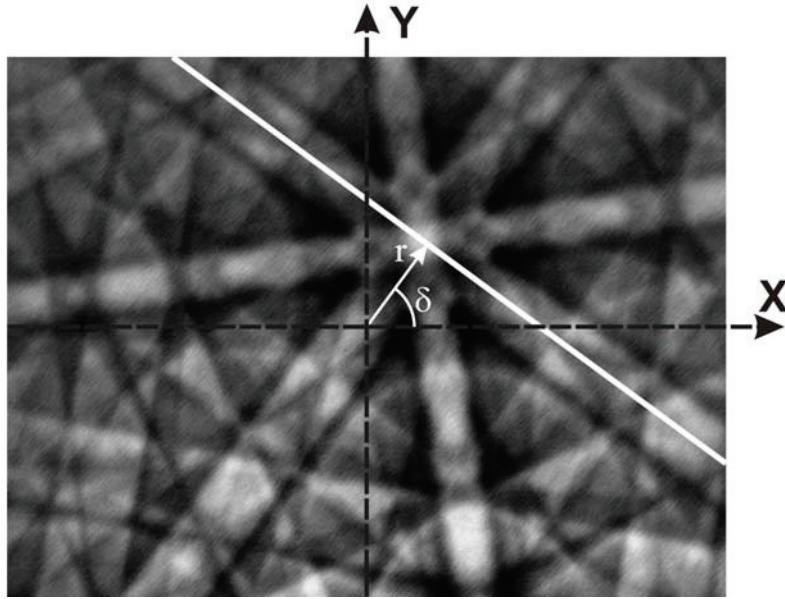


Figure 2.16 – A typical EBSP from a material with FCC structure. Each of the Kikuchi lines can be represented by the two parameters r and δ , where r is the shortest distance from the line to the origin of the x-y coordinate system and δ is the rotation of its normal vector.

The EBSP gives the crystallographic orientation of a position (pixel) on the specimen surface given by the position of the stationary electron beam. When the orientation of the given position is determined, the beam moves to a new position where a new EBSP is generated. The process is repeated several times until the entire area of interest is analysed. The distance on the specimen surface between succeeding positions are commonly referred to as the step size. The image acquisition and calculation of the crystallographic orientations are fully automated and combining state-of-the-art hardware with high tech EBSD software makes it possible to index up to 43 frames/sec (Nordif 2005).

The spatial resolution of EBSD measurements are strongly influenced by the tilt angle, working distance and acceleration voltage. Large sample tilt results in an asymmetric spatial resolution. The optimal resolution is obtained parallel to tilt axis. For a tilt angle of 70° , the resolution perpendicular to the tilt axis is roughly three times the resolution parallel to the tilt axis.

Theoretical background

The high tilt angle increases the backscatter yield as shown in Figure 2.17 where the energy distribution from samples perpendicular and tilted 70° with respect to the electron beam are compared. This is advantageous because the increased signal improves the ability to collect EBSP. It is also important to notice that most of the backscattered electrons in the tilted sample have close to initial electron beam energy. The crystallographic information in the EBSPs is produced by the electrons that have lost very little (the high energy peak) while the remainder of the distribution contribute to the overall background intensity (noise) of the EBSP (Goldstein et al. 2003).

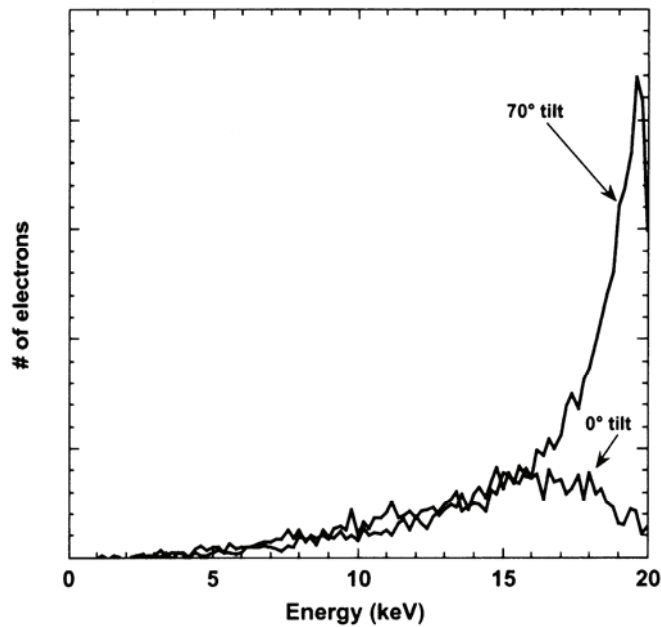


Figure 2.17 – Comparison of energy distribution from a sample perpendicular to and tilted 70° with respect to the electron beam at 20kV acceleration voltage (Goldstein et al. 2003).

Monte Carlo electron trajectory simulations have shown that the resolution of EBSD is related directly to the electron probe size. Hence, it is apparent that higher spatial resolution can be obtained from SEM instruments with field emission (FE) electron guns due to the smaller beam size, provided sufficient beam current is available. The spatial resolution is also a function of the acceleration voltage and the atomic number of the sample (Humphreys et al. 1999). Higher acceleration voltage and lower atomic number will degrade the spatial resolution. One study using an FE electron source operated at

Theoretical background

20kV found the spatial resolution in Al to be approximately 30nm (Humphreys et al. 1999).

The acquired EBSP is achieved from a volume very close to the sample surface since these electrons have lost very little energy. Hence, the size of the interaction volume depends upon the tilt angle (typical 70°), sample material and the energy of the primary electrons. Few experimental studies have been conducted to measure the depth resolution of EBSD, but it is thought to be quite small and of the order of 10-100 nm (Goldstein et al. 2003).

The absolute angular resolution of a crystallite is typically obtained with an accuracy of $\sim 2^\circ$, depending on the sample alignment and EBSD operating conditions (e.g. Humphreys 1999). However, the accuracy in determining the relative orientation between adjacent data points is of greater importance when studying orientation gradients and low angle grain boundaries. This accuracy is related to the precision in which the orientations of data points within the same crystallite can be determined. It would be expected that all the orientations are identical if diffraction patterns are obtained from a single grain within a large-grained polycrystal. However, if the crystallographic orientation is calculated based on several EBSP acquired from a single crystal or the interior of a large grain, small orientation deviations will be observed. This "orientation noise" is mainly a result of the accuracy in the pattern-solving algorithm and are beyond the direct control of the microscopist. However, it has been shown that the angular resolution is affected by the microscope operating-conditions (see e.g. Krieger Lassen 1996 and Humphreys and Brough 1999), and this effect has been measured for a FE SEM as shown in Figure 2.18. The angular resolution obtained with a FE SEM and satisfying operating conditions on aluminium are found to be in the range of $0.6-1.0^\circ$ (Humphreys 2001).

Theoretical background

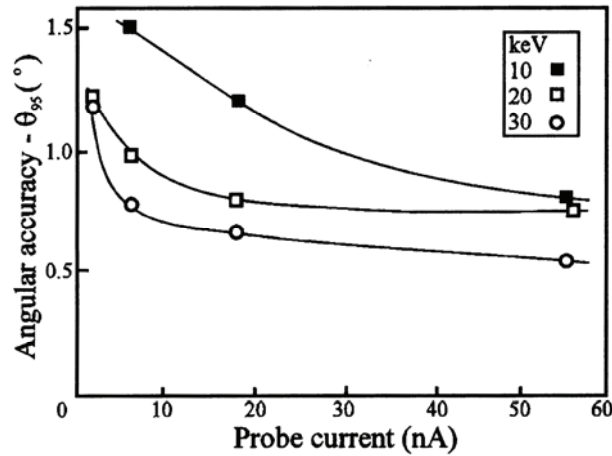


Figure 2.18 – The effect of probe current on the angular accuracy in the FE SEM for single grains in a large-grained aluminium sample (Humphreys and Brough 1999).

2.3.5 Texture components in FCC materials

Deformation texture in FCC metals and alloys are determined primarily by the deformation mode/modes and the stacking fault energy of the material. It is customary to refer to the deformation texture in materials with high stacking fault energy, like aluminium, as “pure metal textures” to distinguish them from the “alloy type textures” characteristic of materials with low stacking fault energy. The “pure metal textures” are often described by a set of four ideal texture components as shown in Table 2.3. However, the observed deformation texture is not satisfactorily described by these ideal components, but more accurately by representing the texture as a continuous tube or fibre of orientations which runs from the Brass through the S to the Copper orientation. By convention the axis of this tube is called the β -fibre and deformation textures are often only presented in the form of orientation densities along this fibre (e.g. Hirsch and Lüke 1988). A second fibre, the α -fibre, is also often used to describe the texture. This fibre extends from the Goss orientation to the Brass orientation (Humphreys and Hatherly 1996). Figure 2.19 presents a schematic representation of the α - and β -fibre.

The observed textures after recrystallization are completely different from the deformation textures. However, the recrystallization texture is strongly dependent upon the deformation texture prior to annealing. Also the recrystallization texture can be described by a set of several ideal texture components as shown in Table 2.3. The Cube

Theoretical background

component is often the most dominating of these components. This orientation has [100] directions aligned with the principle sample axes (extrusion direction (ED), transversal direction (TD) and normal direction (ND)). The recrystallization texture observed in extruded aluminium profiles is often best described as a continuous fibre extending from the Cube (C) orientation to the Goss (G) orientation. This texture is frequently referred to as the ED rotated Cube texture. Figure 2.20 presents a schematic representation of this fibre in the pole figure as well as the $\varphi_2=0$ section of the ODF. This figure also includes an additional texture component introduced to get a better description of the fibre. The CG component is the Cube orientation rotated 22.5° around the ED, i.e. the CG component is oriented halfway between the Cube and Goss orientations.

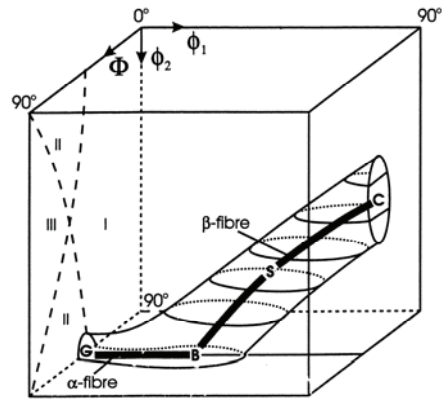


Figure 2.19 - Schematic representation of the FCC rolling texture in the first subspace of the three dimensional Euler angle space. The representation of ideal texture components: Copper (here C), S, Brass (B) and Goss (G) are also indicated (Hirsch and Lüke 1988).

Theoretical background

Table 2.3 – Ideal deformation and recrystallization texture components observed in FCC metals.

Texture component	Miller indices	Euler angles		
	$\{hkl\}\langle uvh \rangle$	φ_1	Φ	φ_2
Deformation				
Copper, Cu	$\{112\}\langle 111 \rangle$	90°	35°	45°
S	$\{123\}\langle 634 \rangle$	59°	37°	63°
Brass, B	$\{011\}\langle 211 \rangle$	35°	45°	$0/90^\circ$
Goss, G	$\{110\}\langle 001 \rangle$	0°	45°	$0/90^\circ$
Recrystallization				
Cube, C	$\{100\}\langle 001 \rangle$	0°	0°	$0/90^\circ$
CG	$\{520\}\langle 001 \rangle$	0°	22.5°	$0/90^\circ$
Goss, G	$\{110\}\langle 001 \rangle$	0°	45°	$0/90^\circ$
ND-rotated Cube	$\{001\}\langle 110 \rangle$	45°	0°	$0/90^\circ$
P	$\{011\}\langle 122 \rangle$	65°	45°	0°
R	$\{124\}\langle 211 \rangle$	57°	29°	63°

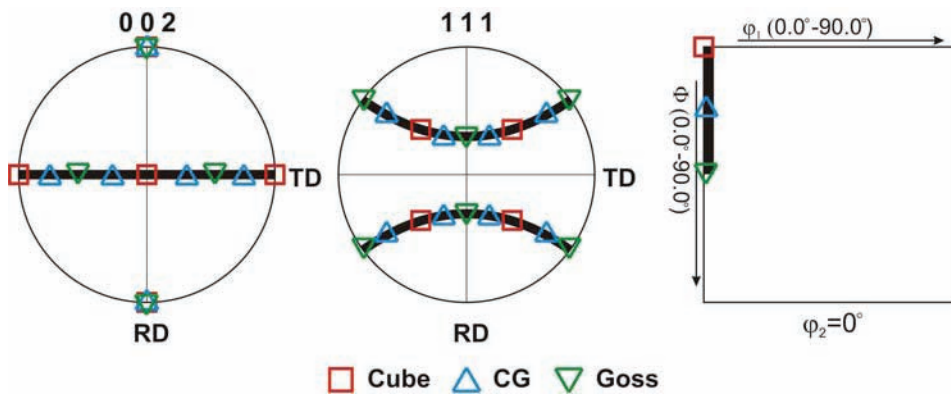


Figure 2.20 – Location of the ideal recrystallization texture components frequently observed in extruded aluminium profiles presented in the 002 and 111 pole figures as well as the $\varphi_2=0^\circ$ section of the ODF.

Theoretical background

2.4 Anisotropy and formability

The formability of a material defines its ability to withstand plastic deformation without failure. The ability to be formed into various geometrical shapes is one of the most important properties of metals and alloys. However, the formability will be strongly dependent on the orientation of the sheet or profile in the forming process. Hence, a good understanding of the directionality of properties may be used to improve and optimise forming operations.

An isotropic material has equal mechanical properties in all directions. Most metals used for practical applications exhibit a directional dependency of the mechanical properties. The tensile properties (yield strength, ductility, r -value etc.) is often observed to vary with the principal direction of deformation, hence relative to the rolling or extrusion direction. This phenomenon is referred to as mechanical anisotropy, and is treated in more detail in the following.

2.4.1 Mechanical anisotropy

Several factors are responsible for the mechanical anisotropy observed in metals and alloys. The most important factor is probably the texture or crystallographic anisotropy. However, also grain shape, precipitates and dislocation structures may influence the mechanical properties (see e.g. Bate et al. 1981, Chung et al. 2000 and Ekstrom et al. 2002).

While a single crystal is highly anisotropic, an aggregate of completely differently orientated grains might be almost isotropic. This relates to the variation in strength of different orientations, which for a tensile test is given by the Schmid value (m) for each individual grain. In a polycrystalline material with crystallographic texture a large number of the individual grains have approximately the same orientation, causing anisotropy.

Mechanical properties like yield strength, ultimate tensile strength, uniform strain and plastic strain ratio are of special interest for manufacturers and other material consumers. The strength parameters are closely connected to the Taylor and Schmid factors. The

Theoretical background

plastic strain ratio is normally given as the r -value or Lankford coefficient. For a tensile test this parameter is defined as

$$r = \frac{\varepsilon_w}{\varepsilon_t} \quad (17)$$

where ε_w is the width or transversal strain and ε_t is the thickness strain. Hence the r -value gives a relation between the contractions in the transverse and normal direction. In the case of $r=1$, the contractions are equal in the two directions and the formability is good. However, if the r -value is small, the thickness contraction is large and the material has a high susceptibility for failure. This happens because the material rapidly goes into a state of plane strain and instability occurs (Marciniak and Duncan 1992).

A classical example of anisotropy and formability is the deep-drawing operation of a cup from a textured sheet. Firstly, as the strength varies with direction, a variation in the resistance towards flow will result in an orientation dependence of the elongation. This appears as “ears” on the top of the cup, since a weak direction will have a low flow resistance with an ear as the result. Secondly, a variation in r -value around the cup circle will give different thinning of the cup wall. Normally, these are undesired effects, as they limit the formability, give varying properties and increase the amount of scrap. However, the mechanical anisotropy can also give beneficial results if taken into account during design and production, e.g. by placing the strong directions at critical positions in the final product.

2.4.2 Texture-based calculations

The mechanical properties and their directional dependency can be approximated based on the crystallographic texture acquired from the EBSD measurements. The Schmid value of all tensile directions can be calculated directly from the crystal orientation of the individual grain and the deformation direction (DD). Further, the Taylor factor in the different directions can be calculated from the different polycrystalline plasticity models like the Taylor and Self-Consistent models. These models can also be used to calculate the theoretical r -values of the material. However, it is important to remember that the

Theoretical background

accuracy of these calculations is dependent on the accuracy of the plasticity model applied.

2.5 Microstructural evolution

The microstructure of a material exposed to plastic deformation will clearly be altered. The generation and migration of dislocations, and the subsequent interaction, storage and recovery of the dislocations are fundamental to evolution of the deformation structure (see e.g. Dieter 1988 and Humphreys and Hatherly 1996). Clear changes in microstructure are evident first at high strains, but some small changes are detectable already at initial plastic deformation much less than 1% plastic strain.

2.5.1 Slip traces

The polished surface of a metal crystal deformed plastically will become covered with one or more sets of parallel fine lines called slip traces, bands or lines. The early work of Ewing and Rosenhain (1900) showed that there were steps in the surface resulting from microscopic shear movements along well-defined crystallographic planes, i.e. surface relief due to slip caused by the plastic deformation on the individual slip planes. Figure 2.21 presents an illustration of the grain structure covered with slip traces. The figure also shows that the deformation of each grain is accomplished by small blocks of the crystal sliding past each other along parallel sets of planes. The slip does not occur on just one plane but are localised to small regions of parallel planes.

Theoretical background

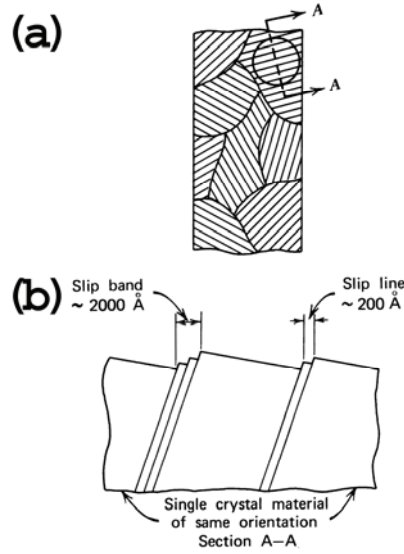


Figure 2.21 – (a) Illustration of grain structure revealed by slip traces. (b) Slip plane intersection with specimen surface due to crystallographic slip (Verhoeven 1975).

The observed slip plane traces are often characterised by the in-plane angle β_{obs} (the angle between the observed slip traces and the DD). The slip direction (\mathbf{s}) and slip plane normal vector (\mathbf{m}) of the 12 potential slip systems for all individual grains are expressed in the specimen axis system as:

$$\mathbf{s} = \mathbf{G}^{-1}\mathbf{s}_0, \quad \mathbf{m} = \mathbf{G}^{-1}\mathbf{m}_0, \quad \mathbf{G} = \mathbf{g}\mathbf{g}' \quad (18)$$

where \mathbf{s}_0 and \mathbf{m}_0 are the slip direction and slip plane normal vectors in the crystallographic frame respectively, \mathbf{g} is the orientation matrix of a grain defining the position of the crystallographic axes with respect to the specimen axis system (Schwartz et al. 2000), and \mathbf{g}' is the rotation from the specimen to the crystallographic system.

Further, the \mathbf{s} and \mathbf{m} vectors from the EBSD results are used to calculate the theoretical angle β_{theo} for the four $\{111\}$ -planes. Another parameter calculated from the same results, is the theoretical out-of-plane angle α_{theo} between the slip direction and the specimen surface normal. This parameter is important because slip planes with a low α_{theo} will not produce visible slip traces since the out-of-plane movement can not be detected. The parameters α_{theo} and β_{theo} were computed according to

Theoretical background

$$\alpha_{theo(i)} = \arccos(S_{z(i)}) \quad \text{and} \quad \beta_{theo(j)} = \arctan\left(\frac{-m_{x(j)}}{m_{y(j)}}\right) \quad (19)$$

where the suffixes i and j represent the inspected slip direction and slip plane respectively.

2.5.2 Transition and kink bands

Microstructural heterogeneities like transition and kink bands may appear at higher strains. Transition bands are defined as bands separating different parts of a grain which has split and rotated away from each other during deformation (Hu 1962). These bands develop when neighbouring volumes of a grain deform on different slip systems and rotate toward different crystallographic orientations. In many cases deformation bands occur with approximately parallel sides and involve a double orientation change A to C and the C to A (i.e. Humphreys and Hatherly 1996). A deformation band of this special type will be called a kink band following the nomenclature of Orowan (1942). Figure 2.22 presents an illustration of both transition and kink bands within a grain.

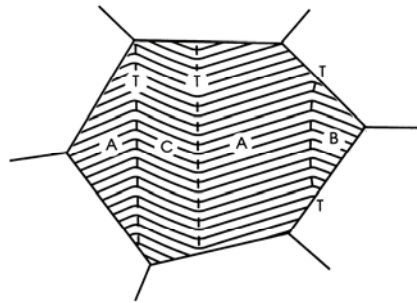


Figure 2.22 – Schematic illustration of transition bands (A-B) and kink bands (A-C-A) (Humphreys and Hatherly 1996).

2.5.3 Shear banding

At high strains (cold rolled material) a new mode of deformation occurs and a new microstructural heterogeneity appears. Shear bands were described in detail by Adcock (1922) but were largely forgotten until the work of Brown (1972). Shear bands are bands of highly strained material formed as a result of strain instability occurring after large deformations. This phenomenon occurs when the dislocation storage capacity of the

Theoretical background

material is almost exhausted. At this stage the material becomes unstable with respect to shear, and shear banding becomes an alternative macroscopic slip mode which accommodates strain accumulation during stage IV hardening. The microstructure inside the bands consists of cells/subgrains that are elongated in the band direction, which appears to be sharply misoriented (10-40°) with respect to the surroundings (Hatherly 1978). The material within the heterogeneity is softer than the surrounding matrix, the bands are non-crystallographic and macroscopic, and are often found with an orientation relationship of 35-38° to the deforming plane (Roven and Nes 1984). Shear bands can extend over distances of several grains or even through the whole specimen. Shear banding in aluminium alloys is often associated with the addition of magnesium, and the shear bands are frequently observed as failure mechanism in quenched Al-Zn-Mg alloys (Chung et al. 1977, King et al. 1982, Sørensen 1997, Fjeldly et al. 2001). For a more comprehensive description of shear banding in aluminium alloys see e.g. Humphreys and Hatherly (1996).

2.6 Strain measurements

The strain introduced to a material during deformation (typically simple tension deformation) is often easily characterised by the average linear strain (e), which is defined as the ratio of change in length (ΔL) to the original length (L_0).

$$e = \frac{\Delta L}{L_0} = \frac{L - L_0}{L_0} \quad (20)$$

This definition of strain is satisfactory for elastic strains where ΔL is very small. However, in plastic deformation the strains are frequently large, and the gauge length changes considerably. Ludwik (1909) first proposed the definition of true or natural strain (ε) which obviates this difficulty. In this definition of strain the change in length is referred to as the instantaneous gauge length, rather than the original gauge length (Dieter 1988).

$$\varepsilon = \int_{L_0}^L \frac{dL}{L} = \ln \frac{L}{L_0} = \ln(e + 1) \quad (21)$$

Theoretical background

The two different definitions of the strains give close to identical results up to a strain of ~ 0.1 but after this point the average linear strain (ϵ) gives much higher results than the true strain.

The change in length during simple tension deformation is normally obtained by using a high accuracy strain-gauge extensometer. However, there are several disadvantages of using extensometers to measure the displacement during deformation. First of all, strain-gauge extensometers provide only a one-dimensional measure of the strain, i.e. two extensometers have to be applied in order to simultaneously measure both the longitudinal and transversal strains. Note that calculations of the plastic strain ratio are based on both strains as shown in section 2.4.1. More important, strain-gauge extensometers only represent the average behaviour of the material in the measurement area, i.e. between the legs of the extensometer. Therefore, the extensometer measure is only valid when the material behaviour is homogeneous within the measurement area. This is especially a problem in materials with very heterogeneous deformation behaviour (Al-Mg-Si and Al-Zn-Mg alloys due to the Portevin-Le Châtelier effect, etc.). Local strain investigations (meso and micro scale) are also very difficult using strain-gauge extensometers.

Over the last two decades new non-contact measurements techniques have appeared. Mostly based on optics, their principles rely on either beam light/sample interaction, i.e. interpretation of interference fringes (see e.g. Tu et al. 1997 and Steinchen et al. 1998) or on correlation techniques, i.e. tracking the motion of geometric grids (see e.g. Chu et al. 1985 and Mguil-Touchal et al. 1997). The two techniques can also be combined as shown by He et al. 2002, Laraba-Abbes et al. 2003 and Zhang et al. 2003.

The accuracy of the former technique is in the order of a few wave-lengths (typically 0.2-0.3 μm). However, they are limited to small displacement gradients i.e. small strains. The latter technique, on the other hand, is less accurate but does not have any limitations with respect to strain. Among those techniques, digital speckle correlation analysis (DSCA) has become widely used. It only requires the surface of the specimen to have a random speckle and pictures of that surface at different instants during deformation. Applications are common at both the macro (Wattrisse et al. 2001, Dumoulin et al. 2003)

Theoretical background

and micro-meter scales (Doumalin et al. 1999, Knauss et al. 2003). In the following section, the theory behind DSCA will be presented in some more detail.

2.6.1 Digital Speckle Correlation Analysis

This strain measurement technique was initially developed by Mguil-Touchal et al. (1997). The principle of the method consists in comparing two digital images of a same object surface with a random surface appearance. The first micrograph is acquired prior to deformation while the second is acquired after deformation (tensile test, shearing test, etc.). When the original specimen surface does not have a random appearance, this must be obtained artificially. For ordinary simple tension specimens where the meso/macro properties are investigated, this can be obtained by some simple black and white spray paints. However, when the strains at the grain level should be investigated, more advanced techniques must be applied. A gold grid deposit on the sample surface is an example of such a technique, and section 4.1.2 describes the production of a gold grid with a grid size of $10\mu\text{m}$ in more detail.

The technique compares the acquired images using a grey level correlation coefficient. In other words, points from the initial image will be found on the final image with a precision lower than a camera pixel.

The image in which the strain is to be analysed is divided into a certain number of grid elements with sides L_p (Figure 2.23), user defined by a given number of pixels. Around each of the four points of a grid element, a square analysis zone or subset is defined by another given number of pixels.

Theoretical background

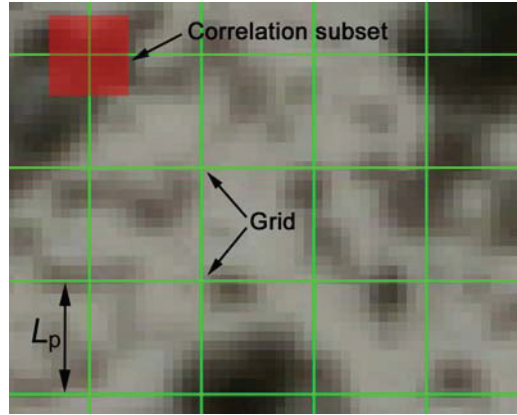


Figure 2.23 – Illustration of the correlation subset and the grid elements on a digital image.

The initial grey level of the micrograph/frame is represented by the discrete function $f(x, y)$ which on the deformed micrograph/frame $f^*(x^*, y^*)$, becomes (Vacher et al. 1997):

$$f^*(x^*, y^*) = f^*[x + u(x, y), y + v(x, y)] \quad (22)$$

with $u(x, y)$ and $v(x, y)$ being the displacement fields for one given grid element as shown in Figure 2.24. These displacement fields are obtained for every grid element by using the correlation method between an initial image grid element and its successor in the deformed micrograph. The calculations are based on the comparison between a subset of the initial image and its counterpart in the deformed image by computing the correlation coefficient (Vacher et al. 1997):

$$\text{Cor} = 1 - \frac{\int_{\Delta S} f(x, y) f^*(x^*, y^*) dx dy}{\sqrt{\int_{\Delta S} f(x, y)^2 dx dy \int_{\Delta S} f^*(x^*, y^*)^2 dx dy}} \quad (23)$$

where ΔS is the area of the concerned correlation pattern on the initial image. For a perfect correlation, $f(x, y) = f^*(x^*, y^*) \Rightarrow \text{Cor} = 0$ and for an imperfect correlation, $0 > \text{Cor} > 1$. The correlation coefficient is used as an indicator of the similarity degree between the two subsets. The first subset is centred on a pixel of the initial micrograph

Theoretical background

and is always square, while the second is in a subpixel position in the deformed micrograph and is a quadrilateral.

When the displacement fields are determined by the correlation technique, these can be used to calculate the local planar strain distribution in the material.

The theoretical background for the DSCA technique presented in this section is based on the work performed by Vacher et al. (1997), thus a more comprehensive review of the DSCA technique may be found in this work.

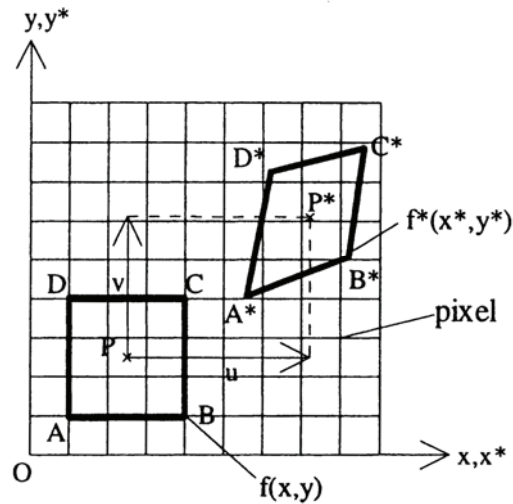


Figure 2.24 – Displacement field $u(x, y)$ and $v(x, y)$ between an initial and a deformed micrograph (Vacher et al. 1997).

2.7 Earlier work – State-of-the-art

So far, Chapter 2 has only given the general theoretical background for the characterisation and plasticity discussed and the experimental techniques applied. The remaining of this chapter will be used to review the state-of-the-art among earlier works within the topics treated in this thesis. The chapter will also include a review of available in-situ techniques as well as an evaluation of their strength and weaknesses.

Theoretical background

2.7.1 Crystal plasticity

Crystal plasticity has been one of the main topics for this work, as it also has for a impressive number of other studies throughout the last century. As already mentioned in Chapter 2.2, crystal plasticity is the bases for the improved knowledge concerning mechanical properties such as anisotropy and forming behaviour.

A better understanding of the deformation mechanisms taking place during deformation stimulated the research of understanding mechanical anisotropy. Experiments performed on single crystals made it possible to study directional dependency in great detail. The early works of e.g. Ewing and Rosenhain (1900) and Schmid and Boas (1935) provided a thorough understanding of the mechanical anisotropy of single crystals. This understanding of anisotropy was based on crystal symmetry. The classical polycrystalline plasticity models are based on this knowledge coupled with the information from the crystallographic texture (Sachs 1928, Taylor 1938, Bishop and Hill 1951). A more detailed description of these models was given in Chapter 2.2.

At the end of last century, crystal plasticity models were combined with finite element (FE) simulations in order to predict material properties after deformation, e.g. texture evolution during forming. Aukrust et al. (1994) simulated the texture development during extrusion of a profile comparable to the profiles investigated in this work by use of the Taylor model integrated into a FE-model. By using this technique, Aukrust et al. (1994) were able to predict the texture variations often observed through the thickness of an extruded profile. These investigations were part of a significant research project initiated by Hydro Aluminium in order to obtain a better understanding of crystal plasticity and how it could be used to understand the mechanical properties after processing (see e.g. Bauger 1994, Aukrust and Vatne 1994, Irgens et al. 1995 and Aukrust et al. 1997).

The knowledge acquired by coupling crystal plasticity and FE-simulations made it possible to better understand the deformation mechanisms operating during deformation. Hence, this knowledge were of great industrial importance and resulted into several great works within the topic “through-process-modelling” (see e.g. Marthinsen et al. 2002, Furu et al. 2004 and Neumann et al. 2005).

2.7.2 Mechanical anisotropy and forming behaviour

Mathematical models utilising crystal plasticity theory and phenomenological models of elastoplasticity have also been used to predict the effect of mechanical anisotropy on formability (see e.g. Lademo et al. 1999, Lademo et al. 2002, Lademo et al. 2005 and Fjeldbo et al. 2005). Forming limit diagrams (FLD) has been computed and compared to experimental results, showing that this technique is able to predict the forming limit of various materials.

Forming of extruded aluminium profiles is important for several industrial applications. Extruded profiles are often found to possess mechanical anisotropy, which has to be fully understood in order to make use of the competitive advantage of utilising these profiles formed to complex shapes. For this reason, it has also been performed several detailed experimental studies of anisotropy in extruded profiles at the Norwegian University of Science and Technology (see e.g. Søreng 1997, Iveland 2000 and Ryen 2003).

Further, it is known that aluminium processed by either extrusion or rolling often possesses through-thickness variations (see e.g. Engler et al. 2000 and Turner et al. 2002). This is especially true for commercial Al-Li based alloys that normally develop strong through-thickness texture gradients (Peters et al. 1986, Bowen 1988, Engler and Lücke 1991). The heterogeneous processing conditions taking place during rolling is assumed to give rise to the gradients observed in rolled sheets. During rolling, the deformation of sheet ingots changes from shear influenced at the surface to plane compression along the centreline. Also the amount of deformation varies quite significantly through the sheet thickness. It is expected that the variation in deformation, coupled with the recrystallization that sometimes occurs during heat-treatment, produce an evident gradient in crystallographic texture through the sheet thickness. The processing taking place during extrusion is normally much more heterogeneous than the processing conditions observed during rolling (Valberg and Malvik 1994). Hence, it is therefore concluded that also extruded products can develop strong through-thickness variations (Przystupa et al. 1994), especially for profiles subjected to large reduction during extrusion (see e.g. Aukrust et al. 1996, Aukrust et al. 1997, Søreng 1997, Pettersen 1999, Fjeldly 1999 and Iveland 2000).

Theoretical background

It is worth noticing that the majority of these investigations have been focusing on explaining the texture evolution that take place during plastic deformation, while only a modest fraction of these works have been devoted to how the forming behaviour is affected by thickness variations. The PhD work of Xiao-Hu Zeng (1995), titled “Anisotropy of Plastic and Elastic Deformation of Al-Li Alloys”, is one of few works totally devoted to the correlation of the plastic properties and the texture gradients. Zeng studied the crystallographic texture changes through the thickness of some rolled sheets. He found from texture-based calculations, that the texture gradient had a strong effect on the shape of the yield loci and the forming limit diagram (FLD) (Zeng et al. 1994, Zeng and Barlat 1994).

2.7.3 Deformation mechanisms

The work of Xiao-Hu Zeng among others was based on the assumption that the yield loci shape was determined by the deformation mechanisms operating locally. Hence, different deformation mechanisms were dominating at different positions through the thickness. For the last decades, the selection of different deformation mechanisms has been a very important topic of research. Computer modelling has tried to implement these mechanisms by developing more advanced crystal plasticity models. The new GIA and ALAMEL models are examples of such more sophisticated models (Van Houtte et al. 2005).

Slip traces have been used for decades in order to study the plastic deformation of crystals. For example, in the middle of the last century the different stages (stage 1-3) of hardening were extensively investigated by use of slip traces (see e.g. Diehl 1955 and Cahn 1950). Detailed investigations of slip traces and how these develop during deformation have also been used to reveal information about the slip planes activated and how the deformation structure develops during deformation (Honeycombe 1984, Sørensen 1997).

This information has been combined with information about the crystallographic orientations and used to predict the number of slip systems activated for individual crystallographic orientations (see e.g. Delaire et al. 2000, Nibur and Bahr 2003, Choi et al. 2004). Delaire et al. (2000), Zhang and Tong (2004) and Henning and Vehoff (2005)

Theoretical background

have all studied the development of secondary slip traces during simple tension of polycrystalline materials and they have shown that the grains deform by multiple slip at very low strains (4% deformation) and close to 50% of the grains investigated develop additional slip traces locally.

Also crystallographic rotations during deformation and how these rotations are related to the deformation mechanisms have been studied to a large extent by these techniques. It has become possible to follow the rotation paths of individual orientations, hence given more insight into how slip enforces crystallographic rotation (see e.g. Han et al. 2004).

Even though it is commonly agreed that the mechanical anisotropy, and by that the forming behaviour, to a large extent is controlled the crystallographic texture (Althoff 1971), the understanding of mechanical anisotropy is still an important topic within material science. The distribution of solute elements and precipitates (Barlat and Liu 1998) and the microstructure (Winther et al. 1997) has also been known to alter the anisotropy. The section below will present earlier work on how age-hardening affect the mechanical anisotropy.

2.7.4 Age-hardening

Age-hardening (particle strengthening) has been studied in great detail after the phenomena was first discovered by Wilm in the beginning of last century (1911). At that time, it was impossible to understand the underlying physical processes. However, the introduction of dislocations (Orowan 1934, Polanyi 1934, Taylor 1934) together with new and more advanced experimental techniques (high-resolution transmission electron microscopy (TEM)) has made it possible to study and explain the observed particle strengthening mechanisms. It has been shown that the particles act as obstacles to the dislocations movement (slip) and thus reduce their mobility. These obstacles can be overcome in two basically different ways, either by shearing or by bypassing (Nembach 1997). The latter mechanism has been suggested by Orowan (1948) and was subsequently named after him (the Orowan mechanism).

In the work of Bate et al. (1981), they studied changes in plastic anisotropy accompanying precipitation from a supersaturated solid solution of an Al-4%Cu. These

Theoretical background

authors showed that the investigated material possesses a strong angular dependency of the plastic strain ratio in supersaturated solid solution. They reported that the anisotropy disappeared after artificial ageing to the peak-aged condition (T6) and reappeared after ageing to the substantially over-aged condition (T7), as shown in Figure 2.25.

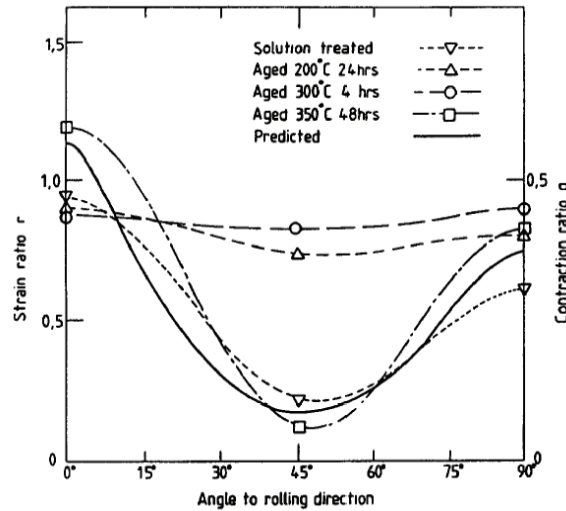


Figure 2.25 – Variation in r -value with test direction in Al-4%Cu in solution treated and artificially aged conditions compared with predictions of texture analysis (Bate et al. 1981).

It has been performed several interesting studies of how the plastic behaviour of a material has been altered due to the introduction of precipitates (see e.g. Hornbogen and Gahr 1975, Barlat and Vasudevan 1991, Hornbogen and Starke 1992, Sehitoglu et al. 2005 and Poole et al. 2005). A common observation is that precipitates alter the coarseness of slip taking place during deformation. During investigations in crystal plasticity, it has been reported that heterogeneous slip is favoured by low stacking fault energy, alloying elements in solid solution, shearable precipitates, when few slip systems are operating and with large grain sizes. Fine slip on the other hand, is favoured by bypassed particles, many operating slip systems and small grain sizes (Hornbogen and Gahr 1975).

Furthermore, the precipitate diameter (d) increases during ageing (see e.g. Hornbogen and Gahr 1975). It has been suggested that the transition from shearable to non-shearable precipitates takes place when the precipitates reach a critical diameter (d_c). Then

Theoretical background

precipitates have to be by-passed by the moving dislocations. Further, this means that a transition between localised and more homogeneous deformation will be dependent on the particle size as indicated in Figure 2.26. As indicated by the figure, dislocations tend to move along well-defined paths (the path of the first dislocations passing through the grain upon early stages of plastic deformation) when the precipitates are shearable (localised deformation). Several explanations have been proposed for this behaviour. Hornbogen and Gahr (1975) suggested that the localisation was related to local softening of the slip plane due to a decrease in precipitate strength. More recent investigations (e.g. see Poole et al. 2005) indicate that this matter is much more complicated and the observed localisation could possibly be more like an intrinsic property of aluminium alloys. In other words, when a dislocation source is activated, this source tends to stay active and will therefore suppress competing dislocation sources. On the other hand, when the dislocations have to overcome the precipitates by by-passing, they try to avoid any interaction with the precipitates, i.e. the slip distribution is more homogeneously distributed when the precipitate size is larger than d_c .

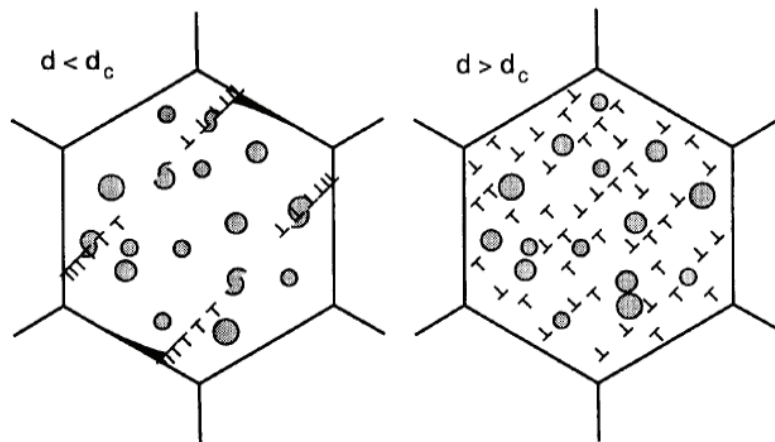


Figure 2.26 – Consequences of d_c on strain localisation. Shearable particles leading to strain localisation (left) and non-shearable particles leading to more distributed deformation (right) (Hornbogen and Starke 1992).

Theoretical background

2.7.5 Available in-situ techniques

The introduction of sophisticated in-situ techniques has inaugurated a new era within material science. These new techniques have made it possible to study deformation mechanisms, annealing behaviour (see e.g. Ferry 1998, Juul Jensen 2005 and Lens et al. 2005) and phase transformations (see e.g. Gourgues-Lorenzon (2007) for a comprehensive review) in a way that were completely unrealistic only a couple of decades ago. In general, these techniques can be utilised for all the topics listed above. However, this section will focus on techniques most frequently used to study deformation mechanisms. Deformation mechanisms can basically be studied by use of three principally different methods:

- Normal characterisation and investigations of pre-deformed samples
- Surface investigations during in-situ deformation
- Bulk investigations during in-situ deformation

Normal characterisation and investigations of pre-deformed samples

Investigations of pre-deformed samples are in many regards the least sophisticated and most “old-fashioned” method, but still very useful to study deformation mechanisms. The PhD-works by Sørensen (1997), Iveland (2000) and Ryen (2003) acquired information of the operating deformation mechanisms by use of this method.

The researchers at the Risø National Laboratory in Denmark have performed several detailed investigations on dislocation boundary formation and the dislocation structure of the material by studying pre-deformed samples in the transmission electron microscope (TEM) (see e.g. Wert et al. 1997, Wert 2002, Wert and Huang 2003, Winther 2004 and Li et al. 2006). The drawback with this method is that it is impossible to investigate the same area several times. Hence, the evolution of individual grains during deformation can not be studied.

Theoretical background

Surface investigations during in-situ deformation

The deformation mechanisms operating at the sample surface can be studied by investigating the sample surface during deformation. Placing a deformation unit inside the chamber of a scanning electron microscope (SEM) allows this type of investigations. Rémi Chiron and his group at the CNRS – PMTM laboratory in Paris have been pioneers when it comes to in-situ deformation in the SEM (Chiron et al. 1996, Delaire et al. 2000). Other groups have also performed detailed investigations of the deformation mechanisms by use of this method in combination with EBSD-investigations. The impressive works by Zhang and Tong (2004) and Han et al. (2003), which have studied the microstructure and crystallographic rotation evolution respectively, are such examples. Also the group at McMaster University in Canada have started to utilise this method in order to obtain a better understanding of deformation mechanisms operating during forming of aluminium (Kang et al. 2005, Kang et al. 2006).

Bulk investigations during in-situ deformation

Bulk investigations are the most advanced method for studying deformation mechanisms. The method is based on diffraction with focused hard x-rays. Consequently, synchrotron radiation facilities are necessary in order to utilise this method. The “Metal Structures in Four Dimensions”-group at the Risø National Laboratory in Denmark should have credit for bringing this work forward, and they have developed methods that make it possible to follow the deformation of individual grains within the bulk material (see e.g. Margulies et al. 2001, Nielsen et al. 2001 and Poulsen et al. 2003). 3D X-ray diffraction (3DXRD) has been widely used both to study rotations taking place during deformation and recrystallization during annealing. By applying this method, it has been possible to study the crystallographic rotation and by that the deformation mechanisms in great detail (Winther et al. 2004, Winther 2005). The method has also been used by other groups (see e.g. Forbød et al. 2007), but the technique is far from being readily available.

Theoretical background

Comparison between different techniques

X-ray diffraction (XRD) has since the introduction of crystallographic texture been the reference technique for measuring texture of polycrystalline materials. The crystallographic texture obtained with XRD and EBSD has been compared several times since the introduction of EBSD in the early nineties (Hjelen 1990). Generally, it has been shown that the measured crystallographic texture is independent of the measuring technique utilised (Bjerkaas and Sjølstad 2003, Saito et al. 2004). However, when the grain size exceeds a certain value (typically 50-100 μm), XRD can no longer provide statistically significant data. For very coarse grained materials (>1mm) and for heterogeneous materials such as welded joints, EBSD can still be used thanks to stage motion in the SEM. In EBSD, the orientation distribution function (ODF) is then directly calculated from the individual orientations by taking one point per grain or by taking all data points and weighting orientation data with the respective area fraction of grains (Gourgues-Lorenzon 2007). One must however, keep in mind that EBSD is a surface analysis technique.

When bulk (high energy x-ray diffraction) is compared to surface (EBSD by use of SEM) investigations, it is clear that bulk studies provide the most reliable results. However, the cost and complexity of this method makes EBSD/SEM the favourable alternative when it comes to studying crystallographic rotations of individual grains of a polycrystalline material. Further, the spatial resolution of 3DXRD is coarser (about a few μm) than that of EBSD but the angular resolution is high ($\sim 0.05^\circ$) (Gourgues-Lorenzon 2007).

As already mentioned above, there is some controversy regarding the results obtained from in-situ EBSD measurements. The EBSD technique has some considerable limitations since it only obtain information from the surface region of the specimen. It can therefore easily be claimed that the technique is insufficient since the acquired results are not representative for bulk deformation of the material. Hence, the results only provide a description of the surface behaviour. The works performed by the Risø group has shown that the rotation paths observed with bulk deformation are consistent with the rotation paths observed by performing in-situ EBSD investigations in the SEM

Theoretical background

(Bjerkaas et al. 2006). This indicates that the EBSD technique is actually able to capture the bulk behaviour during deformation

3 Materials and material processing

This chapter presents the materials investigated as well as the material processing prior and during the present investigations.

3.1 Materials

This work has focused on commercial aluminium alloys representing high volume production in the extrusion industry. Two different precipitation hardening alloys from the Al-Mg-Si system have been investigated (Table 3.1). The two alloys are AA6063 which is a low strength 6xxx series alloy and AA6082 which is a typical high strength alloy. Both alloys were DC-cast and homogenised (see Figure 3.1) by Hydro Aluminium, Sunndal prior to any processing. AA6082 contains somewhat more magnesium and silicon giving rise to higher strength but, more importantly it also contains some manganese (0.54 wt%). Al-Mg-Si alloys with 0.5-0.7 wt% Mn will precipitate small Mn-dispersoids of the $MnAl_6$ -type at temperatures lower than 705°C. These dispersoids will prevent recrystallization during hot deformation (Petzow and Effenberg 1993). As a consequence, AA6063 becomes fully recrystallized while AA6082 develops a fibrous microstructure with a recrystallized surface layer after extrusion. Flat extruded profiles with a cross section of 3 x 205 mm² were received from Hydro Aluminium AS. Previously, these profiles have been characterised and investigated within the VIRFORM project (van der Winden et al., 2002), hence the properties of these materials have already been reported extensively, e.g. Engler (2002), Ryen (2003) and Pedersen et al. (2004). All details regarding these alloys and processing of the investigated profiles are given in Pettersen and Furu (2001a and 2001b).

Table 3.1 – Chemical composition of the two investigated alloys.

Alloy	Wt% Mg	Wt% Si	Wt% Mn	Wt% Fe	Wt% Cu
AA6063	0.46	0.44	0.03	0.19	0.006
AA6082	0.67	1.04	0.54	0.20	0.003

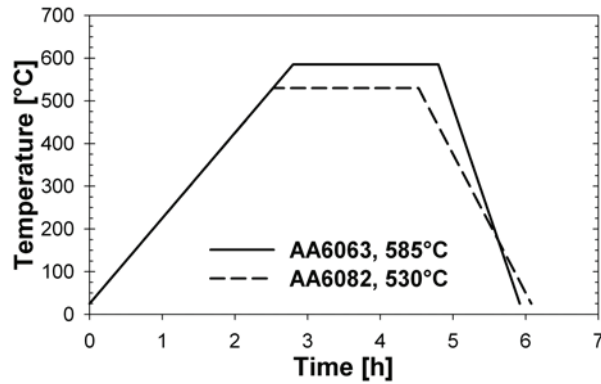


Figure 3.1 – Approximate homogenisation treatments of billets prior to extrusion.

3.2 Material processing

All processing from refining and casting to completion of the final product affects the material properties. It is therefore important to have detailed understanding of the processing taking place prior to the investigations performed in this work.

3.2.1 Extrusion

Billets with a diameter of 203 mm were extruded into flat profiles with a cross section of $3 \times 205 \text{ mm}^2$ by Hydro Aluminium AS. The extrusion process was performed at a reduction ratio of 53 and a ram speed of approximately 15 mm/sec. Immediately after the outlet of the extrusion die, the profiles were cooled with maximum water spray-cooling, followed by forced air-cooling. The press conditions are summed up in Table 3.2. The profiles were stored at room temperature for more than two years prior to further processing and the profiles were therefore received in the naturally stabilised condition, T1.

Table 3.2 – Press conditions for the extruded aluminium profiles.

Alloy	Billet temp.	Container temp.	Ram speed	Profile temp. front
AA6063 ^a	460°C	440°C	14-16 mm/sec.	515-523°C
AA6082 ^b	515°C	440°C	15-16 mm/sec.	520-543°C

Alloy	Profile temp. middle	Profile temp. end	Temp. after spray cooling
AA6063 ^a	511-528°C	505-517°C	~360°C
AA6082 ^b	518-532°C	503-524°C	~360°C

^a Pettersen and Furu (2001a)^b Pettersen and Furu (2001b)

3.2.2 Heat-treatments

Several different heat-treatments were applied to both alloys in order to produce a wide range of material conditions. The solution heat-treatment was performed in an air circulating furnace at 540°C for 20 minutes followed by water quenching, while the artificial age-hardening was performed in an ordinary oil bath at 185°C. The material was stored at room temperature for 10 minutes between the solution heat-treatment and the artificial age-hardening. The ageing behaviour at 185°C was explored in order to determine the ageing times necessary to obtain the peak aged (T6) and over aged (T7) material. This was done by measuring the Vickers hardness after various ageing times and subsequent water quenching. The obtained ageing curves are shown in Figure 3.2. These measurements were performed using a 5 kg load, loading time 15 seconds and a loading speed of 150 $\mu\text{m/s}$. Based on the ageing curve acquired, the T6 condition was expected to be reached at 700 and 250 minutes while ageing times 10,000 and 5000 minutes were necessary to reach the T7 condition for the AA6063 and AA6082 respectively. Specimens were also stored at room temperature for different amounts of time in order to produce naturally aged material conditions. Table 3.3 presents the notations used together with a description of all material conditions investigated herein.

Materials and material processing

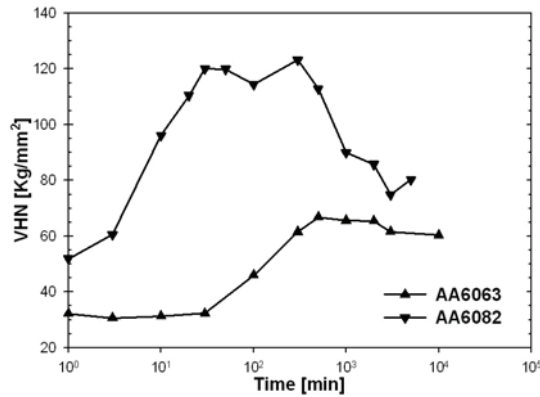


Figure 3.2 – Hardening curves for artificial ageing at 185°C, after solution heat-treatment at 540°C for 20 minutes.

Table 3.3 – Description of the material conditions investigated.

Material Condition	Description
W, 10min	Solution-heat-treated and tested 10 min. after water quenching
T4, 3h	Solution-heat-treated and naturally aged for 3 hours prior to testing
T4, 24h	Solution-heat-treated and naturally aged for 24 hours prior to testing
T4, >1kh	Annealed and naturally aged more than 1000 hours prior to testing
T6	Solution-heat-treated and artificially aged at 185°C to peak strength prior to testing
T7	Solution-heat-treated and artificially aged at 185°C to the over aged condition prior to testing
T1	Naturally aged for more than 2 years after extrusion

3.2.3 Additional processing

Both alloys investigated have a strong crystallographic texture. It was therefore necessary to perform additional investigations on material almost without texture to obtain a more complete understanding of the slip system activation during simple tension. Some additional processing was therefore performed to reduce the texture of the extruded AA6063 profile. The profile was first cross-rolled (50% reduction) at room temperature in a laboratory rolling mill. Cross-rolling reduces the crystallographic

Materials and material processing

texture from extrusion, i.e. the cold rolled profiles developed a weak deformation texture. A consecutive annealing heat-treatment at 520°C for 10 minutes resulted in a fully recrystallized microstructure with a close to random crystallographic texture. The material was stored at room temperature for more than 1000 hours in order to reduce the effect of Mg in supersaturated solid solution.

4 Experimental techniques

A good and comprehensive understanding of the applied experimental techniques is a key element in utilizing the results obtained in this work. For this reason, this chapter will be used to describe the experimental techniques. The background for the selected testing parameters will also be commented.

4.1 Specimen sampling and preparation

Specimen sampling from extruded profiles is critical due to expected through profile variations. Hence, small changes in the sampling position could strongly affect the testing results. Also specimen preparation is of great importance, especially for EBSD investigations, since even minor changes in specimen preparation procedure can lead to significant alteration of the results. The following sections give a detailed description of the specimen sampling procedures and preparation techniques used during this work.

4.1.1 Specimen sampling

Since extruded profiles are believed to be subjected to variations both through the cross-section and along the extrusion direction (ED), it is necessary to use strict sampling procedures in order not to introduce uncertainties.

The profiles investigated were cut into 2-meter-long parts and labelled by Hydro Aluminium AS. However, this labelling did not include any information about the position along the total length, making it impossible to determine any relationship between the different parts and the press cycle. This introduced some uncertainties with regard to possibilities for variations along the profile length but these were neglected in the present work.

It is known that extruded profiles, especially very flat profiles, can develop some variations over the width (Fjeldly 1999). Those investigated in this work had a cross-section (thickness x width) of $3 \times 205 \text{ mm}^2$, hence it was reasonable to assume that they possess such variations. The variations were avoided by sampling all specimens from the centre width position of the profile as shown in Figure 4.1. Consequently, the simple

Experimental techniques

tension specimens were sampled such that the centre specimen position always intersects the centre line of the profile. This figure also indicates that an exception was made for specimens taken parallel to ED. This was done in order to reduce the consumption of material. It was assumed that three parallel specimens could be produced without being influenced by the through width variations. All the simple tension specimens were sampled according to the procedures described above.

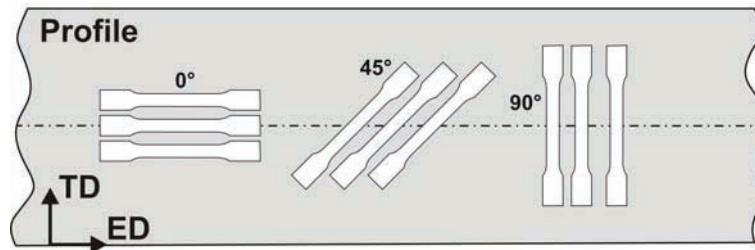


Figure 4.1 – Sampling positions of simple tension specimens where TD and ED are the profile transversal and longitudinal (extrusion) directions.

The full thickness tensile specimens were machined from the extruded profile by using an ordinary CNC cutting machine. The surface was not machined away in order to maintain the true full thickness of the material. The applied specimen geometry of full thickness specimens is shown in Figure 4.2. Sub-size specimens having the same in-plane geometry and 0.3 mm in thickness were sampled from three different positions through the profile thickness. The three positions were labelled Position 1, 2 and 3 and are taken from the centre, middle and surface part of the profile thickness respectively. Figure 4.3 and Figure 4.4 present the thickness direction position of the three sub-size specimens investigated. Investigations on sub-size simple tension specimens were only preformed in material condition T1.

Experimental techniques

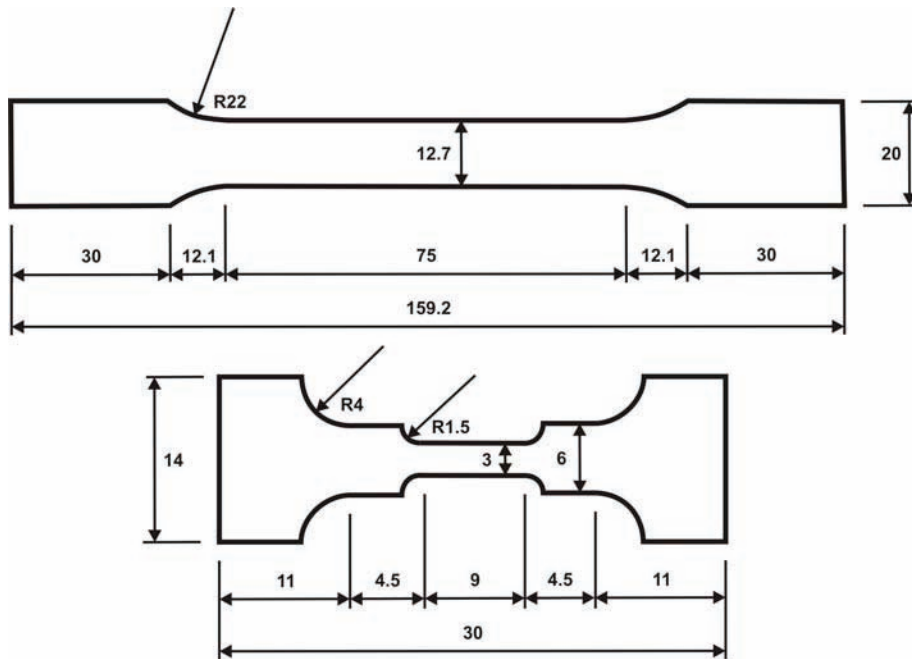


Figure 4.2 – Geometry for standard full-size (top) and in-situ SEM specimens (bottom) for simple tension testing. All dimensions in [mm]. The thickness of the full-size specimens was either 0.3 mm or full profile thickness (3.0 mm), while the typical SEM specimens had a thickness of ~1.0 mm.

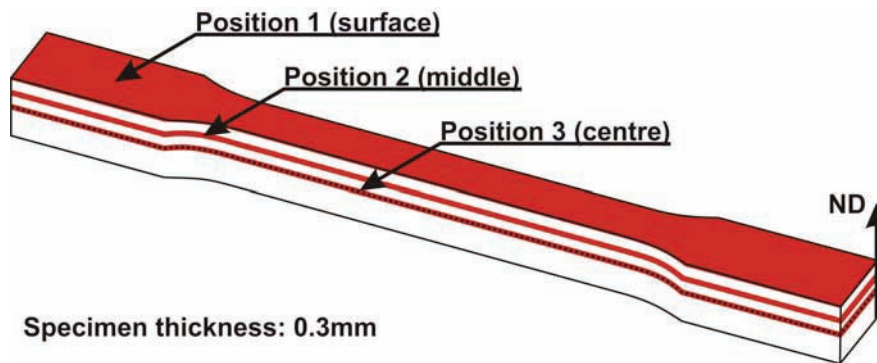


Figure 4.3 – Schematic illustration of simple tension specimens taken from different positions through the profile thickness. Here, ND=profile normal direction.

Experimental techniques

The through-thickness texture variations were investigated by testing specimens sampled from different positions through the thickness. In order to avoid any through width variations, also these specimens were taken close to the centre line (see Figure 4.1). The position along the thickness direction (normal direction) were denoted by an S-value which starts with S=1.0 at the profile surface and ends with S=0.0 in the centre of the profile. Figure 4.4 presents a schematic illustration of the S-value notation used for the different positions. The AA6063 and AA6082 were tested at eight and seven different positions through the thickness, respectively. Table 4.1 summarises the distance beneath the surface for all positions investigated.

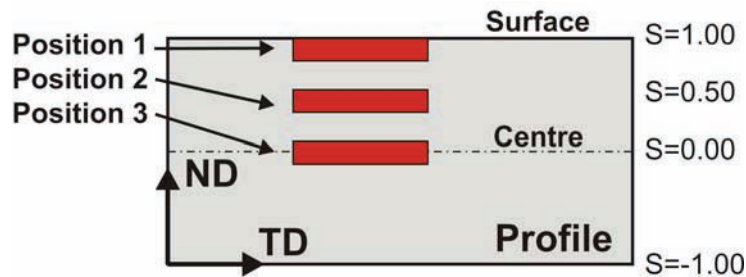


Figure 4.4 – Schematic illustration of the notation used for representing the different positions through the profile thickness.

Table 4.1 – Distances beneath the surface [mm] and corresponding S-notations applied for the different through-thickness positions.

Alloy	S=0.00	S=0.50	S=0.70	S=0.80	S=0.85	S=0.90	S=0.95	S=0.99
AA6063	1.45	0.72	0.43	0.29	0.22	0.14	0.07	0.01
AA6082	1.42	0.71	0.43	0.29	-	0.14	0.07	0.01

The specimens prepared for in-situ testing in the SEM were given a special geometry (Figure 4.2 (bottom)) and a thickness of 1.0 mm. All these specimens were in addition to ordinary machining given some additional metallographic preparation. This is required in order to obtain satisfying EBSD patterns and high quality SE micrographs. It was necessary to remove the heavily deformed surface layer developed during machining. The procedures applied to achieve the required specimen quality will be described in the following paragraph.

Experimental techniques

It was most convenient to study the surface of the gauge length during SEM simple tension deformation. The gauge width of these specimens was 3 mm while the total width of the gripping section was 14 mm (see Figure 4.2 (bottom)). Due to the geometrical limitations set by the SEM chamber, it was not possible to study the through-thickness deformation in the TD plane during in-situ SEM deformation. However, by doing some radical modifications of the specimen geometry, through-thickness investigations were made possible (i.e. see the illustration in Figure 4.5). The gauge length of the specimen was machined as described above and the width of this part corresponds to the profile thickness. In addition, a short 0.8mm thick “notch” was introduced (see Figure 4.5). During straining, the plastic deformation was localised to this area due to 20% reduction of the cross-section. The specimen heads were prefabricated in a material with higher strength in order to avoid plastic deformation of the specimen heads during testing. The prefabricated heads were mounted onto the gauge length piece with two-component epoxy glue. The final specimen assembly is shown in Figure 4.5. However, it is worth noticing that the glued connection will shear off if the “notch” in the parallel part was omitted. Without the “notch”, the full length of the gauge length piece deforms plastically, hence the contraction in width and thickness will weaken the glued connection and the glue would fail.

Experimental techniques

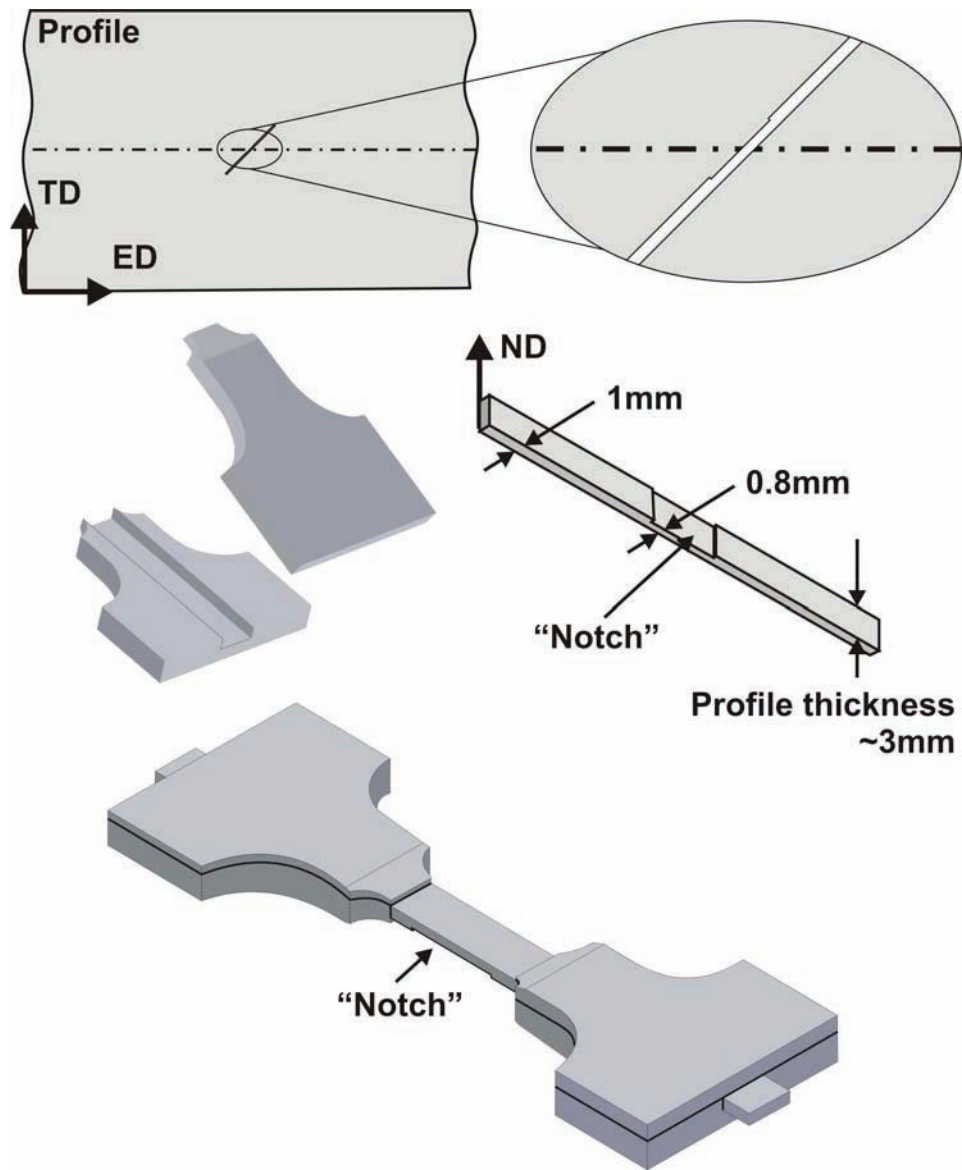


Figure 4.5 – Specimen (45° direction) for investigation of through-thickness deformation in SEM. The gauge length piece is machined from the profile and the width of this part corresponds to the profile thickness. The small “notch” in the gauge length is produced in order to concentrate the plastic deformation. Prefabricated specimen heads are finally glued to the parallel part and the through-thickness deformation can be investigated in the SEM.

4.1.2 Metallographic preparation and surface grids

The sampled specimens developed a heavily deformed surface layer during machining which had to be removed prior to investigations in the light optical microscope or in the SEM. This was obtained by mechanical grinding to ASTM mesh 2400 and subsequent mechanical polishing with 3 and 1 μm diamond paste, followed by “shock” electro-polishing in Struers electrolyte A2 for 4 seconds at 30V and 10°C. The specimens investigated in the light optical microscope were anodized in a 5% HBF₄ aqueous solution (Bakers reagent) (Petzow 1976) for ~2 minutes at 20V and 18°C in order to reveal the grain structure under polarised light.

The undeformed and smooth surface obtained after electro-polishing was necessary for EBSD investigations. However, random features in the specimen surface are absent. Hence, an artificial random speckle had to be created in order to allow EBSD investigations in combination with local strain measurements, using the DSCA technique described later in section 4.4. It was very difficult to produce a sufficiently fine random speckle and a compromise had to be made. In this work an artificial gold grid was produced on the specimen surface. The gold grids were produced in the CNRS – PMTM laboratory at University Paris 13 with a quadratic grid size of 10x10 μm^2 and a grid line width of ~1 μm .

Figure 4.6 presents a schematic illustration of the procedures utilised to produce the gold grid. First, a thin film (~0.4 μm thick) of PMMA (Polymethylmetacrylate) was deposited onto the electro polished surface by spin coating (Figure 4.6 (b)). The specimen was then annealed for 30 minutes at 130°C in order to remove the residual stresses from the spin coating. The grid was produced by exposing the polymer film to the electron beam of a SEM. Movement of the electron beam was controlled by external software and the electron beam broke the polymers down to monomers, which could easily be removed by cleaning the specimen in a solution consisting of 25% ethyl methyl ketone and 75% Propanol-2. The grid became visible in the PMMA film after removal of the monomers (Figure 4.6 (c)). However, this grid could not be investigated in the SEM, so a thin layer of gold was deposited on top of the grid produced in the SEM. The deposition procedure was divided in two operations in order to optimise the adhesiveness between the electro polished surface and the evaporated gold layer. First, a 1nm-thick base Au-layer was

Experimental techniques

sputtered onto the produced grid and then a 20nm thick Au-layer was evaporated on top of the base layer. This gave a continuous layer of gold covering the entire surface of the specimen as shown in Figure 4.6 (d). The remaining PMMA was finally dissolved and removed by cleaning the specimen with ethyl acetate in an ultrasonic bath for 15 minutes, also removing the gold deposit on top of the PMMA. The gold deposit on the specimen surface would not be affected by this cleaning procedure, and the electro polished surface reappeared with an evident gold grid that could be used for strain analysis during investigations in the SEM (Figure 4.6 (e)).

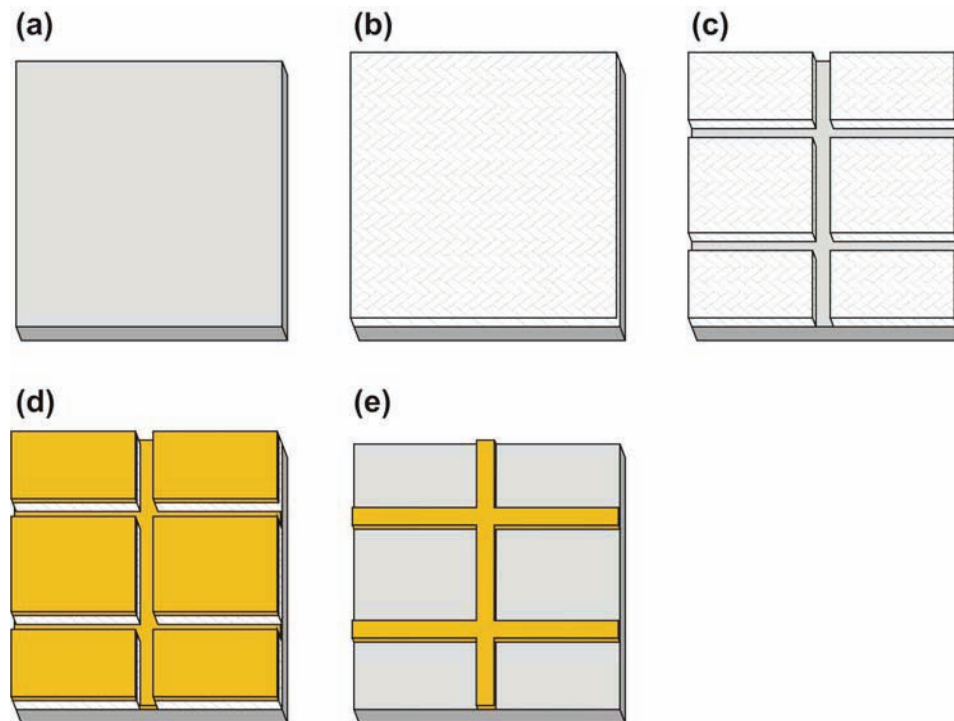


Figure 4.6 – Chronological illustration of the surface grid production procedure. (a) Electro polished specimen surface. (b) Specimen surface with continuous plastic film overlaid. (c) Plastic film with a grid after electron beam exposure. (d) Specimen with gold both in the grid and on the surface of the remaining film. (e) Specimen with gold grid after removal of the remaining film.

4.2 Tensile testing

The tensile testing experiments in this work were performed on two different length scales. The macroscopic results were acquired by use of an ordinary testing machine while a very compact in-situ testing machine was used to investigate the microscopic behaviour in a SEM. Section 4.3.3 gives a detailed description of the simple tension experiments performed in the SEM.

Investigations of the macroscopic behaviour were performed for all the material conditions investigated in this work (see Table 3.3). The tensile specimens were sampled from the extruded profile 0° (parallel to ED), 45° and 90° (parallel to TD) with respect to the extrusion direction (ED). A minimum of three parallels were tested in each direction in order to verify the experimental results. Simple tension experiments were performed in an MTS 880 servo-hydraulic testing machine at a constant ramp rate corresponding to an initial strain rate of $1.1 \times 10^{-3} \text{ s}^{-1}$. The tensile specimens had a width of 12.7mm and a parallel length of 75 mm as shown in Figure 4.2. The transversal and longitudinal strains were measured by a MTS transversal (MTS 632.23F-20) extensometer and a MTS 50mm longitudinal (MTS 632.25F-20) extensometer respectively.

Tensile testing of thin specimens taken from three different positions through the profile thickness was also performed in the same way as described above. Notice that the thickness of these specimens was only 0.3mm, making transversal strain measurements more difficult due to problems with the gripping mechanisms of the extensometer.

4.3 Scanning Electron Microscopy (SEM)

Scanning electron microscopy has been by far the most important tool utilised in this work. The SEM has been used both for metallographic characterisation of the starting material and as a platform for the detailed in-situ deformation behaviour experiments. Two different scanning electron microscopes were used. The first was a very user-friendly conventional tungsten filament SEM with low-vacuum capabilities (Hitachi S3500-N). This microscope was used for the in-situ investigations and characterisation of the recrystallized material. The second microscope was a high resolution field emission SEM (Hitachi S4300-SE) which was used for characterisation of the fibrous

Experimental techniques

fine-scaled microstructure material due to its improved resolution. It is also worth noticing that the Schottky emitter has an extremely stable beam current, which was very convenient for EBSD investigations. The following sections will be used to present the experimental techniques involving scanning electron microscopy and the modification made to the SEM in order to allow in-situ deformation investigations will also be presented.

4.3.1 Electron backscatter diffraction (EBSD)

The electron backscatter diffraction technique has been used to obtain information about the micro and macro texture of the materials investigated. The microstructure and its evolution during deformation have also been determined based on experiments performed with this technique. Important properties of the materials investigated could be determined by use of the crystallographic information obtained by EBSD. EBSD was therefore a very important experimental technique for material characterisation.

The main components of an operating EBSD system is the SEM, the EBSD-detector including a camera that acquires the diffraction patterns and the software that calculates the crystallographic orientation based on these patterns. It is also important to remember that the software should also be able to post-treat the crystallographic orientation information acquired.

The most important properties of the SEM were the beam current and stability. A stable beam current was essential since variations reduce the accuracy of the EBSD measurements. Both microscopes used in this work have a satisfying beam current stability and were very well suited for EBSD investigations.

An important feature of the applied EBSD-detector was the pattern acquisition speed. The camera used was a Nordif digital CD200 EBSD detector with a maximum acquisition speed of 43fps (frames per second). This speed was satisfying for the experiments performed, but it is of course desirable to increase the acquisition speed even further in order to perform fully in-situ investigations with shorter step sizes. This can be obtained when the next generation Nordif EBSD-detectors with acquisition speeds more than 500fps become available.

Experimental techniques

A most critical quality of EBSD software is to calculate the crystallographic orientation accurately and within a short period of time. How easily the orientation data can be post-treated and presented is another important quality. EBSD software from the three most well known suppliers (HKL Channel 5, Oxford Inca and Edax TSL OIM3.5) were all available at the Electron Microscopy laboratory at the Department of Materials Science and Engineering, NTNU. All three were compared with regard to both data acquisition and post-processing. It was concluded, based on an overall evaluation, that the Edax TSL OIM3.5 software and its successors OIM4.X were best suited for this type of work.

This software had a control panel with several available acquisition options, making it easy to optimise the EBSD acquisition parameters for reliable results. However, EBSD acquisition was both material and preparation dependent, so it was almost impossible to give any universal solution for the testing parameters. The testing conditions selected would also affect the testing parameters. For example, the parameters selected for a detailed investigation of the orientation gradient within a deformed grain differs significantly from the parameters used for global texture measurements. Table 4.2 presents the typical software setup for the different types of EBSD investigations. The SEM parameters, on the other hand, were more independent and were normally kept constant for all types of EBSD investigations. A typical microscope setup used for these investigations is given in Table 4.3.

Experimental techniques

Table 4.2 – Normal software setup for EBSD investigations used in the present work. Camera binning is a clocking scheme used to combine the charge collected by several adjacent CCD pixels. This increases both the sensitivity and the acquisition speed of the camera at the expense of resolution. Theta step size describes the resolution of the Hough transform. *Specimens taken from the recrystallized surface area are tested with the same setup as AA6063.

Parameter	AA6063		AA6082*	
	Microstructure	Texture	Microstructure	Texture
Camera binning	8x8	8x8	4x4	4x4
Step size [μm]	2	10-15	0.4	10
Scan size [μm^2]	1500x1500	3000x3000	200x400	1500x3000
Pixel shape	Hexagonal	Hexagonal	Hexagonal	Hexagonal
Binned pattern size	96	96	140	120
Theta step size:	2°	1°	1°	1°

Table 4.3 – Typical SEM setup for EBSD investigations used in this work.

Parameter	Value
Acc. voltage	20 kV
Tilt angle	70°
Probe current	2.0-2.5 nA
Working distance	20mm

The information generated from an EBSD investigation was very dependent on the number of indexed points within the individual grains. It was desirable to have only one orientation per grain for global texture measurement, while more than 1000 orientations were typically necessary to perform detailed studies of the orientation gradients through a grain. The number of measurements within the individual grains could be controlled by choosing an appropriate step size. Hence, the step size selected for microstructure investigations of AA6063 and AA6082 is 2 μm and 0.4 μm respectively. A typical EBSD measurement used to study the microstructure evolution and the development of orientation gradients in deformed aluminium consisted of ~70000 orientations distributed among ~50 grains.

Experimental techniques

It was essential for a global texture measurement to represent the distribution of all possible crystallographic orientations. This was in general obtained by selecting orientations from a large area of the specimen. Large spatial resolution was redundant since the spread in orientation within the individual grains was normally neglectable. The step size was adapted to give only one measurement per grain. However, it was selected equal to the minimum grain size when the material had a very heterogeneous microstructure. The global texture measurements consisted of more than 25.000 orientations due to the large area investigated. A large number of orientations gave a very accurate description of the materials orientation distribution. Engler (2004) stated that the orientation distribution of a specimen can normally be described with only 500 randomly selected orientations. This statement was tested by extracting different numbers of orientations randomly from the global texture measurements, and it was shown that the reduction in the number of mapped orientations only give minor changes. Hence, the scan size used in this work is strongly exaggerated.

4.3.2 In-situ deformation investigations

In-situ deformation investigations in SEM facilitate studies of the deformation behaviour locally. This is a relatively new technique that could be used to study several important metallurgical phenomena. In the present work the tensile deformation process was interrupted in order to perform the surface investigations (SE imaging and EBSD mapping). After each mapping sequence the deformation was continued, and so forth. Hence, these investigations were not fully in-situ but rather “semi-in-situ”.

Two different types of in-situ deformation investigations on the fully recrystallized AA6063 have been performed. In-plane (ED-TD plane) investigations have been used to study the global texture evolution, and more detailed investigations of grain rotations and surface slip-trace development have been performed in-plane. Through-thickness investigations were the second type of in-situ deformation studies performed, i.e. deformation variations over the thickness in a material with a very strong texture gradient.

Experimental techniques

i) In-plane investigations

The in-plane specimens were 1mm thick and were sampled from the centre position in the normal direction (ND), i.e. with specimen geometry as shown in Figure 4.2. Simple tension deformation was performed with a constant stroke rate, giving rise to an initial macroscopic strain rate of $1.1 \times 10^{-4} \text{ s}^{-1}$. The specimens were typically deformed in steps corresponding to $\sim 2.0\%$ nominal strain and SE micrographs were acquired between every step. The specimen was horizontal both during deformation and SE imaging. EBSD investigations were typically performed between every third step (i.e. every $\sim 6.0\%$ nominal strain). The same area was investigated throughout the deformation process allowing the deformation behaviour for a given number of grains to be studied in great detail. The global texture measurements and the detailed investigations of the microstructure consisted of more than 3000 and ~ 40 grains respectively. Microstructural investigations were also performed on specimens with an artificial gold grid.

ii) Through-thickness investigations

In general, the through-thickness investigations were performed in the same way as the in-plane ones. However, the specimen geometry was somewhat more complicated (Figure 4.5) and the specimen width corresponded to the profile thickness ($\sim 3\text{mm}$). The through-thickness variations were investigated by selecting the area of interest equal to the half width ($\sim 1500\mu\text{m}$) of the specimen. Hence, the profile thickness was investigated from the centre ($S=0.00$) to the surface ($S=1.00$). It was not possible to cover the area of interest by using only one micrograph at the desired magnification, hence the SE micrograph consisted of four micrographs stitched together in an image processing software.

4.3.3 Optimisation of in-situ systems

The optimisation of the in-situ system has been one of the most important experimental tasks in this work. It has been mostly motivated by the need for a better understanding of the deformation behaviour. The quality of the results obtained with an in-situ system depends on the in-situ unit and the SEM capabilities. The interaction between these two components was also of primary importance. The following section presents the in-situ system developed during this work.

Experimental techniques

i) Deformation unit

A central part of the in-situ system is the deformation unit. This unit is simply a small tensile machine which can be placed inside the chamber of a SEM (substage). The space available inside a SEM is normally very limited so the tensile machine has a very compact design. The deformation unit implemented to this in-situ system was originally developed at the CNRS – PMTM laboratory at University Paris 13, France (Chiron et al. 1996) and further modified at the Norwegian University of Science and Technology. All the in-situ experiments presented in this work were performed with this deformation unit.

The substage design is very compact ($15.5 \times 9.5 \times 4.5 \text{ cm}^3$) as shown in Figure 4.7. The unit was controlled by external software connected to the substage by a 15pin mini D-sub connector. Deformation took place by simple tension with one fixed and one movable ramp. The movable ramp was screw-driven by an electrical step motor and the strain rate was adapted by the gear. The deformation behaviour could be monitored by the stress vs. strain curves obtained during deformation. The longitudinal strains were calculated based on the stroke movement measured by a LVDT (Linear Variable Differential Transformer) displacements transducer while the deformation force was measured by the load transducer.

Due to the special design, it was possible to tilt the substage 70° without interfering with the objective lens of the SEM. Thus, this in-situ unit was designed for simultaneous deformation and EBSD-mapping. The deformation unit requires specimens with a rectangular cross section and specimen heads specially adapted for the machine as shown in Figure 4.2. Semi-circled alignment parts at both ends forced the specimen to be aligned with the tensile direction during loading. It was important to perform an accurate specimen alignment with regard to the global reference system in order to obtain accurate uniaxial deformation.

This deformation unit could also be combined with a heating unit which allows in-situ simple tension investigations at elevated temperatures. The furnace is simply clamped underneath the parallel part of the specimen and heats the sample locally. The substage could also be used to perform compression experiments. The semi-circled parts are there

Experimental techniques

simply replaced by a compression unit. The compression unit required rectangular specimens with maximum dimensions of $3 \times 3 \times 5 \text{ mm}^3$. Neither compression nor simple tension experiments at elevated temperatures have been performed in this work. It is also worth noticing the large weight (1.6kg) of the deformation unit when it is set up for both straining and heating. For further details concerning the heating-stage, please refer to Appendix A.

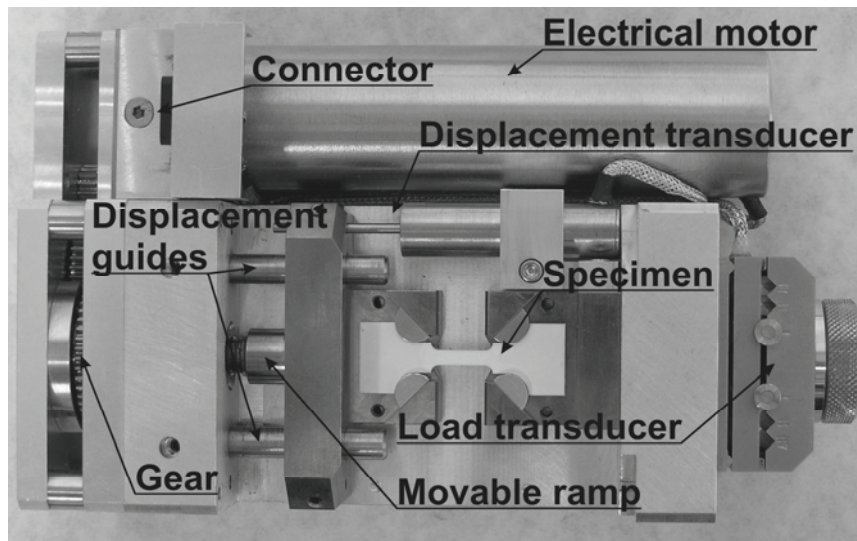


Figure 4.7 – Deformation unit for use in the SEM. Important components are labelled.

ii) The SEM (Hitachi S3500-N)

The conventional Hitachi S3500-N has been the SEM of choice for the in-situ experiments, mainly because this microscope was believed to be more user-friendly with regard to specimen exchange time. The spatial resolution of this instrument was not comparable with the resolution obtained by a field emission SEM. However, this has not been a limiting factor.

There were several potential problems connected to placing a substage inside the chamber of a SEM. The problems that arose during installation in the Hitachi S3500-N will be described in the following. It was desirable to have the specimen surface in the eucentric height (parallel to the tilt axis) since this eases the SEM operations. The height of the deformation unit made it impossible to place the specimen surface in the eucentric

Experimental techniques

plane of the Hitachi S3500-N. Figure 4.8 presents a schematic illustration of the difficulties related to this limitation. The free distance between the substage and the TA (tilt axis) was far too small (Figure 4.8 (a)), which made some modifications of the stage necessary. The bracket performing the Y-direction movement was permanently modified and the rotation unit had to be removed temporarily as shown in Figure 4.9. However, the available space was too small even after these modifications (Figure 4.8 (b)), and the specimen surface was not at eucentric height (Figure 4.8 (c)). Consequently, the specimen surface would therefore move out of the electron beam when tilted 70° (Figure 4.8 (d)) and this had to be compensated by moving the stage perpendicular to the TA (Figure 4.8 (e)). Movement perpendicular to the TA reduced the working distance significantly and the specimen surface was no longer at the optimal working distance for EBSD investigations. The stage had therefore to be moved in the Z-direction in order to reach this optimal working distance (Figure 4.8 (f)). The tilt axis was fixed to the stage, therefore it would also move when the Z-direction position is changed. The machine was mounted to the stage by a simple bracket as shown in Figure 4.10. Non-eucentric specimen mounting introduced much more complicated testing operations and the probability of making fatal errors increased dramatically. In spite of these problems, no damage took place during this experimental work. It was also feared that the large weight of the deformation unit could lead to mechanical vibrations or drift but neither this became any problem at the magnifications used. Also the Hitachi S4300-SE has been modified such that the deformation unit can be mounted into this microscope (see appendix A for details).

Experimental techniques

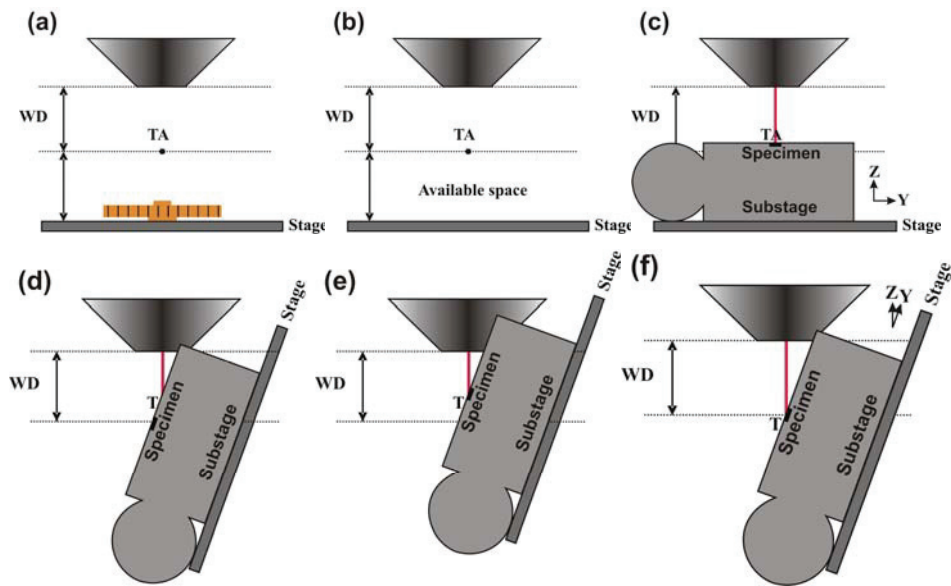


Figure 4.8 – Schematic illustration of the deformation unit inside the Hitachi S3500-N chamber. WD and TA are the optimal working distance for EBSD investigations and the position of tilt axis respectively. The deformation unit must be placed in the available space between the TA and the stage surface. (a) Prior to any modifications (b) After removal of rotation unit (c) Deformation unit placed inside the SEM chamber. The specimen surface is higher than the TA. (d) Stage tilted 70° for EBSD investigation. The specimen surface is rotated away from the electron beam. (e) Stage movement perpendicular to the TA in order to reposition the specimen under the electron beam. (f) Optimal working distance for EBSD investigations are achieved by moving the stage in the Z-direction.

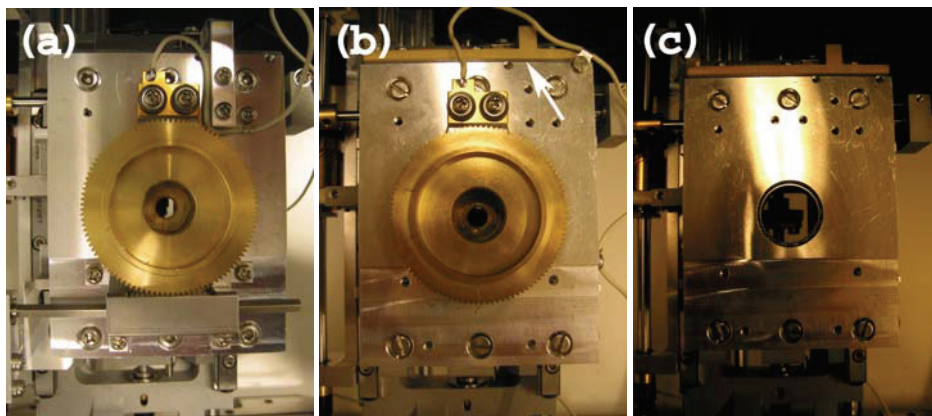


Figure 4.9 – Modifications of the Hitachi S3500-N stage. (a) Prior to any modifications. (b) Permanent redesign of the Y-direction movement bracket. The bracket is indicated by a white arrow. (c) Temporary removed rotation unit in order to allow mounting of deformation unit.

Experimental techniques

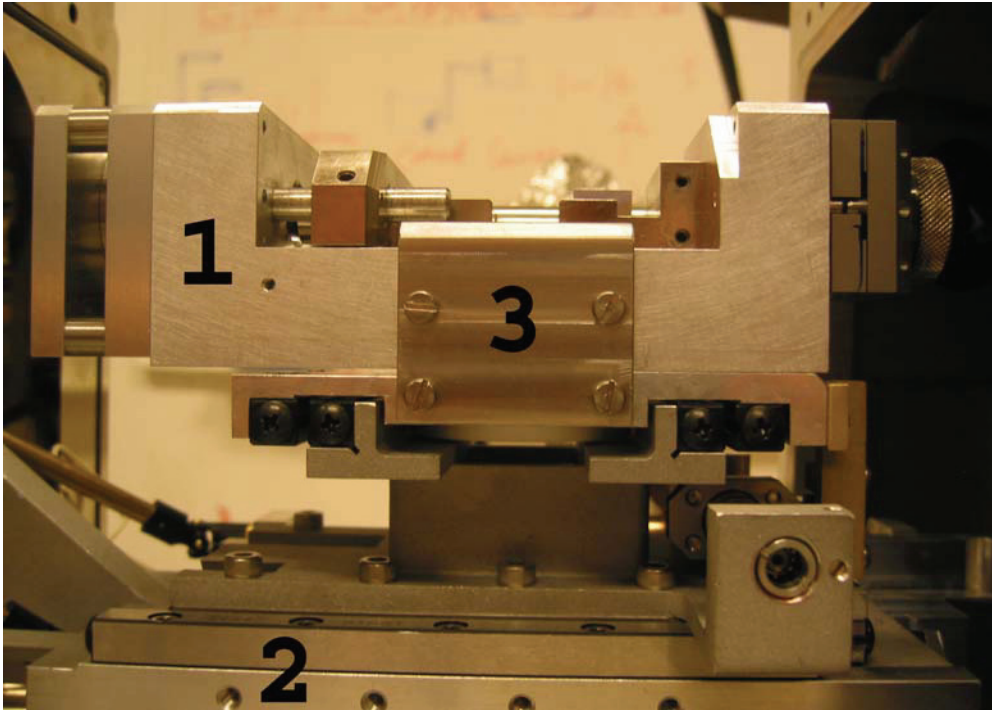


Figure 4.10 – Deformation unit (1) mounted on top of the modified Hitachi S3500-N stage (2) by a simple fixing bracket (3).

4.4 Local strain measurements

The local strain measurements were based on the digital speckle correlation analysis (DSCA) technique (see section 2.6.1 for more details). The commercial software 7XD, developed at INSA – Annecy in France has been used to perform strain measurements of in-situ tensile specimens based on secondary electron (SE) micrographs acquired in the SEM. This technique uses a fixed grid (gold grid) or a random speckle on the specimen surface to correlate the different positions in consecutive micrographs. Further, the strain calculations are related to a micrograph acquired prior to deformation. The two most important parameters for these calculations are the grid size and the binned pattern size. These parameters were selected such that the size of the virtual grid was equivalent to the gold grid produced on the specimen surface (see section 4.1.2 for details regarding preparation of the gold grid). The local strain measurements performed in the SEM with a gauge length of approximately $10\mu\text{m}$ were proven to be equivalent to strain measurements from ordinary simple tension experiments using conventional extensometers.

5 Experimental results

As mentioned above, the main objective of this work has been to investigate and explain the mechanical anisotropy observed in extruded profiles. State-of-the-art experimental techniques have been developed and used in order to investigate the mechanisms taking place in extruded profiles during deformation. Experiments are performed on several length scales, facilitating a better understanding of plastic deformation processes operating during subsequent forming operations. The acquired knowledge can also be used to improve shape tolerances of forward extruded profiles in the future.

The experimental results are organised in two separate parts based on the techniques used and the mechanisms investigated. Part A is titled “Characterisation of materials – Effects of heat-treatment, texture and through-thickness variations”. The basic properties of the selected materials are thoroughly investigated in this part but also the effect of heat-treatment (artificial ageing) on the observed mechanical anisotropy is characterised in great detail. The second part presents the in-situ deformation investigations performed in the SEM, using a new technique developed and implemented during this work: “SEM in-situ investigations of plasticity – Slip activity, grain rotation and texture evolution”. This part contains calculations of slip activity and how this depends on crystallographic texture. Also, crystallographic rotations taking place during deformation are investigated in detail. Local strain distribution during in-situ deformation has been characterised using digital speckle correlation analysis (DSCA).

Part A: Characterisation of materials – Effects of heat-treatment, texture and through-thickness variations

Information about the microstructural and mechanical properties is important in order to understand the mechanical behaviour of a material. The two extruded aluminium profiles investigated in this work are therefore given a thorough characterisation. The effect of heat-treatment on mechanical properties is included, since alteration in mechanical properties is very important in regard to industrial forming operations.

5.1 Characterisation of as-received materials

The properties of the two extruded profiles investigated are determined by the alloy composition and the extrusion process. Extrusion is a non-homogeneous deformation process which gives rise to variations over the profile cross-section. The through-thickness variations in the microstructure have been characterised by applying EBSD investigations at different positions through the thickness.

5.1.1 Microstructure

The microstructure of the two profiles is very different in spite of both being Al-Mg-Si-type alloys. The AA6063 has a fully recrystallized microstructure consisting of relatively equiaxed grains as shown by the light optical micrograph of the longitudinal transverse (ED-ND) plane in Figure 5.1 (a). The corresponding inverse pole figure (IPF) map of the same plane is shown in Figure 5.3(a) and it is clear that the profile possesses an evident through-thickness gradient, especially close to the profile surface. The AA6082 on the other hand, has a fibrous microstructure with a recrystallized surface layer as shown in Figure 5.1 (b) and Figure 5.2. The recrystallized surface layer is approximately 120 μ m thick, giving rise to an even more evident through-thickness texture gradient as shown in Figure 5.3 (b). The figures also show that the size of the recrystallized surface layer is close to constant along the extrusion direction (ED) (Figure 5.1 (b)), and neither is the microstructure affected by the solution heat-treatment (Figure 5.2). However, the fibrous

Experimental results – Part A

part of AA6082 is much more homogeneous than the corresponding part of AA6063. The through-thickness variations observed in these two alloys will be presented in more detail in section 5.1.3.

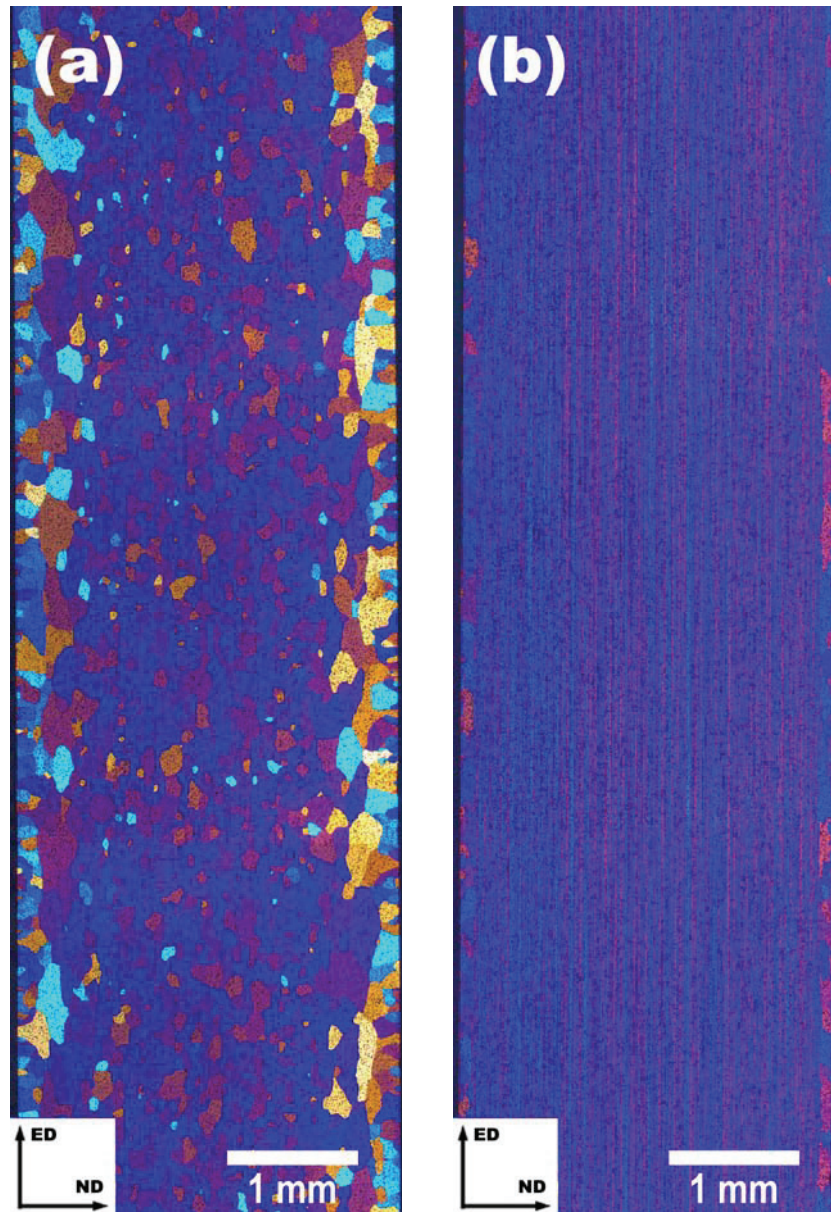


Figure 5.1 – Light optical micrograph of the microstructure in the longitudinal transverse (ED-ND) plane. (a) AA6063 and (b) AA6082.

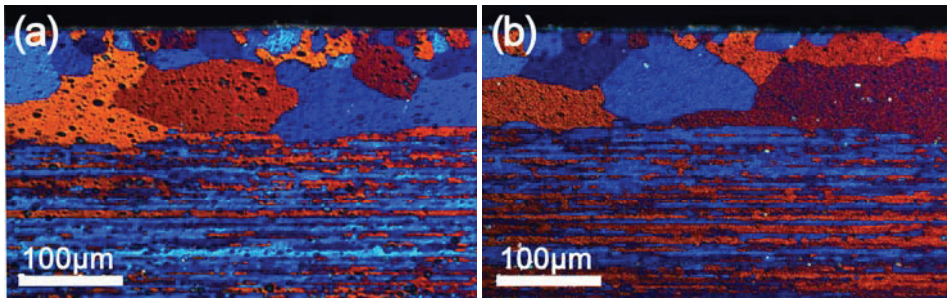


Figure 5.2 – Light optical micrograph of the microstructure close to the surface in the longitudinal transverse (ED-ND) plane of AA6082. (a) Prior to solution heat-treatment. (b) After solution heat-treatment.

The average grain sizes in both the ED and the ND of the two alloys have been measured by use of the linear intercept method and are shown in Table 5.1. The grain sizes are dependent on the minimum misorientation angles selected for the measurements. The measured grain size of AA6063 increases by a factor of 2 when the boundary misorientation angle is increased from 5° to 15° .

It is beyond doubt that the microstructure of AA6063 is fully recrystallized. Hence, the observed changes in grain size as a function of the boundary misorientation angle can not be related to any deformation substructure. The prominent increase in grain size is therefore most likely an intrinsic behaviour of all materials with a strong recrystallized texture, especially materials possessing a rotated recrystallization texture like the investigated AA6063 (see section 5.1.2 for details). Several grains in a material with such a strong texture have close to identical crystallographic orientations. When the number of grains with almost identical orientations is high, it is reasonable to assume that the microstructure will consist of neighbouring grains with close to identical orientation, i.e. the microstructure will consist of grain boundaries with low misorientation angles. For the same reason the measured grain size will be very dependent upon the selected boundary misorientation angle.

Experimental results – Part A

Table 5.1 – Average grain size of both alloys measured by EBSD in conjunction with the linear intercept method by use of different boundary misorientation angles.

Alloy	Boundary misorientation angle	Grain size ED [μm]	Grain size ND [μm]
AA6063	5°	90	63
AA6063	10°	116	83
AA6063	15°	173	98
AA6082	15°	13	4

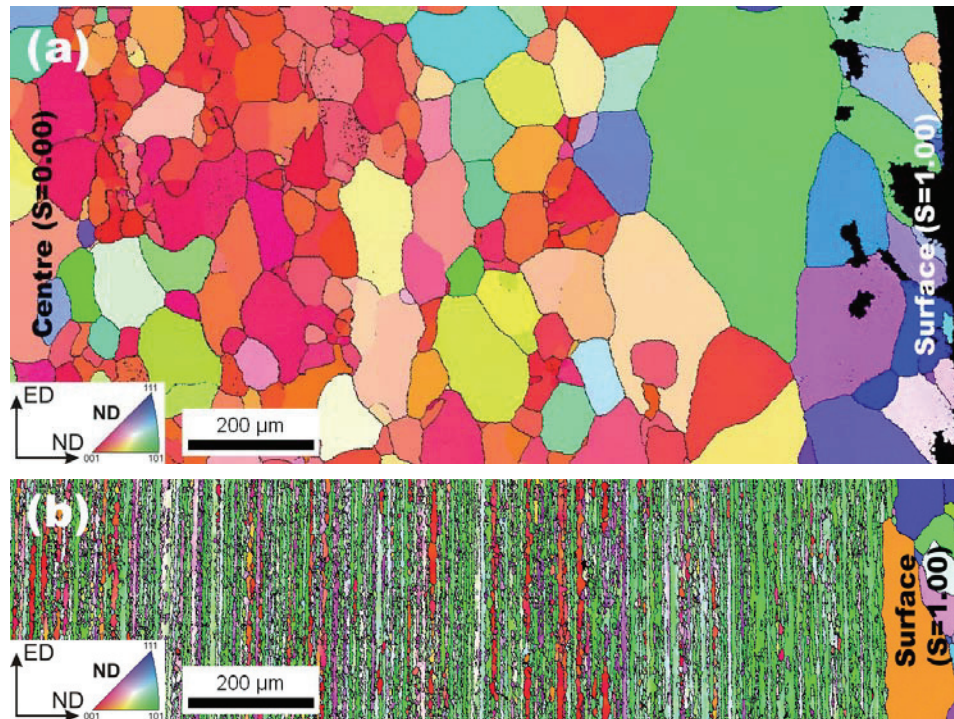


Figure 5.3 – IPF map of the variations in microstructure from the centre to the surface of the investigated profiles. The left hand side represents the centre position while the right hand side represents the surface position of the profile. (a) AA6063 and (b) AA6082.

5.1.2 Crystallographic texture

Evident microstructural variations, like the one observed for the investigated materials, often also give rise to variations in crystallographic texture. The crystallographic texture of AA6063 is very typical for materials with a recrystallized microstructure, i.e. a strong

Experimental results – Part A

texture dominated by the Cube component as presented by pole figures in Figure 5.4. The calculated orientation distribution functions (ODF) are given in Appendix B. Figure 5.5, which presents the area fraction of the most common texture components, shows that the texture also has a relatively large volume fraction of the CG component. Hence, the Cube component is somewhat rotated around the ED towards the CG and Goss component as indicated in Figure 5.4. A material with a perfect cube texture will have symmetrical crystallographic orientations both in the ED and the TD. However, the crystallographic texture of this material is not fully symmetrical since the texture is rotated around the ED, which gives rise to a characteristic fibre along the Φ -axis of the $\varphi_2=0^\circ$ section of the ODF (Appendix B). Figure 5.4 also presents the crystallographic texture of the fibrous AA6082 which possesses a typical deformation texture. Here, the area fraction of the typical recrystallization components (Cube, CG and Goss) is very low. However, the area fraction of the more typical deformation components like Brass and S is quite pronounced. Neither Brass nor S are $0^\circ/90^\circ$ -symmetric, something which means that AA6082 possesses less $0^\circ/90^\circ$ -symmetry than the AA6063 (Figure 5.5).

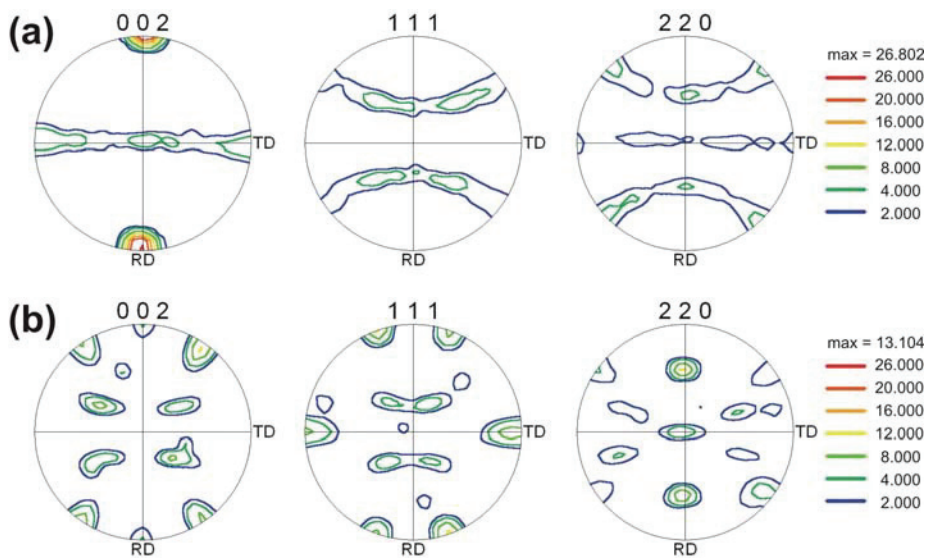


Figure 5.4 – Measured 002, 111 and 220 pole figures representing the initial global texture. (a) AA6063 and (b) AA6082.

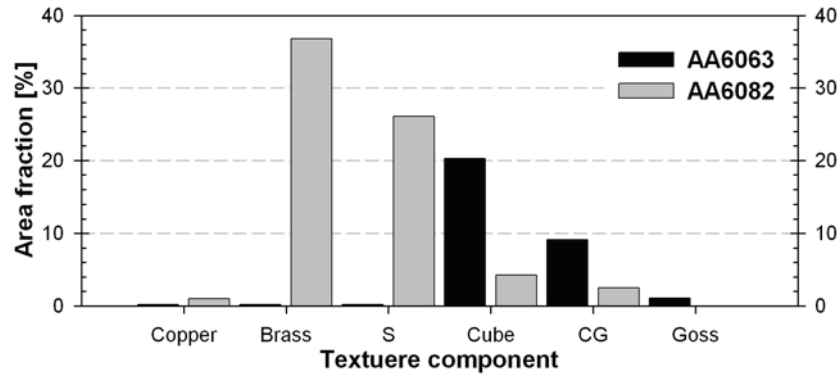


Figure 5.5 – Measured area fraction of the most important texture components through the thickness in the half-width position of the profile. Texture components were defined within 10° from the ideal orientations. Note that the Goss component of AA6082 is absent.

5.1.3 Through-thickness variations

Extruded profiles are expected to have through-thickness variations due to the inhomogeneous deformation taking place through the die during extrusion. The deformation mode at the profile surface ($S=1.0$) is close to perfect shear while the deformation in the centre region of the profile ($S=0.0$) is controlled by plane compression. Strong temperature and deformation mode gradients across the thickness during processing give rise to large textural and microstructural variations. The extent of these through-thickness variations is alloy dependent as will be presented in more detail in the following sections.

AA6063

This profile has a fully recrystallized microstructure but the thickness can be divided into three separate layers based on differences in the microstructure (Figure 5.6). The microstructure consists of equiaxed grains with a grain size of approximately $50\mu\text{m}$ in the centre layer of the profile ($S=0.00 - S=0.70$). In the middle layer ($S=0.70 - S=0.85$) the grain size increases rapidly and the grains become somewhat elongated in the ED. Further toward the surface the grain size decreases and becomes more equiaxed, ending up with a grain size of approximately $40\mu\text{m}$ at $S=0.99$. The measured grain sizes at all investigated positions based on 5° boundary misorientation angle are presented in Table

Experimental results – Part A

5.2. The table also shows that the standard deviation of the grain size measurement is large for all positions investigated, indicating a very heterogeneous microstructure.

Table 5.2 – Measured grain size and standard deviations (Std.) at investigated positions through the profile thickness of AA6063. 5° is used as the minimum misorientation angle for the grain size calculations.

Position	Grain size ED [μm]	Std. ED [μm]	Grain size TD [μm]	Std. TD [μm]
S = 0.00	64	30	55	34
S = 0.50	66	31	56	33
S = 0.70	119	86	104	79
S = 0.80	173	98	159	93
S = 0.85	202	144	198	140
S = 0.90	131	69	103	53
S = 0.95	90	57	82	47
S = 0.99	58	29	51	18

The IPF maps presented in Figure 5.6 give a first indication of an evident texture gradient through the profile thickness. The colours of the IPF maps change dramatically from the centre toward the surface, thus the texture of the material changes. The crystallographic texture can be divided into the same set of layers as used for the microstructure. The centre layer has a strong Cube texture somewhat rotated around the ED (Figure 5.7 (a)). The Cube texture sharpens towards the middle layer where the texture first split into two separate texture components (Cube and Goss) (Figure 5.7 (b)) before it rotates further around the ED, producing a zone circumscribing the equator plane. The texture also becomes more random at the profile surface (Figure 5.7 (c)) with evident traces of texture components typically associated with shear deformation, as shown in Figure 5.8. This leads to a decrease in the maximum texture intensity towards the surface, i.e. the profile has a maximum intensity of 35.1 at S=0.00 and 3.8 at S=0.99 (see Figure 5.7). The area fractions of all the relevant texture components from the different positions through the thickness are given in Figure 5.8. In Appendix C, calculated pole-figures based on orientation data from all positions investigated are included.

Experimental results – Part A

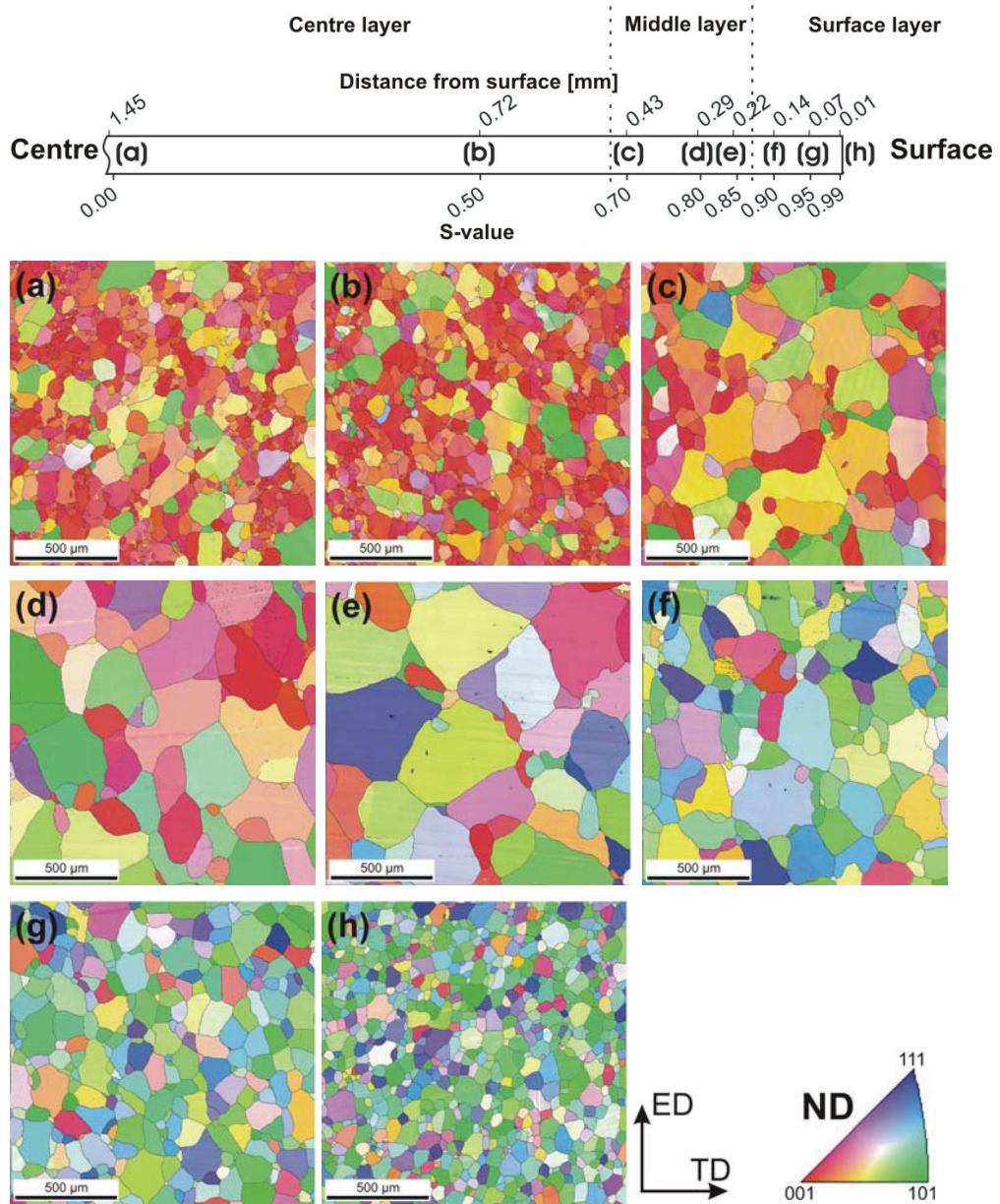


Figure 5.6 – IPF map acquired with a step size of 2μm at different positions through the profile thickness of AA6063. The corresponding positions are shown in the sketch at the top.

Experimental results – Part A

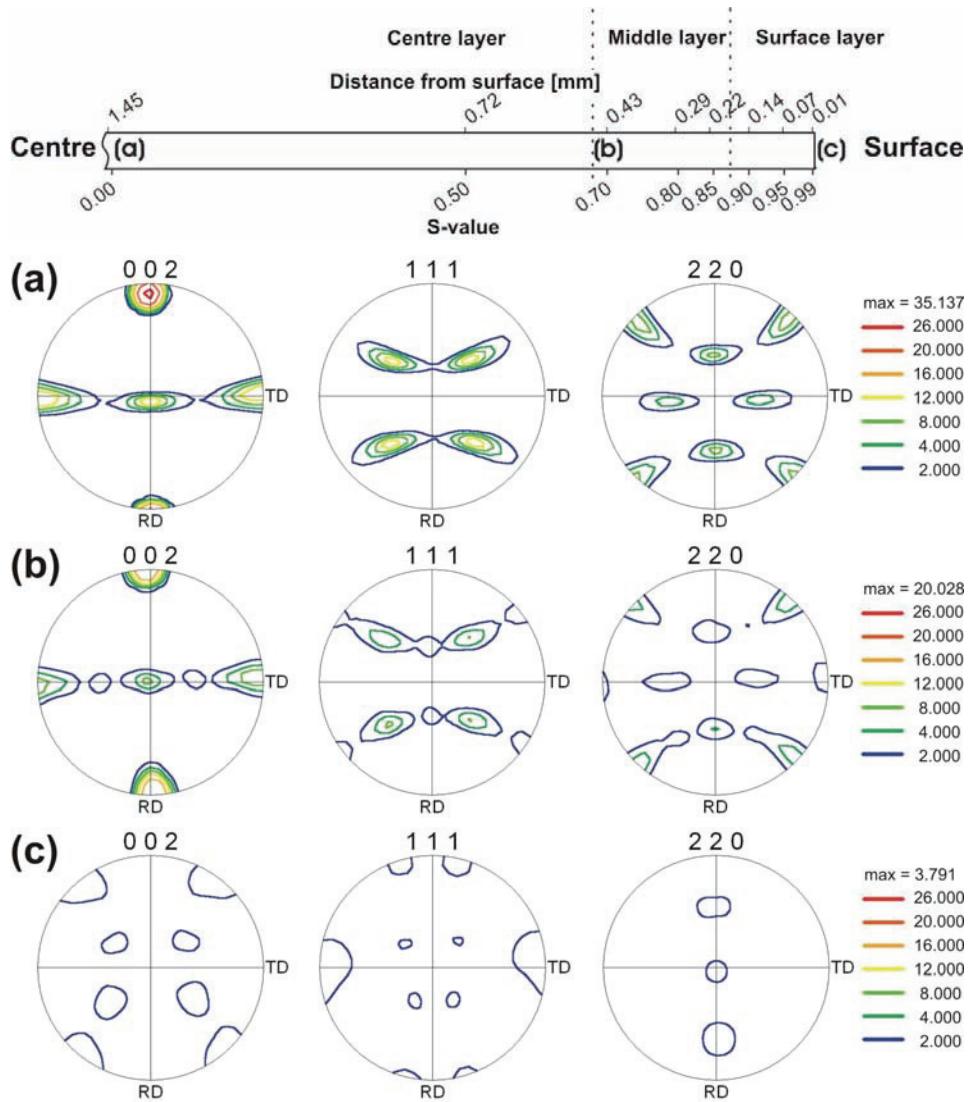


Figure 5.7 – Calculated pole figures based on crystallographic orientation data from different positions through the profile thickness of AA6063. The corresponding positions are shown in the sketch at the top.

Experimental results – Part A

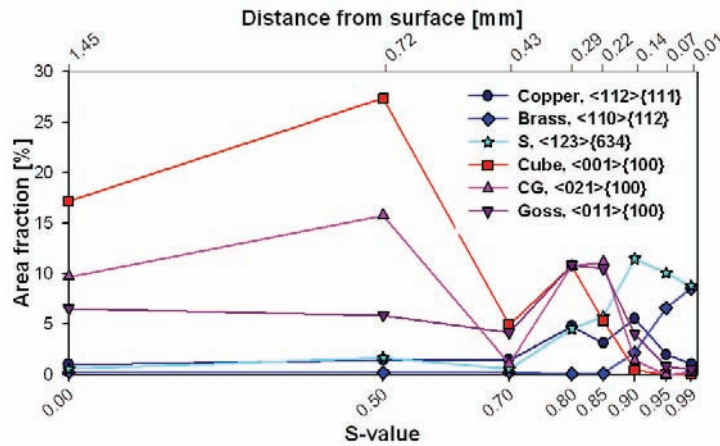


Figure 5.8 – Area fractions of the different texture components at different positions through the thickness of AA6063.

AA6082

The AA6082 has a fibrous microstructure with a recrystallized surface layer, hence the microstructure has evident through-thickness variations as already indicated in conjunction with Figure 5.3. The microstructure consists primarily of two pronounced different layers, i.e. a large centre layer with a deformed microstructure and a recrystallized surface layer with some microstructural variations (Figure 5.9).

Throughout the more or less homogeneous centre layer the grain and sub-grain sizes seem to be independent of the position within the layer. However, the fraction of Cube bands increases toward the centre position. The inverse pole figure map from the centre position (Figure 5.9 (a)) shows a large fraction of grains with Cube orientation aligned along the extrusion direction (Cube bands).

The surface layer, on the other hand, has a microstructure similar to the microstructure observed in the surface layer of AA6063 (Figure 5.6). From the IPF maps presented in Figure 5.9, the size of the recrystallized surface layer is calculated to be approximately 120µm. The green grains in Figure 5.9 (e) are recrystallized grains surrounded by a deformed microstructure. Hence these grains belong to the recrystallized surface layer. The image quality (the quality of the EBSD pattern) provides additional information

Experimental results – Part A

about the deformation structure, and is therefore included in the inverse pole figure maps presented in Figure 5.9.

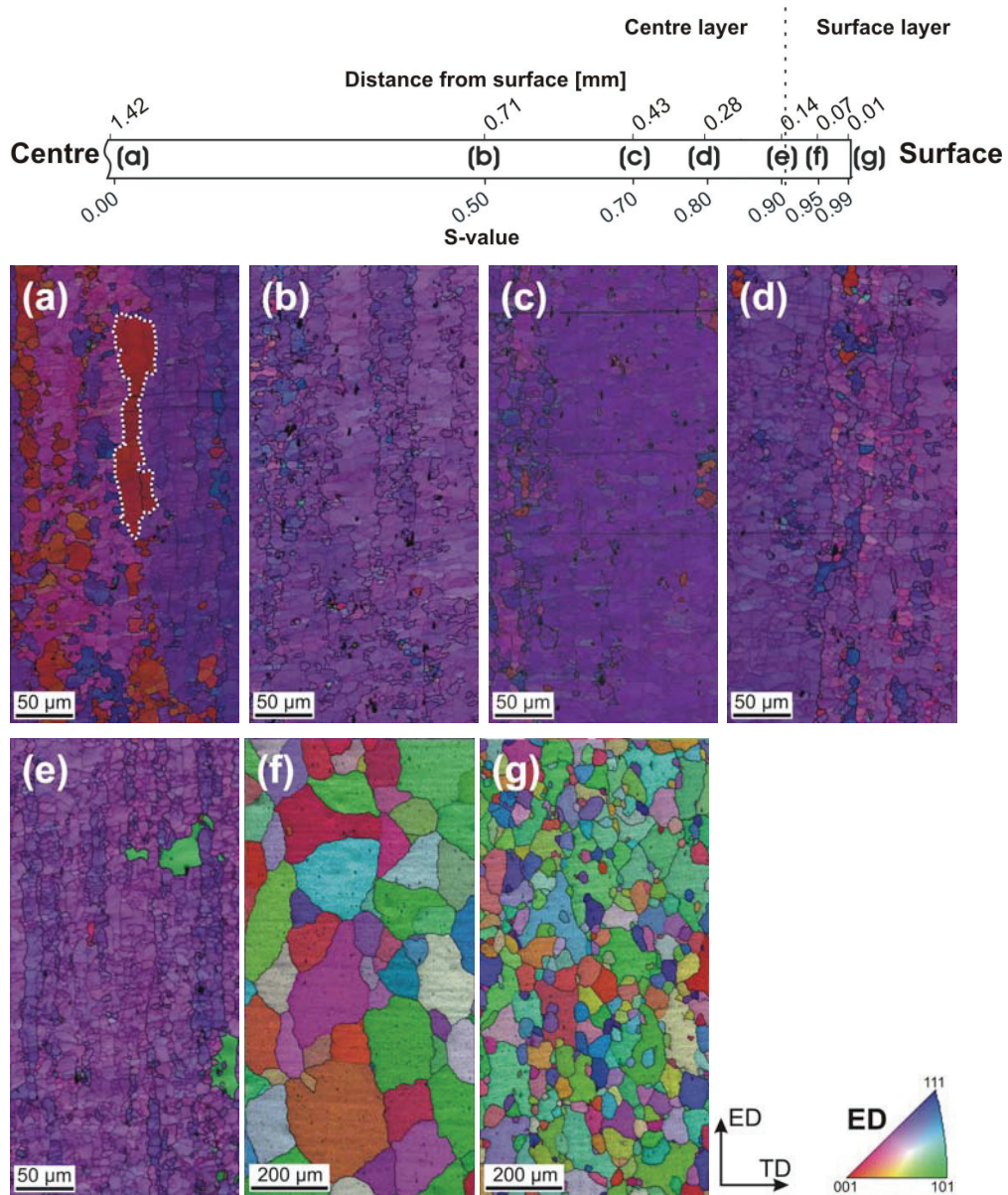


Figure 5.9 – IPF map overlaid the image quality of the EBSD patterns at different positions through the profile thickness of AA6082. The orientation data is acquired at different magnifications with 0.4 μ m and 2.0 μ m step size within the centre (a-e) and surface (f-g) layer respectively. The contour from one of the Cube bands in the centre position is highlighted with a dotted line.

Experimental results – Part A

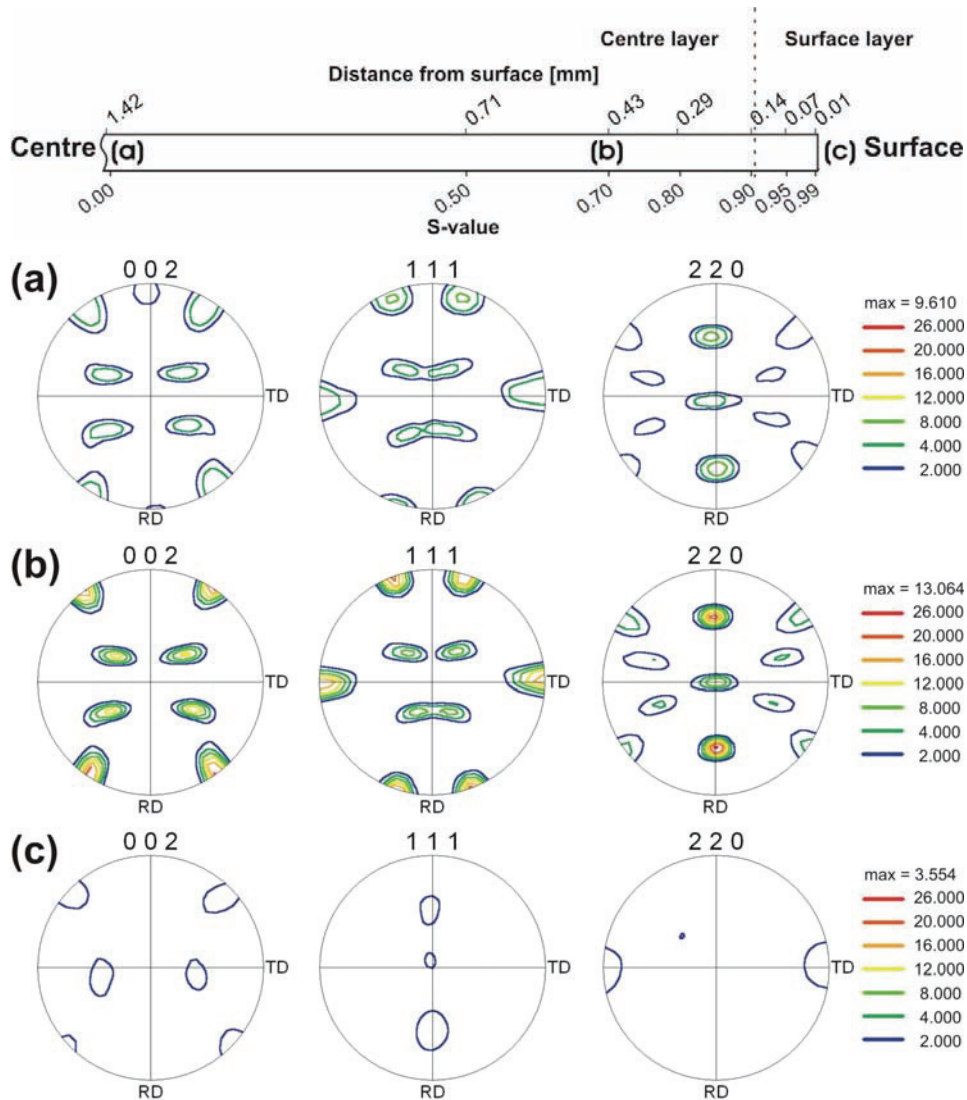


Figure 5.10 – Calculated pole figures based on orientation data at different positions through the profile thickness of AA6082.

The crystallographic texture of AA6082 can be divided into the same set of layers as the microstructure. The different positions within the centre layer ($S=0.00$ to $S=0.90$) of AA6082 have a typical deformation texture while the surface layer has close to a random texture (see e.g. Figure 5.10). Figure 5.11 summarises the area fraction of the most significant texture components through the thickness. The fraction of the Brass and the S components increases from the centre position ($S=0.00$) towards the surface layer

Experimental results – Part A

($S=0.90$) where the area fraction drops very rapidly towards zero. The observed increase of these components must be related to the increased amount of shear deformation taking place closer to the surface. Moreover, the typical recrystallization components are close to absent at all positions through the thickness. Based on the argumentation presented above, it is reasonable to assume that the observed area fractions of the Cube component is related to Cube bands like the one observed in Figure 5.9 (a). In Appendix C, calculated pole-figures based on orientation data from all positions investigated are included.

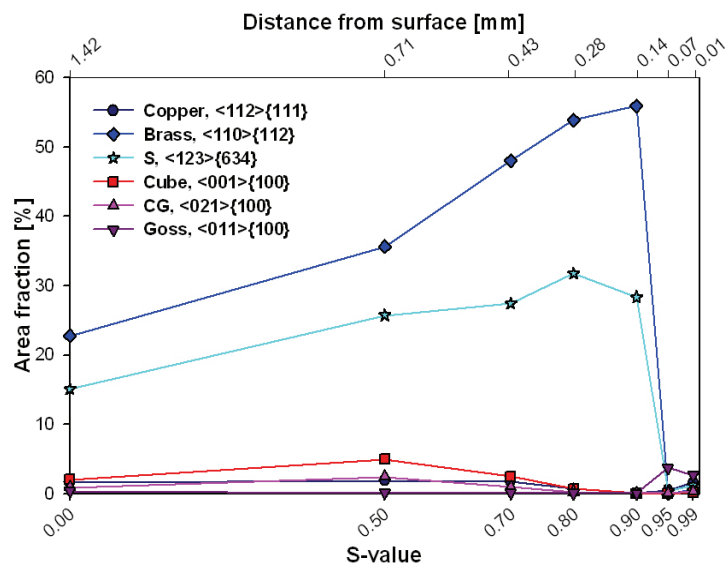


Figure 5.11 – Area fraction of different texture components at different positions through the thickness of AA6082.

5.2 Mechanical properties and anisotropy

Mechanical properties are investigated at different positions through the thickness of both alloys by means of tensile tests. In addition, full thickness specimens are tested after extrusion and subsequent artificial ageing treatments. The tensile specimens are machined from the 0°, 45° and 90° directions related to the ED in order to investigate the directional dependency of the mechanical properties (anisotropy), including the plastic strain ratio (r -value).

5.2.1 Mechanical properties

Anisotropy vs. temper condition (Full thickness studies):

The full thickness true stress-strain curves in Figure 5.12 and Figure 5.13 present the mechanical properties of AA6063 and AA6082 for different temper conditions. Notice that a different scaling of the true strain axis is used for the T6 and T7 conditions. The alloys are investigated in different material conditions at an initial strain rate of $1.1 \times 10^{-3} \text{ s}^{-1}$. From the figures, it is evident that the recrystallized profile (AA6063) has a significantly lower strength than the non-recrystallized AA6082.

Experimental results – Part A

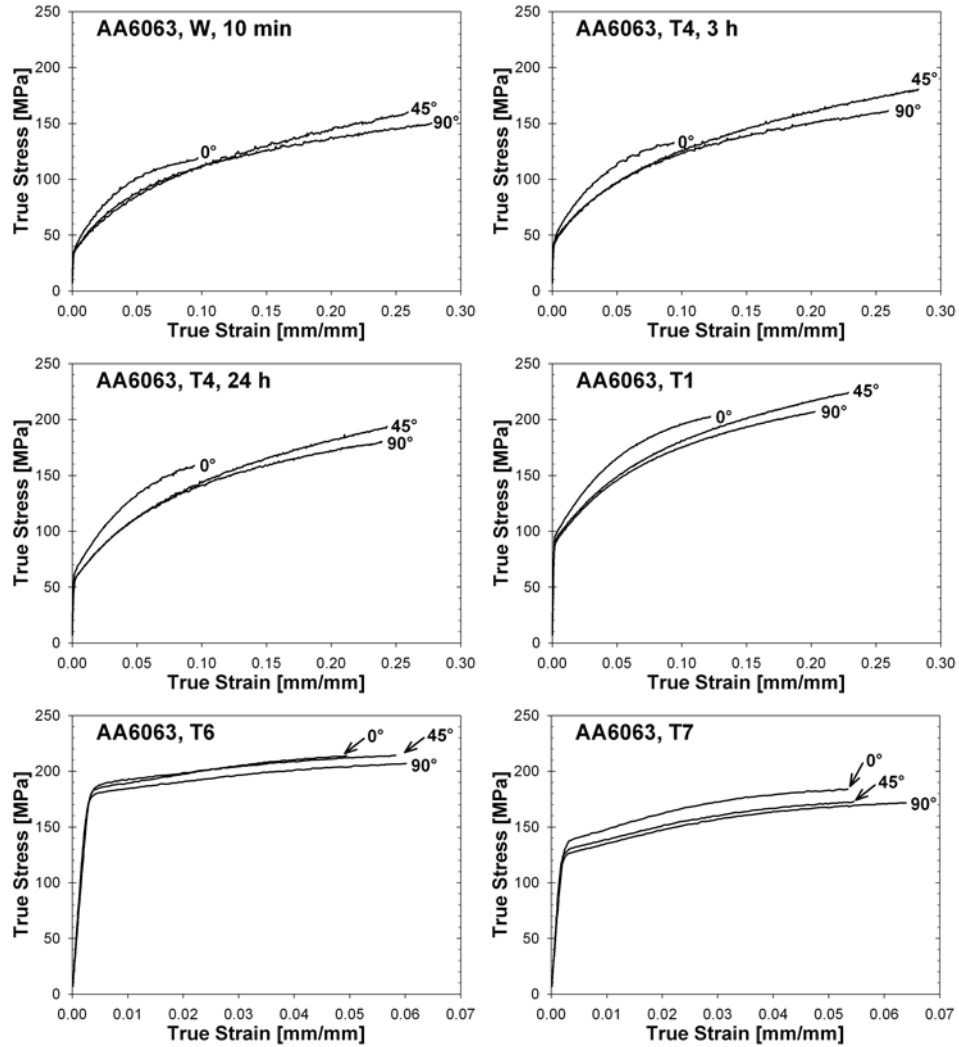


Figure 5.12 – True stress-strain curves 0°, 45° and 90° related to ED at different material conditions of AA6063 obtained with an initial strain rate of $1.1 \times 10^{-3} \text{ s}^{-1}$. Note the change of tensile strain-axis scaling for the two lower figures.

Experimental results – Part A

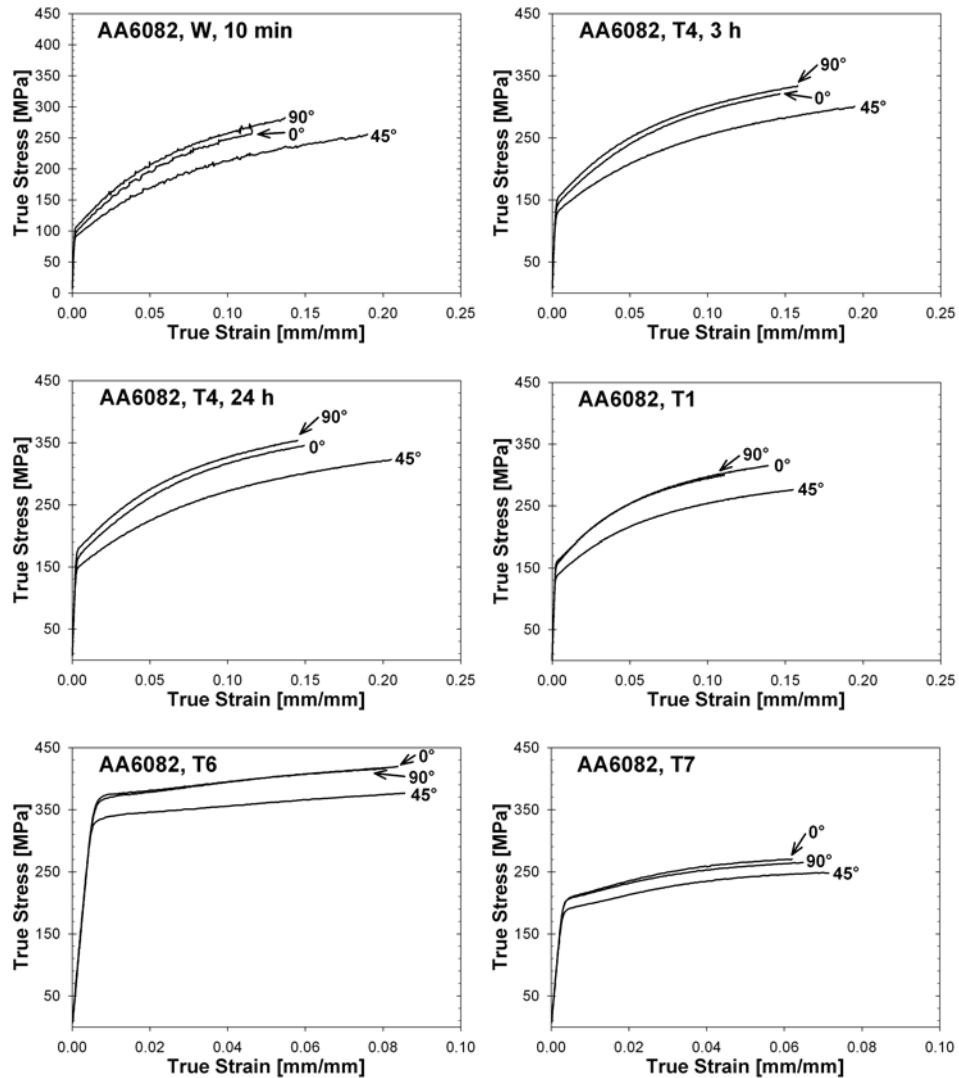


Figure 5.13 – True stress-strain curves 0°, 45° and 90° related to ED at different material conditions of AA6082 obtained with an initial strain rate of $1.1 \times 10^{-3} \text{ s}^{-1}$. Note the change of true true-axis scaling for the two lower figures.

In general it is observed that the mechanical properties are improved after both natural and artificial age-hardening, i.e. the precipitates results in a considerable strengthening contribution. When compared to the solutionised (W) condition, both the yield and ultimate tensile strength of both alloys are close to doubled after age-hardening to the peak aged (T6) condition. The ageing potential of AA6xxx alloys is determined by the chemical composition of β' and β , hence by the amount of Mg and Si in solid solution

Experimental results – Part A

(Martin 1968). The alloys investigated contain approximately the same amount of Mg which is the limiting alloying element. This explains why both alloys have equivalent ageing potential despite relatively large differences in chemical composition.

Another important observation is the significant differences in mechanical properties between the naturally and artificially aged specimens. First of all, the tensile strength increases and the uniform strain decreases when artificially aged. Further, it is observed that the mechanical properties are more isotropic after artificial ageing than after natural ageing. For AA6063, it is shown that the initial yield strength is close to equal for all directions when tested in the supersaturated solid solution (W, 10min) and in the naturally aged (T4, 3 and 24 hours and T1) conditions. However, there are some minor differences when tested after artificial ageing. The 0° and 45° specimens seem to have somewhat higher initial yield stress than the 90° specimens when tested in the T6 condition, while only the 0° specimens seem to have a higher yield stress than the two other directions when tested in the T7 condition. Some variations between the different directions are also observed for AA6082. In general it is observed that the 0° and 90° directions possess close to identical properties with congruent stress-strain curves. These directions are stronger than the 45° direction both with regard to yield stress, work hardening rate and ultimate stress. However, the highest uniform strain is found for the specimens deformed 45° related to ED. As already mentioned, the figures also show that artificial ageing of both alloys results in close to isotropic but low work hardening rate, i.e. the observed anisotropy is strongly reduced. Natural ageing, on the other hand, gives rise to larger anisotropic variations. For AA6063, the specimens deformed parallel to the ED have a higher work hardening rate but considerably lower uniform strain. The work hardening rate of the 45° and 90° specimens is equal at small strains but some differences arise at higher strains. The uniform strain is nevertheless equal for these two directions.

Thickness gradient studies:

As shown above, the mechanical properties of the present two alloys are strongly texture dependent. The texture, on the other hand, is varying through the thickness. Therefore, the effect of the through-thickness gradients has been determined by performing tensile test on 0.3mm thick specimens machined from three different positions through the

Experimental results – Part A

profile thickness (see Chapter 4.2 for more detailed information concerning the sampling procedure). These investigations are only performed in material condition T1.

Figure 5.14 presents the true stress-strain curves for both alloys at the different positions and it is evident that the mechanical properties vary significantly through the profile thickness. The centre and middle positions have similar properties while the surface behaves quite differently. It is clear that the variations observed in uniform strain through-thickness are the most pronounced. Moreover, there are also some differences in initial yield strength and work hardening rate. The 0° specimens taken from the centre and middle positions of AA6063 have a much lower uniform strain than the surface position. Also the yield strength and work hardening rate are higher in these positions when deformed in this direction. On the other hand, all specimens deformed 45° related to ED have close to equal work hardening rate and initial yield strength. However, the uniform strain is significantly higher in the centre and middle positions compared to the surface position. The description of the initial yield strength and uniform strain given for the 45° direction is also valid for the 90° specimens. Moreover, it also seems like the 90° direction has a lower surface work hardening rate than the other positions investigated.

Figure 5.14 also presents the variations observed for the different positions through the thickness of AA6082. Also for this alloy there are some minor differences in work hardening rate and uniform strain. The main differences are, however, related to the initial yield strength. The centre/middle positions have the highest initial yield strength when deformed in the 0° and 45° directions, while the surface position has the highest yield strength when deformed in the transversal direction. It is also worth noticing that no measurements are reported for the middle position of the 45° direction due to problems with the tensile testing machine.

Experimental results – Part A

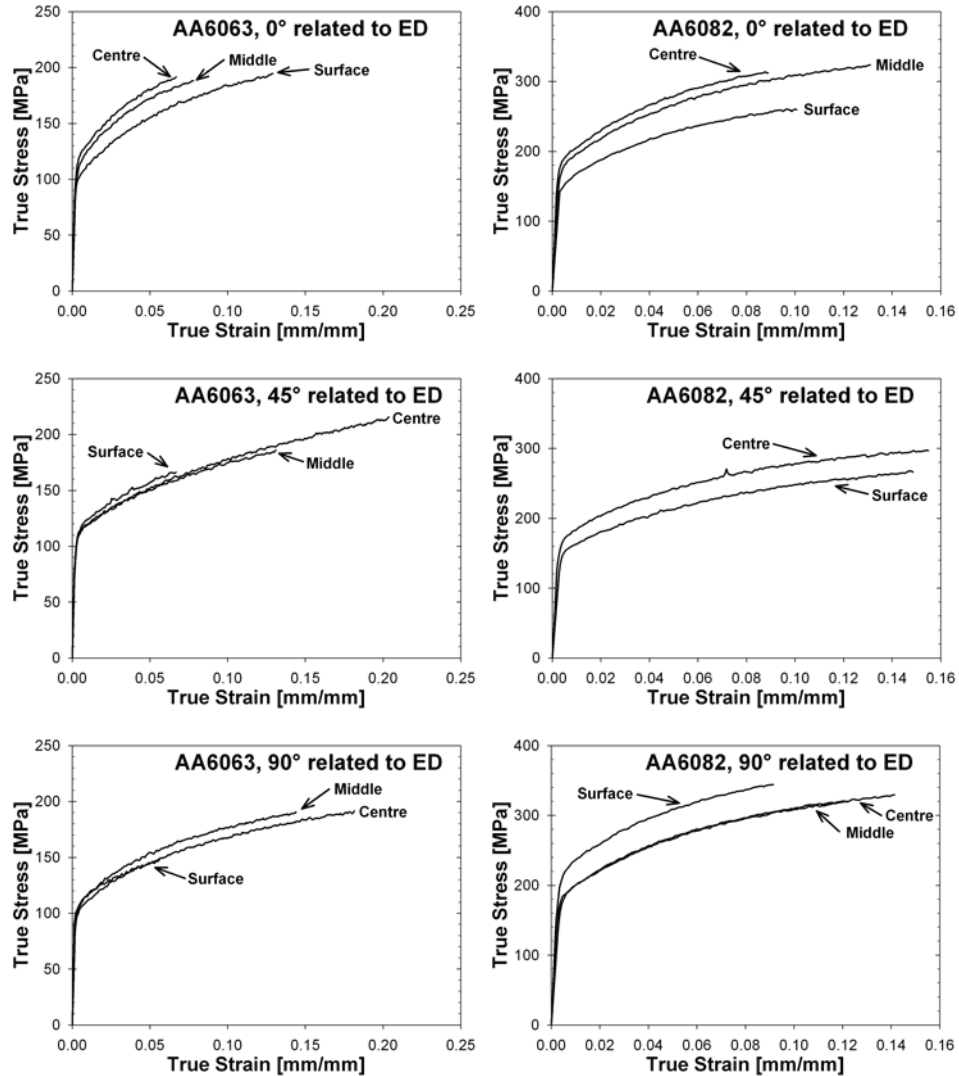


Figure 5.14 – True stress-strain curves 0°, 45° and 90° related to ED at different positions through the profile thickness obtained with an initial strain rate of $1.1 \times 10^{-3} \text{ s}^{-1}$ in material condition T1. AA6063 on the left hand side and AA6082 on the right hand side.

The measured plastic strain ratio (r -values) is also quite anisotropic and varies through the profile thickness (Table 5.3). The centre and middle positions of all directions investigated have comparable r -values for AA6063. Moreover, the plastic strain ratio at the surface is not comparable with the r -values measured in the centre and middle positions. AA6082 on the other hand, do not possess this same type of through-thickness

Experimental results – Part A

variations. This alloy has only minor variations, and the measured r -values vary less than 0.3 over the thickness. Some of these variations could even be explained by the uncertainty of the measurements.

The through-thickness r -value variations give rise to an evident through-thickness displacement gradient on the tensile specimen. This induces bending around the tensile direction during deformation and the specimens develop a transverse curvature. Hence, the fixed transverse extensometer exaggerates the measured transverse strain which again affects the experimental determined plastic strain ratio. The accuracy of the measurements worsens dramatically during deformation due to a strong increase in this transverse curvature. The accuracy of the measurements for some of the investigated positions is therefore of the order of $\pm 35\%$.

Table 5.3 – Experimental determined r -values (at a true strain of 0.05) at different positions through the profile thickness at material condition T1. The accuracy of these measurements is approximately $\pm 35\%$.

Alloy	Direction	Centre	Middle	Surface
AA6063	0°	1.2	1.0	0.4
	45°	0.1	0.1	0.3
	90°	3.5	2.4	1.3
AA6082	0°	0.5	0.3	0.5
	45°	1.1	-	2.8
	90°	1.2	0.9	1.2

5.2.2 Further details regarding age-hardening effects

Influence of properties:

The previous section has shown that the alloys investigated in this work possess significant anisotropic mechanical properties. It has also been shown that the mechanical properties are strongly affected by both natural and artificial age-hardening. In the following, the angular dependency of the mechanical properties of all material conditions is compared.

The effect of age-hardening on the mechanical properties in AA6063 and AA6082 is shown in Figure 5.15 and Figure 5.16 respectively. It is known that mechanical anisotropy in general is affected by age-hardening. The anisotropy in the solution-heat-treated condition (W, 10min) is mainly controlled by the crystallographic texture and in some degree the microstructure, i.e. AA6063 and AA6082 have dissimilar mechanical anisotropy prior to age-hardening. Age-hardening reduces the contribution from crystallographic texture due to introduction of precipitates. The anisotropy of the two alloys will therefore become reduced after both natural and artificial age-hardening.

The true yield stress of both alloys in the W, 10min temper is relatively isotropic. Both natural and artificial ageing result in a close to isotropic increase in yield stress, i.e. the alloys maintain close to isotropic yield properties after age-hardening. AA6082 has a somewhat anisotropic yield stress in the T6 conditions but this anisotropy disappears in the T7 condition. The difference between the minimum and maximum value in the T6 temper is less than 10%. It is also important to remember that it is difficult to accurately determine the yield stress of aluminium alloys, i.e. some of the observed differences can be related to measurement deviations.

The ultimate tensile stress is much more anisotropic than the yield stress. It could be expected that the ultimate tensile stress should follow the same trends as observed for the true yield stress. However, it is important to remember that the work hardening will be strongly affected by precipitation which in turn affects the activation of slip systems.

Experimental results – Part A

However, a main finding is that the observed anisotropy in the ultimate tensile stress is reduced with age-hardening. AA6063 has completely isotropic properties in both the artificially aged conditions while AA6082 maintains some anisotropy in the T6 temper and is fully isotropic in the over-aged condition.

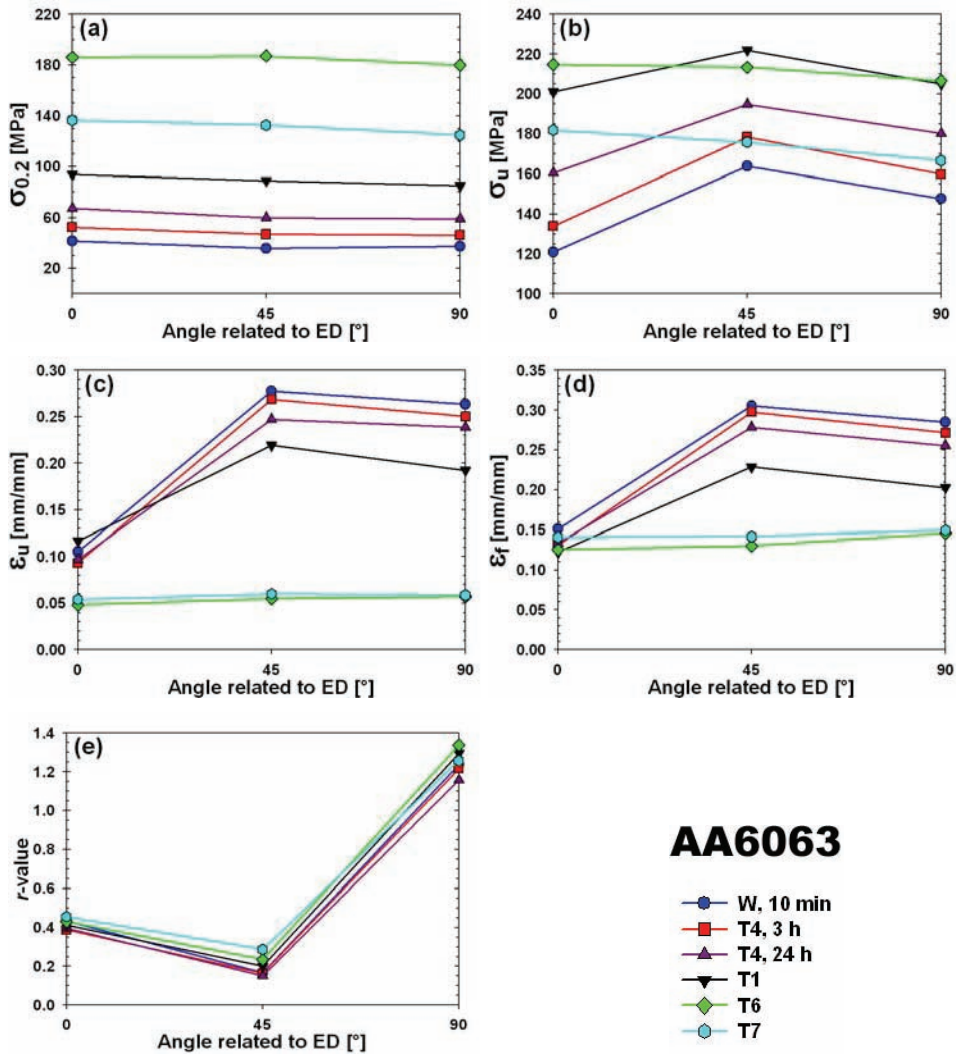


Figure 5.15 – The effect of ageing on mechanical properties and anisotropy of AA6063. (a) Yield stress (b) ultimate tensile stress (c) true uniform strain (d) true fracture strain and (e) r -value at a true strain of 0.05.

Experimental results – Part A

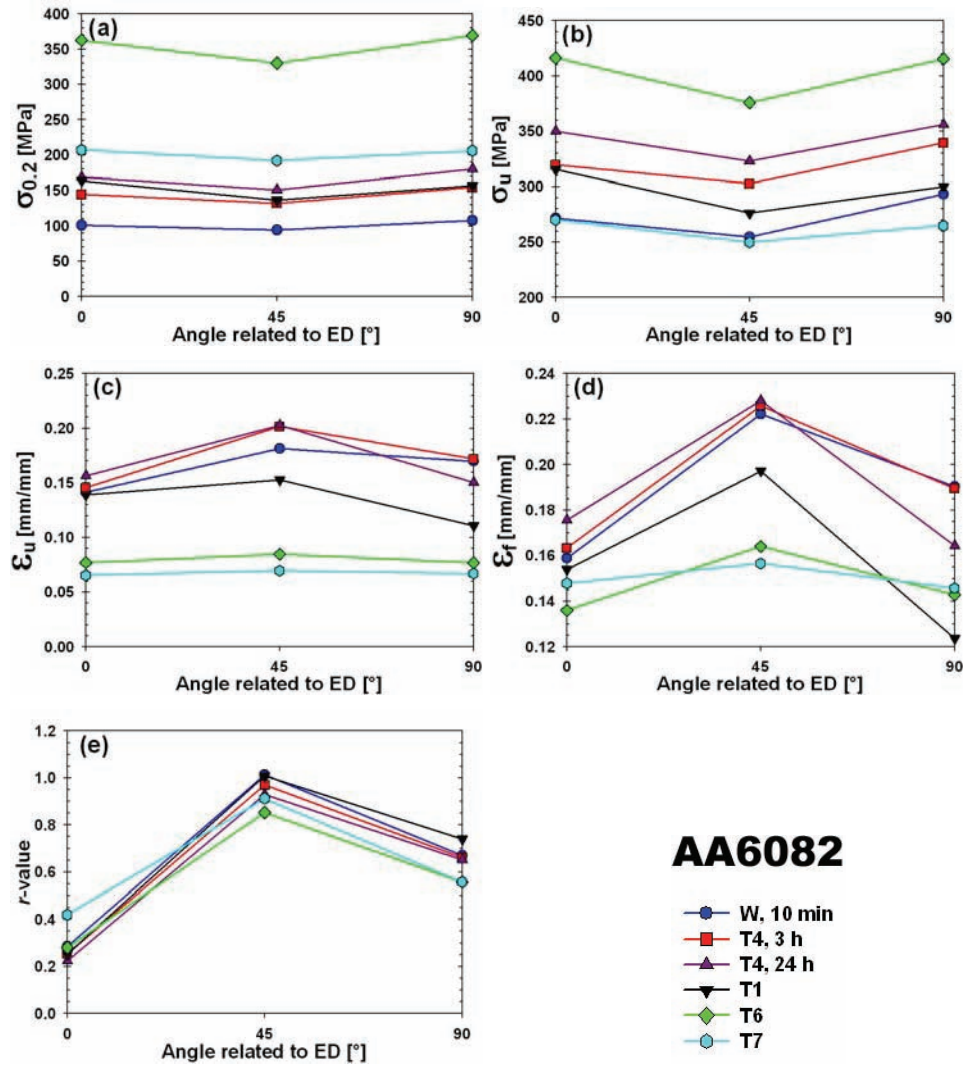


Figure 5.16 – The effect of ageing on mechanical properties and anisotropy of AA6082. (a) Yield stress (b) ultimate tensile stress (c) true uniform strain (d) true fracture strain and (e) r -value at a true strain of 0.05.

Experimental results – Part A

Furthermore, the above curves show that the uniform strain is anisotropic and that the ϵ_u -value is reduced upon both natural and artificial aging. Another main finding for both alloys is that the uniform strain anisotropy is reduced with increasing RT storage time and by artificial aging to tempers T6 and T7, i.e. they are isotropic with regard to uniform strain in the T6 and T7 conditions. Further, the 45° direction has the highest uniform strain when aged at RT and the reduction in the uniform strain upon aging is very pronounced.

The trend observed for the uniform strain is repeated for the fracture strain (ϵ_f), i.e. the anisotropy is reduced with increasing RT storage time and by artificial aging to tempers T6 and T7. However, in the T6 condition the fracture strain is not as isotropic as the uniform strain.

The observed trends for the r -values in the two investigated alloys are more complicated. In the solution-heat-treated condition, the two alloys have completely opposite behaviour with regard to the plastic strain ratio. AA6063 has the highest r -values in the 0 and 90 directions and the lowest r -value in the 45 direction (Figure 5.15), while the behaviour is completely opposite for AA6082 (Figure 5.16).

Notice that the quantitative alteration in r -value during ageing is very limited. It is also important to bear in mind that the accuracy of this type of r -value measurements is poor ($\pm 10\%$) as shown in the previous section. Consequently, some of the alterations are directly related to inaccuracy from the measuring technique. However, the observed trends should still be valid, i.e. also the r -values of both alloys become more isotropic due to age-hardening.

Influence on flow curves

Age-hardening is known to change the mechanical properties of Al-Mg-Si alloys. The changes due to ageing of the specimens deformed 0° related to ED are given in Figure 5.17. Appendix D presents the same set of results from all the deformation directions investigated in this work (0°, 45° and 90°). The strength of both alloys increases substantially during natural ageing. However, stress strain curves indicate that the serrated yielding gives rise to some reduction in uniform strain. In other words, the

Experimental results – Part A

uniform strain increases with longer ageing time at room temperature. For AA6063, the observed serrated yielding is still visible after 24 hours of natural aging, while for AA6082, this jerky flow is only visible in the solution-heat-treated condition (W, 10min).

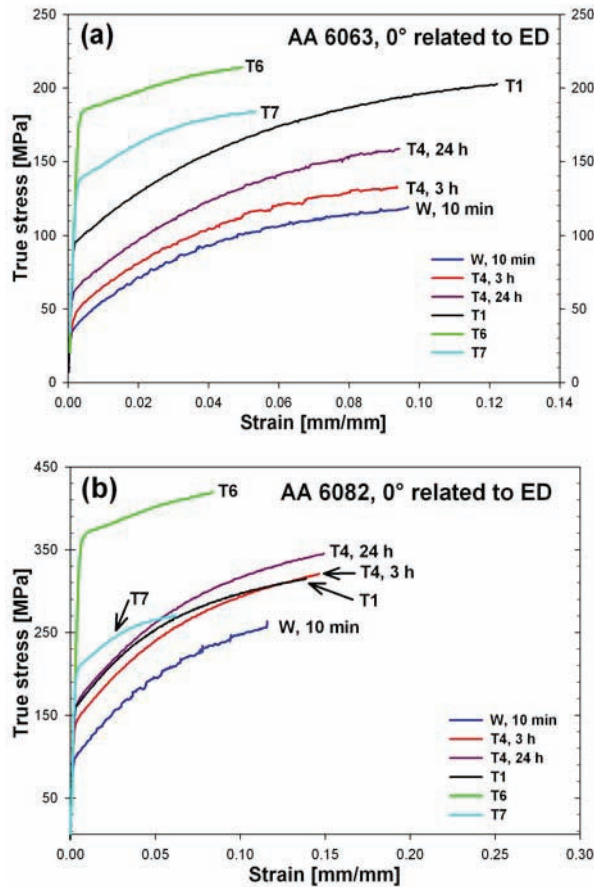


Figure 5.17 – True stress-strain curves parallel to ED for different material conditions. (a) AA6063 and (b) AA6082.

Moreover, Figure 5.17 also shows that the increase in strength and work hardening rate in the naturally aged condition is more than twice as high for AA6082 as for AA6063. Artificial aging to condition T6 exhibits the highest strength while further ageing to the over-aged condition (T7) reduces the strength significantly. The uniform strain is also shown to be heavily reduced after artificial age-hardening. Further, the work hardening rate at low strains is maintained or even improved for the T7 condition compared to the

Experimental results – Part A

T6 condition, even though the strength is considerably reduced. The figure shows that the work hardening rate in the T7 condition is quite similar to the work hardening rates observed after naturally ageing of AA6063, while for AA6082, the work hardening rate is only half of that observed during natural ageing. These reflections are also valid for the 45° and 90° directions as shown in Appendix D.

Influence on plastic strain ratio (*r*-values):

The *r*-value, which is often referred to as the Lankford coefficient or plastic strain ratio, is the ratio between the width and the thickness plastic strain. This parameter is often used to describe the mechanical anisotropy of materials deformed by simple tension. It has been shown that a material with an *r*-value of 1 possesses isotropic mechanical properties. However, it is very difficult to measure the plastic strain ratio accurately by use of extensometers, therefore the accuracy of *r*-value measurements are often of the order of ±10%.

Both alloys investigated show strong mechanical anisotropy in the solution-heat-treated condition (W, 10min), see e.g. Figure 5.12 and Figure 5.13. Calculations of the *r*-values for all the investigated material conditions are therefore performed in order to study the mechanical anisotropy. Figure 5.18 and Figure 5.19 present the evolution in experimental determined *r*-values during simple tension of AA6063 and AA6082 respectively. The figures show that both alloys have very anisotropic properties and the plastic strain ratio is clearly direction-dependent, i.e. large differences were observed between the investigated testing directions.

The *r*-values of AA6063 (Figure 5.18) are approximately 1.2 for all material conditions when tested in the transverse direction. This means that the width strain of AA6063 is roughly 20% larger than the thickness strain. Hence, AA6063 has close to isotropic properties when deformed 90° to ED. However, when tested in the two other directions (0° and 45°), AA6063 possesses very anisotropic and low *r*-values. Here, the *r*-value in the 0° and 45° directions is typically ~0.4 and ~0.2 respectively. Such *r*-values mean that for specimens taken from these directions, the thickness strain is much larger than the width strain. AA6082, on the other hand, has more or less isotropic plastic flow when deformed 45° related to ED, i.e. $r \approx 0.95$. Also for this alloy the *r*-values are lower than

Experimental results – Part A

for the two other directions investigated (0° and 90°). Hence AA6082 possesses anisotropic flow properties when tested in these two directions. Also, the r -value of AA6082 seems to be more dependent upon the material condition than for AA6063. Some distinct differences were observed between the naturally and artificially aged material conditions, especially for the 90° specimen. However, the r -values of the 0° and 90° directions in AA6082 are typically ~ 0.3 and ~ 0.6 respectively.

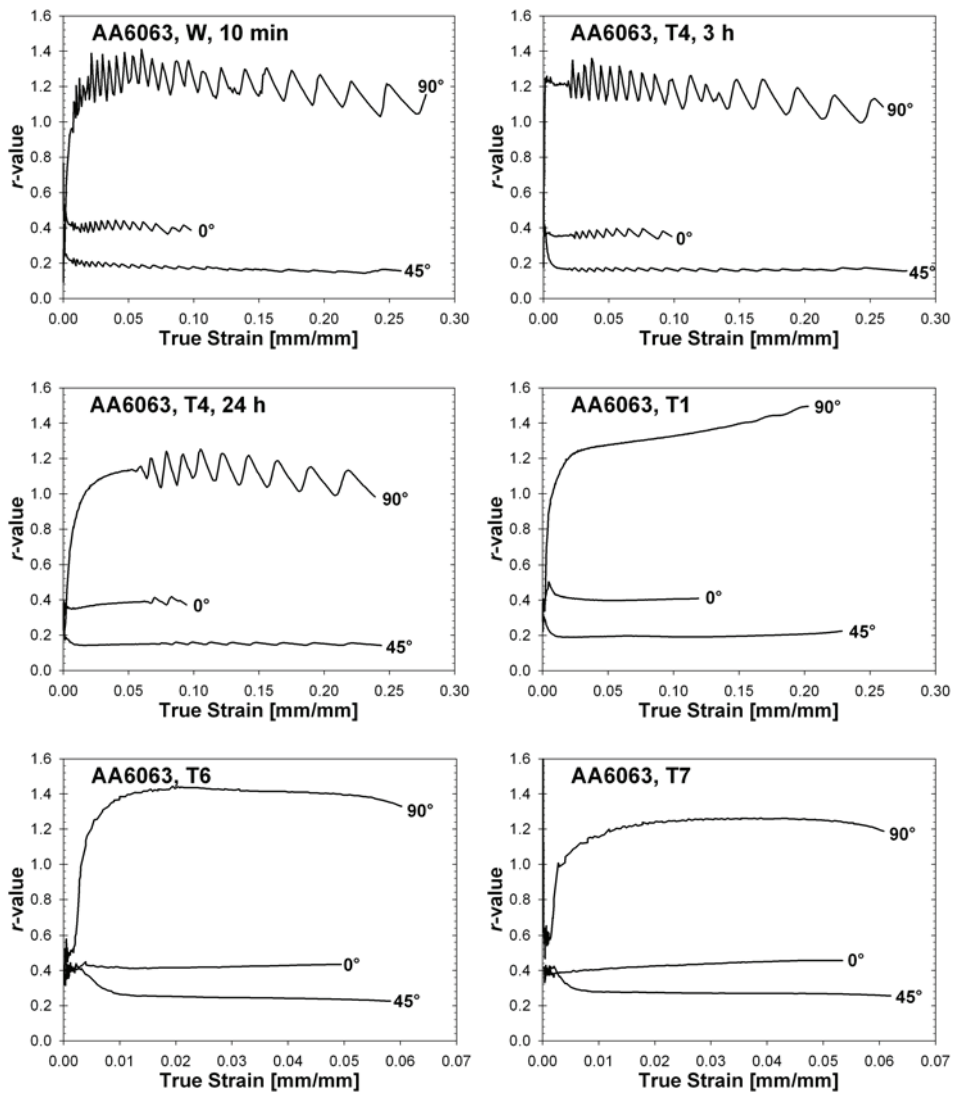


Figure 5.18 – Plastic strain ratio curves 0° , 45° and 90° related to ED at different material conditions of AA6063 obtained with an initial strain rate of $1.1 \times 10^{-3} \text{ s}^{-1}$.

Experimental results – Part A

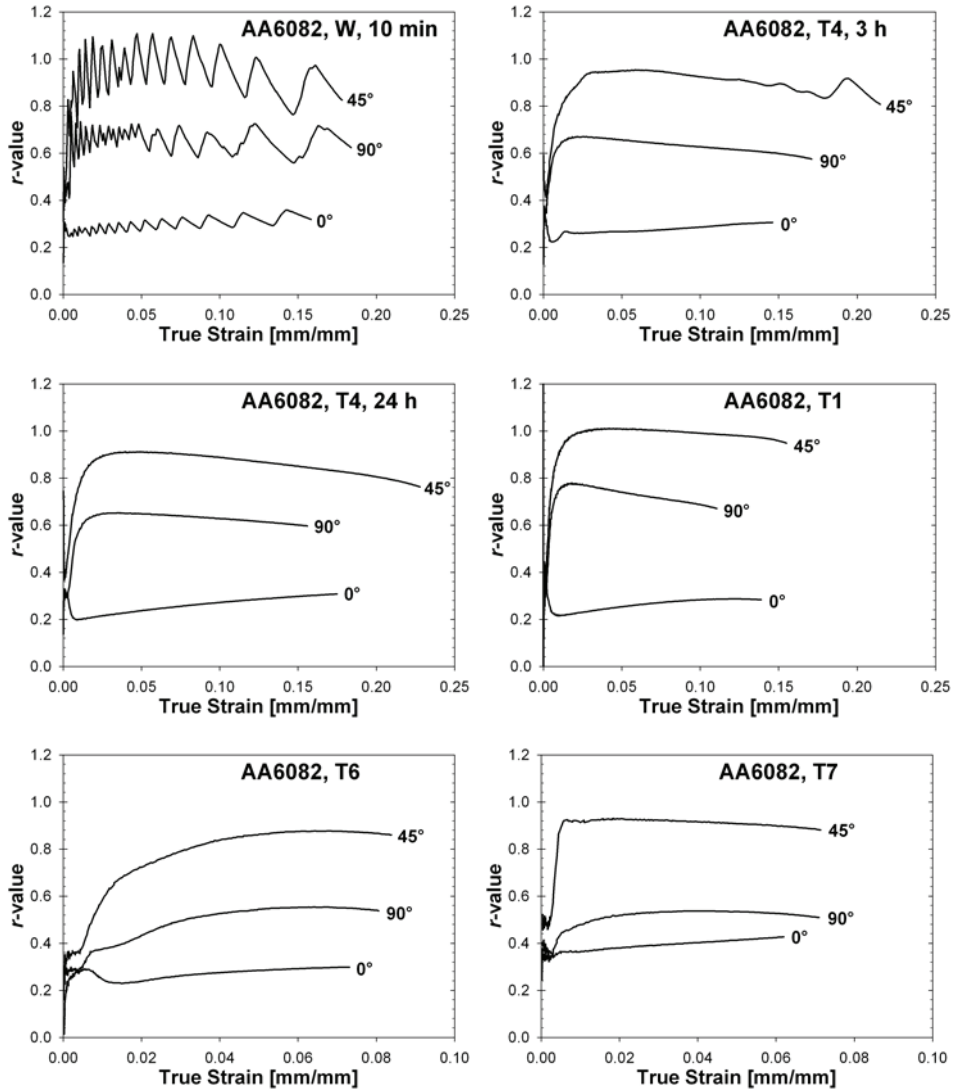


Figure 5.19 – Plastic strain ratio curves 0°, 45° and 90° related to ED at different material conditions of AA6082 obtained with an initial strain rate of $1.1 \times 10^{-3} \text{ s}^{-1}$.

The *r*-value curves obtained from the specimens deformed in the solution-heat-treated condition of both alloys, and the two naturally aged conditions of AA6063 have a characteristic wavy shape. There are also traces of waves in the T4, 3h specimens deformed in the 45° direction of AA6082. This wavy shape is related to the serrated yielding, and each peak in the curves corresponds to a deformation band passing the transverse extensometer. When the band passes the extensometer the negative transverse

Experimental results – Part A

strain will rapidly increase, i.e. the r -value increases. With artificial ageing, the serrated yielding will gradually diminish and the r -value curves become straight lines. It is clear that ageing postpones the onset of serrated yielding to higher strains as shown in both Figure 5.18 and Figure 5.19. It is also noteworthy that the onset-strain of serrated yielding seems to be direction-dependent for alloy AA6063 T4, 24h, but not obvious for the other ageing conditions. Also, the amplitude caused by the serrated yielding is very anisotropic.

Moreover, the general shape of the r -value curves depends on the tensile direction and the alloy composition, i.e. the shape of the r -value curves is texture dependent. The characteristic shape is present also during the wavy behaviour but it is more evident after the serrated yielding has come to an end. The r -values in the 0° and 45° directions of AA6063 are almost strain independent, being constant throughout the deformation process. In general, the 90° direction has a gradual reduction in the r -value with increasing strain, but for the T1 condition the slope is positive.

As a first approximation, all r -value curves for AA6082 have a linear shape, especially in the solution-heat-treated and naturally aged condition. The plastic strain ratio in the 45° and 90° directions is reduced with increasing strain while the opposite behaviour is observed when the specimens are deformed parallel to the ED. Closer investigations of the artificially aged material reveal that the plastic strain ratio increases for all directions at small strains while decreases again at higher strains. This means that the plastic strain rate evolution goes through a local maximum during deformation. Indications of the same behaviour are also observed after artificial ageing of AA6063 (see Figure 5.18).

5.2.3 Age-hardening vs. anisotropy and shape

The end of cross-section shape (Figure 5.20) of both alloys in the solution-heat-treated condition is concave when deformed in the 0° and 90° directions and convex when deformed at 45°. This means that the transverse strain is highest at the surface when deformed in the 45° direction and in the centre part of the profile when deformed in the two other directions.

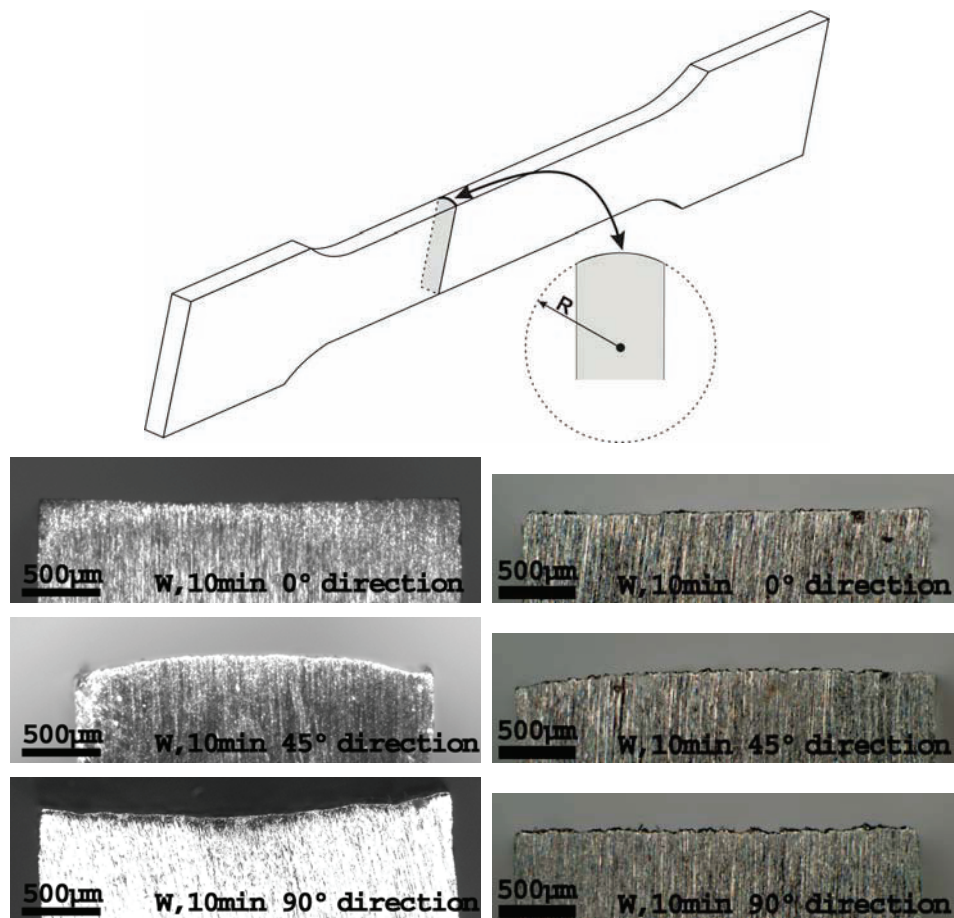


Figure 5.20 – End of cross-section shape after simple tension to the uniform strain in material condition W, 10min. AA6063 (left) and AA6082 (right). The R-value presented in the illustration defines the radius of curvature over the thickness.

Experimental results – Part A

The longitudinal strain is assumed to be independent of the position through the thickness, i.e. the transverse strain is directly linked to the r -values. In other words, the profile has the highest r -value in the centre of the profiles when deformed parallel and perpendicular to the ED and at the surface when deformed 45° related to ED. The effect of the through-thickness gradient is most evident in the 45° and 90° direction specimens. However, it is worth noticing that the affect of the through-thickness variations is more pronounced for AA6063 than for AA6082. Micrographs of the end of cross-section shape for all the specimens investigated are presented in Appendix E.

The end of cross-section shape changes during age-hardening and the through-thickness radius of curvature were determined in order to quantify these changes. Figure 5.21 presents the evolution in the inverse radius of curvature ($1/R$) during ageing of AA6063, and it is evident that the differences over the thickness are strongly reduced during ageing. A large absolute value means that the specimen has a large curvature over the thickness, while a small value means that the specimen thickness is close to constant. It should be noted that it is difficult to determine the radius of curvature accurately especially when the specimen cross-section shape is close to horizontal, i.e. the uncertainty of these measurements is more than $\pm 17\%$.

The end of cross-section shape is also altered due to age-hardening. The characteristic concave and convex shapes of the thickness direction are very evident both in the solution-heat-treated and the naturally aged tempers (Figure 5.20). However, the characteristic shapes disappear when AA6063 is artificially aged to T6 and T7, i.e. $1/R$ becomes close to zero. The material obtains more isotropic properties through the profile thickness and the thickness direction shape is close to horizontal. It is therefore reasonable to claim that age-hardening reduces or even removes the effect of through-thickness gradients.

Experimental results – Part A

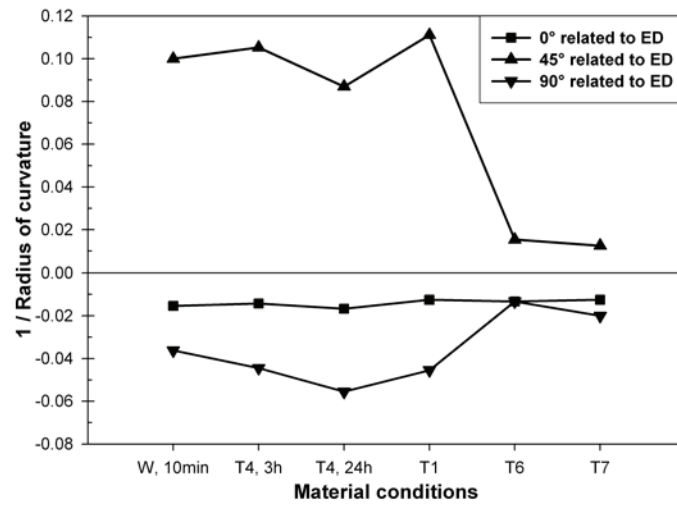


Figure 5.21 – Evolution in the end of cross-section shape of AA6063 during ageing.

Part B: SEM In-situ investigations of plasticity – Slip activity, grain rotation and texture evolution

Part B presents the results from in-situ deformation investigations (simple tension) in the SEM. SEM in-situ investigations facilitates studies on a grain scale, i.e. the grain rotation, plasticity and local strain distribution have been investigated. Also, the global texture evolution has been investigated by performing in-situ global texture measurements using EBSD.

5.3 Initial investigations

This experimental technique is relatively new and has previously never been used on extruded profiles of commercial Al-Mg-Si alloys. It was therefore necessary to verify the testing conditions utilised by performing some initial investigations prior to the in-situ experiments. A recrystallized microstructure is desired in order to obtain high quality EBSD patterns within a reasonable period of time and the SEM in-situ investigations are therefore only performed on the recrystallized AA6063.

First the room temperature (RT) creep rate is determined by performing creep experiments. The creep rate is critical with regard to the testing conditions, since it is important to select a strain rate higher than the current creep rate. It is known that plastic deformation leads to increased creep due to accumulation of internal stresses in the material. This means that the creep rate just prior to the ultimate stress is critical with regard to the in-situ experiments. Creep experiments performed at different nominal stresses in the 0°, 45° and 90° directions are presented in Figure 5.22. This figure confirms that the RT creep rate of AA6063 never exceeds $1 \times 10^{-6} \text{ s}^{-1}$. An initial strain rate of $1 \times 10^{-4} \text{ s}^{-1}$ is therefore selected for the in-situ deformation investigations performed on this material.

Experimental results – Part B

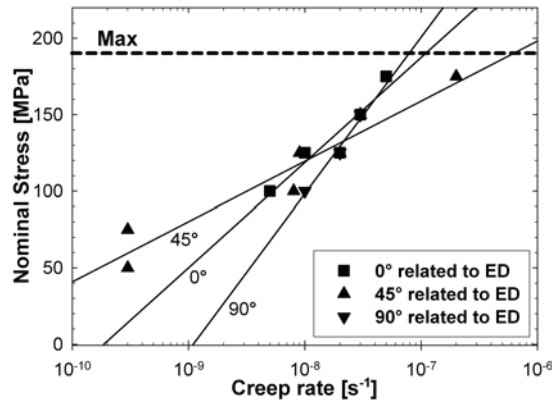


Figure 5.22 – Measured room temperature creep rate at different nominal stresses in the 0°, 45° and 90° directions of AA6063 in material condition T1. The maximal nominal stress is indicated by the dotted line.

Further, the in-situ deformation specimens are deformed in steps of typical 3% axial elongation. The deformation process has to be stopped in order to perform static investigations, i.e. EBSD mapping of the specimen surface. Figure 5.23 presents the average stress vs. strain curve obtained from the load and displacement transducer for typical in-situ experiments 0°, 45° and 90° related to ED. The same figure also presents curves from specimens deformed continuously with the same initial strain rate. The stress drops observed in the in-situ deformed curves correspond to the pauses necessary for the static investigations, and are related to stress relief in the material. However, these stress drops are not expected to have any influence on the deformation process since the overall shape from both sets of stress vs. strain curves is close to identical.

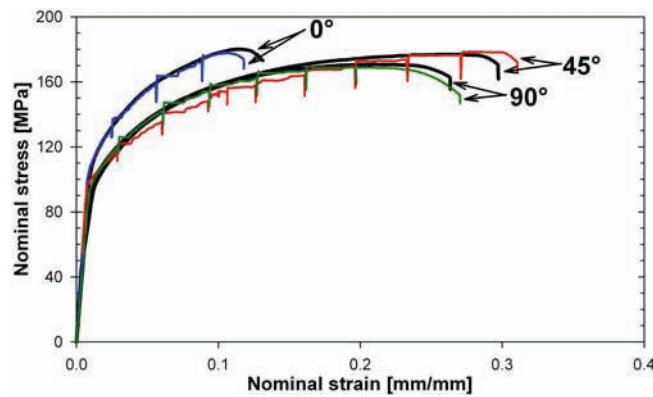


Figure 5.23 – Stress vs. strain curves obtained from the in-situ tensile machine showing no difference between the continuous and discontinuous deformed specimens.

5.4 Global texture evolution with increasing strain

In-situ specimens from the centre layer of AA6063 are deformed 0° , 45° and 90° related to ED with an initial strain rate of $1 \times 10^{-4} \text{ s}^{-1}$. The specimens are deformed in steps of 3% axial elongation in order to perform texture measurements, and in consequence obtain information of the global texture evolution. The initial crystallographic texture of AA6063 consists mainly of the Cube, CG and Goss components as shown in Figure 5.8. Figure 5.24 to Figure 5.26 present the initial texture as well as the texture at the uniform strain and some intermediate strains for specimens deformed in the 0° , 45° and 90° directions respectively.

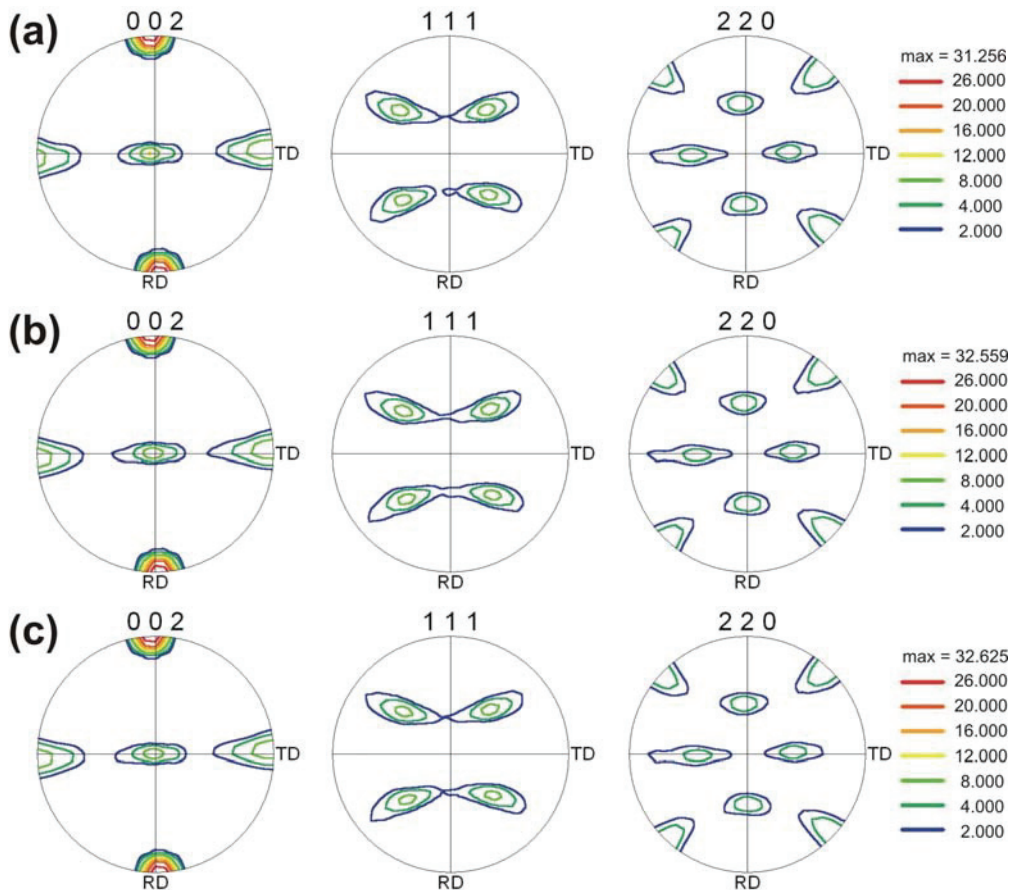
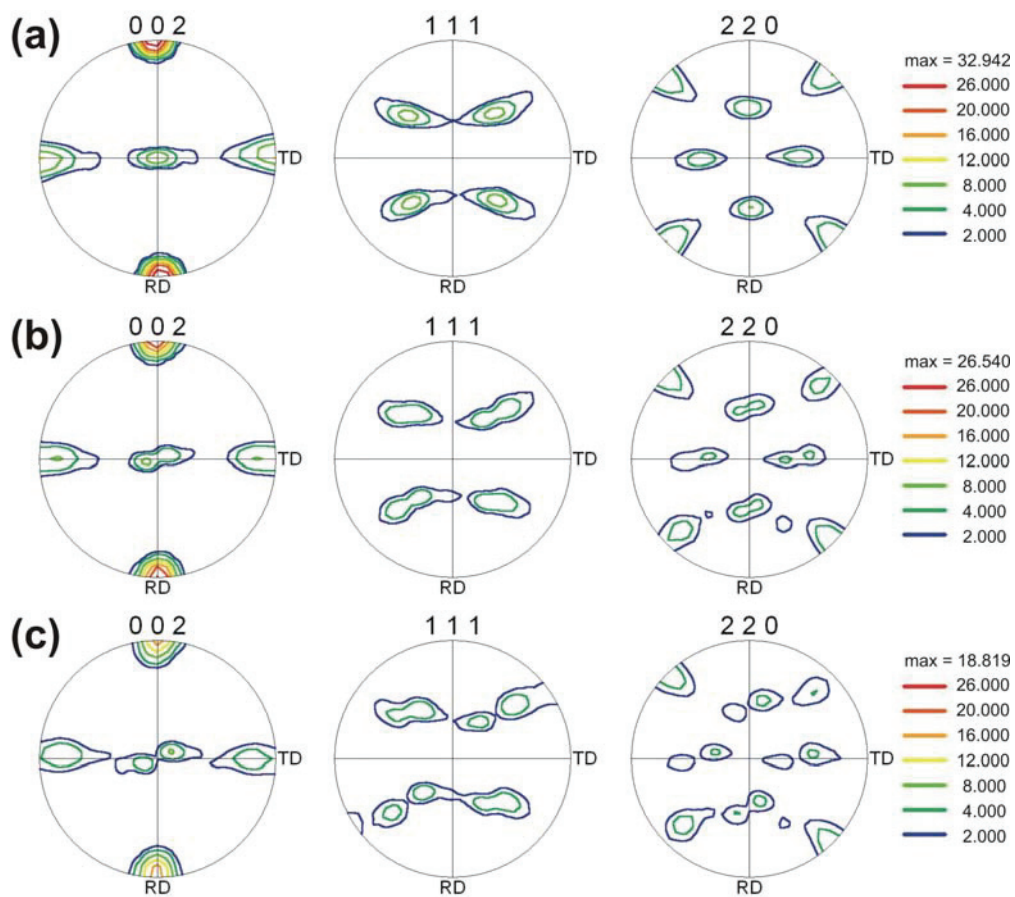


Figure 5.24 – Calculated pole figures based on orientation data after different amounts of axial elongation in the 0° direction. (a) Initial orientation (b) 6% and (c) uniform strain (12%).

Experimental results – Part B

The texture is relatively stable during deformation 0° and 90° related to ED, while deformation in the 45° direction gives rise to quite large crystallographic rotations. Figure 5.24 clearly shows that the crystallographic texture is totally unaffected by deformation parallel to the ED. The pole-figures both after 6% deformation and at the uniform strain are close to identical with the pole-figure calculated based on the orientations acquired prior to deformation. The slight disparities can easily be explained by the inaccuracy of the calculation method.



(Figure continues on next page)

Experimental results – Part B

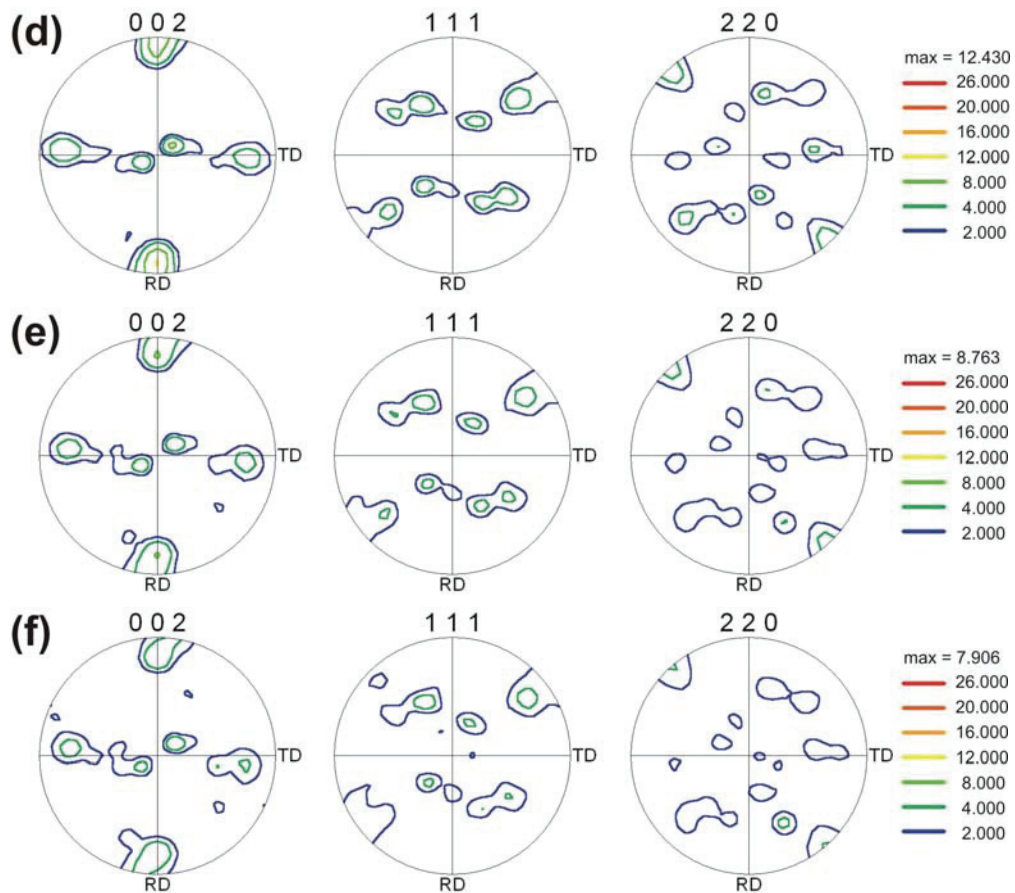


Figure 5.25 – Calculated pole figures based on orientation data after different amounts of axial elongation in the 45° direction. (a) Initial orientation (b) 6% (c) 12% (d) 18% (e) 24% and (f) uniform strain (27%).

As already mentioned, substantial crystallographic rotations are observed when the material is deformed 45° to ED (Figure 5.25). The pole-figures show that the 45° specimen rotates such that the [111] becomes aligned with the deformation direction (DD). Further, the same figure shows that grains initially having a [101] parallel to DD rotate toward more stable orientations with a more random distribution of the [101] direction. Notice also that the material rotates away from having a [100] parallel to the ND.

Experimental results – Part B

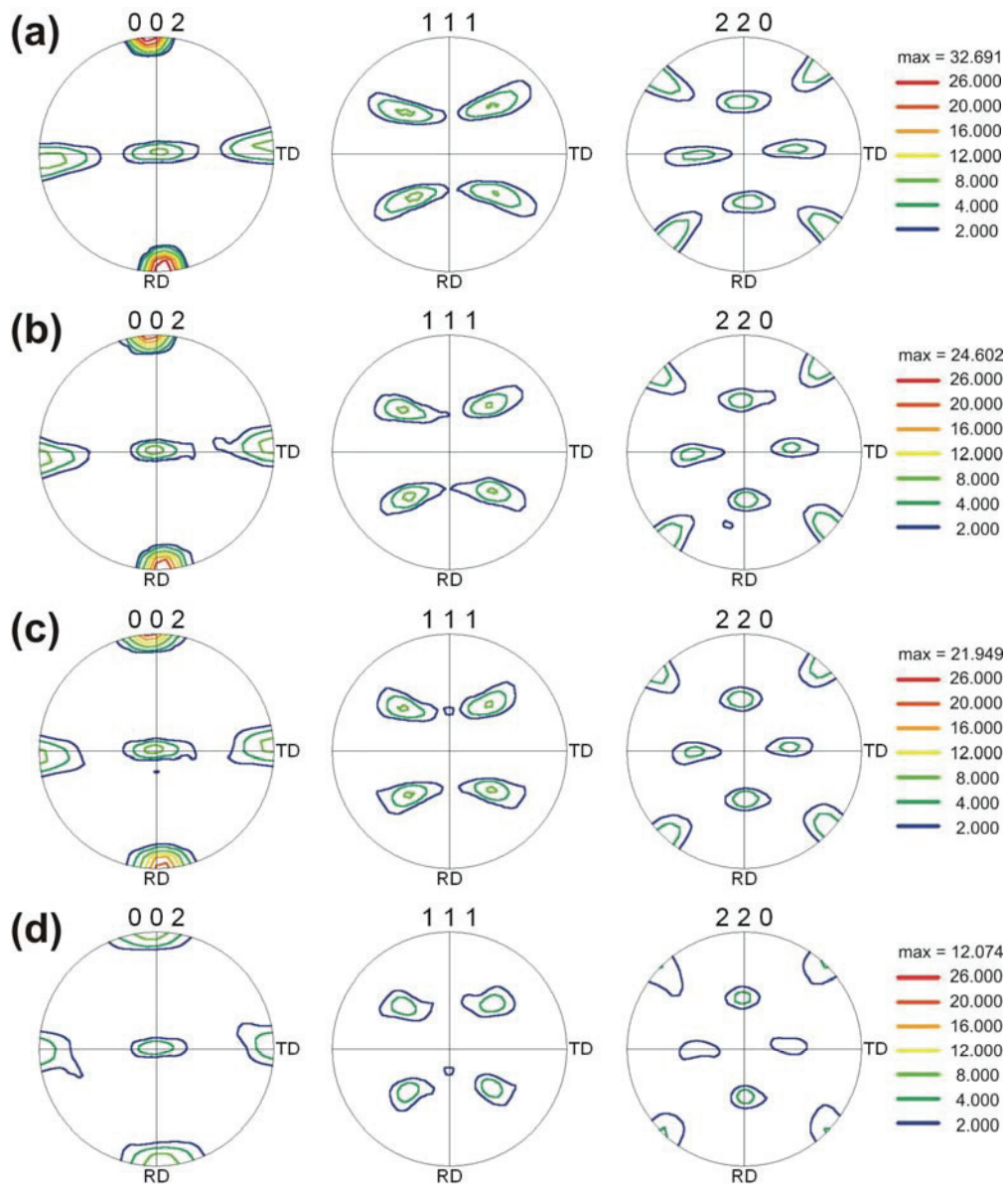


Figure 5.26 – Calculated pole figures based on orientation data after different amounts of axial elongation in the 90° direction. (a) Initial orientation (b) 6% (c) 12% and (d) uniform strain (21%).

Experimental results – Part B

Figure 5.26 shows that the texture hardly is affected when deformed 90° to ED. The orientation of the slip planes and directions resembles those for specimens deformed parallel to ED, hence it should be expected that the crystallographic texture of the 90° specimen was unaffected by deformation. However, there are still some vague indications of texture evolution for this specimen. The pole-figures show that grains initially having close to a $[100]$ parallel to the DD (slightly ED rotated grains), rotate toward aligning the $[100]$ to the DD. This means that the peak close to the transversal direction of the pole-figure becomes somewhat narrower.

Moreover, more detailed examinations of the texture evolution during deformation (Figure 5.27) reveal other important differences between the three directions investigated. The evolution of the three most important texture components (Cube, CG and Goss) has been investigated in great detail. All the investigated texture components have a $[100]$ parallel to the DD when deformed parallel to the ED. Figure 5.27 shows that the intensity of these components is unaffected by deformation, thus indicating that grains having a $[100]$ parallel to the DD tend to be stable. Cube oriented grains also have this $[100]$ direction parallel to the DD when deformed 90° to ED, and the figure shows that the area fraction of Cube oriented grains is close to constant also during deformation in this direction (Figure 5.27). However, the two other texture components are not stable. The area fraction of Goss oriented grains ($[101]$ parallel to the DD) is reduced with approximately 90% when deformed perpendicular to ED. Also the area fraction of the CG component is somewhat reduced. This shows that the Goss and CG components are stable in the 0° direction while the intensity decreases significantly when deformed 90° related to ED. The greatest rotations are observed during deformation of the 45° specimens. This becomes very evident if the area fraction of Cube oriented grains is investigated in detail. The area fraction of this orientation is very high prior to deformation ($\sim 35\%$) but it reduced dramatically (less than 1%) at the uniform strain. This specimen also shows a considerable reduction of the CG component during deformation. On the other hand, the Goss component is almost unaffected by tensile deformation at 45° . However, it is important to bear in mind that the Goss component has close to a $[111]$ parallel to the DD when deformed in this direction. It is also worth noticing that the DD with the most stable texture also has the largest work hardening rate and lowest uniform strain.

Experimental results – Part B

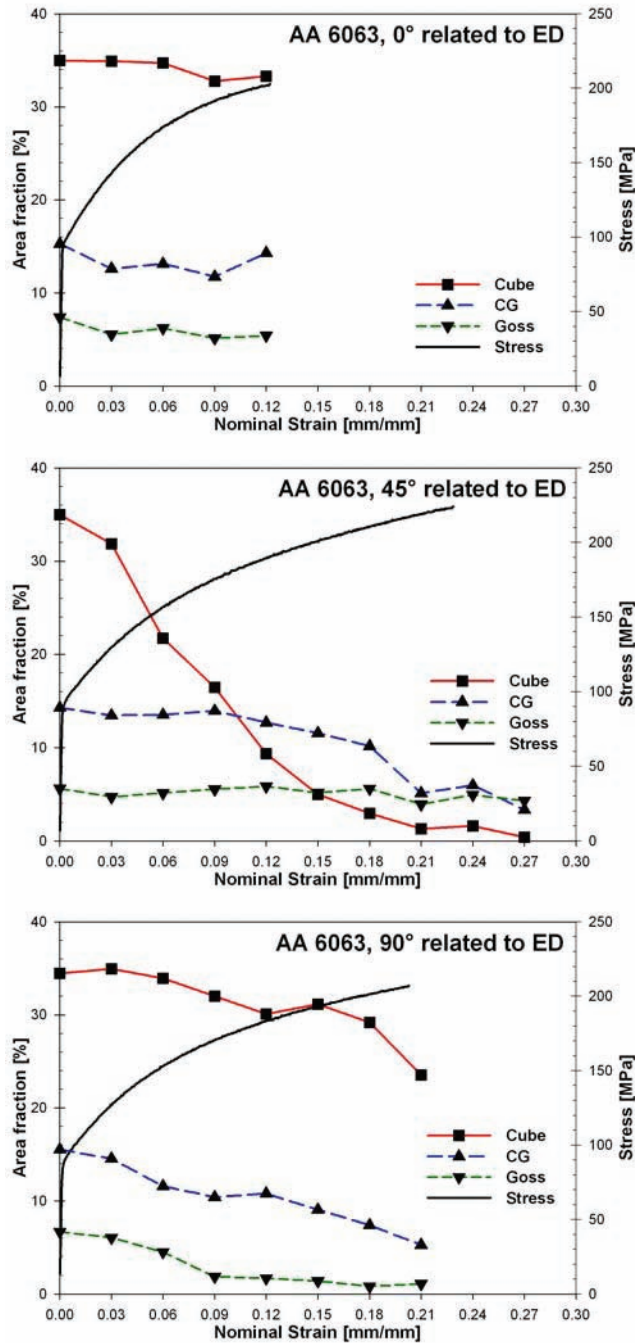


Figure 5.27 – Area fraction evolution of the Cube, CG and Goss components during deformation (nominal strain) of AA6063. The corresponding full thickness true stress-strain curve in material condition T1 is included.

5.5 Grain rotation with increasing strain

SEM experiments with improved resolution (reduced step size) are performed in order to follow the grain rotation of individual grains during simple tension. Also here, 3% axial elongation was selected as an appropriate deformation step size. Each grain is represented by at least 500 orientation measurements and the data is used to calculate both the rotation path and amount of rotation for grains with different initial orientation. Some grains develop internal orientation gradients during deformation and also these gradients are investigated.

5.5.1 Rotation paths – heavily textured material

Inverse pole figures (IPF) present the rotation taking place during deformation. The individual grains primarily rotate by aligning stable crystallographic orientations parallel to the tensile direction (see e.g. Han et al. 2003). Hence, only the inverse pole figures in the deformation direction (DD) are of interest. Figure 5.28 presents DD IPF maps of the initial orientations 0° , 45° and 90° related to ED. The DD IPF map evolutions upon straining of these specimens are given in Figure 5.30 to Figure 5.32. The full range of initial orientations was not covered by these experiments due to the strong crystallographic texture. It was therefore not possible to study the rotations taking place during deformation by simple tension for all possible types of grain orientations. The crystallographic direction parallel to the DD is a combination of the texture and the selected DD. The texture components will therefore behave differently when deformed in different DD, e.g. a grain with Cube orientation has a $[100]$ parallel to the DD when deformed in the 0° and 90° directions and a $[101]$ when deformed in the 45° direction (as indicated in Chapter 5.4). A grain with a Goss orientation, on the other hand, has a $[100]$ and a $[101]$ parallel to DD when deformed in the 0° and 90° directions respectively. When deformed in the 45° direction, this texture component has close to a $[111]$ parallel to the DD, hence the rotation path is very dependent on both the crystallographic orientation and the DD.

Experimental results – Part B

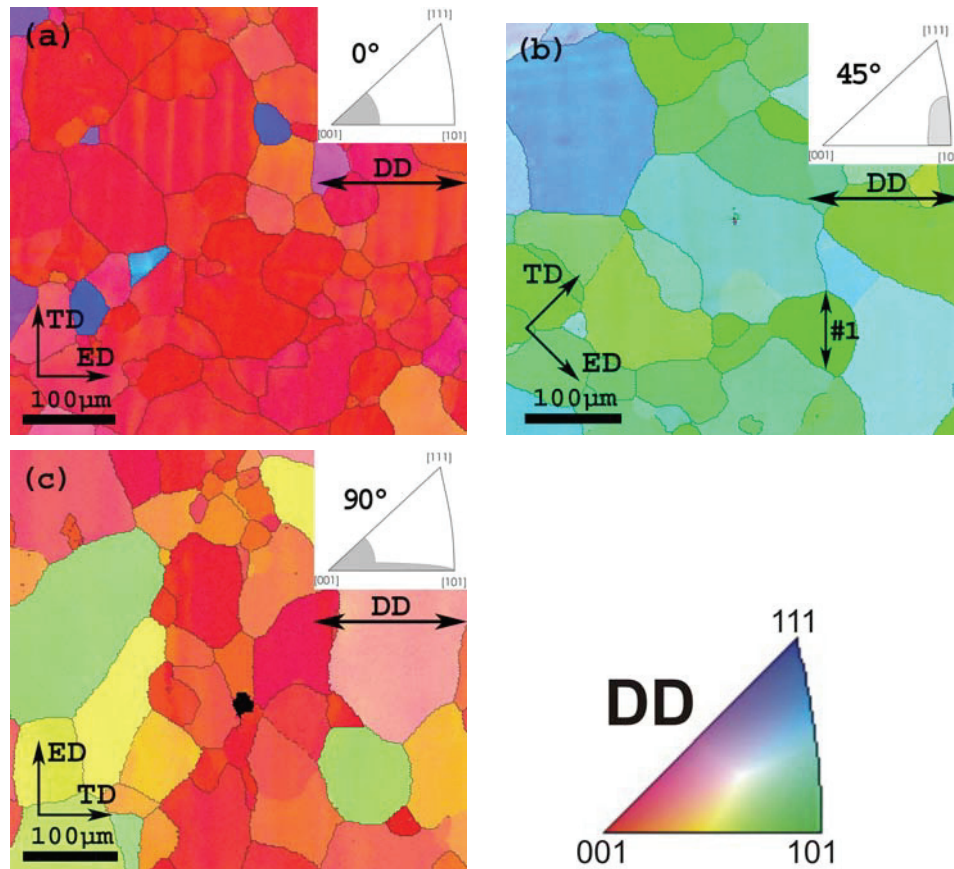


Figure 5.28 – IPF map in the deformation direction of the initial (non-deformed) orientations. The range of directions \parallel DD (parallel to DD) is indicated by an IPF in the upper right corner. (a) 0° direction (b) 45° direction and (c) 90° direction. The black arrow labeled #1 in the figure indicates a grain used for orientation gradients investigations in section 5.5.4.

It has already been shown that the present material has a very strong crystallographic texture. Thus, the microstructure consists of grains with resembling crystallographic orientations, i.e. neighbouring grains have close to equal crystallographic directions parallel to the DD. However, there are some clear differences between the three directions investigated. All the grains from the 0° specimen circumscribe the $001 \parallel$ DD pole of the DD IPF and most of grains from the 45° specimen circumscribe the $111 \parallel$ DD pole, being red and green respectively (Figure 5.28). On the other hand, the grains from the 90° specimen are scattered along the axis connecting the $001 \parallel$ DD and $111 \parallel$ DD poles of the DD IPF. This means that neither of the specimens provides

Experimental results – Part B

information about grains with an initial orientation from the upper part of the IPF. In spite of these limitations, Figure 5.29 shows the rotation path $\langle uvw \rangle \parallel DD$ of a representative selection of grains from specimens deformed 0° , 45° and 90° related to ED. As a first approximation, it seems like the grains rotate toward aligning the crystallographic directions with the $001 \parallel DD$ and the $111 \parallel DD$ poles of the IPF. Successive IPF maps also provide information about the rotation path, since alterations in colour indicate the crystallographic rotation taking place as shown in Figure 5.30 to Figure 5.32. It is evident that the grains rotate toward the $001 \parallel DD$ and $111 \parallel DD$ poles since the colour becomes more red and blue respectively. These figures also show that the deformation process is very heterogeneous since the grains develop strong colour gradients during deformation. Section 5.5.4 will present these heterogeneities in more detail.

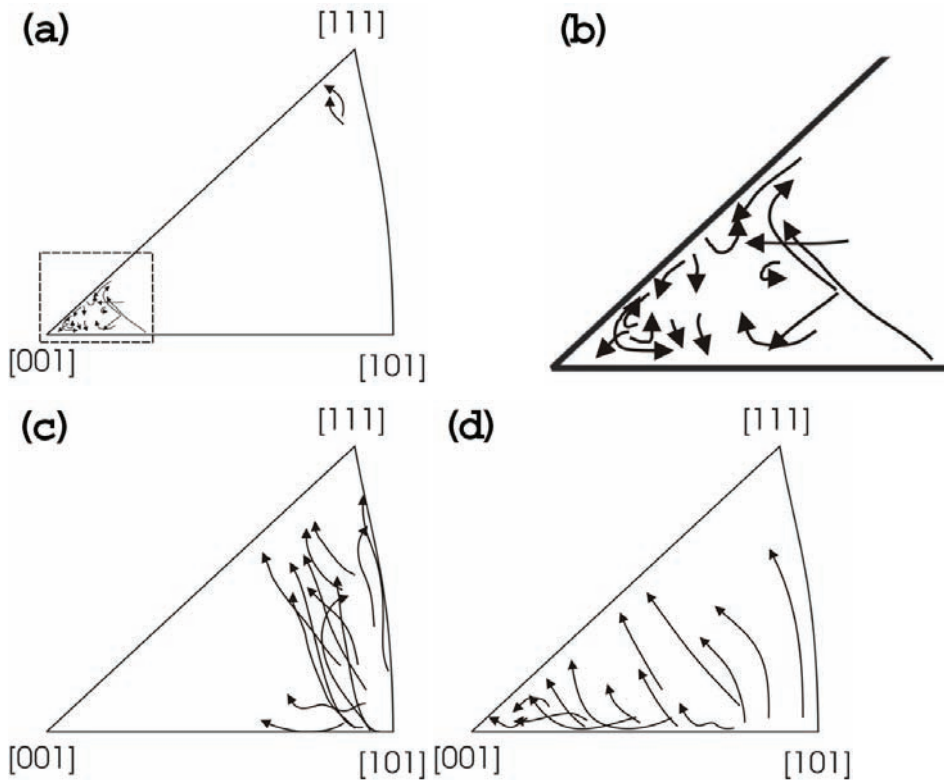


Figure 5.29 – Rotation paths in the IPF parallel to the DD upon straining to the uniform strain. The arrows indicate the rotation path of individual grains. (a) 0° direction (b) zoom of the $[001]$ corner from the 0° direction. (c) 45° direction and (d) 90° direction.

Experimental results – Part B

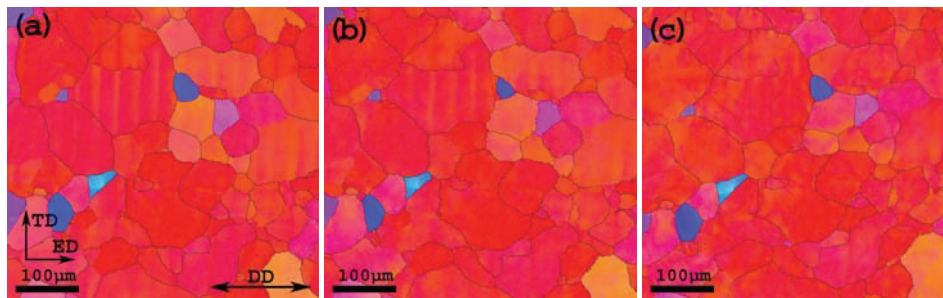


Figure 5.30 – IPF map in the deformation direction based on orientation data after different amounts of axial elongation in the 0° direction. (a) Initial orientation, (b) 6% and (c) at uniform strain (12%).

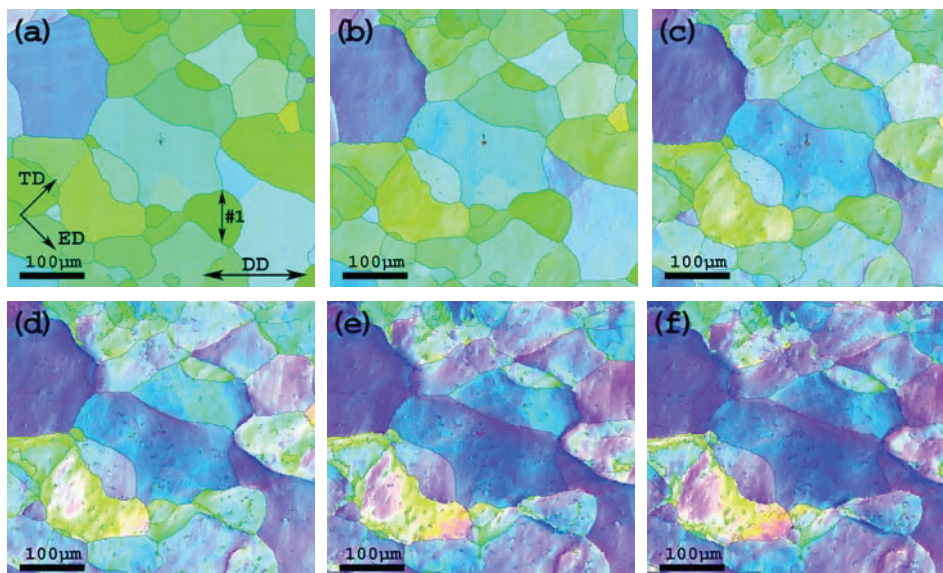


Figure 5.31 – IPF map in the deformation direction based on orientation data after different amounts of axial elongation in the 45° direction. (a) Initial orientation, (b) 6%, (c) 12%, (d) 18%, (e) 24% and (f) at uniform strain (27%). The black arrow labeled #1 in the figure indicates a grain used for orientation gradients investigations in section 5.5.4.

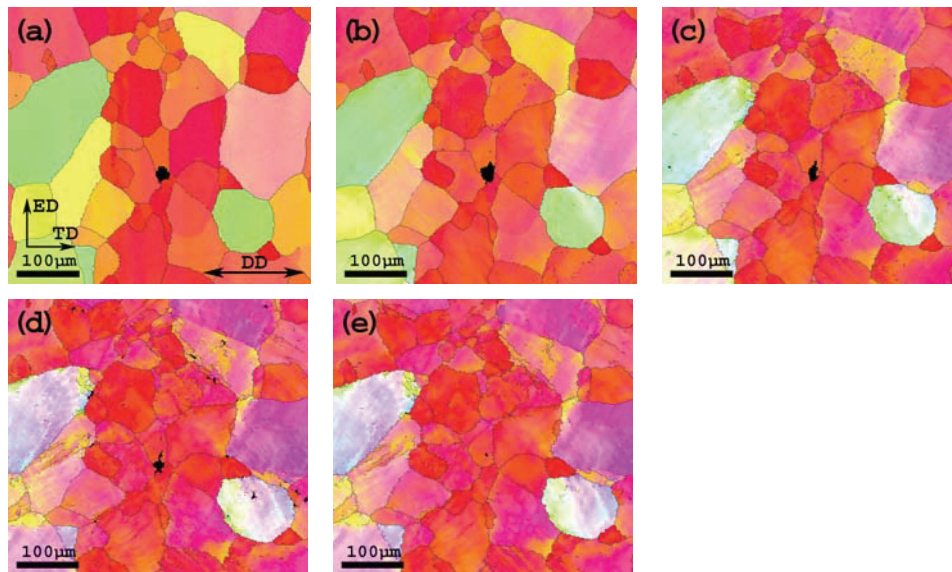


Figure 5.32 – IPF map in the deformation direction based on orientation data after different amounts of axial elongation in the 90° direction. (a) Initial orientation, (b) 6%, (c) 12%, (d) 18% and (e) at uniform strain (21%).

5.5.2 Rotation paths – random textured material

Figure 5.33 shows that specimens taken from the same material after cross-rolling and subsequent heat-treatment possesses close to a random texture, i.e. the material has close to isotropic mechanical properties. Another effect of the random texture is that the initial orientation of the individual grains covers the entire inverse pole figure. Specimens taken from this material are investigated under the same conditions as described above, i.e. studying the rotation paths of grains with initial orientations not covered by the strongly textured specimens. Figure 5.34 presents the IPF map evolution of the DD for a specimen deformed in the 90° direction. It is evident that the crystallographic orientations of the individual grains are widely spread for specimens deformed in this direction, i.e. the grains have different colours in the IPF map. Further, the rotation paths of a larger selection of grains from this specimen are presented in Figure 5.35. In general, the individual grains of this specimen follow the same trends as the material with a strong crystallographic texture. Consequently, the grains rotate toward aligning the crystallographic directions with the 001||DD and 111||DD poles of the IPF.

Experimental results – Part B

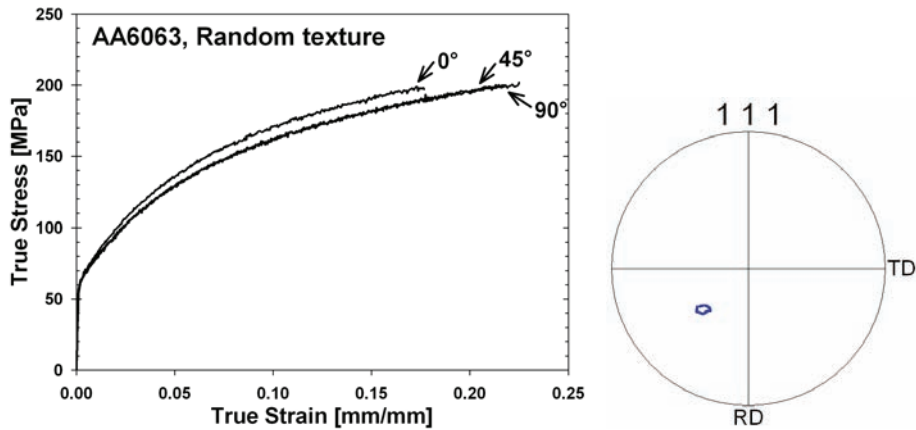


Figure 5.33 – True stress-strain curves 0°, 45° and 90° to ED after cross-rolling and subsequent heat-treatment of AA6063 obtained with an initial strain rate of $1.1 \times 10^{-3} \text{ s}^{-1}$ (left). Calculated 111 pole figure representing the initial texture (i.e. lack of texture) after cross-rolling and subsequent heat-treatment (right).

The area fraction of high angle grain boundaries (HAGB) is extensively increased after the crystallographic texture is removed by cross-rolling and subsequent heat-treatment. This is indicated by the grain boundaries included in the IPF maps presented in Figure 5.34. These maps contain a much higher fraction of HAGBs compared to the maps presenting the microstructure in the as-extruded condition (see e.g. Figure 5.28). The high fraction of HAGBs is consistent with the random texture observed in this material condition.

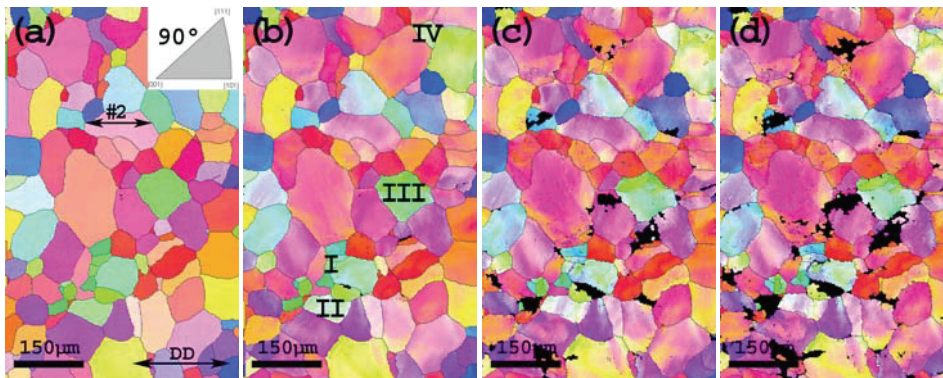


Figure 5.34 – IPF map in the deformation direction based on orientation data after different amount of axial elongation for a specimen with random texture deformed in the 90° direction. (a) Initial orientation, (b) 6%, (c) 12% and (d) uniform strain (18%). The black arrow labeled #2 in figure (a) indicates a grain used for orientation gradients investigations in section 5.5.4. The grains labeled I-IV in figure (b) are the grains used for crystallographic rotation investigations in Figure 6.19.

Experimental results – Part B

The investigations performed on specimens without texture provide information about the relation between rotation of individual grains and the crystallographic orientation of the neighbouring grains. The individual grains in specimens without crystallographic texture are surrounded by grains with a random selection of orientations, while the grains in a specimen with very strong texture are to a large extent surrounded by grains with orientations similar to the orientation of the grain itself. This has allowed investigations of the enforced constraints introduced by the crystallographic orientations of the neighbouring grains.

Notice that some black areas appear toward the end of the deformation process (Figure 5.34). The black areas consist of non-indexed pixels due to low pattern quality, i.e. the crystallographic orientations can not be determined by the EBSD technique. The appearances of these black areas indicate large topography at the specimen surface, causing the pattern quality to drop dramatically in the shadows behind the introduced obstacles.

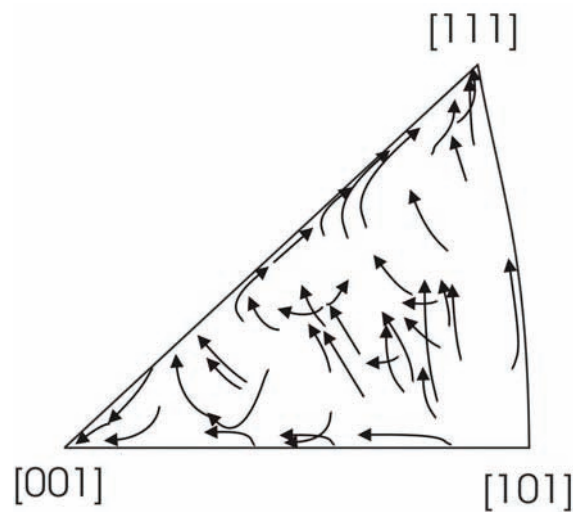


Figure 5.35 – Rotation paths in the IPF parallel to the DD for a specimen with random texture deformed 90° related to ED. The arrows indicate the rotation path of the individual grains, starting at the initial orientation and ending at the orientation at uniform strain.

5.5.3 Amount of rotation

The amount of rotation during deformation is as indicated in the previous section, very dependent on the initial orientation (Figure 5.36 and Figure 5.37). Here, rotation is presented as a function of the macroscopic elongation (global strain) for a selection of grains with different initial orientations. Only the crystallographic direction parallel to the DD is taken into account during the selection of grains. The observations show that grains having a [101] parallel to the DD rotates more than 3 times as much as grains having more stable directions parallel to the DD, e.g. grain E rotates close to 20° during deformation, while both grain A and I rotates less than 6°.

The individual grains in Figure 5.36 were taken from specimens having a strong texture while the grains in Figure 5.37 were taken from specimens where the texture is removed by cross-rolling and subsequent heat-treatment. It is worth noticing that the selection of initial orientations in Figure 5.36 was obtained by choosing different deformation directions from the material with strong texture, i.e. the total amount of deformation (global strain) varies due to anisotropy in uniform strain. The amount of rotation for grains with close to identical crystallographic orientation differs for material with and without any crystallographic texture. Grain C in Figure 5.36 and Grain 3 in Figure 5.37 have almost the same initial crystallographic orientation but the amount of rotation taking place during deformation is 11° and 4° respectively. The results clearly show that the grains in a material with strong crystallographic texture (many of the neighbouring grains have similar orientations) rotate more than grains in a material without a pronounced texture.

Experimental results – Part B

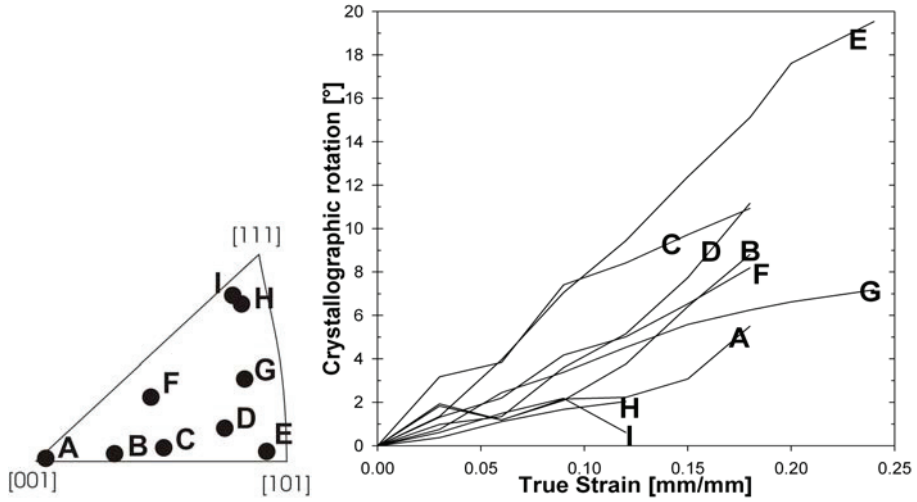


Figure 5.36 – Amount of crystallographic rotation as a function of the global strain for a selection of initial orientations in a material with strong crystallographic texture.

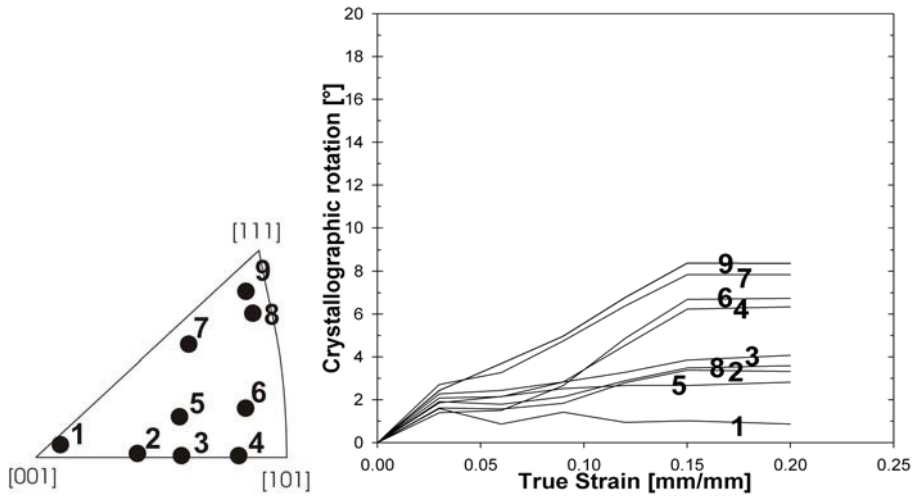


Figure 5.37 – Amount of crystallographic rotation as a function of the global strain for a selection of initial orientations in a material without crystallographic texture.

Experimental results – Part B

The above two figures also show that the amount of rotation during deformation is strongly dependent on the initial orientation. This means that the rotation of a texture component is determined by the selected DD. The rotation behaviour of the Cube, CG and Goss components has been investigated during deformation in the 0°, 45° and 90° directions (Figure 5.38). Specimens from AA6063 (strong ED-rotated Cube texture) have been used for this experiment. The results show a strong effect of the selected DD. The Goss component rotates less than 4° when deformed in the 0° and 45° directions and approximately 12° when deformed 90° related to ED. This observation is consistent with the observations in Figure 5.36 and Figure 5.37. The Goss component has a [100] and close to a [111] parallel to the DD when deformed in the 0° and 45° directions respectively, but a [101] parallel to the DD when deformed in the 90° direction as shown in Figure 5.38. Further, the Cube component has a [100] direction parallel to the DD when deformed 0° and 90° to ED and a [101] parallel to the last direction. It is therefore not surprising that for Cube oriented grains deformed in these three directions (Figure 5.38), only minor rotation is observed in the 0° and 90° directions (less than 4°) while very large rotations (approximately 15°) appear when deformed in the 45° direction. It is also worth noticing that none of the important texture components will give rise to crystallographic rotations when deformed parallel to ED (less than 4°).

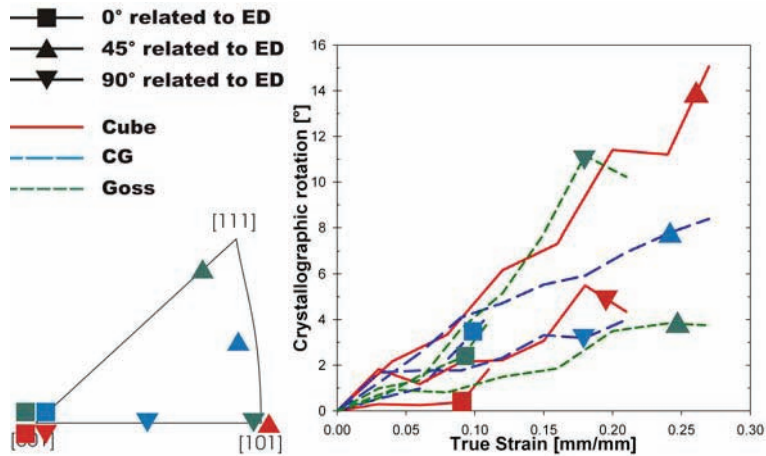


Figure 5.38 – Amount of crystallographic rotation as a function of the global strain for the Cube (red), CG (blue) and Goss (green) orientations deformed 0° (square), 45° (triangle up) and 90° (triangle down) related to ED. The crystallographic direction parallel to the DD for the different texture components and deformation directions are given in the IPF.

5.5.4 Orientation gradients

The individual grains deform heterogeneously during plastic deformation, hence grains develop internal orientation gradients. Orientation gradients develop throughout the deformation process and are often very evident at the uniform strain. However, in some cases, the orientation gradients are visible in the IPF maps already after 6% axial elongation, i.e. the grains develop clear colour gradients which represent changes in orientation across the grains (Figure 5.31). At high strains these colour gradients become very evident and the orientation of the grain interior is represented by several colours.

The orientation gradient can be represented by a misorientation plot, where the reference orientation is the orientation of the pixel in the centre of the grain. Figure 5.39 presents the through grain misorientation evolution for a representative grain (see grain #1 in Figure 5.31) in a specimen deformed 45° related to ED. It is normal that grains have a uniform orientation prior to deformation. This is the case also for this grain. However, the grains often develop very strong orientation gradients toward the grain boundary during deformation. At the uniform strain, a misorientation of 16° is observed between the centre position and the grain boundary, and a steep orientation gradient is evident close to the grain boundary, i.e. the grains deform (rotates) heterogeneously.

Other grains develop more complicated orientation gradients. Figure 5.40 shows the orientation gradient observed in another grain (see grain #2 in Figure 5.34) taken from a specimen without any texture. This orientation gradient is taken parallel to the DD and the grain develops regions of different orientation (substructure) during deformation. However, also this grain develops clear orientation gradients toward the grain boundary. The misorientation between the centre position and the grain boundaries are as high as 10° at the uniform strain.

It should also be noticed that the length of the orientation profile across the grain under consideration changes during deformation. This change in size is enforced by the elongation/contraction of the investigated grain taking place by the plastic deformation process.

Experimental results – Part B

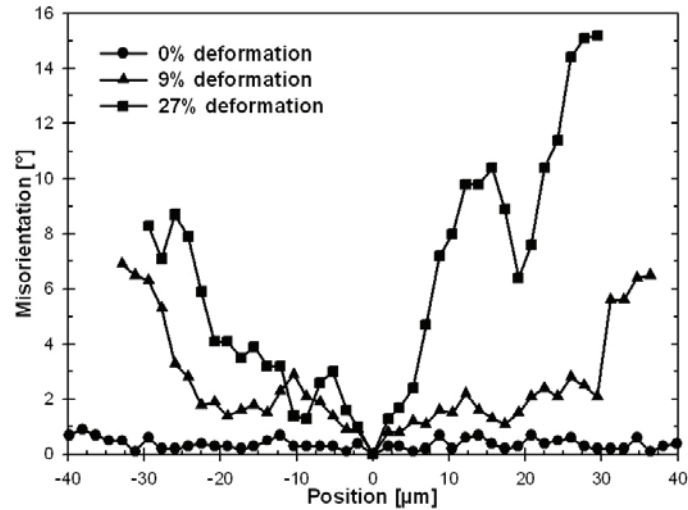


Figure 5.39 – Development of through grain misorientation gradients during deformation of grain #1 (the gradient and centre point position of grain #1 is indicated in Figure 5.28). The length of the plot becomes shorter due to contraction during deformation. The misorientation gradient becomes more evident at high deformation.

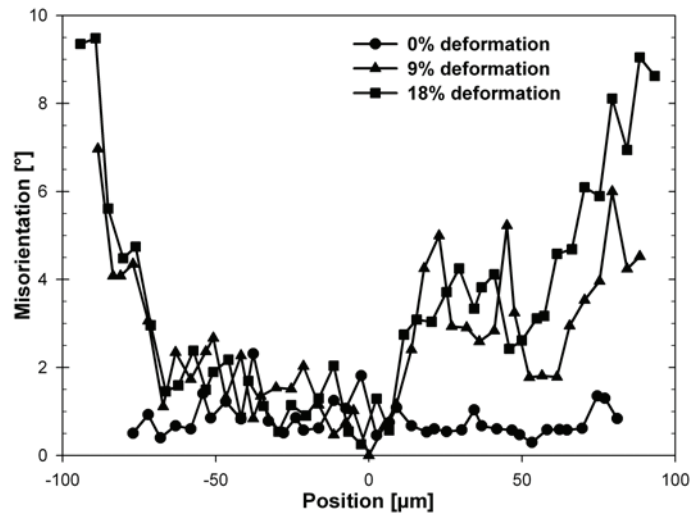


Figure 5.40 – Development of through grain misorientation gradients during deformation of grain #2 (the gradient and centre point position of grain #2 is indicated in Figure 5.34). The length of the plot becomes longer due to axial elongation during deformation. The misorientation gradient becomes more evident at high deformation.

5.6 Plasticity

Aluminium alloys deform plastically with crystallographic slip as the most significant deformation mechanism. Crystallographic slip often gives rise to slip traces at the specimen surface. In the present work, SE micrographs of the specimen surface were used to study the slip trace evolution of the recrystallized alloy during in-situ deformation. Information from the slip trace investigations were also combined with information about the crystallographic orientations, and the slip activity of the individual grains were calculated based on this information. These investigations were performed on AA6063 in material condition T1.

5.6.1 Slip trace evolution

Grains often develop slip traces due to the relative movement of parallel slip planes taking place during dislocation movement. The microstructure often deforms inhomogeneously, i.e. some grains develop visible slip traces earlier than other grains, etc. If no slip traces are observed within a grain, this usually indicates that this grain does not deform plastically, hence the grain is unfavourable oriented for slip. Figure 5.41 to Figure 5.43 present SE-micrographs of the slip trace evolution for specimens with a strong crystallographic texture deformed at 0°, 45° and 90° relative to the ED respectively. Notice that these micrographs correspond to the IPF maps presented above in section 5.5.1. The micrographs clearly show that some grains develop slip traces already after 6% axial elongation and that the specimens taken in the 0° and 90° directions generally start developing slip traces at higher strains than the 45° direction. Also, the specimens deformed in the 45° direction have the most homogeneous distribution of slip traces and only a very limited number of grains do not develop visible slip traces.

Experimental results – Part B

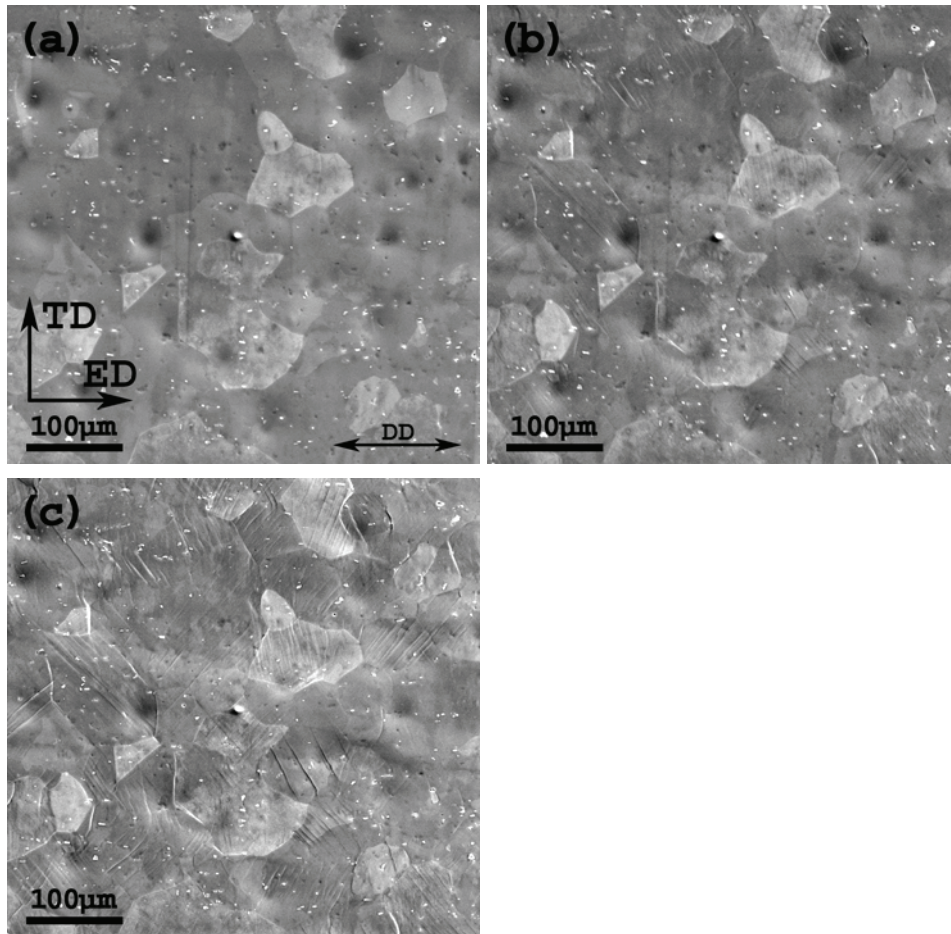


Figure 5.41 – SE micrographs of the same surface area (ED-ND plane) after different amounts of axial elongation in the 0° direction. (a) Initial orientation, (b) 6% and (c) uniform strain (12%). Alloy AA6063 strained in the T1 condition.

Experimental results – Part B

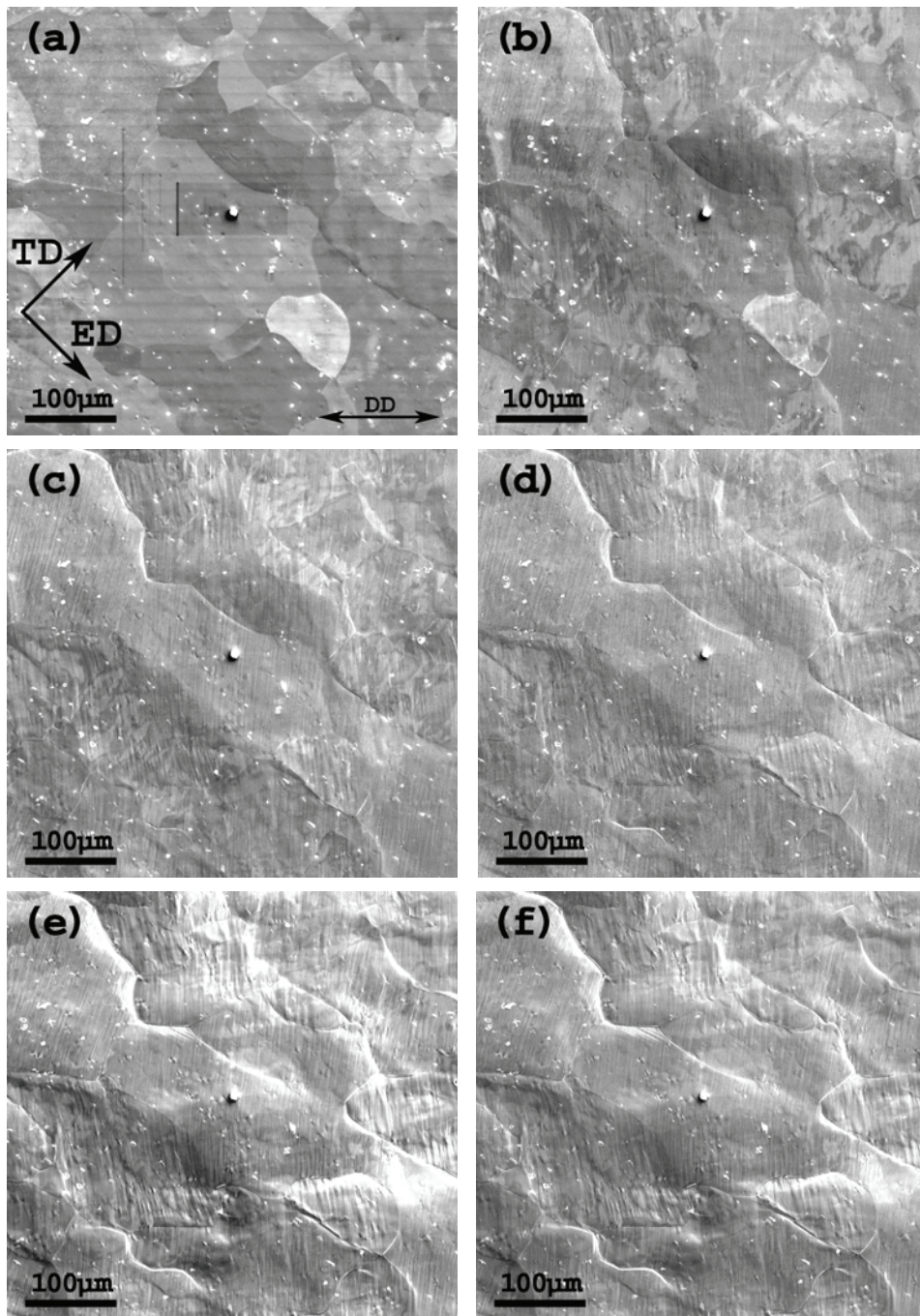


Figure 5.42 – SE micrographs of the same surface area (ED-ND plane) after different amounts of axial elongation in the 45° direction. (a) Initial orientation, (b) 6%, (c) 12%, (d) 18%, (e) 24% and (f) uniform strain (27%). Alloy AA6063 strained in the T1 condition.

Experimental results – Part B

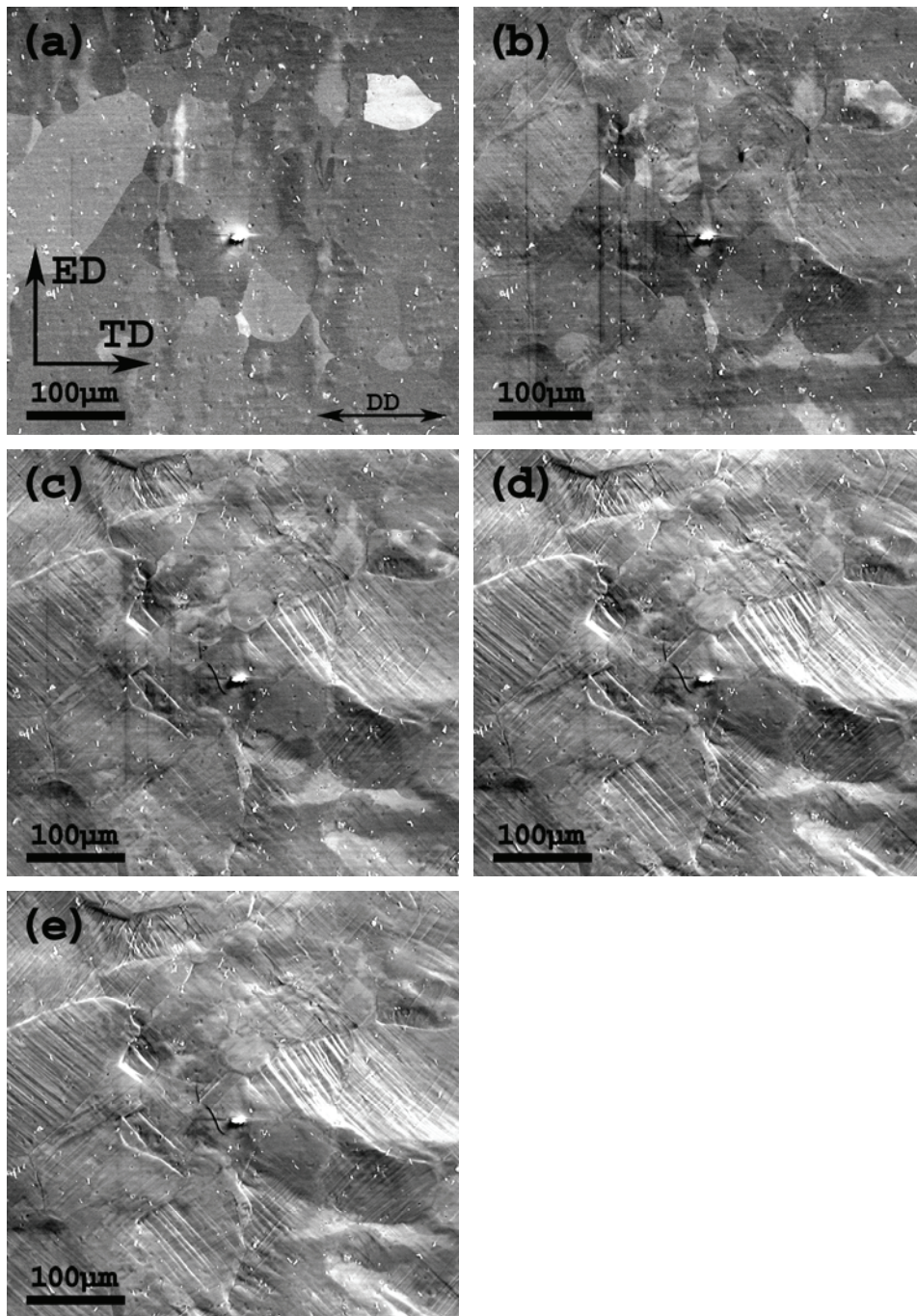


Figure 5.43 – SE micrographs of the same surface area (ED-ND plane) after different amounts of axial elongation in the 90° direction. (a) Initial orientation, (b) 6%, (c) 12%, (d) 18% and (e) uniform strain (21%). Alloy AA6063 strained in the T1 condition.

Experimental results – Part B

In general, the observations show that the individual grains in this material (strong ED-rotated Cube texture) only develop a limited number of non-parallel slip traces. However, it is important to remember that the Cube texture is very symmetrical for the selected deformation directions. Hence, in some special cases, slip on two different slip planes will produce close to parallel slip traces and it becomes difficult to determine the exact number of slip planes activated. Nevertheless, even though the number of slip traces is low for all deformation directions, the number of visible intense slip traces is much higher for the specimen deformed in the 90° direction compared to the other two directions. Figure 5.44 and Figure 5.45 show the evolution in the number of observed slip traces in the individual grains during deformation 45° and 90° related to ED respectively. It is also clear that a more uniform slip trace distribution is observed for the 45° specimens compared to the 90° specimens. Additional slip traces develop only in the neighbourhood of grain boundaries as shown in Figure 5.46, hence the whole grain is seldomly covered with these additional traces. However, in this investigation the number of observed slip traces was determined based on the number of non parallel traces observed within a single grain even though these do not cover the same surface area.

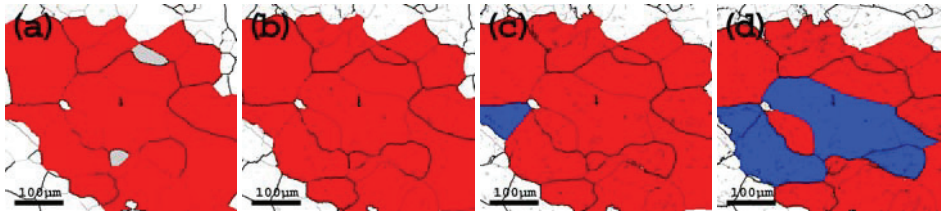


Figure 5.44 – Evolution in number of observed slip traces in the individual grains of a specimen with texture during deformation 45° related to the ED. Grains without any visible slip traces (grey), 1 (red) and 2 (blue) sets of visible slip traces are highlighted. (a) 6%, (b) 12%, (c) 18% and (d) uniform strain (27%).

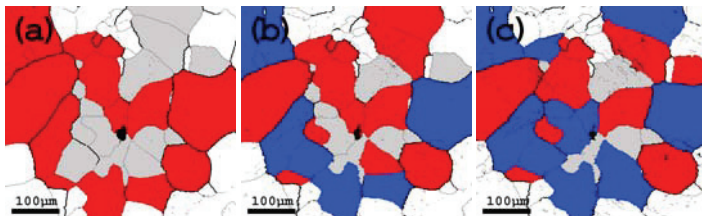


Figure 5.45 – Evolution in number of observed slip traces in the individual grains of a specimen with texture during deformation 90° related to the ED. Grains without any visible slip traces (grey), 1 (red) and 2 (blue) sets of visible slip traces are highlighted. (a) 6%, (b) 12% and (c) uniform strain (18%).

Experimental results – Part B

The trace morphology presented in Figure 5.46, shows that the slip traces often run continuously through the grain interior and in some cases over the grain boundary into the neighbouring grains. In other words, slip traces stretch from one grain into another, often with only minor changes in the intersection angle over the grain boundary. This is very evident for the specimens deformed in the 45° direction where a regular set of slip traces stretches from grain to grain only with $1-2^\circ$ change in orientation. The density of continuous slip traces is not as high for the 90° specimens as for the two other directions. However, also specimens deformed in this direction have several grain boundaries with continuous slip traces, see e.g. Figure 5.47. The changes in orientation over the grain boundary are often somewhat higher for this DD, and it is also more common that the grain surface possesses an additional set of discontinuous slip traces.

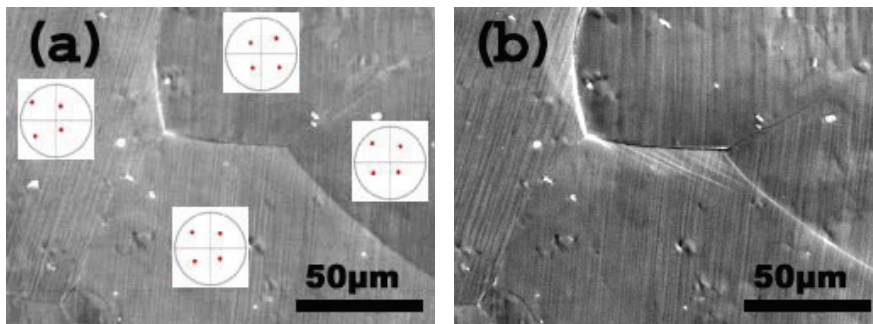


Figure 5.46 – SE micrograph of the observed slip traces at the specimen surface for a specimen deformed 45° to ED. (a) At 9% deformation only one set of slip traces in each grain has developed. 111 pole figures from the individual grains are included in order to show the orientation differences over the grain boundaries. (b) A second set of slip traces develops locally at 21% deformation.

The slip traces seem to be more irregular for the 90° specimens, and this is especially true for grains with an additional set of slip traces (Figure 5.47). Irregular slip traces are also observed in grains with only one set of slip traces. Figure 5.48 shows two grains with irregular slip traces in a specimen deformed parallel to ED. This kind of slip traces is more curved than the regular one. It is also observed that the slip trace separation distance is enlarged for these grains, i.e. coarser slip trace distribution. The slip trace separation distance is as high as $\sim 15\mu\text{m}$ for the grain on the left hand side of Figure 5.48, while the typical value for a grain with regular slip traces is $1-3\mu\text{m}$. It is also worth noticing that the slip traces in grains with a high slip trace separation distance are often thicker than ordinary slip traces.

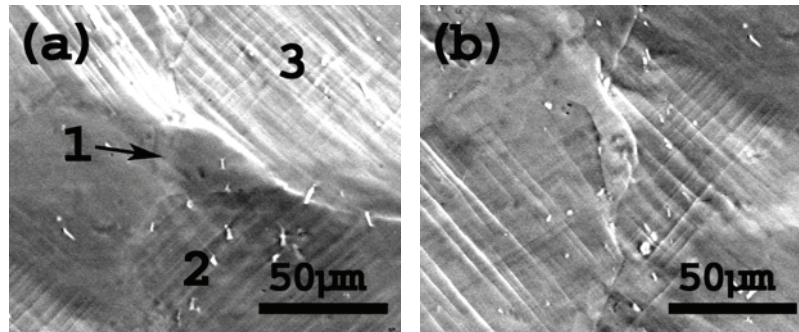


Figure 5.47 – SE micrographs of the observed slip traces at 18% deformation for a specimen deformed 90° to ED. The labelled grains are investigated in more detail in section 5.6.2. (a) Grain without slip traces (#1) surrounded by heavily deformed grains, and (b) two grains with multiple slip.

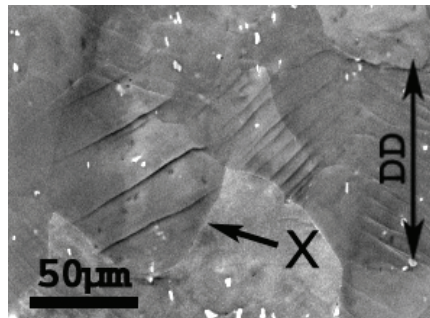


Figure 5.48 - SE micrograph of grains with one set of irregular shaped slip traces for a specimen deformed parallel to ED. Please note the relative large separation distance between the traces (coarse slip) for the grain labelled X.

The slip traces are also investigated for specimens where the crystallographic texture has been more or less removed by cross-rolling and subsequent annealing. It should be noticed that the slip trace distribution of this material condition is somewhat more complicated. Figure 5.49 presents the slip trace evolution of such specimen deformed 90° to ED, and also here the micrographs correspond to the IPF maps presented in section 5.5.1. The observed slip traces are more heterogeneously distributed and some grains develop multiple slip traces already at 6% elongation, while other grains do not develop any visible slip traces even at the uniform strain (Figure 5.50). The micrographs of the slip trace evolution also show that a large fraction of the grains develop as many as 3 sets of slip traces during deformation. The results presented here indicate that during deformation the material without texture develops denser and more multidirectional slip traces compared to the material with strong crystallographic texture.

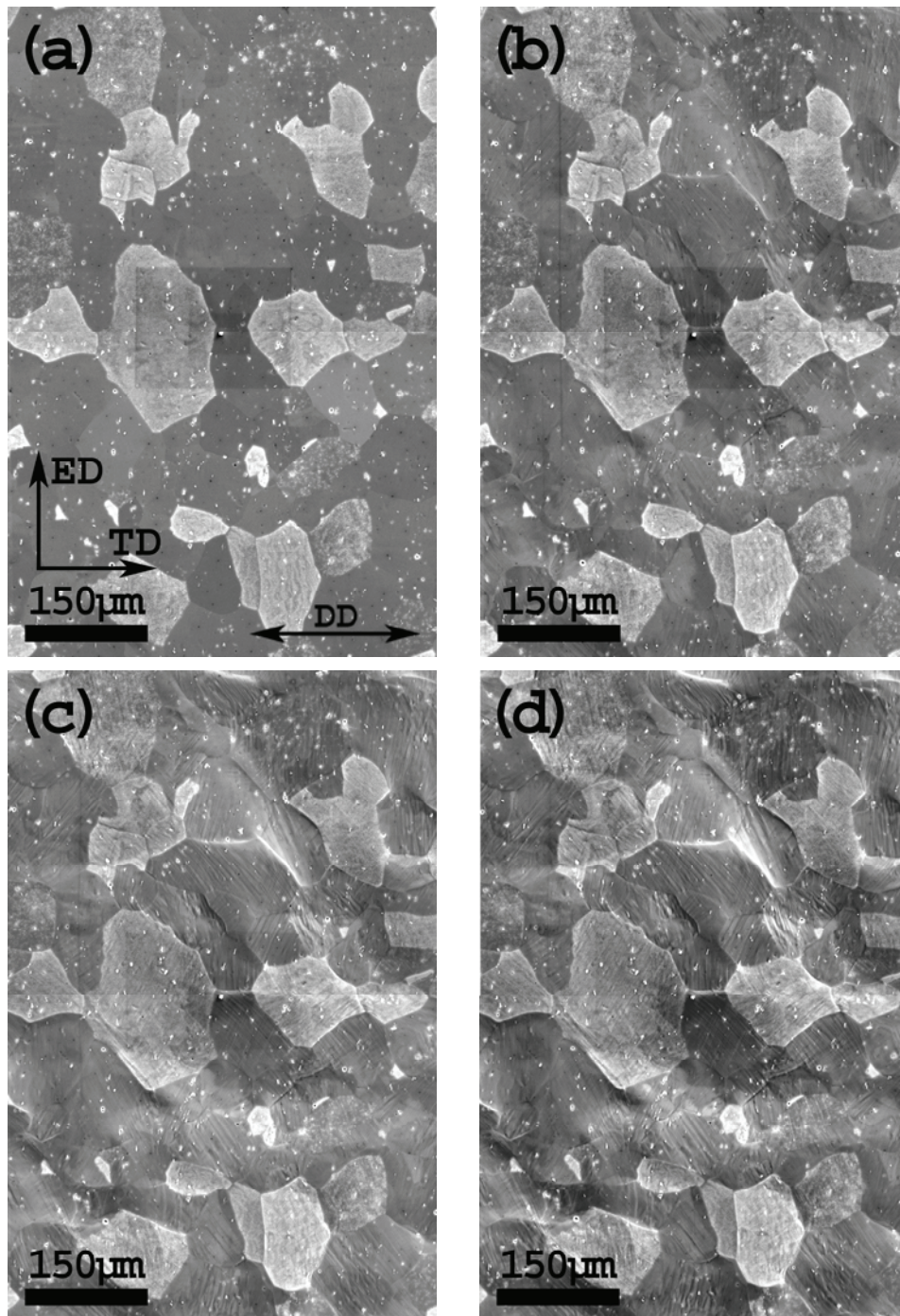


Figure 5.49 – SE micrographs of the specimen surface (ED-ND plane) after different amounts of axial elongation for a specimen with random texture deformed in the 90° direction. (a) 6%, (b) 12% and (c) uniform strain (18%).

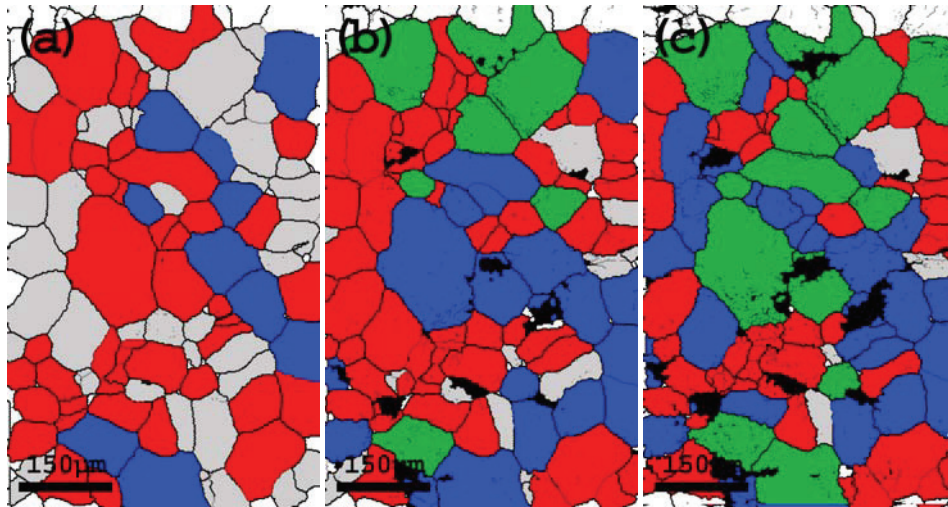


Figure 5.50 – Evolution in the number of observed slip traces in the individual grains during deformation of a specimen without texture 90° related to ED. Grains without any visible slip traces (grey), 1 (red), 2 (blue) and 3 (green) sets of visible slip traces are highlighted. (a) 6%, (b) 12% and at (c) uniform strain (18%).

More detailed slip trace investigations of this specimen at 90° reveal that only a very limited number of slip traces transmit over the grain boundaries. The directional changes over the grain boundary of continuous slip traces are also large compared to the changes observed in the material prior to cross-rolling and subsequent heat-treatment. However, the additional slip traces activated during deformation often coincide with the primary slip traces of a neighbouring grain. Figure 5.51 shows a grain which locally develops two sets of additional slip traces and these coincide with the slip traces of the nearest neighbours. Only one set of slip traces are visible at 6% but one additional set of slip traces develop in the lower right corner of the grain after 12% elongation. This set of slip traces is parallel to the primary slip traces of the grain directly beneath the lower right corner of the grain investigated. Further, when this grain is deformed to a macroscopic strain of 18% also a third set of slip traces has become visible. This set of slip traces develops at the centre of the grain and are perfectly aligned to the slip traces observed in the large grain above. In general, there are several observations showing that additional slip traces developed during deformation are affected by the primary set of slip traces in the neighbouring grains.

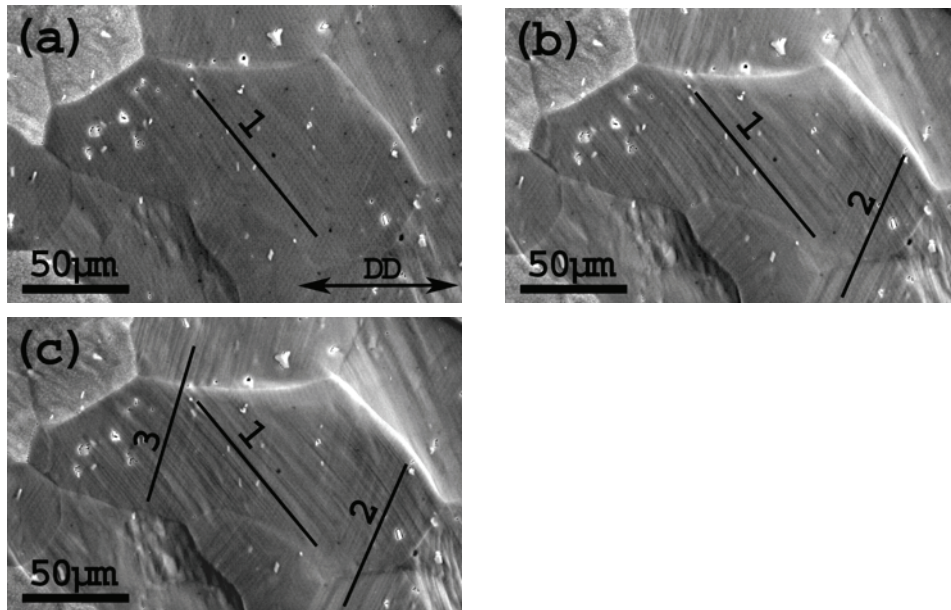


Figure 5.51 – SE micrographs of the observed slip traces in a material with random texture. The lines indicate the observed slip traces and how additional slip traces can coincide with the slip traces from neighbouring grains. (a) 6%, (b) 12% and (c) 18%.

It is worth noticing that it is hard to observe any visible slip traces at the right hand side of the grain investigated in Figure 5.51. Even at the uniform strain there are no visible slip traces close to the grain boundary separating this grain from the two bright grains at the upper left corner of the micrograph. The corresponding Taylor factor map of the same grains (Figure 5.52) shows that the two neighbouring grains have a higher Taylor factor, i.e. these grains are more difficult to deform and will most likely give rise to additional constraint in this region.

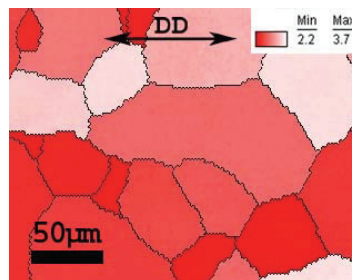


Figure 5.52 – Taylor factor map of the same grain area as presented in Figure 5.51. The calculations were performed by the Taylor FC method and based on the crystallographic orientations prior to deformation.

Experimental results – Part B

The Taylor factor is a direct result of the DD relative to the crystallographic orientations and the calculation-method utilised. The calculated average Taylor factors (here, full constraint approach) of the present AA6063 alloy prior to deformation is 2.5, 2.9 and 2.6 for the 0° , 45° and 90° direction respectively. Hence, this material has close to similar Taylor factors when deformed 0° and 90° related to the ED. However, the Taylor factor change from grain to grain can vary substantially. Figure 5.53 presents the measured area fraction of the Taylor factors for when deformation is utilised in three different directions as well as for a specimen without texture deformed in the 90° direction. The figure shows that the textured material has a large fraction of Taylor factors around 2.45 when deformed parallel to ED. If deformed perpendicular to the ED, some grains have Taylor factors in the range 2.3-2.6 while other grains have Taylor factors of ~ 3.4 . Moreover, these results show that a specimen deformed 45° related to the ED has a higher Taylor factor (close to 3.6) than the two other directions, i.e. see Figure 5.53 – Figure 5.54).

Neither of the grains in the material without crystallographic texture has the same Taylor factors, i.e. this material has a true random orientation distribution. This is further confirmed by the graph in Figure 5.53 where the Taylor factor of the individual grains varies from 2.3 to 3.5 without any evident major peaks. Still, the average Taylor factor of this specimen is similar to the material with texture when deformed in the 0° and 90° directions.

Experimental results – Part B

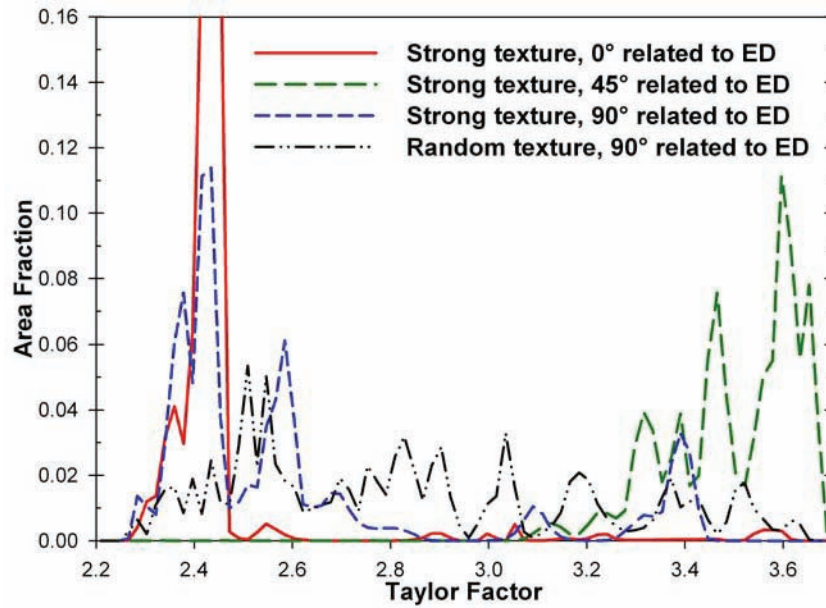


Figure 5.53 – The area fraction of Taylor factors. Calculations performed by the Taylor FC method based on the crystallographic orientations (~100 grains) prior to deformation. The calculations based on a material with random texture are shown for comparison.

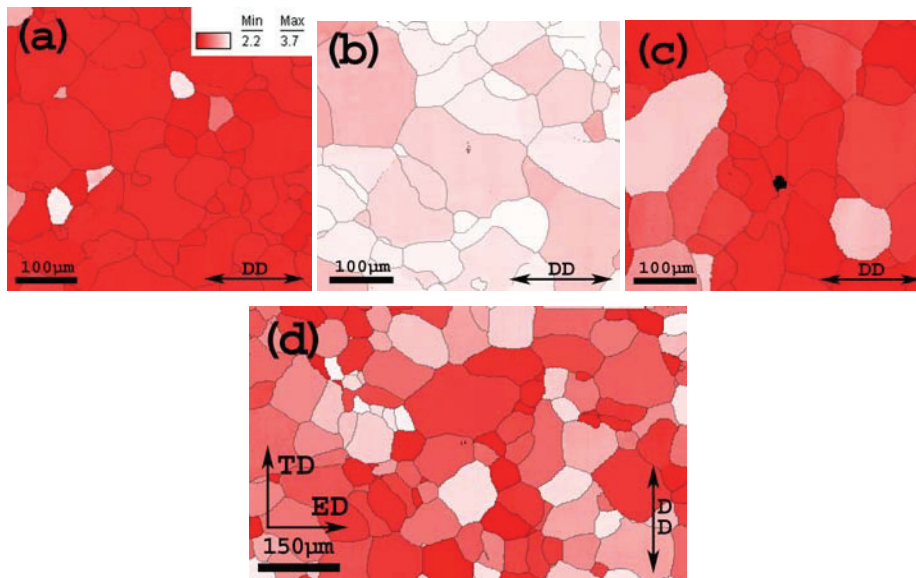


Figure 5.54 – Taylor factor map of specimens in the ED-TD plane with (a to c) and without (d) a strong texture. Calculations performed by the Taylor FC method based on the crystallographic orientations prior to deformation. The colour key represents the Taylor factor of the individual grains. DD parallel to (a) 0°, (b) 45°, (c) 90° and (d) 90° direction.

5.6.2 Slip system activity

The observed surface slip traces give valuable information about the slip activity. They develop due to considerable slip on activated slip planes, and each slip plane consists of three different slip directions, i.e. three different slip systems. Therefore, the probability of slip for each of these slip systems has to be determined. The Schmid value of all slip systems can be calculated based on the crystallographic orientation and the DD (assuming uniaxial deformation in the individual grains). The number of slip systems activated in each grain during simple tension deformation will depend on both the Schmid value distribution among the 12 slip systems and the constraint enforced by the surroundings. It is important to remember that the activated slip systems most likely have to be among the potential active slip systems from a slip trace investigation.

Slip can in general take place without producing any visible slip traces if the plastic deformation of the individual grains is homogeneously distributed in the microstructure. Having said this, the materials investigated in this work seems always to deform in a more localised way, i.e. they always produce slip traces. On the other hand, also this material can in some special cases deform by slip without producing visible slip traces. The slip traces will not be visible if the slip direction (Burgers vector) is parallel to the specimen surface. The slip systems that fulfil this requirement can therefore be activated without producing any visible evidence. The intersection angle between slip direction and the specimen surface can be calculated based on the crystallographic orientation. For this investigation it was assumed that slip systems with an intersection angle larger than 10° will produce visible slip traces.

The Schmid value distribution is entirely controlled by the crystallographic orientations. It has previously been shown that the present material consists of very symmetrical texture components (Figure 5.5). Small rotations can therefore alter the Schmid value distribution significantly. Figure 5.55 presents the Schmid value distribution of different crystallographic orientations along the fibre connecting the Cube and Goss orientation (45° rotation around the ED). The Schmid values of the slip systems are completely independent of the rotation around the ED when deformed parallel to this direction (ED), i.e. all the crystallographic orientations have 8 slip systems with a Schmid value of 0.408 while the remaining 4 slip systems have a Schmid value of zero. However, the rotations

Experimental results – Part B

around the ED strongly affect the Schmid values when deformed in the TD (Figure 5.55 (b)). When deformed in this direction, the two extremes, i.e. the Cube and Goss orientation have 8 and 4 slip systems respectively with a Schmid value of 0.408, while the remaining slip systems are at zero. The figure also shows that rotation as small as 5° changes the Schmid value distribution significantly. The Schmid value of some slip systems was altered as much as 0.039 due to this small rotation. Further, The CG orientation is a less symmetrical orientation with regard to the selected DD and all the slip systems have non-zero Schmid values. Moreover, also for this orientation the difference in Schmid value between the slip systems with the maximum and minimum values is 0.408.

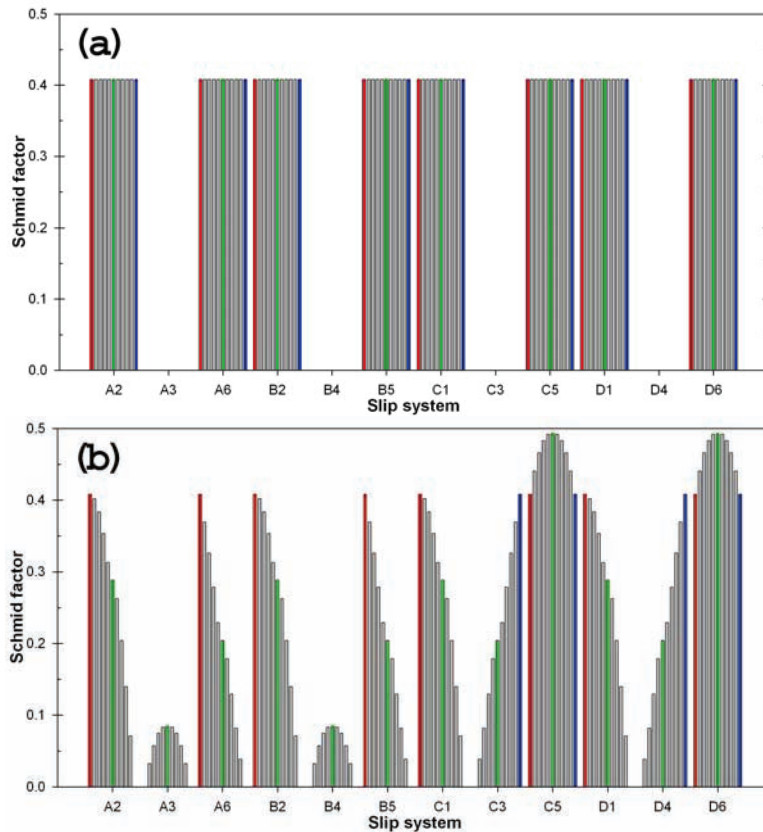


Figure 5.55 – Schmid values for the 12 potential slip systems of different crystallographic orientation along the fibre connecting the Cube and Goss orientation. Each column represents a 5° rotation along the ED-rotated Cube fibre. The Cube, CG and Goss orientation is labelled red, green and blue respectively. Deformed in the (a) ED direction and (b) TD direction.

Experimental results – Part B

The calculated Schmid values presented above clearly show that crystallographic rotation results in alteration of the Schmid value distribution. It has also been shown that the individual grains rotate during simple tension deformation. Thus, also the Schmid value distribution will be altered during deformation. The Schmid value distribution evolution of individual grains with different initial orientations taken from a specimen deformed 90° to ED (Figure 5.47) has been thoroughly investigated (Figure 5.56). It is evident that the Schmid value evolution in grains with a stable crystallographic orientation prior to deformation is relatively low (e.g. see Grain 1). However, there are some clear fluctuations between the eight slip systems with close to identical Schmid values, i.e. the ranking among these slip systems changes several times during deformation.

Further, Figure 5.56 also shows that the alterations in the Schmid value distribution are both more extensive and rapid when the grains have more unstable initial orientations (e.g. see grain 2 and 3). The most favourable orientation of the individual slip systems changes due to the crystallographic rotation, hence the Schmid value of the individual systems changes. In general, it is observed that individual grains have a close to linear Schmid value evolution during straining. It is also worth noticing that the most potential slip systems prior to deformation maintain their high Schmid values at the uniform strain even though the internal ranking may have been altered. This means that the slip systems activated at initial plastic flow tend to stay active throughout the deformation process.

It is very rare that a slip system with a low initial Schmid value rotates in such a way that it becomes a very favourable oriented for slip at the uniform strain. However, in some extreme cases when the initial orientation is very unstable, also this kind of Schmid value evolution is observed. As shown in Figure 5.38, grains having a $[101]$ parallel to the DD can rotate as much as 15° during deformation, hence the Schmid value of the individual slip systems changes dramatically as shown in Figure 5.57.

Experimental results – Part B

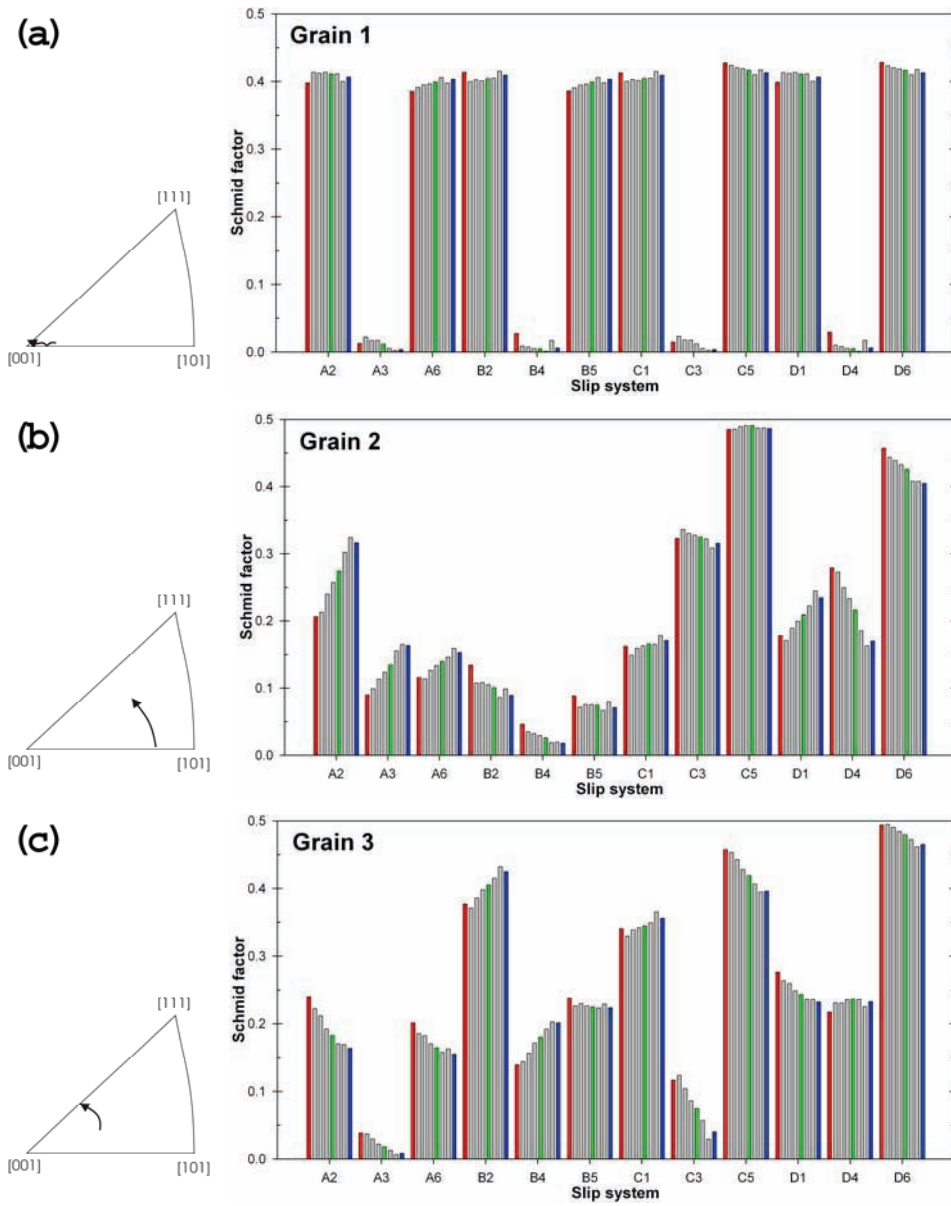


Figure 5.56 – Evolution in Schmid value distribution for grains with various initial orientations deformed 90° related to the ED. The Schmid values after 0% (initial orientation), 12% and 21% (uniform strain) deformation are labelled red, green and blue respectively. The corresponding rotation paths are shown to the left.

Experimental results – Part B

The initial crystallographic orientation (red columns) of grain 4 results in four slip systems having high Schmid values (0.39-0.43), while the remaining slip systems have very low Schmid values (<0.04). The high value slip systems are concentrated to slip systems operating on slip plane A and B (Schmid and Boas notation). The activation of slip systems during deformation and the corresponding grain rotation result in a severe reduction in the Schmid value for the two slip systems on plane A. The reduction in Schmid value after 27% axial elongation (blue columns) of slip system A3 and A6 is 0.24 and 0.15 respectively, while the Schmid values of B4 and B5 are close to constant. However, the experimental results clearly show that the Schmid value of all slip systems on plane C increases as a consequence of this crystallographic rotation. Further, it is clear that the increase in Schmid values on slip system C1 (0.26) and C5 (0.18) are equal to the simultaneous reduction on slip system A3 and A6. From a Schmid value analysis point of view, these Schmid value alterations make slip system C1 and C5 equivalent to slip system A3 and A6 respectively. The crystallographic rotations have resulted in two slip systems maintaining their high Schmid values at the uniform strain, four slip systems have developed intermediate Schmid values (0.17-0.28) while the remaining slip systems maintain values close to zero.

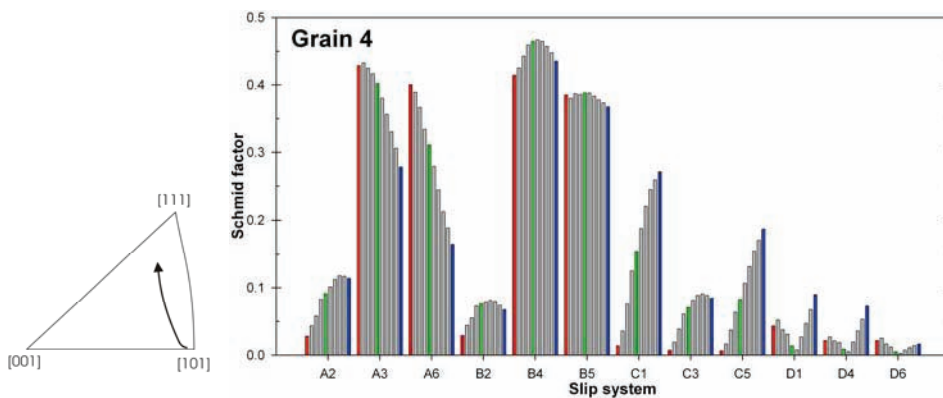


Figure 5.57 – Evolution in Schmid value distribution for a Cube orientated grain deformed 45° related to the ED. The Schmid values after 0% (initial orientation), 12% and 27% (uniform strain) deformation are labelled red, green and blue respectively. The corresponding rotation path are shown to the left. Figure 5.58 presents the slip trace distribution of this grain.

Experimental results – Part B

Moreover, both grain 1 and 4 have a crystallographic orientation close to the perfect Cube orientation (see Figure 5.56 and Figure 5.57). The similarity in crystallographic orientation makes these grains suitable for demonstrating the effect of the DD to the activation of slip systems during deformation. Grain 1 is deformed 90° to ED while grain 4 is deformed 45° to ED. As mentioned above, grain 1 is stable while the orientation of grain 4 is unstable. Grain 1 has a total of eight slip systems with Schmid values close to 0.41 distributed on the four available $\{111\}$ -planes. Since the Schmid value distribution hardly changes, eight slip systems will be available until the material reaches the uniform strain. On the other hand, Grain 4 has only four slip systems with Schmid values close to 0.41 available at initial plastic flow. Further, crystallographic rotation results in only two slip systems having this Schmid value at uniform strain. In other words, the number of available slip systems with Schmid values comparable to the maximum values observed in grain 1 is strongly reduced. In addition to the slip systems maintaining their high Schmid values, grain 4 also has four slip systems with approximately 0.5 times the initial maximum Schmid value.

Calculations of the theoretical slip traces are a favourable supplement to the observed ones. In Figure 5.58 the theoretical slip traces of the four $\{111\}$ -planes are overlaid the observed slip traces after 12% deformation. It is evident that the theoretical slip traces of plane B and in some cases plane A, fully coincide with the observed slip traces. However, even at the uniform strain there are no observed slip traces parallel to the theoretical slip traces of plane C and D.

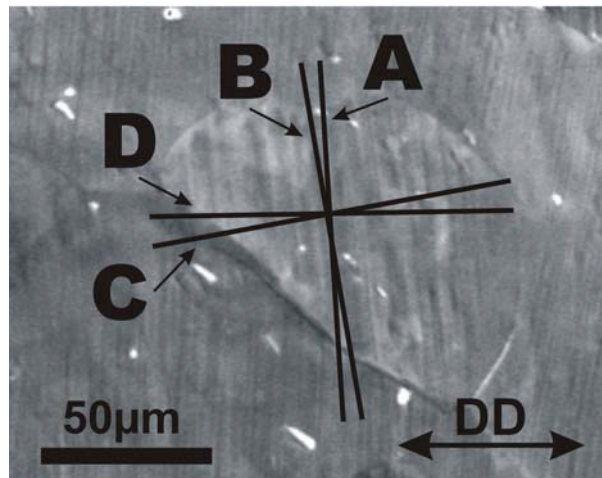


Figure 5.58 – Observed slip traces in Grain 4 after 12% deformation. The orientations of the theoretical slip traces from the four $\{111\}$ -planes are as indicated.

As shown in the previous section, the slip trace evolution is much more heterogeneous in the material after the crystallographic texture has been removed. The results indicate that this is also the case for the slip activity. The slip trace evolution (Figure 5.51) and the corresponding Schmid value distribution evolution (Figure 5.59) of a grain from a material with random texture deformed in the 90° direction has the following characteristics. The observed slip traces labelled 1 to 3 in Figure 5.51 correspond to the theoretical slip traces of plane A, B and C respectively. Slip system A6 has the highest Schmid value, while A2 and A3 have low to intermediate Schmid values after 6% elongation (see Figure 5.59). Further, slip systems B2, B5 and C1 also have high Schmid values at this strain level. However, from the micrographs presented in Figure 5.51, it is evident that the observed slip traces originate from slip activity on slip plane A. Slip traces from plane B become visible locally after 12% deformation. This means that at least one additional slip system on plane B have been activated in this region. Further, when the specimen is deformed to 18%, a second set of additional slip traces develop in another region of the grain. This set of slip traces coincide with the theoretical slip traces of plane C.

These results show that the slip activity is very heterogeneous even within one individual grain. The identified crystallographic orientations possess a substantial spread in Schmid

Experimental results – Part B

values (Figure 5.59) and the slip systems most favourably oriented for slip are distributed among several slip planes.

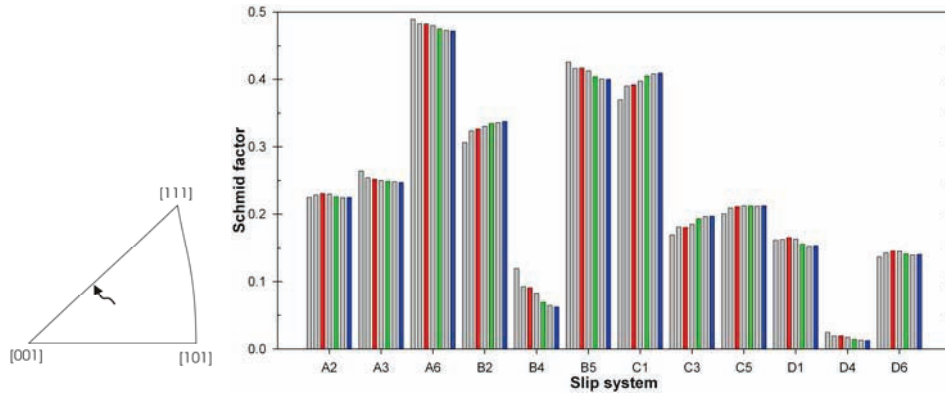


Figure 5.59 – Evolution in Schmid value distribution in a typical grain from a specimen without crystallographic texture. The Schmid values after 6%, 12% and 18% (uniform strain) deformation are labelled red, green and blue respectively.

5.7 Local strain distribution

As shown above, the individual grains have dissimilar slip activity due to variations in crystallographic orientation and the material will therefore develop a local strain distribution during deformation. The slip distribution can even be very heterogeneous within one individual grain, i.e. it develops strain gradients (see the previous section). In the following, the local strain distribution has been quantified on a grain scale in order to understand how different texture components in a recrystallized aluminium alloy deform plastically. The local strain distribution has also been investigated at the meso scale (here; through the profile thickness).

The local strain distribution of the individual grains is obtained by the digital speckle correlation analysis (DSCA) technique based on micrographs acquired in the SEM. The technique is described in more detail in Chapter 2.6. With this technique, it is necessary to produce a structured surface, i.e. it should be textured so that the matching procedure yields a dense distribution array of homologue points. For the specimens investigated, in this work, this was obtained by producing a gold grid on top of the electrochemically polished surface.

5.7.1 Micro scale

The local strain distribution in a specimen deformed 45° related to the ED was investigated in order to study the effect of the initial orientation. It is important to remember that this DD possesses more homogeneous deformation properties than the other directions investigated (see Chapter 5.6 Plasticity). Figure 5.60 presents SEM micrographs of the grid prior to deformation and at the uniform strain (27%). A visual inspection of the distorted grid shows that the deformation is very heterogeneous. The micrographs also show that the strain distribution is heterogeneous even within the individual grains.

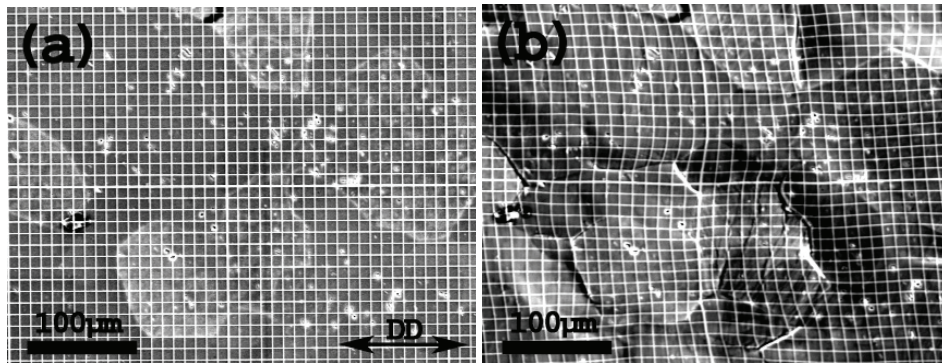


Figure 5.60 – Micrograph of the specimen surface having overlaid a gold grid to visualise the heterogeneous deformation. (a) Prior to deformation and (b) at 27% deformation (uniform strain).

The IPF map shows that the majority of the grains have close to a $[101]$ parallel to the DD (green grains) while some of the grains have close to a $[111]$ parallel to the DD (blue grains) prior to deformation (Figure 5.61). This will again lead to some heterogeneity in the corresponding Taylor factor map as shown in Figure 5.62. The calculated Taylor factors indicate that some grains will deform quite easily while other grains are harder to deform. The Taylor factor map is more or less consistent with the visual observations of the distorted grids presented in Figure 5.60.

Experimental results – Part B

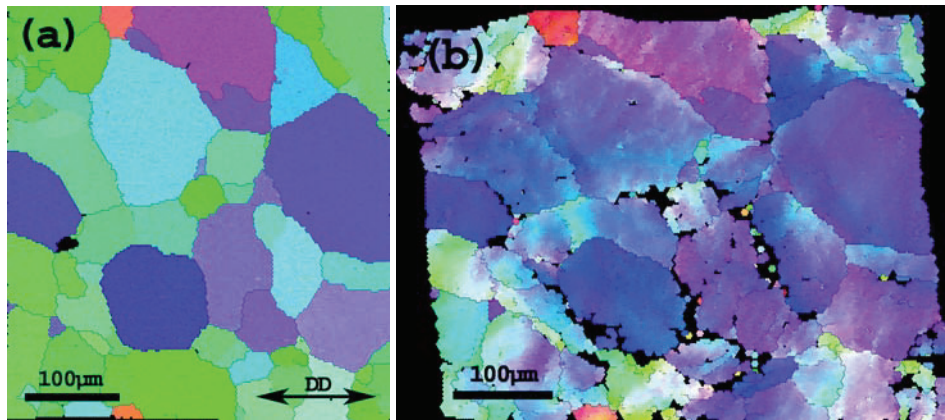


Figure 5.61 – IPF map of the same area (Figure 5.60) in the deformation direction based on orientation data. (a) Initial orientation and (b) at uniform strain (27%).

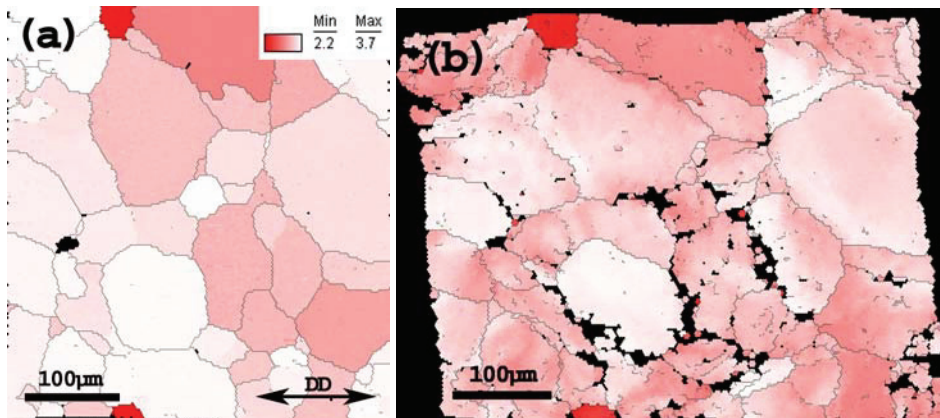


Figure 5.62 – Taylor factor map of the same area as in the two previous figures calculated from the Taylor FC method. The colour key represents the different Taylor factors of the individual grains. (a) Initial orientation (b) uniform strain (27%)

To quantify the deformation heterogeneity, the local in-plane strain distribution was calculated. In Figure 5.63, the major strain distribution after 16% and 27% (uniform strain) axial elongation was calculated based on the SEM micrographs of the distorted grids (Figure 5.60). The grain boundaries from the EBSD investigations are overlaid the strain distribution map in order to separate the individual grains. These strain maps clearly show that some grains are given large deformation while other grains hardly deform at all. The heavily deformed grains deform up to 400% as much as grains with a high Taylor factor. It is also worth noticing that the observed relative differences in amount of deformation are close to constant throughout the tensile experiment. The

Experimental results – Part B

strain distribution maps also confirm the observed heterogeneity within the individual grains. The major strains can vary quite substantially from the centre of the grain toward the grain boundary, and differences up to 40% in relative numbers are often observed.

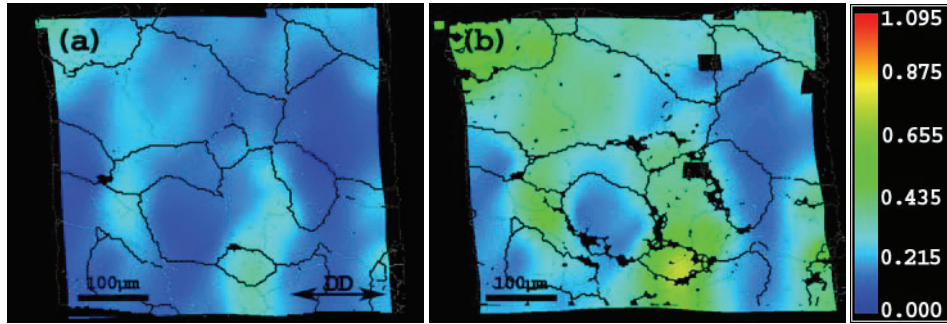


Figure 5.63 – Local major strain distribution of the same area as above, calculated by the DSCA technique from SE micrographs acquired during deformation. (a) 16% (b) uniform strain (27%)

A different and even more pronounced type of local strain distribution becomes evident at higher strains. The deformation localises when the material reaches post-uniform strains and localised shear bands develop. As can be seen from Figure 5.64, further deformation takes place within the band, and the border between the shear band and the surrounding material becomes very evident. It has been shown that all the investigated directions of both alloys develop evident shear bands. However, the characteristics of the shear bands are strongly direction-dependent. Further, the strain distribution within the shear band itself is also very heterogeneous (Figure 5.65).

Experimental results – Part B

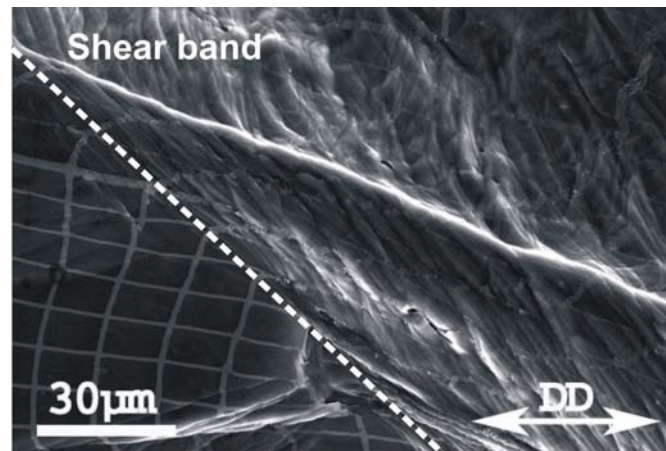


Figure 5.64 – Example of strain gradient at the edge of a shear band. The border between the shear band and the surrounding material is indicated by the dotted line.

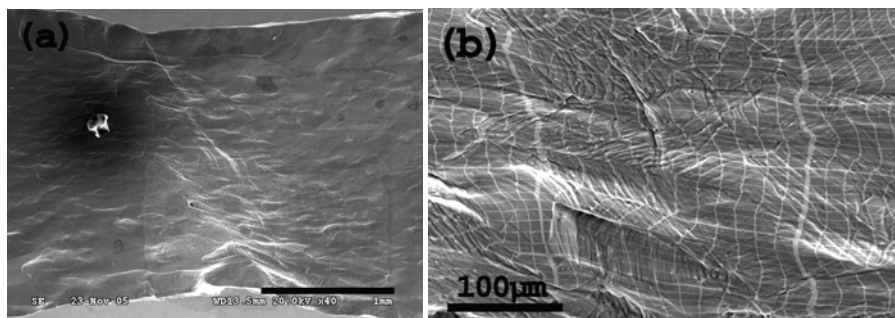


Figure 5.65 – Example of shear band development in the post-uniform strain region (a) and close-up of the corresponding heterogeneous strain distribution (b).

Most of the grains are significantly deformed while other grains are weakly deformed. This leads to extreme strain gradients as shown in Figure 5.66. It is not possible to perform automatic strain measurements based on these micrographs due to the heavy distortion of the gold grid. The grid is therefore reproduced by image processing software and the in-plane strains calculated manually. The results from these calculations show that the strain increases with more than 500% in relative numbers over a distance less than 60µm (Figure 5.67). Hence, the strain gradients observed within the shear band is of the same order as the strain gradients normally observed between the shear band and the surrounding areas.

Experimental results – Part B

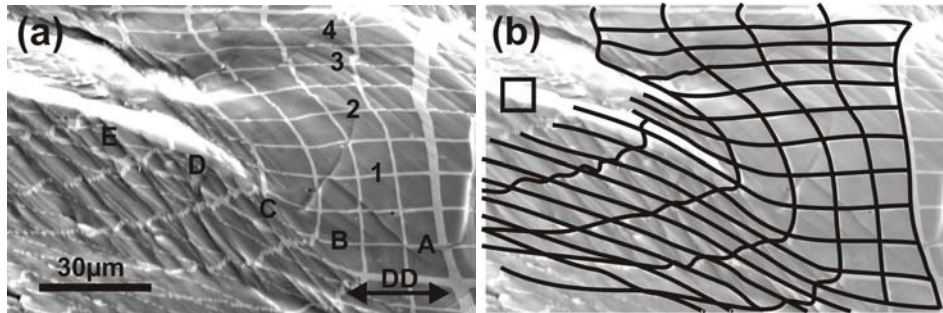


Figure 5.66 – Micrographs presenting the strong deformation gradients observed in a shear band (left part) at the post-uniform strain region. (a) SE micrographs (positions for strain measurements are indicated). (b) Reconstructed grid as used for strain measurements. The size of an initial grid element is also included for comparison.

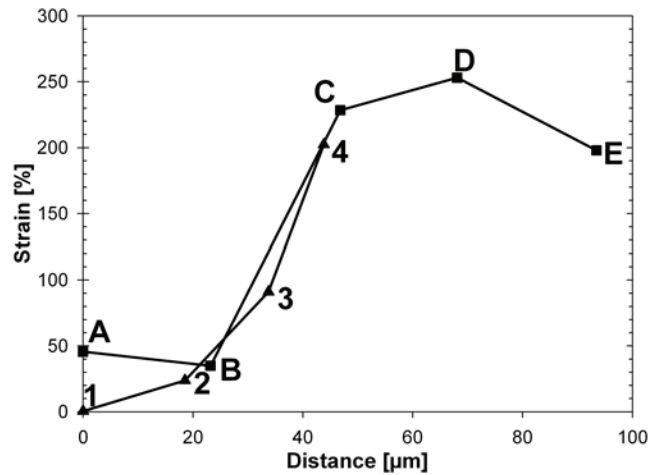


Figure 5.67 – Local strain distribution within the shear band along the two axes indicated in Figure 5.66.

If the local strain distribution in a grain from a specimen with an overlaid grid is investigated in even more detail, it becomes evident that strain and strain measurements on this length scale became complicated. Figure 5.68 presents the observed slip traces in a specimen marked with a gold grid. It is clear that the material deforms by slip on selected slip planes and not as a continuum. Hence, the strain distribution on this length scale can probably not be described by continuum mechanics. The material deforms heavily at the activated slip planes and these planes are separated by more or less undeformed regions (Figure 5.68).

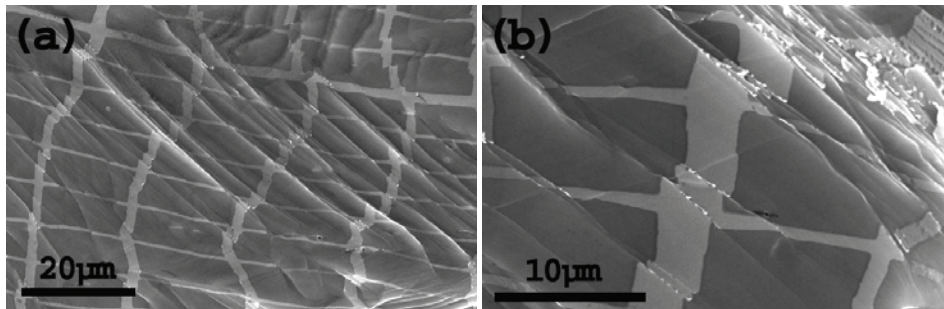


Figure 5.68 – (a) Slip traces and local strain distribution on a grain scale. (b) Close-up of an area with heavily distorted grids.

5.7.2 Meso scale

The meso scale heterogeneities of AA6063 have been studied by deforming in-situ in the SEM (see Chapter 4.1 for the experimental details). The special specimen geometry includes a possibility to perform through-thickness investigations of strain distribution and also of the grain rotations taking place during deformation. Figure 5.69 presents the deformed surface microstructure at uniform strain for specimens tested in the three different directions. They possess meso scale heterogeneities in addition to the micro scale heterogeneities presented in the previous section.

The centre and middle layer ($S=0.00$ to $S=0.85$) of all specimens investigated deforms relatively in-homogeneously, with a large fraction of the grains developing localised coarse slip traces, e.g. see Figure 5.70 and Figure 5.71 for specimens deformed at 0° and 45° respectively. It is clear that the centre region is heavily deformed (pronounced coarse slip) at the uniform strain level regardless of the deformation direction selected, although the coarse slip distribution is not so pronounced in the 90° specimen.

There is also a small directional dependency with regard to deformation/strain development in the surface layer ($S=0.85$ to $S=1.00$). A fine slip distribution is often observed in the surface layer of the 0° specimens. These grains normally develop visible slip traces first at high strains and some of them do not even develop visible slip traces at the uniform strain. The surface layer consists of grains with a very localised and coarse slip distribution in the 45° direction. The extended region between the surface and the centre layer on the other side shows a finer, i.e. more homogeneous slip distribution

Experimental results – Part B

(Figure 5.69 (b)). The 90° direction, on the other hand, deforms with no obvious differences between the different regions and most grains have relatively dense traces of slip. However, some surface grains have localised coarse slip, even with cracking occurring along the traces (Figure 5.69 (c)).

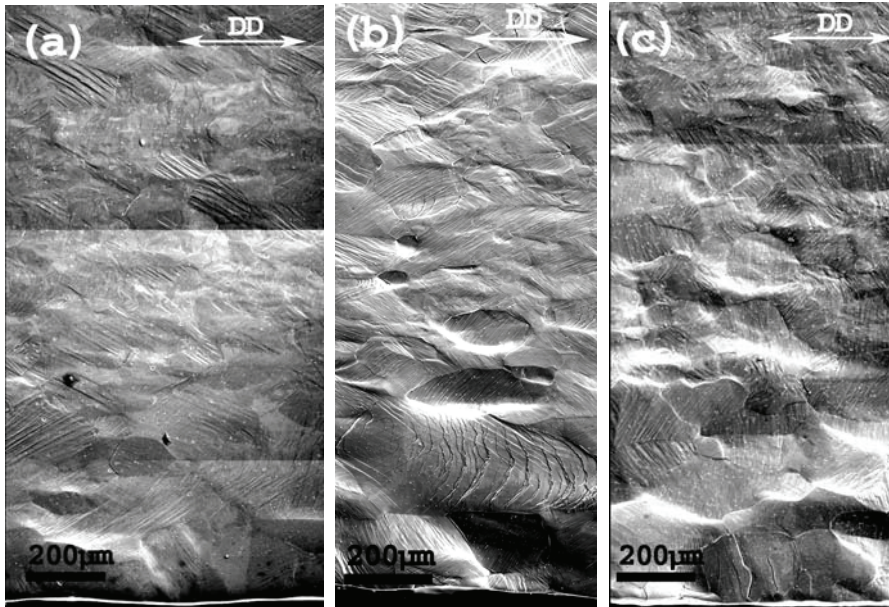


Figure 5.69 – Micrographs over the thickness at the uniform strain. Centre position ($S=0.00$) at the top and surface position ($S=1.00$) at the bottom. (a) 0° , (b) 45° and (c) 90° direction.

Experimental results – Part B

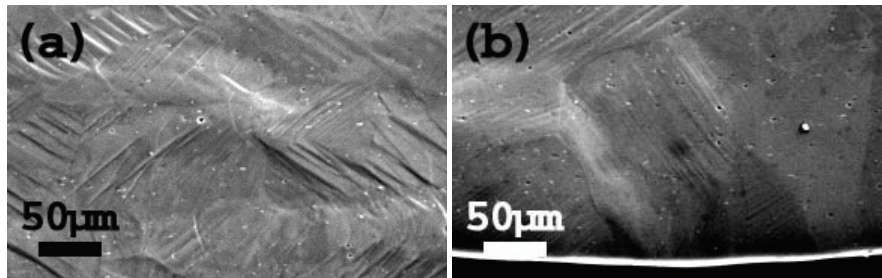


Figure 5.70 – Micrographs showing slip traces at the uniform strain (12%) for a specimen deformed parallel to the ED. (a) centre position and (b) surface position.

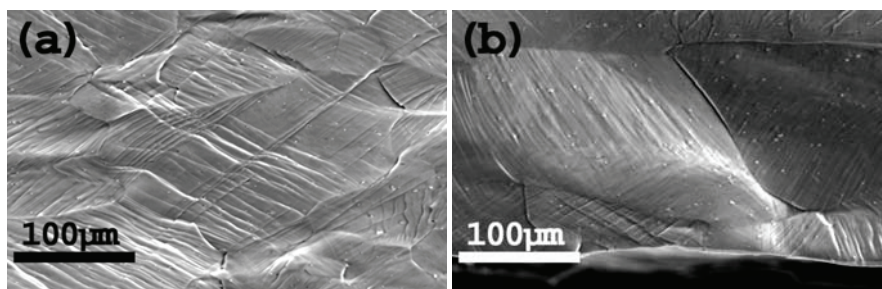


Figure 5.71 – Micrographs of slip traces at the uniform strain (27%) for a specimen deformed 45° related to the ED. (a) centre position and (b) surface position.

Furthermore, the experimental results also show that there are substantial differences between the 0° and 45° directions with regard to crystallographic directions parallel to the DD. It has previously been shown that the material possesses a strong through-thickness gradient (see section 5.1.3) that will affect the deformation properties. When the grains in the centre layer are compared to the grains in the surface layer of specimens deformed 0° and 90° to the ED, it is clear that the surface layer is unfavourably orientated for slip and most of the deformation should therefore take place in the centre region. This is not the case for the 45° specimen where the surface layer is equivalent or even more favourable oriented for slip than the rest of the specimen. Hence, the amount of deformation in the surface and the centre region should be close to equal in this direction.

Experimental results – Part B

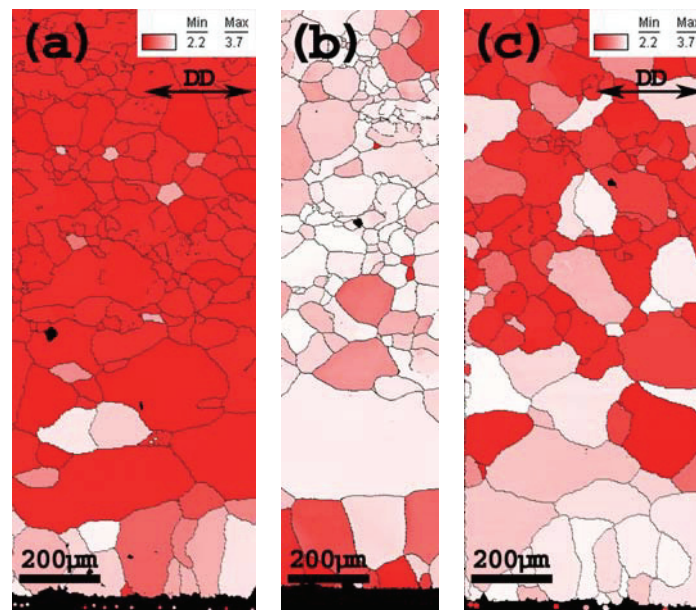


Figure 5.72 – Taylor factor map calculated by the Taylor FC method based on initial crystallographic orientations. Centre position ($S=0.00$) at the top and surface position ($S=1.00$) at the bottom. (a) 0° , (b) 45° and (c) 90° direction.

This is clearly shown by the Taylor factor maps calculated based on the crystallographic orientations prior to deformation (Figure 5.72). Both the 0° and 90° specimens have relatively high Taylor factors (white) in the surface layer, while the Taylor factors in the centre and middle layer of the profile are relatively low (red). The specimen deformed in the 45° direction has the lowest Taylor factors in the surface layer and high to very high Taylor factors in the centre and middle layers. Therefore, the Taylor factor calculations indicate that crystallographic slip is favoured in the centre and middle layer of the profile when deformed parallel and perpendicular to the ED and in the surface layer when deformed in the 45° direction.

In-situ investigations over the profile thickness have also revealed another type of local strain distribution on the meso scale. Strain measurements performed by the DSCA technique show that the strain is localised even prior to the uniform strain. This type of strain localisation appears already after 9% deformation for the specimen deformed in the 45° direction. Here, Figure 5.73 presents the evolution in the local strain distribution during deformation. The software was not able to calculate the strain distribution at uniform strain (27%) due to a large distortion of the grid elements. However, the

Experimental results – Part B

calculated strain distributions show that the deformation is localised bands oriented approximately $\pm 45^\circ$ to the DD. Notice that the distance between these bands seems to be very repeatable.

Further, the specimen surface develops large strains in areas where two bands intersect. In other words, it seems that the deformation carried by the individual bands is additive and the deformation in the intersection area is roughly equal to the sum of the two accumulated strains. Figure 5.73 also shows that these areas can reach up to 63% deformation while the specimen in average has a strain of 22.5%. Hence, the strain observed in strain intensive areas is almost three times as high as the average strain.

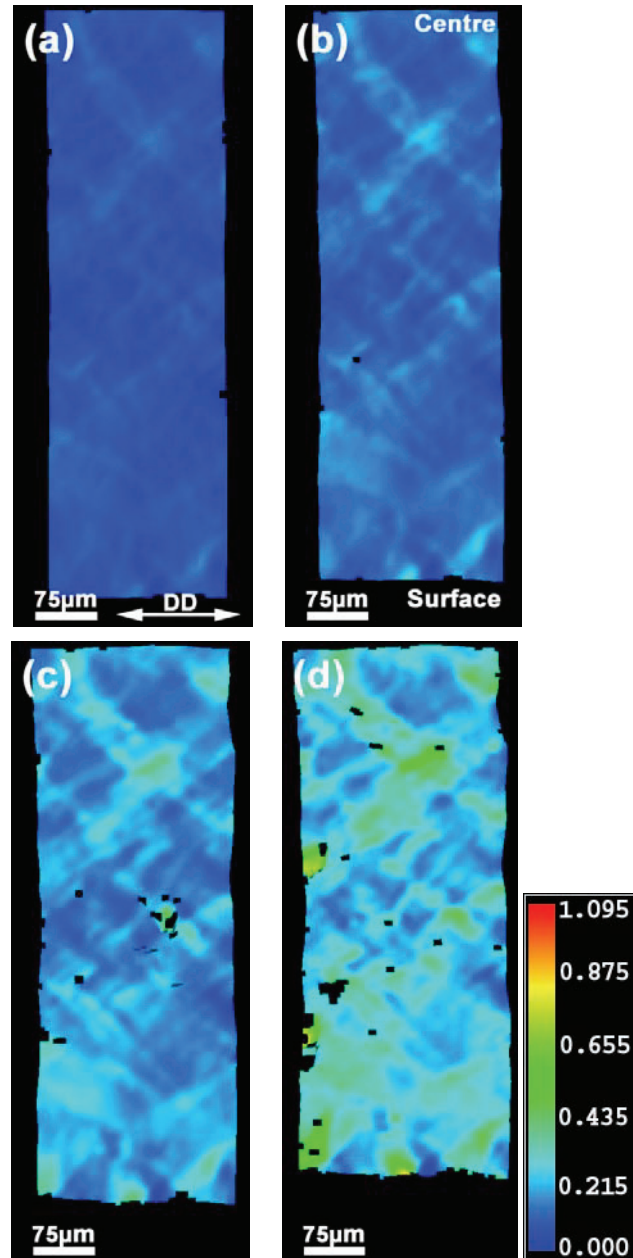


Figure 5.73 – Measured strain distribution evolution (DSCA technique) over the thickness for a specimen deformed 45° related to the ED. Centre position at the top and surface position at the bottom. (a) 9%, (b) 13.5%, (c) 18% and (d) 22.5% deformation. Strain distribution at higher strains was not possible due to a large distortion of the grid.

Experimental results – Part B

Figure 5.74 shows that also specimens deformed parallel to the ED develop localised deformation bands ($\pm 45^\circ$) during straining. However, the bands are not as pronounced for this direction as for the 45° direction. By studying the strain distribution evolution in more detail, it is clear that the localisation takes place at an earlier stage for specimens deformed parallel to ED than for specimens deformed 45° to ED (see e.g. Figure 5.73 (a) and Figure 5.74 (a)). It should also be pointed out that the local peak strain at the uniform strain is comparable for both directions investigated ($\sim 65\%$).

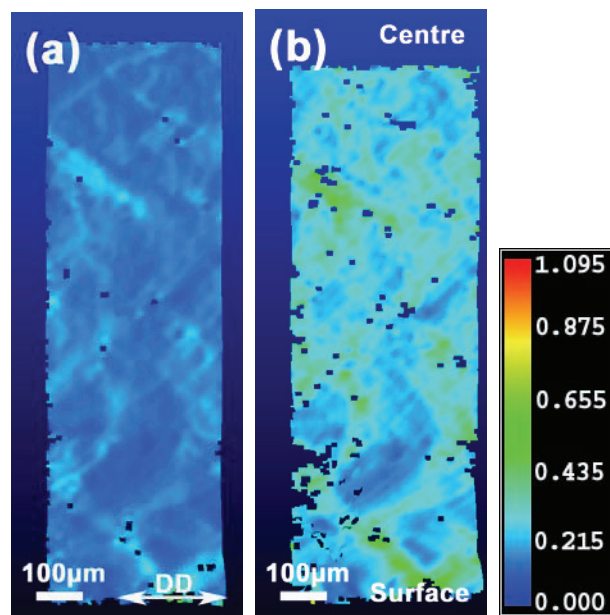


Figure 5.74 – Measured strain distribution evolution (DSCA technique) over the thickness for a specimen deformed parallel to the ED. Centre position at the top and surface position at the bottom. (a) 9% deformation and (b) uniform strain (12%).

6 Discussion

The experimental results presented in the previous chapter deals with many of the fundamental questions related to metallurgy and materials science of aluminium alloys. Hence, the discussion part of this thesis could easily have treated several important topics in a shallow manner. Instead, a more comprehensive discussion of the main objectives has been given, i.e. plasticity and mechanical anisotropy. The first part of this discussion will look at the macroscopic anisotropy observed in the investigated extruded profiles. Later in this chapter, the reasons for this observed macroscopic behaviour will be treated on a microscopic length scale, e.g. distribution of slip. This will be done by looking into the deformation mechanisms operating in individual grains. As a result, this chapter will result in an improved understanding of the plasticity taking place during forming of extruded Al-Mg-Si profiles.

6.1 Mechanical anisotropy

The mechanical anisotropy is in many respects one of the most important mechanical properties of any material that will be plastically formed to its final shape. It is crucial to fully understand the causes for anisotropy, and how these can be governed. This chapter will therefore be used to discuss the different causes for mechanical anisotropy and how these can be explained from a metallurgical point of view.

6.1.1 Crystallographic texture

In order to discuss the observed mechanical anisotropy, it is necessary to repeat some of the main findings related to microstructure and crystallographic texture. The two present alloys have different microstructure and crystallographic texture characteristics. The non-recrystallized alloy (AA6082) has a fibrous microstructure with a typical deformation texture having a maximum intensity of 13 times random. The texture is dominated by the Brass (B) and S components, which are typical for plane strain compression (Humphreys and Hatherly 1996). The microstructure in the centre part of the profile also consist of relatively large amount of retained Cube, as shown by the large fraction of Cube bands at $S=0.00$ (Figure 5.9). This kind of band is often related to plane

Discussion

strain deformation, which also is the deformation mode in the centre part of the profile (Vatne et al. 1996a). The surface region of a profile is subjected to heavy shear deformation during extrusion, hence it could be expected that this area develop a strong shear texture. However, in the surface region, the driving pressure for recrystallization (P_D) exceeds the retarding forces from precipitation of $MnAl_6$ type dispersoids (Petzow and Effenberg 1993). This results in a surface region with a recrystallized microstructure with close to random texture with traces of typical shear components (Humphreys and Hatherly 1996).

AA6063 on the other hand, has a fully recrystallized and equiaxed microstructure with a belonging crystallographic texture. The global texture of this profile is strong, with the most pronounced texture components having intensities close to 27 times random. This is more than twice as high as the intensity observed for the most pronounced texture components of AA6082. The Cube and the ED-rotated Cube (CG and Goss) orientations are the main texture components of this recrystallized profile. Vatne et al. (1996b) have shown that the origin of the Cube (C) orientation is the growth of highly mobile $40^\circ \langle 111 \rangle$ interfaces between grains with retained Cube and S orientation. Further, it is assumed that grains with a Goss orientation can grow out of transition bands within grains having the Brass orientation (Hjelen et al. 1991). From these observations it seems like the recrystallization texture is dependent on the deformation texture prior to recrystallization (see e.g. Furu et al. 2004). The surface layer of this profile is also without any texture due to the same reasons as for AA6082.

It is noticeable that AA6063 most likely possess microstructure and texture equal to AA6082 prior to recrystallization (Furu et al. 2004). This means that the deformation texture of AA6082 might be used to explain the observed texture in AA6063, as suggested by Furu et al. (2004). The centre layer of AA6063 has a very strong Cube texture which diminishes somewhat toward the surface layer (Figure 5.8). This is most likely related to the area fraction of the retained Cube and S orientation prior to recrystallization (Figure 5.11). The area fraction of S orientation increases but the area fraction of retained Cube decreases dramatically. The model presented by Vatne et al. (1996a), suggest that the area fraction of Cube should decrease toward the surface, i.e. in

Discussion

accordance to the present observations. Figure 5.11 also shows that the area fraction of Brass increases a good deal toward the surface of the fibrous microstructure.

Previously, it has been shown that recrystallized grains with Goss orientation originate from heavily deformed Brass-grains exposed to high temperatures (Bowen 1990). It has also been shown by Hjelen (1990) that recrystallized grains with Goss orientation tend to grow into areas with a high fraction of Brass oriented grains. These previously reported results are therefore consistent with the large increase of Goss oriented grains in the middle layer of AA6063.

It is suggested that the strong through-thickness gradients observed in the recrystallized profile can be explained by the heterogeneous deformation in the extrusion die. A more detailed discussion on how Taylor analysis can be used to explain thickness gradient anisotropy will be given below (Chapter 6.2). Furthermore, nature of these gradients and the possible effect of these on formability of extruded profiles will be discussed in more detail in Chapter 6.4.

Age-hardening effects

Natural- and artificial-ageing and ageing mechanisms, in it self, has not been investigated in this work. The focus of this work has rather been to study the effect of age-hardening on the mechanical anisotropy observed in the present two Al-Mg-Si-alloys. The present findings support the theory suggesting that the deformation is heterogeneous and occurs in bands of dislocations on $\langle 111 \rangle$ planes in the case of shearable precipitates, while for non-shearable precipitates, a relatively homogeneous distribution of slip is observed (see section 2.7.4 for details). Section 5.2.3 shows that both alloys posses an evident mechanical anisotropy in the solution-heat-treated condition (W, 10 min). In this condition, the anisotropy is in large extent determined by the crystallographic texture. The tensile test results have shown that naturally ageing to the T4 3h, T4 24h and T1 conditions introduce a substantial quantity of shearable precipitates (i.e. strength increases). These precipitates are normally homogeneously distributed in the matrix hence the most potential slip systems prior to precipitation will probably still be among the most potential slip systems after the shearable dislocations have been introduced.

Discussion

Further, the activated slip systems in the present AA6063 with a strong crystallographic texture will remain or even become more potential when they first have been activated. Hence, the mechanical anisotropy will hardly be affected by the introduction of shearable precipitates. However, when Al-Mg-Si-alloys are artificially aged to the peak aged (T6) and over aged (T7) conditions, the microstructure will consist of a combination of shearable and non-shearable precipitates. Very truly, the introduction of non-shearable particles clearly distributes the deformation and the mechanical properties become more isotropic as shown in Figure 5.15 and Figure 5.16.

Further, it has been pointed out in Chapter 2 that the introduction of particle free zones (PFZ) after ageing to the T7 condition could alter the mechanical anisotropy observed in age-hardenable aluminium alloys (Poole et al. 2005). The PFZ regions might carry a large portion of the strain, which again could make the anisotropy more grain shape dependent. This will not affect AA6063 (equiaxed grains) while the AA6082 could be influenced by these effect due to a fibrous microstructure. If the figures presenting the effect of ageing on the mechanical properties (Figure 5.15 and Figure 5.16) are studied in great detail, it could be argued that AA6063 has more isotropic mechanical properties than AA6082. However, the particle free zones (PFZ) in Al-Mg-Si-alloys are normally very narrow and therefore this effect could most likely be neglected for the alloys investigated in the present work.

Another associated observation regarding the age-hardening – anisotropy interaction is the tensile sample end of cross-section shape (Figure 5.20). This figure shows a strong cross-section curvature in the solutionised condition. This curvature is most likely related to the through-thickness texture variations that will be discussed in the following section. When the specimens are artificially aged, this texture effect is suppressed, and the end of cross-section curvature disappears. Based on the discussion above, it is reasonable to assume that the cross-section curvature disappears because the slip distribution is to a larger extent determined by the introduced precipitates and the influence from crystallographic texture becomes less important. This means, that the slip distribution has become more homogeneous through the cross-section of the profiles.

Discussion

6.1.2 Texture vs. Mechanical observations (mainly AA6063)

Simple tension investigations performed 0° , 45° and 90° related to ED confirms that both AA6063 and AA6082 possess strong mechanical anisotropy in the solutionised condition (see Figure 5.12 and Figure 5.13). AA6063 has an equiaxed microstructure and a strong Cube texture somewhat rotated around the extrusion direction (ED) as shown in Figure 5.4. As a first approximation, one can assume that a material carrying a strong Cube texture has close to isotropic mechanical properties parallel and perpendicular to the ED due to the highly symmetrical Cube orientation (see e.g. Li and Bate 1991 and Lopes et al. 2003). However, the observations in Figure 5.12 indicate that this is not the case for the recrystallized profile investigated in this work. This alloy exhibits significant mechanical anisotropy, i.e. especially when observing the non-artificial aged conditions.

In general, the shear stress (τ) vs. shear strain (γ) curves for materials where the anisotropy is governed by the crystallographic texture is directional independent. This means that materials with texture controlled anisotropy have coincident $\tau - \gamma$ curves in all deformation directions. The shear stress and shear strain can in basic be calculated based on the axial stresses and strains together with the corresponding Taylor factor (M).

$$\tau = \frac{\sigma}{M(\varepsilon)} \quad \text{and} \quad \gamma = \varepsilon \cdot M(\varepsilon) \quad (24)$$

where $M(\varepsilon)$ is the Taylor factor at a given strain (ε). The Taylor factor is calculated from the crystallographic texture applying crystal plasticity models. This means that it is necessary to acquire the texture evolution during deformation in order determine the Taylor factor evolution. It has been shown in previous works that changes in initial texture due to age-hardening of AA6063 are minimal (Li and Van Houtte 2002b, Ryen 2003, Bjerkaas et al. 2005). Taking these observations, the initial Taylor factor seems not dependent on the actual material condition.

Ryen (2003) tried to explain the origin of the observed mechanical anisotropy of AA6063 and AA6082 by comparing the shear stress and shear strain relationship 0° , 45°

Discussion

and 90° related to ED. However, Ryen based his Taylor factor calculation only on texture measurements prior and after simple tension deformation. Further, he assumed a linear Taylor factor evolution during deformation:

$$M(\varepsilon) = M(0) + a \cdot \varepsilon \quad (25)$$

where $M(0)$ is the Taylor factor prior to deformation and a is the slope of the linear Taylor factor evolution. These results showed large variations between the different deformation directions even at the onset of plastic flow, where no work hardening or texture changes have occurred.

The investigations initiated by Ryen (2003) have been continued in the present work in order to fully understand the mechanical anisotropy observed in the two Al-Mg-Si profiles. New Taylor factor calculations were performed using the same software (MTM-FHM software system (Taylor model), see section 2.4.2 for more details). In addition, in-situ deformation experiments in the SEM provided more detailed descriptions of the texture evolution upon tensile deformation.

It has been shown (Figure 6.1) that the calculated Taylor factor evolution with increasing strains actually follows close to a linear relationship. Hence, the above linear assumption made by Ryen (2003) should provide a nearly satisfying description of the crystallographic texture evolution. The corresponding $\tau - \gamma$ curves based on the texture measurements and Taylor factor calculations performed in this work are presented in Figure 6.2. These curves diverge from the experimental non-artificial aged curves (Figure 5.12), since the stress level of directions 45° and 90° have exchanged their relative positions at the highest strain-level. Another discrepancy is that the experimental curves for the 45° and 90° cross each other for the W- and T4-conditions, but the calculated curves in Figure 6.2 do not capture this evolution. However, the calculations are correctly predicting that the 0° -orientation has the highest stress level. Moreover, calculations made by the Taylor relaxed constraint (RC) method seems to provide more coincident results than the full constraint (FC) method since the former indicates less difference in stress levels comparing the different directions. In general, the Taylor based

Discussion

calculations reveals a shear stress level ~20-70% above the experimental values (W-condition).

Further, if the anisotropy is assumed to be caused by crystallographic texture, these calculations reveal that the material tend to deform with fewer activated slip systems than assumed in the classical Taylor full constraint (FC) method. This will be further discussed in Chapter 6.3.

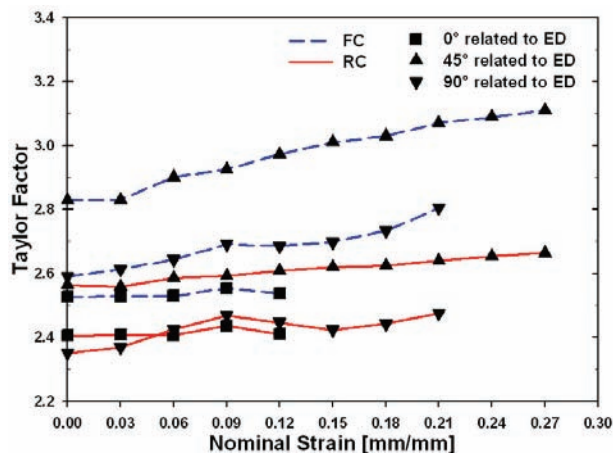


Figure 6.1 – Evolution in Taylor factor during straining of AA6063 0°, 45° and 90° related to ED. Calculations are performed with both full constraint (blue) and the relaxed constraint (red) Taylor model. Please, note that deformation is given in nominal strain.

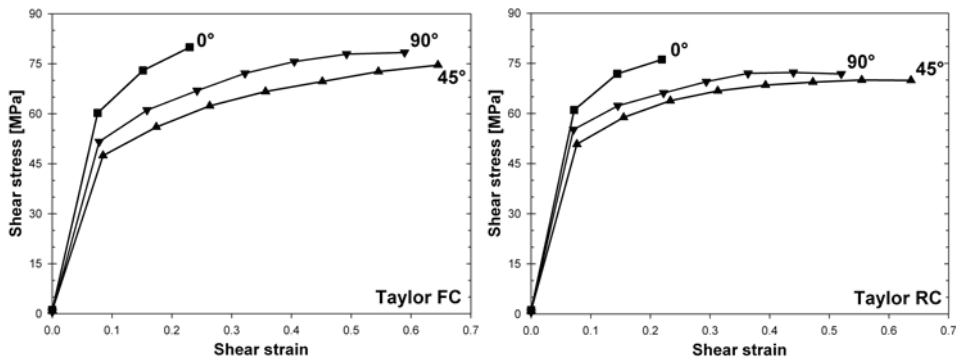


Figure 6.2 – Calculated shear stress vs. shear strain curves for the investigated directions of AA6063. The calculations are based on the Taylor factor evolution during deformation (Figure 6.1). The Taylor factor calculations are performed with both the full constraint (left) and the relaxed constraint (right) Taylor model.

Discussion

In the past several investigations have been performed on materials having a strong Cube texture and it was suggested that the mechanical anisotropy mainly is controlled by the crystallographic texture (e.g. Li and Bate 1991, Lopes et al. 2003 and Wu et al. 2004). Common for all these investigations is the large $0^\circ/90^\circ$ symmetry of the texture. Hence, these materials possess close to equal properties 0° and 90° to the ED. However, the Cube component of the recrystallized AA6063 alloy investigated in this work, is somewhat rotated around the ED. Therefore possesses this material a much more asymmetrical distributed but equally strong Cube texture. Hence, the ED rotated Cube gives rise to differences between the 0° and 90° as shown by the inverse pole figure (IPF) maps presented in Figure 5.28. Almost all the grains (Cube, CG and Goss oriented grains) have a $[100]$ direction parallel to the DD when deformed parallel to ED. When deformed perpendicular to ED, the same grains have non-equal crystallographic directions parallel to the DD. Grains with a CG or Goss orientation have a $[012]$ or a $[110]$ parallel to the DD respectively. This may indicate that the Schmid values of the individual slip systems are strongly altered compared with deformation parallel to ED (Figure 5.55). The spread in crystallographic orientations parallel to the TD means that the probability for slip differs significantly among the individual grains. This is supported by the Taylor factor histogram and maps, given in Figure 5.53 and Figure 5.54 respectively, showing large variations between neighbouring grains in all directions compared to the 0° direction. It has been shown (section 5.6.1) that the orientation spread observed in the 90° specimens leads to a heterogeneous activation of slip systems. Further, it is reasonable to assume that this will affect the macroscopic stress-strain behaviour of the material and could therefore contribute to explain the observed anisotropic stress-strain curves.

Moreover, it has also been reported that the crystallographic orientation parallel to the DD is of great importance for the work hardening, especially at low strains (Honeycombe 1984). Diehl (1956) performed detailed investigations of the work hardening rate at low strains for copper single crystals with a wide range of crystal orientations. He found that crystallites with a $[110]$ parallel to the DD have a lower strain hardening rate than crystallites oriented near the line attaching the $[100]$ and the $[111]$ corners of the inverse pole figure. This behaviour has also been confirmed for aluminium (see e.g. Lucke and Lange 1952, Noggle and Koehler 1957). These observations

Discussion

performed on single crystals may also be valid for deformation of polycrystals. As mentioned above, nearly all the grains have a [100] parallel to the DD when deformed parallel to the ED, while other crystallographic directions are present when deformed perpendicular to the ED. Hence, it is reasonable to assume that the specimens deformed parallel to ED have more pronounced work hardening at low strains. This is consistent with the observed stress vs. strain relationship in the solutionised and natural aged condition for AA6063 as shown in Figure 5.12, i.e. the 0° specimens have a high work hardening rate compared to the two other directions.

The area fraction evolution of the different texture components is also interesting with regard to the observed anisotropy. The texture evolution presented in Figure 5.27 shows that the stability of the different ideal texture components depends on the DD selected. It is important to remember that both the Cube, CG and Goss orientations all have a [100] parallel to the ED (ED rotated Cube orientations). Hence, since the crystallographic orientation parallel to the DD is of main importance with regard to grain rotation during deformation (see Chapter 5.5) these orientations will behave similarly when deformed parallel to the ED. The highly symmetrical Cube orientation is stable both parallel and perpendicular to the ED during deformation to low and intermediate strains. The intensity of the Cube orientation is however slightly reduced at high strains ($>15\%$) when deformed in the 90° direction. This means, at least at low and intermediate strains, that the cube oriented grains are expected to give the same work hardening and stress vs. strain relationship contribution when deformed 0° and 90° related to ED. However, for this assumption to be valid, the orientation of the neighbouring grains should not affect the slip behaviour of individual grains. This assumption is therefore not completely valid, but it should at least give a good indication of the work hardening contribution from Cube oriented grains.

The Goss grains on the other hand have a more unsymmetrical crystallographic orientation with regard to the 0° and 90° deformation directions. Hence, the stability of this orientation is more dependent of the selected DD. Figure 5.27 shows that the Goss orientation is stable during deformation parallel to the ED while very unstable during deformation perpendicular to the ED. Grains with a Goss orientation have as already mentioned several times, a [100] and a [110] parallel to the DD when deformed parallel

Discussion

and perpendicular to the ED respectively. As a consequence, the activation of slip systems will differ substantially during deformation in these two deformation directions, and both work hardening and the stress vs. strain contribution from these grains will be strongly directionally dependent.

The same argumentation can be used for the CG orientation. However, the differences are not expected to be as large as for the Goss orientation since the CG orientation is more stable in the 90° direction. When studying the different texture components during deformation, it is also conspicuous that the Cube orientation is extremely unstable during deformation 45° related to ED. The Cube orientation has a [110] parallel to the DD when deformed in this direction hence it is reasonable to expect a large reduction in the area fraction of Cube oriented grains during deformation in the 45° direction. It is also worth noticing that the texture evolution during tensile deformation is consistent with the grain rotation path and amount of rotation results presented in Chapter 5.5. From the above discussion, seems reasonable to believe that the observed texture evolution upon tensile straining could be used to support a texture dependent mechanical anisotropy.

However, it could be claimed that the above discussion does not take the interaction between the neighbouring grains into account. The accumulation and movement of dislocations in the vicinity of the grain boundaries are normally dependent on the orientation of the neighbouring grains and will therefore substantially affect the work hardening contribution of the different texture components. The slip-trace investigations presented in section 5.6.1 show that there is an evident directional dependency on how slip traces intersect the grain boundaries (see e.g. Figure 5.46 and Figure 5.47). The micrographs indicate that the slip traces intersect the grain boundaries quite easily when deformed 45° to ED, while intersections seem to be more difficult when deformed parallel or perpendicular to ED. However, the latter statement is difficult to prove. Deformed specimens should therefore be investigated in a transmission electron microscope (TEM) in order to determine any slip activation differences between the 0° and 90° directions. Anyway, if a statistically significant variation with regard to the crystallographic orientations of the neighbouring grains exists, this is governed by the texture. Hence, also this issue supports a texture determined mechanical anisotropy.

Discussion

Further, Figure 6.3 presents the $\sigma - \varepsilon$ curves for AA6063 in material condition T1 at the onset of plastic flow. These curves show that the specimens deformed parallel to the ED and to some extent 45° to, ED have much sharper elastic to plastic transition than the 90° specimens. This is most likely related to the activation of slip systems in the individual grains. The spread in Schmid values for the 90° specimens means that the individual grains will reach the critical resolved shear stress (τ_c^s) after various amounts of deformation, hence the material has a “soft” yield point. All the grains in the 0° specimen on the other hand, have a close to identical Schmid value distribution and will therefore reach the critical resolved shear stress at approximately the same strain, hence the 0° direction possesses a sharp elastic-plastic transition. To be mentioned, the crystallographic texture of AA6082 on the other hand, indicates that all the investigated directions have the same spread in Schmid values. This results in a similar transition for all directions.

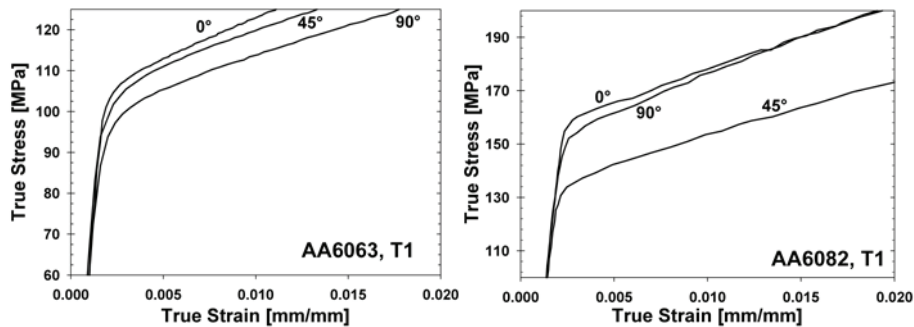


Figure 6.3 – Stress vs. strain behaviour at the onset of plastic flow for AA6063 (left) and AA6082 (right). Please note that this is segment of the whole true stress vs. strain curve.

The observed differences between the 0° and 90° specimens on one side and the 45° specimens on the other side are therefore related to differences in the Taylor factor, i.e. crystallographic texture variations. Hence, the anisotropy in yield strength and plastic deformation properties of AA6063 can be related both to variations in crystallographic texture and variations in crystallographic texture distribution (texture spread).

6.2 Observations and Taylor analyses regarding through-thickness variations

The results presented in Chapter 5 clearly showed that the investigated profiles possess evident through-thickness variations. There are different approaches to obtain an understanding of and the causes for these effects. The through-thickness variations can be engaged either by Taylor-type calculations or experimental investigations. This chapter will be used to discuss through-thickness variations as well as limitations with both methods of engaging this problem.

6.2.1 Taylor analyses

As already shown, the profiles investigated in this work possess strong texture and grain morphology gradients (see section 5.1.3). It is therefore reasonable to assume that Taylor-type calculations based on orientation data taken from the different position through the thickness will give rise to variations in mechanical properties. Therefore, initial crystallographic orientations have been used as input to Taylor method calculations of materials properties through the Taylor factor (M -factor). Also, the plastic strain ratio, or r -value, can be calculated based on the crystallographic orientation data. Taylor method calculations are performed at all the positions through the profile thickness ($S=0.00$ to $S=0.99$) with deformation tensors corresponding to simple tension at 0° , 45° and 90° related to ED. The Taylor full constraint (FC) and the relaxed constraint (RC) methods are used to predict properties for recrystallized (AA6063) and fibrous (AA6082) microstructures respectively. However, the evaluations are based on both methods in order to fully evaluate the texture-based calculations (e.g. see Figure 6.4).

The calculations based on the RC method show that the M -factor of AA6063 increases toward the surface when deformed in the 0° and 90° directions and decreases when deformed in the 45° (Figure 6.4). It is worth noticing that the RC method calculations of AA6082 give rise to the opposite behaviour as to AA6063, i.e. the Taylor factor decreases toward the surface when deformed 0° and 90° related to ED and increases when deformed in the 45° direction (see Figure 6.4). However, the Taylor factor increases toward the surface in all deformation directions when calculated by the FC

Discussion

method. The only difference between the two calculation procedures is the relaxation of two shear directions (ε_{13} and ε_{23}) for the RC-method (pancake shaped grains). Hence, the number of activated slip systems is five and three slip systems for the FC and RC method respectively. By comparing the results from these two methods one can evaluate whether the Taylor factor gradient can be directly linked to the activation of slip systems during deformation.

As mentioned above, the anisotropy differences in the M -factor between the FC and the RC calculations are more pronounced for AA6082 than for AA6063. The Taylor factor calculations of AA6082 made by the FC method are generally twice as high as the RC calculations. This indicates that AA6082 is more dependent upon the number of slip systems physically activated. Further, the calculations indicate that the resistance towards deformation increases more for AA6082 than for AA6063 if the material needs to activate five instead of three slip systems in order to deform. As expected, the FC calculations will always give a higher Taylor factor than the RC calculation and this is simply related to the activation of slip systems. The RC method takes use of the three slip systems most favourable oriented for slip, while the FC method has to add two additional slip systems which are more unfavourable oriented. Thus, the FC method will therefore always give a higher M -factor. However, a more detailed discussion on the number of slip systems activated during deformation and how this correlates to the different calculation methods will be discussed further in Chapter 6.3.

Discussion

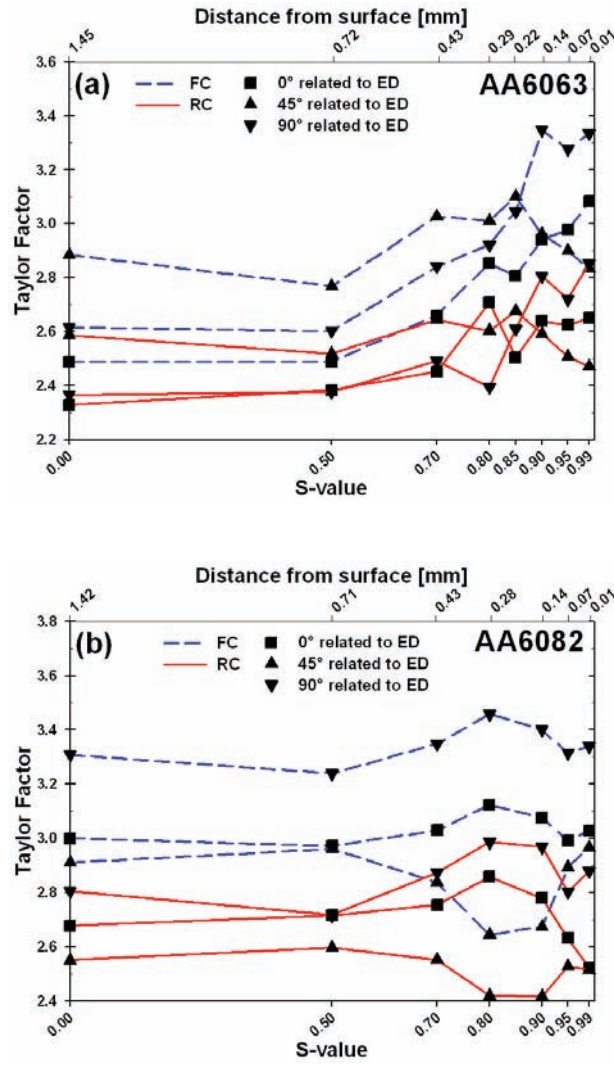


Figure 6.4 – Texture-based calculations of Taylor factors at different positions through the profile thickness. (a) AA6063 and (b) AA6082.

Discussion

6.2.2 Evaluation of the Voce-type model

Furthermore, the observed through-thickness variations will affect the mechanical properties of the different layers through the thickness. Also the Taylor factor calculations indicate that the mechanical properties should vary significantly through the profile thickness. Fjeldbo et al. (2005) have calculated the mechanical properties of the different layers of AA6063 (0° direction), based on the orientation data acquired in this work (M -factors). In the latter work, the critical resolved shear stress (τ) has been expressed as a function of the resolved shear strain (γ) by an extended Voce expression (Voce 1948):

$$\tau = \tau_0 + \sum_{i=1}^2 Q_i [1 - \exp(-C_i \gamma)] \quad (26)$$

where τ_0, Q_1, C_1, Q_2 and C_2 are fitted parameters, determined from the experimental behaviour of a full thickness specimen. Further, the resolved shear stress and strain is here related to the true stress (σ) and strain (ε) by use of equation 25 with $M(\varepsilon) = M(0)$:

$$\bar{\sigma} = M \left(\tau_0 + \sum_{i=1}^2 Q_i [1 - \exp(-MC_i \bar{\varepsilon})] \right) \quad (27)$$

From the last expression, it is clear that the initial yield stress is scaled against $M\tau_0$, where τ_0 is strongly dependent upon the microstructure. Further, also the curve shape is a product of both the fitting parameters and the calculated Taylor factor. This means that the calculated stress strain behaviour (Figure 6.5) will be independent of microstructural variations between the individual layers, but is fully based on variations in crystallographic texture. Consequently, the relative ranking between the different layers through the thickness is fully determined by the differences in texture (M -factor).

Discussion

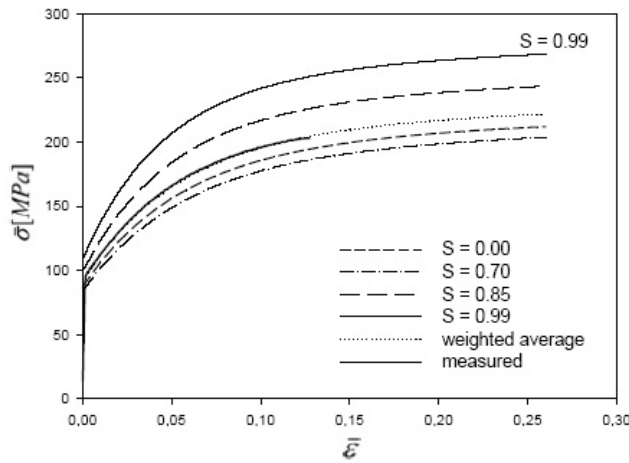


Figure 6.5 – Calculated variations of stress-strain curves parallel to the ED at different positions through the thickness of AA6063 (after Fjeldbo et al. 2005).

As expected, these texture-based calculations show that the mechanical properties of the different layers vary significantly. The calculations for the 0° orientation show that both the initial yield strength and the work-hardening rate is high for the surface layer ($S=0.99$) compared to the centre region ($S=0.00 - S=0.70$). However, these calculations by Fjeldbo et al. (2005) are in contradiction to the experimental results obtained from simple tension experiments performed in this work. Specimens taken from the different positions through the profile thickness have been tested (Figure 5.14) and the behaviour is completely opposite of the texture-based calculations. This means that in this direction (0°) the highest yield strength and work-hardening rate were found in the centre region (centre and middle positions) while the surface position ($S=0.99$) possessed both lower strength and less work-hardening.

As shown in Chapter 5, the AA6063 profile possesses an evident through-thickness microstructural gradient (Figure 5.6). It is expected that such variations will affect both the yield stress and the overall work-hardening rate (shape of the stress-strain curve), layer by layer. This is especially true close to the specimen surface, where the differences in grain sizes are extremely large (Table 5.1). Microstructural heterogeneities can be taken into account by varying the initial shear strain (τ_0) through the profile thickness ($\tau_0(S)$). Such variations are not included in the mentioned calculations, something which certainly reduces the validity.

Discussion

Further, it could be claimed that the observed differences between calculations and experiments are basically linked to the errors in the yield stress calculations. Hence, the shape of the stress-strain curves should be predicted satisfactorily by use of the Taylor factors as input to the Voce type model. However, none of the experimental curves can be predicted correctly by the calculated M -factors. Although, there is an adequate fit for the specimens taken from the centre region, and the texture of this region is equivalent to the global texture (which has been used for calibration of the fitting parameters). Therefore, it is only in this central layer that the calculated curves fit the experimental observations. One can, of course, claim that the observed differences can be related to an intrinsic error in the Voce type model, but it is more reasonable to assume that the disparities are related to the utilised Taylor factors.

Another important shortage with these calculations is not to include the Taylor factor evolution during deformation. One can expect that the M -factor in the centre region is almost unaffected since specimens with this type of texture tend to be stable during deformation in the strain-range typically associated with simple tension (see Figure 5.24). However, the surface region of the specimen (random texture) is not stable and is therefore expected to rotate toward more stable orientations (indicated by change of colour in the IPF maps in Figure 5.34), thus altering the Taylor factors.

Moreover, also the plasticity model utilised will affect the calculated results (M -factor), thus also the stress-strain curve. The alterations introduced by selecting another plasticity model are normally negligible, and it is therefore not reasonable to assume that the accuracy can have been improved by switching from the FC to the RC, or vice versa. However, if one can assume that the constraint from the neighbouring grains alters through the thickness, it can be expected that the number of activated slip systems can vary among the different layers. This means that the different layers is best described with various plasticity models, e.g. the surface layers is described by a Sachs type model (1-2 slip systems) while the centre region is best described by a Taylor FC type model (5 slip systems). Such variations will introduce predictions approaching the observed behaviour of the material.

6.2.3 Experimental effects

It is important to remember that also the experimental results hold some significant limitations. The thickness of the used specimens (0.3 mm) in combination with the actual grain sizes in the normal direction (Table 5.2), especially close to the specimen surface (60-200 μm), means that the specimens from the latter position consist of a very limited number of grains. It is known that this can affect the deformation behaviour, i.e. the mechanical properties. The low number of neighbouring grains relaxes the constraint, making the specimen able to deform by a reduced number of activated slip systems. In addition, the effects from the free surfaces become more important for these specimens.

Furthermore, it is observed that the thin specimens taken from the profile surface develop a vigorous ‘orange peel’ surface topography during deformation (Figure 6.6 (a)). However, no orange peel is observed on the full thickness specimen surface (Figure 6.6 (b)). It has been reported that orange peel normally develops due to deformation on very limited number of slip systems (see e.g. Choi et al. 2004). This confirms that the deformation behaviour of the surface specimens have been altered due to reduced constraint conditions. It is therefore reasonable to assume that the surface stress-strain curve should have shifted towards higher stress levels if a more “correct” number of slip systems was activated during deformation. In such a case, the predictions (ref. Figure 6.5) and the experimental flow curves could approach each other.

Discussion

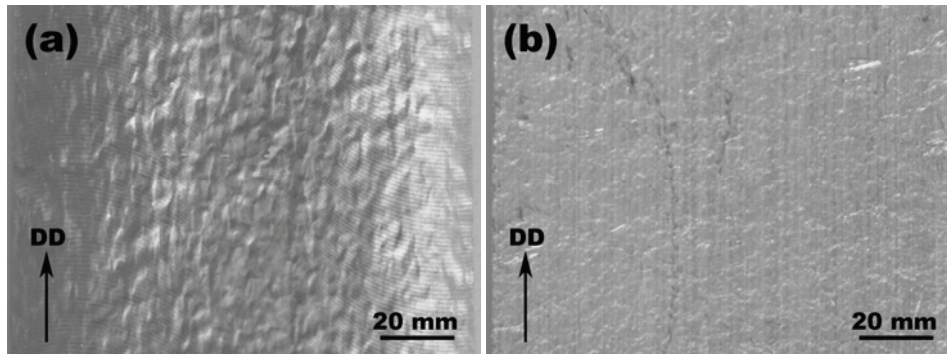


Figure 6.6 – The surface roughness of AA6063 after deformation to the uniform strain. (a) Thin specimen (0.3 mm thick) taken from the surface layer showing vigorous ‘orange peel’. (b) Full thickness specimen without any pronounced surface roughness. Please remember that the texture and grain size for both specimens is equal ($\sim 55\mu\text{m}$) since both are taken from the same position.

Also, it can be suggested that the initial yield strength of the thin specimens can be altered due to the reduced number of grains across the thickness. In some special cases, the specimen cross-section only consists of ~ 100 grains. Based on this fact, it can be expected that some coarse grained regions of the cross-section is more favourable oriented for slip (do not really represent the layer properties), and can therefore start to deform plastically prior to the “actual” yield stress, i.e. the measured yield strength is reduced. This is most likely not the case for the thin surface specimens investigated in this work, since the initial surface yield strength is equal to the full thickness yield strength, i.e. see Figure 6.7. Not surprisingly this figure illustrate that the full thickness data is roughly an average of the sub-layer properties for this test direction. On the other hand, both the experimental (Figure 6.7) and the calculated (Figure 6.5) differences between the surface layer (random texture) and the centre layer (strong Cube texture) can be questioned when compared to the stress-strain behaviour of full thickness specimens.

Discussion

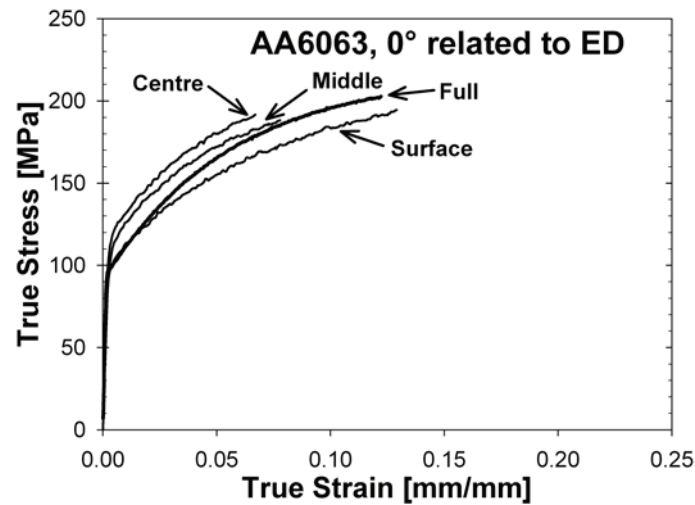


Figure 6.7 – Comparison of stress-strain behaviour from different positions through the thickness and bulk properties of AA6063.

Furthermore, simple tension specimens of AA6063 with both strong Cube (extruded profiles) and random texture (same material, but subsequently cross-rolled and annealed) have been investigated by Furu and Pedersen (2006) in the W, 10min condition (Figure 6.8). In this case, microstructural investigations revealed just minor differences in the microstructure (the cross-rolled material possesses somewhat smaller grain sizes). The idea was here to explore whether a random texture behaved differently from the strongly textured profile dominated by the Cube texture. Hence, the differences in stress-strain behaviour should be related to the crystallographic texture. The results showed that the textured specimen possesses a somewhat larger work-hardening rate (at low strains) and lower uniform strain than the specimen with random texture. However, it is clear that the deformation behaviour of the two specimens is comparable in spite of evident differences in texture (Figure 6.8).

Discussion

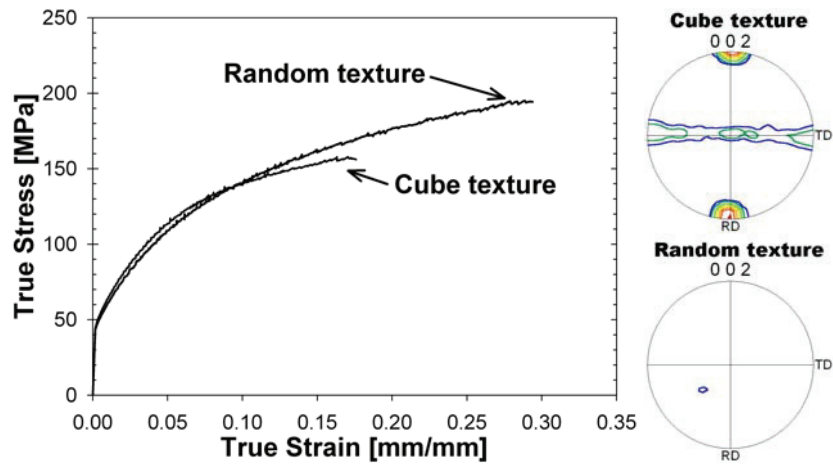


Figure 6.8 – Comparison of the stress-strain behaviour of a specimen with strong Cube texture and a specimen with random texture (after Furu and Pedersen 2006).

From the experimental results obtained by Furu and Pedersen (2006), it is reasonable to assume that the mechanical properties in the centre and surface layer of the AA6063 profile should be comparable when deformed parallel to ED. However, this assumption requires that the slip distribution (the number of activated slip systems) and the microstructure is independent of the through-thickness position. This is not the case (Figure 5.6), and some variations should therefore be expected. Based on the enlarged grain sizes and the reduced constraint from the surroundings close to the profile surface, it could be expected that the yield stress in the surface layer is somewhat reduced. This speculation is supported by the experimental results shown in Figure 5.14. However, the observed lower stress level can hardly be attributed to the real microstructure alone, but is most likely exaggerated do to the above discussed specimen thickness effect.

6.2.4 Final comments on the Voce-type modelling

On the other hand, the calculations performed by Fjeldbo et al. (2005) are in fact based on the assumption (homogeneous slip distribution and microstructure), thus these calculations should therefore be expected to provide only minor differences between the different layers. Consequently, the predicted results (Figure 6.5) are in strong contrast to the results found by Furu and Pedersen (2006) and the present results. This fact directs towards questioning the validity of the plasticity model used for these calculations, since neither the yield point nor the work-hardening rate is described satisfactorily.

Discussion

6.2.5 Internal stresses

The issue of internal stresses and corresponding strains during deformation is another important feature which has not been treated in the above discussion. Internal stresses are known to develop at the grain boundaries due to compatibility requirements (Li and Bretheau 1989). Further, it is known that micro-textural variations will increase the amount of internal stresses, since heterogeneities will worsen the compatibility conditions at the grain boundaries. This means that strong texture gradients could lead to large internal stresses in extruded profiles like the present AA6063 alloy. Internal stresses can assist to accommodate for the interaction between the different layers through the profile thickness. However, it is very difficult to quantify such stresses on a local scale, but it is to some extent possible to obtain qualitative information by investigating the specimen behaviour during unloading.

Measurements of the internal stress evolution have not been performed in the present case. However, it is observed that thin specimens taken from the surface layer of both alloys, exhibit a curved shape after unloading (Figure 6.9). This curvature can of course be attributed to development of internal stresses, but it can also be linked to variations in the plastic strain ratio (due to crystallographic texture and the associated slip distribution) as will be discussed later.

Based on the discussions above, it seems evident that the effect of through-thickness variations on the mechanical properties is a very complicated topic. It is subjected to several counteracting phenomena which separately need to be understood in great detail in order to obtain a full understanding of the overall effect. However, it is clear that the texture gradient is a key element for such an understanding, but the interpretation of the texture effects and how they affect the crystal plasticity is not fully known.

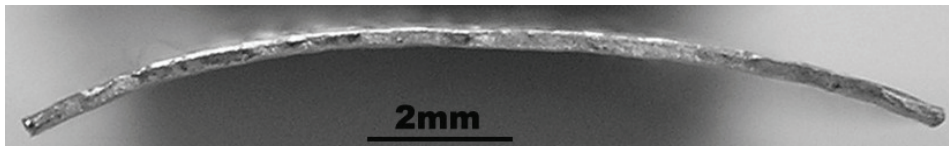


Figure 6.9 - Cross-section shape with evident curvature in the width direction of a specimen from the surface layer of AA6063 deformed to the uniform strain and unloaded.

Discussion

6.2.6 Plastic strain ratios

As part of the thickness gradient study, the local r -values have been determined from simple tension investigations using thin specimens sampled from different positions through the thickness (Table 5.3). However, the accuracy of these measurements is very limited due to inaccuracy of the transversal strain measurements. This is mostly related to the reduced specimen thickness (0.3 mm) since the mounting of the transversal extensometer is very unstable. Some of these problems could have been overcome by utilizing the local strain measurement procedure known as the DSCA technique (Vacher et al. 1999) (Section 2.6.1 provides a description of this technique.). However, such measurements have not been performed in this work. It is therefore recommended that these measurements should be used only as an indication of the plastic strain ratio at the different positions investigated.

As mentioned above, the plastic strain ratio of different positions through the thickness has also been calculated based on the crystallographic texture (Figure 5.7 and Figure 5.10). Both the Taylor FC and RC methods have been utilised for these calculations (Figure 6.10). This figure clearly shows that the plastic strain ratio of AA6063 is almost unaffected by the calculation method utilised (especially in the centre region), while the r -values of AA6082 are very method dependent. This is most likely related to the orientation of the different slip systems with regard to the investigated deformation directions. It has been shown that the centre region of AA6063 is dominated by the symmetrical Cube orientation where the Burgers vectors of several of the most favourable oriented slip systems are parallel. The plastic strain ratio is therefore not so dependent upon the number of slip systems activated, since the net Burgers vector is almost unaffected. AA6082 on the other hand has a more unsymmetrical slip system distribution and will therefore be more dependent upon the number of slip systems activated. Consequently, the plastic strain ratio is strongly affected by the Taylor model utilised.

It seems clear from these calculations that the plastic strain ratio is strongly angular dependent. A macroscopic (full thickness) consideration shows that AA6063 has large r -values in the 0° and 90° directions and r -values close to zero when deformed 45° related to ED. AA6082 on the other hand, has a large r -value when deformed in the 45°

Discussion

direction while the 0° and 90° directions have lower and quite similar r -values. The angular dependency of the plastic strain ratios will certainly give rise to the macroscopic anisotropy as seen in Chapter 5.2. However, more importantly, the plastic strain ratio changes dramatically through the thickness. Figure 6.10 also shows the evolution of the calculated r -values from the centre ($S=0.00$) towards the surface ($S=0.99$). The variations in the actual plastic strain ratio can also affect the deformation behaviour locally. This means that the differences in mechanical properties observed in the different layers of the profiles (Figure 5.14) can partly be explained by variations in three dimensional plastic flow.

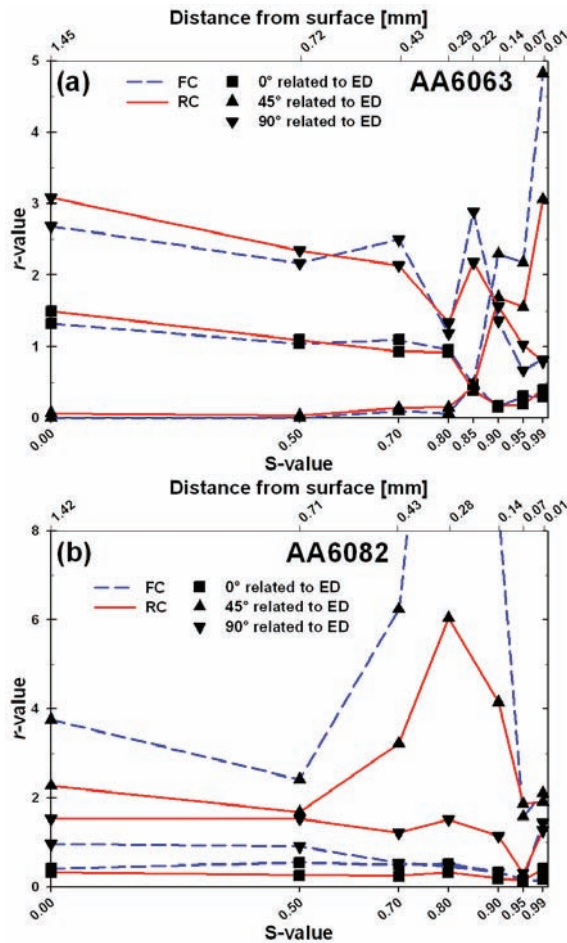


Figure 6.10 – Texture-based calculations of r -values at different positions through the profile thickness, applying both the FC and RC models. (a) AA6063 and (b) AA6082.

Discussion

The through-thickness variations in plastic strain ratio have been investigated in more detail by comparing texture-based calculations of r -values from three different positions through the thickness (Figure 6.11). Here, $S=0.00$ corresponds to the centre position of both alloys, $S=0.80$ corresponds to the middle layer of AA6063 and the outer part of the centre layer of AA6082, while $S=0.99$ corresponds to the outer surface layer. The centre and middle parts of AA6063 have a concave r -value shape (r -value as a function of deformation angle), i.e. these positions possess the highest r -values when deformed parallel or perpendicular to the ED and lowest when deformed 45° related to ED.

In fact, this is the typical r -value shape of materials having a recrystallized texture (Cube texture) like AA6063 (see e.g. Fjeldly 1999). However, the surface layer possesses the opposite behaviour, i.e. the 45° direction possesses the highest plastic strain ratio. From the graphs in Figure 6.11, it is evident that the two alloys behave fundamentally different with regard to the straining direction, i.e. the overall r -value shape of AA6082 is convex. Also for this alloy, the surface layer possesses more extreme r -values than the centre part of the profile. The calculated variations between the centre and surface layers observed for AA6063 and AA6082 are typical for extruded profiles with a recrystallized and fibrous microstructure respectively. Sørensen (1997) observed from experiments the same behaviour when studying the local plastic strain ratios of extruded AA7030 (recrystallized) and AA7108 (fibrous) profiles.

Discussion

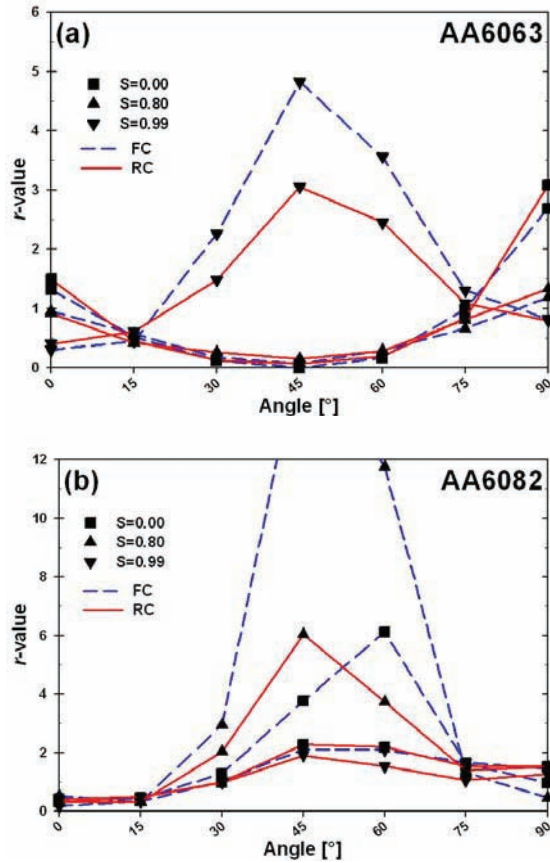


Figure 6.11 – Texture-based calculations of r -values at three different positions through the profile thickness as function of the tensile direction. (a) AA6063 and (b) AA6082.

Furthermore, the r -values calculated with the Taylor RC model corresponds remarkably well to the experimental values (Table 5.3). It is also clear that the FC method provides a qualitatively reasonable description of the plastic strain ratio. However, the FC method strongly exaggerates the r -values for both alloys. Fjeldly (1999) has performed the same type of calculations for one recrystallized (AA7030) and one fibrous (AA7108) profile by use of several different plasticity models. This author found that the qualitative results of all the models were satisfying, but only the less constricted models like the Sachs (AA7030) and the Taylor RC (AA7108) were able to provide quantitative reliable results. This behaviour can be explained by the localised deformation often observed for this type of alloys (Sørensen 1997).

Discussion

This means that models activating only a limited number of slip systems are more accurate than the conventional Taylor FC model. The same explanation could be used for the coinciding results obtained in this work since also the deformation of AA6063 and AA6082 tend to localise.

The through-thickness variations in plastic strain ratio can therefore be used to explain the through-specimen-thickness-curvatures observed after simple tension deformation in different directions (see Figure 5.20 and Appendix D). Since,

$$r = \frac{\varepsilon_w}{\varepsilon_t} \quad (28)$$

this means that a material obtains a large r -value if ε_w is relatively large (or ε_t is relatively low). Implicitly, the material obtains a low r -value if ε_w is relatively low (or ε_t is relatively large). The transversal strain is directly linked to the initial and final width of the specimen:

$$\varepsilon_w = \ln \frac{w}{w_0} \quad (29)$$

I.e. the through-thickness final width of the specimen can be used as a direct measure of the local plastic strain ratio through the thickness. A large r -value will result in a significant reduction of the width, while the initial and final width of a specimen with a low r -value is almost equal. Hence,

$$\text{Large } r \Rightarrow \text{Large } \varepsilon_w \Rightarrow w \ll w_0 \quad (30)$$

$$\text{Low } r \Rightarrow \text{Low } \varepsilon_w \Rightarrow w \approx w_0 \quad (31)$$

By using the measured transversal strain as input to the plastic strain ratio determination, it seems clear that a material with the largest plastic strain ratio in the centre will develop a concave cross-sectional shape. The same argumentation indicates that a material with the largest r -values at the profile surface will develop a convex shape during deformation (Figure 6.12).

Discussion

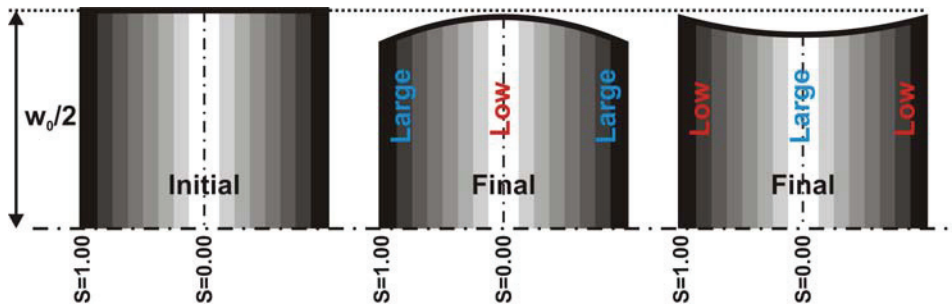


Figure 6.12 – Schematic illustration presenting the effect of r -ratio variations through the thickness of a simple tension specimen. A specimen with low r -values at the surface and a large value in the centre will develop a concave shape. The opposite r -value distribution will result in a convex through-specimen-thickness-curvature.

Comparisons of the calculated r -values from the centre and surface positions with the through-specimen-thickness-curvatures, confirms that the variations in plastic strain ratio can be used as an explanation of the observed curvatures (Table 6.1). The results even show that the radius of curvature (Figure 5.21) is consistent with the differences in r -values observed between the centre and the surface layer. However, the behaviour of the specimens deformed in the 45° direction (AA6082) is different from the other orientations. The r -value variations in this deformation direction should develop a concave shape, however a weak convex shape is observed. This latter behaviour can not be explained based on the results obtained in this work.

Table 6.1 – Texture-based calculations of the plastic strain ratio using the Taylor RC method, and the corresponding observed tensile cross-sectional shape.

Alloy	Direction	Calculated r -value		Observed shape
		Centre	Surface	
AA6063	0°	1.5	0.4	Concave
	45°	0.1	3.1	Convex
	90°	3.1	0.8	Concave
AA6082	0°	0.3	0.4	Straight
	45°	2.3	1.9	Convex
	90°	1.5	1.3	Straight

6.2.7 Final comments on profile thickness strain distribution

Both simple tension experiments with reduced specimen thickness (Figure 5.14) and the observed end of cross-section shape (Figure 5.20) indicate a very heterogeneous through-thickness strain distribution for the investigated profiles. This is further supported by the local strain distribution measurements of AA6063 presented in Chapter 5.7. The calculated strain distribution maps from measurements show that strain localisation takes place in well-defined straight bands through the profile thickness. The thickness and density seem to be dependent upon the deformation direction and Chapter 6.3 will treat this topic in more detail.

Even though the origin of the observed strain heterogeneities take place in areas with low Taylor factors, the localised deformation seems to grow into bands with a 45° angle related to the deformation direction. These bands expand through the thickness of the specimen and are most likely the precursors to macroscopic shear localisation (see Figure 5.73 and Figure 5.74). When the through-thickness strain distribution is compared with the Taylor factor maps of the same area (Figure 5.72), it is evident that there is no correlation between the localised bands and the Taylor factor of the individual grains. In other words, Taylor factor heterogeneities may act as nucleation points for the macroscopic strain heterogeneities. This assumption is strongly supported by Duan et al. (2005), who were able to predict the formation of shear localisation during simple tension deformation simulations of an Al-Mg alloy by taking advantage of the heterogeneities in mechanical properties, i.e. variation in Taylor factors. The variations are clearly directional dependent, i.e. they are most likely linked to the crystallographic texture.

To summarise, the observed strain distribution is consistent with both observations of variations in plastic strain ratios (r -values), end of cross-section shape and the results from texture-based calculations. Also the measured through-thickness strain distribution supports the above findings. Such effects can therefore complicate the understanding of extruded aluminium profiles with regard to forming behaviour (see Chapter 6.4).

6.3 Deformation mechanisms and crystal plasticity

The work presented so far has shown that extruded profiles often possess strong mechanical anisotropy. It has also been shown that the through-thickness variations often observed in these profiles may influence the profile shape due to variations in anisotropy. Through-thickness variations will therefore often make it more difficult to predict and control final shapes after a given forming operation. It has previously been shown (see e.g. Yau and Wagoner 1993, Han et al. 2004 and Winther 2004) that the actual activation of slip systems is a determining factor for the observed mechanical anisotropy during deformation. This section will therefore address a discussion concerned with plasticity in textured materials carrying microstructural and textural gradients. A close evaluation of the microstructure evolution upon plastic deformation will be given, before the crystallographic rotations and activation of slip systems will be discussed in detail.

6.3.1 The nature of slip traces

The experimental results presented in Chapter 5 show that the crystallographic texture and microstructure evolution has been carefully monitored by performing EBSD investigations and acquiring SE micrographs at different strains during deformation. SE micrographs reveal that AA6063 tend to deform in a localised manner, i.e. produces evident slip traces.

The theoretical in-plane slip trace angle (β_{theo}) of all crystallographic planes can be calculated based on the crystallographic orientation of the grain (section 2.5.1). This information in combination with the observed orientation of the visible slip traces (β_{obs}) can then be used to identify the slip planes activated during deformation. The calculations performed for all investigated grains showed that the difference between β_{obs} and β_{theo} from one of the $\{111\}$ -planes never exceeded 3° . This fact clearly confirms that the plastic deformation of aluminium takes place on the closed-packed $\{111\}$ -planes.

Microstructure micrographs at different strain states (Figure 5.41-Figure 5.43) reveal that the slip trace evolution is strongly dependent upon the deformation direction selected.

Discussion

The same micrographs also show that the slip trace appearance and density varies significantly from grain to grain within one deformation direction, especially for the specimens deformed 0° and 90° related to ED. Earlier works, i.e. Delaire et al. (2000), Zhang and Tong (2004) and Henning and Vehoff (2005) have reported more extensive development of secondary slip traces during simple tension of polycrystalline materials than observed in the present work. In other words, they observe that the grains deform by multiple slip at very low strains (4%) and close to 50% of the grains investigated developed additional slip traces. To be noticed, most of the grains from the present material with a strong crystallographic texture have their primary slip systems aligned in a similar way, hence the compatibility requirements are probably reduced and there is less need for activating additional slip systems.

The specimens deformed in the 45° direction possess a much more homogeneous slip trace distribution compared to the other two directions and all the grains develop slip traces very early in the deformation process, e.g. most of the grains have developed visible slip traces already after 3% deformation. The DD IPF in Figure 5.28 (b) indicates that the majority of the grains have a $101\parallel DD$ when deformed 45° to ED. Most of the grains have quite similar initial orientations, i.e. the slip systems possess a similar resolved shear stresses (τ_{res}) distribution and all the individual grains will therefore behave similarly. This is also confirmed by the Taylor factor map presented in Figure 5.54. Most of the grains have a $100\parallel DD$ (Figure 5.28 (a)) when deformed parallel to ED. The different slip systems within the individual grains will also in this DD possess similar τ_{res} -values. As a consequence, all grains should therefore start to deform (produce visible slip traces) simultaneously as already discussed in section 6.1.2. However, this is not the case observed, as shown in Figure 5.41. Some grains develop visible slip traces already after 3% deformation while other grains do not produce visible slip traces even at the uniform strain (12% deformation). This is most likely do to the intrinsic nature of aluminium deformed parallel to a $\langle 100 \rangle$ direction, i.e. 8 of 12 slip systems have equal and very high Schmid values (Figure 5.55). It is reason to believe that both constraint from the neighbouring grains and only small deviations from the perfect Cube orientation will alter the slip distribution, hence altering the slip trace distribution. However, these considerations will be treated more thorough in the following sections. Section 6.1.2 also showed that the specimens deformed 90° have a

Discussion

“soft” yield point which was attributed to the initiation of slip in the different slip systems. This is also confirmed by the slip trace evolution (Figure 5.43) where it is clear that some grains develop visible slip traces prior to other grains.

Further, it has been shown that grains deformed in the 45° direction (Figure 5.44) generally develop only one set of slip traces (primary slip traces) below 12%, while the number of visible slip traces varies significantly when deformed in the two other directions, especially when deformed perpendicular to the ED (Figure 5.45). However, grains from the 45° direction also develop additional set of slip traces (secondary slip traces) at higher strains (15%). The additional sets of slip traces are always seen close to grain boundaries or triple junctions (see e.g. Figure 5.46). Local slip traces probably develop because the already activated slip systems are not able to accommodate the deformation enforced by the surroundings (i.e. compatibility requirements). The enforced constraint will most likely give a shear stress contribution, $\Delta\tau$. This means that the local resolved shear stress experienced (τ_{loc}), is increased by the amount $\Delta\tau$ such that it exceeds the critical resolved shear stress τ_{CRSS} for the additional activated slip system. This means that an additional slip system is activated when;

$$\tau_{loc} = \tau_{res} + \Delta\tau \geq \tau_{CRSS} \quad (32)$$

It has been shown that the slip trace direction is crystallographic dependent, i.e. β_{obs} is determined by the crystallographic orientation. However, detailed slip trace investigations showed that some grains possess non-linear slip traces. The divergence from the linear appearance could in some cases be explained by crystallographic through-grain orientation gradients. Non-linearity related to orientation gradients is in general very smooth and do often enhance toward to the grain boundary as shown for a grain deformed to the uniform strain (Figure 6.13). The smoothly curved slip traces and the enhanced curvature for this grain which is deformed 45° related ED are consistent with the orientation gradients observed after deformation to intermediate and high strains (see Figure 5.39). This has been confirmed by calculating β_{theo} of the four $\{111\}$ -planes at different position along the orientation gradient and comparing these values to the β_{obs} at the corresponding positions (Figure 6.14). Based on this information, it is reasonable to claim that this type of observed curvatures is related to orientation gradients, i.e. the

Discussion

observed curvatures originate from crystallographic rotations and not from activation of additional slip systems since β_{obs} is identical to one of the β_{theo} numbers along this line.

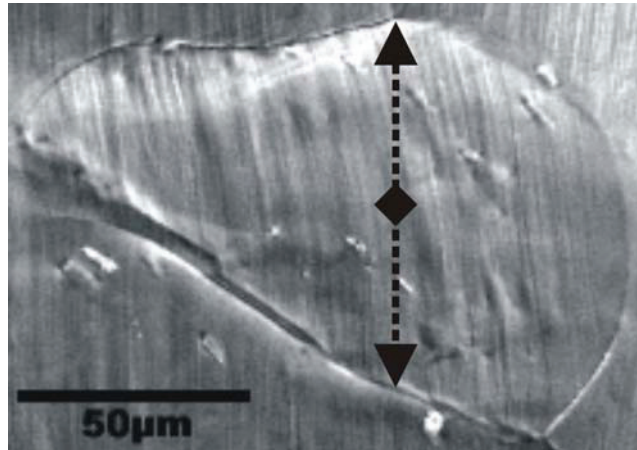


Figure 6.13 – Observed slip traces in grain labelled #1 in Figure 5.28 at 27% deformation. The observed slip traces are curved due to orientation gradients. The black two-headed arrow indicates the location on the grain surface of the orientation profile presented in Figure 5.39 and Figure 6.14.

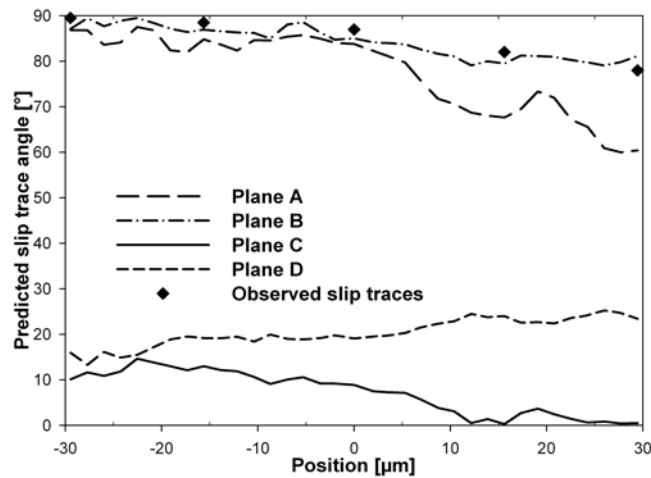


Figure 6.14 – Evolution of theoretical in plane slip traces angle (β_{theo}) for the four $\{111\}$ -planes based on orientation profile through the grain labelled #1 in Figure 5.31 at 27% deformation. The observed angle (β_{obs}) along the orientation profile is also included.

As a result of these significant misorientation gradients, the slip traces would no longer be straight lines crossing through the grains but rather they would become curved, e.g. see Fig. 11. The same figure also presents parameters β_{obs} and β_{theo} of the four $\{111\}$ -

Discussion

planes along a line crossing through grain number 2 after 27% deformation. Again, it is evident that the observed curvatures were related to crystallographic rotation and not to activation of additional slip systems since β_{obs} is identical to one of the β_{theo} numbers along this line.

However, also another type of non-linear slip traces is observed. This type is more discontinuous and the appearance is somewhat wavier. It is also worth noticing that the slip trace distance is often enhanced for this type of grains. The big grain labelled X in Figure 5.48 is a perfect example with clearly non-linear slip traces. From the illustration of this grain (Figure 6.15), it is clear that slip traces can be divided into different regions belonging to different crystallographic planes. The different segments are all crystallographic dependent, but the overall slip-trace-shape is wavy. Irregular slip traces like this is only observed for orientations with two almost parallel theoretical slip traces, i.e. slip systems from two different slip planes have close to identical Schmid values. Hence, this type of slip traces is often observed for grains with close to a $100\parallel DD$. As indicated, the reason why these grains behave in this remarkable way is most likely related to the Schmid value distribution. Slip systems from both slip planes have close to identical Schmid values and the activation of slip systems are determined by external constraints, as will be discussed in more details in the following section.

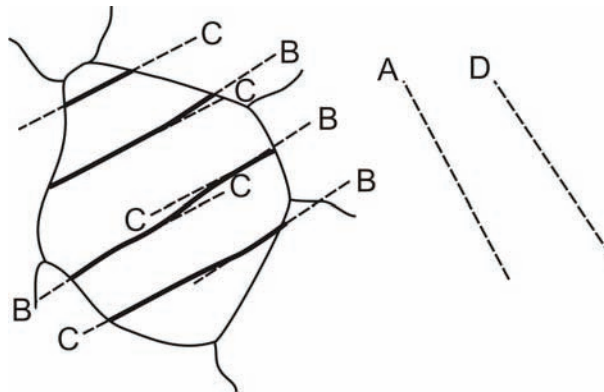


Figure 6.15 – Illustration of the irregular slip traces observed at the specimen surface of the big grain labelled X in Figure 5.48. The primary slip traces consist of different sections belonging to plane B and plane C respectively. Hence, the slip traces are not linear but rather curved. None of the parallel sections within the slip traces belong to plane A or plane D. The theoretical in-plane angle of slip plane A and D is indicated on the right hand side.

Discussion

Further, the slip traces of an individual grain can be affected by the deformation mechanisms taking place at the nearest neighbours as illustrated in Figure 6.16. The primary slip traces (violet) are produced do to deformation on the slip system/systems with the highest Schmid value/values. Further, additional slip traces induced by the nearest neighbours can be categorised based on their appearance. Some slip traces can intersect the grain boundary and continuous through the entire grain in question (green). This is most common for neighbouring grains having slip planes with close to identical orientation (see e.g. the specimens of AA6063 deformed 45° related to ED). Further, in some cases, the induced slip traces are not able to continue through the entire grain but are terminated close to the grain boundary (blue). This means that the slip systems on the slip plane corresponding to the primary slip traces on the neighbouring grain have low Schmid values. Hence, the terminated slip traces observed are generated only in order to fulfil the compatibility requirements over the grain boundary. The red slip traces also intersect the grain boundary, but do hardly continue into the centre grain. However, some of these slip traces are also observed close to the grain boundary between the centre and top grain, and are most likely activated to fulfil the compatibility close to the triple junction.

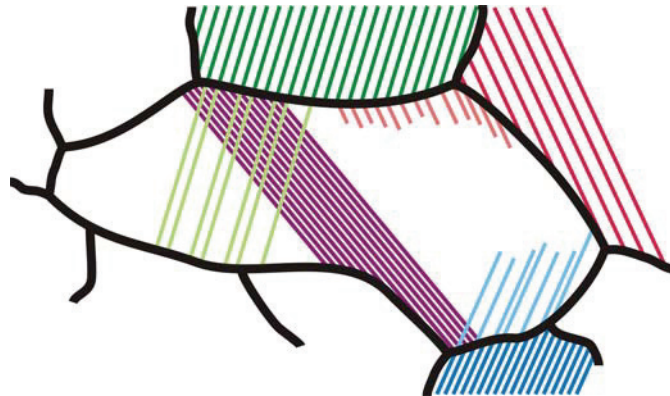


Figure 6.16 – Schematic illustration showing the effect of primary slip traces observed in neighbouring grains. The violet traces illustrate the primary slip traces of the centre grain. The green slip traces are the primary slip traces of the top grain, but similarly oriented traces are continuing in the center grain (light green). The primary slip traces of the bottom right grain also intersect the grain boundary, but these slip traces are not able to continue through the centre grain. The red slip traces observed in the top right grain also intersect the grain boundary, but do hardly continue into the centre grain.

6.3.2 Crystallographic rotations during deformation

It is beyond doubt that most grains tend to rotate during deformation. As already explained in section 2.2.3, crystallographic rotation is not a direct consequence of plastic deformation but rather an effect of the constraint enforced by the surroundings. The most important elements concerning the rotation path are therefore closely linked to the activation of slip systems in the grain itself. However, the activation of slip systems in the neighbouring grains, the grain size and shape can also affect the rotation paths.

Further, it has been shown (see e.g. Figure 5.35) that both the amount of rotation and the rotation paths are strongly dependent upon the initial orientation. Crystallographic rotation of both single- and poly-crystals has been studied in great detail in the past, and it has been shown that the rotation paths are usually quite well described by the Taylor (1938) model (see e.g. Bunge and Fuchs 1969, Han et al. 2003 and Winther et al. 2004). The Taylor model states that grains rotate toward aligning either a [100] or [111] parallel to the DD.

In order to comprehend the rotations taking place, it is important to realise why grains having these directions parallel to the DD tend to be stable, while grains not having this configuration often contend to align these axis to the DD. From the discussion above, it is reasonable to assume that the stable behaviour of these orientations is related to the Schmid value distribution. The experimental results have clearly shown that eight of the twelve slip systems (two from each slip plane) have identical Schmid values when the grain has a [100] parallel to the DD (Figure 5.55). Moreover, when a grain has a [111] parallel to the DD, six slip systems from three different slip planes have identical Schmid values. In other words, the Schmid value distribution for both these orientations is very special.

Further, it is known that when a slip system is activated in grains with one of these orientations, the accompanying rotation give rise to an increase in Schmid value for the slip systems on the other planes, while the Schmid value of the activated slip system itself is reduced. As a consequence, the Schmid value distribution is slightly altered. The slip system originally activated is no longer the most potential, and often another slip system will be activated instead. This will in turn slightly alter the Schmid value

Discussion

distribution, and a third or the originally activated slip system will become the most potential. These repeating alterations in Schmid values will only lead to a very small fluctuation in crystallographic orientation and the orientation appears to be stable.

Also grains with a $[101]$ parallel to the DD have this special Schmid value distribution with four slip systems having identical Schmid values and the remaining having Schmid values equal to zero (Figure 5.55). However, still this orientation behaves quite differently. The rotation accompanying activation of one of these highly potential systems leads to a Schmid value increase, i.e. the initially activated slip systems will tend to remain active. In other words, the grain will continue to rotate in the same direction as shown in Figure 5.57.

To summarise, it is clear that some grains are stable because the activation of slip systems results in a small alteration of Schmid value distribution while other orientations are unstable because activation of slip systems leads to Schmid value strengthening of the same systems.

In general, the results presented in this investigation clearly confirm the statements above, i.e. the majority of the grains rotate in accordance with the predictions made by Taylor (see e.g. Figure 5.29 and Figure 5.35). However, it is also observed that grains initially having close to identical crystallographic orientations rotate in opposite directions. The three grains in Figure 6.17 illustrate such rotation behaviour for a sample with random crystallographic texture deformed perpendicular to the ED. The crystallographic rotations predicted by the Taylor model are a direct result of the embedded rules for activation of slip systems. This means that deviation from the predicted rotation behaviour indicates a deficiency in the prediction of slip activation.

Discussion

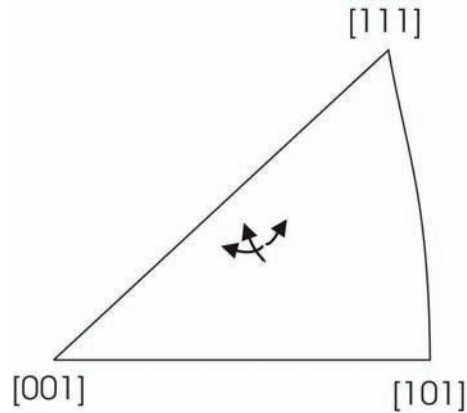


Figure 6.17 – Example of grains with close to identical crystallographic orientation prior to deformation rotating in different directions during deformation.

Also the amount of rotation is determined by the selection of activated slip systems. Since the only input for Taylor model calculations is the initial texture, the predicted amount of rotation is determined by the grains crystallographic orientation alone. However, the results presented in section 5.5.3 show that the rotations taking place are to a large extent dependent upon the orientation of the surroundings. Grains in a material with strong crystallographic texture (Figure 5.36) tend to rotate more than grains in a material without crystallographic texture (Figure 5.37). Again, this is most likely related to activation of slip systems. The constraint enforced by the surroundings is dependent on the compatibility between the deformation (activation of slip system) taking place in the grain itself and the nearest neighbours. A strong crystallographic texture means that a considerable fraction of the neighbouring grains have a comparable crystallographic orientation. This means that the constraint enforced by the surroundings is expected to be large for a material with strong crystallographic texture compared to a material without texture. As a consequence, the constraint enforced by the surroundings should be reduced for materials without texture. In other words, a material with random texture needs to activate more slip systems than a material with strong texture.

Further, the mathematics from basic crystal plasticity shows that the amount of rotation taking place will be reduced with an increased number of slip systems activated. The correlation between number of slip systems activated and the rotation taking place is very well illustrated in a number of works (see e.g. Margulies et al. 2001, Poulsen 2003

Discussion

and Winther et al. 2004). Figure 6.18 presents the rotations taking place during deformation by use of Sachs (one active slip system) and Taylor FC (five active slip systems) type models. The results clearly show that the rotations predicted by the Sachs model exceed the predicted amount of rotation taking place when more slip systems are activated. The differences observed by varying the number of activated systems are comparable to the observed differences between a material without and with strong crystallographic texture. Hence, these observations support texture dependent rotations, i.e. materials with strong texture will rotate more than materials without texture due to a reduced number of slip systems activated.

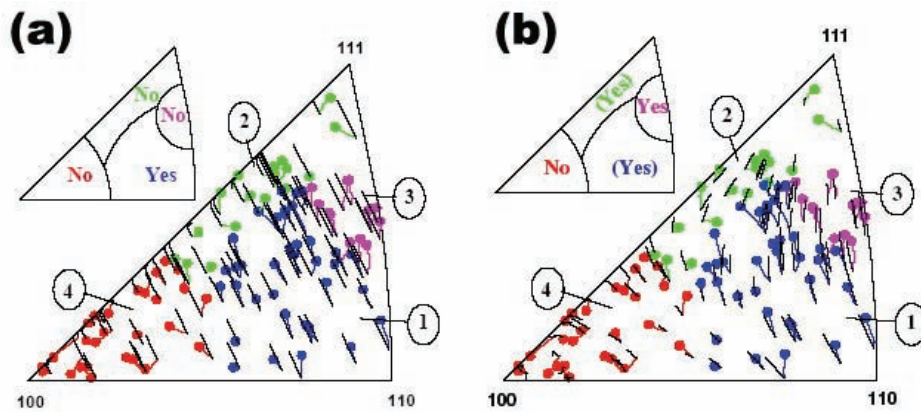


Figure 6.18 – Predictions of the rotations of the tensile direction by different plasticity models are shown as black lines together with the experimental data. The small stereographic triangle shows in which areas acceptable agreement between experimental and predictions are found. (a) Sachs model and (b) Taylor FC model (after Winther et al. 2004).

Another important phenomenon with regard to crystallographic rotation is the effect of grain size. It is almost impossible to isolate the grain size effect since at the same time also other parameters will affect the rotation behaviour. An example of such a parameter is the influence from the surroundings, i.e. crystallographic orientation of the nearest neighbours. The present investigations of the grain size effect were performed on material with random crystallographic texture in order to minimise the influence from the surroundings. Figure 6.19 presents the measured rotations taking place during deformation to the uniform strain for a given orientation parallel to DD as a function of the initial grain size. The grain labelled IV in this figure deviates from the linear relationship between the amount of rotation and grain size. Grain IV has due to a

Discussion

different crystallographic direction parallel to ND a low Taylor factor compared to the other grains. This could be used to explain the reduced amount of rotation. If the shown results are representative for rotations taking place, one can assume that an increased grain size leads to reduced crystallographic rotation upon deformation. The one reason for such behaviour could be that large grains are not as affected by the surroundings as a smaller grain would be.

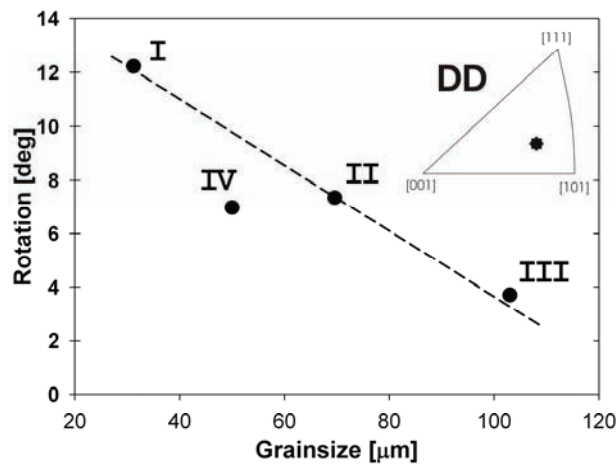


Figure 6.19 – Detected rotation from the initial orientation at the uniform strain as a function of grain size for four different grains (see Figure 5.34) with identical orientation parallel to the DD prior to deformation. The initial orientation prior to deformation is included in the DD IPF. The grain labelled IV has a different crystallographic direction parallel to ND compared to the other grains. Notice the linear relationship between misorientation and grain size as indicated by the dotted line.

Plastic deformation may also lead to a completely different type of crystallographic rotation. This type of rotations is observed within individual grains. Grains often produce internal orientation gradients during deformation which in turn leads to the smoothly curved slip traces discussed in the previous section. The orientation gradients develop more or less continuously during deformation and become more distinct close to the grain boundary (Figure 5.39). In some cases, the gradients develop in a more discontinuous manner, i.e. the grains consist of several regions of slightly different orientation. The measurements shown in Figure 5.40 are an example of such behaviour. Even though the grain possesses an evident through grain orientation gradient, the grain interior can be divided into three separate regions with close to constant orientation (Figure 6.20).

Discussion

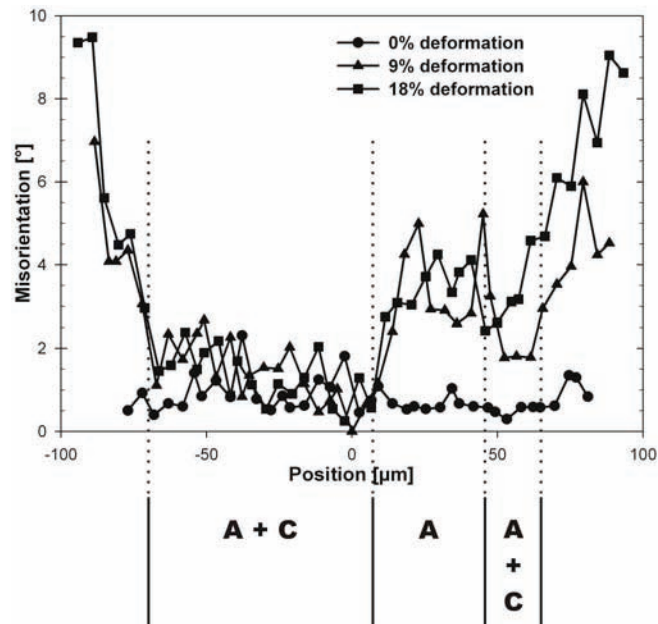


Figure 6.20 – Orientation gradient through the grain labelled #2 in Figure 5.34. The dotted lines indicate the different regions of comparable orientation. Also the slip planes activated within these regions based on the slip traces observed are indicated in Figure 5.51.

Figure 5.51 presents the slip trace evolution for the same grain as where the orientation gradient was investigated (orientation gradient parallel to DD). By comparing Figure 6.20 and Figure 5.51, it becomes clear that the shape of the orientation gradient is corresponding to the different slip trace-regions. Hence, it is reasonable to assume that there is a direct relation between slip traces, i.e. activation of slip systems, and the observed orientation gradients.

Orientation gradients seem to develop due to compatibility requirements. It has been shown that deformation within individual grains is primarily determined by the crystallographic orientation. However, since the material in question is a polycrystal, the deformation is also affected by the neighbours. The grain boundaries are therefore of great importance when it comes to compatibility. This can also be investigated by evaluating the slip traces intersecting the grain boundaries, since the ease of such intersections is related to the compatibility (see section 6.3.1 for more details).

Discussion

During plastic deformation of aluminium, the effect of grain boundaries have been thoroughly discussed in the past (see e.g. Raabe et al. 2001). It is commonly agreed that grains split up into subgrains etc., during deformation. Formation of subgrains may be the most energy efficient way to satisfy the strain compatibility requirements. The observed orientation gradients are in other words the first step in producing a substructure.

Moreover, from the figures presenting the observed orientation gradients, it could be argued that grains with orientation gradients in average activate more slip systems than other grains. Based on the discussion above, this could explain way the experimental results show that grains with orientation gradients tend to rotate less than homogeneously oriented grains.

6.3.3 Selection of slip systems

Several decades ago, it was discovered that slip is the most important deformation mechanism for room temperature deformation of aluminium (see e.g. Verhoeven 1975 and Honeycombe 1984). Activation of a slip system means that slip takes place on that particular system, i.e. accumulation of dislocation and dislocation movement. Introduction and movement of dislocations lead to an increase of energy for the system. Hence, the most favourable oriented slip systems are therefore the first to be activated during deformation. The early works on single crystals by Garstone et al. (1956), Diehl (1956) and McKinnom (quoted in Clarebrough and Hardreaves 1959) all showed the close relationship between activation of slip systems and initial crystallographic orientation (Schmid value). The same authors have also treated the effect of crystallographic orientation on the local work-hardening.

As stated above, the Schmid value is among other factors often used to evaluate the potential for activation of the various slip systems. Further, the previous sections have shown that also grain size, morphology etc., can affect the activation of slip systems. However, the Schmid value, i.e. the crystallographic texture is by fare the most important in order to determine the activated slip systems.

Discussion

In general, the number of slip systems activated can not be determined by the Schmid value distribution alone. Ideally, a combination of Schmid values, slip traces, crystallographic rotations and if possible, local strain measurements should be utilised to obtain a reliable description of the amount of slip on the individual slip systems. However, in practise, the Schmid value distribution and the orientation of the observed slip traces are sufficient for determining the number of slip systems activated.

As was shown in section 2.2.2, the Schmid value distribution is determined by the given combination of crystallographic orientation and enforced deformation mode. Some orientations have 1-2 slip systems with high to very high Schmid values, while for other orientations almost all the slip systems have high Schmid values. Further, also combinations of orientation and deformation mode where all the slip systems have medium to low Schmid values exist. In other words, the Schmid value distribution throughout the microstructure varies substantial from grain-to-grain. From this relatively simple consideration, it is reasonable to assume that the number of activated slip systems will vary substantially through the microstructure. The observed slip trace evolution can be used to support this assumption. Frequently, only one set of slip traces is observed, something, which indicates that only slip systems on the corresponding slip plane are activated. In the case of congruent slip traces, slip systems from both slip planes can be activated. To illustrate how the Schmid values and the slip traces of the individual grains can be utilised to determine the number of systems activated, two different grains are discussed in more detail.

The first grain that will be treated is the grain labelled #1 in Figure 5.31. This grain is taken from a specimen deformed 45° direction and has a very unstable crystallographic orientation, i.e. a $101\parallel DD$. As already mentioned in section 6.3.2, this orientation gives rise to a special Schmid value distribution with four slip systems from two different slip planes (plane A and B) having very high Schmid values (Figure 5.57). Figure 6.13 presents the slip traces from this grain at 27% deformation and Figure 6.14 presents both the theoretical and observed in-plane slip trace angles from the same grain. From these figures it is clear that the grain possesses only one set of slip traces even though it could be argued that these traces originate from slip on both slip plane A and B. However, when the potential planes for producing this slip traces are compared with the Schmid

Discussion

value distribution, it becomes evident that the slip traces must have been produced by slip on plane B. In other words, there is no slip activity on plane A during deformation to the uniform strain. Further, this confirms that if any slip should have taken place on slip plane A, this must have been early in the deformation process. The reason for this statement is that during deformation, the Schmid values of these systems are reduced to the same values as the slip systems on plane C (see Figure 5.57) hence the probability for slip on plane A and C are equivalent. As a consequence, it is reasonable to assume that this grain only activates two slip systems (B4 and B5) and that these systems tend to stay active until the material reaches the uniform strain.

Also the grain labelled #2 in Figure 5.34 illustrate very well how the use of slip traces together with the Schmid value evolution can be used to determine the number of slip systems activated in a material with random texture. Figure 5.51 and Figure 5.59 from section 5.6.2 present the slip trace evolution and the Schmid value distribution evolution of this grain. The Schmid value distribution gives the most favourable oriented slip systems, while slip traces combined with information about the crystallographic orientation provide information about the slip planes actually activated (Figure 6.20). Section 5.6.2 clearly shows that this grain only activate one slip system (A6) at low strains. Moreover, while some regions activate other slip systems at higher strains, A6 seems to remain as the only activated slip system in the centre region (the region labelled A in Figure 6.20). It has also been shown that at higher strains, this grain locally develops additional slip traces. This locally activated slip planes correspond with the slip systems of high to intermediate Schmid values, hence it is reasonable to assume that these slip systems are activated in these regions. Based on this, the two neighbouring regions with additional slip traces (the regions labelled A+C and A+B in Figure 6.20) most likely activate two (A6 and C1) and three (A6, B5 and B2) slip systems respectively. Again this confirms that the combinations of Schmid values and slip traces can be used to determine the number of slip systems activated. It also shows that the slip activity is very heterogeneous even within one individual grain.

The surface topography is another important indicator for activation of slip systems. It has been shown that the material condition with strong crystallographic texture tends to rotate more than the material condition without any texture (section 5.5.3). In the previous

Discussion

section, it was argued that the reduced rotation observed in the material without texture is caused by the increased number of activated slip systems compared to the textured material. The surface-topography investigations clearly support this statement. The material will develop a more vigorous surface-topography when a reduced number of slip systems are activated (Choi et al. 2004). Few activated slip systems means that the limited number of slip systems has to carry all the enforced deformation. In other words, the relative movement (displacement) between activated slip planes is large compared to a material with many slip systems activated. Deformation on few slip systems will therefore clearly lead to a more vigorous surface-topography. This is also observed for the material investigated in this work as shown by the SE-micrographs in Figure 5.43 and Figure 5.49. The increased surface-topography observed for the material without crystallographic texture is also indicated by the IPF-maps presented in Figure 5.32 and Figure 5.34. The topography blocks the electron beam from reaching the “valleys” at the surface and the crystallographic orientation of that point can not be determined. As a consequence, a non-indexed point will become black on the IPF-map. The amount of non-indexed points is very large for the material without texture (Figure 5.34) compared to the material with texture (Figure 5.32). As discussed in section 6.2.2, this argument was also used to support the observed variations in slip activity through the material thickness.

From the discussion above, it seems clear that the number of slip systems activated varies substantially from grain-to-grain, and variations even within one individual grain are often observed. It is also indicated that the number of slip systems activated is less than predicted by the classical and widely used Taylor model. This will be treated more thoroughly in the next section (“Activation of slip systems – experimental observations vs. texture-based calculations”).

However, another important observation regarding activation of slip systems should first be treated. The Taylor factor gives an indication on how easy a material can be deformed. From a slip system point of view, it is reasonable to assume that a grain with a low Taylor factor needs to activate fewer slip systems than a grain which is harder to deform (high Taylor factor). In spite of this, the above observations can be summarised by stating that the number of activated slip traces seems to be more dependent upon the

Discussion

spread in Taylor factor than the value of the Taylor factor itself. It is also important to remember that the calculation method selected will affect the Taylor value more than the spread in the results.

Also there is some controversy regarding the results obtained from in-situ EBSD measurements. As presented in section 2.7.5, the EBSD technique has some considerable limitations since it only obtain information from the surface region of the specimen. It can therefore easily be claimed that the technique is insufficient since the acquired results are not representative for bulk deformation of the material. Hence, the results only provide a description of the surface behaviour, i.e. this work is only a study of near surface plasticity.

As already mentioned, the “Metal Structures in Four Dimensions”-group at Risø National Laboratory in Denmark is one of the groups which really has studied bulk rotations of individual grains by use of 3D X-ray diffraction (3DXRD). The rotation paths observed in several works performed at Risø is consistent with the rotation paths observed in this works (see e.g. Margulies et al. 2001 and Poulsen 2003). This indicate that the EBSD technique is actually able to capture the bulk behaviour during deformation, and it should therefore be reasonable to assume that the obtained observations can be used to determine the number of slip systems activated.

If a grain, for both conservatism and simplicity, is assumed to have a cubic shape and one cube plane is parallel to the surface, 5/6 of the grain surface will be surrounded by other grains. Hence, the enforced constraint should be comparable to the constraint experienced by a bulk grain. Hence, also from this point of view, in-situ deformation in combination with EBSD investigations should be able to capture the true grain rotations during deformation.

6.3.4 Activation of slip systems – experimental observations vs. texture-based calculations

Crystal plasticity models attempt to describe the plastic deformation by utilising mathematical formulations. As already described in Chapter 2, both the mathematical formulations and the boundary conditions utilised vary from one plasticity model to

Discussion

another. From a crystal plasticity point of view, the variations among these models are related to how they engage and determine the number of slip systems activated for the individual grains. So called 1-point approach models like the Taylor model (Taylor 1938) are the simplest and roughest of the plasticity models. The Taylor model simply state that each crystal of a polycrystalline aggregate (i.e. grain) deforms such that the outer deformation state is fulfilled (see section 2.2.5 for more detailed information concerning the model). These models engage a given number of slip systems in order to accommodate the enforced macroscopic deformation and this number is independent of crystallographic orientation. Further, these models also state that the same number of slip systems remains active throughout the whole deformation process. The number of slip systems activated is based on the constraint, and the Taylor full constraint (FC) assumes activation of 5 different slip systems. Based on the grain shape and/or the stress continuity consideration, some shear requirements may be relaxed, i.e. not prescribed. This leads to the relaxed constraint (RC) Taylor models (Honneff and Mecking 1978). The Taylor RC lath and pancake models relax one and two shear components respectively, i.e. the number of activated slip systems become 4 and 3 respectively (Van Houtte et al. 2005). The original Sachs model (1928) states, as opposed to the Taylor model, that a polycrystal is an aggregate of independently deforming single crystals which only activates one slip system for each individual grain (section 2.2.4). Hence, the Sachs model is the other extremity when it comes to 1-point approach models.

Further, it is well established that the slip systems most easily activated are the ones having the highest Schmid values. The results presented in section 5.6.2 show that the grain-to-grain Schmid value distribution varies significantly. Hence, some orientations have a homogeneous Schmid value distribution while other orientations engage a limited number of slip systems with Schmid values that diverge considerably compared to the remaining slip systems. As already thoroughly discussed in the previous section, it seems reasonable to assume that the number of activated slip systems can vary quite substantially for the various grains in a given microstructure. Therefore, it is important that the applied plasticity model captures these local variations.

Established algorithms for simulating plastic deformation of metals are normally calibrated and compared to tensile test curves. However, this global mechanical

Discussion

behaviour is just an average over all heterogeneities included in the sample. So, although simulations may agree well with the specimen behaviour as a whole, the mathematical models are not able to describe the material behaviour locally (Kalidindi et al. 2003, Henning and Vehoff 2005). Section 6.3.5 discusses the effect and nature of these local strain heterogeneities in more detail.

Based on this, the calculated number of activated slip systems by static plasticity models at the best, is an average of the actual number of slip systems activated. For most applications, this type of models gives a sufficient description. Taylor type models are therefore frequently used to predict texture evolution during deformation (se e.g. Aukrust et al. 1997). However, this type of models is inadequate when used to predict anisotropy in mechanical properties as shown in Chapter 6.2. Previously, Fjeldly (1999) has evaluated the capabilities of several different plasticity models by predicting the angular dependence of mechanical properties (yield stress, flow stress and r -value) for two different Al-Zn-Mg-alloys. The results are consistent with the findings in this work, and clearly show that static plasticity models are not able to predict the observed mechanical anisotropy behaviours sufficiently.

During the last couple of decades, several new and more flexible N-point approach models like the LAMEL/ALAMEL models developed by Van Houtte and co-workers (2005) and the GIA model developed by Crumbach and colleagues (Crumbach et al. 2001) have been introduced. These models take grain-to-grain interactions into account, i.e. the number of slip systems activated is also dependent on the orientation of the surrounding grains. In this approach, plastic deformation can be described more accurately and prediction of mechanical anisotropy becomes more realistic. The overview made by Li and Van Houtte (2002a) clearly shows that the LAMEL method is clearly superior to the above classical models. The experimental observations made in this work support the findings made by Li and Van Houtte.

Further, Li and Van Houtte (2002a) also showed that LAMEL is more accurate than the Crystal Plasticity Finite Element Method (CPFEM). However, also the finite element technique is able to satisfactorily capture the overall mechanical anisotropy. Even though the CPFEM is practically impossible to use for industrial forming simulations (enormous calculation time), the interest for this type of modelling has been rapidly growing with

Discussion

the growth of the computing capacity of the average workstation. The work by Delaire et al. (2000) use the CPFEM in combination with deformation field and crystallographic orientation measurements in order to better understand the history of slip in each grain and help establish which slip systems are activated at a local level. The comparisons between orientations, measurements and simulations have shown good overall agreement to observed strain and local orientations quantities. The kinetics of plastic deformation was also accurately described, with no discrepancy between methods for the determination of locally active slip systems.

This type of complex calculations has been outside the scope of this work. However, a very simplified method for determining the number of slip systems activated gives similar results, hence supporting the findings reported by Delaire et al. (2000). In the present work all potential slip systems with a Schmid factor satisfying the condition:

$$m \geq 0.75m_{max} = m_{crit} \quad (33)$$

seem to activate. Here, the Schmid factor of the slip system most likely to be active is m_{max} and m_{crit} is the appurtenant critical Schmid factor. Most of the grains in the present material having a strong crystallographic texture (deformed 45° to ED), had an initial orientation where 3-4 slip systems could satisfy the above criteria. However, up to as much as a strain of 12%, the number of slip systems satisfying this criterion was only two (as shown in Figure 6.21). These two slip systems were frequently co-planar but in some cases the slip systems belonged to different slip planes.

Discussion

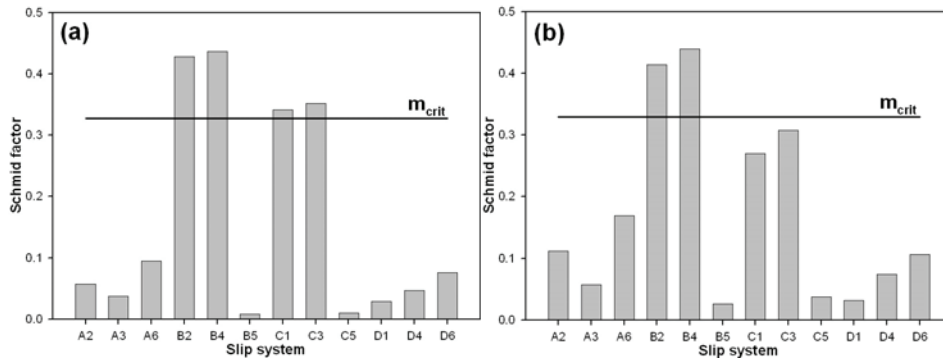


Figure 6.21 – Calculated Schmid factor of all slip systems based on crystallographic orientation of a typical grain investigated in this work. The assumed critical Schmid factor is indicated with a horizontal line. (a) initial orientation (undeformed) and (b) 12% deformation.

At 27% deformation only 1-2 slip systems were satisfying the above criteria, and the grains with a high probability for activating two slip systems were the grains having multiple slip traces, hence not co-planar slip systems. By combining information from slip traces, crystallographic orientation and local strain measurements, this type of relation was found for all directions investigated.

6.3.5 Strain heterogeneities

Strain heterogeneities are almost inevitable during plastic deformation. It is generally accepted that formability of semi-products is closely related to the microstructure inherited from the upstream processing. Textural components, grain-size and morphology as well as the second phase particles are typically inhomogeneously distributed in the microstructure. For that reason, the strain is never completely homogeneous throughout the structure and the materials tend to develop some sort of strain localisation. The different types of strain heterogeneities/localisations can be divided into different categories based on their origin and length scale.

It is beyond doubt that the local strain distribution by itself is a very complex matter. If a material develops visible strain heterogeneities or not during deformation is strongly dependent upon the length scale in which the strains are evaluated. Materials which seem to possess a very homogeneous strain distribution on a given length-scale can easily

Discussion

possess vigorous strain heterogeneities on a finer length-scale. Aluminium is a typical example of such a material.

The most well known strain heterogeneity at the macroscopic length scale is the strain localisation taking place during necking initiated at the uniform strain, ref. the Considere criterion (Considere 1885). This criterion states that the onset of necking and the end of uniform elongation (homogeneous deformation on a macroscopic length scale) occurs when the true work hardening rate exactly equals the true strain (Wagoner and Chenot 1996):

$$\frac{d\sigma}{d\varepsilon} = \sigma \quad (34)$$

At this point, the deformation is localised into the necking area while the remaining part of the material is strain relaxed and almost no more deformation takes place. Hence, beyond this point the material develops evident severe strain heterogeneities as shown by the micrograph presented in Figure 5.65.

Further, the Piobert-Lüders (PL) and the Portevin-Le Châtelier (PLC) effects are other strain heterogeneities which are evident at the macroscopic scale in alloys with Mg in solid solution. The PL phenomenon is a strain softening type instability and is characterised by the presence of a plateau of almost constant stress after the onset of yielding (Baird 1963). The PLC effect is a strain rate softening type instability and manifests itself as serrations in the stress-strain curve during the work-hardening stage of deformation (Thomas 1966). Both these effects are frequently observed on the macroscopic stress-strain curve of aluminium alloys containing magnesium. The alloys investigated in this work, which are from the Al-Mg-Si system, possesses therefore this type of strain heterogeneities as shown in Figure 5.12 and Figure 5.13.

In a parallel work associated to this PhD-thesis, the PLC effect has been investigated by use of the DSCA-technique. The results from these investigations will be reported elsewhere. Experimental results from earlier work (e.g. Sørensen 1997) have shown that the PLC-effect has a negative impact on the forming behaviour. This is most likely related to the altered strain distribution as suggested by Sørensen (1997). Locally, the material has to activate additional slip systems when the moving deformation band

Discussion

passes. Additional slip systems activated will lead to increased dislocation interactions which clearly have a negative impact on the forming behaviour (Kocks 1970). This is another example where the experimental results clearly confirm the correlation between the number of slip systems activated, strain heterogeneities and the forming behaviour.

As shown in Figure 5.18 and Figure 5.19, heat-treatment leads to significant alterations in the amount of PLC activity, and the PLC-effect is not visible for the specimens deformed in the SEM (AA6063, T1 condition). This is confirmed by the stress vs. strain curves obtained from the in-situ experiments (Figure 5.23). Hence, AA6063 has in condition T1 a homogeneous strain distribution on the macroscopic scale. However, when this material condition is investigated more carefully in the SEM, it becomes clear that the material has a quite heterogeneous strain distribution on a finer length-scale (microscopic).

The slip traces observed on the specimen surface (section 5.6.1) are by themselves strain heterogeneities. This type of local strain heterogeneities develops on a much finer length-scale than what can be observed with the naked eye. On this length-scale, some regions do not deform at all, while other regions develop very significant strains. Hence, also strain localisation on a microscopic scale is an intrinsic property for this type of alloys. Previously it has been reported that this type of strain heterogeneities might be suppressed by artificial age-hardening to peak- and over-aged conditions (Poole et al. 2005). However, the present observations for AA6063 clearly contradict this since slip traces evidently develops in condition T1.

Within the microstructure, the amount of slip traces, appearance and consistency with neighbouring grains varies significantly from grain to grain. It is also worth noticing that these slip trace characteristic is strongly dependent on the deformation direction. As shown in section 5.6.1, these features varies significantly through the microstructure for specimens deformed perpendicular to ED. Hence, some grains possess fine slip traces, while other grains possess thick discontinuous and wavy slip traces. The specimen deformed 45° to ED possesses very fine and homogeneous slip traces through the whole microstructure. These evident variations in slip traces, i.e. local strain heterogeneities, are directly linked to the crystallographic texture, which again is related to slip

Discussion

activation. It is therefore clear that also the amount of strain heterogeneities on this finer length-scale is texture dependent.

When slip traces are studied in even more detail, micrographs illustrate that deformation by slip clearly is a discontinuous deformation process (Figure 5.68). Hence, by using ordinary definitions of strain very locally, the strain can be almost infinity in one region, while the neighbouring regions are more or less undeformed. As already indicated in section 5.7.1, this fact makes it impossible to treat the material as a continuum at this length-scale. The very significant strains will make the material collapse locally (i.e. the material reaches the ultimate strain in these regions), which again will lead macroscopic failure. In other words, the forming behaviour of a material is to a large extent determined by the local strain distribution taking place on all length-scales. To illustrate this even further, the in-situ deformation experiments will be discussed to explain the effect of texture and activation of slip systems on the local strain distribution taking place during deformation.

6.3.6 Hard vs. soft orientations

As mentioned above, it is a common understanding that microstructural heterogeneities like crystallographic texture, grain size and shape, and second phase particles lead to strain heterogeneities. During the last century, several studies have been performed on how the local strain distribution is controlled by microstructural heterogeneities. Raabe et al. (2003) studied an Al-Mg-Si sheet (AA6022) and found that the existence of soft and hard inclusions gave rise to strong strain heterogeneities at the specimen surface. This observation is comparable to the observation made by Wittridge and Knutsen (1999), which found that strain localisation was produced when colonies of the strong R-texture components were embedded within the soft matrix with Cube texture. This observation confirmed the fact that grain-scale roughening first produces microscopic strain localization in the incipient stages of plastic straining and eventually macroscopic through-thickness strain localisation. In agreement with earlier work along these lines, the authors concluded that ridging phenomena could be attributed to texture inhomogeneity.

Discussion

The present study has shown that alloy AA6063 also develops similar type of strain localisation due to texture heterogeneities. The soft grains, having several slip systems with high to very high Schmid values can easily activate many slip systems (see section 6.3.3 for more details) and are therefore easy to deform. The hard grains have a more unfavourable Schmid value distribution and would therefore like to avoid activating any slip systems. As a consequence, the number of slip systems activated varies significantly from grain to grain, which again affect the strain distribution during deformation. This is very well illustrated in Figure 5.63, which presents the measured major strain distribution deformed to a global strain of 27%. Here, the grain boundaries determined by EBSD are overlaid, and it becomes clear that the strain heterogeneities are related to variations in crystallographic orientation. The IPF-map of the same area (Figure 5.61) confirms that there exist a close correlation between the crystallographic orientation and the local strain distribution. In other words, microstructures consisting of both “hard” and “soft” grains will develop local strain heterogeneities during deformation, i.e. some grains are deformed significantly more than others. The soft grains have to compensate for the lack of deformation taking place in the hard grains. This again means that the enforced global deformation mainly is picked up by grains having soft crystallographic orientations, i.e. the strain is localised to soft regions. Soft grains can therefore be deformed to strains approximately three times as high as the global strain and more than four times as high as neighbouring hard grains as shown in Figure 5.63. The consequences of such variations have also been investigated by Duan et al. (2005) and were discussed above in Chapter 6.2.

The fact that all grains have some slip systems more favourable oriented for slip has been known since the earliest days of crystal plasticity. All the classical plasticity models are even based on this assumption (Sachs, Taylor). An example of a Taylor factor map of the microstructure (Figure 5.62) illustrates quite evidently how the crystallographic texture determines deformation easiness. The grains having a high Taylor factor correspond to the least deformed grains at the macroscopic uniform strain. Further, the maps presented in Figure 5.54 clearly illustrate how the Taylor factor of a given material is determined by the applied deformation direction (a-c), as well as the texture heterogeneity. Consequently, the material with random texture (d) has large variations in the Taylor factors compared to the material with strong texture (a-c).

Discussion

Further, it appears that a clear correlation between the number of slip traces observed and the local strain distribution exists. In general, grains developing low strain, i.e. high Taylor factor, rarely develop strong slip traces. Further, it is observed that the grains exhibiting high strain often develop a limited number but very vigorous slip traces. However, it is also observed that such grains develop multiple slip traces, especially close to the grain boundaries. This can be explained by the Schmid value distribution. Hence, heavily deformed grains has some slip systems which are extremely well oriented for slip and can therefore accommodate large strains on a limited number of slip systems. However, at very high strains, other slip systems have to be activated in order to fulfil the compatibility requirements. On the other hand, there are examples of grains deformed to very high strains, where no evident slip traces are observed. This could mean that the strain either is evenly distributed among a high number of slip systems (homogeneous deformation), which is in strong contrast to the discussions regarding activation of slip systems, or, strain is distributed on a limited number of slip systems which not produces visible slip traces. Neither of these solutions seems very likely, so it is difficult to fully explain the relationship between the number of slip traces observed and the amount of strain heterogeneities. From the discussion above, the amount of deformation taking place in individual grains is to a large extent determined by their crystallographic orientation. However, it has also been shown that other factors could introduce strain heterogeneities.

6.3.7 Effects of nearest neighbours

As already mentioned several times, the number of slip systems activated is strongly dependent on the global texture. For the individual grains, also another given difference comes into effect. Almost all grains in a material with very strong crystallographic texture have close to similar orientation. Hence, individual grains have several neighbouring grains with comparable orientation and they will therefore activate the same number of slip systems during deformation. For the same reason, they will deform in a similar manner, hence internal compatibility is also improved. Contrary, in a material with random texture, all the surrounding grains will have dissimilar orientations. The compatibility requirements are more demanding and the grain has to activate a higher number of slip systems. This is very well illustrated comparing the

Discussion

maps presenting the number of slip traces activated by the individual grains during deformation (Figure 5.44, Figure 5.45 and Figure 5.50). These figures show that AA6063 has to activate a higher number of slip traces when the crystallographic texture is more or less removed. As a consequence, this material will have a more heterogeneous strain distribution when the crystallographic texture has been removed by cross-rolling. This is also well illustrated by comparing the two figures presenting the local strain distribution of the material with strong texture deformed parallel and 45° to ED (Figure 5.73 and Figure 5.74). The specimen deformed parallel to ED, which also has the most uniform Taylor factor distribution, has a much more homogeneous strain distribution than the specimen deformed 45° to ED.

The effect of nearest neighbours can also indirectly affect the strain distribution. In many ways, it could be reasonable to compare the macroscopic uniform strain of a material with a chain. The chain is not stronger than its weakest segment and neither a material can be deformed further than until the microstructure reaches the uniform strain locally. In other words, a material with vigorous strain localisation will reach the macroscopic uniform strain earlier than a material with homogeneous strain distribution. When this statement is transferred to the investigated material, it becomes evident that the observed strain heterogeneities will have a negative impact on the macroscopic uniform strain. The amount of strain localisation is dependent on the deformation direction. Hence, it could be claimed that these variations explain the variations in uniform strain when deformed 0° , 45° and 90° to ED. These variations might be insufficient to explain the variations observed in macroscopic mechanical properties alone, but the angular dependency of the local strain heterogeneities are undoubtedly consistent with variations in mechanical properties.

In other words, not only the crystallographic texture determines the strain distribution taking place in the material. This is explicitly illustrated when the through-thickness variations in crystallographic texture for AA6063 prior to cross-rolling is compared to the local strain measurements of the same area. Figure 5.72 shows that there are large variations in Taylor factors through the profile thickness, due to the evident texture gradient discussed in Chapter 6.2. From a Taylor factor point of view, the 0° and 90° specimens would develop heavy strain localisation at the specimen surface, while the

Discussion

surface of the 45° specimens would hardly deform at all. In contrast, the local strain distribution clearly show that this is not the case, even though the first traces of strain localisation take place in areas of low Taylor factor. The material has to overcome the compatibility requirements, underlining the fact that the material is dependent on the nearest neighbours in order to overcome the enforced global deformation.

6.4 Impact and relevance to shape of extrusions

The through-thickness variations developed during extrusion will certainly affect all subsequent forming processes. It has been shown above in Chapter 6.2 that the deformation behaviour of the different layers varies significantly. Further, it has been assumed that the observed gradients are symmetrical about the profile centre plane ($S=0.00$), which is expected for simple extrusions like the flat geometries investigated in this work. However, due to the complicated texture evolution during extrusion, such simple symmetrical texture variations are not expected for more complicated geometries. When more complicated profiles are investigated, they often possess unsymmetrical gradients, hence predictions of the forming behaviour become very challenging.

Imagine a fairly simple V-shaped extruded profile (Figure 6.22). During extrusion of such profile geometries, the die design will normally enforce a flow pattern where texture differences are developing between the inside and outside surface layer. Based on the results and discussions presented above, it seems clear that the mechanical properties will differ through the wall thickness. This will, of course, alter the deformation behaviour of the different layers which again can appear like minor alterations of the profile geometry.

Discussion

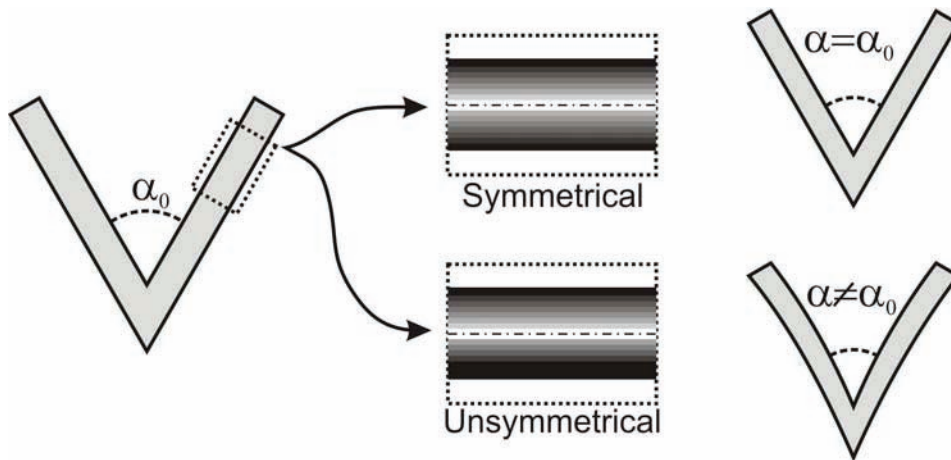


Figure 6.22 – V-shaped extruded profile (complicated geometry). Profiles with symmetrical texture will maintain their geometry after axial deformation (top), while the geometry will be altered if the gradient is unsymmetrical (bottom).

Extruded profiles are normally subjected to a stretching procedure immediately after extrusion in order to remove curvatures introduced for example from uneven cooling or material flow through the die. In this operation, the profiles are given an axial elongation of typically 0.5-1.5%. This deformation is in some cases observed to be sufficient in order to adjust the geometrical shape. However, very frequently the shape after stretching is becoming outside the geometry tolerances, i.e. the angle α_0 (Figure 6.22) can be shifted during stretching. If a profile with a symmetrical texture gradient is stretched, the deformation is expected to take place symmetrical around the centre plane ($S=0.00$). Each layer will deform differently but the profile will maintain its geometrical shape since the outer and inner side of the profile deforms equally and by that neutralise potential bending of the profile walls. However, if a profile with an unsymmetrical gradient is deformed by tension, the inner and outer side will deform differently (Figure 6.23). The differences in deformation behaviour, independent of the cause (internal stresses, gradients, plastic strain ratios etc.), could introduce some alterations of the profile shape ($\alpha \neq \alpha_0$). If, for the sake of simplicity, the variation in plastic strain ratio is the only cause of variations through the thickness, the differences in r -values could introduce larger transversal strains (Figure 6.23). These strains can alter the profile shape which again makes it more difficult to reach the target shape after forming. It is therefore very important both to understand the effect from and to control the development of through-thickness variations in order to improve the forming behaviour.

Discussion

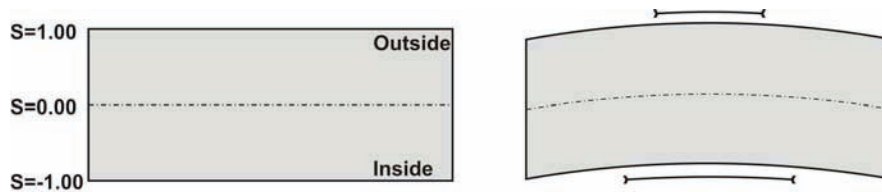


Figure 6.23 – Illustration of the leg from a V-shaped extruded profile with evident through-thickness variations before stretching (left). In the shown case, the transversal strains at the inside of the profile are assumed larger than the outside strains due to differences in plastic strain ratio. This leads to strain gradients which manifest as a curvature (shape change) of the profile after stretching.

6.5 In-situ deformation in the SEM – status and challenges

The discussion presented above clearly shows that in-situ deformation in the SEM is a powerful tool that allows a new type of experimental investigations and thereby provides insight to important metallurgical phenomena. Still, the technique is not fully developed and is confronted with several challenges that have to be overcome. This chapter will be used to discuss the status and challenges for this promising technique.

6.5.1 In-situ deformation unit

For the last decade, there has been an enormous evolution when it comes to in-situ deformation capabilities in the SEM. At the initiation of this work, only a modest number of works related to this topic was published. The group at the CNRS – PMTM laboratory in Paris was one of the exceptions, and had already published several impressive works utilising simple-tension deformation (Chiron et al. 1996, Delaire et al. 2000) (see section 2.7.5 for more details). At the beginning of this decade, the interest boosted and several groups around the world started to utilise this technique. As a consequence, the number of publications has increased vigorously. Most of these publications are related to simple-tension deformation.

The Norwegian University of Science and Technology (NTNU) has collaborated closely with the CNRS – PMTM laboratory for several years. In 2001, this collaboration was extended also include in-situ investigations in the SEM. Consequently, NTNU acquired the deformation unit developed by Rémi Chiron and his group at CNRS – PMTM. This

Discussion

deformation unit is very compact, allowing it to be mounted to most SEMs available today. In addition, this deformation unit is not only capable of deforming the sample by simple-tension, but also other deformation modes like compression and bending are available. Furthermore, these different modes of deformation can be combined with a heating unit, allowing deformation at elevated temperatures. The capabilities are extensive when this deformation unit is combined with EBSD measurements (and/or local strain measurements).

When designing experimental equipment like the one described here, it is always a compromise between different functionalities, i.e. EBSD performance and deformation mode capabilities. These functionalities are very well balanced for the deformation unit applied in this work. Hence, the machine developed by Rémi Chiron and co-workers is really state-of-the-art when it comes to in-situ deformation in the SEM (see section 4.3.3 for more details concerning this deformation unit).

6.5.2 Challenges (related to in-situ deformation in the SEM)

As already mentioned above, there are still some challenges that have to be overcome even though in-situ deformation in the SEM is a powerful tool. There are some important limitations for the EBSD technique.

When the specimen is deformed with a strain rate of $1.1 \times 10^{-4} \text{ s}^{-1}$ and the time necessary to perform a detailed scan of the microstructure is ~ 45 minutes, the specimen will be given a deformation equal to 30% during on scan. Consequently, the deformation has to be interrupted in order to perform these investigations. Hence, this type of investigations is not fully in-situ but rather “semi-in-situ”. The pattern acquisition speed of the EBSD technique has been improved significantly since the introduction of the technique. At that time, it was almost impossible to acquire 1fps, while modern EBSD systems easily acquire up to 43fps (see section 4.3.1). In the near future, it is reasonable to assume a pattern acquisition speed of 300-500fps will be available (Schwarzer 2007). With this acquisition speed, it will be possible to perform fully in-situ EBSD investigations.

Discussion

The strict surface requirements for EBSD investigations are another important limitation for the EBSD technique. As pointed out in section 4.1.2, the specimen surface has to be electro-polished in order to obtain the required pattern quality. Further, it is well known that the specimen surface contaminate due to the electron beam, and this reduces the pattern quality. In addition, the specimens often develop surface topography that makes it difficult to perform high-quality EBSD investigations at high strains (see e.g. Figure 5.49). To avoid these problems, it would have been desirable to repolish the specimen surface during deformation. The new dual-beam microscopes (combined Focused Ion Beam (FIB) – Scanning Electron Microscope (SEM)) allow this type of repolishing. However, since both these techniques are fairly novel, there are still not reported any works where FIB is used to repolish the specimen during in-situ deformation investigations.

Further, repolishing will also remove the slip traces at the specimen surface. Hence, it could be argued that information about the slip planes activated is lost. On the other hand, it will become possible to study when the different slip traces are produced. As an example, some grains develop additional slip traces at high strains, indicating that other slip systems are activated at this strain range. By repolishing the surface, it would be possible to answer whether the initial slip systems stay active, or if these systems become inactive at higher strains. In other words, this type of supplement provides new possibilities for in-situ deformation investigations. However, the repolishing must be used with consideration since it alters the investigated surface.

6.5.3 Focused Ion Beam (FIB)

As already mentioned above, FIB has been introduced as a new and very interesting technique for performing microstructural investigations. The technique has evolved substantially since it first was introduced more than thirty years ago (Bischoff and Teichert 1997, Tseng 2004). For the last couple of years, FIB has for different reasons been substantially applied together with EBSD.

FIB can for example be used to prepare the surface of a material for EBSD investigations (Matteson et al. 2002). Repolishing can as discussed above be necessary during in-situ deformation investigations. Further, there are also applications where the

Discussion

material of interest has to be prepared in vacuum, since an oxide layer can develop at the specimen surface and obscure the backscattered signal. For example, when exposed to atmosphere, nano-scale metallic interconnects, used in microelectronic devices, can oxidize rapidly, making them very difficult to analyze by EBSD (Farrer et al. 2002).

More relevant for this thesis is the use of dual-beam microscopes for 3D microstructural investigations, especially when FIB is used together with EBSD. Combining the successive removal by FIB with sequential EBSD maps and high-resolution imaging by the electron beam, reveal detailed information through the specimen thickness. The different sections can then be used to generate a full 3D sample reconstruction. The technique is in other words perfect for obtaining information about the microstructure that can be used as input for computer simulations of various forming operations. Further, FIB-EBSD can also be used to obtain detailed information about orientation gradients developing e.g. close to grain boundaries and primary particles.

Another important feature is that the spatial resolution of combined FIB and EBSD investigations conveniently fits in between the electron tomography (few Angstroms) and the 3DXRD (several microns) techniques, and is suitable for looking at microstructures with feature sizes of tens of nanometres to tens of microns (Mulders and Day 2005, Zaefferer et al. 2005). Dual-beam investigations have already been used to obtain a better understanding of 3D orientation gradients (see e.g. Konrad et al. 2006).

Due to the destructive nature of FIB-sectioning, this type of experiments never can be combined with in-situ investigations. Still, combined FIB-EBSD experiments clearly supplement the EBSD in-situ experiments. Hence, if performed correctly, the results from both methods provide a better understanding of 3D plasticity. Due to the limitations with these methods, in-situ 3D plasticity investigations still have to be performed by the 3DXRD or similar techniques as pointed out in section 2.7.5. Even though 3DXRD is superior to the in-situ deformation technique in the SEM when it comes to 3D plasticity, the discussion above has shown the enormous potential for this technique. It is reasonable to assume that in the future, in-situ deformation in SEM will help scientist understand the basics of the mechanisms operating during deformation.

7 Conclusion

The present work has been concerned with experimental investigations of extruded sheets from two commercial Al-Mg-Si alloys with different microstructure. The main objective has been to obtain a better understanding of the deformation mechanisms operating during plastic forming of extruded aluminium profiles. This has been obtained by discussing the experimental results, which are organised in two separate parts based on the techniques applied and the mechanisms investigated. The main conclusions based on these examinations, can be summarised as follows:

- The mechanical anisotropy observed between the 0° and 90° direction of AA6063 is related to the ED-rotated Cube texture. The Schmid value distribution for the dominant texture components is not symmetrically distributed. Hence, the activation of slip systems varies significantly.
- Crystallographic texture is the main reason for mechanical anisotropy. However, also artificial and to some extent natural age-hardening affect mechanical anisotropy due to the introduction of non-shearable particles that reduces the texture effect. Hence, both AA6063 and AA6082 possess more isotropic mechanical properties after artificial ageing.
- Extruded profiles with microstructural and textural through-thickness variations will possess evident variations in through-thickness mechanical properties and can develop significant anisotropic cross-sectional shape variations when subjected to uniaxial tensile deformation. The prediction of the forming behaviour becomes more complicated by the introduction of such a variation.
- Grains having a [100] or a [111] parallel to the deformation direction (DD) are stable during simple tension deformation while other crystallographic orientations tend to obtain such a configuration. Further, the accumulated lattice rotation for individual grains is reduced when the grain size is large.

Conclusion

- Combined slip trace and Schmid value distribution analysis can be used to determine the number of slip systems activated.
- Comparison of experimental results and texture based calculations show that the plastic strain ratio for the present Al-Mg-Si profiles is better described by the Taylor RC than the FC method. The static plasticity models (e.g. Sachs, Taylor models) are not able to provide sufficiently accurate predictions of the mechanical anisotropy. The accuracy of texture based calculations can be improved by applying more advanced and dynamic models like the GIA and LAMEL models.
- The number of slip systems activated (typically 1-2 slip systems) is very heterogeneous and is normally less than the number predicted by the classical Taylor model. Generally, it has been shown that materials without texture need to activate a higher number of slip systems than a material carrying a strong crystallographic texture.
- Strain heterogeneities lead to reduced macroscopic uniform strain. Different types of heterogeneities are observed at all length-scales, and all types of strain heterogeneities should be evaluated in order to determine the macroscopic forming behaviour of a material.
- Microstructures consisting of both “hard” and “soft” grains develop local strain heterogeneities during deformation. Consequently, the enforced global deformation is mainly picked up by grains having soft crystallographic orientations, i.e. the strain is localised to soft regions.
- In-situ deformation in the SEM combined with EBSD is a powerful tool for investigating plasticity of materials. The technique has some important limitations, but still, the results obtained with this technique are comparable to the observations obtained with the more advanced 3DXRD technique.

References

References

- Adcock F., *J. Inst. Met.*, **27**, p. 73, 1922
- Althoff J., Drefahl K., Wincierz P., *Zeitschrift für Metallkunde*, **62**, p. 765, 1971
- Aukrust T., Vatne H.E., SINTEF Materials Technology, Report STF24 A94044, p. 63, 1994
- Aukrust T., Tjøtta S., Skauvik I., Vatne H.E., Van Houtte P., Proc. 15th Risø International Symposium on Materials Science, Denmark, p. 219, 1994
- Aukrust T., Lohne O., Vatne H.E., Furu T., Tjøtta S., Proc. ET96: 6th International Aluminum Extrusion Technology Seminar, Chicago, Illinois, p. 171, 1996
- Aukrust T., Tjøtta S., Vatne H.E., Van Houtte P., *Int. J. Plasticity*, **13**, p. 111, 1997
- Backofen W.A., *Deformation Processing*, Addison-Wesley Pub. Co., 1972
- Baird J.D., *Iron Steel*, **36**, p. 186, 1963
- Barlat F., Liu J., *Mater. Sci. Eng.*, **A257**, p. 47, 1998
- Barlat F., Vasudevan A.K., *Acta Metall. Mater.*, **39**, p. 391, 1991
- Bate P., *Phil. Trans. R. Soc. A*, **357**, p. 1589, 1999
- Bate P., Roberts W.T., Wilson D.V., *Acta Metall.*, **29**, p. 1797, 1981
- Bauger Ø., SINTEF Materials Technology, Report STF24 A94649, p. 33, 1994
- Bischoff L., Teichert J., *Mater. Sci. For.*, **248-249**, p. 445, 1997
- Bishop J.F.W., Hill R., *Phil. Mag.*, **42**, p. 414, 1951
- Bjerkaas H., Sjølstad K., Proc. SCANDEM 2002, ed. Keränen J., Sillanpää K., Tampere, Finland, p. 51, 2002
- Bjerkaas H., Fjeldbo S.K., Roven H.J., Hjelen J., Furu T., Proc. TMS 134th Annual Meeting & Exhibition, Trends in Materials Manufacturing Technologies for Transportation Industries, p. 251, 2005
- Bjerkaas H., Fjeldbo S.K., Roven H.J., Hjelen J., Cjiron R., Furu T., *Mater. Sci. For.*, **519-521**, p. 809, 2006
- Bowen A.W., Proc. ICOTOM 8, ed. Kallend J.S., Gottstein G., Warrendale, PA, p. 971, 1988
- Bowen A.W., *Mater. Sci. Tech.*, **6**, p. 1058, 1990
- Brown K., *J. Inst. Met.*, **100**, p. 341, 1972
- Bunge H.J., *Texture analysis in Materials science - Mathematical methods*, Butterworth, London, 1983
- Bunge H.J., Fuchs R., *Phys. Stat. Sol.*, **32**, p. 169, 1969
- Bunge H.J., Nielsen I., *Int. J. Plasticity*, **13**, p. 435, 1997

References

- Cahn, J. *Inst. Metals*, **79**, p. 129, 1950
- Chiron R., Fryet J., Viaris de Lesegno P., *Proc. Symposium on Local Strain and Temperature measurement in Non-uniform Fields at Elevated Temperatures*, Berlin, 1996
- Choi Y.S., Piehler H.R., Rollett A.D., *Matall. Mater. Trans.*, **35A**, p. 513, 2004
- Chu T.C., Ranson W.F., Sutton M.A., Peters W.H., *Exp. Mech.*, **25**, p. 232, 1985
- Chung N., Embury D., Evensen J.D., Hoagland R.G., Sargent C.M., *Acta Metall.*, **25**, p. 377, 1977
- Chung Y.H., Cho K.K., Han J.H., Shin M.C., *Scripta Mater.*, **43**, p. 759, 2000
- Cizek P., Wynne B.P., Hong Lu, Parker B.A., *Mater. Sci. Eng.*, **A219**, p. 44, 1996
- Clarebrough L.M., Hardreaves M.E., *Progress in Metal Physics*, 8, Pergamon Press, Oxford, 1959
- Considerere A., *Ann. Ponts Chaussees*, **9**, p. 574, 1885
- Cox H.L., Sopwith D.G., *Proc. Phys. Soc.*, **49**, p. 134, 1937
- Crumbach M., Pomana P., Wagner P., Gottstein G., *Proc. 1st joint Conf. On Recrystallization and Grain Growth*, ed. G. Gottstein and D.A. Molodov, p. 1053, 2001
- Crumbach M., Goerdeler M., Gottstein G., Neumann L., Aretz H., Kopp P., *Modelling Simul. Mater. Sci. Eng.*, **12**, p. S1, 2004
- Delaire F., Raphanel J.L., Rey C., *Acta. Mater.*, **48**, p. 1075, 2000
- Diehl J., *Z. Metallk.*, **46**, p. 650, 1955
- Diehl J., *Z. Metallk.*, **47**, p. 331, 1956
- Dieter G.E., *Mechanical Metallurgy*, McGraw-Hill, London, 1988
- Dillamore I.L., Roberts W.T., *Met. Rev.*, **10**, p. 271, 1965
- Dingley D.J., *Scanning Electron Microscopy*, **2**, p. 569, 1984
- Doumalin P., Bornert M., Caldemaison D., *Proc. International Conference on Advanced Technology in Experimental Mechanics '99*, Ube, Japan, p.81, 1999
- Duan X., Jain B., Metzger D., Kang J., Wilkinson D.S., Embury J.D., *Mater. Sci. Eng.*, **A394**, p. 192, 2005
- Dumoulin S., Tabourot L., Chappuis C., Vacher P., Arrieux R., *J. Mat. Proc. Tech.*, **133**, p. 79, 2003
- Ekstrom H.E., Furu T., Mishin O.V., Pettersen T., Olsson B., *Aluminium*, **78**, p. 930, 2002
- Engler O., *VIRFORM-report*, Hydro Aluminium, Deutschland, 2002
- Engler O., *Lecture notes*, March 16th, 2004
- Engler O., Lüke K., *Mater. Sci. Eng.*, **A148**, p. 15, 1991
- Engler O., Crumbach M., Li S., *Acta Mater.*, **53**, p. 2241, 2005

References

- Ewing J.A., Rosenhain W., *Phil. Trans. Royal Soc.*, **193A**, p. 353, 1900
- Farrer J.K., Chipman M.C., Tiner M., *Microsc. Microanal.*, **8**, p. 544, 2002
- Ferry M., *Proc. Materials 98*, ed. M. Ferry, Wollongong, p. 439, 1998
- Fjeldbo S.K., Holmedal B., Lademo O.-G., Bjerkaas H., Støren S., Roven H.J., Hjelen J., Hopperstad O.S., Berstad T., Pedersen K.O., Furu T., *Proc. ESAFORM 2005*, Cluj-Napoca, Romania, 2005
- Fjeldly T.A., *Dr.Ing. Thesis*, NTNU, 1999
- Fjeldly T.A., Sørøng A., Roven H.J., *Mater. Sci. Eng.*, **A300**, p. 515, 2001
- Forbord B., Mathiesen R.H., Roven H.J., *Mater. Sci. For.*, **558-559**, p. 1299, 2007
- Furu T., Pedersen K.O., *Mater. Sci. For.*, **519-521**, p. 1611, 2006
- Furu T., Johansen A., Sæther J.A., Dons A.L., Pedersen K., Berstad T., Lademo O.-G., Holmedal B., Marthinsen K., Hopperstad O.S., Nes E., Mortensen D., *Aluminium*, **80**, p. 707, 2004
- Gambin W., *Plasticity and Textures*, Kluwer Academic Publishers, Dordrecht, 2001
- Garstone J., Honeycombe R.W.K., Greetham G., *Acta Metall.*, **4**, p. 485, 1956
- Goldstein J., Newbury D., Joy D., Lyman C., Echlin P., Lifshin E., Sawyer L., Michael J., *Scanning Electron Microscopy and X-Ray Microanalysis-3th ed.*, Kluwer/Academic Press, New York, 2003
- Gourgues-Lorenzon A.F., *Inter. Mater. Rev.*, **52**, p. 65, 2007
- Gray III G.T., *Acta Metall.*, **36**, p. 1745, 1988
- Hallem H., *PhD Thesis*, NTNU, 2005
- Han J.H., Jee K.K., Oh K.H., *Int. J. Mech. Sci.*, **45**, p. 1613, 2003
- Han J.H., Kim D.I., Jee K.K., Oh K.H., *Mater. Sci. Eng.*, **A387-389**, p. 60, 2004
- Hatherly M., *Proc. ICOTOM 5*, ed. Gottstein G. and Lücke K., **1**, p. 265, 1978
- He X.Y., Kang X., Quan C., Tay C.J., Wang S.H., Shang H.M., *Proc. SPIE*, **4537**, p. 63, 2002
- Henning M., Vehoff H., *Acta Mater.*, **53**, p. 1285, 2005
- Hirsch J., *Proc. ICAA9*, ed. Nie J.F., Morton A.J., Muddle B.C., Brisbane, Australia, p. 15, 2004
- Hirsch J., Lücke K., *Acta Metall.*, **36**, p. 2863, 1988
- Hjelen J., *PhD Thesis*, University of Trondheim, 1990
- Hjelen J., Ørsund R., Nes E., *Acta Metall.*, **39**, p. 1377, 1991
- Hjelen J., Qvale A.H., Gomo Ø., *Proc. ICOTOM 10*, ed. Bunge H.j., Clausthal, Germany, p. 137, 1993
- Honeycombe R.W.K., *The Plastic Deformation of Metals-2nd ed.*, Edward Arnold, Australia, 1984

References

- Honneff H., Mecking H., *Texture of Materials*, Aachen, Germany, p. 265, 1978
- Honneff H., Mecking H., *Proc. ICOTOM 6*, **1**, Tokyo, p. 347, 1981
- Hornbogen E., Gahr K.H.Z., *Metallography*, **8**, p. 181, 1975
- Hornbogen E., Starke E.A., *Acta Metall. Mater.*, **41**, p. 1, 1993
- Hu H., *Trans. Met. Soc. AIME*, **224**, p. 75, 1962
- Humphreys F.J., *J. Microsc.*, **195**, p. 170, 1999
- Humphreys F.J., *J Mater. Sci.*, **36**, p. 3833, 2001
- Humphreys F.J., Brough I., *J. Microsc.*, **195**, p. 6, 1999
- Humphreys F.J., Hatherly M., *Recrystallization and related annealing phenomena*, Pergamon, Oxford, 1996
- Humphreys F.J., Huang Y., Brough I., Harris C., *J. Microsc.*, **195**, p. 212, 1999
- Irgens F., Bauger Ø., Andersson B., *SINTEF Materials Technology, Report STF24 A95564*, p. 24, 1995
- International Organization for Standardization, *ISO 2107:2004*, 2004
- Iveland T, *Dr.Ing. Thesis, NTNU*, 2000
- Iwahashi Y., Horita Z., Nemoto M., Langdon T.G., *Acta Mater.*, **45**, p.4733, 1997
- Juul Jensen D., *Mater. Sci. Tech.*, **21**, p. 1365, 2005
- Kahn A.S., Huang S., *Continuum Theory of Plasticity*, John Wiley & Sons, New York, 1995
- Kalidindi S.R., Bronkhorst C.A., Anand L., *J. Mech. Phys. Solids*, **40**, p. 537, 1992
- Kalidindi S.R., Bhattacharyya A., Doherty R.D., *Adv. Mater*, **15**, p. 1345, 2003
- Kang J., Jain M., Wilkinson D.S., Embury J.D., *J. Strain. Anal. Eng. Des.*, **40**, p. 559, 2005
- Kang J., Wilkinson D.S., Jain M., Embury J.D., Beaudoin A.J., Kim S., Mishira R., Sachdev A.K., *Acta Mater.*, **54**, p. 209, 2006
- Karlsen M., Norum H., Hjelen J., Grong Ø., Frigaard Ø., *Proc. EMC 2004*, ed. Van Tendeloo G., Antwerp, Belgium, p. 623, 2004
- King J.E., You C.P., Knott J.F., *Acta Metall.*, **29**, p. 1553, 1981
- Knauss W.G., Chasiotis I., Huang Y., *Mech. Mat.*, **35**, p. 217, 2003
- Kobberrød O.K., Johannessen K., Heiberg G., Hjelen J., *Proc. ICEM 14*, ed. Calderón Benavides H.A., José Yacamán M., Cancun, Mexico, p. 543, 1998
- Kochendörfer A., Swanson M., *Arch. Eisenhüttenw.*, **31**, p. 549, 1960
- Kocks U.F., *Met. Trans.*, **1**, p. 1121, 1970
- Kocks U.F., Chandra H., *Acta Metall.*, **30**, p. 695, 1982
- Konrad J., Zaefferer S., Raabe D., *Acta Mater.*, **54**, p. 1369, 2006

References

- Korsnes T., Norum H., Karlsen M., Hjelen J., Proc. EMC 2004, ed. Van Tendeloo G., Antwerp, Belgium, p. 625, 2004
- Krieger Lassen N.C., J. Microsc., **181**, p. 72, 1996
- Krieger Lassen N.C., Juul Jensen D., Conradsen K., Scanning Microscopy, **6**, (1), p. 115, 1992
- Lademo O.-G., Hopperstad O.S., Langseth M., Int. J. Plasticity, **15**, p. 191, 1999
- Lademo O.-G., Hopperstad O.S., Malo K.A., Pedersen K.O., J. Mater. Proc. Tech., **125-126**, p. 84, 2002
- Lademo O.-G., Hopperstad O.S., Berstad T., Langseth M., J. Mater. Proc. Tech., **166**, p. 247, 2005
- Laraba-Abbes F., Ienny P., Piques R., Polymer, **44**, p. 807, 2003
- Lebensohn R.A., Tomé C.N., Acta Metall. Mater., **41**, p. 2611, 1993
- Leinum J.R., Moen K., Hjelen J., Malvik T., Proc. EMC 2004, ed. Van Tendeloo G., Antwerp, Belgium, p. 563, 2004
- Lens A., Maurice C., Driver J.H., Mater. Sci. Eng., **A403**, p. 144, 2005
- Li F., Bate P.S., Acta Mater. Metall., **39**, p. 2639, 1991
- Li C., Bretheau T., Acta Metall., **37**, p. 2645, 1989
- Li S., Van Houtte P., VIRFORM Report, Katholieke Universitet Leuven, Belgium
- Li S., Van Houtte P., Aluminium, **78**, p. 918, 2002a
- Li S., Van Houtte P., VIRFORM Report 13D, Katholieke Universitet Leuven, Belgium, 2002b
- Li Z.J., Winther G., Hansen N., Acta Mater., **54**, p. 401, 2006
- Liu Y.S., Kang S.B., Ko H.S., Scripta Mater., **37**, p. 411, 1997
- Liu Q., Wert J., Hansen N., Acta Mater., **48**, p. 4267, 2000
- Lopes A.B., Barlat F., Gracio J.J., Ferreira Duarte J.F., Rauch E.F., Int. J. Plasticity, **19**, p. 1, 2003
- Lucke K., Lange H., Z. Metallk., **43**, p. 55, 1952
- Ludwik P., Elemente der technologischen Mechanik, Springer-Verlag OHG, Berlin, 1909
- Marciniak Z., Duncan J., Mechanics of Sheet Metal Forming, 1992
- Margulies L., Winther G., Poulsen H.F., Science, **291**, p. 2392, 2001
- Marthinsen K., Abthai S., Nes E., Holmedal B., Aluminium, **78**, p. 869, 2002
- Martin J.W., Precipitation Hardening, Pergamon Press, New York, 1968
- Matteson T.L., Schwarz S.W., Houge E.C., Kempshall B.W., Giannuzzi L.A., J. Electron. Mater., **31**, p. 33, 2002

References

- Mguil-Touchal S., Morestin F., Brunet M., Proc. Eighth International Conference on Computational Methods and Experimental Measurements, ed. Brebbia C.A., Anagnostopoulos P., Carlomagno G.M., Rhodes, Greece, p. 45, 1997
- Mika D.P., Dawson P.R., Acta Mater., **47**, p. 1355, 1999
- Moen K., Malvik T., Hjelen J., Leinum J.R., Alnæs L., Proc. Applied Mineralogy 2004
- Mulders J.J.L., Day A.P., Mater. Sci. For., **495-497**, p. 348, 2005
- Nembach E., Particle Strengthening of Metals and Alloys, John Wiley & Sons, New York, 1997
- Neumann L., Kopp R., Aretz H., Crumbach M., Goerdeler M., Gottstein G., Mater. Sci. For., **495-497**, p. 1657, 2005
- Nibur K.A., Bahr D.F., Scripta Mater., **49**, p. 1055, 2003
- Nielsen S.F., Lauridsen E.M., Juul Jensen d., Poulsen H.F., Mater. Sci. Eng., **A319-321**, p. 179, 2001
- Noggle T.S., Koehler J.S., J. Appl. Phys., **29**, p. 53, 1957
- Nordif, Digital EBSD detectors, <http://www.Nordif.com>, 2005
- Orowan E., Z. Phys., **89**, p. 634, 1934
- Orowan E., Nature, **149**, p. 643, 1942
- Orowan E., discussion in: Symposium on Internal Stresses in Metals and Alloys, Institute of Metals, London, p. 451, 1948
- Pedersen K., Segle P., Hagsrtöm J., Furu T., Ekström H.E., Aluminium, **80**, p. 747, 2004
- Perocheau F., Driver J.H., Int. J. Plasticity, **18**, p. 185, 2002
- Peters M., Eschweiler J., Welpmann K., Scripta Metall., **20**, p. 259, 1986
- Pettersen T., Dr.Ing. Thesis, NTNU, 1999
- Pettersen T., Furu T., AA6063 Basic Characterisation, VIRFORM-report, Hydro Aluminium, Norway, 2001a
- Pettersen T., Furu T., AA6082 Basic Characterisation, VIRFORM-report, Hydro Aluminium, Norway, 2001b
- Petzow G., Metallographic Etching, American Society for Metals, Ohio, 1976
- Petzow G., Effenberg G., Ternary Alloys, A Comprehensive Compendium of Evaluated Constitutional Data and Phase Diagrams, 7, VCH Publishers, New York, 1993
- Polanyi M., Z. Phys., **89**, p. 660, 1934
- Polmear I.J., Proc. ICAA9, ed. Nie J.F., Morton A.J., Muddle B.C., Brisbane, Australia, p. 1, 2004
- Poole W.J., Wang X., Lloyd D.J., Embury J.D., Phil. Mag., **85**, p. 3113, 2005
- Poulsen H.F., Margulies L., Schmidt S., Winther G., Acta Mater., **51**, p. 3821, 2003
- Przystupa M.A., Vasudévan A.K., Rollet A.D., Mater. Sci. Eng., **A186**, p. 35, 1994

References

- Randle V., Engler O., Introduction to Texture Analysis: Macro texture, Microtexture and Orientation Mapping, Gordon and Breach, New York, 2000
- Reimer L., Scanning Electron Microscopy: Physics of Image Formation and Microanalysis, Springer, New York, 1998
- Roven H.J., Nes E., Metal Science, **18**, p. 515, 1984
- Ryen Ø., Dr.Ing. Thesis, NTNU, 2003
- Raabe D., Sachtleber M., Zhao Z., Roters F., Zaefferer S., Acta Metall. Mater., **49**, p. 3433, 2001
- Raabe D., Sachtleber M., Weiland W., Scheele G., Zhao Z., Acta Mater., **51**, p. 1539, 2003
- Sachs G., Z. Verein Deut. Ing., **72**, p.734, 1928
- Saito C., Furuya Y., Okazaki T., Matzusaki T., Watanabe T, Mater. Trans., **45**, p. 192, 2004
- Schmid E., Boas W., Kristallplastizität, Springer Verlag, Berlin, 1935
- Schwartz A.J., Kumar M., Adams B.L., Electron Backscatter Diffraction in Materials Science, Kluwer/Academic Press, New York, 2000
- Schwarzer R., Proc. DGM-DVM AK-Treffen "Mikrostrukturuntersuchungen im REM" 2007, Zürich, Switzerland, 2007
- Schwink C., Phys. Stat. Sol., **8**, p. 457, 1965
- Schwink C., VorbruggW., Z. Naturforsch., **22a**, p. 626, 1967
- Sehitoglu H., Foglesong T., Maier H.J., Matall. Mater. Trans., **36A**, p. 749, 2005
- Sjølstad K., Dr.Ing. Thesis, NTNU, 2003
- Skjervold S.R., Dr.Ing. Thesis, NTH, 1993
- Steinchen W., Yang L.X., Kupfer G., Maeckel P., Voessing F., J. Strain Analysis Eng. Design, **33**, p. 171, 1998
- Søreng A., Dr.Ing. thesis NTNU, 1997
- Tangen S., Dr.Ing. Thesis, NTNU, 2004
- Tangen S., Hjelen J., Furu T., Ryum N., Proc. SCANDEM 2001, Stockholm, Sweden, p. 90, 2001
- Tangen S., Hjelen J., Sjølstad K., Proc. SCANDEM 2002, ed. Keränen J., Sillanpää K., Tampere, Finland, p. 122, 2002
- Tangen S., Bjerkaas H., Hjelen J., Proc. SCANDEM 2003, ed. Jørgensen S., Gunnæs A.E., Oslo, Norway, p. 141, 2003
- Tatschl A., Kolednik O., Mater. Sci. Eng., **A342**, p. 152, 2003
- Taylor G.I., Proc. R. Soc. London A, **145**, p. 364, 1934
- Taylor G.I., J. Inst. Metals, **62**, p. 307, 1938

References

- Thomas T., *Acta Metall.*, **14**, p. 1363, 1966
- Tong W., Hector L.G., Weiland H., Wieserman L.F., *Scripta Mater.*, **36**, p. 1339, 1997
- Tseng A.A., *J. Micromech. Microeng.*, **14**, p. R15, 2004
- Tu M., Gielisse P.J., Xu W., *Exp. Mech.*, **37**, p. 188, 1997
- Turner T.J., Miller M.P., Barton N.R., *Mech. Mater.*, **34**, p. 605, 2002
- Vacher P., Dumoulin S., Morestin F., Mguil-Touchal S., *Proc. Instn. Mech. Engrs.*, **213 C**, p. 811, 1999
- Valberg H., Malvik T., *Int. J. Mater. Prod. Tech.*, **9**, p.428, 1994
- van der Winden M.R., Grün G.-U., Furu T., Asboell K., *Aluminium*, **78**, p. 816, 2002
- Van Houtte P., *Mater. Sci. Eng.*, **55**, p. 69, 1982
- Van Houtte P., Delannay L., Kalidindi S.R., *Int. J. Plasticity*, **18**, p. 359, 2002
- Van Houtte P., Li S., Seefeldt M., Delannay L., *Int. J. Plasticity*, **21**, p. 589, 2005
- Vatne H.E., Shahani R., Nes E., *Acta Mater.*, **44**, p. 4447, 1996a
- Vatne H.E., Furu T., Ørsund R., Nes E., *Acta Mater.*, **44**, p. 4463, 1996b
- Verhoeven J.D., *Fundamentals of Physical Metallurgy*, John Wiley & Sons, New York, 1975
- Voce E., *J. Inst. Metals*, **74**, p. 537, 1948
- Wagoner R.H., Chenot J.L., *Fundamentals of Metal Forming*, John Wiley & Sons, New York, 1996
- Wattrisse B., Chrysochoos A., Muracciole J.M., Némoz-Gaillard M., *Exp. Mech.*, **41**, p. 29, 2001
- Wells O.C., *Scanning*, **21**, p. 368, 1999
- Wenk H.R., Van Houtte P., *Rep. Prog. Phys.*, **67**, p. 1367, 2004
- Werenskiold J.C., *Dr.Ing. thesis NTNU*, 2004
- Wert J.A., *Acta Mater.*, **50**, p. 3125, 2002
- Wert J.A., Huang X., *Phil. Mag.*, **83**, p. 969, 2003
- Wert J.A., Liu Q., Hansen N., *Acta Mater.*, **45**, p. 2565, 1997
- Wilkinson D.S., Maire E., Embury J.D., *Mater. Sci. Eng.*, **A233**, p. 145, 1997
- Wilm A., *Metallurgi*, **8**, p. 225, 1911
- Winther G., *Proc. 25th Risø International Symposium on Materials Science*, ed. Gundlach C., Haldrup K., Hansen N., Huang X., Juul Jensen D., Leffers T., Li Z.J., Nielsen S.F., Pantleon W., Wert J.A., Winther G., Denmark, p. 211, 2004
- Winther G., *Mater. Sci. Forum*, **495-497**, p. 1013, 2005
- Winther G., Juul Jensen D., Hansen N., *Acta Mater.*, **45**, p. 2455, 1997

References

- Winther G., Margulies L., Schmidt S., Poulsen H.F., *Acta Mater.*, **52**, p. 2863, 2004
- Wittridge N.J., Knutsen R.D., *Mater. Sci. Eng.*, **A269**, p. 205, 1999
- Wu P.D., MacEwen S.R., Lloyd D.J., Neale K.W., *Mater. Sci. Eng.*, **A364**, p. 182, 2004
- Yao Z., Wagoner R.H., *Acta Metall. Mater.*, **41**, p. 451, 1993
- Zaefferer S., Konrad J., Raabe D., *Proc. Microscopy Conference 2005*, p. 63, Davos, Switzerland, 2005
- Zankl G., *Z. Naturforsch.*, **18a**, p.795, 1963
- Zeng X.H., PhD Thesis, Linköping University, Sweden, 1995
- Zeng X.H., Barlat F., *Metall. Trans.*, **25A**, p. 2783, 1994
- Zeng X.H., Ahmad M., Engler O., *Mater. Sci. Tech.*, **10**, p. 581, 1994
- Zhang N., Tong W., *Int. J. Plasticity*, **20**, p. 523, 2004
- Zhang J., Jin G.C., Meng L.B., Jian L.H., Wang A.Y., Lu S.B., *Proc. SPIE*, **4961**, p.191, 2003
- Aluminium Association of the United States, <http://www.aluminum.org/>, 1970

Appendix A – Heating unit

The main purpose of the heating unit is to allow simple tension experiments at elevated temperatures. It was developed at the CNRS – PMTM laboratory at University Paris 13, France and is simply a small furnace that is clamped underneath the in-situ specimen (Figure A.1). The heat generated by the furnace is directly transferred to the specimen. However, the heating unit has been modified such that the same unit can be used to perform dedicated heating experiments (Figure A.2). The furnace is designed for heating up to 600°C but the actual limit could be lower due to limitations from the surrounding. Over heating the system can destroy some of the fragile components in a SEM. However, this problem can be overcome by attaching a cooling unit to the substage. Such a cooling unit has been developed for the Hitachi S4300-SE (Figure A.3).



Figure A.1 – Small furnace clamped to the specimen. The specimen can easily be mounted in the deformation stage.

Appendix A – Heating unit

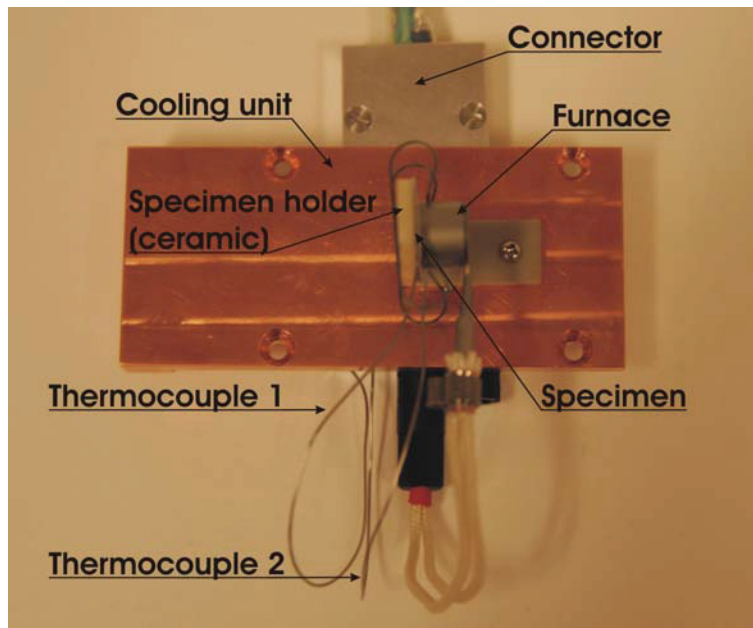


Figure A.2 – Furnace mounted to a dedicated substage for heating experiments. The cooling unit is coupled to a cold finger by a ductile copper cable (see. Figure A.3).

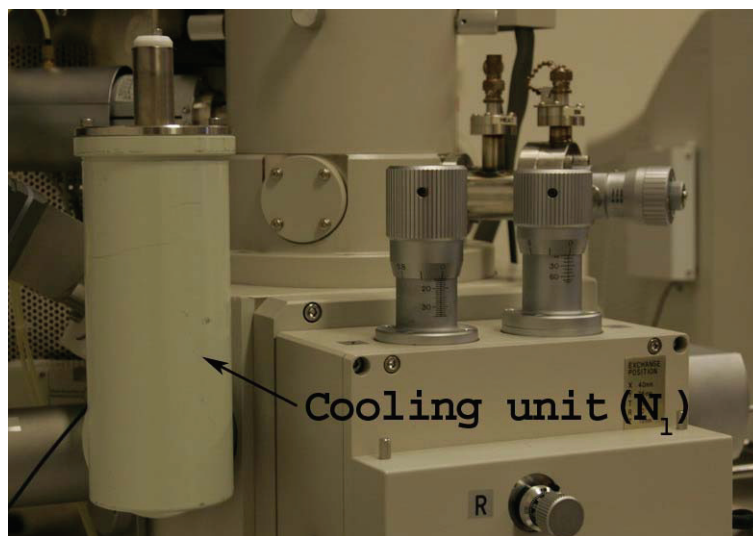


Figure A.3 – Cooling unit mounted to the chamber of Hitachi S4300-SE. The cold finger transfer the heat generated in the microscope to the cooling medium (liquid nitrogen (N₁)) through a ductile copper cable.

Appendix B – Calculated ODFs

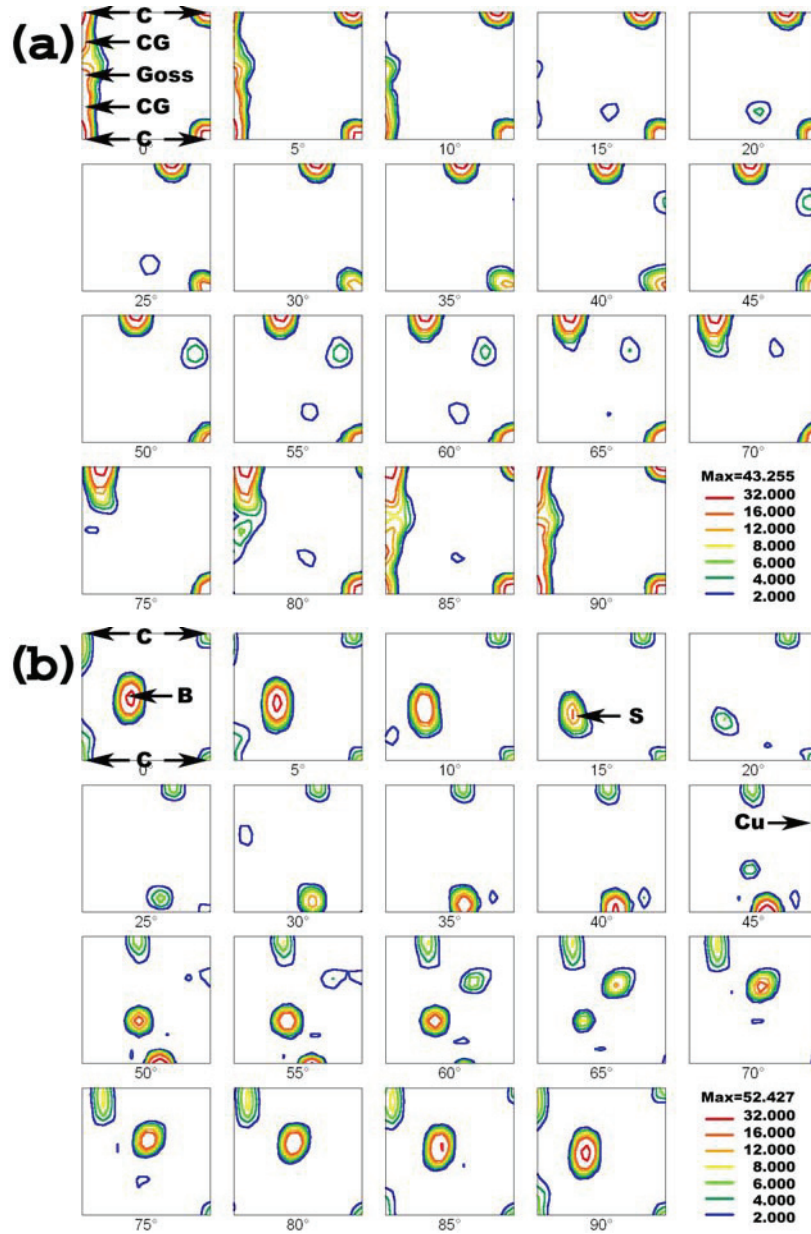
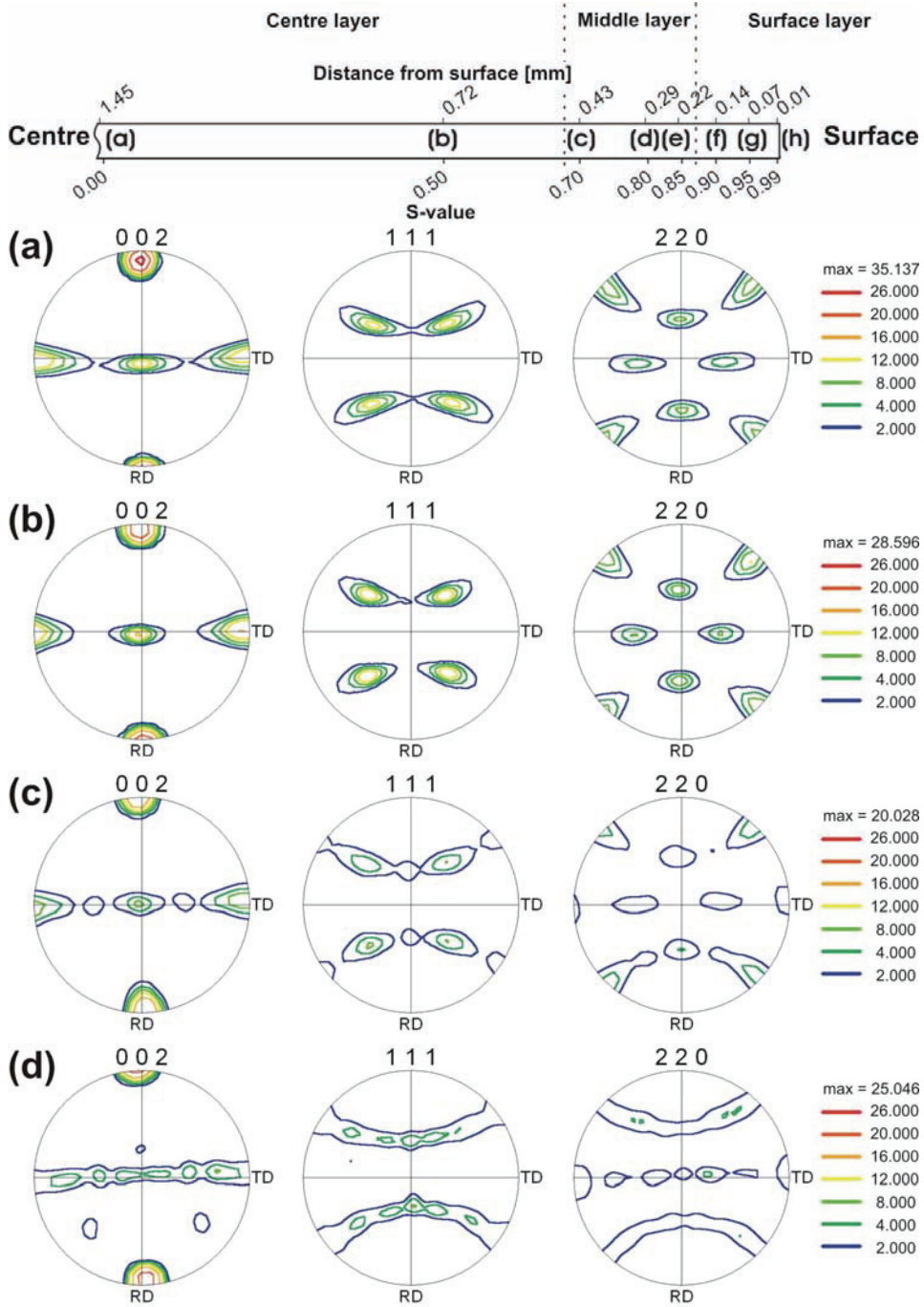


Figure A.4 – Measured ODF representing the initial global texture. Positions of important texture components are given by their notation letters. (a) AA6063 (b) AA6082

Appendix C – Through-thickness variations



Appendix C – Through-thickness variations

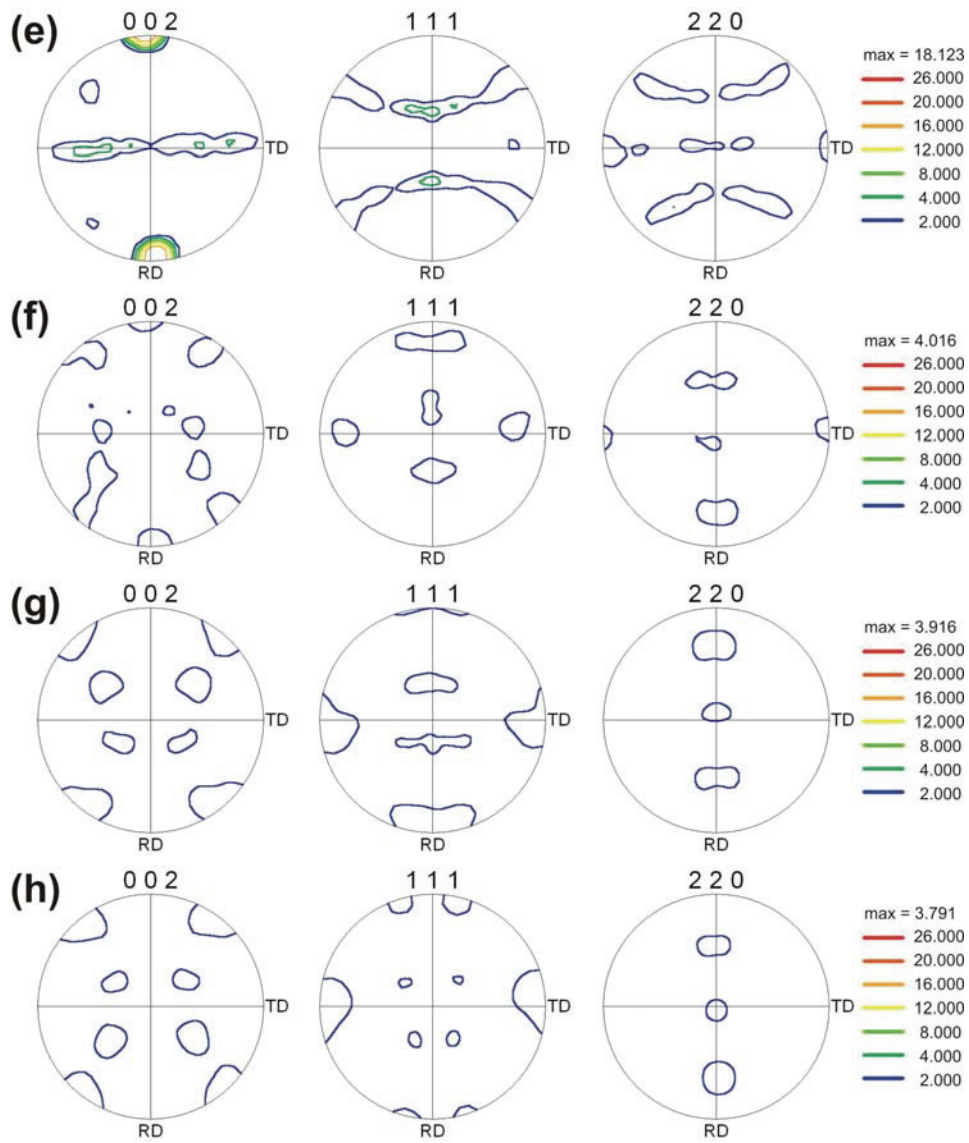
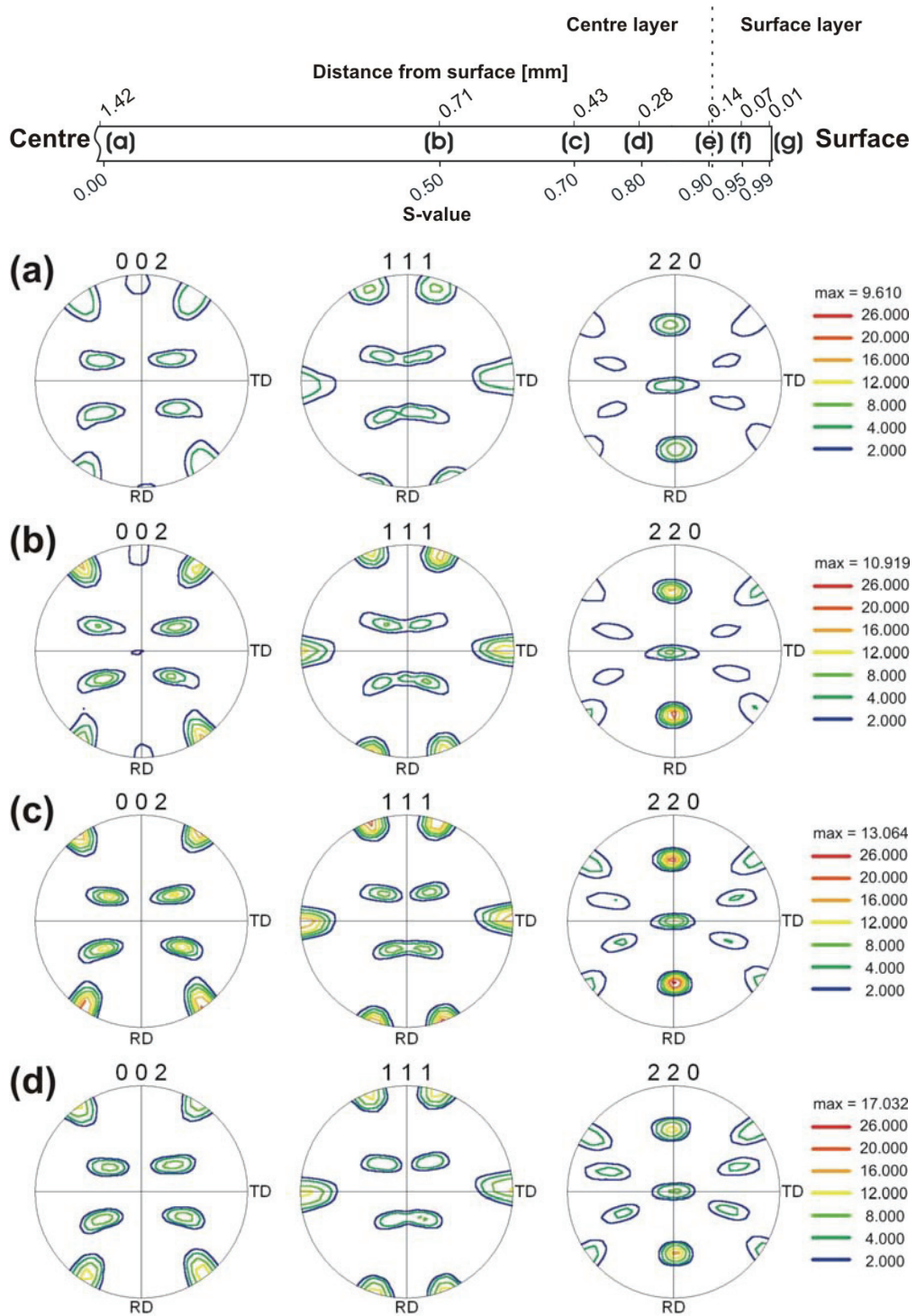


Figure A.5 – Calculated pole figures based on orientation data at different positions through the profile thickness of AA6063.

Appendix C – Through-thickness variations



Appendix C – Through-thickness variations

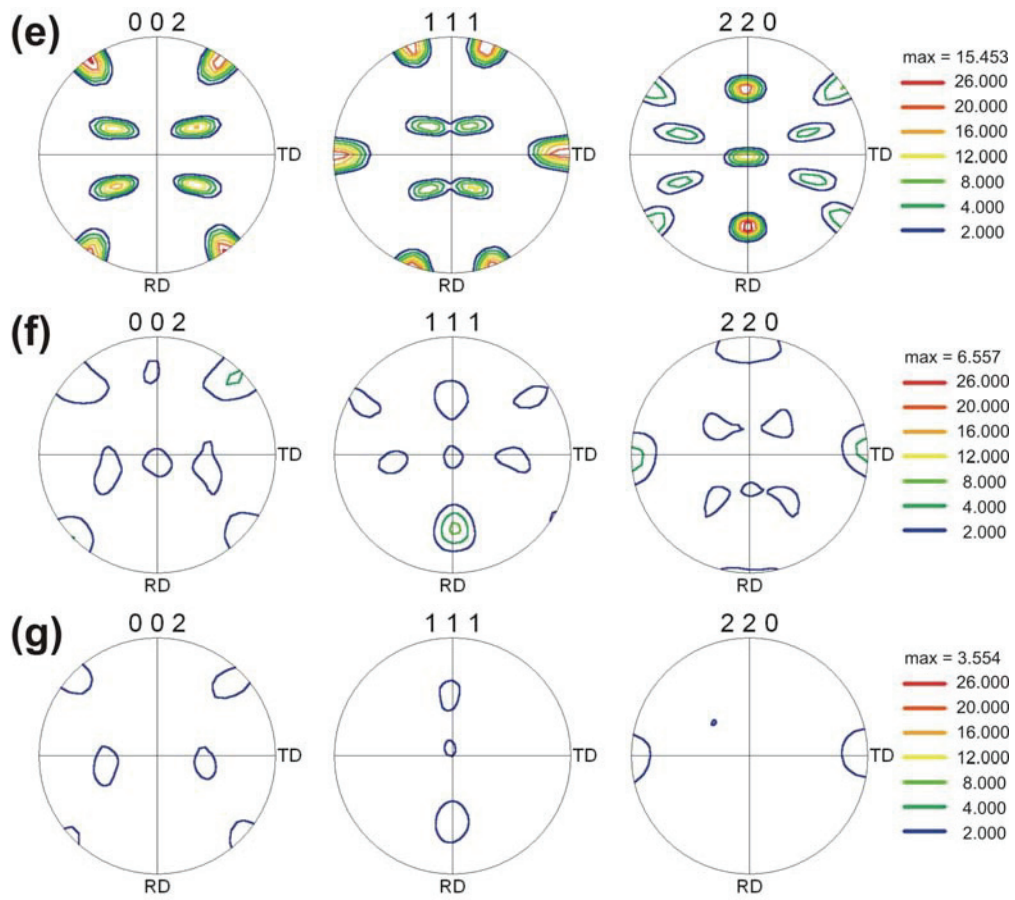
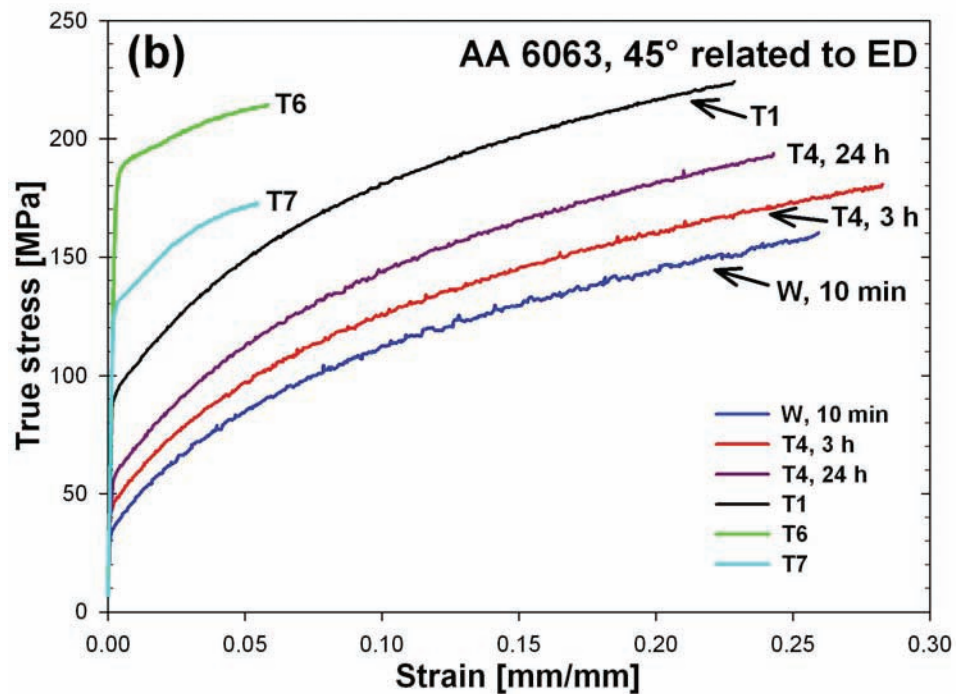
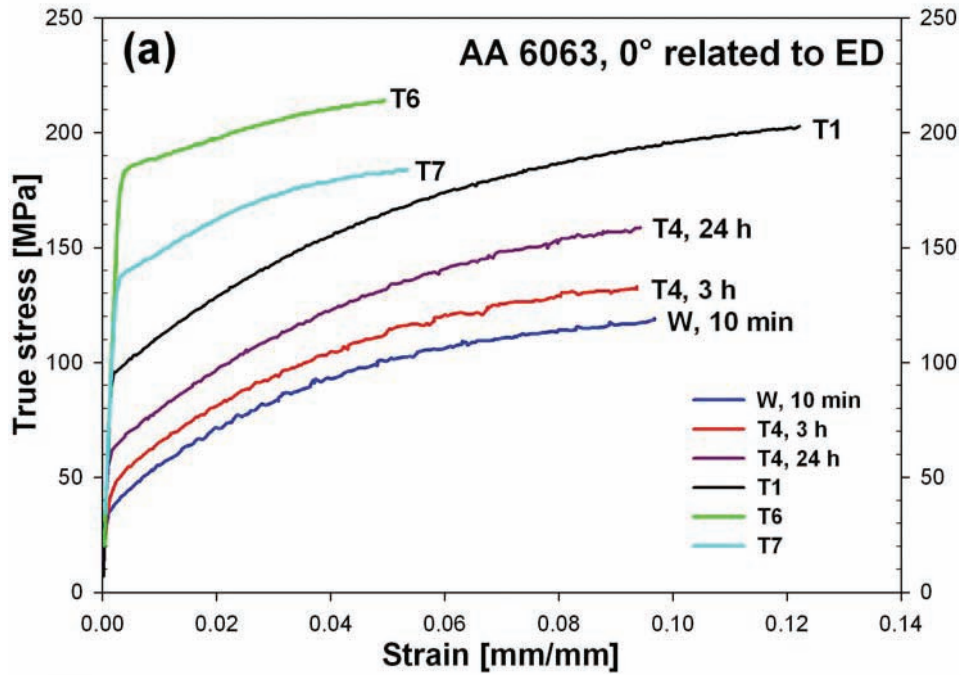


Figure A.6 – Calculated pole figures based on orientation data at different positions through the profile thickness of AA6082.

Appendix D – Effect of age-hardening



Appendix D – Effect of age-hardening

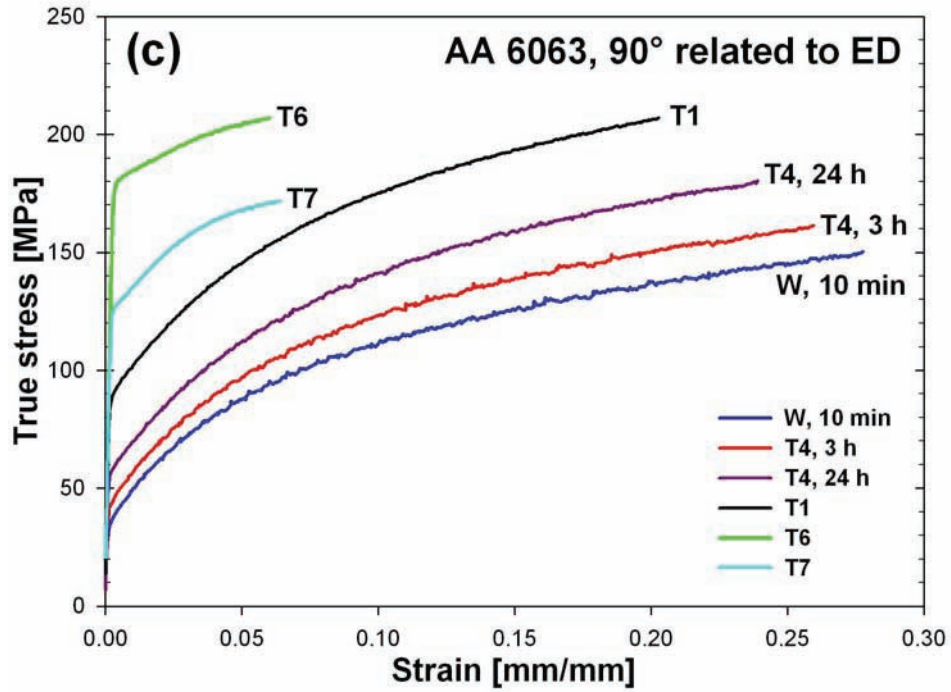
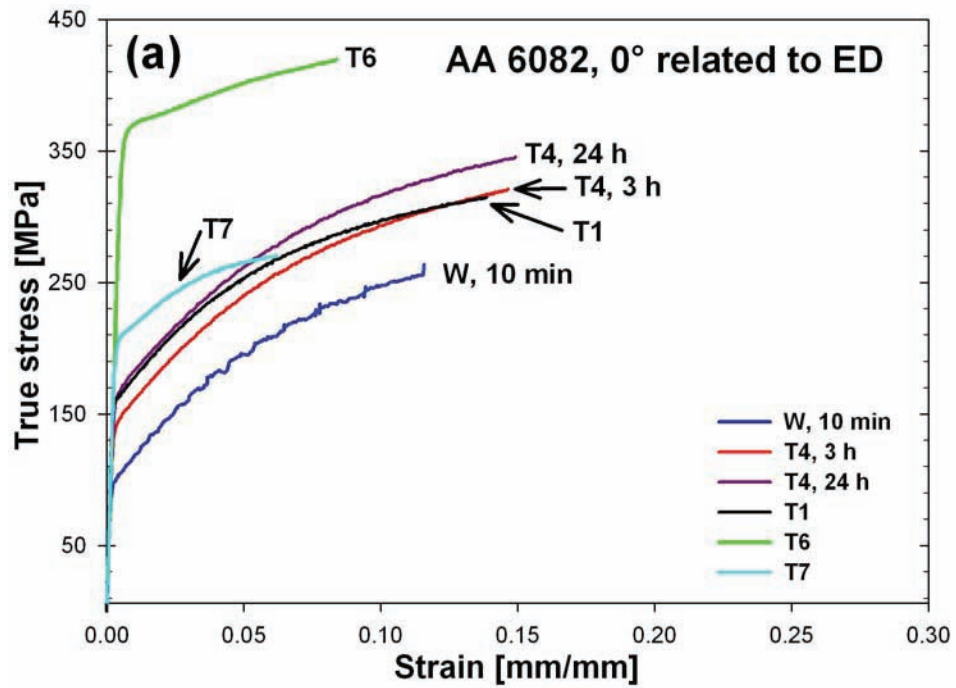


Figure A.7 – True stress-strain curves at different material conditions for AA6063. (a) 0° (b) 45° (c) 90° related to ED.



Appendix D – Effect of age-hardening

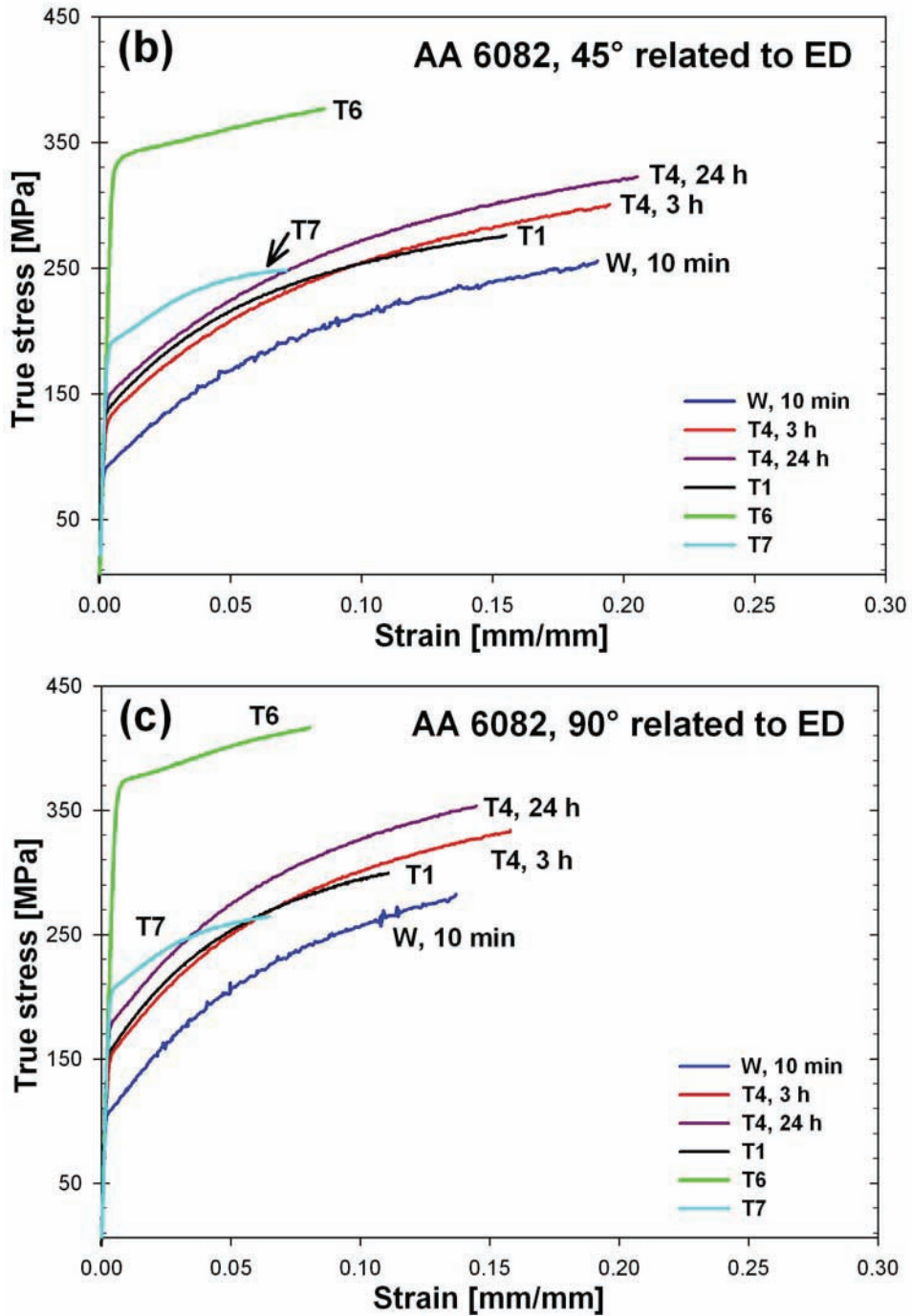
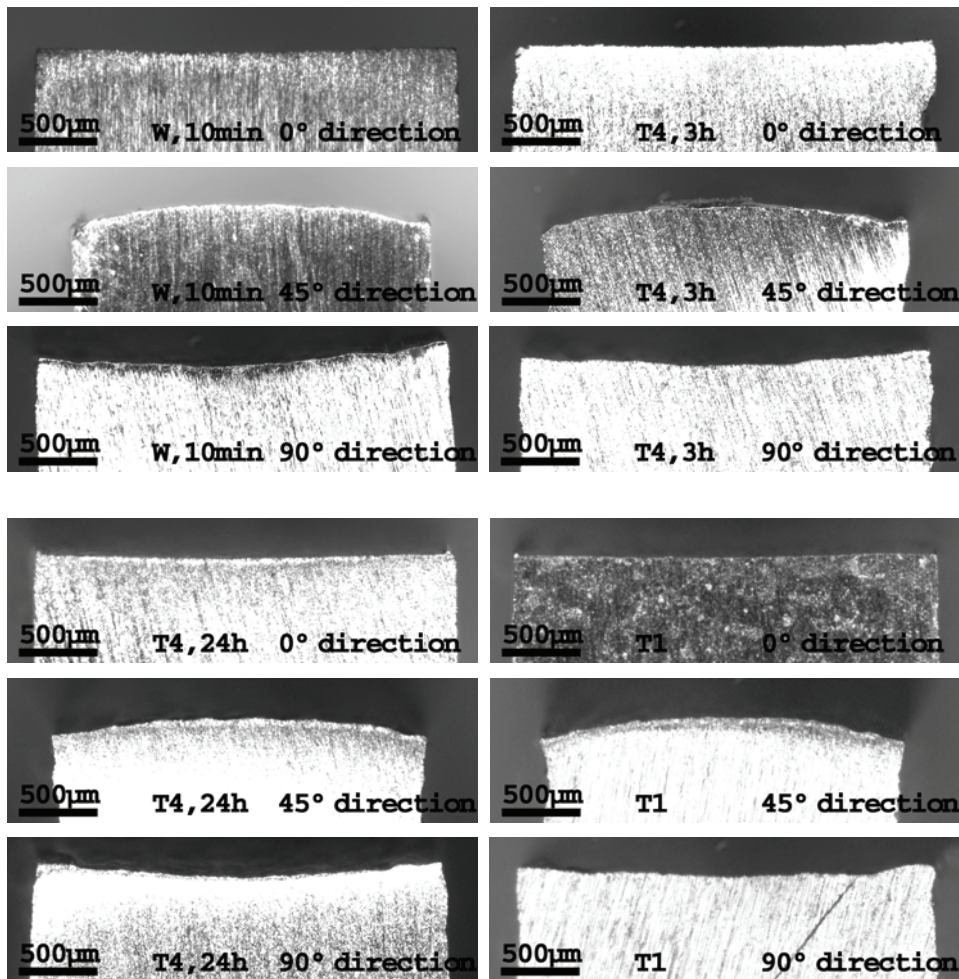
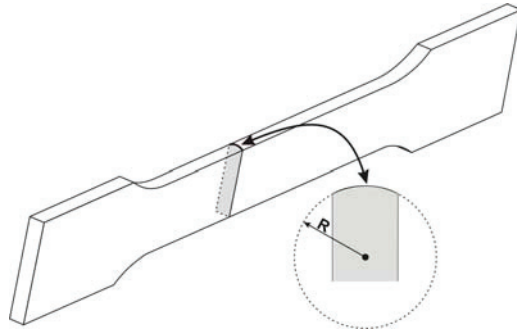


Figure A.8 – True stress-strain curves at different material conditions for AA6082. (a) 0° (b) 45° (c) 90° related to ED.

Appendix E – Through-specimen-thickness-curvatures



Appendix E – Through-specimen-thickness-curvatures

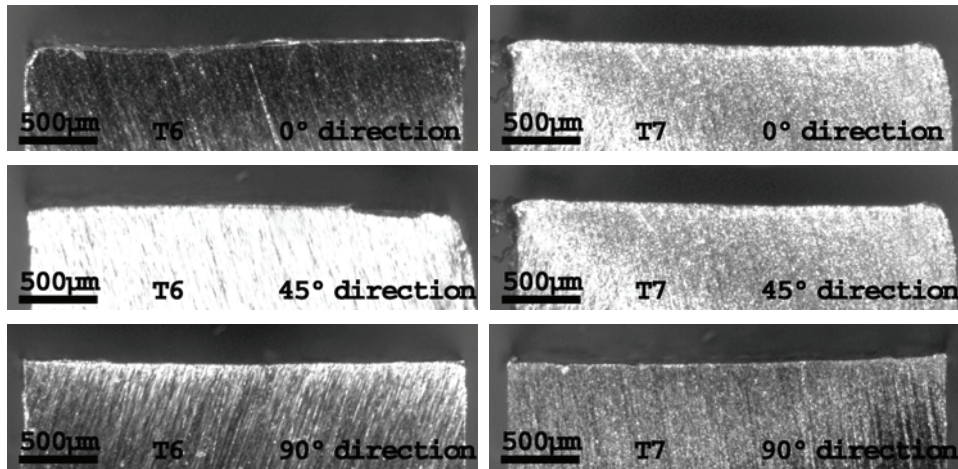


Figure A.9 – Micrographs of the through-specimen-thickness-curvature in AA6063 after simple tension to the uniform strain 0°, 45° and 90° related to ED. All temper conditions investigated are presented.

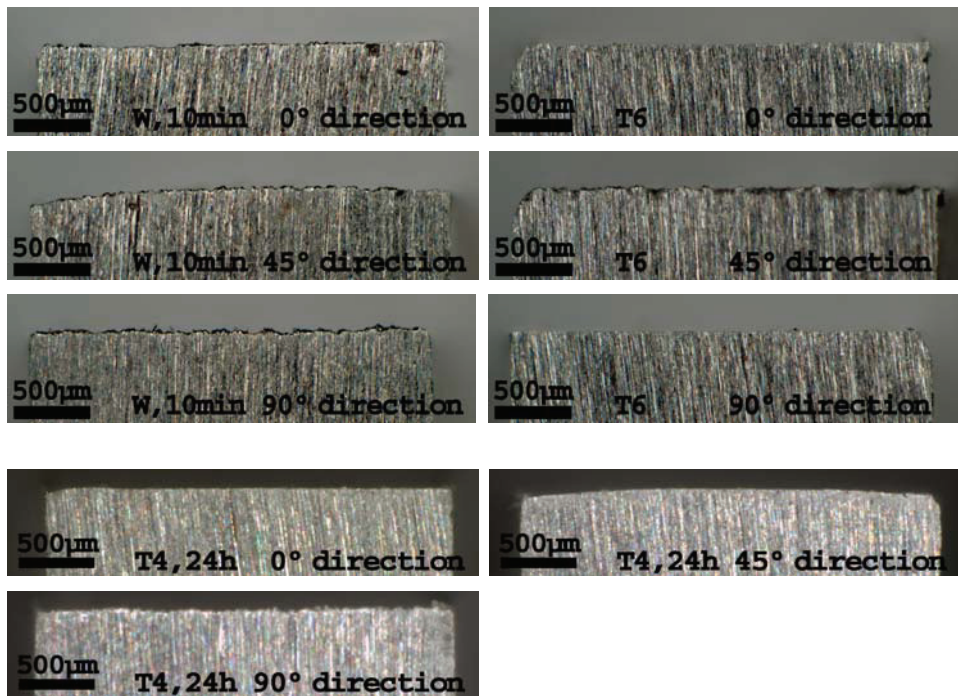


Figure A.10 – Micrographs of the through-specimen-thickness-curvature in AA6082 after simple tension to the uniform strain 0°, 45° and 90° related to ED. Material conditions W, 10min, T4, 24h and T6 are presented.

Appendix E – Through-specimen-thickness-curvatures

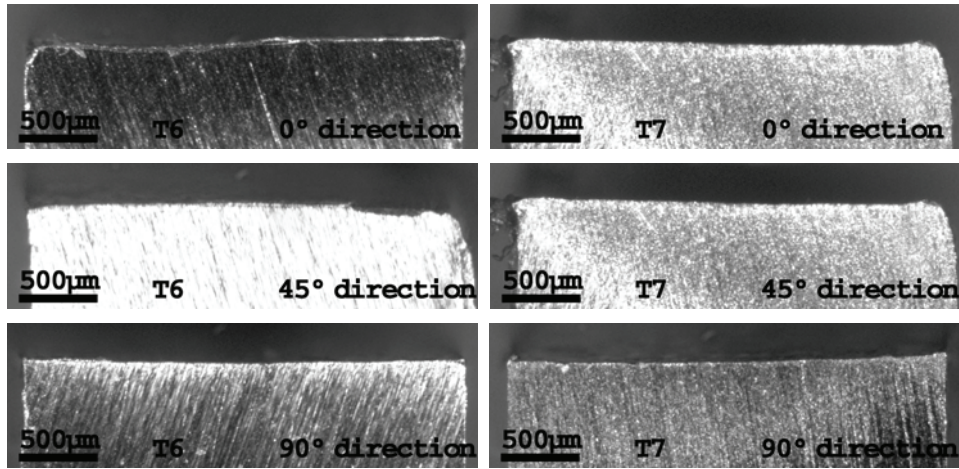


Figure A.9 – Micrographs of the through-specimen-thickness-curvature in AA6063 after simple tension to the uniform strain 0°, 45° and 90° related to ED. All temper conditions investigated are presented.

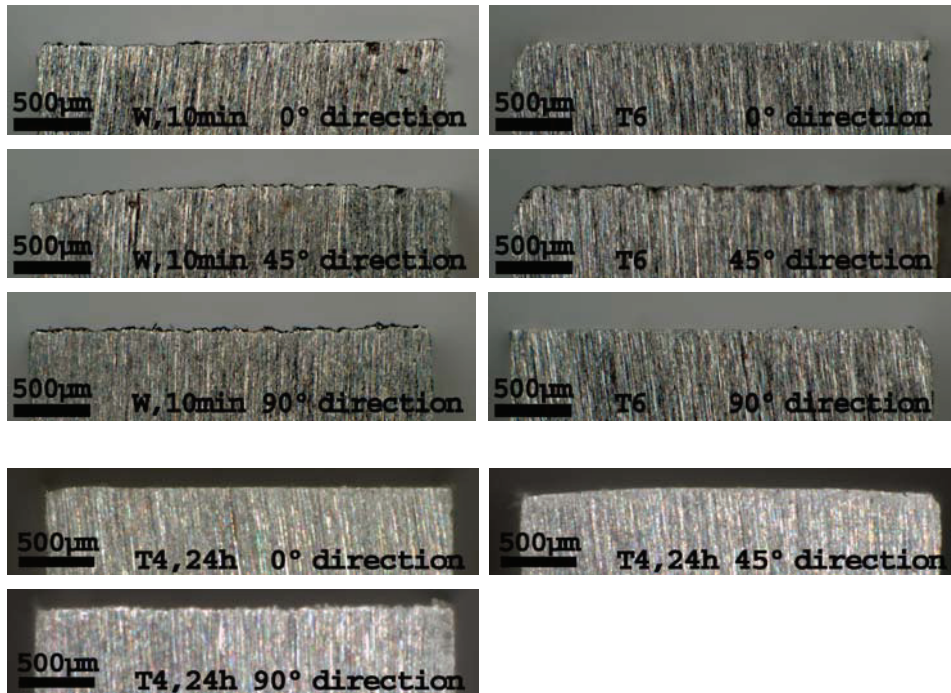
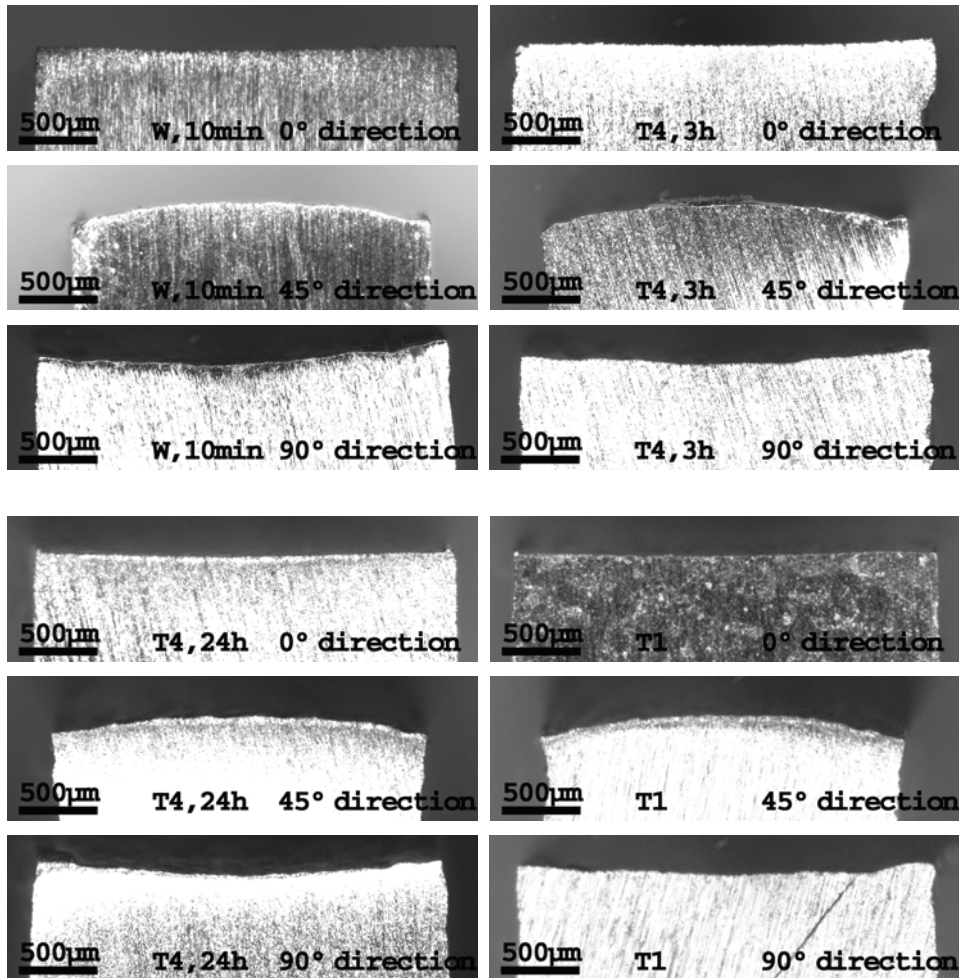
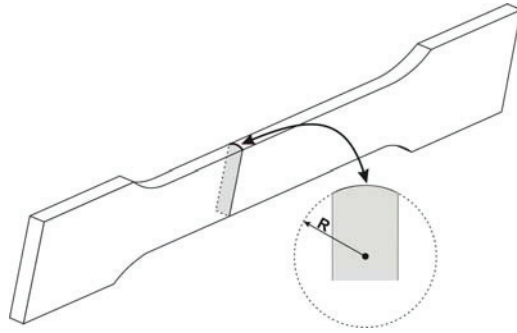


Figure A.10 – Micrographs of the through-specimen-thickness-curvature in AA6082 after simple tension to the uniform strain 0°, 45° and 90° related to ED. Material conditions W, 10min, T4, 24h and T6 are presented.

Appendix E – Through-specimen-thickness-curvatures



Appendix D – Effect of age-hardening

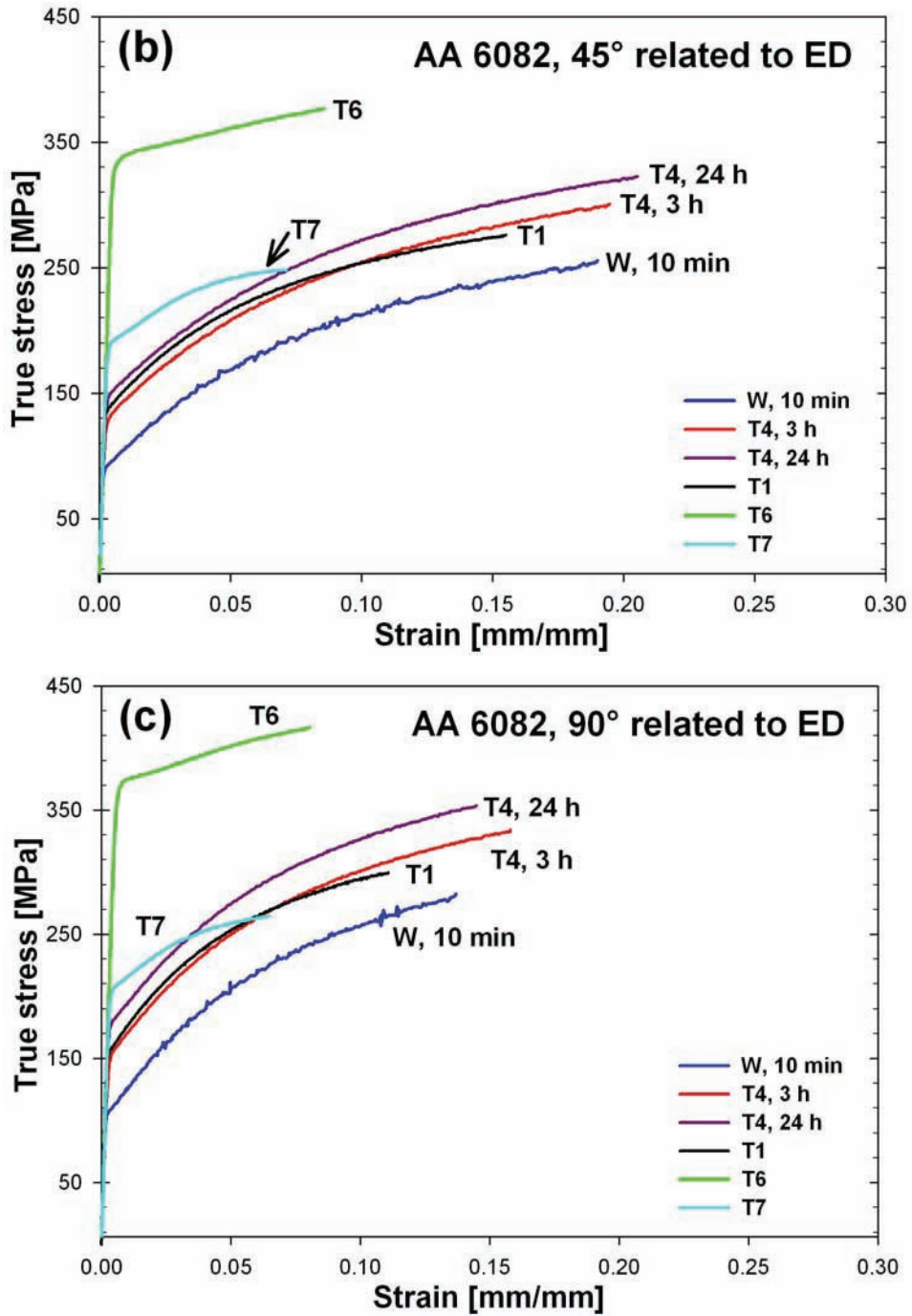


Figure A.8 – True stress-strain curves at different material conditions for AA6082. (a) 0° (b) 45° (c) 90° related to ED.

Appendix D – Effect of age-hardening

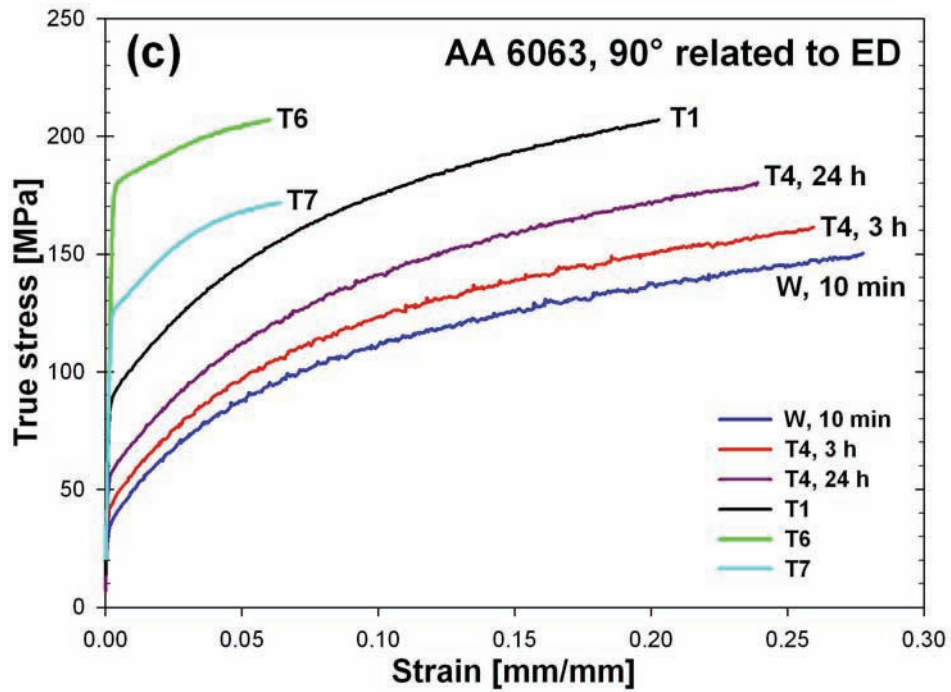
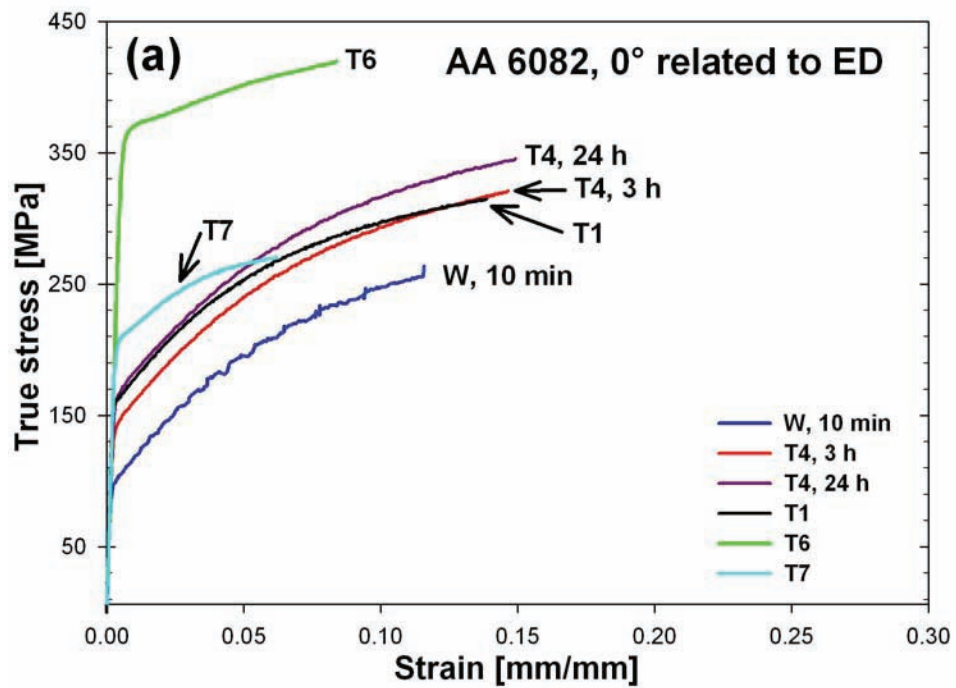
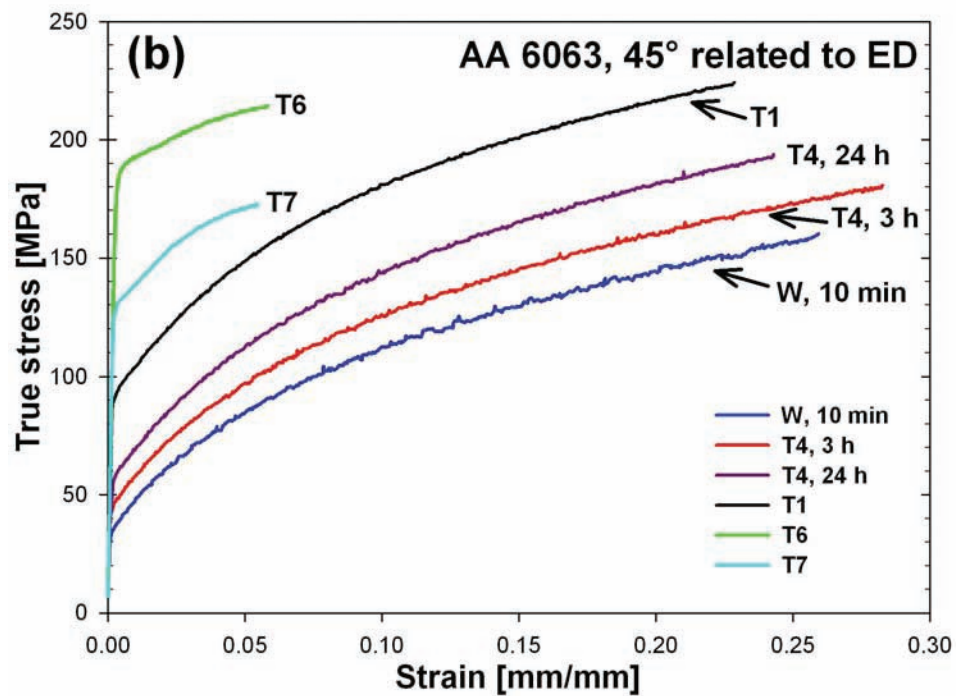
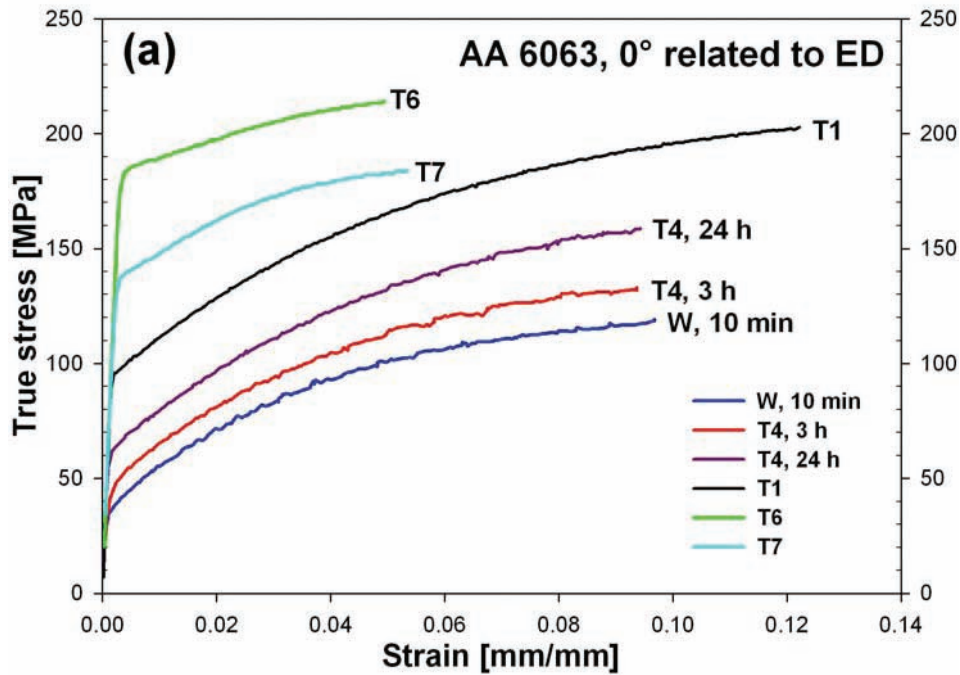


Figure A.7 – True stress-strain curves at different material conditions for AA6063. (a) 0° (b) 45° (c) 90° related to ED.



Appendix D – Effect of age-hardening



Appendix C – Through-thickness variations

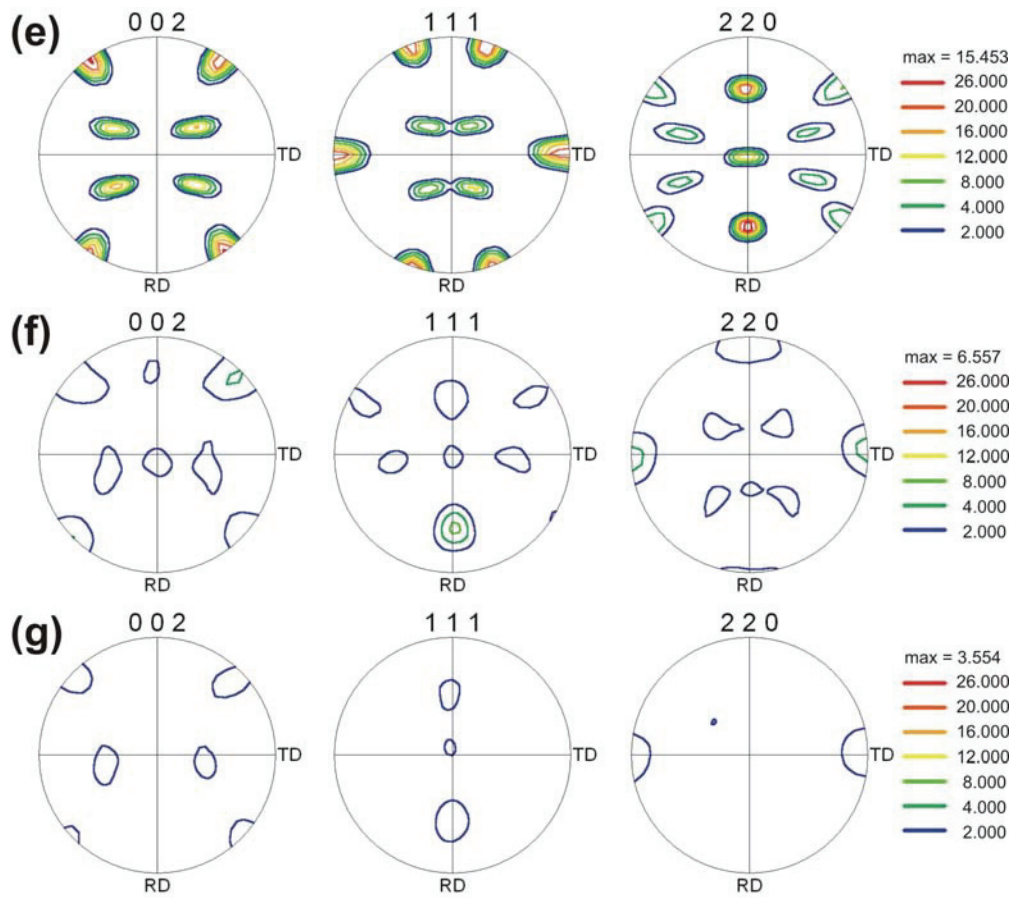
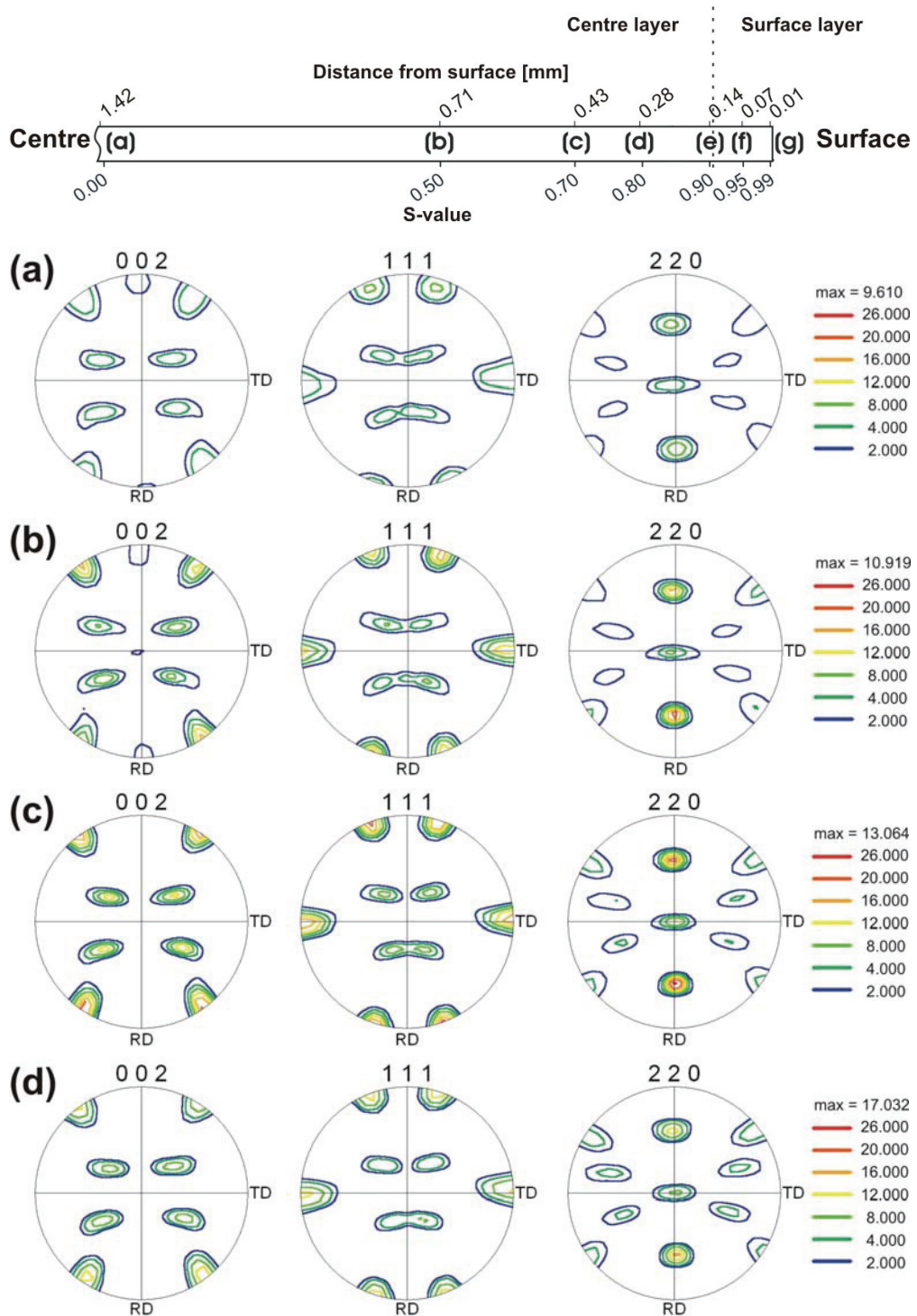


Figure A.6 – Calculated pole figures based on orientation data at different positions through the profile thickness of AA6082.

Appendix C – Through-thickness variations



Appendix C – Through-thickness variations

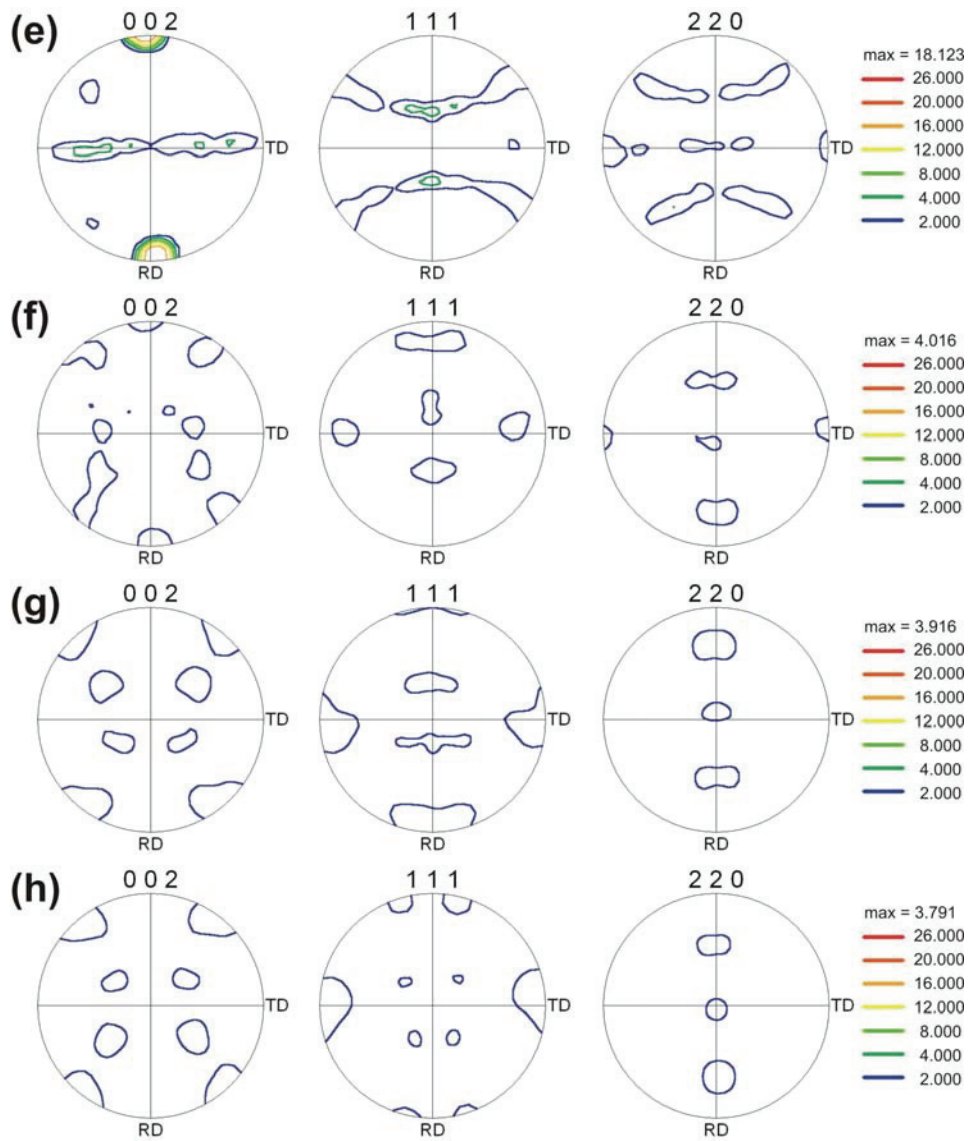
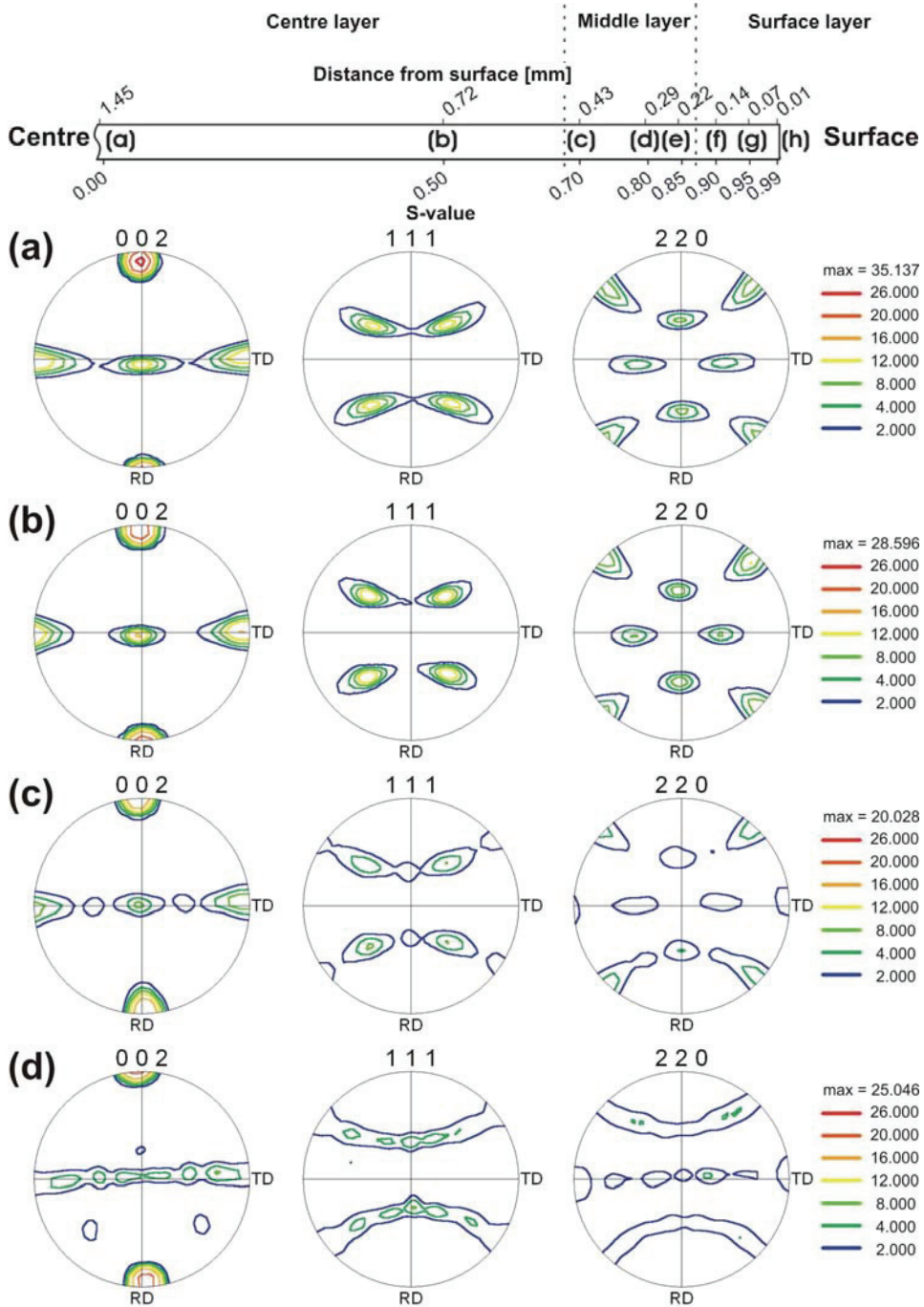


Figure A.5 – Calculated pole figures based on orientation data at different positions through the profile thickness of AA6063.

Appendix C – Through-thickness variations



Appendix B – Calculated ODFs

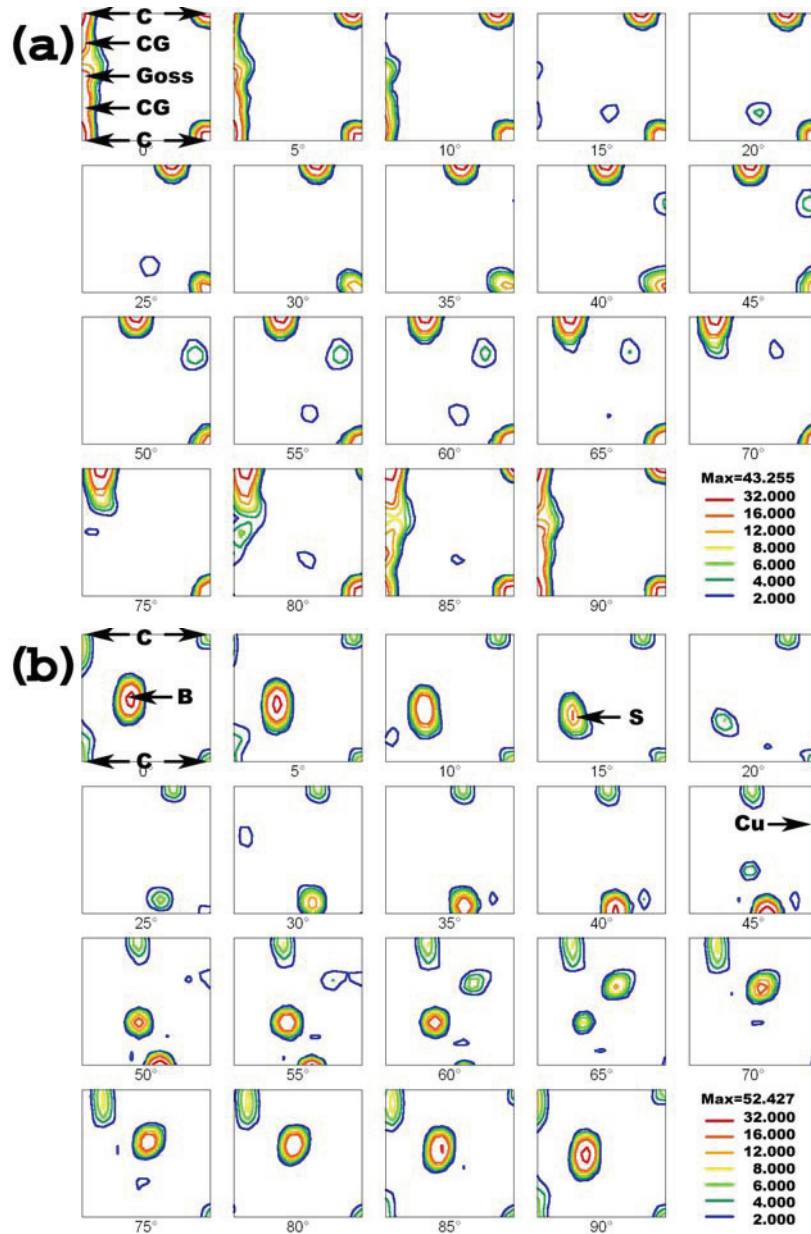


Figure A.4 – Measured ODF representing the initial global texture. Positions of important texture components are given by their notation letters. (a) AA6063 (b) AA6082

Appendix A – Heating unit

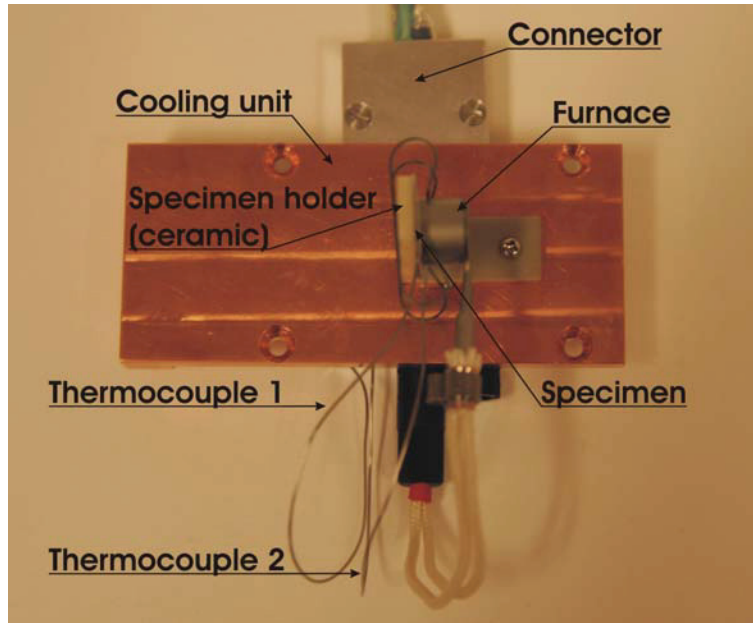


Figure A.2 – Furnace mounted to a dedicated substage for heating experiments. The cooling unit is coupled to a cold finger by a ductile copper cable (see. Figure A.3).

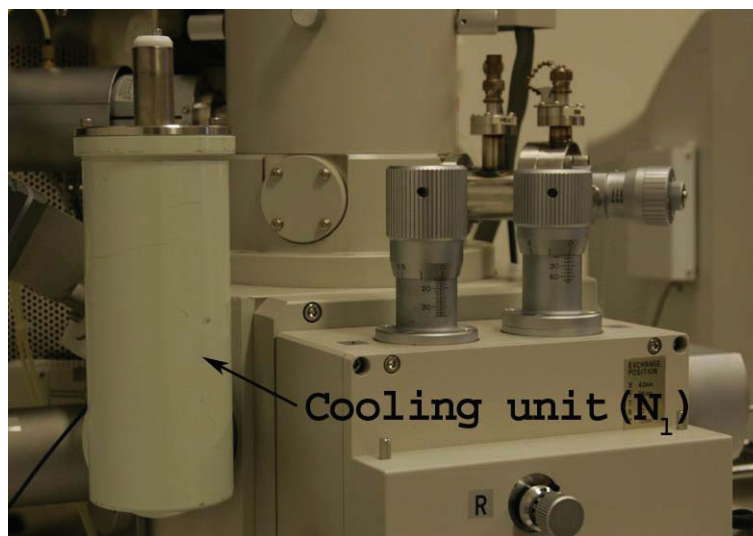


Figure A.3 – Cooling unit mounted to the chamber of Hitachi S4300-SE. The cold finger transfer the heat generated in the microscope to the cooling medium (liquid nitrogen (N_l)) through a ductile copper cable.

Appendix A – Heating unit

The main purpose of the heating unit is to allow simple tension experiments at elevated temperatures. It was developed at the CNRS – PMTM laboratory at University Paris 13, France and is simply a small furnace that is clamped underneath the in-situ specimen (Figure A.1). The heat generated by the furnace is directly transferred to the specimen. However, the heating unit has been modified such that the same unit can be used to perform dedicated heating experiments (Figure A.2). The furnace is designed for heating up to 600°C but the actual limit could be lower due to limitations from the surrounding. Over heating the system can destroy some of the fragile components in a SEM. However, this problem can be overcome by attaching a cooling unit to the substage. Such a cooling unit has been developed for the Hitachi S4300-SE (Figure A.3).



Figure A.1 – Small furnace clamped to the specimen. The specimen can easily be mounted in the deformation stage.

References

- Winther G., Margulies L., Schmidt S., Poulsen H.F., *Acta Mater.*, **52**, p. 2863, 2004
- Wittridge N.J., Knutsen R.D., *Mater. Sci. Eng.*, **A269**, p. 205, 1999
- Wu P.D., MacEwen S.R., Lloyd D.J., Neale K.W., *Mater. Sci. Eng.*, **A364**, p. 182, 2004
- Yao Z., Wagoner R.H., *Acta Metall. Mater.*, **41**, p. 451, 1993
- Zaefferer S., Konrad J., Raabe D., *Proc. Microscopy Conference 2005*, p. 63, Davos, Switzerland, 2005
- Zankl G., *Z. Naturforsch.*, **18a**, p.795, 1963
- Zeng X.H., PhD Thesis, Linköping University, Sweden, 1995
- Zeng X.H., Barlat F., *Metall. Trans.*, **25A**, p. 2783, 1994
- Zeng X.H., Ahmad M., Engler O., *Mater. Sci. Tech.*, **10**, p. 581, 1994
- Zhang N., Tong W., *Int. J. Plasticity*, **20**, p. 523, 2004
- Zhang J., Jin G.C., Meng L.B., Jian L.H., Wang A.Y., Lu S.B., *Proc. SPIE*, **4961**, p.191, 2003
- Aluminium Association of the United States, <http://www.aluminum.org/>, 1970

References

- Thomas T., *Acta Metall.*, **14**, p. 1363, 1966
- Tong W., Hector L.G., Weiland H., Wieserman L.F., *Scripta Mater.*, **36**, p. 1339, 1997
- Tseng A.A., *J. Micromech. Microeng.*, **14**, p. R15, 2004
- Tu M., Gielisse P.J., Xu W., *Exp. Mech.*, **37**, p. 188, 1997
- Turner T.J., Miller M.P., Barton N.R., *Mech. Mater.*, **34**, p. 605, 2002
- Vacher P., Dumoulin S., Morestin F., Mguil-Touchal S., *Proc. Instn. Mech. Engrs.*, **213 C**, p. 811, 1999
- Valberg H., Malvik T., *Int. J. Mater. Prod. Tech.*, **9**, p.428, 1994
- van der Winden M.R., Grün G.-U., Furu T., Asboell K., *Aluminium*, **78**, p. 816, 2002
- Van Houtte P., *Mater. Sci. Eng.*, **55**, p. 69, 1982
- Van Houtte P., Delannay L., Kalidindi S.R., *Int. J. Plasticity*, **18**, p. 359, 2002
- Van Houtte P., Li S., Seefeldt M., Delannay L., *Int. J. Plasticity*, **21**, p. 589, 2005
- Vatne H.E., Shahani R., Nes E., *Acta Mater.*, **44**, p. 4447, 1996a
- Vatne H.E., Furu T., Ørsund R., Nes E., *Acta Mater.*, **44**, p. 4463, 1996b
- Verhoeven J.D., *Fundamentals of Physical Metallurgy*, John Wiley & Sons, New York, 1975
- Voce E., *J. Inst. Metals*, **74**, p. 537, 1948
- Wagoner R.H., Chenot J.L., *Fundamentals of Metal Forming*, John Wiley & Sons, New York, 1996
- Wattrisse B., Chrysochoos A., Muracciole J.M., Némoz-Gaillard M., *Exp. Mech.*, **41**, p. 29, 2001
- Wells O.C., *Scanning*, **21**, p. 368, 1999
- Wenk H.R., Van Houtte P., *Rep. Prog. Phys.*, **67**, p. 1367, 2004
- Werenskiold J.C., *Dr.Ing. thesis NTNU*, 2004
- Wert J.A., *Acta Mater.*, **50**, p. 3125, 2002
- Wert J.A., Huang X., *Phil. Mag.*, **83**, p. 969, 2003
- Wert J.A., Liu Q., Hansen N., *Acta Mater.*, **45**, p. 2565, 1997
- Wilkinson D.S., Maire E., Embury J.D., *Mater. Sci. Eng.*, **A233**, p. 145, 1997
- Wilm A., *Metallurgi*, **8**, p. 225, 1911
- Winther G., *Proc. 25th Risø International Symposium on Materials Science*, ed. Gundlach C., Haldrup K., Hansen N., Huang X., Juul Jensen D., Leffers T., Li Z.J., Nielsen S.F., Pantleon W., Wert J.A., Winther G., Denmark, p. 211, 2004
- Winther G., *Mater. Sci. Forum*, **495-497**, p. 1013, 2005
- Winther G., Juul Jensen D., Hansen N., *Acta Mater.*, **45**, p. 2455, 1997

References

- Randle V., Engler O., Introduction to Texture Analysis: Macro texture, Microtexture and Orientation Mapping, Gordon and Breach, New York, 2000
- Reimer L., Scanning Electron Microscopy: Physics of Image Formation and Microanalysis, Springer, New York, 1998
- Roven H.J., Nes E., Metal Science, **18**, p. 515, 1984
- Ryen Ø., Dr.Ing. Thesis, NTNU, 2003
- Raabe D., Sachtleber M., Zhao Z., Roters F., Zaefferer S., Acta Metall. Mater., **49**, p. 3433, 2001
- Raabe D., Sachtleber M., Weiland W., Scheele G., Zhao Z., Acta Mater., **51**, p. 1539, 2003
- Sachs G., Z. Verein Deut. Ing., **72**, p.734, 1928
- Saito C., Furuya Y., Okazaki T., Matsumaki T., Watanabe T, Mater. Trans., **45**, p. 192, 2004
- Schmid E., Boas W., Kristallplastizität, Springer Verlag, Berlin, 1935
- Schwartz A.J., Kumar M., Adams B.L., Electron Backscatter Diffraction in Materials Science, Kluwer/Academic Press, New York, 2000
- Schwarzer R., Proc. DGM-DVM AK-Treffen "Mikrostrukturuntersuchungen im REM" 2007, Zürich, Switzerland, 2007
- Schwink C., Phys. Stat. Sol., **8**, p. 457, 1965
- Schwink C., VorbruggW., Z. Naturforsch., **22a**, p. 626, 1967
- Sehitoglu H., Foglesong T., Maier H.J., Matall. Mater. Trans., **36A**, p. 749, 2005
- Sjølstad K., Dr.Ing. Thesis, NTNU, 2003
- Skjervold S.R., Dr.Ing. Thesis, NTH, 1993
- Steinchen W., Yang L.X., Kupfer G., Maeckel P., Voessing F., J. Strain Analysis Eng. Design, **33**, p. 171, 1998
- Søreng A., Dr.Ing. thesis NTNU, 1997
- Tangen S., Dr.Ing. Thesis, NTNU, 2004
- Tangen S., Hjelen J., Furu T., Ryum N., Proc. SCANDEM 2001, Stockholm, Sweden, p. 90, 2001
- Tangen S., Hjelen J., Sjølstad K., Proc. SCANDEM 2002, ed. Keränen J., Sillanpää K., Tampere, Finland, p. 122, 2002
- Tangen S., Bjerkaas H., Hjelen J., Proc. SCANDEM 2003, ed. Jørgensen S., Gunnæs A.E., Oslo, Norway, p. 141, 2003
- Tatschl A., Kolednik O., Mater. Sci. Eng., **A342**, p. 152, 2003
- Taylor G.I., Proc. R. Soc. London A, **145**, p. 364, 1934
- Taylor G.I., J. Inst. Metals, **62**, p. 307, 1938

References

- Mguil-Touchal S., Morestin F., Brunet M., Proc. Eighth International Conference on Computational Methods and Experimental Measurements, ed. Brebbia C.A., Anagnostopoulos P., Carlomagno G.M., Rhodes, Greece, p. 45, 1997
- Mika D.P., Dawson P.R., Acta Mater., **47**, p. 1355, 1999
- Moen K., Malvik T., Hjelen J., Leinum J.R., Alnæs L., Proc. Applied Mineralogy 2004
- Mulders J.J.L., Day A.P., Mater. Sci. For., **495-497**, p. 348, 2005
- Nembach E., Particle Strengthening of Metals and Alloys, John Wiley & Sons, New York, 1997
- Neumann L., Kopp R., Aretz H., Crumbach M., Goerdeler M., Gottstein G., Mater. Sci. For., **495-497**, p. 1657, 2005
- Nibur K.A., Bahr D.F., Scripta Mater., **49**, p. 1055, 2003
- Nielsen S.F., Lauridsen E.M., Juul Jensen d., Poulsen H.F., Mater. Sci. Eng., **A319-321**, p. 179, 2001
- Noggle T.S., Koehler J.S., J. Appl. Phys., **29**, p. 53, 1957
- Nordif, Digital EBSD detectors, <http://www.Nordif.com>, 2005
- Orowan E., Z. Phys., **89**, p. 634, 1934
- Orowan E., Nature, **149**, p. 643, 1942
- Orowan E., discussion in: Symposium on Internal Stresses in Metals and Alloys, Institute of Metals, London, p. 451, 1948
- Pedersen K., Segle P., Hagsrtöm J., Furu T., Ekström H.E., Aluminium, **80**, p. 747, 2004
- Perocheau F., Driver J.H., Int. J. Plasticity, **18**, p. 185, 2002
- Peters M., Eschweiler J., Welpmann K., Scripta Metall., **20**, p. 259, 1986
- Pettersen T., Dr.Ing. Thesis, NTNU, 1999
- Pettersen T., Furu T., AA6063 Basic Characterisation, VIRFORM-report, Hydro Aluminium, Norway, 2001a
- Pettersen T., Furu T., AA6082 Basic Characterisation, VIRFORM-report, Hydro Aluminium, Norway, 2001b
- Petzw G., Metallographic Etching, American Society for Metals, Ohio, 1976
- Petzw G., Effenberg G., Ternary Alloys, A Comprehensive Compendium of Evaluated Constitutional Data and Phase Diagrams, 7, VCH Publishers, New York, 1993
- Polanyi M., Z. Phys., **89**, p. 660, 1934
- Polmear I.J., Proc. ICAA9, ed. Nie J.F., Morton A.J., Muddle B.C., Brisbane, Australia, p. 1, 2004
- Poole W.J., Wang X., Lloyd D.J., Embury J.D., Phil. Mag., **85**, p. 3113, 2005
- Poulsen H.F., Margulies L., Schmidt S., Winther G., Acta Mater., **51**, p. 3821, 2003
- Przystupa M.A., Vasudévan A.K., Rollet A.D., Mater. Sci. Eng., **A186**, p. 35, 1994

References

- Korsnes T., Norum H., Karlsen M., Hjelen J., Proc. EMC 2004, ed. Van Tendeloo G., Antwerp, Belgium, p. 625, 2004
- Krieger Lassen N.C., J. Microsc., **181**, p. 72, 1996
- Krieger Lassen N.C., Juul Jensen D., Conradsen K., Scanning Microscopy, **6**, (1), p. 115, 1992
- Lademo O.-G., Hopperstad O.S., Langseth M., Int. J. Plasticity, **15**, p. 191, 1999
- Lademo O.-G., Hopperstad O.S., Malo K.A., Pedersen K.O., J. Mater. Proc. Tech., **125-126**, p. 84, 2002
- Lademo O.-G., Hopperstad O.S., Berstad T., Langseth M., J. Mater. Proc. Tech., **166**, p. 247, 2005
- Laraba-Abbes F., Ienny P., Piques R., Polymer, **44**, p. 807, 2003
- Lebensohn R.A., Tomé C.N., Acta Metall. Mater., **41**, p. 2611, 1993
- Leinum J.R., Moen K., Hjelen J., Malvik T., Proc. EMC 2004, ed. Van Tendeloo G., Antwerp, Belgium, p. 563, 2004
- Lens A., Maurice C., Driver J.H., Mater. Sci. Eng., **A403**, p. 144, 2005
- Li F., Bate P.S., Acta Mater. Metall., **39**, p. 2639, 1991
- Li C., Bretheau T., Acta Metall., **37**, p. 2645, 1989
- Li S., Van Houtte P., VIRFORM Report, Katholieke Universitet Leuven, Belgium
- Li S., Van Houtte P., Aluminium, **78**, p. 918, 2002a
- Li S., Van Houtte P., VIRFORM Report 13D, Katholieke Universitet Leuven, Belgium, 2002b
- Li Z.J., Winther G., Hansen N., Acta Mater., **54**, p. 401, 2006
- Liu Y.S., Kang S.B., Ko H.S., Scripta Mater., **37**, p. 411, 1997
- Liu Q., Wert J., Hansen N., Acta Mater., **48**, p. 4267, 2000
- Lopes A.B., Barlat F., Gracio J.J., Ferreira Duarte J.F., Rauch E.F., Int. J. Plasticity, **19**, p. 1, 2003
- Lucke K., Lange H., Z. Metallk., **43**, p. 55, 1952
- Ludwik P., Elemente der technologischen Mechanik, Springer-Verlag OHG, Berlin, 1909
- Marciniak Z., Duncan J., Mechanics of Sheet Metal Forming, 1992
- Margulies L., Winther G., Poulsen H.F., Science, **291**, p. 2392, 2001
- Marthinsen K., Abthai S., Nes E., Holmedal B., Aluminium, **78**, p. 869, 2002
- Martin J.W., Precipitation Hardening, Pergamon Press, New York, 1968
- Matteson T.L., Schwarz S.W., Houge E.C., Kempshall B.W., Giannuzzi L.A., J. Electron. Mater., **31**, p. 33, 2002

References

- Honneff H., Mecking H., *Texture of Materials*, Aachen, Germany, p. 265, 1978
- Honneff H., Mecking H., *Proc. ICOTOM 6*, **1**, Tokyo, p. 347, 1981
- Hornbogen E., Gahr K.H.Z., *Metallography*, **8**, p. 181, 1975
- Hornbogen E., Starke E.A., *Acta Metall. Mater.*, **41**, p. 1, 1993
- Hu H., *Trans. Met. Soc. AIME*, **224**, p. 75, 1962
- Humphreys F.J., *J. Microsc.*, **195**, p. 170, 1999
- Humphreys F.J., *J Mater. Sci.*, **36**, p. 3833, 2001
- Humphreys F.J., Brough I., *J. Microsc.*, **195**, p. 6, 1999
- Humphreys F.J., Hatherly M., *Recrystallization and related annealing phenomena*, Pergamon, Oxford, 1996
- Humphreys F.J., Huang Y., Brough I., Harris C., *J. Microsc.*, **195**, p. 212, 1999
- Irgens F., Bauger Ø., Andersson B., *SINTEF Materials Technology, Report STF24 A95564*, p. 24, 1995
- International Organization for Standardization, *ISO 2107:2004*, 2004
- Iveland T, *Dr.Ing. Thesis, NTNU*, 2000
- Iwahashi Y., Horita Z., Nemoto M., Langdon T.G., *Acta Mater.*, **45**, p.4733, 1997
- Juul Jensen D., *Mater. Sci. Tech.*, **21**, p. 1365, 2005
- Kahn A.S., Huang S., *Continuum Theory of Plasticity*, John Wiley & Sons, New York, 1995
- Kalidindi S.R., Bronkhorst C.A., Anand L., *J. Mech. Phys. Solids*, **40**, p. 537, 1992
- Kalidindi S.R., Bhattacharyya A., Doherty R.D., *Adv. Mater*, **15**, p. 1345, 2003
- Kang J., Jain M., Wilkinson D.S., Embury J.D., *J. Strain. Anal. Eng. Des.*, **40**, p. 559, 2005
- Kang J., Wilkinson D.S., Jain M., Embury J.D., Beaudoin A.J., Kim S., Mishira R., Sachdev A.K., *Acta Mater.*, **54**, p. 209, 2006
- Karlsen M., Norum H., Hjelen J., Grong Ø., Frigaard Ø., *Proc. EMC 2004*, ed. Van Tendeloo G., Antwerp, Belgium, p. 623, 2004
- King J.E., You C.P., Knott J.F., *Acta Metall.*, **29**, p. 1553, 1981
- Knauss W.G., Chasiotis I., Huang Y., *Mech. Mat.*, **35**, p. 217, 2003
- Kobberrød O.K., Johannessen K., Heiberg G., Hjelen J., *Proc. ICEM 14*, ed. Calderón Benavides H.A., José Yacamán M., Cancun, Mexico, p. 543, 1998
- Kochendörfer A., Swanson M., *Arch. Eisenhüttenw.*, **31**, p. 549, 1960
- Kocks U.F., *Met. Trans.*, **1**, p. 1121, 1970
- Kocks U.F., Chandra H., *Acta Metall.*, **30**, p. 695, 1982
- Konrad J., Zaeferrer S., Raabe D., *Acta Mater.*, **54**, p. 1369, 2006

References

- Ewing J.A., Rosenhain W., *Phil. Trans. Royal Soc.*, **193A**, p. 353, 1900
- Farrer J.K., Chipman M.C., Tiner M., *Microsc. Microanal.*, **8**, p. 544, 2002
- Ferry M., *Proc. Materials 98*, ed. M. Ferry, Wollongong, p. 439, 1998
- Fjeldbo S.K., Holmedal B., Lademo O.-G., Bjerkaas H., Støren S., Roven H.J., Hjelen J., Hopperstad O.S., Berstad T., Pedersen K.O., Furu T., *Proc. ESAFORM 2005*, Cluj-Napoca, Romania, 2005
- Fjeldly T.A., *Dr.Ing. Thesis*, NTNU, 1999
- Fjeldly T.A., Sørensen A., Roven H.J., *Mater. Sci. Eng.*, **A300**, p. 515, 2001
- Forbord B., Mathiesen R.H., Roven H.J., *Mater. Sci. For.*, **558-559**, p. 1299, 2007
- Furu T., Pedersen K.O., *Mater. Sci. For.*, **519-521**, p. 1611, 2006
- Furu T., Johansen A., Sæther J.A., Dons A.L., Pedersen K., Berstad T., Lademo O.-G., Holmedal B., Marthinsen K., Hopperstad O.S., Nes E., Mortensen D., *Aluminium*, **80**, p. 707, 2004
- Gambin W., *Plasticity and Textures*, Kluwer Academic Publishers, Dordrecht, 2001
- Garstone J., Honeycombe R.W.K., Greetham G., *Acta Metall.*, **4**, p. 485, 1956
- Goldstein J., Newbury D., Joy D., Lyman C., Echlin P., Lifshin E., Sawyer L., Michael J., *Scanning Electron Microscopy and X-Ray Microanalysis-3th ed.*, Kluwer/Academic Press, New York, 2003
- Gourgues-Lorenzon A.F., *Inter. Mater. Rev.*, **52**, p. 65, 2007
- Gray III G.T., *Acta Metall.*, **36**, p. 1745, 1988
- Hallem H., *PhD Thesis*, NTNU, 2005
- Han J.H., Jee K.K., Oh K.H., *Int. J. Mech. Sci.*, **45**, p. 1613, 2003
- Han J.H., Kim D.I., Jee K.K., Oh K.H., *Mater. Sci. Eng.*, **A387-389**, p. 60, 2004
- Hatherly M., *Proc. ICOTOM 5*, ed. Gottstein G. and Lücke K., **1**, p. 265, 1978
- He X.Y., Kang X., Quan C., Tay C.J., Wang S.H., Shang H.M., *Proc. SPIE*, **4537**, p. 63, 2002
- Henning M., Vehoff H., *Acta Mater.*, **53**, p. 1285, 2005
- Hirsch J., *Proc. ICAA9*, ed. Nie J.F., Morton A.J., Muddle B.C., Brisbane, Australia, p. 15, 2004
- Hirsch J., Lücke K., *Acta Metall.*, **36**, p. 2863, 1988
- Hjelen J., *PhD Thesis*, University of Trondheim, 1990
- Hjelen J., Ørsund R., Nes E., *Acta Metall.*, **39**, p. 1377, 1991
- Hjelen J., Qvale A.H., Gomo Ø., *Proc. ICOTOM 10*, ed. Bunge H.j., Clausthal, Germany, p. 137, 1993
- Honeycombe R.W.K., *The Plastic Deformation of Metals-2nd ed.*, Edward Arnold, Australia, 1984

References

- Cahn, J. *Inst. Metals*, **79**, p. 129, 1950
- Chiron R., Fryet J., Viaris de Lesegno P., *Proc. Symposium on Local Strain and Temperature measurement in Non-uniform Fields at Elevated Temperatures*, Berlin, 1996
- Choi Y.S., Piehler H.R., Rollett A.D., *Matall. Mater. Trans.*, **35A**, p. 513, 2004
- Chu T.C., Ranson W.F., Sutton M.A., Peters W.H., *Exp. Mech.*, **25**, p. 232, 1985
- Chung N., Embury D., Evensen J.D., Hoagland R.G., Sargent C.M., *Acta Metall.*, **25**, p. 377, 1977
- Chung Y.H., Cho K.K., Han J.H., Shin M.C., *Scripta Mater.*, **43**, p. 759, 2000
- Cizek P., Wynne B.P., Hong Lu, Parker B.A., *Mater. Sci. Eng.*, **A219**, p. 44, 1996
- Clarebrough L.M., Hardreaves M.E., *Progress in Metal Physics*, 8, Pergamon Press, Oxford, 1959
- Considerere A., *Ann. Ponts Chaussees*, **9**, p. 574, 1885
- Cox H.L., Sopwith D.G., *Proc. Phys. Soc.*, **49**, p. 134, 1937
- Crumbach M., Pomana P., Wagner P., Gottstein G., *Proc. 1st joint Conf. On Recrystallization and Grain Growth*, ed. G. Gottstein and D.A. Molodov, p. 1053, 2001
- Crumbach M., Goerdeler M., Gottstein G., Neumann L., Aretz H., Kopp P., *Modelling Simul. Mater. Sci. Eng.*, **12**, p. S1, 2004
- Delaire F., Raphanel J.L., Rey C., *Acta. Mater.*, **48**, p. 1075, 2000
- Diehl J., *Z. Metallk.*, **46**, p. 650, 1955
- Diehl J., *Z. Metallk.*, **47**, p. 331, 1956
- Dieter G.E., *Mechanical Metallurgy*, McGraw-Hill, London, 1988
- Dillamore I.L., Roberts W.T., *Met. Rev.*, **10**, p. 271, 1965
- Dingley D.J., *Scanning Electron Microscopy*, **2**, p. 569, 1984
- Doumalin P., Bornert M., Caldemaïson D., *Proc. International Conference on Advanced Technology in Experimental Mechanics '99*, Ube, Japan, p.81, 1999
- Duan X., Jain B., Metzger D., Kang J., Wilkinson D.S., Embury J.D., *Mater. Sci. Eng.*, **A394**, p. 192, 2005
- Dumoulin S., Tabourot L., Chappuis C., Vacher P., Arrieux R., *J. Mat. Proc. Tech.*, **133**, p. 79, 2003
- Ekstrom H.E., Furu T., Mishin O.V., Pettersen T., Olsson B., *Aluminium*, **78**, p. 930, 2002
- Engler O., *VIRFORM-report*, Hydro Aluminium, Deutschland, 2002
- Engler O., *Lecture notes*, March 16th, 2004
- Engler O., Lüke K., *Mater. Sci. Eng.*, **A148**, p. 15, 1991
- Engler O., Crumbach M., Li S., *Acta Mater.*, **53**, p. 2241, 2005

References

References

- Adcock F., *J. Inst. Met.*, **27**, p. 73, 1922
- Althoff J., Drefahl K., Wincierz P., *Zeitschrift für Metallkunde*, **62**, p. 765, 1971
- Aukrust T., Vatne H.E., SINTEF Materials Technology, Report STF24 A94044, p. 63, 1994
- Aukrust T., Tjøtta S., Skauvik I., Vatne H.E., Van Houtte P., Proc. 15th Risø International Symposium on Materials Science, Denmark, p. 219, 1994
- Aukrust T., Lohne O., Vatne H.E., Furu T., Tjøtta S., Proc. ET96: 6th International Aluminum Extrusion Technology Seminar, Chicago, Illinois, p. 171, 1996
- Aukrust T., Tjøtta S., Vatne H.E., Van Houtte P., *Int. J. Plasticity*, **13**, p. 111, 1997
- Backofen W.A., *Deformation Processing*, Addison-Wesley Pub. Co., 1972
- Baird J.D., *Iron Steel*, **36**, p. 186, 1963
- Barlat F., Liu J., *Mater. Sci. Eng.*, **A257**, p. 47, 1998
- Barlat F., Vasudevan A.K., *Acta Metall. Mater.*, **39**, p. 391, 1991
- Bate P., *Phil. Trans. R. Soc. A*, **357**, p. 1589, 1999
- Bate P., Roberts W.T., Wilson D.V., *Acta Metall.*, **29**, p. 1797, 1981
- Bauger Ø., SINTEF Materials Technology, Report STF24 A94649, p. 33, 1994
- Bischoff L., Teichert J., *Mater. Sci. For.*, **248-249**, p. 445, 1997
- Bishop J.F.W., Hill R., *Phil. Mag.*, **42**, p. 414, 1951
- Bjerkaas H., Sjølstad K., Proc. SCANDEM 2002, ed. Keränen J., Sillanpää K., Tampere, Finland, p. 51, 2002
- Bjerkaas H., Fjeldbo S.K., Roven H.J., Hjelen J., Furu T., Proc. TMS 134th Annual Meeting & Exhibition, Trends in Materials Manufacturing Technologies for Transportation Industries, p. 251, 2005
- Bjerkaas H., Fjeldbo S.K., Roven H.J., Hjelen J., Cjiron R., Furu T., *Mater. Sci. For.*, **519-521**, p. 809, 2006
- Bowen A.W., Proc. ICOTOM 8, ed. Kallend J.S., Gottstein G., Warrendale, PA, p. 971, 1988
- Bowen A.W., *Mater. Sci. Tech.*, **6**, p. 1058, 1990
- Brown K., *J. Inst. Met.*, **100**, p. 341, 1972
- Bunge H.J., *Texture analysis in Materials science - Mathematical methods*, Butterworth, London, 1983
- Bunge H.J., Fuchs R., *Phys. Stat. Sol.*, **32**, p. 169, 1969
- Bunge H.J., Nielsen I., *Int. J. Plasticity*, **13**, p. 435, 1997

Conclusion

- Combined slip trace and Schmid value distribution analysis can be used to determine the number of slip systems activated.
- Comparison of experimental results and texture based calculations show that the plastic strain ratio for the present Al-Mg-Si profiles is better described by the Taylor RC than the FC method. The static plasticity models (e.g. Sachs, Taylor models) are not able to provide sufficiently accurate predictions of the mechanical anisotropy. The accuracy of texture based calculations can be improved by applying more advanced and dynamic models like the GIA and LAMEL models.
- The number of slip systems activated (typically 1-2 slip systems) is very heterogeneous and is normally less than the number predicted by the classical Taylor model. Generally, it has been shown that materials without texture need to activate a higher number of slip systems than a material carrying a strong crystallographic texture.
- Strain heterogeneities lead to reduced macroscopic uniform strain. Different types of heterogeneities are observed at all length-scales, and all types of strain heterogeneities should be evaluated in order to determine the macroscopic forming behaviour of a material.
- Microstructures consisting of both “hard” and “soft” grains develop local strain heterogeneities during deformation. Consequently, the enforced global deformation is mainly picked up by grains having soft crystallographic orientations, i.e. the strain is localised to soft regions.
- In-situ deformation in the SEM combined with EBSD is a powerful tool for investigating plasticity of materials. The technique has some important limitations, but still, the results obtained with this technique are comparable to the observations obtained with the more advanced 3DXRD technique.

7 Conclusion

The present work has been concerned with experimental investigations of extruded sheets from two commercial Al-Mg-Si alloys with different microstructure. The main objective has been to obtain a better understanding of the deformation mechanisms operating during plastic forming of extruded aluminium profiles. This has been obtained by discussing the experimental results, which are organised in two separate parts based on the techniques applied and the mechanisms investigated. The main conclusions based on these examinations, can be summarised as follows:

- The mechanical anisotropy observed between the 0° and 90° direction of AA6063 is related to the ED-rotated Cube texture. The Schmid value distribution for the dominant texture components is not symmetrically distributed. Hence, the activation of slip systems varies significantly.
- Crystallographic texture is the main reason for mechanical anisotropy. However, also artificial and to some extent natural age-hardening affect mechanical anisotropy due to the introduction of non-shearable particles that reduces the texture effect. Hence, both AA6063 and AA6082 possess more isotropic mechanical properties after artificial ageing.
- Extruded profiles with microstructural and textural through-thickness variations will possess evident variations in through-thickness mechanical properties and can develop significant anisotropic cross-sectional shape variations when subjected to uniaxial tensile deformation. The prediction of the forming behaviour becomes more complicated by the introduction of such a variation.
- Grains having a [100] or a [111] parallel to the deformation direction (DD) are stable during simple tension deformation while other crystallographic orientations tend to obtain such a configuration. Further, the accumulated lattice rotation for individual grains is reduced when the grain size is large.

Discussion

material of interest has to be prepared in vacuum, since an oxide layer can develop at the specimen surface and obscure the backscattered signal. For example, when exposed to atmosphere, nano-scale metallic interconnects, used in microelectronic devices, can oxidize rapidly, making them very difficult to analyze by EBSD (Farrer et al. 2002).

More relevant for this thesis is the use of dual-beam microscopes for 3D microstructural investigations, especially when FIB is used together with EBSD. Combining the successive removal by FIB with sequential EBSD maps and high-resolution imaging by the electron beam, reveal detailed information through the specimen thickness. The different sections can then be used to generate a full 3D sample reconstruction. The technique is in other words perfect for obtaining information about the microstructure that can be used as input for computer simulations of various forming operations. Further, FIB-EBSD can also be used to obtain detailed information about orientation gradients developing e.g. close to grain boundaries and primary particles.

Another important feature is that the spatial resolution of combined FIB and EBSD investigations conveniently fits in between the electron tomography (few Angstroms) and the 3DXRD (several microns) techniques, and is suitable for looking at microstructures with feature sizes of tens of nanometres to tens of microns (Mulders and Day 2005, Zaefferer et al. 2005). Dual-beam investigations have already been used to obtain a better understanding of 3D orientation gradients (see e.g. Konrad et al. 2006).

Due to the destructive nature of FIB-sectioning, this type of experiments never can be combined with in-situ investigations. Still, combined FIB-EBSD experiments clearly supplement the EBSD in-situ experiments. Hence, if performed correctly, the results from both methods provide a better understanding of 3D plasticity. Due to the limitations with these methods, in-situ 3D plasticity investigations still have to be performed by the 3DXRD or similar techniques as pointed out in section 2.7.5. Even though 3DXRD is superior to the in-situ deformation technique in the SEM when it comes to 3D plasticity, the discussion above has shown the enormous potential for this technique. It is reasonable to assume that in the future, in-situ deformation in SEM will help scientist understand the basics of the mechanisms operating during deformation.

Discussion

The strict surface requirements for EBSD investigations are another important limitation for the EBSD technique. As pointed out in section 4.1.2, the specimen surface has to be electro-polished in order to obtain the required pattern quality. Further, it is well known that the specimen surface contaminate due to the electron beam, and this reduces the pattern quality. In addition, the specimens often develop surface topography that makes it difficult to perform high-quality EBSD investigations at high strains (see e.g. Figure 5.49). To avoid these problems, it would have been desirable to repolish the specimen surface during deformation. The new dual-beam microscopes (combined Focused Ion Beam (FIB) – Scanning Electron Microscope (SEM)) allow this type of repolishing. However, since both these techniques are fairly novel, there are still not reported any works where FIB is used to repolish the specimen during in-situ deformation investigations.

Further, repolishing will also remove the slip traces at the specimen surface. Hence, it could be argued that information about the slip planes activated is lost. On the other hand, it will become possible to study when the different slip traces are produced. As an example, some grains develop additional slip traces at high strains, indicating that other slip systems are activated at this strain range. By repolishing the surface, it would be possible to answer whether the initial slip systems stay active, or if these systems become inactive at higher strains. In other words, this type of supplement provides new possibilities for in-situ deformation investigations. However, the repolishing must be used with consideration since it alters the investigated surface.

6.5.3 Focused Ion Beam (FIB)

As already mentioned above, FIB has been introduced as a new and very interesting technique for performing microstructural investigations. The technique has evolved substantially since it first was introduced more than thirty years ago (Bischoff and Teichert 1997, Tseng 2004). For the last couple of years, FIB has for different reasons been substantially applied together with EBSD.

FIB can for example be used to prepare the surface of a material for EBSD investigations (Matteson et al. 2002). Repolishing can as discussed above be necessary during in-situ deformation investigations. Further, there are also applications where the

Discussion

deformation unit is very compact, allowing it to be mounted to most SEMs available today. In addition, this deformation unit is not only capable of deforming the sample by simple-tension, but also other deformation modes like compression and bending are available. Furthermore, these different modes of deformation can be combined with a heating unit, allowing deformation at elevated temperatures. The capabilities are extensive when this deformation unit is combined with EBSD measurements (and/or local strain measurements).

When designing experimental equipment like the one described here, it is always a compromise between different functionalities, i.e. EBSD performance and deformation mode capabilities. These functionalities are very well balanced for the deformation unit applied in this work. Hence, the machine developed by Rémi Chiron and co-workers is really state-of-the-art when it comes to in-situ deformation in the SEM (see section 4.3.3 for more details concerning this deformation unit).

6.5.2 Challenges (related to in-situ deformation in the SEM)

As already mentioned above, there are still some challenges that have to be overcome even though in-situ deformation in the SEM is a powerful tool. There are some important limitations for the EBSD technique.

When the specimen is deformed with a strain rate of $1.1 \times 10^{-4} \text{ s}^{-1}$ and the time necessary to perform a detailed scan of the microstructure is ~ 45 minutes, the specimen will be given a deformation equal to 30% during on scan. Consequently, the deformation has to be interrupted in order to perform these investigations. Hence, this type of investigations is not fully in-situ but rather “semi-in-situ”. The pattern acquisition speed of the EBSD technique has been improved significantly since the introduction of the technique. At that time, it was almost impossible to acquire 1fps, while modern EBSD systems easily acquire up to 43fps (see section 4.3.1). In the near future, it is reasonable to assume a pattern acquisition speed of 300-500fps will be available (Schwarzer 2007). With this acquisition speed, it will be possible to perform fully in-situ EBSD investigations.

Discussion

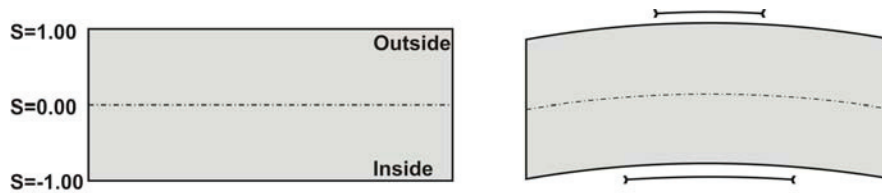


Figure 6.23 – Illustration of the leg from a V-shaped extruded profile with evident through-thickness variations before stretching (left). In the shown case, the transversal strains at the inside of the profile are assumed larger than the outside strains due to differences in plastic strain ratio. This leads to strain gradients which manifest as a curvature (shape change) of the profile after stretching.

6.5 In-situ deformation in the SEM – status and challenges

The discussion presented above clearly shows that in-situ deformation in the SEM is a powerful tool that allows a new type of experimental investigations and thereby provides insight to important metallurgical phenomena. Still, the technique is not fully developed and is confronted with several challenges that have to be overcome. This chapter will be used to discuss the status and challenges for this promising technique.

6.5.1 In-situ deformation unit

For the last decade, there has been an enormous evolution when it comes to in-situ deformation capabilities in the SEM. At the initiation of this work, only a modest number of works related to this topic was published. The group at the CNRS – PMTM laboratory in Paris was one of the exceptions, and had already published several impressive works utilising simple-tension deformation (Chiron et al. 1996, Delaire et al. 2000) (see section 2.7.5 for more details). At the beginning of this decade, the interest boosted and several groups around the world started to utilise this technique. As a consequence, the number of publications has increased vigorously. Most of these publications are related to simple-tension deformation.

The Norwegian University of Science and Technology (NTNU) has collaborated closely with the CNRS – PMTM laboratory for several years. In 2001, this collaboration was extended also include in-situ investigations in the SEM. Consequently, NTNU acquired the deformation unit developed by Rémi Chiron and his group at CNRS – PMTM. This

Discussion

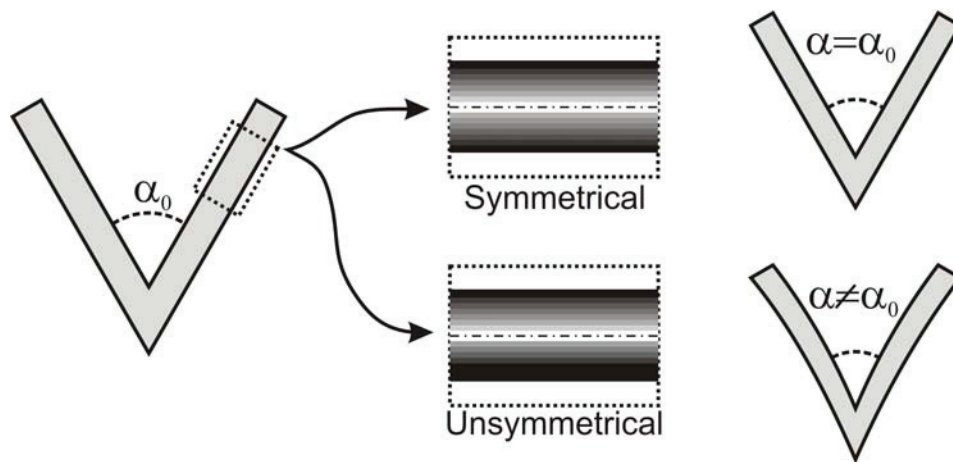


Figure 6.22 – V-shaped extruded profile (complicated geometry). Profiles with symmetrical texture will maintain their geometry after axial deformation (top), while the geometry will be altered if the gradient is unsymmetrical (bottom).

Extruded profiles are normally subjected to a stretching procedure immediately after extrusion in order to remove curvatures introduced for example from uneven cooling or material flow through the die. In this operation, the profiles are given an axial elongation of typically 0.5-1.5%. This deformation is in some cases observed to be sufficient in order to adjust the geometrical shape. However, very frequently the shape after stretching is becoming outside the geometry tolerances, i.e. the angle α_0 (Figure 6.22) can be shifted during stretching. If a profile with a symmetrical texture gradient is stretched, the deformation is expected to take place symmetrical around the centre plane ($S=0.00$). Each layer will deform differently but the profile will maintain its geometrical shape since the outer and inner side of the profile deforms equally and by that neutralise potential bending of the profile walls. However, if a profile with an unsymmetrical gradient is deformed by tension, the inner and outer side will deform differently (Figure 6.23). The differences in deformation behaviour, independent of the cause (internal stresses, gradients, plastic strain ratios etc.), could introduce some alterations of the profile shape ($\alpha \neq \alpha_0$). If, for the sake of simplicity, the variation in plastic strain ratio is the only cause of variations through the thickness, the differences in r -values could introduce larger transversal strains (Figure 6.23). These strains can alter the profile shape which again makes it more difficult to reach the target shape after forming. It is therefore very important both to understand the effect from and to control the development of through-thickness variations in order to improve the forming behaviour.

Discussion

surface of the 45° specimens would hardly deform at all. In contrast, the local strain distribution clearly show that this is not the case, even though the first traces of strain localisation take place in areas of low Taylor factor. The material has to overcome the compatibility requirements, underlining the fact that the material is dependent on the nearest neighbours in order to overcome the enforced global deformation.

6.4 Impact and relevance to shape of extrusions

The through-thickness variations developed during extrusion will certainly affect all subsequent forming processes. It has been shown above in Chapter 6.2 that the deformation behaviour of the different layers varies significantly. Further, it has been assumed that the observed gradients are symmetrical about the profile centre plane ($S=0.00$), which is expected for simple extrusions like the flat geometries investigated in this work. However, due to the complicated texture evolution during extrusion, such simple symmetrical texture variations are not expected for more complicated geometries. When more complicated profiles are investigated, they often possess unsymmetrical gradients, hence predictions of the forming behaviour become very challenging.

Imagine a fairly simple V-shaped extruded profile (Figure 6.22). During extrusion of such profile geometries, the die design will normally enforce a flow pattern where texture differences are developing between the inside and outside surface layer. Based on the results and discussions presented above, it seems clear that the mechanical properties will differ through the wall thickness. This will, of course, alter the deformation behaviour of the different layers which again can appear like minor alterations of the profile geometry.

Discussion

maps presenting the number of slip traces activated by the individual grains during deformation (Figure 5.44, Figure 5.45 and Figure 5.50). These figures show that AA6063 has to activate a higher number of slip traces when the crystallographic texture is more or less removed. As a consequence, this material will have a more heterogeneous strain distribution when the crystallographic texture has been removed by cross-rolling. This is also well illustrated by comparing the two figures presenting the local strain distribution of the material with strong texture deformed parallel and 45° to ED (Figure 5.73 and Figure 5.74). The specimen deformed parallel to ED, which also has the most uniform Taylor factor distribution, has a much more homogeneous strain distribution than the specimen deformed 45° to ED.

The effect of nearest neighbours can also indirectly affect the strain distribution. In many ways, it could be reasonable to compare the macroscopic uniform strain of a material with a chain. The chain is not stronger than its weakest segment and neither a material can be deformed further than until the microstructure reaches the uniform strain locally. In other words, a material with vigorous strain localisation will reach the macroscopic uniform strain earlier than a material with homogeneous strain distribution. When this statement is transferred to the investigated material, it becomes evident that the observed strain heterogeneities will have a negative impact on the macroscopic uniform strain. The amount of strain localisation is dependent on the deformation direction. Hence, it could be claimed that these variations explain the variations in uniform strain when deformed 0°, 45° and 90° to ED. These variations might be insufficient to explain the variations observed in macroscopic mechanical properties alone, but the angular dependency of the local strain heterogeneities are undoubtedly consistent with variations in mechanical properties.

In other words, not only the crystallographic texture determines the strain distribution taking place in the material. This is explicitly illustrated when the through-thickness variations in crystallographic texture for AA6063 prior to cross-rolling is compared to the local strain measurements of the same area. Figure 5.72 shows that there are large variations in Taylor factors through the profile thickness, due to the evident texture gradient discussed in Chapter 6.2. From a Taylor factor point of view, the 0° and 90° specimens would develop heavy strain localisation at the specimen surface, while the

Discussion

Further, it appears that a clear correlation between the number of slip traces observed and the local strain distribution exists. In general, grains developing low strain, i.e. high Taylor factor, rarely develop strong slip traces. Further, it is observed that the grains exhibiting high strain often develop a limited number but very vigorous slip traces. However, it is also observed that such grains develop multiple slip traces, especially close to the grain boundaries. This can be explained by the Schmid value distribution. Hence, heavily deformed grains has some slip systems which are extremely well oriented for slip and can therefore accommodate large strains on a limited number of slip systems. However, at very high strains, other slip systems have to be activated in order to fulfil the compatibility requirements. On the other hand, there are examples of grains deformed to very high strains, where no evident slip traces are observed. This could mean that the strain either is evenly distributed among a high number of slip systems (homogeneous deformation), which is in strong contrast to the discussions regarding activation of slip systems, or, strain is distributed on a limited number of slip systems which not produces visible slip traces. Neither of these solutions seems very likely, so it is difficult to fully explain the relationship between the number of slip traces observed and the amount of strain heterogeneities. From the discussion above, the amount of deformation taking place in individual grains is to a large extent determined by their crystallographic orientation. However, it has also been shown that other factors could introduce strain heterogeneities.

6.3.7 Effects of nearest neighbours

As already mentioned several times, the number of slip systems activated is strongly dependent on the global texture. For the individual grains, also another given difference comes into effect. Almost all grains in a material with very strong crystallographic texture have close to similar orientation. Hence, individual grains have several neighbouring grains with comparable orientation and they will therefore activate the same number of slip systems during deformation. For the same reason, they will deform in a similar manner, hence internal compatibility is also improved. Contrary, in a material with random texture, all the surrounding grains will have dissimilar orientations. The compatibility requirements are more demanding and the grain has to activate a higher number of slip systems. This is very well illustrated comparing the

Discussion

The present study has shown that alloy AA6063 also develops similar type of strain localisation due to texture heterogeneities. The soft grains, having several slip systems with high to very high Schmid values can easily activate many slip systems (see section 6.3.3 for more details) and are therefore easy to deform. The hard grains have a more unfavourable Schmid value distribution and would therefore like to avoid activating any slip systems. As a consequence, the number of slip systems activated varies significantly from grain to grain, which again affect the strain distribution during deformation. This is very well illustrated in Figure 5.63, which presents the measured major strain distribution deformed to a global strain of 27%. Here, the grain boundaries determined by EBSD are overlaid, and it becomes clear that the strain heterogeneities are related to variations in crystallographic orientation. The IPF-map of the same area (Figure 5.61) confirms that there exist a close correlation between the crystallographic orientation and the local strain distribution. In other words, microstructures consisting of both “hard” and “soft” grains will develop local strain heterogeneities during deformation, i.e. some grains are deformed significantly more than others. The soft grains have to compensate for the lack of deformation taking place in the hard grains. This again means that the enforced global deformation mainly is picked up by grains having soft crystallographic orientations, i.e. the strain is localised to soft regions. Soft grains can therefore be deformed to strains approximately three times as high as the global strain and more than four times as high as neighbouring hard grains as shown in Figure 5.63. The consequences of such variations have also been investigated by Duan et al. (2005) and were discussed above in Chapter 6.2.

The fact that all grains have some slip systems more favourable oriented for slip has been known since the earliest days of crystal plasticity. All the classical plasticity models are even based on this assumption (Sachs, Taylor). An example of a Taylor factor map of the microstructure (Figure 5.62) illustrates quite evidently how the crystallographic texture determines deformation easiness. The grains having a high Taylor factor correspond to the least deformed grains at the macroscopic uniform strain. Further, the maps presented in Figure 5.54 clearly illustrate how the Taylor factor of a given material is determined by the applied deformation direction (a-c), as well as the texture heterogeneity. Consequently, the material with random texture (d) has large variations in the Taylor factors compared to the material with strong texture (a-c).

Discussion

activation. It is therefore clear that also the amount of strain heterogeneities on this finer length-scale is texture dependent.

When slip traces are studied in even more detail, micrographs illustrate that deformation by slip clearly is a discontinuous deformation process (Figure 5.68). Hence, by using ordinary definitions of strain very locally, the strain can be almost infinity in one region, while the neighbouring regions are more or less undeformed. As already indicated in section 5.7.1, this fact makes it impossible to treat the material as a continuum at this length-scale. The very significant strains will make the material collapse locally (i.e. the material reaches the ultimate strain in these regions), which again will lead macroscopic failure. In other words, the forming behaviour of a material is to a large extent determined by the local strain distribution taking place on all length-scales. To illustrate this even further, the in-situ deformation experiments will be discussed to explain the effect of texture and activation of slip systems on the local strain distribution taking place during deformation.

6.3.6 Hard vs. soft orientations

As mentioned above, it is a common understanding that microstructural heterogeneities like crystallographic texture, grain size and shape, and second phase particles lead to strain heterogeneities. During the last century, several studies have been performed on how the local strain distribution is controlled by microstructural heterogeneities. Raabe et al. (2003) studied an Al-Mg-Si sheet (AA6022) and found that the existence of soft and hard inclusions gave rise to strong strain heterogeneities at the specimen surface. This observation is comparable to the observation made by Wittridge and Knutsen (1999), which found that strain localisation was produced when colonies of the strong R-texture components were embedded within the soft matrix with Cube texture. This observation confirmed the fact that grain-scale roughening first produces microscopic strain localization in the incipient stages of plastic straining and eventually macroscopic through-thickness strain localisation. In agreement with earlier work along these lines, the authors concluded that ridging phenomena could be attributed to texture inhomogeneity.

Discussion

passes. Additional slip systems activated will lead to increased dislocation interactions which clearly have a negative impact on the forming behaviour (Kocks 1970). This is another example where the experimental results clearly confirm the correlation between the number of slip systems activated, strain heterogeneities and the forming behaviour.

As shown in Figure 5.18 and Figure 5.19, heat-treatment leads to significant alterations in the amount of PLC activity, and the PLC-effect is not visible for the specimens deformed in the SEM (AA6063, T1 condition). This is confirmed by the stress vs. strain curves obtained from the in-situ experiments (Figure 5.23). Hence, AA6063 has in condition T1 a homogeneous strain distribution on the macroscopic scale. However, when this material condition is investigated more carefully in the SEM, it becomes clear that the material has a quite heterogeneous strain distribution on a finer length-scale (microscopic).

The slip traces observed on the specimen surface (section 5.6.1) are by themselves strain heterogeneities. This type of local strain heterogeneities develops on a much finer length-scale than what can be observed with the naked eye. On this length-scale, some regions do not deform at all, while other regions develop very significant strains. Hence, also stain localisation on a microscopic scale is an intrinsic property for this type of alloys. Previously it has been reported that this type of strain heterogeneities might be suppressed by artificial age-hardening to peak- and over-aged conditions (Poole et al. 2005). However, the present observations for AA6063 clearly contradict this since slip traces evidently develops in condition T1.

Within the microstructure, the amount of slip traces, appearance and consistency with neighbouring grains varies significantly from grain to grain. It is also worth noticing that these slip trace characteristic is strongly dependent on the deformation direction. As shown in section 5.6.1, these features varies significantly trough the microstructure for specimens deformed perpendicular to ED. Hence, some grains possess fine slip traces, while other grains possess thick discontinuous and wavy slip traces. The specimen deformed 45° to ED possesses very fine and homogeneous slip traces through the whole microstructure. These evident variations in slip traces, i.e. local strain heterogeneities, are directly linked to the crystallographic texture, which again is related to slip

Discussion

possess vigorous strain heterogeneities on a finer length-scale. Aluminium is a typical example of such a material.

The most well known strain heterogeneity at the macroscopic length scale is the strain localisation taking place during necking initiated at the uniform strain, ref. the Considere criterion (Considere 1885). This criterion states that the onset of necking and the end of uniform elongation (homogeneous deformation on a macroscopic length scale) occurs when the true work hardening rate exactly equals the true strain (Wagoner and Chenot 1996):

$$\frac{d\sigma}{d\varepsilon} = \sigma \quad (34)$$

At this point, the deformation is localised into the necking area while the remaining part of the material is strain relaxed and almost no more deformation takes place. Hence, beyond this point the material develops evident severe strain heterogeneities as shown by the micrograph presented in Figure 5.65.

Further, the Piobert-Lüders (PL) and the Portevin-Le Châtelier (PLC) effects are other strain heterogeneities which are evident at the macroscopic scale in alloys with Mg in solid solution. The PL phenomenon is a strain softening type instability and is characterised by the presence of a plateau of almost constant stress after the onset of yielding (Baird 1963). The PLC effect is a strain rate softening type instability and manifests itself as serrations in the stress-strain curve during the work-hardening stage of deformation (Thomas 1966). Both these effects are frequently observed on the macroscopic stress-strain curve of aluminium alloys containing magnesium. The alloys investigated in this work, which are from the Al-Mg-Si system, possess therefore this type of strain heterogeneities as shown in Figure 5.12 and Figure 5.13.

In a parallel work associated to this PhD-thesis, the PLC effect has been investigated by use of the DSCA-technique. The results from these investigations will be reported elsewhere. Experimental results from earlier work (e.g. Sørensen 1997) have shown that the PLC-effect has a negative impact on the forming behaviour. This is most likely related to the altered strain distribution as suggested by Sørensen (1997). Locally, the material has to activate additional slip systems when the moving deformation band

Discussion

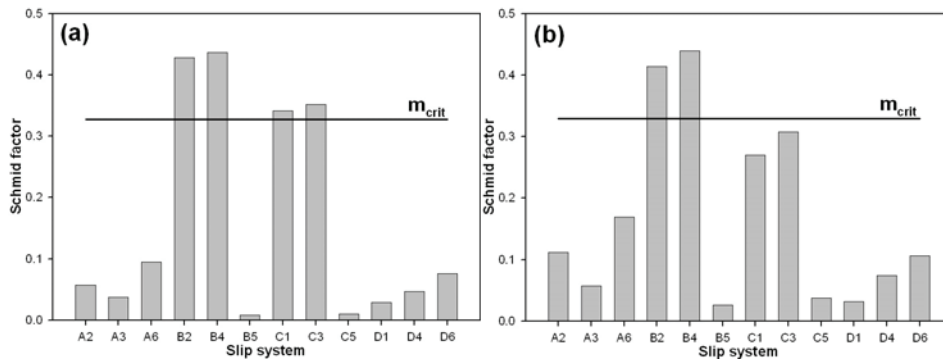


Figure 6.21 – Calculated Schmid factor of all slip systems based on crystallographic orientation of a typical grain investigated in this work. The assumed critical Schmid factor is indicated with a horizontal line. (a) initial orientation (undeformed) and (b) 12% deformation.

At 27% deformation only 1-2 slip systems were satisfying the above criteria, and the grains with a high probability for activating two slip systems were the grains having multiple slip traces, hence not co-planar slip systems. By combining information from slip traces, crystallographic orientation and local strain measurements, this type of relation was found for all directions investigated.

6.3.5 Strain heterogeneities

Strain heterogeneities are almost inevitable during plastic deformation. It is generally accepted that formability of semi-products is closely related to the microstructure inherited from the upstream processing. Textural components, grain-size and morphology as well as the second phase particles are typically inhomogeneously distributed in the microstructure. For that reason, the strain is never completely homogeneous throughout the structure and the materials tend to develop some sort of strain localisation. The different types of strain heterogeneities/localisations can be divided into different categories based on their origin and length scale.

It is beyond doubt that the local strain distribution by itself is a very complex matter. If a material develops visible strain heterogeneities or not during deformation is strongly dependent upon the length scale in which the strains are evaluated. Materials which seem to possess a very homogeneous strain distribution on a given length-scale can easily

Discussion

the growth of the computing capacity of the average workstation. The work by Delaire et al. (2000) use the CPFEM in combination with deformation field and crystallographic orientation measurements in order to better understand the history of slip in each grain and help establish which slip systems are activated at a local level. The comparisons between orientations, measurements and simulations have shown good overall agreement to observed strain and local orientations quantities. The kinetics of plastic deformation was also accurately described, with no discrepancy between methods for the determination of locally active slip systems.

This type of complex calculations has been outside the scope of this work. However, a very simplified method for determining the number of slip systems activated gives similar results, hence supporting the findings reported by Delaire et al. (2000). In the present work all potential slip systems with a Schmid factor satisfying the condition:

$$m \geq 0.75m_{max} = m_{crit} \quad (33)$$

seem to activate. Here, the Schmid factor of the slip system most likely to be active is m_{max} and m_{crit} is the appurtenant critical Schmid factor. Most of the grains in the present material having a strong crystallographic texture (deformed 45° to ED), had an initial orientation where 3-4 slip systems could satisfy the above criteria. However, up to as much as a strain of 12%, the number of slip systems satisfying this criterion was only two (as shown in Figure 6.21). These two slip systems were frequently co-planar but in some cases the slip systems belonged to different slip planes.

Discussion

behaviour is just an average over all heterogeneities included in the sample. So, although simulations may agree well with the specimen behaviour as a whole, the mathematical models are not able to describe the material behaviour locally (Kalidindi et al. 2003, Henning and Vehoff 2005). Section 6.3.5 discusses the effect and nature of these local strain heterogeneities in more detail.

Based on this, the calculated number of activated slip systems by static plasticity models at the best, is an average of the actual number of slip systems activated. For most applications, this type of models gives a sufficient description. Taylor type models are therefore frequently used to predict texture evolution during deformation (see e.g. Aukrust et al. 1997). However, this type of models is inadequate when used to predict anisotropy in mechanical properties as shown in Chapter 6.2. Previously, Fjeldly (1999) has evaluated the capabilities of several different plasticity models by predicting the angular dependence of mechanical properties (yield stress, flow stress and r -value) for two different Al-Zn-Mg-alloys. The results are consistent with the findings in this work, and clearly show that static plasticity models are not able to predict the observed mechanical anisotropy behaviours sufficiently.

During the last couple of decades, several new and more flexible N-point approach models like the LAMEL/ALAMEL models developed by Van Houtte and co-workers (2005) and the GIA model developed by Crumbach and colleagues (Crumbach et al. 2001) have been introduced. These models take grain-to-grain interactions into account, i.e. the number of slip systems activated is also dependent on the orientation of the surrounding grains. In this approach, plastic deformation can be described more accurately and prediction of mechanical anisotropy becomes more realistic. The overview made by Li and Van Houtte (2002a) clearly shows that the LAMEL method is clearly superior to the above classical models. The experimental observations made in this work support the findings made by Li and Van Houtte.

Further, Li and Van Houtte (2002a) also showed that LAMEL is more accurate than the Crystal Plasticity Finite Element Method (CPFEM). However, also the finite element technique is able to satisfactorily capture the overall mechanical anisotropy. Even though the CPFEM is practically impossible to use for industrial forming simulations (enormous calculation time), the interest for this type of modelling has been rapidly growing with

Discussion

another. From a crystal plasticity point of view, the variations among these models are related to how they engage and determine the number of slip systems activated for the individual grains. So called 1-point approach models like the Taylor model (Taylor 1938) are the simplest and roughest of the plasticity models. The Taylor model simply state that each crystal of a polycrystalline aggregate (i.e. grain) deforms such that the outer deformation state is fulfilled (see section 2.2.5 for more detailed information concerning the model). These models engage a given number of slip systems in order to accommodate the enforced macroscopic deformation and this number is independent of crystallographic orientation. Further, these models also state that the same number of slip systems remains active throughout the whole deformation process. The number of slip systems activated is based on the constraint, and the Taylor full constraint (FC) assumes activation of 5 different slip systems. Based on the grain shape and/or the stress continuity consideration, some shear requirements may be relaxed, i.e. not prescribed. This leads to the relaxed constraint (RC) Taylor models (Honneff and Mecking 1978). The Taylor RC lath and pancake models relax one and two shear components respectively, i.e. the number of activated slip systems become 4 and 3 respectively (Van Houtte et al. 2005). The original Sachs model (1928) states, as opposed to the Taylor model, that a polycrystal is an aggregate of independently deforming single crystals which only activates one slip system for each individual grain (section 2.2.4). Hence, the Sachs model is the other extremity when it comes to 1-point approach models.

Further, it is well established that the slip systems most easily activated are the ones having the highest Schmid values. The results presented in section 5.6.2 show that the grain-to-grain Schmid value distribution varies significantly. Hence, some orientations have a homogeneous Schmid value distribution while other orientations engage a limited number of slip systems with Schmid values that diverge considerably compared to the remaining slip systems. As already thoroughly discussed in the previous section, it seems reasonable to assume that the number of activated slip systems can vary quite substantially for the various grains in a given microstructure. Therefore, it is important that the applied plasticity model captures these local variations.

Established algorithms for simulating plastic deformation of metals are normally calibrated and compared to tensile test curves. However, this global mechanical

Discussion

spread in Taylor factor than the value of the Taylor factor itself. It is also important to remember that the calculation method selected will affect the Taylor value more than the spread in the results.

Also there is some controversy regarding the results obtained from in-situ EBSD measurements. As presented in section 2.7.5, the EBSD technique has some considerable limitations since it only obtain information from the surface region of the specimen. It can therefore easily be claimed that the technique is insufficient since the acquired results are not representative for bulk deformation of the material. Hence, the results only provide a description of the surface behaviour, i.e. this work is only a study of near surface plasticity.

As already mentioned, the “Metal Structures in Four Dimensions”-group at Risø National Laboratory in Denmark is one of the groups which really has studied bulk rotations of individual grains by use of 3D X-ray diffraction (3DXRD). The rotation paths observed in several works performed at Risø is consistent with the rotation paths observed in this works (see e.g. Margulies et al. 2001 and Poulsen 2003). This indicate that the EBSD technique is actually able to capture the bulk behaviour during deformation, and it should therefore be reasonable to assume that the obtained observations can be used to determine the number of slip systems activated.

If a grain, for both conservatism and simplicity, is assumed to have a cubic shape and one cube plane is parallel to the surface, $5/6$ of the grain surface will be surrounded by other grains. Hence, the enforced constraint should be comparable to the constraint experienced by a bulk grain. Hence, also from this point of view, in-situ deformation in combination with EBSD investigations should be able to capture the true grain rotations during deformation.

6.3.4 Activation of slip systems – experimental observations vs. texture-based calculations

Crystal plasticity models attempt to describe the plastic deformation by utilising mathematical formulations. As already described in Chapter 2, both the mathematical formulations and the boundary conditions utilised vary from one plasticity model to

Discussion

section, it was argued that the reduced rotation observed in the material without texture is caused by the increased number of activated slip systems compared to the textured material. The surface-topography investigations clearly support this statement. The material will develop a more vigorous surface-topography when a reduced number of slip systems are activated (Choi et al. 2004). Few activated slip systems means that the limited number of slip systems has to carry all the enforced deformation. In other words, the relative movement (displacement) between activated slip planes is large compared to a material with many slip systems activated. Deformation on few slip systems will therefore clearly lead to a more vigorous surface-topography. This is also observed for the material investigated in this work as shown by the SE-micrographs in Figure 5.43 and Figure 5.49. The increased surface-topography observed for the material without crystallographic texture is also indicated by the IPF-maps presented in Figure 5.32 and Figure 5.34. The topography blocks the electron beam from reaching the “valleys” at the surface and the crystallographic orientation of that point can not be determined. As a consequence, a non-indexed point will become black on the IPF-map. The amount of non-indexed points is very large for the material without texture (Figure 5.34) compared to the material with texture (Figure 5.32). As discussed in section 6.2.2, this argument was also used to support the observed variations in slip activity through the material thickness.

From the discussion above, it seems clear that the number of slip systems activated varies substantially from grain-to-grain, and variations even within one individual grain are often observed. It is also indicated that the number of slip systems activated is less than predicted by the classical and widely used Taylor model. This will be treated more thoroughly in the next section (“Activation of slip systems – experimental observations vs. texture-based calculations”).

However, another important observation regarding activation of slip systems should first be treated. The Taylor factor gives an indication on how easy a material can be deformed. From a slip system point of view, it is reasonable to assume that a grain with a low Taylor factor needs to activate fewer slip systems than a grain which is harder to deform (high Taylor factor). In spite of this, the above observations can be summarised by stating that the number of activated slip traces seems to be more dependent upon the

Discussion

value distribution, it becomes evident that the slip traces must have been produced by slip on plane B. In other words, there is no slip activity on plane A during deformation to the uniform strain. Further, this confirms that if any slip should have taken place on slip plane A, this must have been early in the deformation process. The reason for this statement is that during deformation, the Schmid values of these systems are reduced to the same values as the slip systems on plane C (see Figure 5.57) hence the probability for slip on plane A and C are equivalent. As a consequence, it is reasonable to assume that this grain only activates two slip systems (B4 and B5) and that these systems tend to stay active until the material reaches the uniform strain.

Also the grain labelled #2 in Figure 5.34 illustrate very well how the use of slip traces together with the Schmid value evolution can be used to determine the number of slip systems activated in a material with random texture. Figure 5.51 and Figure 5.59 from section 5.6.2 present the slip trace evolution and the Schmid value distribution evolution of this grain. The Schmid value distribution gives the most favourable oriented slip systems, while slip traces combined with information about the crystallographic orientation provide information about the slip planes actually activated (Figure 6.20). Section 5.6.2 clearly shows that this grain only activate one slip system (A6) at low strains. Moreover, while some regions activate other slip systems at higher strains, A6 seems to remain as the only activated slip system in the centre region (the region labelled A in Figure 6.20). It has also been shown that at higher strains, this grain locally develops additional slip traces. This locally activated slip planes correspond with the slip systems of high to intermediate Schmid values, hence it is reasonable to assume that these slip systems are activated in these regions. Based on this, the two neighbouring regions with additional slip traces (the regions labelled A+C and A+B in Figure 6.20) most likely activate two (A6 and C1) and three (A6, B5 and B2) slip systems respectively. Again this confirms that the combinations of Schmid values and slip traces can be used to determine the number of slip systems activated. It also shows that the slip activity is very heterogeneous even within one individual grain.

The surface topography is another important indicator for activation of slip systems. It has been shown that the material condition with strong crystallographic texture tends to rotate more than the material condition without any texture (section 5.5.3). In the previous

Discussion

In general, the number of slip systems activated can not be determined by the Schmid value distribution alone. Ideally, a combination of Schmid values, slip traces, crystallographic rotations and if possible, local strain measurements should be utilised to obtain a reliable description of the amount of slip on the individual slip systems. However, in practise, the Schmid value distribution and the orientation of the observed slip traces are sufficient for determining the number of slip systems activated.

As was shown in section 2.2.2, the Schmid value distribution is determined by the given combination of crystallographic orientation and enforced deformation mode. Some orientations have 1-2 slip systems with high to very high Schmid values, while for other orientations almost all the slip systems have high Schmid values. Further, also combinations of orientation and deformation mode where all the slip systems have medium to low Schmid values exist. In other words, the Schmid value distribution throughout the microstructure varies substantial from grain-to-grain. From this relatively simple consideration, it is reasonable to assume that the number of activated slip systems will vary substantially through the microstructure. The observed slip trace evolution can be used to support this assumption. Frequently, only one set of slip traces is observed, something, which indicates that only slip systems on the corresponding slip plane are activated. In the case of congruent slip traces, slip systems from both slip planes can be activated. To illustrate how the Schmid values and the slip traces of the individual grains can be utilised to determine the number of systems activated, two different grains are discussed in more detail.

The first grain that will be treated is the grain labelled #1 in Figure 5.31. This grain is taken from a specimen deformed 45° direction and has a very unstable crystallographic orientation, i.e. a $101\parallel DD$. As already mentioned in section 6.3.2, this orientation gives rise to a special Schmid value distribution with four slip systems from two different slip planes (plane A and B) having very high Schmid values (Figure 5.57). Figure 6.13 presents the slip traces from this grain at 27% deformation and Figure 6.14 presents both the theoretical and observed in-plane slip trace angles from the same grain. From these figures it is clear that the grain possesses only one set of slip traces even though it could be argued that these traces originate from slip on both slip plane A and B. However, when the potential planes for producing this slip traces are compared with the Schmid

Discussion

During plastic deformation of aluminium, the effect of grain boundaries have been thoroughly discussed in the past (see e.g. Raabe et al. 2001). It is commonly agreed that grains split up into subgrains etc., during deformation. Formation of subgrains may be the most energy efficient way to satisfy the strain compatibility requirements. The observed orientation gradients are in other words the first step in producing a substructure.

Moreover, from the figures presenting the observed orientation gradients, it could be argued that grains with orientation gradients in average activate more slip systems than other grains. Based on the discussion above, this could explain way the experimental results show that grains with orientation gradients tend to rotate less than homogeneously oriented grains.

6.3.3 Selection of slip systems

Several decades ago, it was discovered that slip is the most important deformation mechanism for room temperature deformation of aluminium (see e.g. Verhoeven 1975 and Honeycombe 1984). Activation of a slip system means that slip takes place on that particular system, i.e. accumulation of dislocation and dislocation movement. Introduction and movement of dislocations lead to an increase of energy for the system. Hence, the most favourable oriented slip systems are therefore the first to be activated during deformation. The early works on single crystals by Garstone et al. (1956), Diehl (1956) and McKinnom (quoted in Clarebrough and Hardreaves 1959) all showed the close relationship between activation of slip systems and initial crystallographic orientation (Schmid value). The same authors have also treated the effect of crystallographic orientation on the local work-hardening.

As stated above, the Schmid value is among other factors often used to evaluate the potential for activation of the various slip systems. Further, the previous sections have shown that also grain size, morphology etc., can affect the activation of slip systems. However, the Schmid value, i.e. the crystallographic texture is by fare the most important in order to determine the activated slip systems.

Discussion

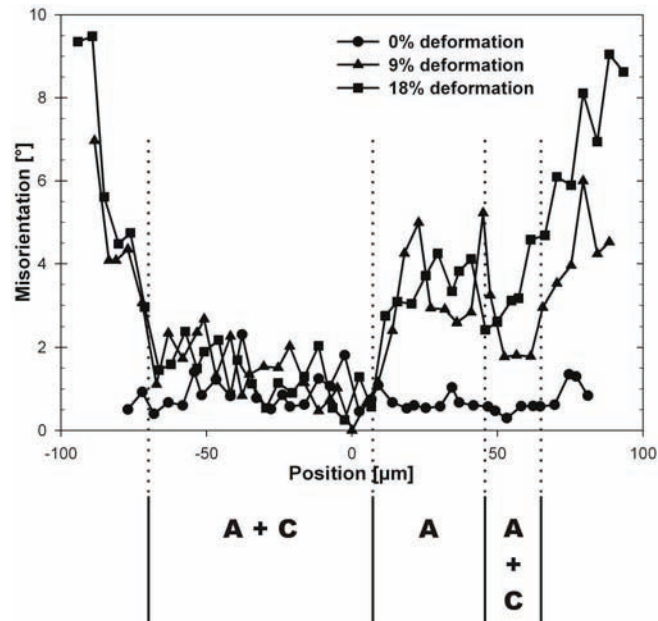


Figure 6.20 – Orientation gradient through the grain labelled #2 in Figure 5.34. The dotted lines indicate the different regions of comparable orientation. Also the slip planes activated within these regions based on the slip traces observed are indicated in Figure 5.51.

Figure 5.51 presents the slip trace evolution for the same grain as where the orientation gradient was investigated (orientation gradient parallel to DD). By comparing Figure 6.20 and Figure 5.51, it becomes clear that the shape of the orientation gradient is corresponding to the different slip trace-regions. Hence, it is reasonable to assume that there is a direct relation between slip traces, i.e. activation of slip systems, and the observed orientation gradients.

Orientation gradients seem to develop due to compatibility requirements. It has been shown that deformation within individual grains is primarily determined by the crystallographic orientation. However, since the material in question is a polycrystal, the deformation is also affected by the neighbours. The grain boundaries are therefore of great importance when it comes to compatibility. This can also be investigated by evaluating the slip traces intersecting the grain boundaries, since the ease of such intersections is related to the compatibility (see section 6.3.1 for more details).

Discussion

different crystallographic direction parallel to ND a low Taylor factor compared to the other grains. This could be used to explain the reduced amount of rotation. If the shown results are representative for rotations taking place, one can assume that an increased grain size leads to reduced crystallographic rotation upon deformation. The one reason for such behaviour could be that large grains are not as affected by the surroundings as a smaller grain would be.

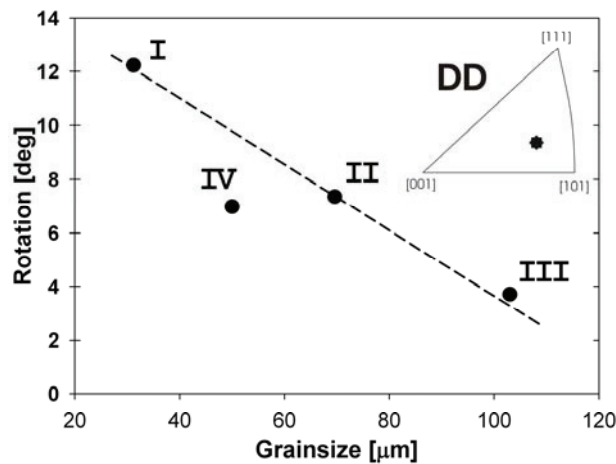


Figure 6.19 – Detected rotation from the initial orientation at the uniform strain as a function of grain size for four different grains (see Figure 5.34) with identical orientation parallel to the DD prior to deformation. The initial orientation prior to deformation is included in the DD IPF. The grain labelled IV has a different crystallographic direction parallel to ND compared to the other grains. Notice the linear relationship between misorientation and grain size as indicated by the dotted line.

Plastic deformation may also lead to a completely different type of crystallographic rotation. This type of rotations is observed within individual grains. Grains often produce internal orientation gradients during deformation which in turn leads to the smoothly curved slip traces discussed in the previous section. The orientation gradients develop more or less continuously during deformation and become more distinct close to the grain boundary (Figure 5.39). In some cases, the gradients develop in a more discontinuous manner, i.e. the grains consist of several regions of slightly different orientation. The measurements shown in Figure 5.40 are an example of such behaviour. Even though the grain possesses an evident through grain orientation gradient, the grain interior can be divided into three separate regions with close to constant orientation (Figure 6.20).

Discussion

and Winther et al. 2004). Figure 6.18 presents the rotations taking place during deformation by use of Sachs (one active slip system) and Taylor FC (five active slip systems) type models. The results clearly show that the rotations predicted by the Sachs model exceed the predicted amount of rotation taking place when more slip systems are activated. The differences observed by varying the number of activated systems are comparable to the observed differences between a material without and with strong crystallographic texture. Hence, these observations support texture dependent rotations, i.e. materials with strong texture will rotate more than materials without texture due to a reduced number of slip systems activated.

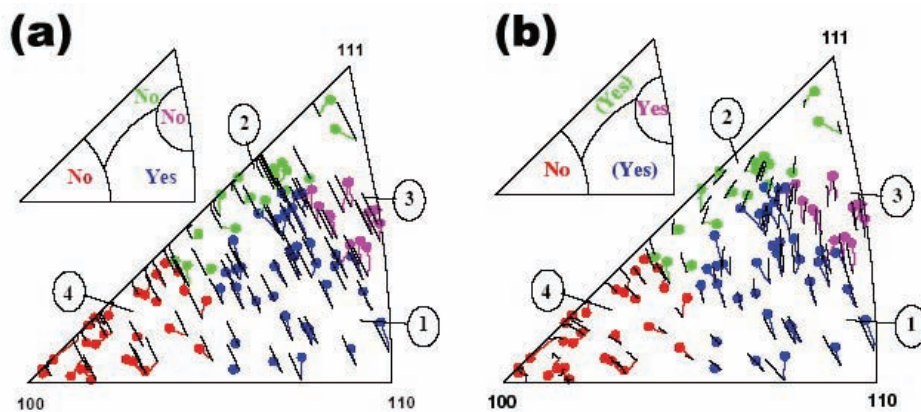


Figure 6.18 – Predictions of the rotations of the tensile direction by different plasticity models are shown as black lines together with the experimental data. The small stereographic triangle shows in which areas acceptable agreement between experimental and predictions are found. (a) Sachs model and (b) Taylor FC model (after Winther et al. 2004).

Another important phenomenon with regard to crystallographic rotation is the effect of grain size. It is almost impossible to isolate the grain size effect since at the same time also other parameters will affect the rotation behaviour. An example of such a parameter is the influence from the surroundings, i.e. crystallographic orientation of the nearest neighbours. The present investigations of the grain size effect were performed on material with random crystallographic texture in order to minimise the influence from the surroundings. Figure 6.19 presents the measured rotations taking place during deformation to the uniform strain for a given orientation parallel to DD as a function of the initial grain size. The grain labelled IV in this figure deviates from the linear relationship between the amount of rotation and grain size. Grain IV has due to a

Discussion

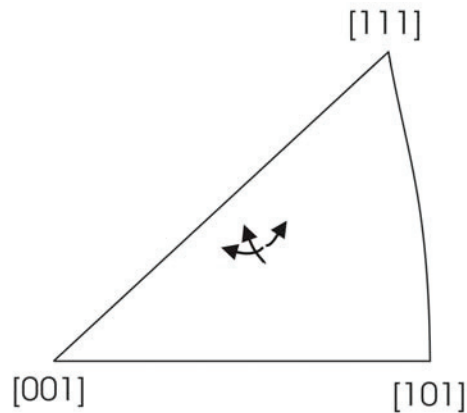


Figure 6.17 – Example of grains with close to identical crystallographic orientation prior to deformation rotating in different directions during deformation.

Also the amount of rotation is determined by the selection of activated slip systems. Since the only input for Taylor model calculations is the initial texture, the predicted amount of rotation is determined by the grains crystallographic orientation alone. However, the results presented in section 5.5.3 show that the rotations taking place are to a large extent dependent upon the orientation of the surroundings. Grains in a material with strong crystallographic texture (Figure 5.36) tend to rotate more than grains in a material without crystallographic texture (Figure 5.37). Again, this is most likely related to activation of slip systems. The constraint enforced by the surroundings is dependent on the compatibility between the deformation (activation of slip system) taking place in the grain itself and the nearest neighbours. A strong crystallographic texture means that a considerable fraction of the neighbouring grains have a comparable crystallographic orientation. This means that the constraint enforced by the surroundings is expected to be large for a material with strong crystallographic texture compared to a material without texture. As a consequence, the constraint enforced by the surroundings should be reduced for materials without texture. In other words, a material with random texture needs to activate more slip systems than a material with strong texture.

Further, the mathematics from basic crystal plasticity shows that the amount of rotation taking place will be reduced with an increased number of slip systems activated. The correlation between number of slip systems activated and the rotation taking place is very well illustrated in a number of works (see e.g. Margulies et al. 2001, Poulsen 2003

Discussion

distribution, and a third or the originally activated slip system will become the most potential. These repeating alterations in Schmid values will only lead to a very small fluctuation in crystallographic orientation and the orientation appears to be stable.

Also grains with a $[101]$ parallel to the DD have this special Schmid value distribution with four slip systems having identical Schmid values and the remaining having Schmid values equal to zero (Figure 5.55). However, still this orientation behaves quite differently. The rotation accompanying activation of one of these highly potential systems leads to a Schmid value increase, i.e. the initially activated slip systems will tend to remain active. In other words, the grain will continue to rotate in the same direction as shown in Figure 5.57.

To summarise, it is clear that some grains are stable because the activation of slip systems results in a small alteration of Schmid value distribution while other orientations are unstable because activation of slip systems leads to Schmid value strengthening of the same systems.

In general, the results presented in this investigation clearly confirm the statements above, i.e. the majority of the grains rotate in accordance with the predictions made by Taylor (see e.g. Figure 5.29 and Figure 5.35). However, it is also observed that grains initially having close to identical crystallographic orientations rotate in opposite directions. The three grains in Figure 6.17 illustrate such rotation behaviour for a sample with random crystallographic texture deformed perpendicular to the ED. The crystallographic rotations predicted by the Taylor model are a direct result of the embedded rules for activation of slip systems. This means that deviation from the predicted rotation behaviour indicates a deficiency in the prediction of slip activation.

6.3.2 Crystallographic rotations during deformation

It is beyond doubt that most grains tend to rotate during deformation. As already explained in section 2.2.3, crystallographic rotation is not a direct consequence of plastic deformation but rather an effect of the constraint enforced by the surroundings. The most important elements concerning the rotation path are therefore closely linked to the activation of slip systems in the grain itself. However, the activation of slip systems in the neighbouring grains, the grain size and shape can also affect the rotation paths.

Further, it has been shown (see e.g. Figure 5.35) that both the amount of rotation and the rotation paths are strongly dependent upon the initial orientation. Crystallographic rotation of both single- and poly-crystals has been studied in great detail in the past, and it has been shown that the rotation paths are usually quite well described by the Taylor (1938) model (see e.g. Bunge and Fuchs 1969, Han et al. 2003 and Winther et al. 2004). The Taylor model states that grains rotate toward aligning either a [100] or [111] parallel to the DD.

In order to comprehend the rotations taking place, it is important to realise why grains having these directions parallel to the DD tend to be stable, while grains not having this configuration often contend to align these axis to the DD. From the discussion above, it is reasonable to assume that the stable behaviour of these orientations is related to the Schmid value distribution. The experimental results have clearly shown that eight of the twelve slip systems (two from each slip plane) have identical Schmid values when the grain has a [100] parallel to the DD (Figure 5.55). Moreover, when a grain has a [111] parallel to the DD, six slip systems from three different slip planes have identical Schmid values. In other words, the Schmid value distribution for both these orientations is very special.

Further, it is known that when a slip system is activated in grains with one of these orientations, the accompanying rotation give rise to an increase in Schmid value for the slip systems on the other planes, while the Schmid value of the activated slip system itself is reduced. As a consequence, the Schmid value distribution is slightly altered. The slip system originally activated is no longer the most potential, and often another slip system will be activated instead. This will in turn slightly alter the Schmid value

Discussion

Further, the slip traces of an individual grain can be affected by the deformation mechanisms taking place at the nearest neighbours as illustrated in Figure 6.16. The primary slip traces (violet) are produced due to deformation on the slip system/systems with the highest Schmid value/values. Further, additional slip traces induced by the nearest neighbours can be categorised based on their appearance. Some slip traces can intersect the grain boundary and continue through the entire grain in question (green). This is most common for neighbouring grains having slip planes with close to identical orientation (see e.g. the specimens of AA6063 deformed 45° related to ED). Further, in some cases, the induced slip traces are not able to continue through the entire grain but are terminated close to the grain boundary (blue). This means that the slip systems on the slip plane corresponding to the primary slip traces on the neighbouring grain have low Schmid values. Hence, the terminated slip traces observed are generated only in order to fulfil the compatibility requirements over the grain boundary. The red slip traces also intersect the grain boundary, but do hardly continue into the centre grain. However, some of these slip traces are also observed close to the grain boundary between the centre and top grain, and are most likely activated to fulfil the compatibility close to the triple junction.

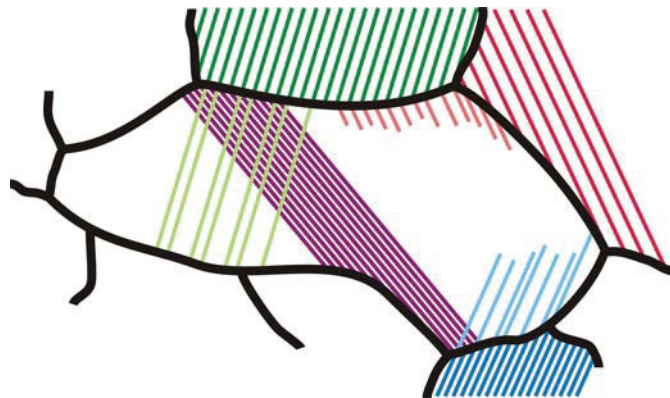


Figure 6.16 – Schematic illustration showing the effect of primary slip traces observed in neighbouring grains. The violet traces illustrate the primary slip traces of the centre grain. The green slip traces are the primary slip traces of the top grain, but similarly oriented traces are continuing in the center grain (light green). The primary slip traces of the bottom right grain also intersect the grain boundary, but these slip traces are not able to continue through the centre grain. The red slip traces observed in the top right grain also intersect the grain boundary, but do hardly continue into the centre grain.

Discussion

planes along a line crossing through grain number 2 after 27% deformation. Again, it is evident that the observed curvatures were related to crystallographic rotation and not to activation of additional slip systems since β_{obs} is identical to one of the β_{theo} numbers along this line.

However, also another type of non-linear slip traces is observed. This type is more discontinuous and the appearance is somewhat wavier. It is also worth noticing that the slip trace distance is often enhanced for this type of grains. The big grain labelled X in Figure 5.48 is a perfect example with clearly non-linear slip traces. From the illustration of this grain (Figure 6.15), it is clear that slip traces can be divided into different regions belonging to different crystallographic planes. The different segments are all crystallographic dependent, but the overall slip-trace-shape is wavy. Irregular slip traces like this is only observed for orientations with two almost parallel theoretical slip traces, i.e. slip systems from two different slip planes have close to identical Schmid values. Hence, this type of slip traces is often observed for grains with close to a $100\parallel DD$. As indicated, the reason why these grains behave in this remarkable way is most likely related to the Schmid value distribution. Slip systems from both slip planes have close to identical Schmid values and the activation of slip systems are determined by external constraints, as will be discussed in more details in the following section.

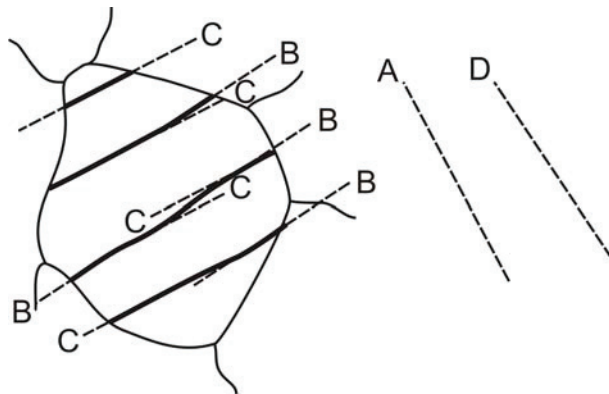


Figure 6.15 – Illustration of the irregular slip traces observed at the specimen surface of the big grain labelled X in Figure 5.48. The primary slip traces consist of different sections belonging to plane B and plane C respectively. Hence, the slip traces are not linear but rather curved. None of the parallel sections within the slip traces belong to plane A or plane D. The theoretical in-plane angle of slip plane A and D is indicated on the right hand side.

Discussion

observed curvatures originate from crystallographic rotations and not from activation of additional slip systems since β_{obs} is identical to one of the β_{theo} numbers along this line.

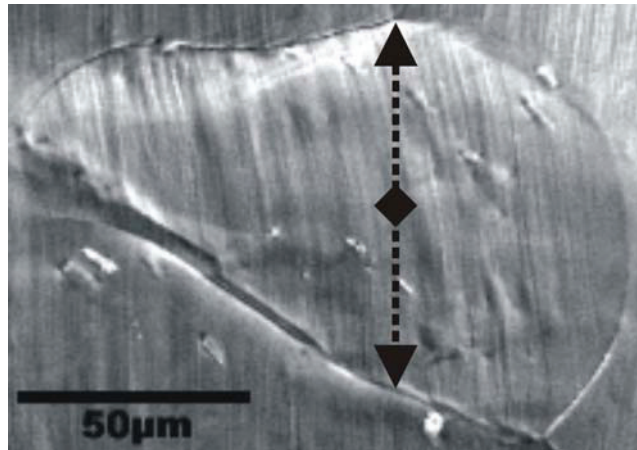


Figure 6.13 – Observed slip traces in grain labelled #1 in Figure 5.28 at 27% deformation. The observed slip traces are curved due to orientation gradients. The black two-headed arrow indicates the location on the grain surface of the orientation profile presented in Figure 5.39 and Figure 6.14.

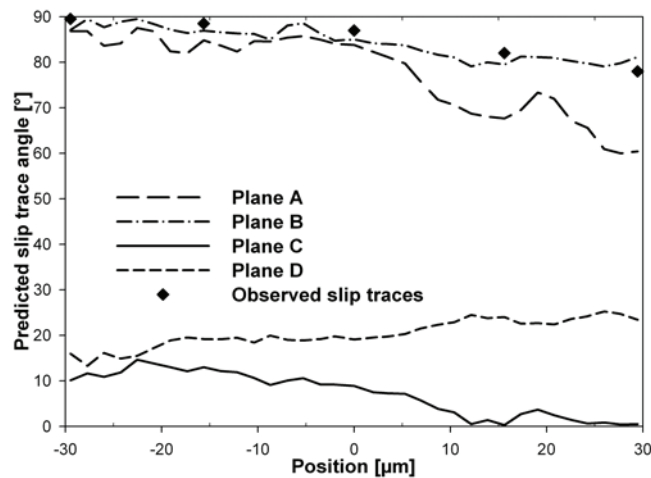


Figure 6.14 – Evolution of theoretical in plane slip traces angle (β_{theo}) for the four $\{111\}$ -planes based on orientation profile through the grain labelled #1 in Figure 5.31 at 27% deformation. The observed angle (β_{obs}) along the orientation profile is also included.

As a result of these significant misorientation gradients, the slip traces would no longer be straight lines crossing through the grains but rather they would become curved, e.g. see Fig. 11. The same figure also presents parameters β_{obs} and β_{theo} of the four $\{111\}$ -

Discussion

“soft” yield point which was attributed to the initiation of slip in the different slip systems. This is also confirmed by the slip trace evolution (Figure 5.43) where it is clear that some grains develop visible slip traces prior to other grains.

Further, it has been shown that grains deformed in the 45° direction (Figure 5.44) generally develop only one set of slip traces (primary slip traces) below 12%, while the number of visible slip traces varies significantly when deformed in the two other directions, especially when deformed perpendicular to the ED (Figure 5.45). However, grains from the 45° direction also develop additional set of slip traces (secondary slip traces) at higher strains (15%). The additional sets of slip traces are always seen close to grain boundaries or triple junctions (see e.g. Figure 5.46). Local slip traces probably develop because the already activated slip systems are not able to accommodate the deformation enforced by the surroundings (i.e. compatibility requirements). The enforced constraint will most likely give a shear stress contribution, $\Delta\tau$. This means that the local resolved shear stress experienced (τ_{loc}), is increased by the amount $\Delta\tau$ such that it exceeds the critical resolved shear stress τ_{CRSS} for the additional activated slip system. This means that an additional slip system is activated when;

$$\tau_{loc} = \tau_{res} + \Delta\tau \geq \tau_{CRSS} \quad (32)$$

It has been shown that the slip trace direction is crystallographic dependent, i.e. β_{obs} is determined by the crystallographic orientation. However, detailed slip trace investigations showed that some grains possess non-linear slip traces. The divergence from the linear appearance could in some cases be explained by crystallographic through-grain orientation gradients. Non-linearity related to orientation gradients is in general very smooth and do often enhance toward to the grain boundary as shown for a grain deformed to the uniform strain (Figure 6.13). The smoothly curved slip traces and the enhanced curvature for this grain which is deformed 45° related ED are consistent with the orientation gradients observed after deformation to intermediate and high strains (see Figure 5.39). This has been confirmed by calculating β_{theo} of the four $\{111\}$ -planes at different position along the orientation gradient and comparing these values to the β_{obs} at the corresponding positions (Figure 6.14). Based on this information, it is reasonable to claim that this type of observed curvatures is related to orientation gradients, i.e. the

Discussion

The same micrographs also show that the slip trace appearance and density varies significantly from grain to grain within one deformation direction, especially for the specimens deformed 0° and 90° related to ED. Earlier works, i.e. Delaire et al. (2000), Zhang and Tong (2004) and Henning and Vehoff (2005) have reported more extensive development of secondary slip traces during simple tension of polycrystalline materials than observed in the present work. In other words, they observe that the grains deform by multiple slip at very low strains (4%) and close to 50% of the grains investigated developed additional slip traces. To be noticed, most of the grains from the present material with a strong crystallographic texture have their primary slip systems aligned in a similar way, hence the compatibility requirements are probably reduced and there is less need for activating additional slip systems.

The specimens deformed in the 45° direction possess a much more homogeneous slip trace distribution compared to the other two directions and all the grains develop slip traces very early in the deformation process, e.g. most of the grains have developed visible slip traces already after 3% deformation. The DD IPF in Figure 5.28 (b) indicates that the majority of the grains have a $101\parallel DD$ when deformed 45° to ED. Most of the grains have quite similar initial orientations, i.e. the slip systems possess a similar resolved shear stresses (τ_{res}) distribution and all the individual grains will therefore behave similarly. This is also confirmed by the Taylor factor map presented in Figure 5.54. Most of the grains have a $100\parallel DD$ (Figure 5.28 (a)) when deformed parallel to ED. The different slip systems within the individual grains will also in this DD possess similar τ_{res} -values. As a consequence, all grains should therefore start to deform (produce visible slip traces) simultaneously as already discussed in section 6.1.2. However, this is not the case observed, as shown in Figure 5.41. Some grains develop visible slip traces already after 3% deformation while other grains do not produce visible slip traces even at the uniform strain (12% deformation). This is most likely do to the intrinsic nature of aluminium deformed parallel to a $\langle 100 \rangle$ direction, i.e. 8 of 12 slip systems have equal and very high Schmid values (Figure 5.55). It is reason to believe that both constraint from the neighbouring grains and only small deviations from the perfect Cube orientation will alter the slip distribution, hence altering the slip trace distribution. However, these considerations will be treated more thorough in the following sections. Section 6.1.2 also showed that the specimens deformed 90° have a

6.3 Deformation mechanisms and crystal plasticity

The work presented so far has shown that extruded profiles often possess strong mechanical anisotropy. It has also been shown that the through-thickness variations often observed in these profiles may influence the profile shape due to variations in anisotropy. Through-thickness variations will therefore often make it more difficult to predict and control final shapes after a given forming operation. It has previously been shown (see e.g. Yau and Wagoner 1993, Han et al. 2004 and Winther 2004) that the actual activation of slip systems is a determining factor for the observed mechanical anisotropy during deformation. This section will therefore address a discussion concerned with plasticity in textured materials carrying microstructural and textural gradients. A close evaluation of the microstructure evolution upon plastic deformation will be given, before the crystallographic rotations and activation of slip systems will be discussed in detail.

6.3.1 The nature of slip traces

The experimental results presented in Chapter 5 show that the crystallographic texture and microstructure evolution has been carefully monitored by performing EBSD investigations and acquiring SE micrographs at different strains during deformation. SE micrographs reveal that AA6063 tends to deform in a localised manner, i.e. produces evident slip traces.

The theoretical in-plane slip trace angle (β_{theo}) of all crystallographic planes can be calculated based on the crystallographic orientation of the grain (section 2.5.1). This information in combination with the observed orientation of the visible slip traces (β_{obs}) can then be used to identify the slip planes activated during deformation. The calculations performed for all investigated grains showed that the difference between β_{obs} and β_{theo} from one of the $\{111\}$ -planes never exceeded 3° . This fact clearly confirms that the plastic deformation of aluminium takes place on the closed-packed $\{111\}$ -planes.

Microstructure micrographs at different strain states (Figure 5.41-Figure 5.43) reveal that the slip trace evolution is strongly dependent upon the deformation direction selected.

6.2.7 Final comments on profile thickness strain distribution

Both simple tension experiments with reduced specimen thickness (Figure 5.14) and the observed end of cross-section shape (Figure 5.20) indicate a very heterogeneous through-thickness strain distribution for the investigated profiles. This is further supported by the local strain distribution measurements of AA6063 presented in Chapter 5.7. The calculated strain distribution maps from measurements show that strain localisation takes place in well-defined straight bands through the profile thickness. The thickness and density seem to be dependent upon the deformation direction and Chapter 6.3 will treat this topic in more detail.

Even though the origin of the observed strain heterogeneities take place in areas with low Taylor factors, the localised deformation seems to grow into bands with a 45° angle related to the deformation direction. These bands expand through the thickness of the specimen and are most likely the precursors to macroscopic shear localisation (see Figure 5.73 and Figure 5.74). When the through-thickness strain distribution is compared with the Taylor factor maps of the same area (Figure 5.72), it is evident that there is no correlation between the localised bands and the Taylor factor of the individual grains. In other words, Taylor factor heterogeneities may act as nucleation points for the macroscopic strain heterogeneities. This assumption is strongly supported by Duan et al. (2005), who were able to predict the formation of shear localisation during simple tension deformation simulations of an Al-Mg alloy by taking advantage of the heterogeneities in mechanical properties, i.e. variation in Taylor factors. The variations are clearly directional dependent, i.e. they are most likely linked to the crystallographic texture.

To summarise, the observed strain distribution is consistent with both observations of variations in plastic strain ratios (r -values), end of cross-section shape and the results from texture-based calculations. Also the measured through-thickness strain distribution supports the above findings. Such effects can therefore complicate the understanding of extruded aluminium profiles with regard to forming behaviour (see Chapter 6.4).

Discussion

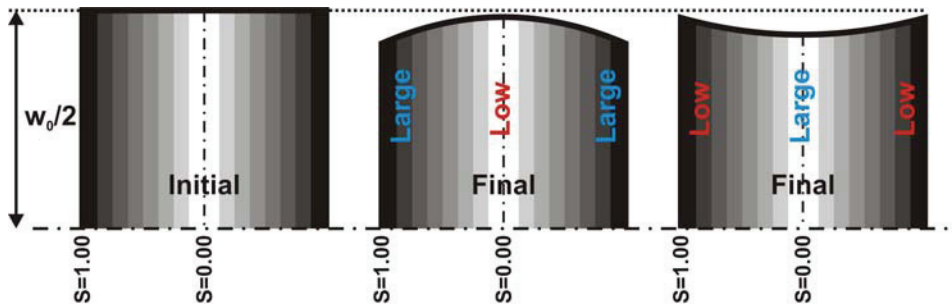


Figure 6.12 – Schematic illustration presenting the effect of r -ratio variations through the thickness of a simple tension specimen. A specimen with low r -values at the surface and a large value in the centre will develop a concave shape. The opposite r -value distribution will result in a convex through-specimen-thickness-curvature.

Comparisons of the calculated r -values from the centre and surface positions with the through-specimen-thickness-curvatures, confirms that the variations in plastic strain ratio can be used as an explanation of the observed curvatures (Table 6.1). The results even show that the radius of curvature (Figure 5.21) is consistent with the differences in r -values observed between the centre and the surface layer. However, the behaviour of the specimens deformed in the 45° direction (AA6082) is different from the other orientations. The r -value variations in this deformation direction should develop a concave shape, however a weak convex shape is observed. This latter behaviour can not be explained based on the results obtained in this work.

Table 6.1 – Texture-based calculations of the plastic strain ratio using the Taylor RC method, and the corresponding observed tensile cross-sectional shape.

Alloy	Direction	Calculated r -value		Observed shape
		Centre	Surface	
AA6063	0°	1.5	0.4	Concave
	45°	0.1	3.1	Convex
	90°	3.1	0.8	Concave
AA6082	0°	0.3	0.4	Straight
	45°	2.3	1.9	Convex
	90°	1.5	1.3	Straight

Discussion

This means that models activating only a limited number of slip systems are more accurate than the conventional Taylor FC model. The same explanation could be used for the coinciding results obtained in this work since also the deformation of AA6063 and AA6082 tend to localise.

The through-thickness variations in plastic strain ratio can therefore be used to explain the through-specimen-thickness-curvatures observed after simple tension deformation in different directions (see Figure 5.20 and Appendix D). Since,

$$r = \frac{\varepsilon_w}{\varepsilon_t} \quad (28)$$

this means that a material obtains a large r -value if ε_w is relatively large (or ε_t is relatively low). Implicitly, the material obtains a low r -value if ε_w is relatively low (or ε_t is relatively large). The transversal strain is directly linked to the initial and final width of the specimen:

$$\varepsilon_w = \ln \frac{w}{w_0} \quad (29)$$

I.e. the through-thickness final width of the specimen can be used as a direct measure of the local plastic strain ratio through the thickness. A large r -value will result in a significant reduction of the width, while the initial and final width of a specimen with a low r -value is almost equal. Hence,

$$\text{Large } r \Rightarrow \text{Large } \varepsilon_w \Rightarrow w \ll w_0 \quad (30)$$

$$\text{Low } r \Rightarrow \text{Low } \varepsilon_w \Rightarrow w \approx w_0 \quad (31)$$

By using the measured transversal strain as input to the plastic strain ratio determination, it seems clear that a material with the largest plastic strain ratio in the centre will develop a concave cross-sectional shape. The same argumentation indicates that a material with the largest r -values at the profile surface will develop a convex shape during deformation (Figure 6.12).

Discussion

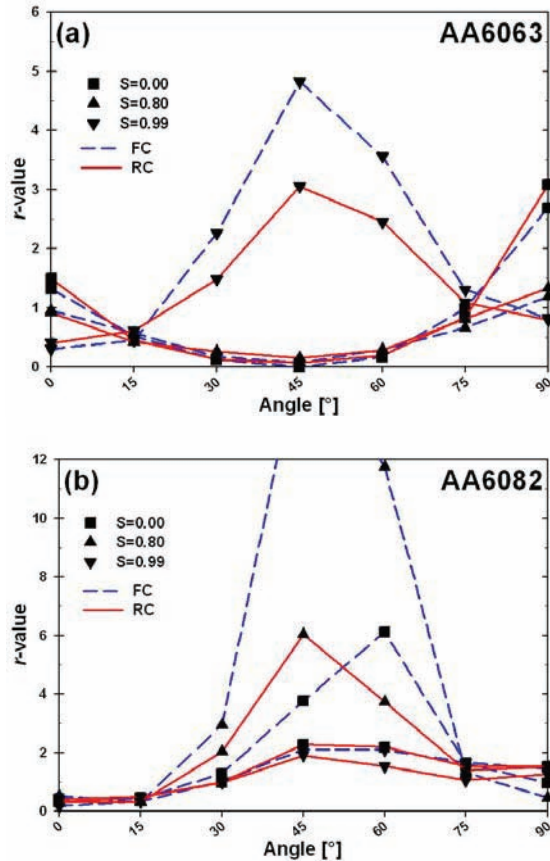


Figure 6.11 – Texture-based calculations of r -values at three different positions through the profile thickness as function of the tensile direction. (a) AA6063 and (b) AA6082.

Furthermore, the r -values calculated with the Taylor RC model corresponds remarkably well to the experimental values (Table 5.3). It is also clear that the FC method provide a qualitatively reasonable description of the plastic strain ratio. However, the FC method strongly exaggerated the r -values for both alloys. Fjeldly (1999) has performed the same type of calculations for one recrystallized (AA7030) and one fibrous (AA7108) profile by use of several different plasticity models. This author found that the qualitative results of all the models were satisfying, but only the less constricted models like the Sachs (AA7030) and the Taylor RC (AA7108) were able to provide quantitative reliable results. This behaviour can be explained by the localised deformation often observed for this type of alloys (Søreng 1997).

Discussion

The through-thickness variations in plastic strain ratio have been investigated in more detail by comparing texture-based calculations of r -values from three different positions through the thickness (Figure 6.11). Here, $S=0.00$ corresponds to the centre position of both alloys, $S=0.80$ corresponds to the middle layer of AA6063 and the outer part of the centre layer of AA6082, while $S=0.99$ corresponds to the outer surface layer. The centre and middle parts of AA6063 have a concave r -value shape (r -value as a function of deformation angle), i.e. these positions possess the highest r -values when deformed parallel or perpendicular to the ED and lowest when deformed 45° related to ED.

In fact, this is the typical r -value shape of materials having a recrystallized texture (Cube texture) like AA6063 (see e.g. Fjeldly 1999). However, the surface layer possesses the opposite behaviour, i.e. the 45° direction possesses the highest plastic strain ratio. From the graphs in Figure 6.11, it is evident that the two alloys behave fundamentally different with regard to the straining direction, i.e. the overall r -value shape of AA6082 is convex. Also for this alloy, the surface layer possesses more extreme r -values than the centre part of the profile. The calculated variations between the centre and surface layers observed for AA6063 and AA6082 are typical for extruded profiles with a recrystallized and fibrous microstructure respectively. Sørensen (1997) observed from experiments the same behaviour when studying the local plastic strain ratios of extruded AA7030 (recrystallized) and AA7108 (fibrous) profiles.

Discussion

direction while the 0° and 90° directions have lower and quite similar r -values. The angular dependency of the plastic strain ratios will certainly give rise to the macroscopic anisotropy as seen in Chapter 5.2. However, more importantly, the plastic strain ratio changes dramatically through the thickness. Figure 6.10 also shows the evolution of the calculated r -values from the centre ($S=0.00$) towards the surface ($S=0.99$). The variations in the actual plastic strain ratio can also affect the deformation behaviour locally. This means that the differences in mechanical properties observed in the different layers of the profiles (Figure 5.14) can partly be explained by variations in three dimensional plastic flow.

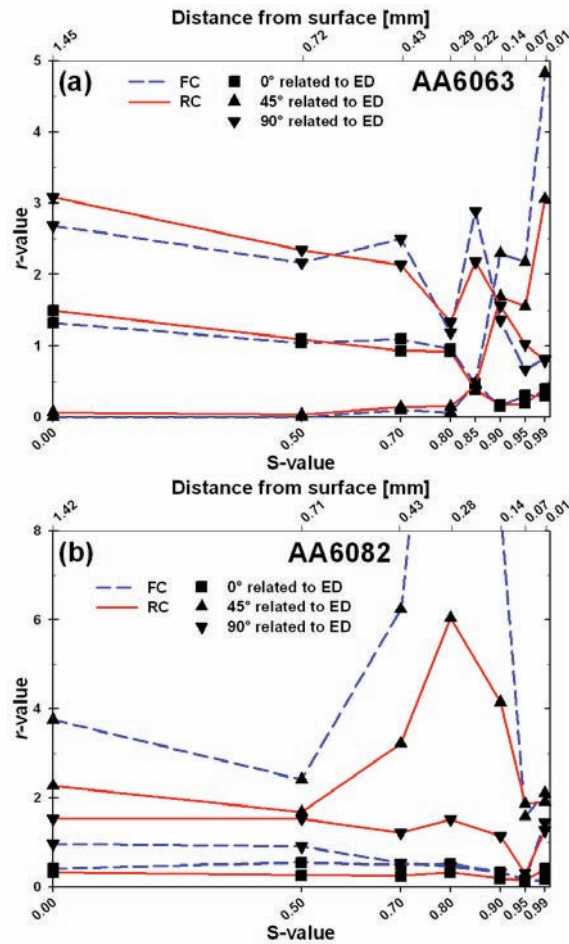


Figure 6.10 – Texture-based calculations of r -values at different positions through the profile thickness, applying both the FC and RC models. (a) AA6063 and (b) AA6082.

Discussion

6.2.6 Plastic strain ratios

As part of the thickness gradient study, the local r -values have been determined from simple tension investigations using thin specimens sampled from different positions through the thickness (Table 5.3). However, the accuracy of these measurements is very limited due to inaccuracy of the transversal strain measurements. This is mostly related to the reduced specimen thickness (0.3 mm) since the mounting of the transversal extensometer is very unstable. Some of these problems could have been overcome by utilizing the local strain measurement procedure known as the DSCA technique (Vacher et al. 1999) (Section 2.6.1 provides a description of this technique.). However, such measurements have not been performed in this work. It is therefore recommended that these measurements should be used only as an indication of the plastic strain ratio at the different positions investigated.

As mentioned above, the plastic strain ratio of different positions through the thickness has also been calculated based on the crystallographic texture (Figure 5.7 and Figure 5.10). Both the Taylor FC and RC methods have been utilised for these calculations (Figure 6.10). This figure clearly shows that the plastic strain ratio of AA6063 is almost unaffected by the calculation method utilised (especially in the centre region), while the r -values of AA6082 are very method dependent. This is most likely related to the orientation of the different slip systems with regard to the investigated deformation directions. It has been shown that the centre region of AA6063 is dominated by the symmetrical Cube orientation where the Burgers vectors of several of the most favourable oriented slip systems are parallel. The plastic strain ratio is therefore not so dependent upon the number of slip systems activated, since the net Burgers vector is almost unaffected. AA6082 on the other hand has a more unsymmetrical slip system distribution and will therefore be more dependent upon the number of slip systems activated. Consequently, the plastic strain ratio is strongly affected by the Taylor model utilised.

It seems clear from these calculations that the plastic strain ratio is strongly angular dependent. A macroscopic (full thickness) consideration shows that AA6063 has large r -values in the 0° and 90° directions and r -values close to zero when deformed 45° related to ED. AA6082 on the other hand, has a large r -value when deformed in the 45°

Discussion

6.2.5 Internal stresses

The issue of internal stresses and corresponding strains during deformation is another important feature which has not been treated in the above discussion. Internal stresses are known to develop at the grain boundaries due to compatibility requirements (Li and Bretheau 1989). Further, it is known that micro-textural variations will increase the amount of internal stresses, since heterogeneities will worsen the compatibility conditions at the grain boundaries. This means that strong texture gradients could lead to large internal stresses in extruded profiles like the present AA6063 alloy. Internal stresses can assist to accommodate for the interaction between the different layers through the profile thickness. However, it is very difficult to quantify such stresses on a local scale, but it is to some extent possible to obtain qualitative information by investigating the specimen behaviour during unloading.

Measurements of the internal stress evolution have not been performed in the present case. However, it is observed that thin specimens taken from the surface layer of both alloys, exhibit a curved shape after unloading (Figure 6.9). This curvature can of course be attributed to development of internal stresses, but it can also be linked to variations in the plastic strain ratio (due to crystallographic texture and the associated slip distribution) as will be discussed later.

Based on the discussions above, it seems evident that the effect of through-thickness variations on the mechanical properties is a very complicated topic. It is subjected to several counteracting phenomena which separately need to be understood in great detail in order to obtain a full understanding of the overall effect. However, it is clear that the texture gradient is a key element for such an understanding, but the interpretation of the texture effects and how they affect the crystal plasticity is not fully known.

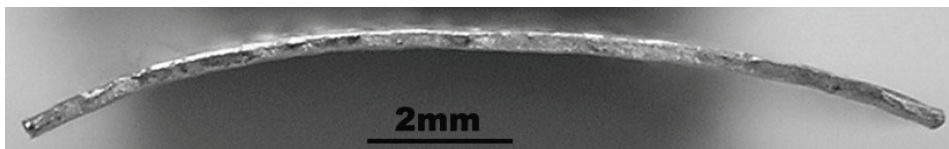


Figure 6.9 - Cross-section shape with evident curvature in the width direction of a specimen from the surface layer of AA6063 deformed to the uniform strain and unloaded.

Discussion

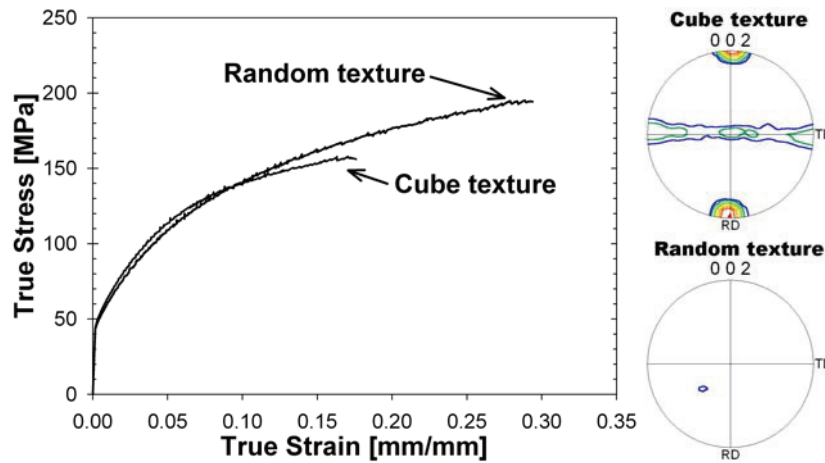


Figure 6.8 – Comparison of the stress-strain behaviour of a specimen with strong Cube texture and a specimen with random texture (after Furu and Pedersen 2006).

From the experimental results obtained by Furu and Pedersen (2006), it is reasonable to assume that the mechanical properties in the centre and surface layer of the AA6063 profile should be comparable when deformed parallel to ED. However, this assumption requires that the slip distribution (the number of activated slip systems) and the microstructure is independent of the through-thickness position. This is not the case (Figure 5.6), and some variations should therefore be expected. Based on the enlarged grain sizes and the reduced constraint from the surroundings close to the profile surface, it could be expected that the yield stress in the surface layer is somewhat reduced. This speculation is supported by the experimental results shown in Figure 5.14. However, the observed lower stress level can hardly be attributed to the real microstructure alone, but is most likely exaggerated do to the above discussed specimen thickness effect.

6.2.4 Final comments on the Voce-type modelling

On the other hand, the calculations performed by Fjeldbo et al. (2005) are in fact based on the assumption (homogeneous slip distribution and microstructure), thus these calculations should therefore be expected to provide only minor differences between the different layers. Consequently, the predicted results (Figure 6.5) are in strong contrast to the results found by Furu and Pedersen (2006) and the present results. This fact directs towards questioning the validity of the plasticity model used for these calculations, since neither the yield point nor the work-hardening rate is described satisfactorily.

Discussion

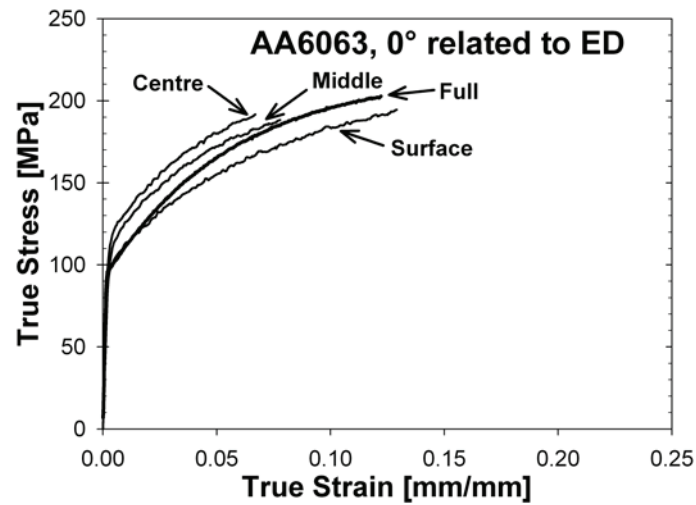


Figure 6.7 – Comparison of stress-strain behaviour from different positions through the thickness and bulk properties of AA6063.

Furthermore, simple tension specimens of AA6063 with both strong Cube (extruded profiles) and random texture (same material, but subsequently cross-rolled and annealed) have been investigated by Furu and Pedersen (2006) in the W, 10min condition (Figure 6.8). In this case, microstructural investigations revealed just minor differences in the microstructure (the cross-rolled material possesses somewhat smaller grain sizes). The idea was here to explore whether a random texture behaved differently from the strongly textured profile dominated by the Cube texture. Hence, the differences in stress-strain behaviour should be related to the crystallographic texture. The results showed that the textured specimen possesses a somewhat larger work-hardening rate (at low strains) and lower uniform strain than the specimen with random texture. However, it is clear that the deformation behaviour of the two specimens is comparable in spite of evident differences in texture (Figure 6.8).

Discussion

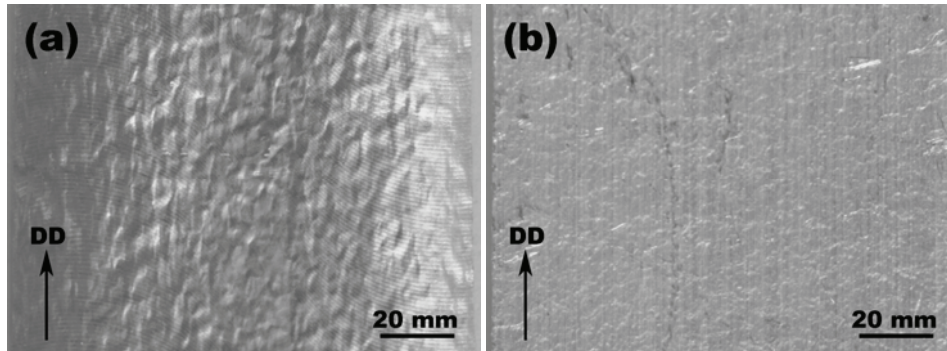


Figure 6.6 – The surface roughness of AA6063 after deformation to the uniform strain. (a) Thin specimen (0.3 mm thick) taken from the surface layer showing vigorous ‘orange peel’. (b) Full thickness specimen without any pronounced surface roughness. Please remember that the texture and grain size for both specimens is equal ($\sim 55\mu\text{m}$) since both are taken from the same position.

Also, it can be suggested that the initial yield strength of the thin specimens can be altered due to the reduced number of grains across the thickness. In some special cases, the specimen cross-section only consists of ~ 100 grains. Based on this fact, it can be expected that some coarse grained regions of the cross-section is more favourable oriented for slip (do not really represent the layer properties), and can therefore start to deform plastically prior to the “actual” yield stress, i.e. the measured yield strength is reduced. This is most likely not the case for the thin surface specimens investigated in this work, since the initial surface yield strength is equal to the full thickness yield strength, i.e. see Figure 6.7. Not surprisingly this figure illustrate that the full thickness data is roughly an average of the sub-layer properties for this test direction. On the other hand, both the experimental (Figure 6.7) and the calculated (Figure 6.5) differences between the surface layer (random texture) and the centre layer (strong Cube texture) can be questioned when compared to the stress-strain behaviour of full thickness specimens.

6.2.3 Experimental effects

It is important to remember that also the experimental results hold some significant limitations. The thickness of the used specimens (0.3 mm) in combination with the actual grain sizes in the normal direction (Table 5.2), especially close to the specimen surface (60-200 μm), means that the specimens from the latter position consist of a very limited number of grains. It is known that this can affect the deformation behaviour, i.e. the mechanical properties. The low number of neighbouring grains relaxes the constraint, making the specimen able to deform by a reduced number of activated slip systems. In addition, the effects from the free surfaces become more important for these specimens.

Furthermore, it is observed that the thin specimens taken from the profile surface develop a vigorous ‘orange peel’ surface topography during deformation (Figure 6.6 (a)). However, no orange peel is observed on the full thickness specimen surface (Figure 6.6 (b)). It has been reported that orange peel normally develops due to deformation on very limited number of slip systems (see e.g. Choi et al. 2004). This confirms that the deformation behaviour of the surface specimens have been altered due to reduced constraint conditions. It is therefore reasonable to assume that the surface stress-strain curve should have shifted towards higher stress levels if a more “correct” number of slip systems was activated during deformation. In such a case, the predictions (ref. Figure 6.5) and the experimental flow curves could approach each other.

Discussion

Further, it could be claimed that the observed differences between calculations and experiments are basically linked to the errors in the yield stress calculations. Hence, the shape of the stress-strain curves should be predicted satisfactorily by use of the Taylor factors as input to the Voce type model. However, none of the experimental curves can be predicted correctly by the calculated M -factors. Although, there is an adequate fit for the specimens taken from the centre region, and the texture of this region is equivalent to the global texture (which has been used for calibration of the fitting parameters). Therefore, it is only in this central layer that the calculated curves fit the experimental observations. One can, of course, claim that the observed differences can be related to an intrinsic error in the Voce type model, but it is more reasonable to assume that the disparities are related to the utilised Taylor factors.

Another important shortage with these calculations is not to include the Taylor factor evolution during deformation. One can expect that the M -factor in the centre region is almost unaffected since specimens with this type of texture tend to be stable during deformation in the strain-range typically associated with simple tension (see Figure 5.24). However, the surface region of the specimen (random texture) is not stable and is therefore expected to rotate toward more stable orientations (indicated by change of colour in the IPF maps in Figure 5.34), thus altering the Taylor factors.

Moreover, also the plasticity model utilised will affect the calculated results (M -factor), thus also the stress-strain curve. The alterations introduced by selecting another plasticity model are normally negligible, and it is therefore not reasonable to assume that the accuracy can have been improved by switching from the FC to the RC, or vice versa. However, if one can assume that the constraint from the neighbouring grains alters through the thickness, it can be expected that the number of activated slip systems can vary among the different layers. This means that the different layers is best described with various plasticity models, e.g. the surface layers is described by a Sachs type model (1-2 slip systems) while the centre region is best described by a Taylor FC type model (5 slip systems). Such variations will introduce predictions approaching the observed behaviour of the material.

Discussion

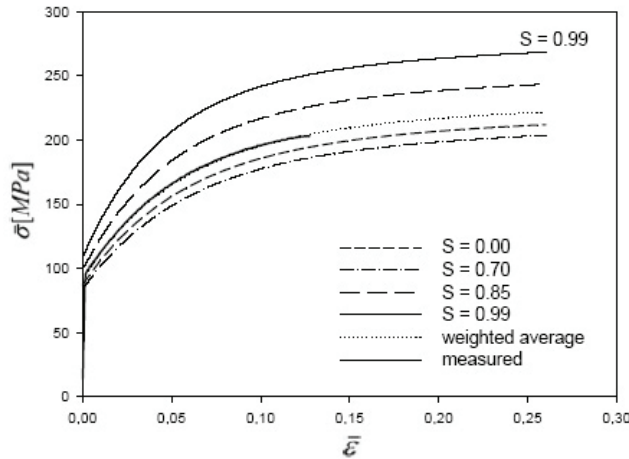


Figure 6.5 – Calculated variations of stress-strain curves parallel to the ED at different positions through the thickness of AA6063 (after Fjeldbo et al. 2005).

As expected, these texture-based calculations show that the mechanical properties of the different layers vary significantly. The calculations for the 0° orientation show that both the initial yield strength and the work-hardening rate is high for the surface layer ($S=0.99$) compared to the centre region ($S=0.00 - S=0.70$). However, these calculations by Fjeldbo et al. (2005) are in contradiction to the experimental results obtained from simple tension experiments performed in this work. Specimens taken from the different positions through the profile thickness have been tested (Figure 5.14) and the behaviour is completely opposite of the texture-based calculations. This means that in this direction (0°) the highest yield strength and work-hardening rate were found in the centre region (centre and middle positions) while the surface position ($S=0.99$) possessed both lower strength and less work-hardening.

As shown in Chapter 5, the AA6063 profile possesses an evident through-thickness microstructural gradient (Figure 5.6). It is expected that such variations will affect both the yield stress and the overall work-hardening rate (shape of the stress-strain curve), layer by layer. This is especially true close to the specimen surface, where the differences in grain sizes are extremely large (Table 5.1). Microstructural heterogeneities can be taken into account by varying the initial shear strain (τ_0) through the profile thickness ($\tau_0(S)$). Such variations are not included in the mentioned calculations, something which certainly reduces the validity.

Discussion

6.2.2 Evaluation of the Voce-type model

Furthermore, the observed through-thickness variations will affect the mechanical properties of the different layers through the thickness. Also the Taylor factor calculations indicate that the mechanical properties should vary significantly through the profile thickness. Fjeldbo et al. (2005) have calculated the mechanical properties of the different layers of AA6063 (0° direction), based on the orientation data acquired in this work (M -factors). In the latter work, the critical resolved shear stress (τ) has been expressed as a function of the resolved shear strain (γ) by an extended Voce expression (Voce 1948):

$$\tau = \tau_0 + \sum_{i=1}^2 Q_i [1 - \exp(-C_i \gamma)] \quad (26)$$

where τ_0, Q_1, C_1, Q_2 and C_2 are fitted parameters, determined from the experimental behaviour of a full thickness specimen. Further, the resolved shear stress and strain is here related to the true stress (σ) and strain (ε) by use of equation 25 with $M(\varepsilon) = M(0)$:

$$\bar{\sigma} = M \left(\tau_0 + \sum_{i=1}^2 Q_i [1 - \exp(-MC_i \bar{\varepsilon})] \right) \quad (27)$$

From the last expression, it is clear that the initial yield stress is scaled against $M\tau_0$, where τ_0 is strongly dependent upon the microstructure. Further, also the curve shape is a product of both the fitting parameters and the calculated Taylor factor. This means that the calculated stress strain behaviour (Figure 6.5) will be independent of microstructural variations between the individual layers, but is fully based on variations in crystallographic texture. Consequently, the relative ranking between the different layers through the thickness is fully determined by the differences in texture (M -factor).

Discussion

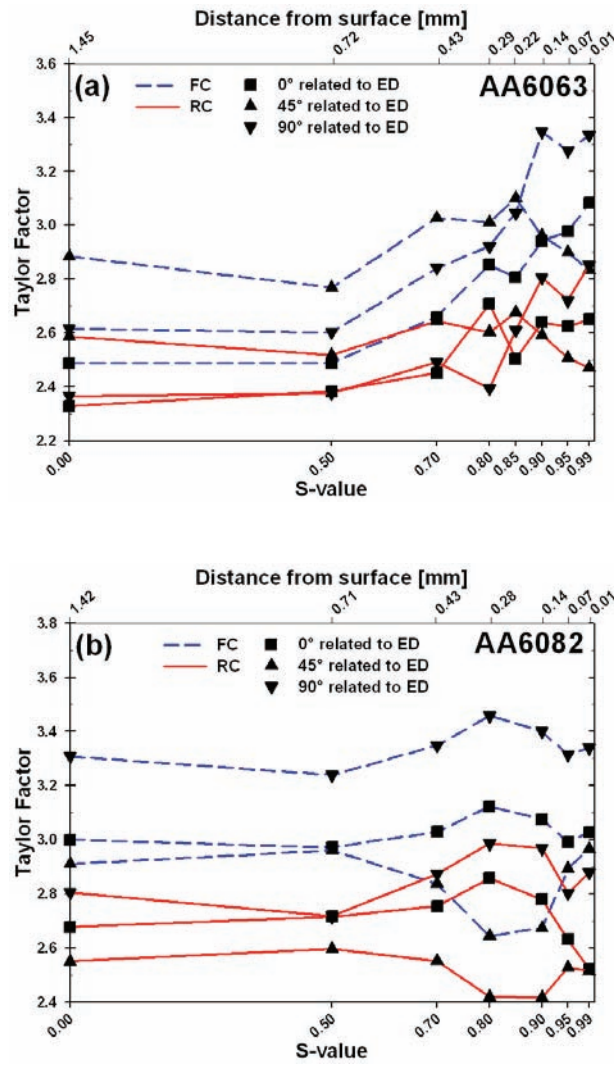


Figure 6.4 – Texture-based calculations of Taylor factors at different positions through the profile thickness. (a) AA6063 and (b) AA6082.

Discussion

method. The only difference between the two calculation procedures is the relaxation of two shear directions (ε_{13} and ε_{23}) for the RC-method (pancake shaped grains). Hence, the number of activated slip systems is five and three slip systems for the FC and RC method respectively. By comparing the results from these two methods one can evaluate whether the Taylor factor gradient can be directly linked to the activation of slip systems during deformation.

As mentioned above, the anisotropy differences in the M -factor between the FC and the RC calculations are more pronounced for AA6082 than for AA6063. The Taylor factor calculations of AA6082 made by the FC method are generally twice as high as the RC calculations. This indicates that AA6082 is more dependent upon the number of slip systems physically activated. Further, the calculations indicate that the resistance towards deformation increases more for AA6082 than for AA6063 if the material needs to activate five instead of three slip systems in order to deform. As expected, the FC calculations will always give a higher Taylor factor than the RC calculation and this is simply related to the activation of slip systems. The RC method takes use of the three slip systems most favourable oriented for slip, while the FC method has to add two additional slip systems which are more unfavourable oriented. Thus, the FC method will therefore always give a higher M -factor. However, a more detailed discussion on the number of slip systems activated during deformation and how this correlates to the different calculation methods will be discussed further in Chapter 6.3.

6.2 Observations and Taylor analyses regarding through-thickness variations

The results presented in Chapter 5 clearly showed that the investigated profiles possess evident through-thickness variations. There are different approaches to obtain an understanding of and the causes for these effects. The through-thickness variations can be engaged either by Taylor-type calculations or experimental investigations. This chapter will be used to discuss through-thickness variations as well as limitations with both methods of engaging this problem.

6.2.1 Taylor analyses

As already shown, the profiles investigated in this work possess strong texture and grain morphology gradients (see section 5.1.3). It is therefore reasonable to assume that Taylor-type calculations based on orientation data taken from the different position through the thickness will give rise to variations in mechanical properties. Therefore, initial crystallographic orientations have been used as input to Taylor method calculations of materials properties through the Taylor factor (M -factor). Also, the plastic strain ratio, or r -value, can be calculated based on the crystallographic orientation data. Taylor method calculations are performed at all the positions through the profile thickness ($S=0.00$ to $S=0.99$) with deformation tensors corresponding to simple tension at 0° , 45° and 90° related to ED. The Taylor full constraint (FC) and the relaxed constraint (RC) methods are used to predict properties for recrystallized (AA6063) and fibrous (AA6082) microstructures respectively. However, the evaluations are based on both methods in order to fully evaluate the texture-based calculations (e.g. see Figure 6.4).

The calculations based on the RC method show that the M -factor of AA6063 increases toward the surface when deformed in the 0° and 90° directions and decreases when deformed in the 45° (Figure 6.4). It is worth noticing that the RC method calculations of AA6082 give rise to the opposite behaviour as to AA6063, i.e. the Taylor factor decreases toward the surface when deformed 0° and 90° related to ED and increases when deformed in the 45° direction (see Figure 6.4). However, the Taylor factor increases toward the surface in all deformation directions when calculated by the FC

Discussion

Further, Figure 6.3 presents the $\sigma - \varepsilon$ curves for AA6063 in material condition T1 at the onset of plastic flow. These curves show that the specimens deformed parallel to the ED and to some extent 45° to, ED have much sharper elastic to plastic transition than the 90° specimens. This is most likely related to the activation of slip systems in the individual grains. The spread in Schmid values for the 90° specimens means that the individual grains will reach the critical resolved shear stress (τ_c^s) after various amounts of deformation, hence the material has a “soft” yield point. All the grains in the 0° specimen on the other hand, have a close to identical Schmid value distribution and will therefore reach the critical resolved shear stress at approximately the same strain, hence the 0° direction possesses a sharp elastic-plastic transition. To be mentioned, the crystallographic texture of AA6082 on the other hand, indicates that all the investigated directions have the same spread in Schmid values. This results in a similar transition for all directions.

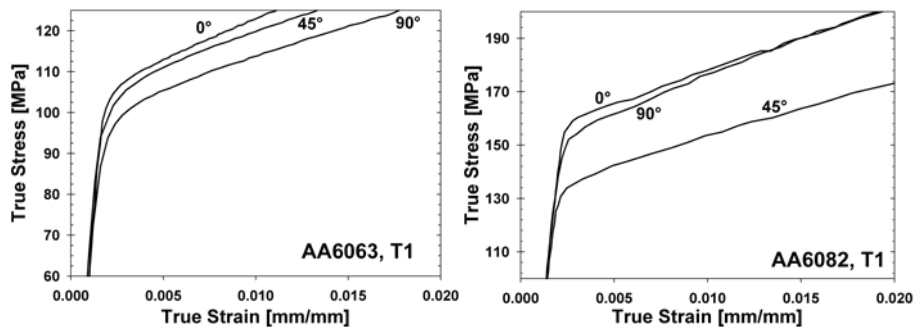


Figure 6.3 – Stress vs. strain behaviour at the onset of plastic flow for AA6063 (left) and AA6082 (right). Please note that this is segment of the whole true stress vs. strain curve.

The observed differences between the 0° and 90° specimens on one side and the 45° specimens on the other side are therefore related to differences in the Taylor factor, i.e. crystallographic texture variations. Hence, the anisotropy in yield strength and plastic deformation properties of AA6063 can be related both to variations in crystallographic texture and variations in crystallographic texture distribution (texture spread).

Discussion

and perpendicular to the ED respectively. As a consequence, the activation of slip systems will differ substantially during deformation in these two deformation directions, and both work hardening and the stress vs. strain contribution from these grains will be strongly directionally dependent.

The same argumentation can be used for the CG orientation. However, the differences are not expected to be as large as for the Goss orientation since the CG orientation is more stable in the 90° direction. When studying the different texture components during deformation, it is also conspicuous that the Cube orientation is extremely unstable during deformation 45° related to ED. The Cube orientation has a [110] parallel to the DD when deformed in this direction hence it is reasonable to expect a large reduction in the area fraction of Cube oriented grains during deformation in the 45° direction. It is also worth noticing that the texture evolution during tensile deformation is consistent with the grain rotation path and amount of rotation results presented in Chapter 5.5. From the above discussion, seems reasonable to believe that the observed texture evolution upon tensile straining could be used to support a texture dependent mechanical anisotropy.

However, it could be claimed that the above discussion does not take the interaction between the neighbouring grains into account. The accumulation and movement of dislocations in the vicinity of the grain boundaries are normally dependent on the orientation of the neighbouring grains and will therefore substantially affect the work hardening contribution of the different texture components. The slip-trace investigations presented in section 5.6.1 show that there is an evident directional dependency on how slip traces intersect the grain boundaries (see e.g. Figure 5.46 and Figure 5.47). The micrographs indicate that the slip traces intersect the grain boundaries quite easily when deformed 45° to ED, while intersections seem to be more difficult when deformed parallel or perpendicular to ED. However, the latter statement is difficult to prove. Deformed specimens should therefore be investigated in a transmission electron microscope (TEM) in order to determine any slip activation differences between the 0° and 90° directions. Anyway, if a statistically significant variation with regard to the crystallographic orientations of the neighbouring grains exists, this is governed by the texture. Hence, also this issue supports a texture determined mechanical anisotropy.

Discussion

performed on single crystals may also be valid for deformation of polycrystals. As mentioned above, nearly all the grains have a [100] parallel to the DD when deformed parallel to the ED, while other crystallographic directions are present when deformed perpendicular to the ED. Hence, it is reasonable to assume that the specimens deformed parallel to ED have more pronounced work hardening at low strains. This is consistent with the observed stress vs. strain relationship in the solutionised and natural aged condition for AA6063 as shown in Figure 5.12, i.e. the 0° specimens have a high work hardening rate compared to the two other directions.

The area fraction evolution of the different texture components is also interesting with regard to the observed anisotropy. The texture evolution presented in Figure 5.27 shows that the stability of the different ideal texture components depends on the DD selected. It is important to remember that both the Cube, CG and Goss orientations all have a [100] parallel to the ED (ED rotated Cube orientations). Hence, since the crystallographic orientation parallel to the DD is of main importance with regard to grain rotation during deformation (see Chapter 5.5) these orientations will behave similarly when deformed parallel to the ED. The highly symmetrical Cube orientation is stable both parallel and perpendicular to the ED during deformation to low and intermediate strains. The intensity of the Cube orientation is however slightly reduced at high strains ($>15\%$) when deformed in the 90° direction. This means, at least at low and intermediate strains, that the cube oriented grains are expected to give the same work hardening and stress vs. strain relationship contribution when deformed 0° and 90° related to ED. However, for this assumption to be valid, the orientation of the neighbouring grains should not affect the slip behaviour of individual grains. This assumption is therefore not completely valid, but it should at least give a good indication of the work hardening contribution from Cube oriented grains.

The Goss grains on the other hand have a more unsymmetrical crystallographic orientation with regard to the 0° and 90° deformation directions. Hence, the stability of this orientation is more dependent of the selected DD. Figure 5.27 shows that the Goss orientation is stable during deformation parallel to the ED while very unstable during deformation perpendicular to the ED. Grains with a Goss orientation have as already mentioned several times, a [100] and a [110] parallel to the DD when deformed parallel

Discussion

In the past several investigations have been performed on materials having a strong Cube texture and it was suggested that the mechanical anisotropy mainly is controlled by the crystallographic texture (e.g. Li and Bate 1991, Lopes et al. 2003 and Wu et al. 2004). Common for all these investigations is the large $0^\circ/90^\circ$ symmetry of the texture. Hence, these materials possess close to equal properties 0° and 90° to the ED. However, the Cube component of the recrystallized AA6063 alloy investigated in this work, is somewhat rotated around the ED. Therefore possesses this material a much more asymmetrical distributed but equally strong Cube texture. Hence, the ED rotated Cube gives rise to differences between the 0° and 90° as shown by the inverse pole figure (IPF) maps presented in Figure 5.28. Almost all the grains (Cube, CG and Goss oriented grains) have a $[100]$ direction parallel to the DD when deformed parallel to ED. When deformed perpendicular to ED, the same grains have non-equal crystallographic directions parallel to the DD. Grains with a CG or Goss orientation have a $[012]$ or a $[110]$ parallel to the DD respectively. This may indicate that the Schmid values of the individual slip systems are strongly altered compared with deformation parallel to ED (Figure 5.55). The spread in crystallographic orientations parallel to the TD means that the probability for slip differs significantly among the individual grains. This is supported by the Taylor factor histogram and maps, given in Figure 5.53 and Figure 5.54 respectively, showing large variations between neighbouring grains in all directions compared to the 0° direction. It has been shown (section 5.6.1) that the orientation spread observed in the 90° specimens leads to a heterogeneous activation of slip systems. Further, it is reasonable to assume that this will affect the macroscopic stress-strain behaviour of the material and could therefore contribute to explain the observed anisotropic stress-strain curves.

Moreover, it has also been reported that the crystallographic orientation parallel to the DD is of great importance for the work hardening, especially at low strains (Honeycombe 1984). Diehl (1956) performed detailed investigations of the work hardening rate at low strains for copper single crystals with a wide range of crystal orientations. He found that crystallites with a $[110]$ parallel to the DD have a lower strain hardening rate than crystallites oriented near the line attaching the $[100]$ and the $[111]$ corners of the inverse pole figure. This behaviour has also been confirmed for aluminium (see e.g. Lucke and Lange 1952, Noggle and Koehler 1957). These observations

Discussion

calculations reveals a shear stress level ~20-70% above the experimental values (W-condition).

Further, if the anisotropy is assumed to be caused by crystallographic texture, these calculations reveal that the material tend to deform with fewer activated slip systems than assumed in the classical Taylor full constraint (FC) method. This will be further discussed in Chapter 6.3.

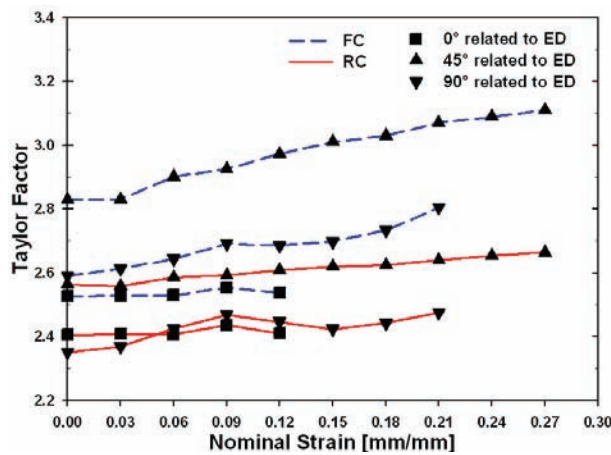


Figure 6.1 – Evolution in Taylor factor during straining of AA6063 0°, 45° and 90° related to ED. Calculations are performed with both full constraint (blue) and the relaxed constraint (red) Taylor model. Please, note that deformation is given in nominal strain.

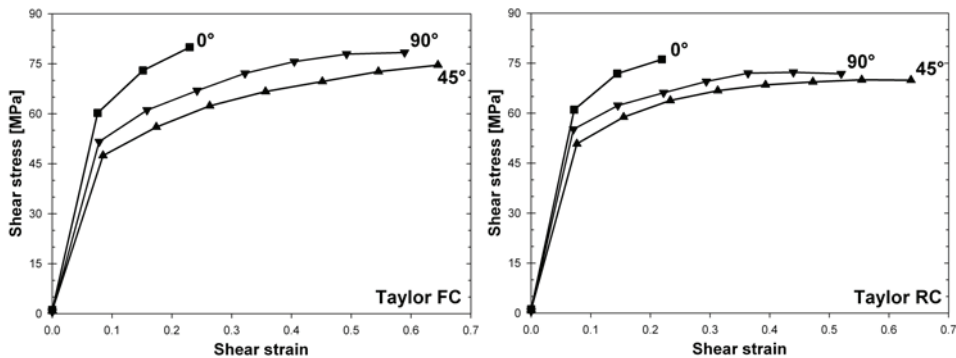


Figure 6.2 – Calculated shear stress vs. shear strain curves for the investigated directions of AA6063. The calculations are based on the Taylor factor evolution during deformation (Figure 6.1). The Taylor factor calculations are performed with both the full constraint (left) and the relaxed constraint (right) Taylor model.

Discussion

and 90° related to ED. However, Ryen based his Taylor factor calculation only on texture measurements prior and after simple tension deformation. Further, he assumed a linear Taylor factor evolution during deformation:

$$M(\varepsilon) = M(0) + a \cdot \varepsilon \quad (25)$$

where $M(0)$ is the Taylor factor prior to deformation and a is the slope of the linear Taylor factor evolution. These results showed large variations between the different deformation directions even at the onset of plastic flow, where no work hardening or texture changes have occurred.

The investigations initiated by Ryen (2003) have been continued in the present work in order to fully understand the mechanical anisotropy observed in the two Al-Mg-Si profiles. New Taylor factor calculations were performed using the same software (MTM-FHM software system (Taylor model), see section 2.4.2 for more details). In addition, in-situ deformation experiments in the SEM provided more detailed descriptions of the texture evolution upon tensile deformation.

It has been shown (Figure 6.1) that the calculated Taylor factor evolution with increasing strains actually follows close to a linear relationship. Hence, the above linear assumption made by Ryen (2003) should provide a nearly satisfying description of the crystallographic texture evolution. The corresponding $\tau - \gamma$ curves based on the texture measurements and Taylor factor calculations performed in this work are presented in Figure 6.2. These curves diverge from the experimental non-artificial aged curves (Figure 5.12), since the stress level of directions 45° and 90° have exchanged their relative positions at the highest strain-level. Another discrepancy is that the experimental curves for the 45° and 90° cross each other for the W- and T4-conditions, but the calculated curves in Figure 6.2 do not capture this evolution. However, the calculations are correctly predicting that the 0° -orientation has the highest stress level. Moreover, calculations made by the Taylor relaxed constraint (RC) method seems to provide more coincident results than the full constraint (FC) method since the former indicates less difference in stress levels comparing the different directions. In general, the Taylor based

Discussion

6.1.2 Texture vs. Mechanical observations (mainly AA6063)

Simple tension investigations performed 0° , 45° and 90° related to ED confirms that both AA6063 and AA6082 possess strong mechanical anisotropy in the solutionised condition (see Figure 5.12 and Figure 5.13). AA6063 has an equiaxed microstructure and a strong Cube texture somewhat rotated around the extrusion direction (ED) as shown in Figure 5.4. As a first approximation, one can assume that a material carrying a strong Cube texture has close to isotropic mechanical properties parallel and perpendicular to the ED due to the highly symmetrical Cube orientation (see e.g. Li and Bate 1991 and Lopes et al. 2003). However, the observations in Figure 5.12 indicate that this is not the case for the recrystallized profile investigated in this work. This alloy exhibits significant mechanical anisotropy, i.e. especially when observing the non-artificial aged conditions.

In general, the shear stress (τ) vs. shear strain (γ) curves for materials where the anisotropy is governed by the crystallographic texture is directional independent. This means that materials with texture controlled anisotropy have coincident $\tau - \gamma$ curves in all deformation directions. The shear stress and shear strain can in basic be calculated based on the axial stresses and strains together with the corresponding Taylor factor (M).

$$\tau = \frac{\sigma}{M(\varepsilon)} \quad \text{and} \quad \gamma = \varepsilon \cdot M(\varepsilon) \quad (24)$$

where $M(\varepsilon)$ is the Taylor factor at a given strain (ε). The Taylor factor is calculated from the crystallographic texture applying crystal plasticity models. This means that it is necessary to acquire the texture evolution during deformation in order determine the Taylor factor evolution. It has been shown in previous works that changes in initial texture due to age-hardening of AA6063 are minimal (Li and Van Houtte 2002b, Ryen 2003, Bjerkaas et al. 2005). Taking these observations, the initial Taylor factor seems not dependent on the actual material condition.

Ryen (2003) tried to explain the origin of the observed mechanical anisotropy of AA6063 and AA6082 by comparing the shear stress and shear strain relationship 0° , 45°

Discussion

Further, the activated slip systems in the present AA6063 with a strong crystallographic texture will remain or even become more potential when they first have been activated. Hence, the mechanical anisotropy will hardly be affected by the introduction of shearable precipitates. However, when Al-Mg-Si-alloys are artificially aged to the peak aged (T6) and over aged (T7) conditions, the microstructure will consist of a combination of shearable and non-shearable precipitates. Very truly, the introduction of non-shearable particles clearly distributes the deformation and the mechanical properties become more isotropic as shown in Figure 5.15 and Figure 5.16.

Further, it has been pointed out in Chapter 2 that the introduction of particle free zones (PFZ) after ageing to the T7 condition could alter the mechanical anisotropy observed in age-hardenable aluminium alloys (Poole et al. 2005). The PFZ regions might carry a large portion of the strain, which again could make the anisotropy more grain shape dependent. This will not affect AA6063 (equiaxed grains) while the AA6082 could be influenced by these effect due to a fibrous microstructure. If the figures presenting the effect of ageing on the mechanical properties (Figure 5.15 and Figure 5.16) are studied in great detail, it could be argued that AA6063 has more isotropic mechanical properties than AA6082. However, the particle free zones (PFZ) in Al-Mg-Si-alloys are normally very narrow and therefore this effect could most likely be neglected for the alloys investigated in the present work.

Another associated observation regarding the age-hardening – anisotropy interaction is the tensile sample end of cross-section shape (Figure 5.20). This figure shows a strong cross-section curvature in the solutionised condition. This curvature is most likely related to the through-thickness texture variations that will be discussed in the following section. When the specimens are artificially aged, this texture effect is suppressed, and the end of cross-section curvature disappears. Based on the discussion above, it is reasonable to assume that the cross-section curvature disappears because the slip distribution is to a larger extent determined by the introduced precipitates and the influence from crystallographic texture becomes less important. This means, that the slip distribution has become more homogeneous through the cross-section of the profiles.

Discussion

accordance to the present observations. Figure 5.11 also shows that the area fraction of Brass increases a good deal toward the surface of the fibrous microstructure.

Previously, it has been shown that recrystallized grains with Goss orientation originate from heavily deformed Brass-grains exposed to high temperatures (Bowen 1990). It has also been shown by Hjelen (1990) that recrystallized grains with Goss orientation tend to grow into areas with a high fraction of Brass oriented grains. These previously reported results are therefore consistent with the large increase of Goss oriented grains in the middle layer of AA6063.

It is suggested that the strong through-thickness gradients observed in the recrystallized profile can be explained by the heterogeneous deformation in the extrusion die. A more detailed discussion on how Taylor analysis can be used to explain thickness gradient anisotropy will be given below (Chapter 6.2). Furthermore, nature of these gradients and the possible effect of these on formability of extruded profiles will be discussed in more detail in Chapter 6.4.

Age-hardening effects

Natural- and artificial-ageing and ageing mechanisms, in it self, has not been investigated in this work. The focus of this work has rather been to study the effect of age-hardening on the mechanical anisotropy observed in the present two Al-Mg-Si-alloys. The present findings support the theory suggesting that the deformation is heterogeneous and occurs in bands of dislocations on $\langle 111 \rangle$ planes in the case of shearable precipitates, while for non-shearable precipitates, a relatively homogeneous distribution of slip is observed (see section 2.7.4 for details). Section 5.2.3 shows that both alloys posses an evident mechanical anisotropy in the solution-heat-treated condition (W, 10 min). In this condition, the anisotropy is in large extent determined by the crystallographic texture. The tensile test results have shown that naturally ageing to the T4 3h, T4 24h and T1 conditions introduce a substantial quantity of shearable precipitates (i.e. strength increases). These precipitates are normally homogeneously distributed in the matrix hence the most potential slip systems prior to precipitation will probably still be among the most potential slip systems after the shearable dislocations have been introduced.

Discussion

strain deformation, which also is the deformation mode in the centre part of the profile (Vatne et al. 1996a). The surface region of a profile is subjected to heavy shear deformation during extrusion, hence it could be expected that this area develop a strong shear texture. However, in the surface region, the driving pressure for recrystallization (P_D) exceeds the retarding forces from precipitation of $MnAl_6$ type dispersoids (Petzow and Effenberg 1993). This results in a surface region with a recrystallized microstructure with close to random texture with traces of typical shear components (Humphreys and Hatherly 1996).

AA6063 on the other hand, has a fully recrystallized and equiaxed microstructure with a belonging crystallographic texture. The global texture of this profile is strong, with the most pronounced texture components having intensities close to 27 times random. This is more than twice as high as the intensity observed for the most pronounced texture components of AA6082. The Cube and the ED-rotated Cube (CG and Goss) orientations are the main texture components of this recrystallized profile. Vatne et al. (1996b) have shown that the origin of the Cube (C) orientation is the growth of highly mobile $40^\circ \langle 111 \rangle$ interfaces between grains with retained Cube and S orientation. Further, it is assumed that grains with a Goss orientation can grow out of transition bands within grains having the Brass orientation (Hjelen et al. 1991). From these observations it seems like the recrystallization texture is dependent on the deformation texture prior to recrystallization (see e.g. Furu et al. 2004). The surface layer of this profile is also without any texture due to the same reasons as for AA6082.

It is noticeable that AA6063 most likely possess microstructure and texture equal to AA6082 prior to recrystallization (Furu et al. 2004). This means that the deformation texture of AA6082 might be used to explain the observed texture in AA6063, as suggested by Furu et al. (2004). The centre layer of AA6063 has a very strong Cube texture which diminishes somewhat toward the surface layer (Figure 5.8). This is most likely related to the area fraction of the retained Cube and S orientation prior to recrystallization (Figure 5.11). The area fraction of S orientation increases but the area fraction of retained Cube decreases dramatically. The model presented by Vatne et al. (1996a), suggest that the area fraction of Cube should decrease toward the surface, i.e. in

6 Discussion

The experimental results presented in the previous chapter deals with many of the fundamental questions related to metallurgy and materials science of aluminium alloys. Hence, the discussion part of this thesis could easily have treated several important topics in a shallow manner. Instead, a more comprehensive discussion of the main objectives has been given, i.e. plasticity and mechanical anisotropy. The first part of this discussion will look at the macroscopic anisotropy observed in the investigated extruded profiles. Later in this chapter, the reasons for this observed macroscopic behaviour will be treated on a microscopic length scale, e.g. distribution of slip. This will be done by looking into the deformation mechanisms operating in individual grains. As a result, this chapter will result in an improved understanding of the plasticity taking place during forming of extruded Al-Mg-Si profiles.

6.1 Mechanical anisotropy

The mechanical anisotropy is in many respects one of the most important mechanical properties of any material that will be plastically formed to its final shape. It is crucial to fully understand the causes for anisotropy, and how these can be governed. This chapter will therefore be used to discuss the different causes for mechanical anisotropy and how these can be explained from a metallurgical point of view.

6.1.1 Crystallographic texture

In order to discuss the observed mechanical anisotropy, it is necessary to repeat some of the main findings related to microstructure and crystallographic texture. The two present alloys have different microstructure and crystallographic texture characteristics. The non-recrystallized alloy (AA6082) has a fibrous microstructure with a typical deformation texture having a maximum intensity of 13 times random. The texture is dominated by the Brass (B) and S components, which are typical for plane strain compression (Humphreys and Hatherly 1996). The microstructure in the centre part of the profile also consist of relatively large amount of retained Cube, as shown by the large fraction of Cube bands at $S=0.00$ (Figure 5.9). This kind of band is often related to plane

Experimental results – Part B

Figure 5.74 shows that also specimens deformed parallel to the ED develop localised deformation bands ($\pm 45^\circ$) during straining. However, the bands are not as pronounced for this direction as for the 45° direction. By studying the strain distribution evolution in more detail, it is clear that the localisation takes place at an earlier stage for specimens deformed parallel to ED than for specimens deformed 45° to ED (see e.g. Figure 5.73 (a) and Figure 5.74 (a)). It should also be pointed out that the local peak strain at the uniform strain is comparable for both directions investigated ($\sim 65\%$).

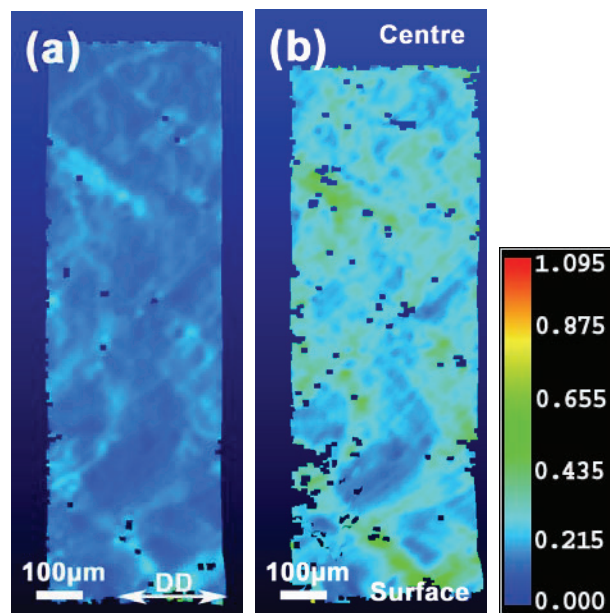


Figure 5.74 – Measured strain distribution evolution (DSCA technique) over the thickness for a specimen deformed parallel to the ED. Centre position at the top and surface position at the bottom. (a) 9% deformation and (b) uniform strain (12%).

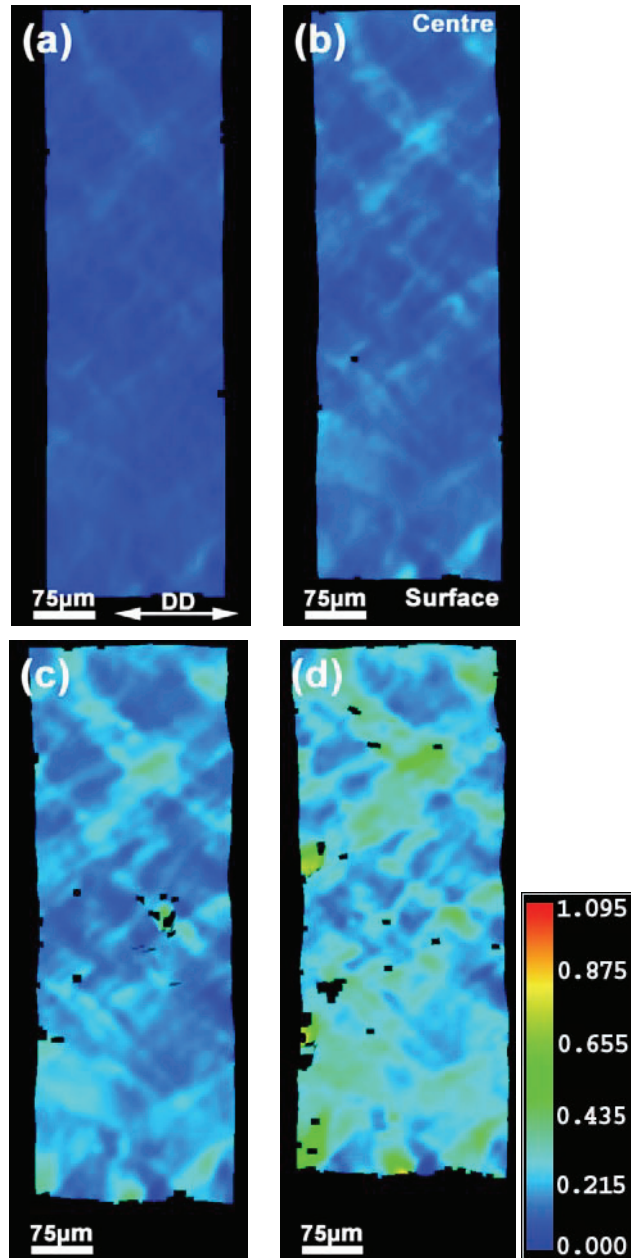


Figure 5.73 – Measured strain distribution evolution (DSCA technique) over the thickness for a specimen deformed 45° related to the ED. Centre position at the top and surface position at the bottom. (a) 9%, (b) 13.5%, (c) 18% and (d) 22.5% deformation. Strain distribution at higher strains was not possible due to a large distortion of the grid.

Experimental results – Part B

calculated strain distributions show that the deformation is localised bands oriented approximately $\pm 45^\circ$ to the DD. Notice that the distance between these bands seems to be very repeatable.

Further, the specimen surface develops large strains in areas where two bands intersect. In other words, it seems that the deformation carried by the individual bands is additive and the deformation in the intersection area is roughly equal to the sum of the two accumulated strains. Figure 5.73 also shows that these areas can reach up to 63% deformation while the specimen in average has a strain of 22.5%. Hence, the strain observed in strain intensive areas is almost three times as high as the average strain.

Experimental results – Part B

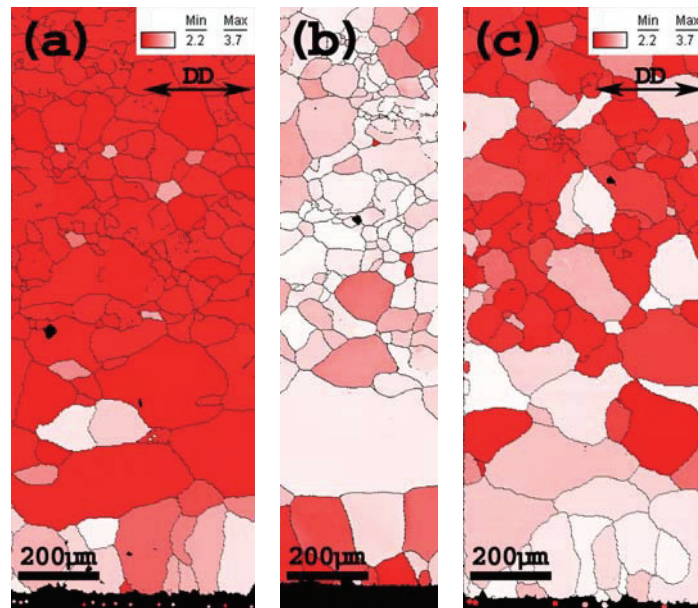


Figure 5.72 – Taylor factor map calculated by the Taylor FC method based on initial crystallographic orientations. Centre position ($S=0.00$) at the top and surface position ($S=1.00$) at the bottom. (a) 0° , (b) 45° and (c) 90° direction.

This is clearly shown by the Taylor factor maps calculated based on the crystallographic orientations prior to deformation (Figure 5.72). Both the 0° and 90° specimens have relatively high Taylor factors (white) in the surface layer, while the Taylor factors in the centre and middle layer of the profile are relatively low (red). The specimen deformed in the 45° direction has the lowest Taylor factors in the surface layer and high to very high Taylor factors in the centre and middle layers. Therefore, the Taylor factor calculations indicate that crystallographic slip is favoured in the centre and middle layer of the profile when deformed parallel and perpendicular to the ED and in the surface layer when deformed in the 45° direction.

In-situ investigations over the profile thickness have also revealed another type of local strain distribution on the meso scale. Strain measurements performed by the DSCA technique show that the strain is localised even prior to the uniform strain. This type of strain localisation appears already after 9% deformation for the specimen deformed in the 45° direction. Here, Figure 5.73 presents the evolution in the local strain distribution during deformation. The software was not able to calculate the strain distribution at uniform strain (27%) due to a large distortion of the grid elements. However, the

Experimental results – Part B

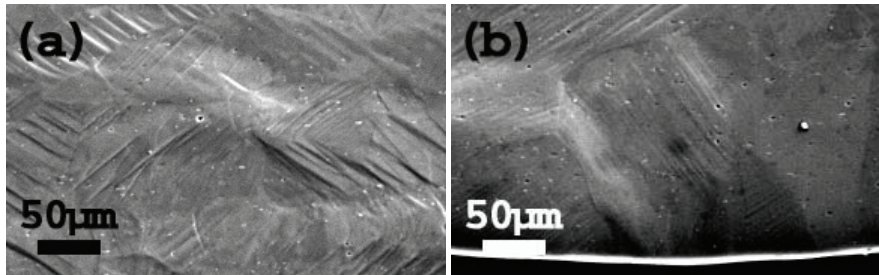


Figure 5.70 – Micrographs showing slip traces at the uniform strain (12%) for a specimen deformed parallel to the ED. (a) centre position and (b) surface position.

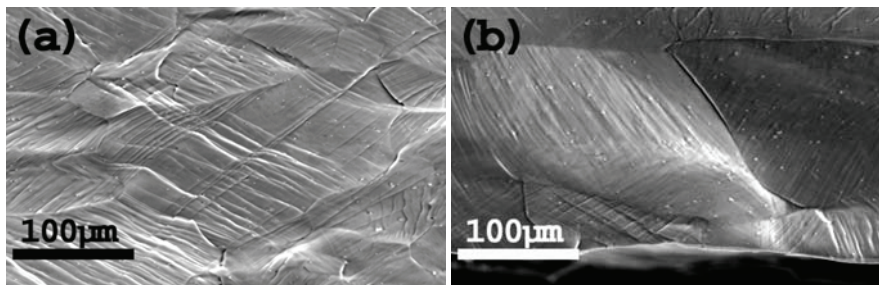


Figure 5.71 – Micrographs of slip traces at the uniform strain (27%) for a specimen deformed 45° related to the ED. (a) centre position and (b) surface position.

Furthermore, the experimental results also show that there are substantial differences between the 0° and 45° directions with regard to crystallographic directions parallel to the DD. It has previously been shown that the material possesses a strong through-thickness gradient (see section 5.1.3) that will affect the deformation properties. When the grains in the centre layer are compared to the grains in the surface layer of specimens deformed 0° and 90° to the ED, it is clear that the surface layer is unfavourably orientated for slip and most of the deformation should therefore take place in the centre region. This is not the case for the 45° specimen where the surface layer is equivalent or even more favourable oriented for slip than the rest of the specimen. Hence, the amount of deformation in the surface and the centre region should be close to equal in this direction.

Experimental results – Part B

(Figure 5.69 (b)). The 90° direction, on the other hand, deforms with no obvious differences between the different regions and most grains have relatively dense traces of slip. However, some surface grains have localised coarse slip, even with cracking occurring along the traces (Figure 5.69 (c)).

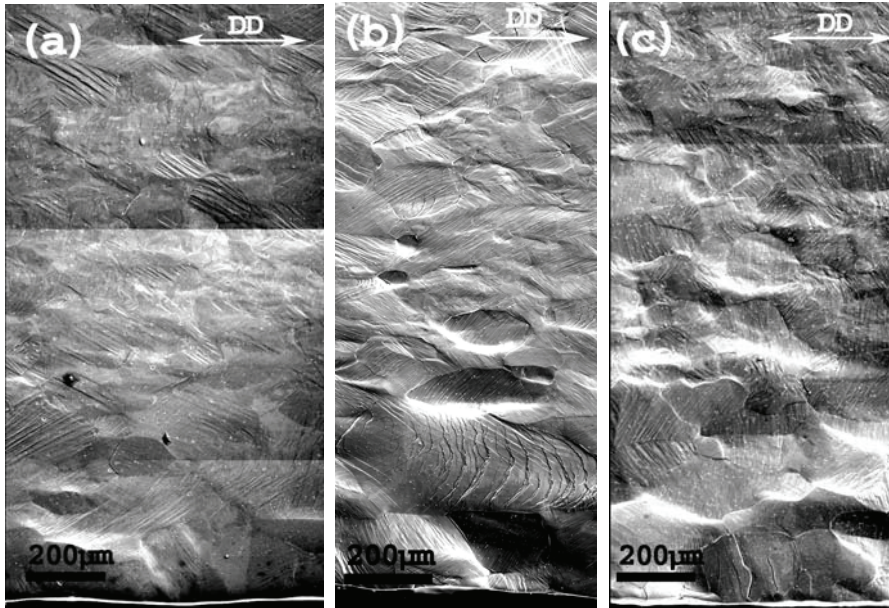


Figure 5.69 – Micrographs over the thickness at the uniform strain. Centre position ($S=0.00$) at the top and surface position ($S=1.00$) at the bottom. (a) 0° , (b) 45° and (c) 90° direction.

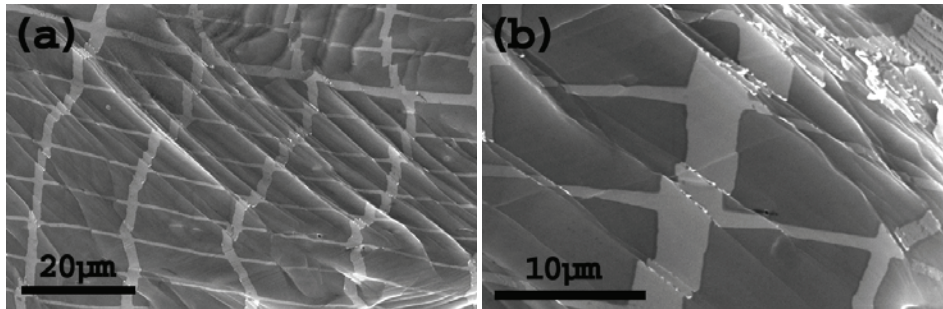


Figure 5.68 – (a) Slip traces and local strain distribution on a grain scale. (b) Close-up of an area with heavily distorted grids.

5.7.2 Meso scale

The meso scale heterogeneities of AA6063 have been studied by deforming in-situ in the SEM (see Chapter 4.1 for the experimental details). The special specimen geometry includes a possibility to perform through-thickness investigations of strain distribution and also of the grain rotations taking place during deformation. Figure 5.69 presents the deformed surface microstructure at uniform strain for specimens tested in the three different directions. They possess meso scale heterogeneities in addition to the micro scale heterogeneities presented in the previous section.

The centre and middle layer ($S=0.00$ to $S=0.85$) of all specimens investigated deforms relatively in-homogeneously, with a large fraction of the grains developing localised coarse slip traces, e.g. see Figure 5.70 and Figure 5.71 for specimens deformed at 0° and 45° respectively. It is clear that the centre region is heavily deformed (pronounced coarse slip) at the uniform strain level regardless of the deformation direction selected, although the coarse slip distribution is not so pronounced in the 90° specimen.

There is also a small directional dependency with regard to deformation/strain development in the surface layer ($S=0.85$ to $S=1.00$). A fine slip distribution is often observed in the surface layer of the 0° specimens. These grains normally develop visible slip traces first at high strains and some of them do not even develop visible slip traces at the uniform strain. The surface layer consists of grains with a very localised and coarse slip distribution in the 45° direction. The extended region between the surface and the centre layer on the other side shows a finer, i.e. more homogeneous slip distribution

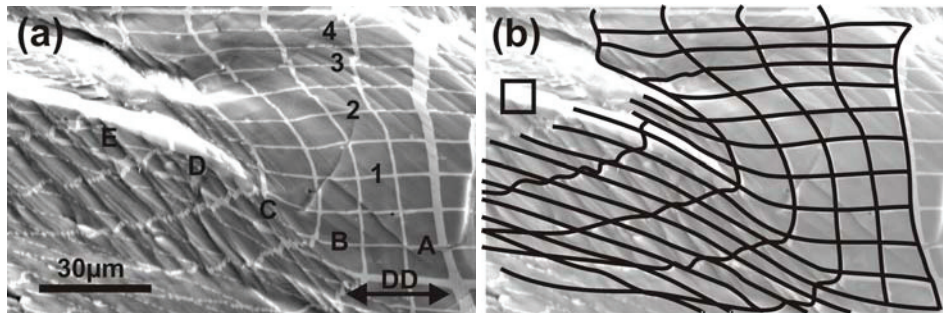


Figure 5.66 – Micrographs presenting the strong deformation gradients observed in a shear band (left part) at the post-uniform strain region. (a) SE micrographs (positions for strain measurements are indicated). (b) Reconstructed grid as used for strain measurements. The size of an initial grid element is also included for comparison.

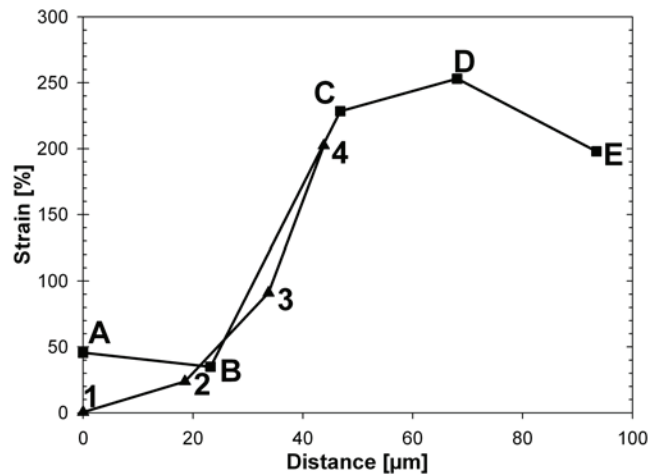


Figure 5.67 – Local strain distribution within the shear band along the two axes indicated in Figure 5.66.

If the local strain distribution in a grain from a specimen with an overlaid grid is investigated in even more detail, it becomes evident that strain and strain measurements on this length scale became complicated. Figure 5.68 presents the observed slip traces in a specimen marked with a gold grid. It is clear that the material deforms by slip on selected slip planes and not as a continuum. Hence, the strain distribution on this length scale can probably not be described by continuum mechanics. The material deforms heavily at the activated slip planes and these planes are separated by more or less undeformed regions (Figure 5.68).

Experimental results – Part B

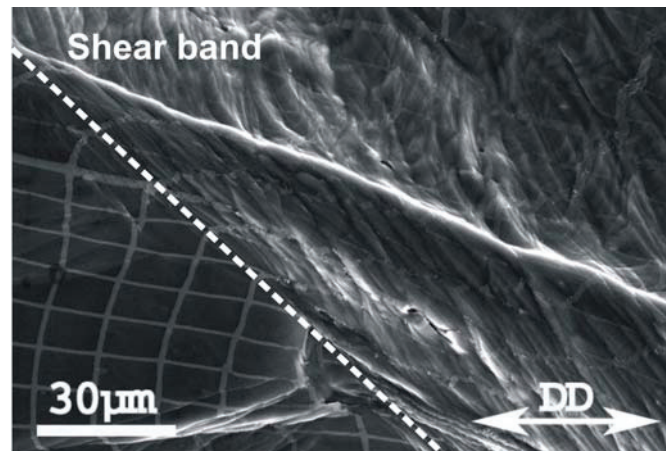


Figure 5.64 – Example of strain gradient at the edge of a shear band. The border between the shear band and the surrounding material is indicated by the dotted line.

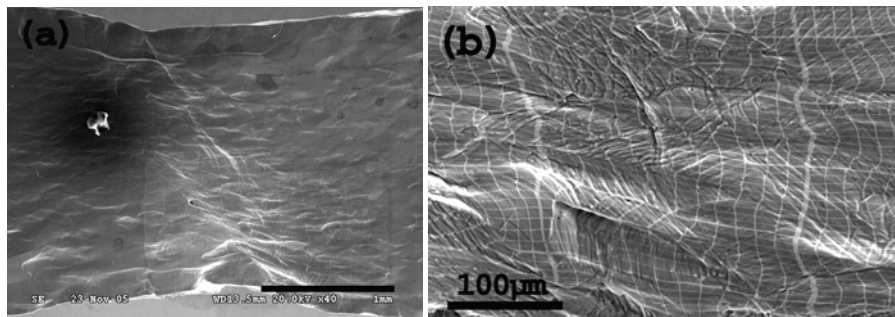


Figure 5.65 – Example of shear band development in the post-uniform strain region (a) and close-up of the corresponding heterogeneous strain distribution (b).

Most of the grains are significantly deformed while other grains are weakly deformed. This leads to extreme strain gradients as shown in Figure 5.66. It is not possible to perform automatic strain measurements based on these micrographs due to the heavy distortion of the gold grid. The grid is therefore reproduced by image processing software and the in-plane strains calculated manually. The results from these calculations show that the strain increases with more than 500% in relative numbers over a distance less than 60µm (Figure 5.67). Hence, the strain gradients observed within the shear band is of the same order as the strain gradients normally observed between the shear band and the surrounding areas.

Experimental results – Part B

strain distribution maps also confirm the observed heterogeneity within the individual grains. The major strains can vary quite substantially from the centre of the grain toward the grain boundary, and differences up to 40% in relative numbers are often observed.

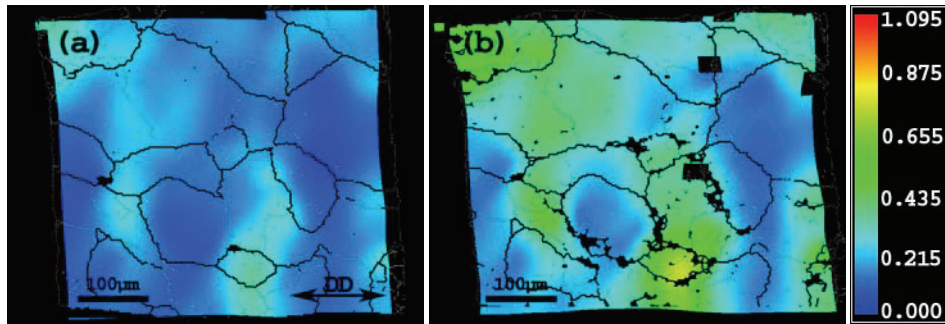


Figure 5.63 – Local major strain distribution of the same area as above, calculated by the DSCA technique from SE micrographs acquired during deformation. (a) 16% (b) uniform strain (27%)

A different and even more pronounced type of local strain distribution becomes evident at higher strains. The deformation localises when the material reaches post-uniform strains and localised shear bands develop. As can be seen from Figure 5.64, further deformation takes place within the band, and the border between the shear band and the surrounding material becomes very evident. It has been shown that all the investigated directions of both alloys develop evident shear bands. However, the characteristics of the shear bands are strongly direction-dependent. Further, the strain distribution within the shear band itself is also very heterogeneous (Figure 5.65).

Experimental results – Part B

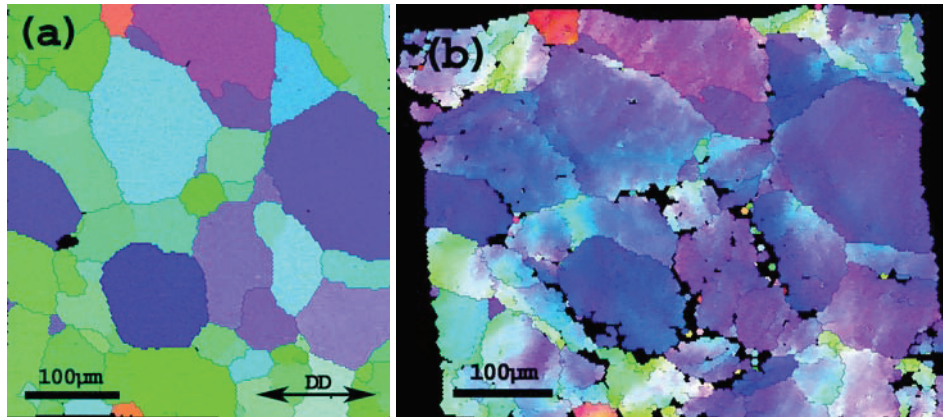


Figure 5.61 – IPF map of the same area (Figure 5.60) in the deformation direction based on orientation data. (a) Initial orientation and (b) at uniform strain (27%).

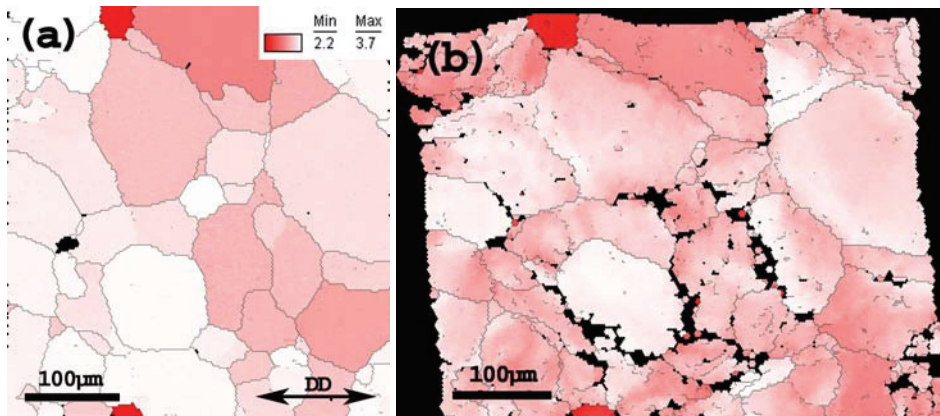


Figure 5.62 – Taylor factor map of the same area as in the two previous figures calculated from the Taylor FC method. The colour key represents the different Taylor factors of the individual grains. (a) Initial orientation (b) uniform strain (27%)

To quantify the deformation heterogeneity, the local in-plane strain distribution was calculated. In Figure 5.63, the major strain distribution after 16% and 27% (uniform strain) axial elongation was calculated based on the SEM micrographs of the distorted grids (Figure 5.60). The grain boundaries from the EBSD investigations are overlaid the strain distribution map in order to separate the individual grains. These strain maps clearly show that some grains are given large deformation while other grains hardly deform at all. The heavily deformed grains deform up to 400% as much as grains with a high Taylor factor. It is also worth noticing that the observed relative differences in amount of deformation are close to constant throughout the tensile experiment. The

5.7.1 Micro scale

The local strain distribution in a specimen deformed 45° related to the ED was investigated in order to study the effect of the initial orientation. It is important to remember that this DD possesses more homogeneous deformation properties than the other directions investigated (see Chapter 5.6 Plasticity). Figure 5.60 presents SEM micrographs of the grid prior to deformation and at the uniform strain (27%). A visual inspection of the distorted grid shows that the deformation is very heterogeneous. The micrographs also show that the strain distribution is heterogeneous even within the individual grains.

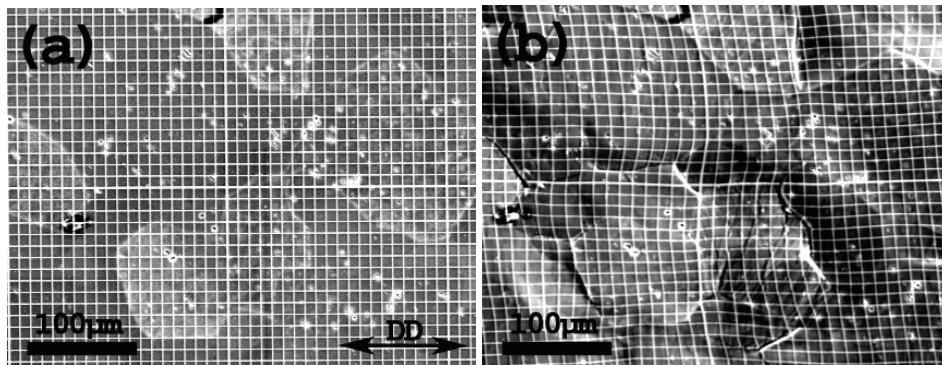


Figure 5.60 – Micrograph of the specimen surface having overlaid a gold grid to visualise the heterogeneous deformation. (a) Prior to deformation and (b) at 27% deformation (uniform strain).

The IPF map shows that the majority of the grains have close to a $[101]$ parallel to the DD (green grains) while some of the grains have close to a $[111]$ parallel to the DD (blue grains) prior to deformation (Figure 5.61). This will again lead to some heterogeneity in the corresponding Taylor factor map as shown in Figure 5.62. The calculated Taylor factors indicate that some grains will deform quite easily while other grains are harder to deform. The Taylor factor map is more or less consistent with the visual observations of the distorted grids presented in Figure 5.60.

Experimental results – Part B

values (Figure 5.59) and the slip systems most favourably oriented for slip are distributed among several slip planes.

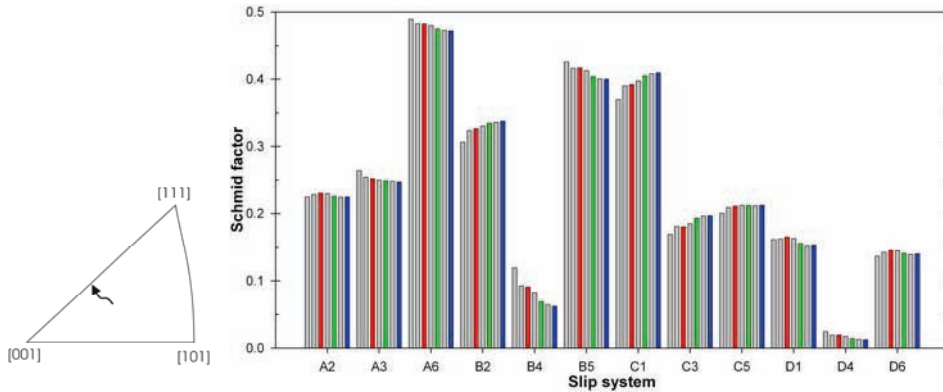


Figure 5.59 – Evolution in Schmid value distribution in a typical grain from a specimen without crystallographic texture. The Schmid values after 6%, 12% and 18% (uniform strain) deformation are labelled red, green and blue respectively.

5.7 Local strain distribution

As shown above, the individual grains have dissimilar slip activity due to variations in crystallographic orientation and the material will therefore develop a local strain distribution during deformation. The slip distribution can even be very heterogeneous within one individual grain, i.e. it develops strain gradients (see the previous section). In the following, the local strain distribution has been quantified on a grain scale in order to understand how different texture components in a recrystallized aluminium alloy deform plastically. The local strain distribution has also been investigated at the meso scale (here; through the profile thickness).

The local strain distribution of the individual grains is obtained by the digital speckle correlation analysis (DSCA) technique based on micrographs acquired in the SEM. The technique is described in more detail in Chapter 2.6. With this technique, it is necessary to produce a structured surface, i.e. it should be textured so that the matching procedure yields a dense distribution array of homologue points. For the specimens investigated, in this work, this was obtained by producing a gold grid on top of the electrochemically polished surface.

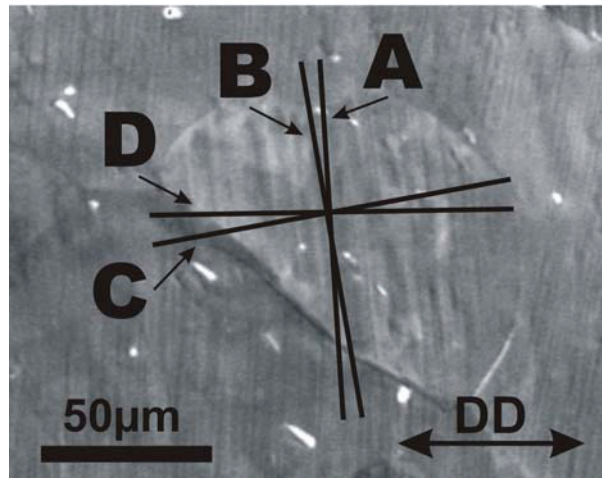


Figure 5.58 – Observed slip traces in Grain 4 after 12% deformation. The orientations of the theoretical slip traces from the four $\{111\}$ -planes are as indicated.

As shown in the previous section, the slip trace evolution is much more heterogeneous in the material after the crystallographic texture has been removed. The results indicate that this is also the case for the slip activity. The slip trace evolution (Figure 5.51) and the corresponding Schmid value distribution evolution (Figure 5.59) of a grain from a material with random texture deformed in the 90° direction has the following characteristics. The observed slip traces labelled 1 to 3 in Figure 5.51 correspond to the theoretical slip traces of plane A, B and C respectively. Slip system A6 has the highest Schmid value, while A2 and A3 have low to intermediate Schmid values after 6% elongation (see Figure 5.59). Further, slip systems B2, B5 and C1 also have high Schmid values at this strain level. However, from the micrographs presented in Figure 5.51, it is evident that the observed slip traces originate from slip activity on slip plane A. Slip traces from plane B become visible locally after 12% deformation. This means that at least one additional slip system on plane B have been activated in this region. Further, when the specimen is deformed to 18%, a second set of additional slip traces develop in another region of the grain. This set of slip traces coincide with the theoretical slip traces of plane C.

These results show that the slip activity is very heterogeneous even within one individual grain. The identified crystallographic orientations possess a substantial spread in Schmid

Experimental results – Part B

Moreover, both grain 1 and 4 have a crystallographic orientation close to the perfect Cube orientation (see Figure 5.56 and Figure 5.57). The similarity in crystallographic orientation makes these grains suitable for demonstrating the effect of the DD to the activation of slip systems during deformation. Grain 1 is deformed 90° to ED while grain 4 is deformed 45° to ED. As mentioned above, grain 1 is stable while the orientation of grain 4 is unstable. Grain 1 has a total of eight slip systems with Schmid values close to 0.41 distributed on the four available $\{111\}$ -planes. Since the Schmid value distribution hardly changes, eight slip systems will be available until the material reaches the uniform strain. On the other hand, Grain 4 has only four slip systems with Schmid values close to 0.41 available at initial plastic flow. Further, crystallographic rotation results in only two slip systems having this Schmid value at uniform strain. In other words, the number of available slip systems with Schmid values comparable to the maximum values observed in grain 1 is strongly reduced. In addition to the slip systems maintaining their high Schmid values, grain 4 also has four slip systems with approximately 0.5 times the initial maximum Schmid value.

Calculations of the theoretical slip traces are a favourable supplement to the observed ones. In Figure 5.58 the theoretical slip traces of the four $\{111\}$ -planes are overlaid the observed slip traces after 12% deformation. It is evident that the theoretical slip traces of plane B and in some cases plane A, fully coincide with the observed slip traces. However, even at the uniform strain there are no observed slip traces parallel to the theoretical slip traces of plane C and D.

Experimental results – Part B

The initial crystallographic orientation (red columns) of grain 4 results in four slip systems having high Schmid values (0.39-0.43), while the remaining slip systems have very low Schmid values (<0.04). The high value slip systems are concentrated to slip systems operating on slip plane A and B (Schmid and Boas notation). The activation of slip systems during deformation and the corresponding grain rotation result in a severe reduction in the Schmid value for the two slip systems on plane A. The reduction in Schmid value after 27% axial elongation (blue columns) of slip system A3 and A6 is 0.24 and 0.15 respectively, while the Schmid values of B4 and B5 are close to constant. However, the experimental results clearly show that the Schmid value of all slip systems on plane C increases as a consequence of this crystallographic rotation. Further, it is clear that the increase in Schmid values on slip system C1 (0.26) and C5 (0.18) are equal to the simultaneous reduction on slip system A3 and A6. From a Schmid value analysis point of view, these Schmid value alterations make slip system C1 and C5 equivalent to slip system A3 and A6 respectively. The crystallographic rotations have resulted in two slip systems maintaining their high Schmid values at the uniform strain, four slip systems have developed intermediate Schmid values (0.17-0.28) while the remaining slip systems maintain values close to zero.

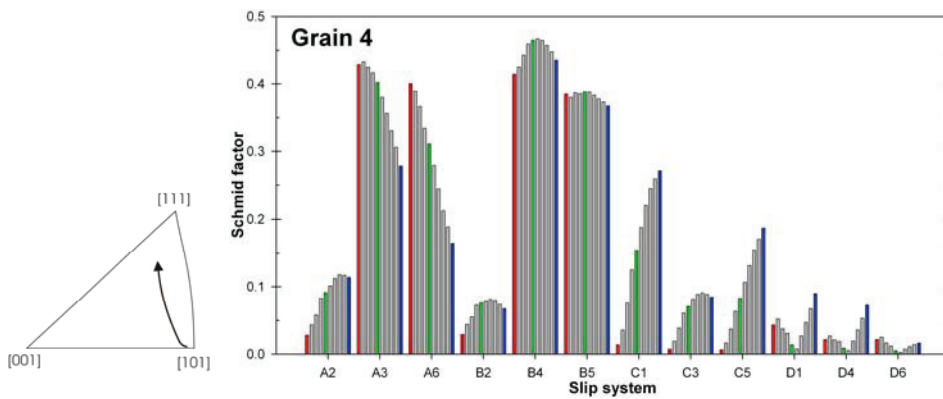


Figure 5.57 – Evolution in Schmid value distribution for a Cube orientated grain deformed 45° related to the ED. The Schmid values after 0% (initial orientation), 12% and 27% (uniform strain) deformation are labelled red, green and blue respectively. The corresponding rotation path are shown to the left. Figure 5.58 presents the slip trace distribution of this grain.

Experimental results – Part B

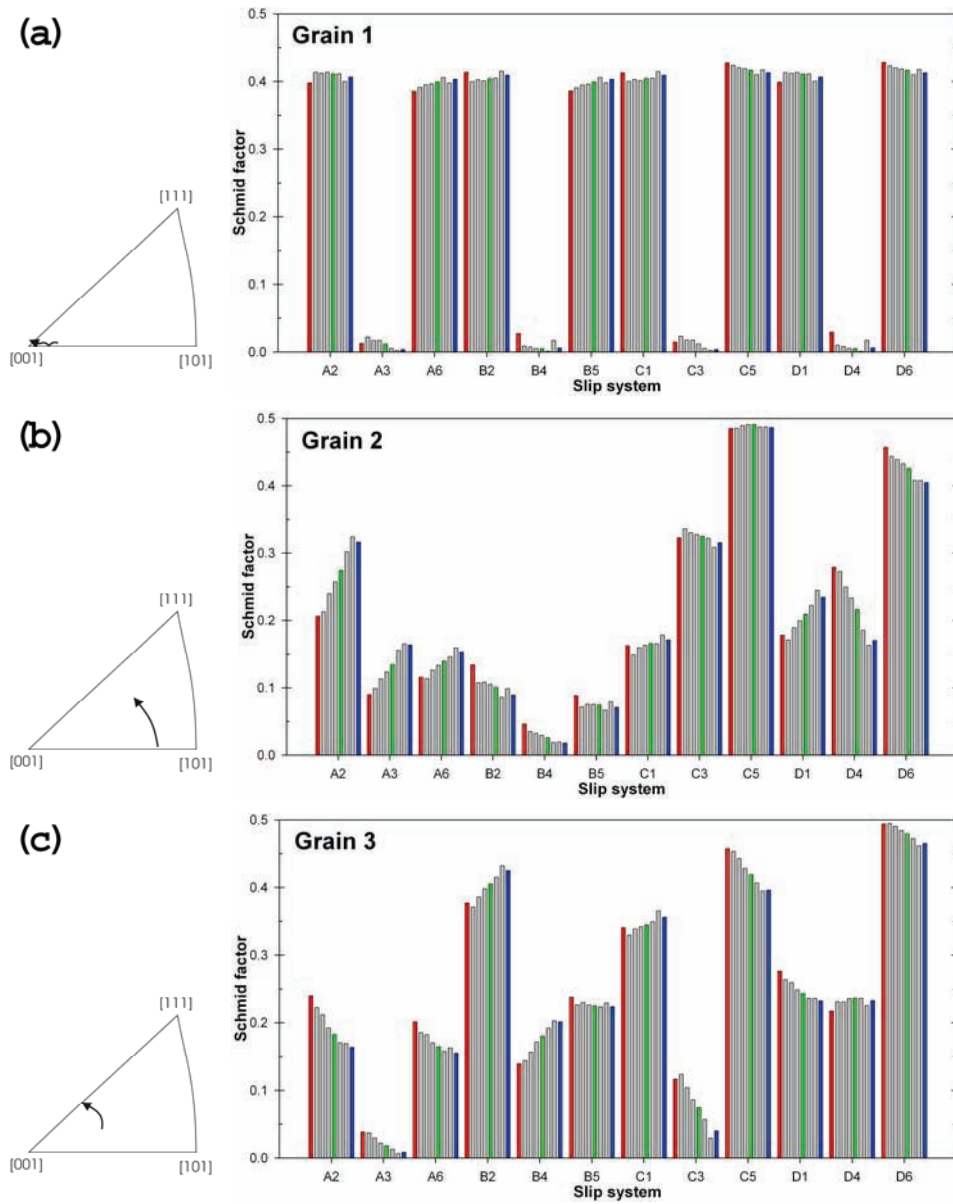


Figure 5.56 – Evolution in Schmid value distribution for grains with various initial orientations deformed 90° related to the ED. The Schmid values after 0% (initial orientation), 12% and 21% (uniform strain) deformation are labelled red, green and blue respectively. The corresponding rotation paths are shown to the left.

Experimental results – Part B

The calculated Schmid values presented above clearly show that crystallographic rotation results in alteration of the Schmid value distribution. It has also been shown that the individual grains rotate during simple tension deformation. Thus, also the Schmid value distribution will be altered during deformation. The Schmid value distribution evolution of individual grains with different initial orientations taken from a specimen deformed 90° to ED (Figure 5.47) has been thoroughly investigated (Figure 5.56). It is evident that the Schmid value evolution in grains with a stable crystallographic orientation prior to deformation is relatively low (e.g. see Grain 1). However, there are some clear fluctuations between the eight slip systems with close to identical Schmid values, i.e. the ranking among these slip systems changes several times during deformation.

Further, Figure 5.56 also shows that the alterations in the Schmid value distribution are both more extensive and rapid when the grains have more unstable initial orientations (e.g. see grain 2 and 3). The most favourable orientation of the individual slip systems changes due to the crystallographic rotation, hence the Schmid value of the individual systems changes. In general, it is observed that individual grains have a close to linear Schmid value evolution during straining. It is also worth noticing that the most potential slip systems prior to deformation maintain their high Schmid values at the uniform strain even though the internal ranking may have been altered. This means that the slip systems activated at initial plastic flow tend to stay active throughout the deformation process.

It is very rare that a slip system with a low initial Schmid value rotates in such a way that it becomes a very favourable oriented for slip at the uniform strain. However, in some extreme cases when the initial orientation is very unstable, also this kind of Schmid value evolution is observed. As shown in Figure 5.38, grains having a $[101]$ parallel to the DD can rotate as much as 15° during deformation, hence the Schmid value of the individual slip systems changes dramatically as shown in Figure 5.57.

Experimental results – Part B

around the ED strongly affect the Schmid values when deformed in the TD (Figure 5.55 (b)). When deformed in this direction, the two extremes, i.e. the Cube and Goss orientation have 8 and 4 slip systems respectively with a Schmid value of 0.408, while the remaining slip systems are at zero. The figure also shows that rotation as small as 5° changes the Schmid value distribution significantly. The Schmid value of some slip systems was altered as much as 0.039 due to this small rotation. Further, The CG orientation is a less symmetrical orientation with regard to the selected DD and all the slip systems have non-zero Schmid values. Moreover, also for this orientation the difference in Schmid value between the slip systems with the maximum and minimum values is 0.408.

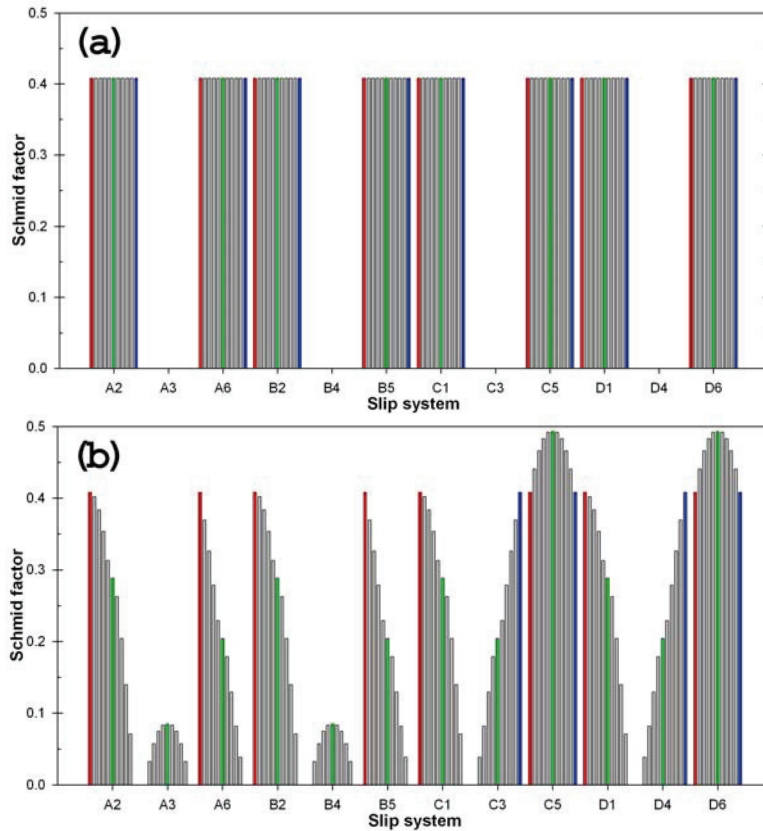


Figure 5.55 – Schmid values for the 12 potential slip systems of different crystallographic orientation along the fibre connecting the Cube and Goss orientation. Each column represents a 5° rotation along the ED-rotated Cube fibre. The Cube, CG and Goss orientation is labelled red, green and blue respectively. Deformed in the (a) ED direction and (b) TD direction.

5.6.2 Slip system activity

The observed surface slip traces give valuable information about the slip activity. They develop due to considerable slip on activated slip planes, and each slip plane consists of three different slip directions, i.e. three different slip systems. Therefore, the probability of slip for each of these slip systems has to be determined. The Schmid value of all slip systems can be calculated based on the crystallographic orientation and the DD (assuming uniaxial deformation in the individual grains). The number of slip systems activated in each grain during simple tension deformation will depend on both the Schmid value distribution among the 12 slip systems and the constraint enforced by the surroundings. It is important to remember that the activated slip systems most likely have to be among the potential active slip systems from a slip trace investigation.

Slip can in general take place without producing any visible slip traces if the plastic deformation of the individual grains is homogeneously distributed in the microstructure. Having said this, the materials investigated in this work seems always to deform in a more localised way, i.e. they always produce slip traces. On the other hand, also this material can in some special cases deform by slip without producing visible slip traces. The slip traces will not be visible if the slip direction (Burgers vector) is parallel to the specimen surface. The slip systems that fulfil this requirement can therefore be activated without producing any visible evidence. The intersection angle between slip direction and the specimen surface can be calculated based on the crystallographic orientation. For this investigation it was assumed that slip systems with an intersection angle larger than 10° will produce visible slip traces.

The Schmid value distribution is entirely controlled by the crystallographic orientations. It has previously been shown that the present material consists of very symmetrical texture components (Figure 5.5). Small rotations can therefore alter the Schmid value distribution significantly. Figure 5.55 presents the Schmid value distribution of different crystallographic orientations along the fibre connecting the Cube and Goss orientation (45° rotation around the ED). The Schmid values of the slip systems are completely independent of the rotation around the ED when deformed parallel to this direction (ED), i.e. all the crystallographic orientations have 8 slip systems with a Schmid value of 0.408 while the remaining 4 slip systems have a Schmid value of zero. However, the rotations

Experimental results – Part B

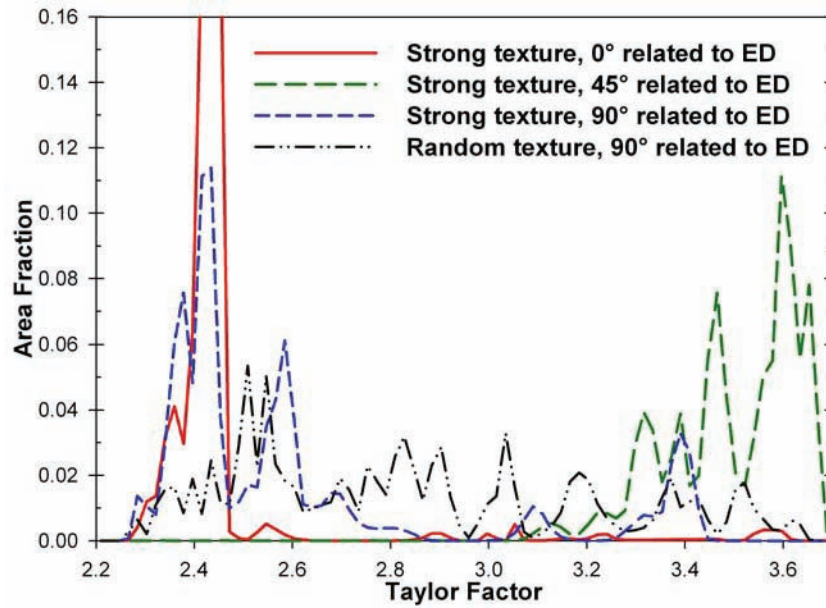


Figure 5.53 – The area fraction of Taylor factors. Calculations performed by the Taylor FC method based on the crystallographic orientations (~100 grains) prior to deformation. The calculations based on a material with random texture are shown for comparison.

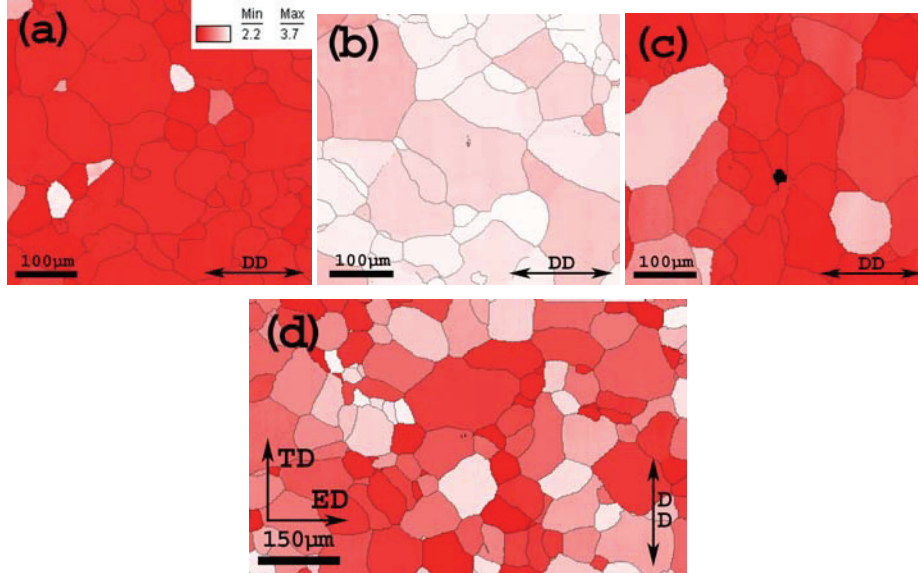


Figure 5.54 – Taylor factor map of specimens in the ED-TD plane with (a to c) and without (d) a strong texture. Calculations performed by the Taylor FC method based on the crystallographic orientations prior to deformation. The colour key represents the Taylor factor of the individual grains. DD parallel to (a) 0°, (b) 45°, (c) 90° and (d) 90° direction.

Experimental results – Part B

The Taylor factor is a direct result of the DD relative to the crystallographic orientations and the calculation-method utilised. The calculated average Taylor factors (here, full constraint approach) of the present AA6063 alloy prior to deformation is 2.5, 2.9 and 2.6 for the 0° , 45° and 90° direction respectively. Hence, this material has close to similar Taylor factors when deformed 0° and 90° related to the ED. However, the Taylor factor change from grain to grain can vary substantially. Figure 5.53 presents the measured area fraction of the Taylor factors for when deformation is utilised in three different directions as well as for a specimen without texture deformed in the 90° direction. The figure shows that the textured material has a large fraction of Taylor factors around 2.45 when deformed parallel to ED. If deformed perpendicular to the ED, some grains have Taylor factors in the range 2.3-2.6 while other grains have Taylor factors of ~ 3.4 . Moreover, these results show that a specimen deformed 45° related to the ED has a higher Taylor factor (close to 3.6) than the two other directions, i.e. see Figure 5.53 – Figure 5.54).

Neither of the grains in the material without crystallographic texture has the same Taylor factors, i.e. this material has a true random orientation distribution. This is further confirmed by the graph in Figure 5.53 where the Taylor factor of the individual grains varies from 2.3 to 3.5 without any evident major peaks. Still, the average Taylor factor of this specimen is similar to the material with texture when deformed in the 0° and 90° directions.

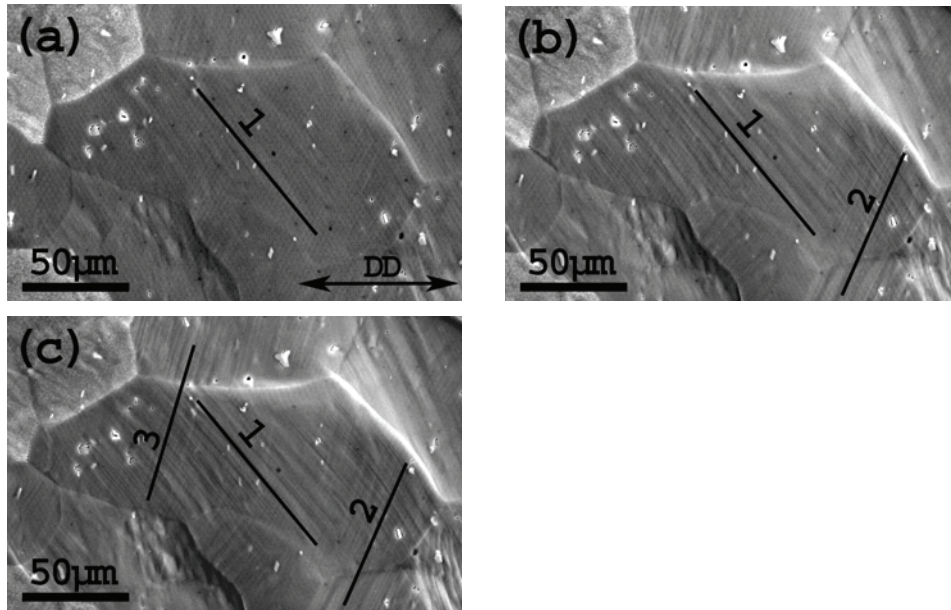


Figure 5.51 – SE micrographs of the observed slip traces in a material with random texture. The lines indicate the observed slip traces and how additional slip traces can coincide with the slip traces from neighbouring grains. (a) 6%, (b) 12% and (c) 18%.

It is worth noticing that it is hard to observe any visible slip traces at the right hand side of the grain investigated in Figure 5.51. Even at the uniform strain there are no visible slip traces close to the grain boundary separating this grain from the two bright grains at the upper left corner of the micrograph. The corresponding Taylor factor map of the same grains (Figure 5.52) shows that the two neighbouring grains have a higher Taylor factor, i.e. these grains are more difficult to deform and will most likely give rise to additional constraint in this region.

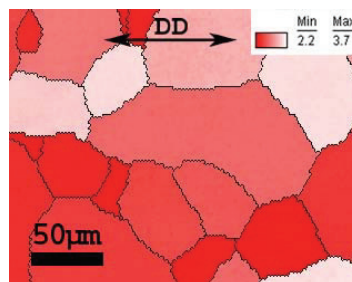


Figure 5.52 – Taylor factor map of the same grain area as presented in Figure 5.51. The calculations were performed by the Taylor FC method and based on the crystallographic orientations prior to deformation.

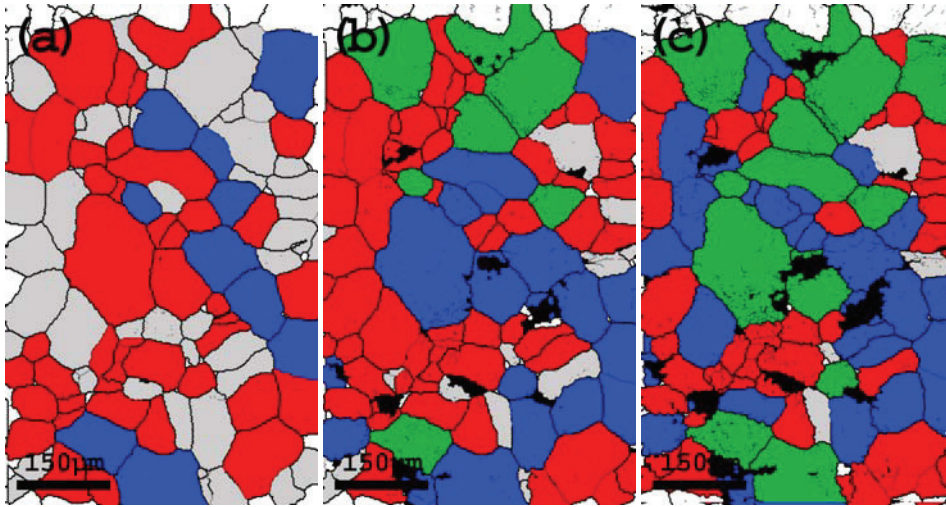


Figure 5.50 – Evolution in the number of observed slip traces in the individual grains during deformation of a specimen without texture 90° related to ED. Grains without any visible slip traces (grey), 1 (red), 2 (blue) and 3 (green) sets of visible slip traces are highlighted. (a) 6%, (b) 12% and at (c) uniform strain (18%).

More detailed slip trace investigations of this specimen at 90° reveal that only a very limited number of slip traces transmit over the grain boundaries. The directional changes over the grain boundary of continuous slip traces are also large compared to the changes observed in the material prior to cross-rolling and subsequent heat-treatment. However, the additional slip traces activated during deformation often coincide with the primary slip traces of a neighbouring grain. Figure 5.51 shows a grain which locally develops two sets of additional slip traces and these coincide with the slip traces of the nearest neighbours. Only one set of slip traces are visible at 6% but one additional set of slip traces develop in the lower right corner of the grain after 12% elongation. This set of slip traces is parallel to the primary slip traces of the grain directly beneath the lower right corner of the grain investigated. Further, when this grain is deformed to a macroscopic strain of 18% also a third set of slip traces has become visible. This set of slip traces develops at the centre of the grain and are perfectly aligned to the slip traces observed in the large grain above. In general, there are several observations showing that additional slip traces developed during deformation are affected by the primary set of slip traces in the neighbouring grains.

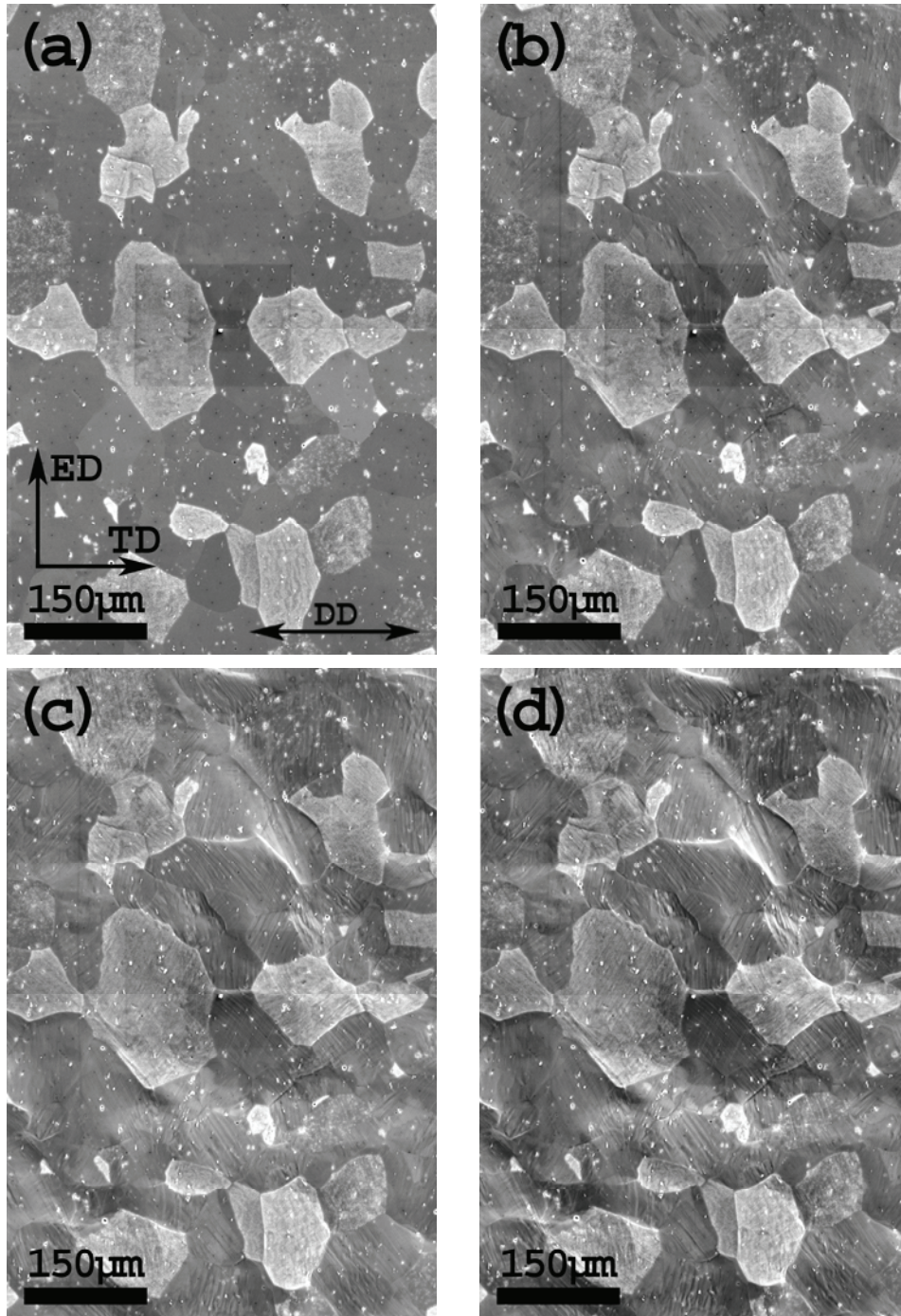


Figure 5.49 – SE micrographs of the specimen surface (ED-ND plane) after different amounts of axial elongation for a specimen with random texture deformed in the 90° direction. (a) 6%, (b) 12% and (c) uniform strain (18%).

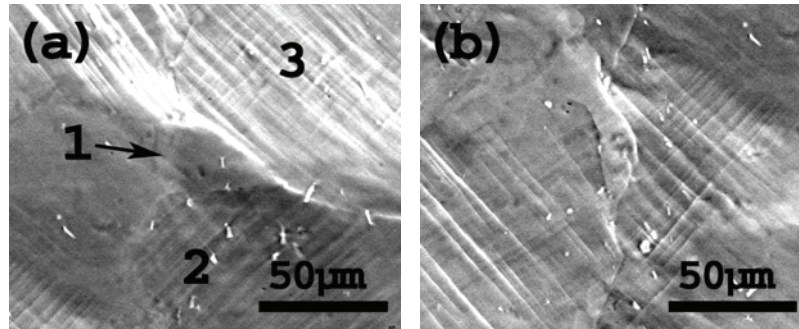


Figure 5.47 – SE micrographs of the observed slip traces at 18% deformation for a specimen deformed 90° to ED. The labelled grains are investigated in more detail in section 5.6.2. (a) Grain without slip traces (#1) surrounded by heavily deformed grains, and (b) two grains with multiple slip.

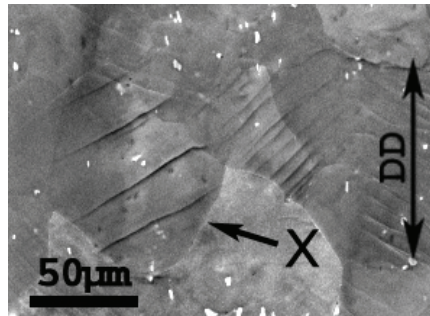


Figure 5.48 - SE micrograph of grains with one set of irregular shaped slip traces for a specimen deformed parallel to ED. Please note the relative large separation distance between the traces (coarse slip) for the grain labelled X.

The slip traces are also investigated for specimens where the crystallographic texture has been more or less removed by cross-rolling and subsequent annealing. It should be noticed that the slip trace distribution of this material condition is somewhat more complicated. Figure 5.49 presents the slip trace evolution of such specimen deformed 90° to ED, and also here the micrographs correspond to the IPF maps presented in section 5.5.1. The observed slip traces are more heterogeneously distributed and some grains develop multiple slip traces already at 6% elongation, while other grains do not develop any visible slip traces even at the uniform strain (Figure 5.50). The micrographs of the slip trace evolution also show that a large fraction of the grains develop as many as 3 sets of slip traces during deformation. The results presented here indicate that during deformation the material without texture develops denser and more multidirectional slip traces compared to the material with strong crystallographic texture.

Experimental results – Part B

The trace morphology presented in Figure 5.46, shows that the slip traces often run continuously through the grain interior and in some cases over the grain boundary into the neighbouring grains. In other words, slip traces stretch from one grain into another, often with only minor changes in the intersection angle over the grain boundary. This is very evident for the specimens deformed in the 45° direction where a regular set of slip traces stretches from grain to grain only with $1-2^\circ$ change in orientation. The density of continuous slip traces is not as high for the 90° specimens as for the two other directions. However, also specimens deformed in this direction have several grain boundaries with continuous slip traces, see e.g. Figure 5.47. The changes in orientation over the grain boundary are often somewhat higher for this DD, and it is also more common that the grain surface possesses an additional set of discontinuous slip traces.

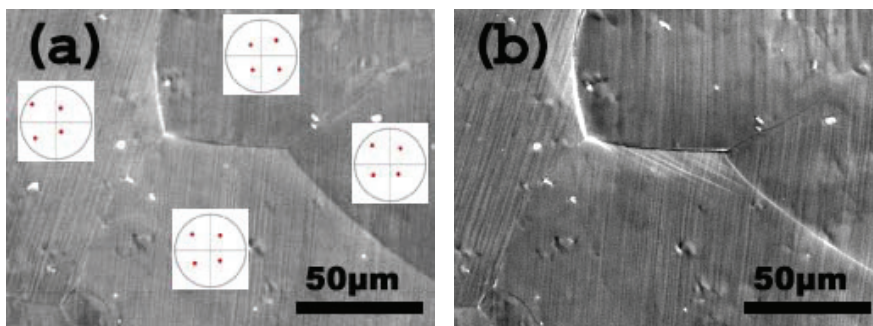


Figure 5.46 – SE micrograph of the observed slip traces at the specimen surface for a specimen deformed 45° to ED. (a) At 9% deformation only one set of slip traces in each grain has developed. 111 pole figures from the individual grains are included in order to show the orientation differences over the grain boundaries. (b) A second set of slip traces develops locally at 21% deformation.

The slip traces seem to be more irregular for the 90° specimens, and this is especially true for grains with an additional set of slip traces (Figure 5.47). Irregular slip traces are also observed in grains with only one set of slip traces. Figure 5.48 shows two grains with irregular slip traces in a specimen deformed parallel to ED. This kind of slip traces is more curved than the regular one. It is also observed that the slip trace separation distance is enlarged for these grains, i.e. coarser slip trace distribution. The slip trace separation distance is as high as $\sim 15\mu\text{m}$ for the grain on the left hand side of Figure 5.48, while the typical value for a grain with regular slip traces is $1-3\mu\text{m}$. It is also worth noticing that the slip traces in grains with a high slip trace separation distance are often thicker than ordinary slip traces.

Experimental results – Part B

In general, the observations show that the individual grains in this material (strong ED-rotated Cube texture) only develop a limited number of non-parallel slip traces. However, it is important to remember that the Cube texture is very symmetrical for the selected deformation directions. Hence, in some special cases, slip on two different slip planes will produce close to parallel slip traces and it becomes difficult to determine the exact number of slip planes activated. Nevertheless, even though the number of slip traces is low for all deformation directions, the number of visible intense slip traces is much higher for the specimen deformed in the 90° direction compared to the other two directions. Figure 5.44 and Figure 5.45 show the evolution in the number of observed slip traces in the individual grains during deformation 45° and 90° related to ED respectively. It is also clear that a more uniform slip trace distribution is observed for the 45° specimens compared to the 90° specimens. Additional slip traces develop only in the neighbourhood of grain boundaries as shown in Figure 5.46, hence the whole grain is seldomly covered with these additional traces. However, in this investigation the number of observed slip traces was determined based on the number of non parallel traces observed within a single grain even though these do not cover the same surface area.

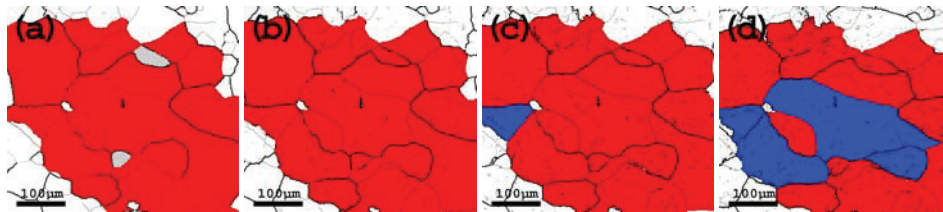


Figure 5.44 – Evolution in number of observed slip traces in the individual grains of a specimen with texture during deformation 45° related to the ED. Grains without any visible slip traces (grey), 1 (red) and 2 (blue) sets of visible slip traces are highlighted. (a) 6%, (b) 12%, (c) 18% and (d) uniform strain (27%).

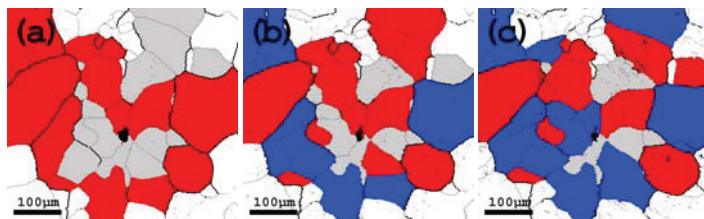


Figure 5.45 – Evolution in number of observed slip traces in the individual grains of a specimen with texture during deformation 90° related to the ED. Grains without any visible slip traces (grey), 1 (red) and 2 (blue) sets of visible slip traces are highlighted. (a) 6%, (b) 12% and (c) uniform strain (18%).

Experimental results – Part B

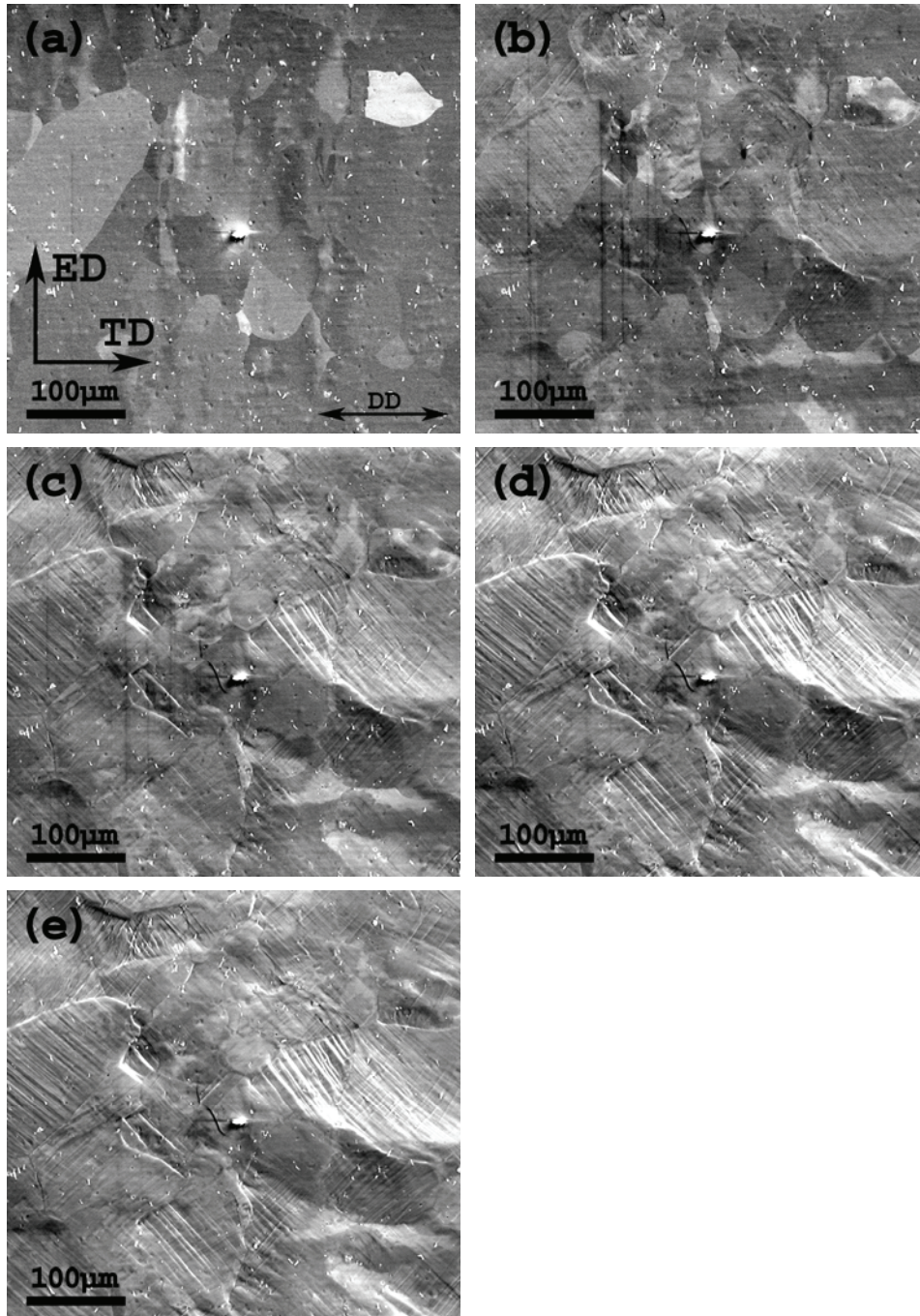


Figure 5.43 – SE micrographs of the same surface area (ED-ND plane) after different amounts of axial elongation in the 90° direction. (a) Initial orientation, (b) 6%, (c) 12%, (d) 18% and (e) uniform strain (21%). Alloy AA6063 strained in the T1 condition.

Experimental results – Part B

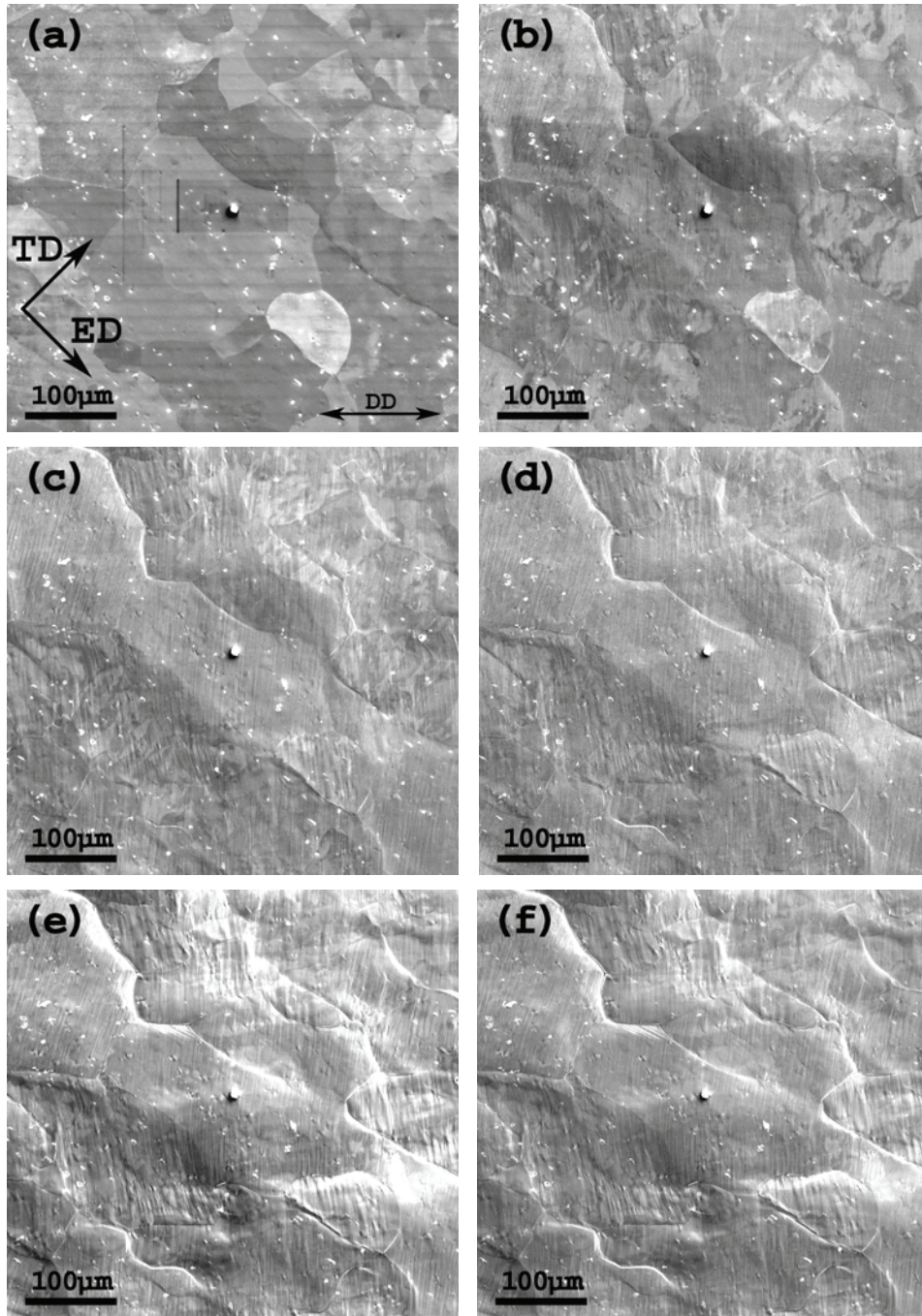


Figure 5.42 – SE micrographs of the same surface area (ED-ND plane) after different amounts of axial elongation in the 45° direction. (a) Initial orientation, (b) 6%, (c) 12%, (d) 18%, (e) 24% and (f) uniform strain (27%). Alloy AA6063 strained in the T1 condition.

Experimental results – Part B

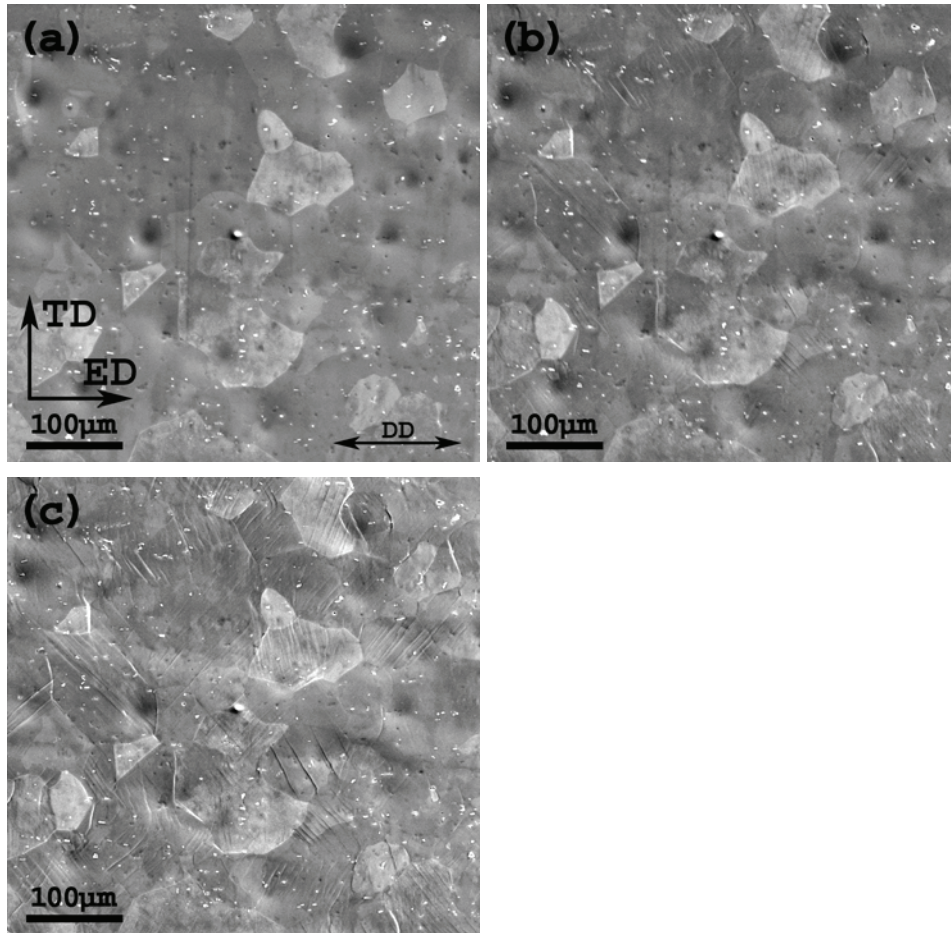


Figure 5.41 – SE micrographs of the same surface area (ED-ND plane) after different amounts of axial elongation in the 0° direction. (a) Initial orientation, (b) 6% and (c) uniform strain (12%). Alloy AA6063 strained in the T1 condition.

5.6 Plasticity

Aluminium alloys deform plastically with crystallographic slip as the most significant deformation mechanism. Crystallographic slip often gives rise to slip traces at the specimen surface. In the present work, SE micrographs of the specimen surface were used to study the slip trace evolution of the recrystallized alloy during in-situ deformation. Information from the slip trace investigations were also combined with information about the crystallographic orientations, and the slip activity of the individual grains were calculated based on this information. These investigations were performed on AA6063 in material condition T1.

5.6.1 Slip trace evolution

Grains often develop slip traces due to the relative movement of parallel slip planes taking place during dislocation movement. The microstructure often deforms inhomogeneously, i.e. some grains develop visible slip traces earlier than other grains, etc. If no slip traces are observed within a grain, this usually indicates that this grain does not deform plastically, hence the grain is unfavourable oriented for slip. Figure 5.41 to Figure 5.43 present SE-micrographs of the slip trace evolution for specimens with a strong crystallographic texture deformed at 0°, 45° and 90° relative to the ED respectively. Notice that these micrographs correspond to the IPF maps presented above in section 5.5.1. The micrographs clearly show that some grains develop slip traces already after 6% axial elongation and that the specimens taken in the 0° and 90° directions generally start developing slip traces at higher strains than the 45° direction. Also, the specimens deformed in the 45° direction have the most homogeneous distribution of slip traces and only a very limited number of grains do not develop visible slip traces.

Experimental results – Part B

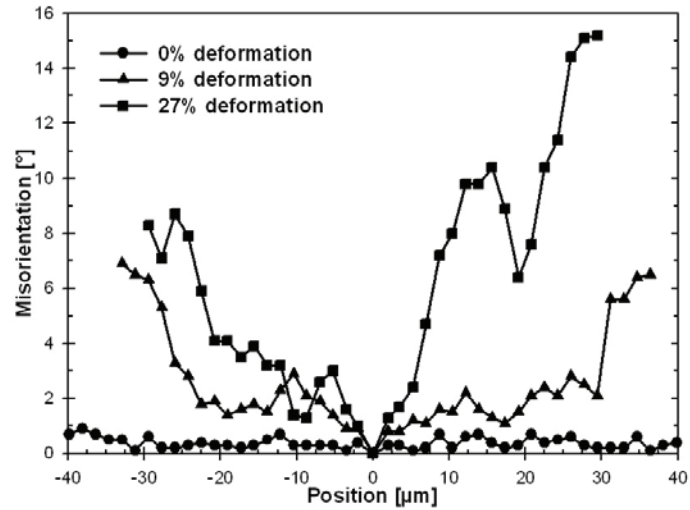


Figure 5.39 – Development of through grain misorientation gradients during deformation of grain #1 (the gradient and centre point position of grain #1 is indicated in Figure 5.28). The length of the plot becomes shorter due to contraction during deformation. The misorientation gradient becomes more evident at high deformation.

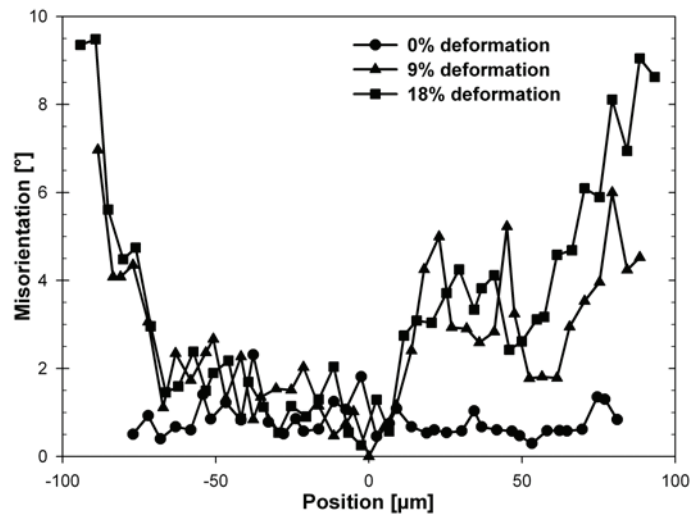


Figure 5.40 – Development of through grain misorientation gradients during deformation of grain #2 (the gradient and centre point position of grain #2 is indicated in Figure 5.34). The length of the plot becomes longer due to axial elongation during deformation. The misorientation gradient becomes more evident at high deformation.

5.5.4 Orientation gradients

The individual grains deform heterogeneously during plastic deformation, hence grains develop internal orientation gradients. Orientation gradients develop throughout the deformation process and are often very evident at the uniform strain. However, in some cases, the orientation gradients are visible in the IPF maps already after 6% axial elongation, i.e. the grains develop clear colour gradients which represent changes in orientation across the grains (Figure 5.31). At high strains these colour gradients become very evident and the orientation of the grain interior is represented by several colours.

The orientation gradient can be represented by a misorientation plot, where the reference orientation is the orientation of the pixel in the centre of the grain. Figure 5.39 presents the through grain misorientation evolution for a representative grain (see grain #1 in Figure 5.31) in a specimen deformed 45° related to ED. It is normal that grains have a uniform orientation prior to deformation. This is the case also for this grain. However, the grains often develop very strong orientation gradients toward the grain boundary during deformation. At the uniform strain, a misorientation of 16° is observed between the centre position and the grain boundary, and a steep orientation gradient is evident close to the grain boundary, i.e. the grains deform (rotates) heterogeneously.

Other grains develop more complicated orientation gradients. Figure 5.40 shows the orientation gradient observed in another grain (see grain #2 in Figure 5.34) taken from a specimen without any texture. This orientation gradient is taken parallel to the DD and the grain develops regions of different orientation (substructure) during deformation. However, also this grain develops clear orientation gradients toward the grain boundary. The misorientation between the centre position and the grain boundaries are as high as 10° at the uniform strain.

It should also be noticed that the length of the orientation profile across the grain under consideration changes during deformation. This change in size is enforced by the elongation/contraction of the investigated grain taking place by the plastic deformation process.

Experimental results – Part B

The above two figures also show that the amount of rotation during deformation is strongly dependent on the initial orientation. This means that the rotation of a texture component is determined by the selected DD. The rotation behaviour of the Cube, CG and Goss components has been investigated during deformation in the 0°, 45° and 90° directions (Figure 5.38). Specimens from AA6063 (strong ED-rotated Cube texture) have been used for this experiment. The results show a strong effect of the selected DD. The Goss component rotates less than 4° when deformed in the 0° and 45° directions and approximately 12° when deformed 90° related to ED. This observation is consistent with the observations in Figure 5.36 and Figure 5.37. The Goss component has a [100] and close to a [111] parallel to the DD when deformed in the 0° and 45° directions respectively, but a [101] parallel to the DD when deformed in the 90° direction as shown in Figure 5.38. Further, the Cube component has a [100] direction parallel to the DD when deformed 0° and 90° to ED and a [101] parallel to the last direction. It is therefore not surprising that for Cube oriented grains deformed in these three directions (Figure 5.38), only minor rotation is observed in the 0° and 90° directions (less than 4°) while very large rotations (approximately 15°) appear when deformed in the 45° direction. It is also worth noticing that none of the important texture components will give rise to crystallographic rotations when deformed parallel to ED (less than 4°).

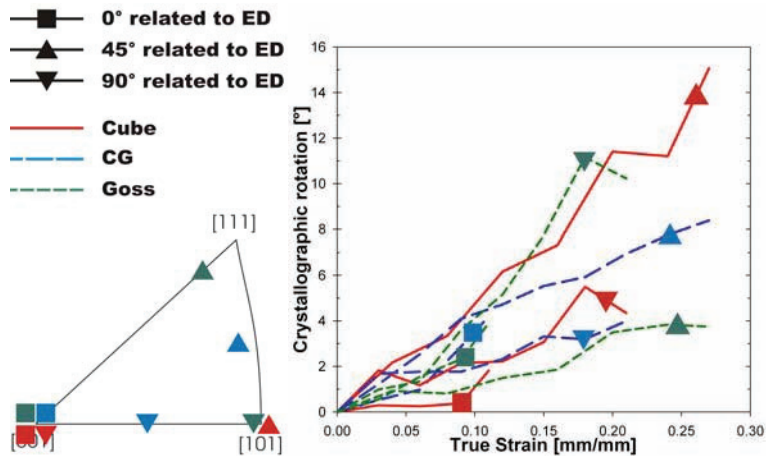


Figure 5.38 – Amount of crystallographic rotation as a function of the global strain for the Cube (red), CG (blue) and Goss (green) orientations deformed 0° (square), 45° (triangle up) and 90° (triangle down) related to ED. The crystallographic direction parallel to the DD for the different texture components and deformation directions are given in the IPF.

Experimental results – Part B

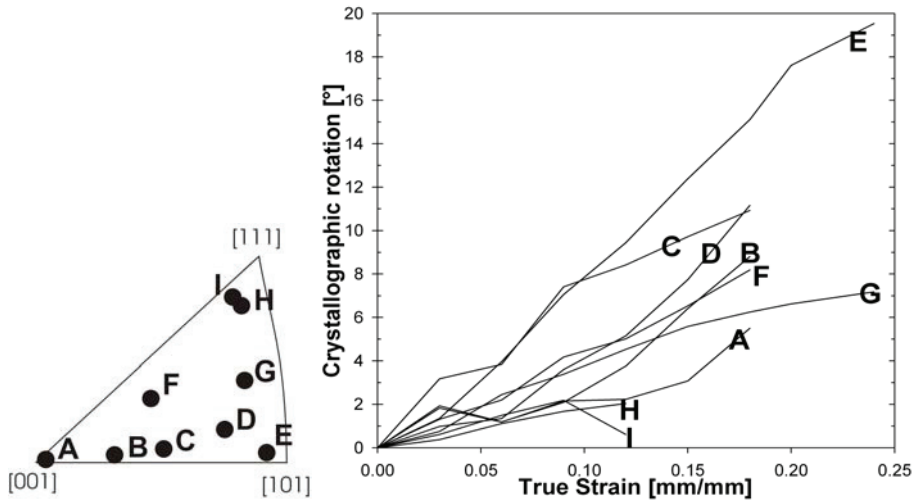


Figure 5.36 – Amount of crystallographic rotation as a function of the global strain for a selection of initial orientations in a material with strong crystallographic texture.

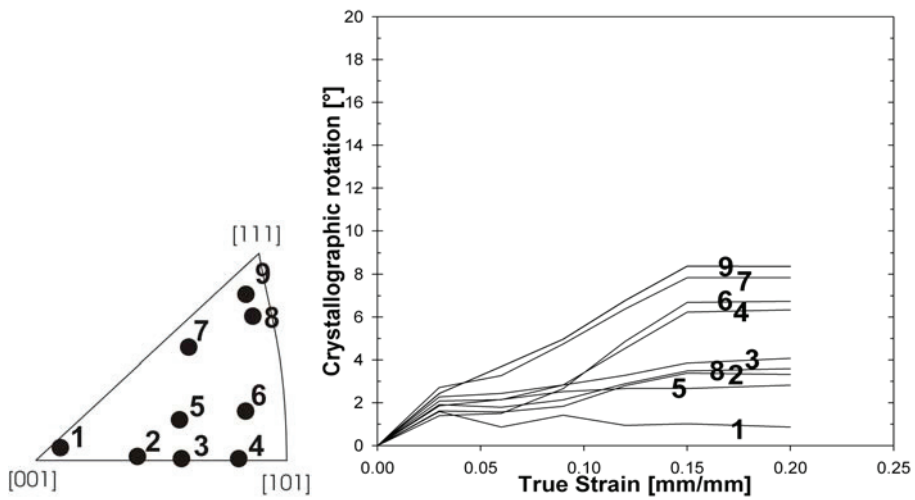


Figure 5.37 – Amount of crystallographic rotation as a function of the global strain for a selection of initial orientations in a material without crystallographic texture.

5.5.3 Amount of rotation

The amount of rotation during deformation is as indicated in the previous section, very dependent on the initial orientation (Figure 5.36 and Figure 5.37). Here, rotation is presented as a function of the macroscopic elongation (global strain) for a selection of grains with different initial orientations. Only the crystallographic direction parallel to the DD is taken into account during the selection of grains. The observations show that grains having a [101] parallel to the DD rotates more than 3 times as much as grains having more stable directions parallel to the DD, e.g. grain E rotates close to 20° during deformation, while both grain A and I rotates less than 6°.

The individual grains in Figure 5.36 were taken from specimens having a strong texture while the grains in Figure 5.37 were taken from specimens where the texture is removed by cross-rolling and subsequent heat-treatment. It is worth noticing that the selection of initial orientations in Figure 5.36 was obtained by choosing different deformation directions from the material with strong texture, i.e. the total amount of deformation (global strain) varies due to anisotropy in uniform strain. The amount of rotation for grains with close to identical crystallographic orientation differs for material with and without any crystallographic texture. Grain C in Figure 5.36 and Grain 3 in Figure 5.37 have almost the same initial crystallographic orientation but the amount of rotation taking place during deformation is 11° and 4° respectively. The results clearly show that the grains in a material with strong crystallographic texture (many of the neighbouring grains have similar orientations) rotate more than grains in a material without a pronounced texture.

Experimental results – Part B

The investigations performed on specimens without texture provide information about the relation between rotation of individual grains and the crystallographic orientation of the neighbouring grains. The individual grains in specimens without crystallographic texture are surrounded by grains with a random selection of orientations, while the grains in a specimen with very strong texture are to a large extent surrounded by grains with orientations similar to the orientation of the grain itself. This has allowed investigations of the enforced constraints introduced by the crystallographic orientations of the neighbouring grains.

Notice that some black areas appear toward the end of the deformation process (Figure 5.34). The black areas consist of non-indexed pixels due to low pattern quality, i.e. the crystallographic orientations can not be determined by the EBSD technique. The appearances of these black areas indicate large topography at the specimen surface, causing the pattern quality to drop dramatically in the shadows behind the introduced obstacles.

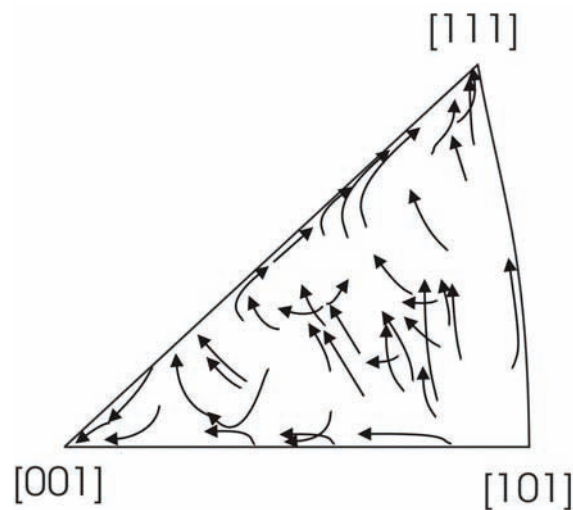


Figure 5.35 – Rotation paths in the IPF parallel to the DD for a specimen with random texture deformed 90° related to ED. The arrows indicate the rotation path of the individual grains, starting at the initial orientation and ending at the orientation at uniform strain.

Experimental results – Part B

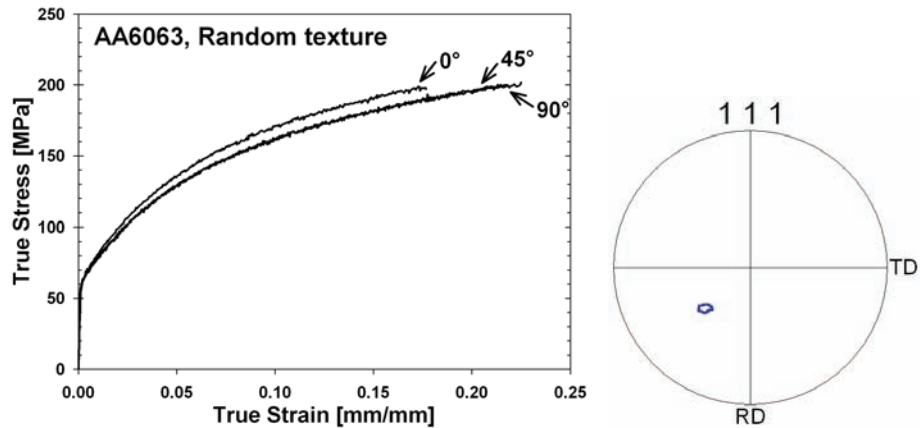


Figure 5.33 – True stress-strain curves 0°, 45° and 90° to ED after cross-rolling and subsequent heat-treatment of AA6063 obtained with an initial strain rate of $1.1 \times 10^{-3} \text{ s}^{-1}$ (left). Calculated 111 pole figure representing the initial texture (i.e. lack of texture) after cross-rolling and subsequent heat-treatment (right).

The area fraction of high angle grain boundaries (HAGB) is extensively increased after the crystallographic texture is removed by cross-rolling and subsequent heat-treatment. This is indicated by the grain boundaries included in the IPF maps presented in Figure 5.34. These maps contain a much higher fraction of HAGBs compared to the maps presenting the microstructure in the as-extruded condition (see e.g. Figure 5.28). The high fraction of HAGBs is consistent with the random texture observed in this material condition.

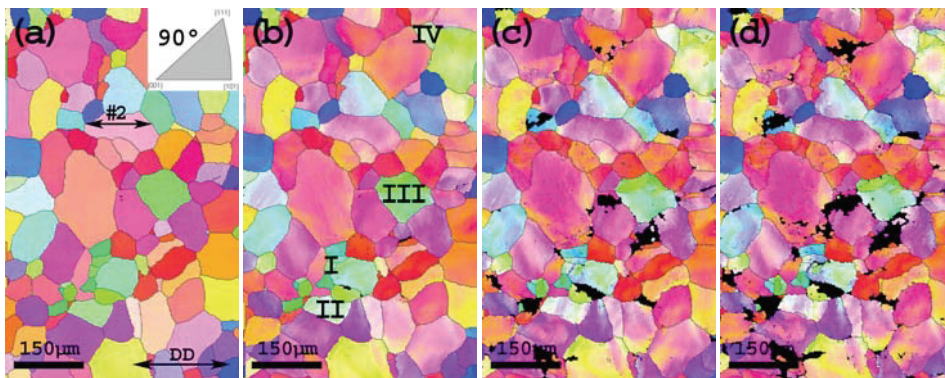


Figure 5.34 – IPF map in the deformation direction based on orientation data after different amount of axial elongation for a specimen with random texture deformed in the 90° direction. (a) Initial orientation, (b) 6%, (c) 12% and (d) uniform strain (18%). The black arrow labeled #2 in figure (a) indicates a grain used for orientation gradients investigations in section 5.5.4. The grains labeled I-IV in figure (b) are the grains used for crystallographic rotation investigations in Figure 6.19.

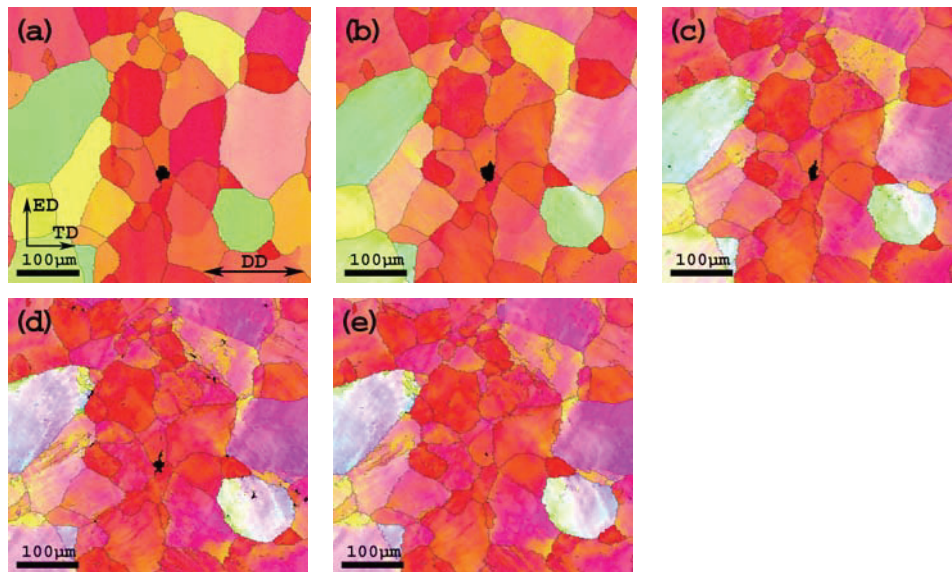


Figure 5.32 – IPF map in the deformation direction based on orientation data after different amounts of axial elongation in the 90° direction. (a) Initial orientation, (b) 6%, (c) 12%, (d) 18% and (e) at uniform strain (21%).

5.5.2 Rotation paths – random textured material

Figure 5.33 shows that specimens taken from the same material after cross-rolling and subsequent heat-treatment possesses close to a random texture, i.e. the material has close to isotropic mechanical properties. Another effect of the random texture is that the initial orientation of the individual grains covers the entire inverse pole figure. Specimens taken from this material are investigated under the same conditions as described above, i.e. studying the rotation paths of grains with initial orientations not covered by the strongly textured specimens. Figure 5.34 presents the IPF map evolution of the DD for a specimen deformed in the 90° direction. It is evident that the crystallographic orientations of the individual grains are widely spread for specimens deformed in this direction, i.e. the grains have different colours in the IPF map. Further, the rotation paths of a larger selection of grains from this specimen are presented in Figure 5.35. In general, the individual grains of this specimen follow the same trends as the material with a strong crystallographic texture. Consequently, the grains rotate toward aligning the crystallographic directions with the 001||DD and 111||DD poles of the IPF.

Experimental results – Part B

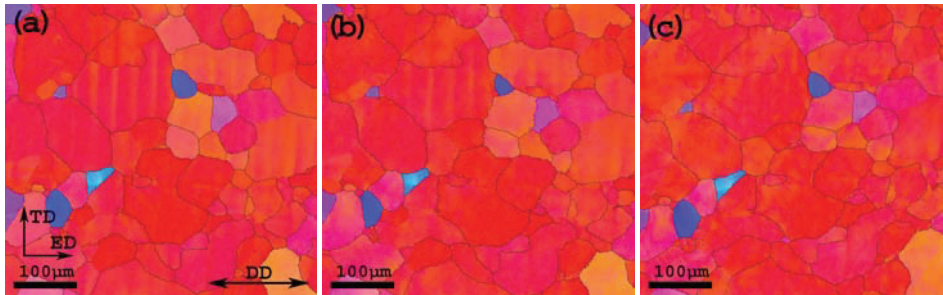


Figure 5.30 – IPF map in the deformation direction based on orientation data after different amounts of axial elongation in the 0° direction. (a) Initial orientation, (b) 6% and (c) at uniform strain (12%).

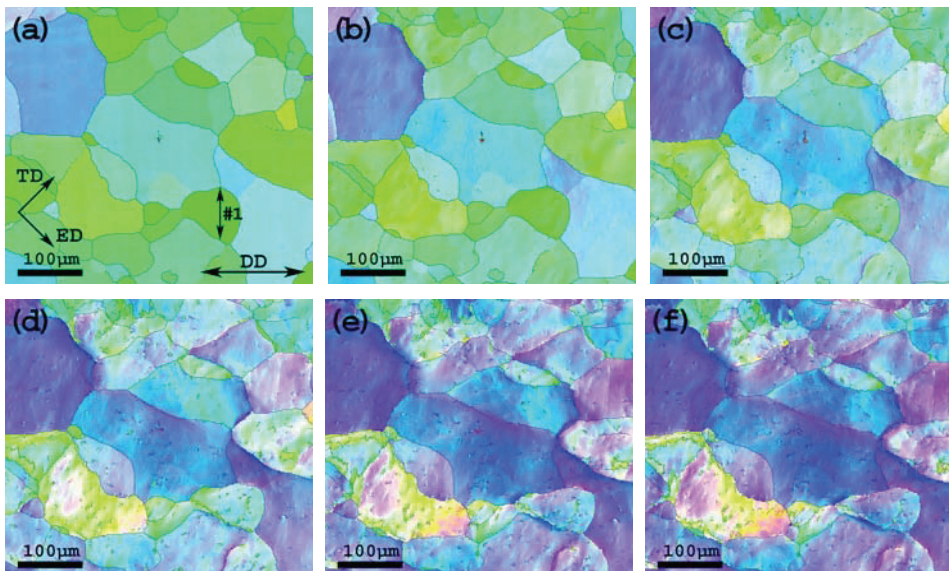


Figure 5.31 – IPF map in the deformation direction based on orientation data after different amounts of axial elongation in the 45° direction. (a) Initial orientation, (b) 6%, (c) 12%, (d) 18%, (e) 24% and (f) at uniform strain (27%). The black arrow labeled #1 in the figure indicates a grain used for orientation gradients investigations in section 5.5.4.

Experimental results – Part B

information about grains with an initial orientation from the upper part of the IPF. In spite of these limitations, Figure 5.29 shows the rotation path $\langle uvw \rangle \parallel DD$ of a representative selection of grains from specimens deformed 0° , 45° and 90° related to ED. As a first approximation, it seems like the grains rotate toward aligning the crystallographic directions with the $001 \parallel DD$ and the $111 \parallel DD$ poles of the IPF. Successive IPF maps also provide information about the rotation path, since alterations in colour indicate the crystallographic rotation taking place as shown in Figure 5.30 to Figure 5.32. It is evident that the grains rotate toward the $001 \parallel DD$ and $111 \parallel DD$ poles since the colour becomes more red and blue respectively. These figures also show that the deformation process is very heterogeneous since the grains develop strong colour gradients during deformation. Section 5.5.4 will present these heterogeneities in more detail.

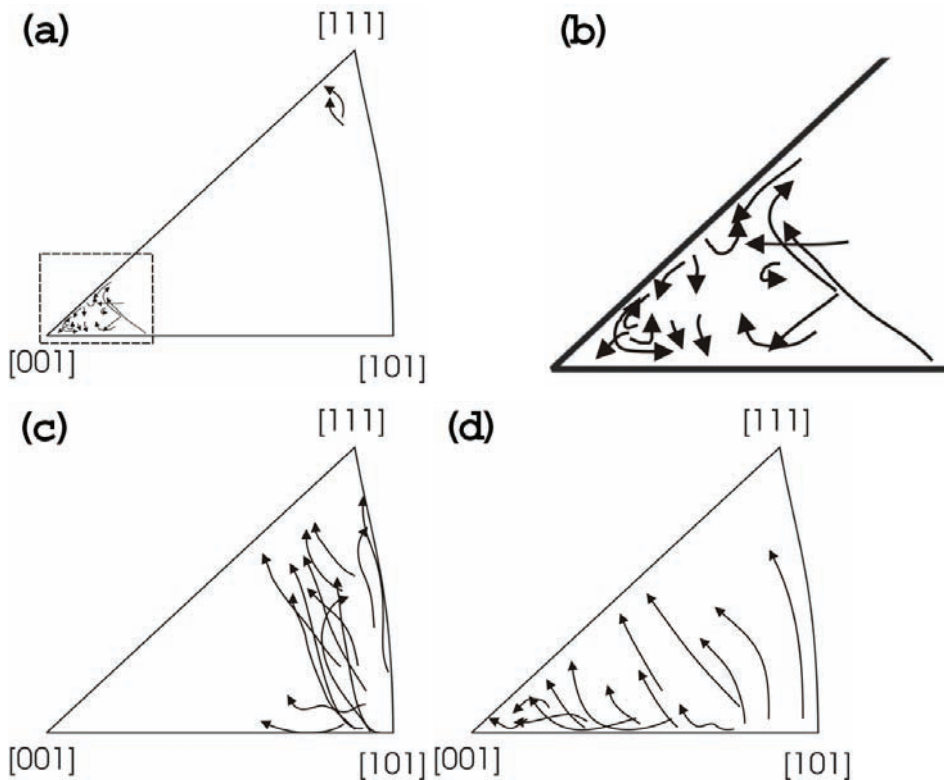


Figure 5.29 – Rotation paths in the IPF parallel to the DD upon straining to the uniform strain. The arrows indicate the rotation path of individual grains. (a) 0° direction (b) zoom of the $[001]$ corner from the 0° direction. (c) 45° direction and (d) 90° direction.

Experimental results – Part B

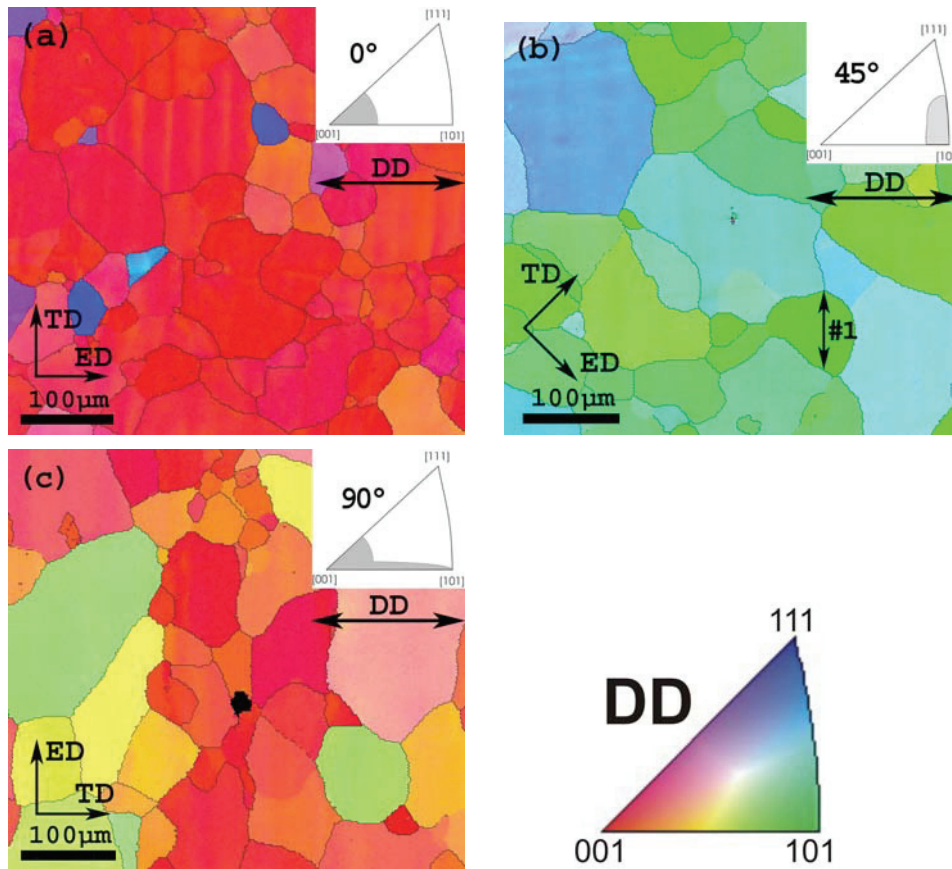


Figure 5.28 – IPF map in the deformation direction of the initial (non-deformed) orientations. The range of directions \parallel DD (parallel to DD) is indicated by an IPF in the upper right corner. (a) 0° direction (b) 45° direction and (c) 90° direction. The black arrow labeled #1 in the figure indicates a grain used for orientation gradients investigations in section 5.5.4.

It has already been shown that the present material has a very strong crystallographic texture. Thus, the microstructure consists of grains with resembling crystallographic orientations, i.e. neighbouring grains have close to equal crystallographic directions parallel to the DD. However, there are some clear differences between the three directions investigated. All the grains from the 0° specimen circumscribe the $001 \parallel$ DD pole of the DD IPF and most of grains from the 45° specimen circumscribe the $110 \parallel$ DD pole, being red and green respectively (Figure 5.28). On the other hand, the grains from the 90° specimen are scattered along the axis connecting the $001 \parallel$ DD and $110 \parallel$ DD poles of the DD IPF. This means that neither of the specimens provides

5.5 Grain rotation with increasing strain

SEM experiments with improved resolution (reduced step size) are performed in order to follow the grain rotation of individual grains during simple tension. Also here, 3% axial elongation was selected as an appropriate deformation step size. Each grain is represented by at least 500 orientation measurements and the data is used to calculate both the rotation path and amount of rotation for grains with different initial orientation. Some grains develop internal orientation gradients during deformation and also these gradients are investigated.

5.5.1 Rotation paths – heavily textured material

Inverse pole figures (IPF) present the rotation taking place during deformation. The individual grains primarily rotate by aligning stable crystallographic orientations parallel to the tensile direction (see e.g. Han et al. 2003). Hence, only the inverse pole figures in the deformation direction (DD) are of interest. Figure 5.28 presents DD IPF maps of the initial orientations 0° , 45° and 90° related to ED. The DD IPF map evolutions upon straining of these specimens are given in Figure 5.30 to Figure 5.32. The full range of initial orientations was not covered by these experiments due to the strong crystallographic texture. It was therefore not possible to study the rotations taking place during deformation by simple tension for all possible types of grain orientations. The crystallographic direction parallel to the DD is a combination of the texture and the selected DD. The texture components will therefore behave differently when deformed in different DD, e.g. a grain with Cube orientation has a $[100]$ parallel to the DD when deformed in the 0° and 90° directions and a $[101]$ when deformed in the 45° direction (as indicated in Chapter 5.4). A grain with a Goss orientation, on the other hand, has a $[100]$ and a $[101]$ parallel to DD when deformed in the 0° and 90° directions respectively. When deformed in the 45° direction, this texture component has close to a $[111]$ parallel to the DD, hence the rotation path is very dependent on both the crystallographic orientation and the DD.

Experimental results – Part B

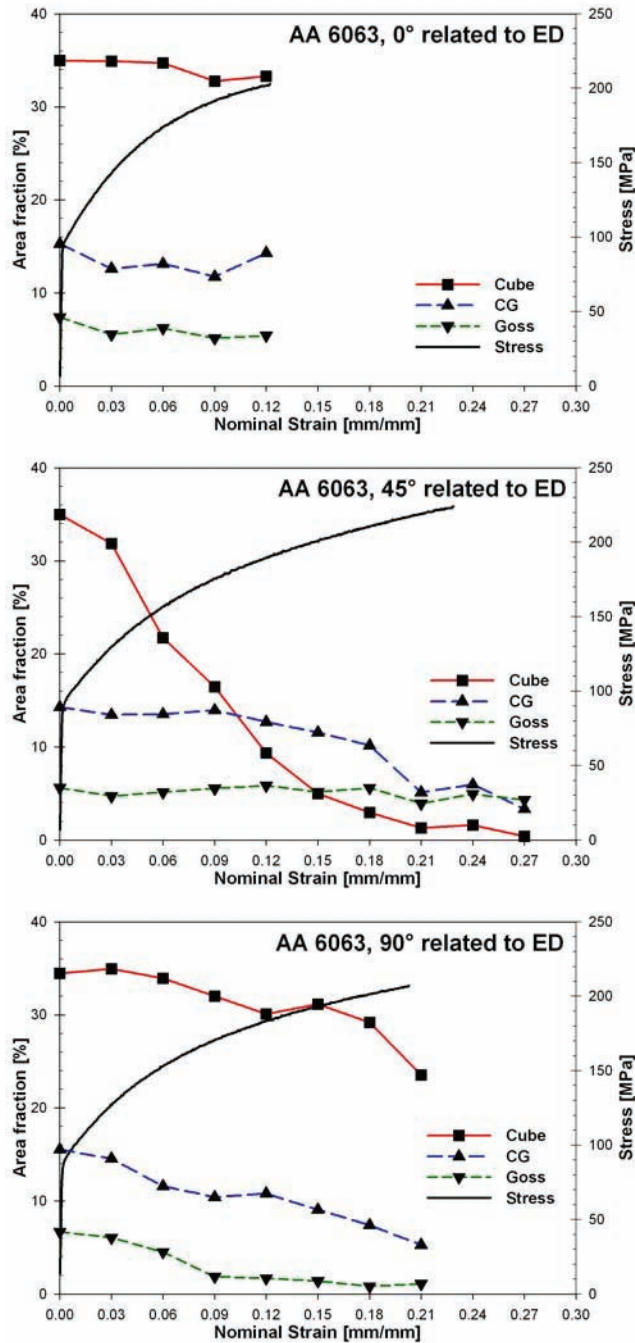


Figure 5.27 – Area fraction evolution of the Cube, CG and Goss components during deformation (nominal strain) of AA6063. The corresponding full thickness true stress-strain curve in material condition T1 is included.

Experimental results – Part B

Figure 5.26 shows that the texture hardly is affected when deformed 90° to ED. The orientation of the slip planes and directions resembles those for specimens deformed parallel to ED, hence it should be expected that the crystallographic texture of the 90° specimen was unaffected by deformation. However, there are still some vague indications of texture evolution for this specimen. The pole-figures show that grains initially having close to a $[100]$ parallel to the DD (slightly ED rotated grains), rotate toward aligning the $[100]$ to the DD. This means that the peak close to the transversal direction of the pole-figure becomes somewhat narrower.

Moreover, more detailed examinations of the texture evolution during deformation (Figure 5.27) reveal other important differences between the three directions investigated. The evolution of the three most important texture components (Cube, CG and Goss) has been investigated in great detail. All the investigated texture components have a $[100]$ parallel to the DD when deformed parallel to the ED. Figure 5.27 shows that the intensity of these components is unaffected by deformation, thus indicating that grains having a $[100]$ parallel to the DD tend to be stable. Cube oriented grains also have this $[100]$ direction parallel to the DD when deformed 90° to ED, and the figure shows that the area fraction of Cube oriented grains is close to constant also during deformation in this direction (Figure 5.27). However, the two other texture components are not stable. The area fraction of Goss oriented grains ($[101]$ parallel to the DD) is reduced with approximately 90% when deformed perpendicular to ED. Also the area fraction of the CG component is somewhat reduced. This shows that the Goss and CG components are stable in the 0° direction while the intensity decreases significantly when deformed 90° related to ED. The greatest rotations are observed during deformation of the 45° specimens. This becomes very evident if the area fraction of Cube oriented grains is investigated in detail. The area fraction of this orientation is very high prior to deformation ($\sim 35\%$) but it reduced dramatically (less than 1%) at the uniform strain. This specimen also shows a considerable reduction of the CG component during deformation. On the other hand, the Goss component is almost unaffected by tensile deformation at 45° . However, it is important to bear in mind that the Goss component has close to a $[111]$ parallel to the DD when deformed in this direction. It is also worth noticing that the DD with the most stable texture also has the largest work hardening rate and lowest uniform strain.

Experimental results – Part B

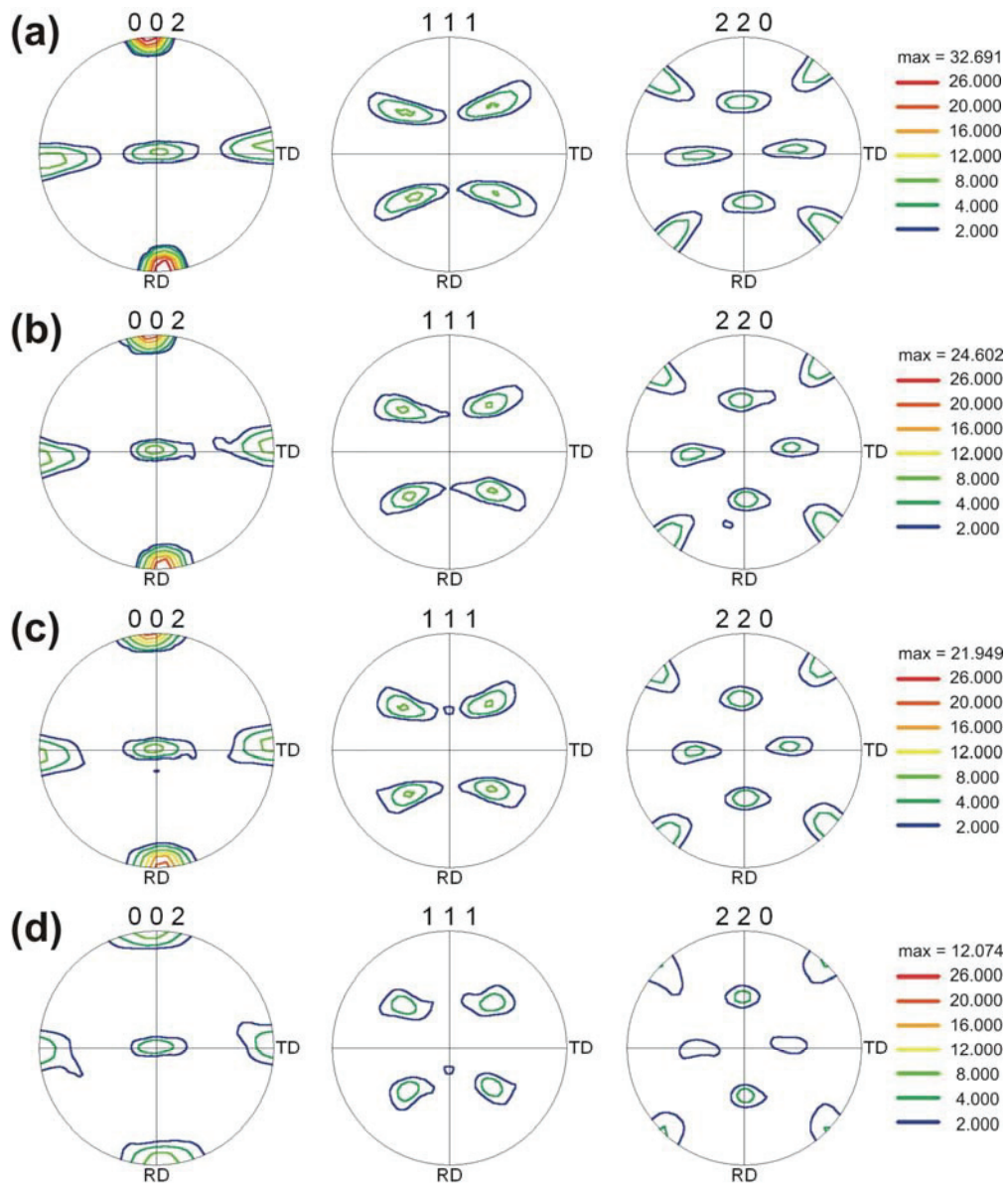


Figure 5.26 – Calculated pole figures based on orientation data after different amounts of axial elongation in the 90° direction. (a) Initial orientation (b) 6% (c) 12% and (d) uniform strain (21%).

Experimental results – Part B

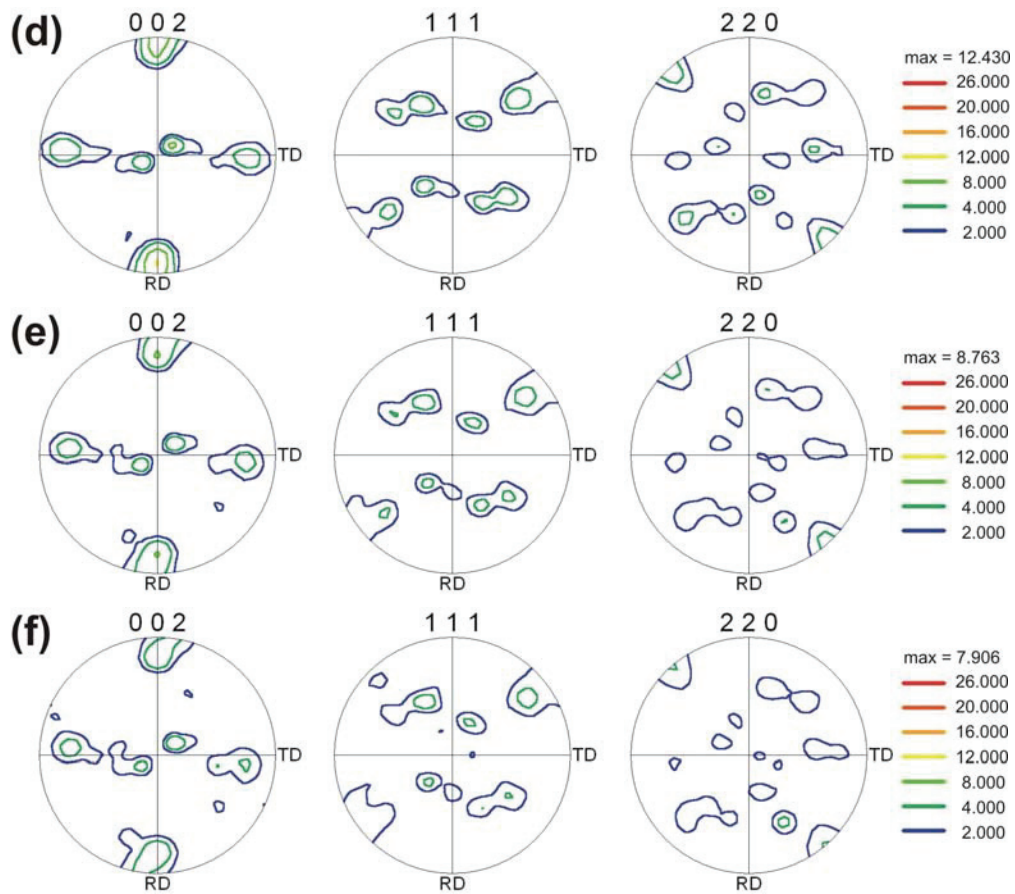
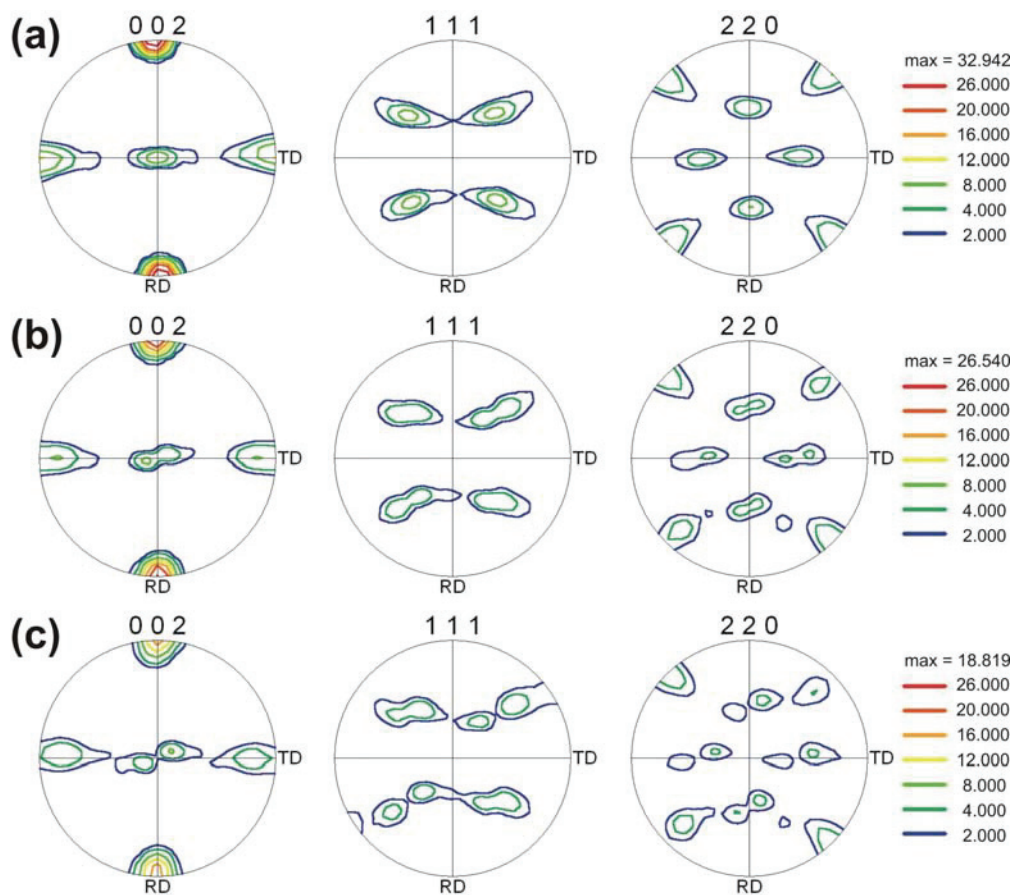


Figure 5.25 – Calculated pole figures based on orientation data after different amounts of axial elongation in the 45° direction. (a) Initial orientation (b) 6% (c) 12% (d) 18% (e) 24% and (f) uniform strain (27%).

As already mentioned, substantial crystallographic rotations are observed when the material is deformed 45° to ED (Figure 5.25). The pole-figures show that the 45° specimen rotates such that the $[111]$ becomes aligned with the deformation direction (DD). Further, the same figure shows that grains initially having a $[101]$ parallel to DD rotate toward more stable orientations with a more random distribution of the $[101]$ direction. Notice also that the material rotates away from having a $[100]$ parallel to the ND.

Experimental results – Part B

The texture is relatively stable during deformation 0° and 90° related to ED, while deformation in the 45° direction gives rise to quite large crystallographic rotations. Figure 5.24 clearly shows that the crystallographic texture is totally unaffected by deformation parallel to the ED. The pole-figures both after 6% deformation and at the uniform strain are close to identical with the pole-figure calculated based on the orientations acquired prior to deformation. The slight disparities can easily be explained by the inaccuracy of the calculation method.



(Figure continues on next page)

5.4 Global texture evolution with increasing strain

In-situ specimens from the centre layer of AA6063 are deformed 0° , 45° and 90° related to ED with an initial strain rate of $1 \times 10^{-4} \text{ s}^{-1}$. The specimens are deformed in steps of 3% axial elongation in order to perform texture measurements, and in consequence obtain information of the global texture evolution. The initial crystallographic texture of AA6063 consists mainly of the Cube, CG and Goss components as shown in Figure 5.8. Figure 5.24 to Figure 5.26 present the initial texture as well as the texture at the uniform strain and some intermediate strains for specimens deformed in the 0° , 45° and 90° directions respectively.

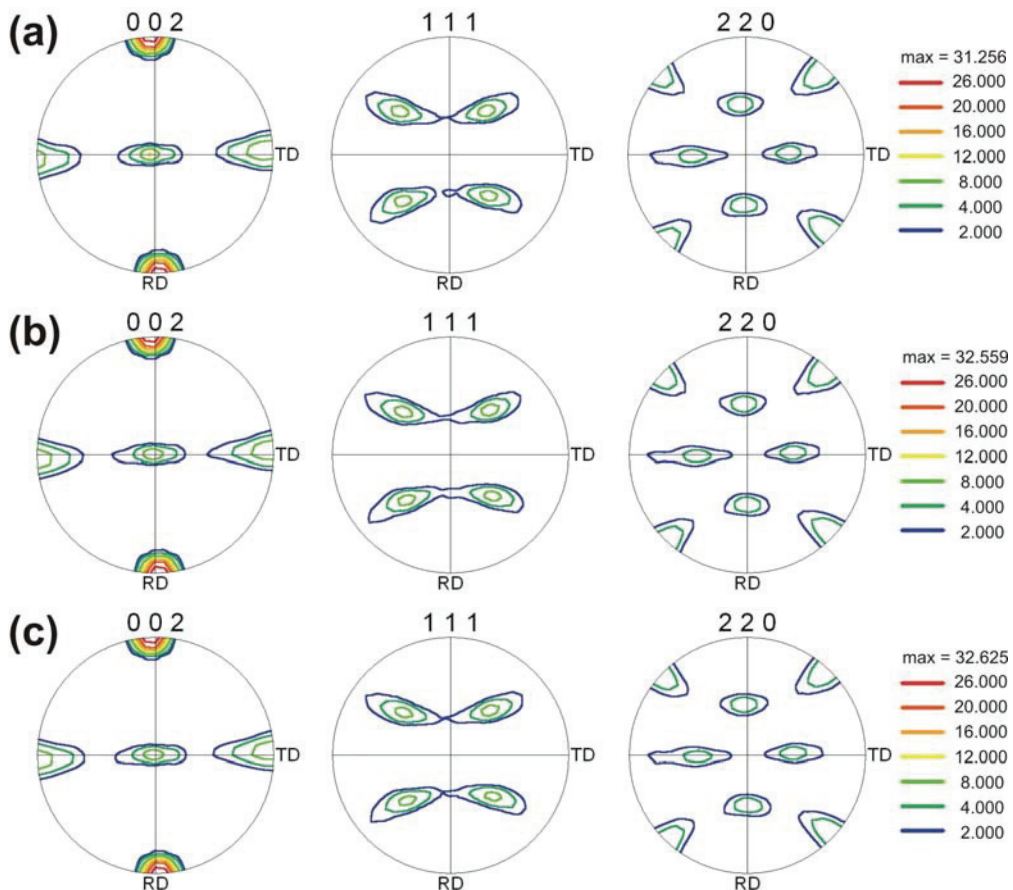


Figure 5.24 – Calculated pole figures based on orientation data after different amounts of axial elongation in the 0° direction. (a) Initial orientation (b) 6% and (c) uniform strain (12%).

Experimental results – Part B

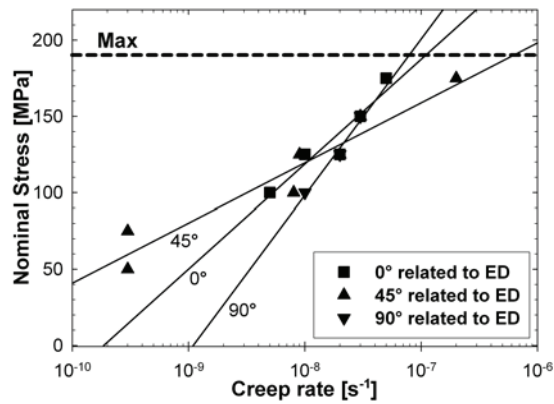


Figure 5.22 – Measured room temperature creep rate at different nominal stresses in the 0°, 45° and 90° directions of AA6063 in material condition T1. The maximal nominal stress is indicated by the dotted line.

Further, the in-situ deformation specimens are deformed in steps of typical 3% axial elongation. The deformation process has to be stopped in order to perform static investigations, i.e. EBSD mapping of the specimen surface. Figure 5.23 presents the average stress vs. strain curve obtained from the load and displacement transducer for typical in-situ experiments 0°, 45° and 90° related to ED. The same figure also presents curves from specimens deformed continuously with the same initial strain rate. The stress drops observed in the in-situ deformed curves correspond to the pauses necessary for the static investigations, and are related to stress relief in the material. However, these stress drops are not expected to have any influence on the deformation process since the overall shape from both sets of stress vs. strain curves is close to identical.

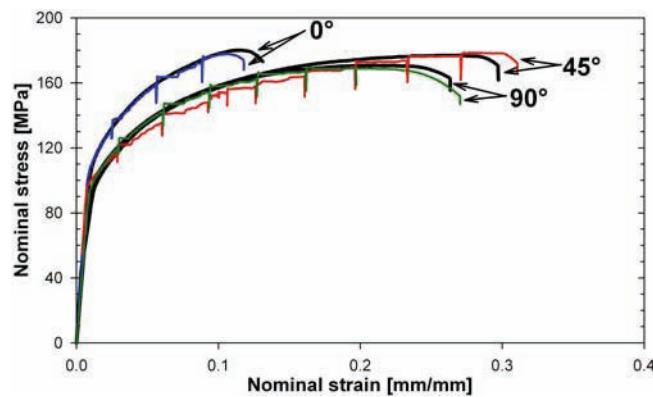


Figure 5.23 – Stress vs. strain curves obtained from the in-situ tensile machine showing no difference between the continuous and discontinuous deformed specimens.

Part B: SEM In-situ investigations of plasticity – Slip activity, grain rotation and texture evolution

Part B presents the results from in-situ deformation investigations (simple tension) in the SEM. SEM in-situ investigations facilitates studies on a grain scale, i.e. the grain rotation, plasticity and local strain distribution have been investigated. Also, the global texture evolution has been investigated by performing in-situ global texture measurements using EBSD.

5.3 Initial investigations

This experimental technique is relatively new and has previously never been used on extruded profiles of commercial Al-Mg-Si alloys. It was therefore necessary to verify the testing conditions utilised by performing some initial investigations prior to the in-situ experiments. A recrystallized microstructure is desired in order to obtain high quality EBSD patterns within a reasonable period of time and the SEM in-situ investigations are therefore only performed on the recrystallized AA6063.

First the room temperature (RT) creep rate is determined by performing creep experiments. The creep rate is critical with regard to the testing conditions, since it is important to select a strain rate higher than the current creep rate. It is known that plastic deformation leads to increased creep due to accumulation of internal stresses in the material. This means that the creep rate just prior to the ultimate stress is critical with regard to the in-situ experiments. Creep experiments performed at different nominal stresses in the 0°, 45° and 90° directions are presented in Figure 5.22. This figure confirms that the RT creep rate of AA6063 never exceeds $1 \times 10^{-6} \text{ s}^{-1}$. An initial strain rate of $1 \times 10^{-4} \text{ s}^{-1}$ is therefore selected for the in-situ deformation investigations performed on this material.

Experimental results – Part A

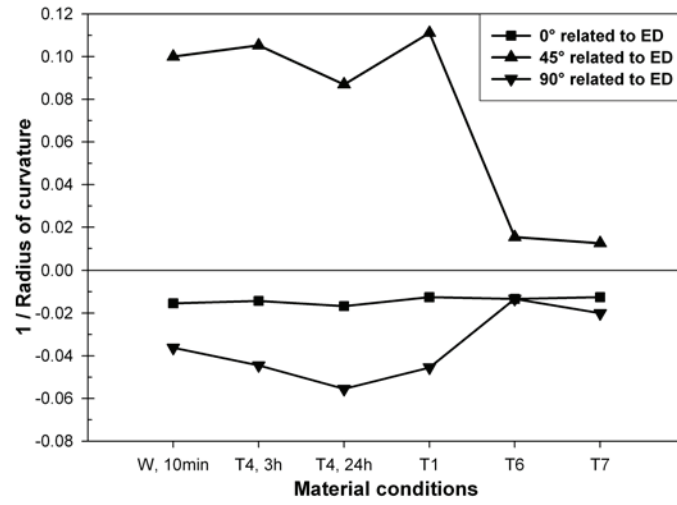


Figure 5.21 – Evolution in the end of cross-section shape of AA6063 during ageing.

Experimental results – Part A

The longitudinal strain is assumed to be independent of the position through the thickness, i.e. the transverse strain is directly linked to the r -values. In other words, the profile has the highest r -value in the centre of the profiles when deformed parallel and perpendicular to the ED and at the surface when deformed 45° related to ED. The effect of the through-thickness gradient is most evident in the 45° and 90° direction specimens. However, it is worth noticing that the affect of the through-thickness variations is more pronounced for AA6063 than for AA6082. Micrographs of the end of cross-section shape for all the specimens investigated are presented in Appendix E.

The end of cross-section shape changes during age-hardening and the through-thickness radius of curvature were determined in order to quantify these changes. Figure 5.21 presents the evolution in the inverse radius of curvature ($1/R$) during ageing of AA6063, and it is evident that the differences over the thickness are strongly reduced during ageing. A large absolute value means that the specimen has a large curvature over the thickness, while a small value means that the specimen thickness is close to constant. It should be noted that it is difficult to determine the radius of curvature accurately especially when the specimen cross-section shape is close to horizontal, i.e. the uncertainty of these measurements is more than $\pm 17\%$.

The end of cross-section shape is also altered due to age-hardening. The characteristic concave and convex shapes of the thickness direction are very evident both in the solution-heat-treated and the naturally aged tempers (Figure 5.20). However, the characteristic shapes disappear when AA6063 is artificially aged to T6 and T7, i.e. $1/R$ becomes close to zero. The material obtains more isotropic properties through the profile thickness and the thickness direction shape is close to horizontal. It is therefore reasonable to claim that age-hardening reduces or even removes the effect of through-thickness gradients.

5.2.3 Age-hardening vs. anisotropy and shape

The end of cross-section shape (Figure 5.20) of both alloys in the solution-heat-treated condition is concave when deformed in the 0° and 90° directions and convex when deformed at 45°. This means that the transverse strain is highest at the surface when deformed in the 45° direction and in the centre part of the profile when deformed in the two other directions.

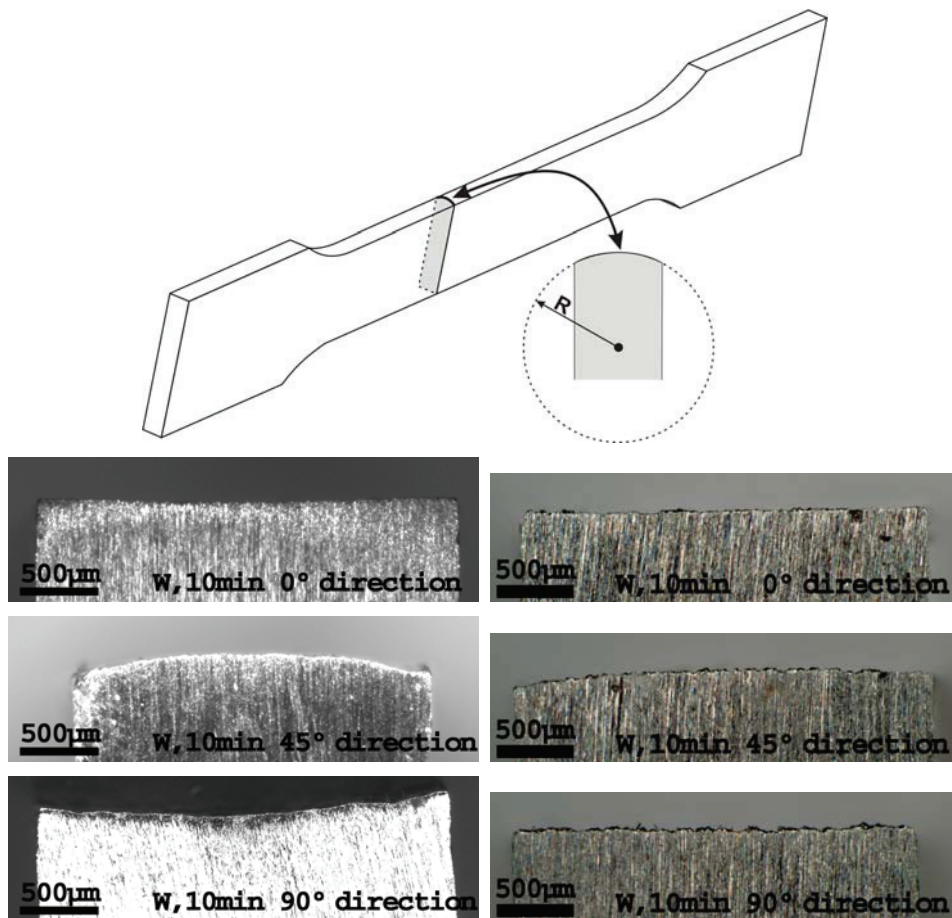


Figure 5.20 – End of cross-section shape after simple tension to the uniform strain in material condition W, 10min. AA6063 (left) and AA6082 (right). The R-value presented in the illustration defines the radius of curvature over the thickness.

Experimental results – Part A

strain will rapidly increase, i.e. the r -value increases. With artificial ageing, the serrated yielding will gradually diminish and the r -value curves become straight lines. It is clear that ageing postpones the onset of serrated yielding to higher strains as shown in both Figure 5.18 and Figure 5.19. It is also noteworthy that the onset-strain of serrated yielding seems to be direction-dependent for alloy AA6063 T4, 24h, but not obvious for the other ageing conditions. Also, the amplitude caused by the serrated yielding is very anisotropic.

Moreover, the general shape of the r -value curves depends on the tensile direction and the alloy composition, i.e. the shape of the r -value curves is texture dependent. The characteristic shape is present also during the wavy behaviour but it is more evident after the serrated yielding has come to an end. The r -values in the 0° and 45° directions of AA6063 are almost strain independent, being constant throughout the deformation process. In general, the 90° direction has a gradual reduction in the r -value with increasing strain, but for the T1 condition the slope is positive.

As a first approximation, all r -value curves for AA6082 have a linear shape, especially in the solution-heat-treated and naturally aged condition. The plastic strain ratio in the 45° and 90° directions is reduced with increasing strain while the opposite behaviour is observed when the specimens are deformed parallel to the ED. Closer investigations of the artificially aged material reveal that the plastic strain ratio increases for all directions at small strains while decreases again at higher strains. This means that the plastic strain rate evolution goes through a local maximum during deformation. Indications of the same behaviour are also observed after artificial ageing of AA6063 (see Figure 5.18).

Experimental results – Part A

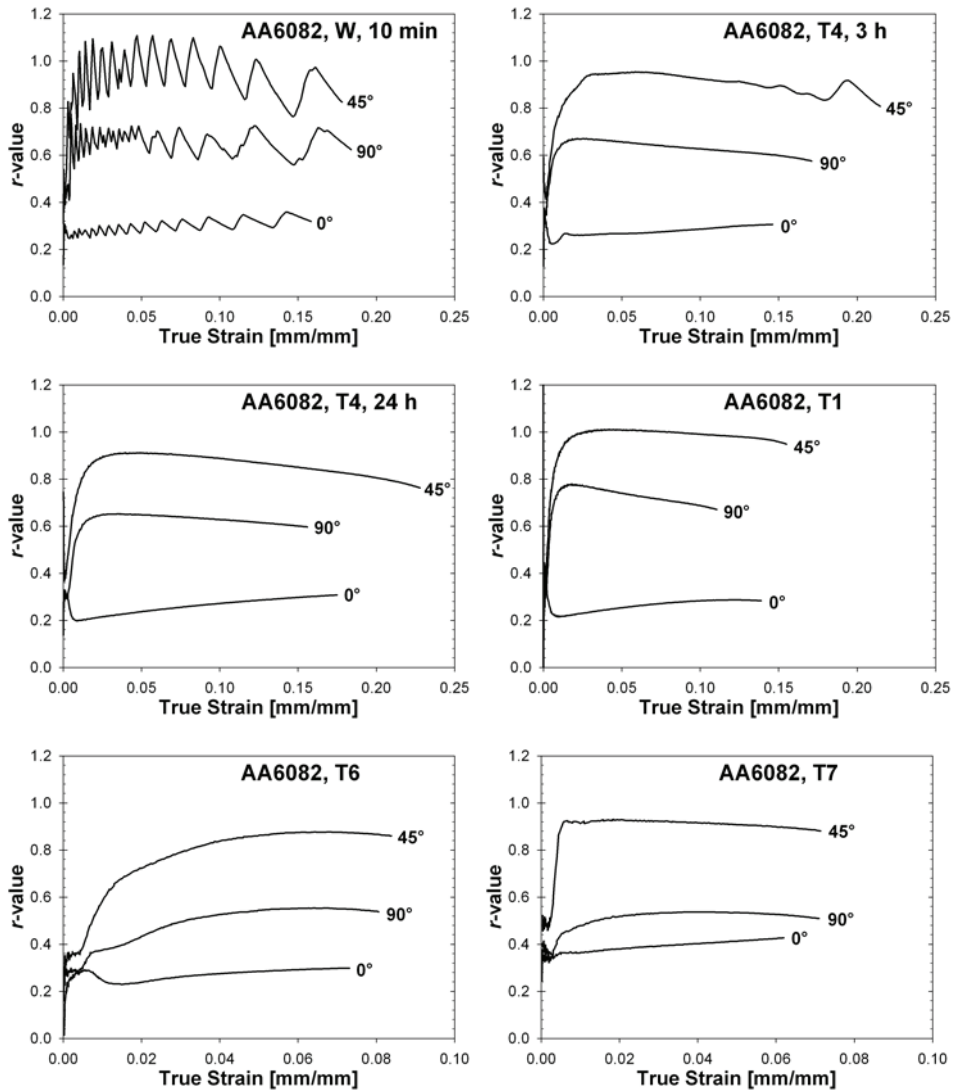


Figure 5.19 – Plastic strain ratio curves 0°, 45° and 90° related to ED at different material conditions of AA6082 obtained with an initial strain rate of $1.1 \times 10^{-3} \text{ s}^{-1}$.

The *r*-value curves obtained from the specimens deformed in the solution-heat-treated condition of both alloys, and the two naturally aged conditions of AA6063 have a characteristic wavy shape. There are also traces of waves in the T4, 3h specimens deformed in the 45° direction of AA6082. This wavy shape is related to the serrated yielding, and each peak in the curves corresponds to a deformation band passing the transverse extensometer. When the band passes the extensometer the negative transverse

Experimental results – Part A

for the two other directions investigated (0° and 90°). Hence AA6082 possesses anisotropic flow properties when tested in these two directions. Also, the r -value of AA6082 seems to be more dependent upon the material condition than for AA6063. Some distinct differences were observed between the naturally and artificially aged material conditions, especially for the 90° specimen. However, the r -values of the 0° and 90° directions in AA6082 are typically ~ 0.3 and ~ 0.6 respectively.

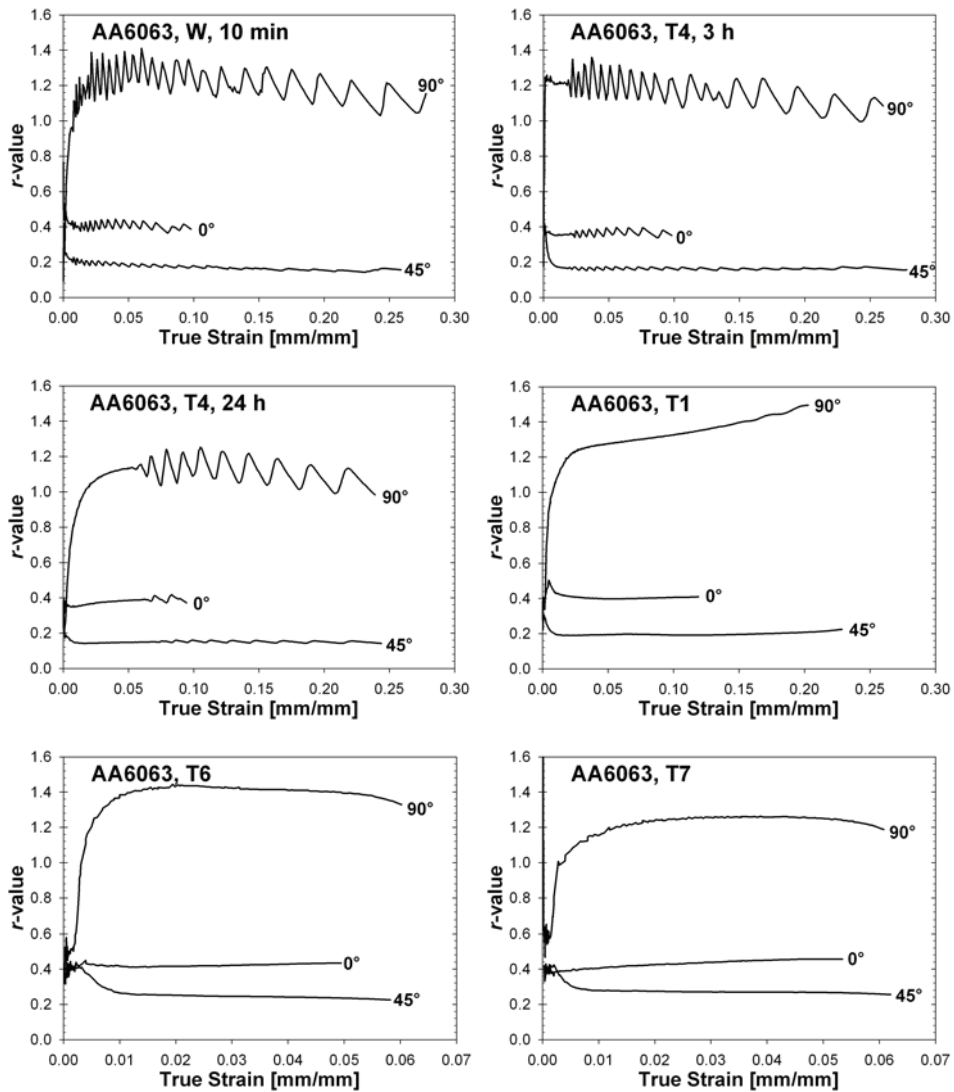


Figure 5.18 – Plastic strain ratio curves 0° , 45° and 90° related to ED at different material conditions of AA6063 obtained with an initial strain rate of $1.1 \times 10^{-3} \text{ s}^{-1}$.

Experimental results – Part A

T6 condition, even though the strength is considerably reduced. The figure shows that the work hardening rate in the T7 condition is quite similar to the work hardening rates observed after naturally ageing of AA6063, while for AA6082, the work hardening rate is only half of that observed during natural ageing. These reflections are also valid for the 45° and 90° directions as shown in Appendix D.

Influence on plastic strain ratio (*r*-values):

The *r*-value, which is often referred to as the Lankford coefficient or plastic strain ratio, is the ratio between the width and the thickness plastic strain. This parameter is often used to describe the mechanical anisotropy of materials deformed by simple tension. It has been shown that a material with an *r*-value of 1 possesses isotropic mechanical properties. However, it is very difficult to measure the plastic strain ratio accurately by use of extensometers, therefore the accuracy of *r*-value measurements are often of the order of $\pm 10\%$.

Both alloys investigated show strong mechanical anisotropy in the solution-heat-treated condition (W, 10min), see e.g. Figure 5.12 and Figure 5.13. Calculations of the *r*-values for all the investigated material conditions are therefore performed in order to study the mechanical anisotropy. Figure 5.18 and Figure 5.19 present the evolution in experimental determined *r*-values during simple tension of AA6063 and AA6082 respectively. The figures show that both alloys have very anisotropic properties and the plastic strain ratio is clearly direction-dependent, i.e. large differences were observed between the investigated testing directions.

The *r*-values of AA6063 (Figure 5.18) are approximately 1.2 for all material conditions when tested in the transverse direction. This means that the width strain of AA6063 is roughly 20% larger than the thickness strain. Hence, AA6063 has close to isotropic properties when deformed 90° to ED. However, when tested in the two other directions (0° and 45°), AA6063 possesses very anisotropic and low *r*-values. Here, the *r*-value in the 0° and 45° directions is typically ~ 0.4 and ~ 0.2 respectively. Such *r*-values mean that for specimens taken from these directions, the thickness strain is much larger than the width strain. AA6082, on the other hand, has more or less isotropic plastic flow when deformed 45° related to ED, i.e. $r \approx 0.95$. Also for this alloy the *r*-values are lower than

Experimental results – Part A

uniform strain increases with longer ageing time at room temperature. For AA6063, the observed serrated yielding is still visible after 24 hours of natural aging, while for AA6082, this jerky flow is only visible in the solution-heat-treated condition (W, 10min).

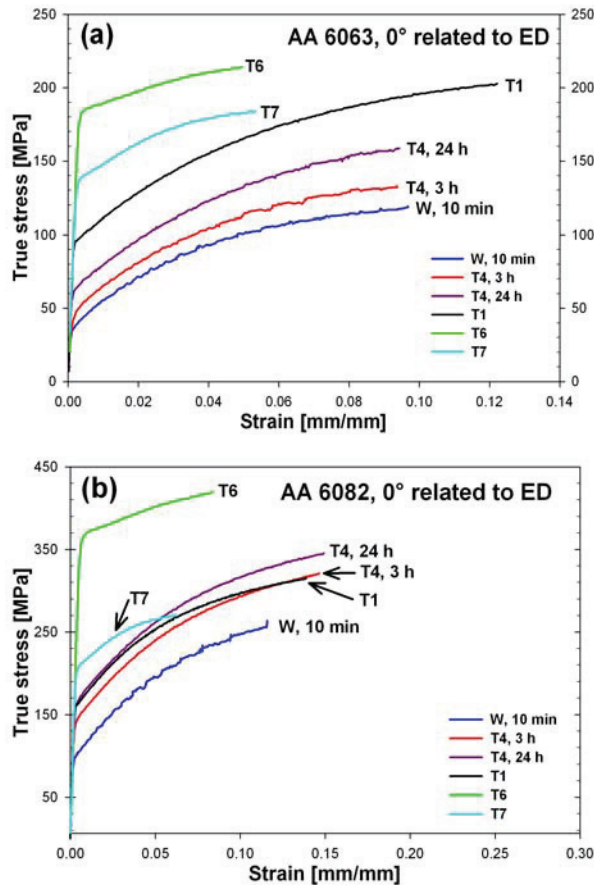


Figure 5.17 – True stress-strain curves parallel to ED for different material conditions. (a) AA6063 and (b) AA6082.

Moreover, Figure 5.17 also shows that the increase in strength and work hardening rate in the naturally aged condition is more than twice as high for AA6082 as for AA6063. Artificial aging to condition T6 exhibits the highest strength while further ageing to the over-aged condition (T7) reduces the strength significantly. The uniform strain is also shown to be heavily reduced after artificial age-hardening. Further, the work hardening rate at low strains is maintained or even improved for the T7 condition compared to the

Experimental results – Part A

Furthermore, the above curves show that the uniform strain is anisotropic and that the ϵ_u -value is reduced upon both natural and artificial aging. Another main finding for both alloys is that the uniform strain anisotropy is reduced with increasing RT storage time and by artificial aging to tempers T6 and T7, i.e. they are isotropic with regard to uniform strain in the T6 and T7 conditions. Further, the 45° direction has the highest uniform strain when aged at RT and the reduction in the uniform strain upon aging is very pronounced.

The trend observed for the uniform strain is repeated for the fracture strain (ϵ_f), i.e. the anisotropy is reduced with increasing RT storage time and by artificial aging to tempers T6 and T7. However, in the T6 condition the fracture strain is not as isotropic as the uniform strain.

The observed trends for the r -values in the two investigated alloys are more complicated. In the solution-heat-treated condition, the two alloys have completely opposite behaviour with regard to the plastic strain ratio. AA6063 has the highest r -values in the 0 and 90 directions and the lowest r -value in the 45 direction (Figure 5.15), while the behaviour is completely opposite for AA6082 (Figure 5.16).

Notice that the quantitative alteration in r -value during ageing is very limited. It is also important to bear in mind that the accuracy of this type of r -value measurements is poor ($\pm 10\%$) as shown in the previous section. Consequently, some of the alterations are directly related to inaccuracy from the measuring technique. However, the observed trends should still be valid, i.e. also the r -values of both alloys become more isotropic due to age-hardening.

Influence on flow curves

Age-hardening is known to change the mechanical properties of Al-Mg-Si alloys. The changes due to ageing of the specimens deformed 0° related to ED are given in Figure 5.17. Appendix D presents the same set of results from all the deformation directions investigated in this work (0°, 45° and 90°). The strength of both alloys increases substantially during natural ageing. However, stress strain curves indicate that the serrated yielding gives rise to some reduction in uniform strain. In other words, the

Experimental results – Part A

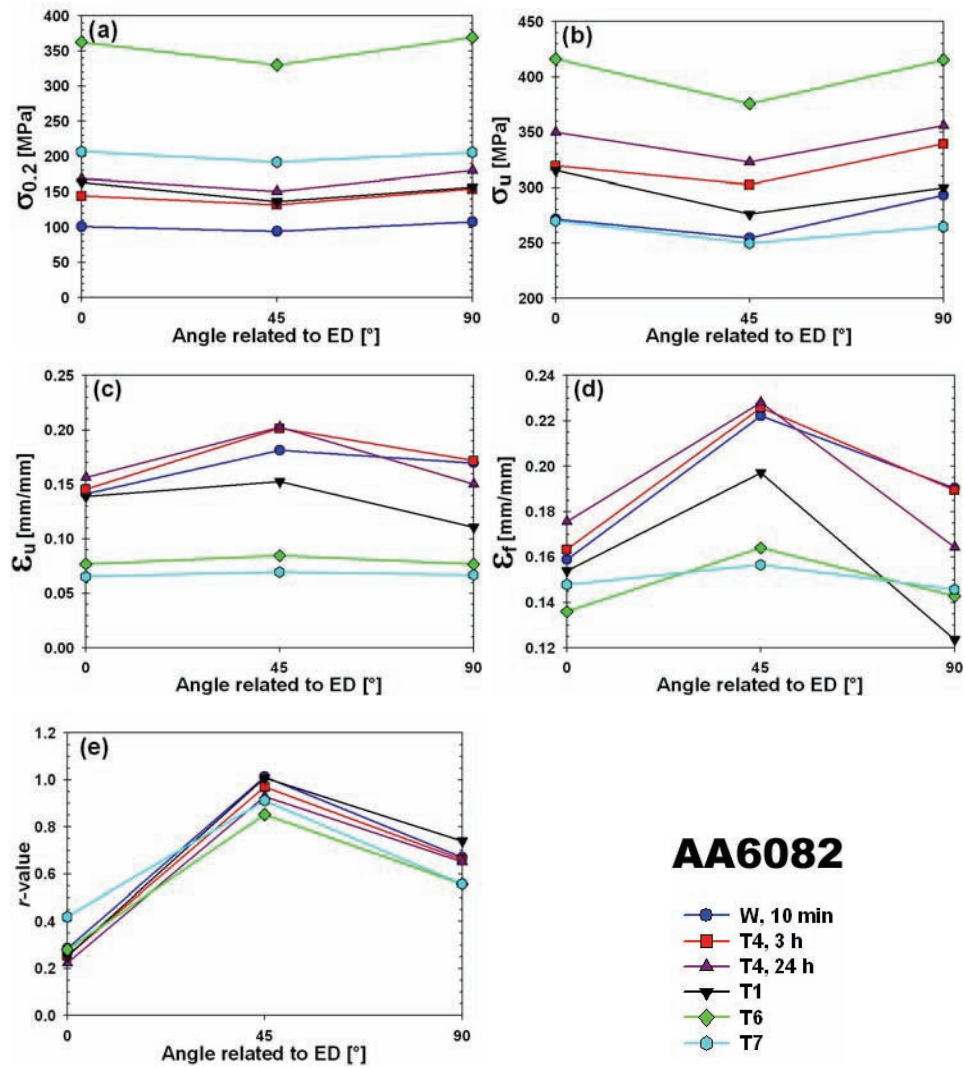


Figure 5.16 – The effect of ageing on mechanical properties and anisotropy of AA6082. (a) Yield stress (b) ultimate tensile stress (c) true uniform strain (d) true fracture strain and (e) r -value at a true strain of 0.05.

Experimental results – Part A

However, a main finding is that the observed anisotropy in the ultimate tensile stress is reduced with age-hardening. AA6063 has completely isotropic properties in both the artificially aged conditions while AA6082 maintains some anisotropy in the T6 temper and is fully isotropic in the over-aged condition.

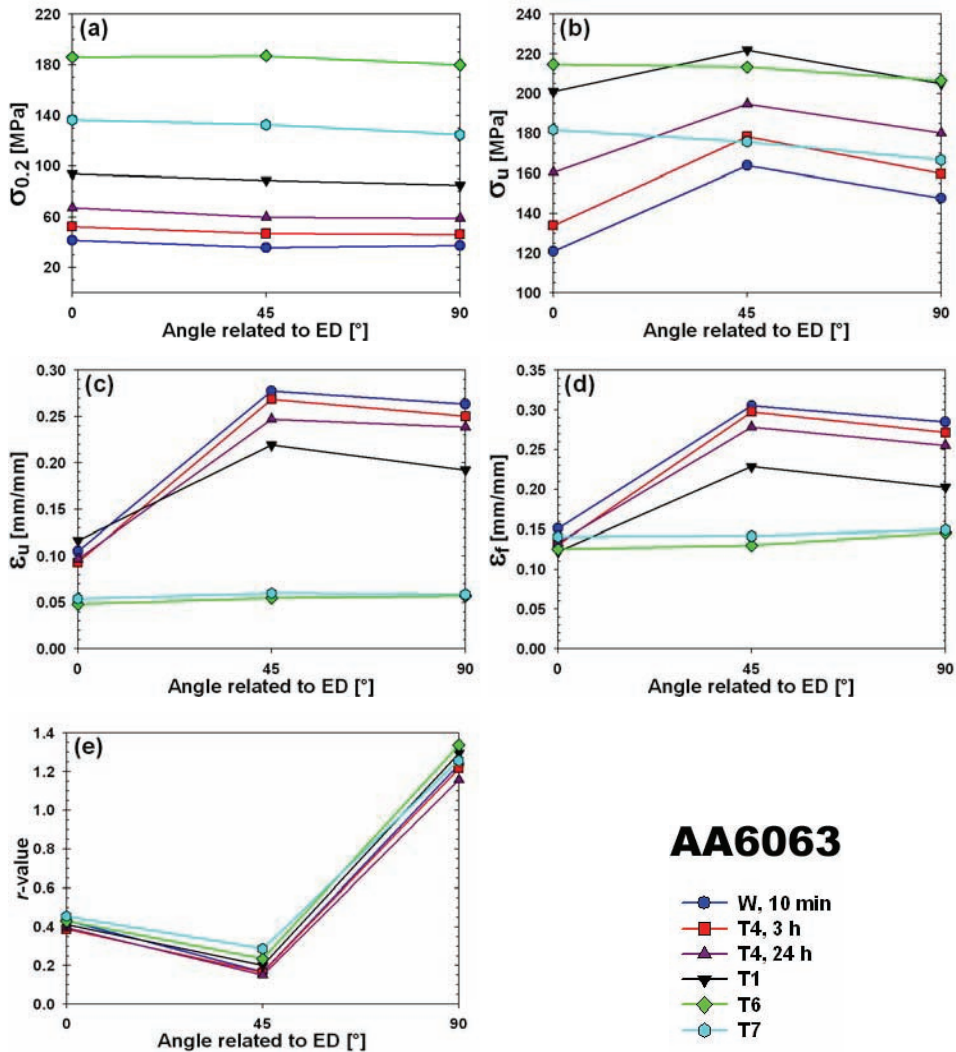


Figure 5.15 – The effect of ageing on mechanical properties and anisotropy of AA6063. (a) Yield stress (b) ultimate tensile stress (c) true uniform strain (d) true fracture strain and (e) r -value at a true strain of 0.05.

5.2.2 Further details regarding age-hardening effects

Influence of properties:

The previous section has shown that the alloys investigated in this work possess significant anisotropic mechanical properties. It has also been shown that the mechanical properties are strongly affected by both natural and artificial age-hardening. In the following, the angular dependency of the mechanical properties of all material conditions is compared.

The effect of age-hardening on the mechanical properties in AA6063 and AA6082 is shown in Figure 5.15 and Figure 5.16 respectively. It is known that mechanical anisotropy in general is affected by age-hardening. The anisotropy in the solution-heat-treated condition (W, 10min) is mainly controlled by the crystallographic texture and in some degree the microstructure, i.e. AA6063 and AA6082 have dissimilar mechanical anisotropy prior to age-hardening. Age-hardening reduces the contribution from crystallographic texture due to introduction of precipitates. The anisotropy of the two alloys will therefore become reduced after both natural and artificial age-hardening.

The true yield stress of both alloys in the W, 10min temper is relatively isotropic. Both natural and artificial ageing result in a close to isotropic increase in yield stress, i.e. the alloys maintain close to isotropic yield properties after age-hardening. AA6082 has a somewhat anisotropic yield stress in the T6 conditions but this anisotropy disappears in the T7 condition. The difference between the minimum and maximum value in the T6 temper is less than 10%. It is also important to remember that it is difficult to accurately determine the yield stress of aluminium alloys, i.e. some of the observed differences can be related to measurement deviations.

The ultimate tensile stress is much more anisotropic than the yield stress. It could be expected that the ultimate tensile stress should follow the same trends as observed for the true yield stress. However, it is important to remember that the work hardening will be strongly affected by precipitation which in turn affects the activation of slip systems.

Experimental results – Part A

variations. This alloy has only minor variations, and the measured r -values vary less than 0.3 over the thickness. Some of these variations could even be explained by the uncertainty of the measurements.

The through-thickness r -value variations give rise to an evident through-thickness displacement gradient on the tensile specimen. This induces bending around the tensile direction during deformation and the specimens develop a transverse curvature. Hence, the fixed transverse extensometer exaggerates the measured transverse strain which again affects the experimental determined plastic strain ratio. The accuracy of the measurements worsens dramatically during deformation due to a strong increase in this transverse curvature. The accuracy of the measurements for some of the investigated positions is therefore of the order of $\pm 35\%$.

Table 5.3 – Experimental determined r -values (at a true strain of 0.05) at different positions through the profile thickness at material condition T1. The accuracy of these measurements is approximately $\pm 35\%$.

Alloy	Direction	Centre	Middle	Surface
AA6063	0°	1.2	1.0	0.4
	45°	0.1	0.1	0.3
	90°	3.5	2.4	1.3
AA6082	0°	0.5	0.3	0.5
	45°	1.1	-	2.8
	90°	1.2	0.9	1.2

Experimental results – Part A

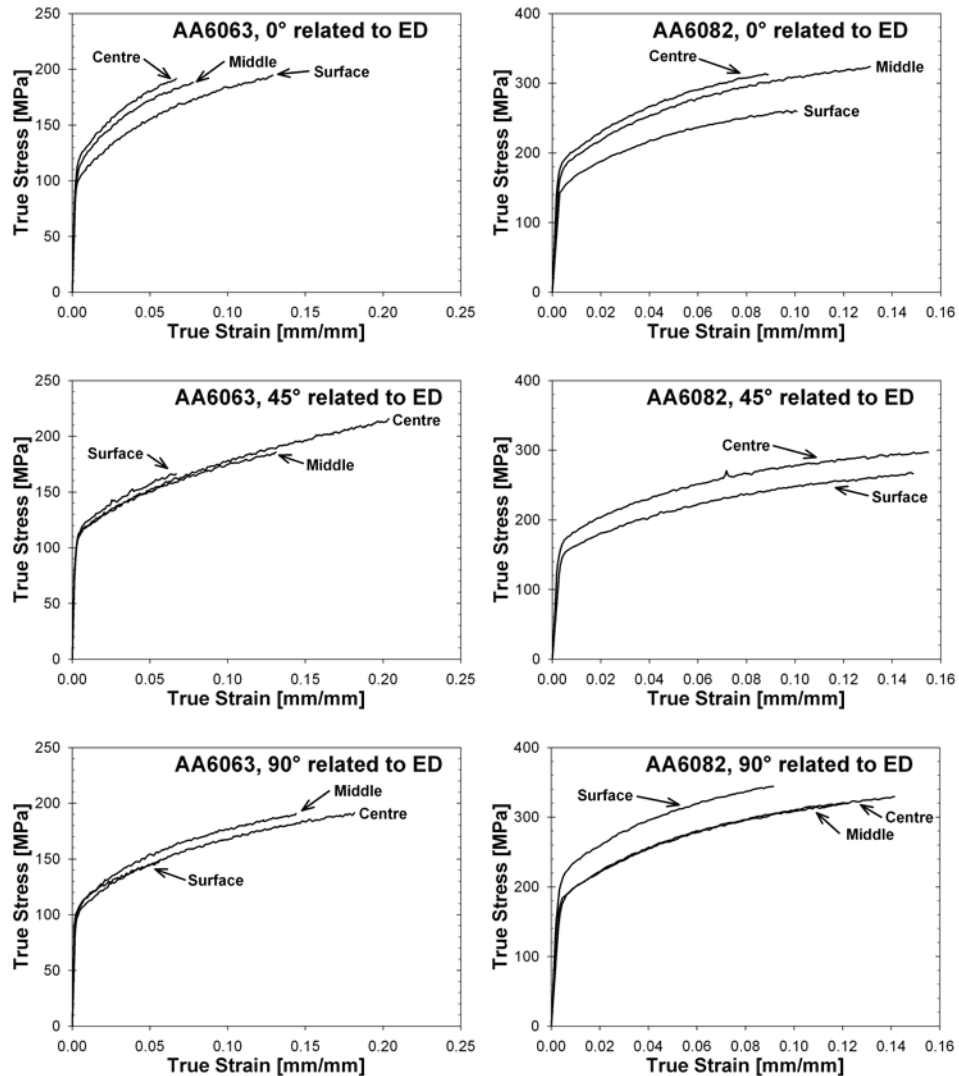


Figure 5.14 – True stress-strain curves 0°, 45° and 90° related to ED at different positions through the profile thickness obtained with an initial strain rate of $1.1 \times 10^{-3} \text{ s}^{-1}$ in material condition T1. AA6063 on the left hand side and AA6082 on the right hand side.

The measured plastic strain ratio (r -values) is also quite anisotropic and varies through the profile thickness (Table 5.3). The centre and middle positions of all directions investigated have comparable r -values for AA6063. Moreover, the plastic strain ratio at the surface is not comparable with the r -values measured in the centre and middle positions. AA6082 on the other hand, do not possess this same type of through-thickness

Experimental results – Part A

profile thickness (see Chapter 4.2 for more detailed information concerning the sampling procedure). These investigations are only performed in material condition T1.

Figure 5.14 presents the true stress-strain curves for both alloys at the different positions and it is evident that the mechanical properties vary significantly through the profile thickness. The centre and middle positions have similar properties while the surface behaves quite differently. It is clear that the variations observed in uniform strain through-thickness are the most pronounced. Moreover, there are also some differences in initial yield strength and work hardening rate. The 0° specimens taken from the centre and middle positions of AA6063 have a much lower uniform strain than the surface position. Also the yield strength and work hardening rate are higher in these positions when deformed in this direction. On the other hand, all specimens deformed 45° related to ED have close to equal work hardening rate and initial yield strength. However, the uniform strain is significantly higher in the centre and middle positions compared to the surface position. The description of the initial yield strength and uniform strain given for the 45° direction is also valid for the 90° specimens. Moreover, it also seems like the 90° direction has a lower surface work hardening rate than the other positions investigated.

Figure 5.14 also presents the variations observed for the different positions through the thickness of AA6082. Also for this alloy there are some minor differences in work hardening rate and uniform strain. The main differences are, however, related to the initial yield strength. The centre/middle positions have the highest initial yield strength when deformed in the 0° and 45° directions, while the surface position has the highest yield strength when deformed in the transversal direction. It is also worth noticing that no measurements are reported for the middle position of the 45° direction due to problems with the tensile testing machine.

Experimental results – Part A

(Martin 1968). The alloys investigated contain approximately the same amount of Mg which is the limiting alloying element. This explains why both alloys have equivalent ageing potential despite relatively large differences in chemical composition.

Another important observation is the significant differences in mechanical properties between the naturally and artificially aged specimens. First of all, the tensile strength increases and the uniform strain decreases when artificially aged. Further, it is observed that the mechanical properties are more isotropic after artificial ageing than after natural ageing. For AA6063, it is shown that the initial yield strength is close to equal for all directions when tested in the supersaturated solid solution (W, 10min) and in the naturally aged (T4, 3 and 24 hours and T1) conditions. However, there are some minor differences when tested after artificial ageing. The 0° and 45° specimens seem to have somewhat higher initial yield stress than the 90° specimens when tested in the T6 condition, while only the 0° specimens seem to have a higher yield stress than the two other directions when tested in the T7 condition. Some variations between the different directions are also observed for AA6082. In general it is observed that the 0° and 90° directions possess close to identical properties with congruent stress-strain curves. These directions are stronger than the 45° direction both with regard to yield stress, work hardening rate and ultimate stress. However, the highest uniform strain is found for the specimens deformed 45° related to ED. As already mentioned, the figures also show that artificial ageing of both alloys results in close to isotropic but low work hardening rate, i.e. the observed anisotropy is strongly reduced. Natural ageing, on the other hand, gives rise to larger anisotropic variations. For AA6063, the specimens deformed parallel to the ED have a higher work hardening rate but considerably lower uniform strain. The work hardening rate of the 45° and 90° specimens is equal at small strains but some differences arise at higher strains. The uniform strain is nevertheless equal for these two directions.

Thickness gradient studies:

As shown above, the mechanical properties of the present two alloys are strongly texture dependent. The texture, on the other hand, is varying through the thickness. Therefore, the effect of the through-thickness gradients has been determined by performing tensile test on 0.3mm thick specimens machined from three different positions through the

Experimental results – Part A

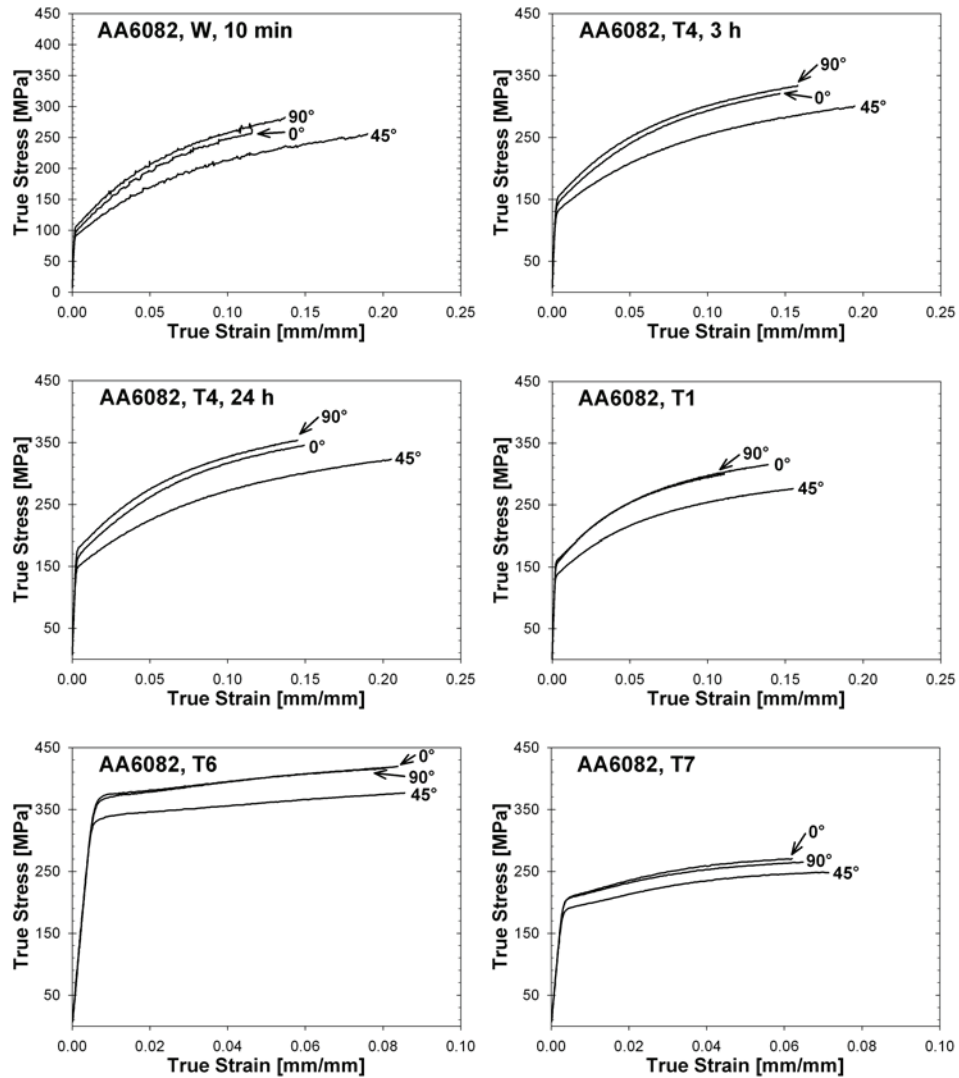


Figure 5.13 – True stress-strain curves 0° , 45° and 90° related to ED at different material conditions of AA6082 obtained with an initial strain rate of $1.1 \times 10^{-3} \text{ s}^{-1}$. Note the change of true true-axis scaling for the two lower figures.

In general it is observed that the mechanical properties are improved after both natural and artificial age-hardening, i.e. the precipitates results in a considerable strengthening contribution. When compared to the solutionised (W) condition, both the yield and ultimate tensile strength of both alloys are close to doubled after age-hardening to the peak aged (T6) condition. The ageing potential of AA6xxx alloys is determined by the chemical composition of β' and β , hence by the amount of Mg and Si in solid solution

Experimental results – Part A

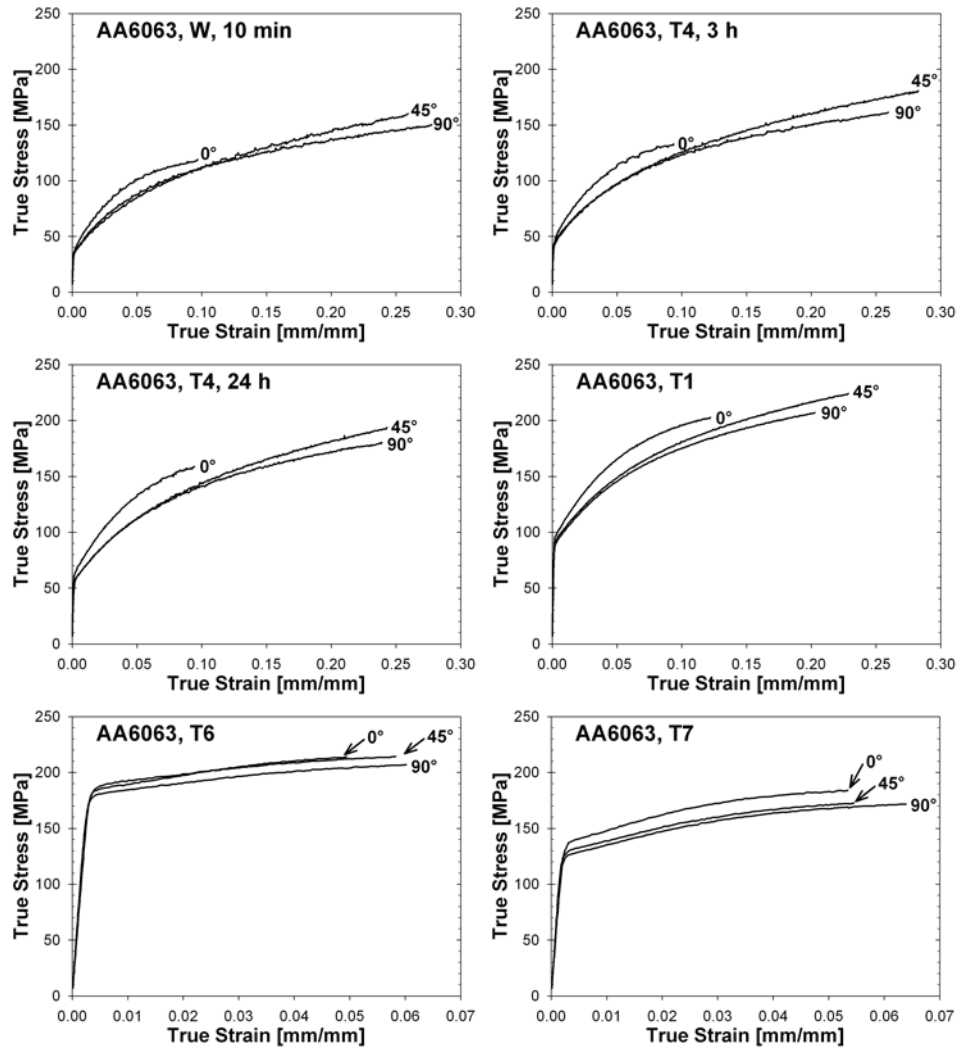


Figure 5.12 – True stress-strain curves 0°, 45° and 90° related to ED at different material conditions of AA6063 obtained with an initial strain rate of $1.1 \times 10^{-3} \text{ s}^{-1}$. Note the change of tensile strain-axis scaling for the two lower figures.

5.2 Mechanical properties and anisotropy

Mechanical properties are investigated at different positions through the thickness of both alloys by means of tensile tests. In addition, full thickness specimens are tested after extrusion and subsequent artificial ageing treatments. The tensile specimens are machined from the 0°, 45° and 90° directions related to the ED in order to investigate the directional dependency of the mechanical properties (anisotropy), including the plastic strain ratio (*r*-value).

5.2.1 Mechanical properties

Anisotropy vs. temper condition (Full thickness studies):

The full thickness true stress-strain curves in Figure 5.12 and Figure 5.13 present the mechanical properties of AA6063 and AA6082 for different temper conditions. Notice that a different scaling of the true strain axis is used for the T6 and T7 conditions. The alloys are investigated in different material conditions at an initial strain rate of $1.1 \times 10^{-3} \text{ s}^{-1}$. From the figures, it is evident that the recrystallized profile (AA6063) has a significantly lower strength than the non-recrystallized AA6082.

Experimental results – Part A

($S=0.90$) where the area fraction drops very rapidly towards zero. The observed increase of these components must be related to the increased amount of shear deformation taking place closer to the surface. Moreover, the typical recrystallization components are close to absent at all positions through the thickness. Based on the argumentation presented above, it is reasonable to assume that the observed area fractions of the Cube component is related to Cube bands like the one observed in Figure 5.9 (a). In Appendix C, calculated pole-figures based on orientation data from all positions investigated are included.

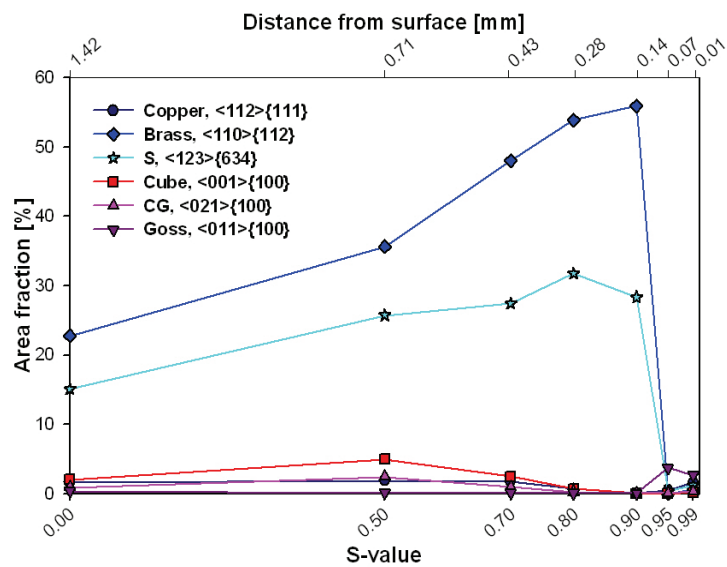


Figure 5.11 – Area fraction of different texture components at different positions through the thickness of AA6082.

Experimental results – Part A

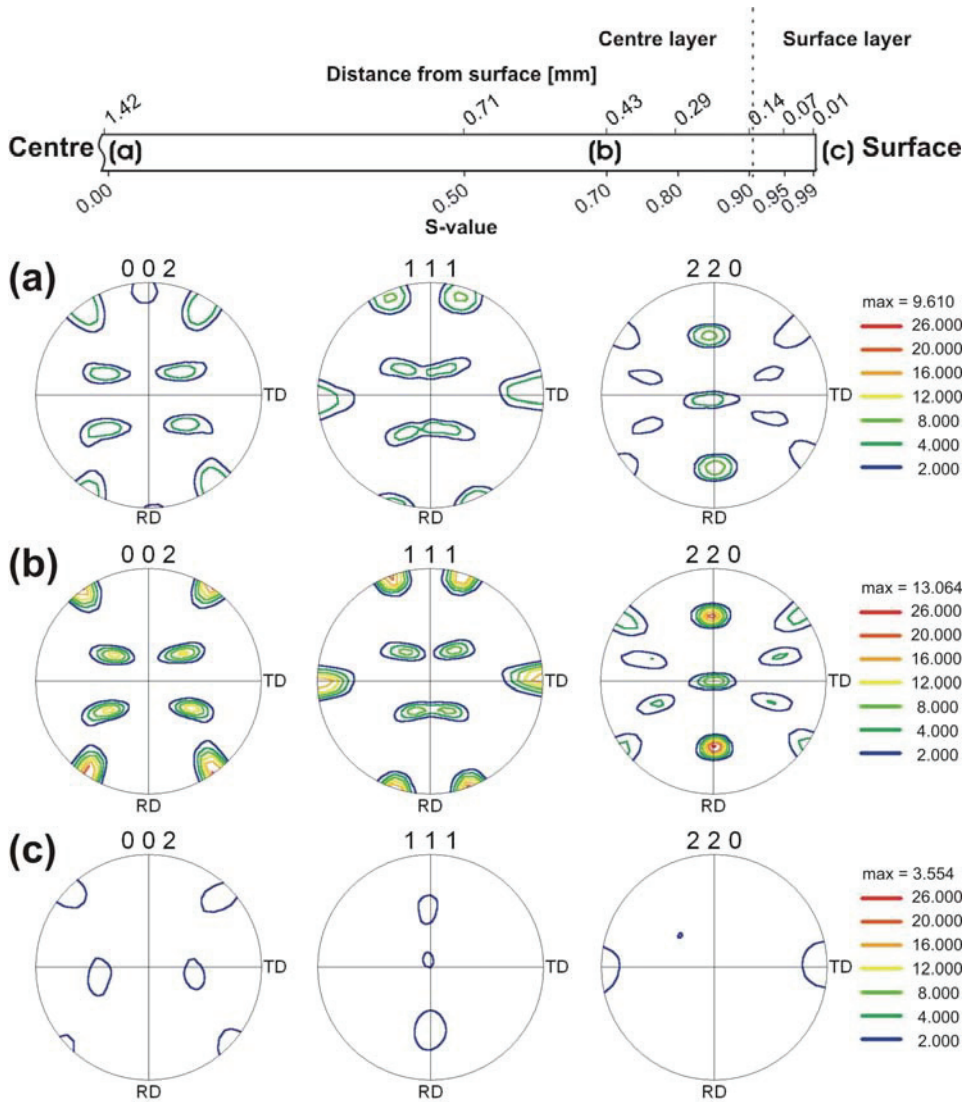


Figure 5.10 – Calculated pole figures based on orientation data at different positions through the profile thickness of AA6082.

The crystallographic texture of AA6082 can be divided into the same set of layers as the microstructure. The different positions within the centre layer (S=0.00 to S=0.90) of AA6082 have a typical deformation texture while the surface layer has close to a random texture (see e.g. Figure 5.10). Figure 5.11 summarises the area fraction of the most significant texture components through the thickness. The fraction of the Brass and the S components increases from the centre position (S=0.00) towards the surface layer

Experimental results – Part A

about the deformation structure, and is therefore included in the inverse pole figure maps presented in Figure 5.9.

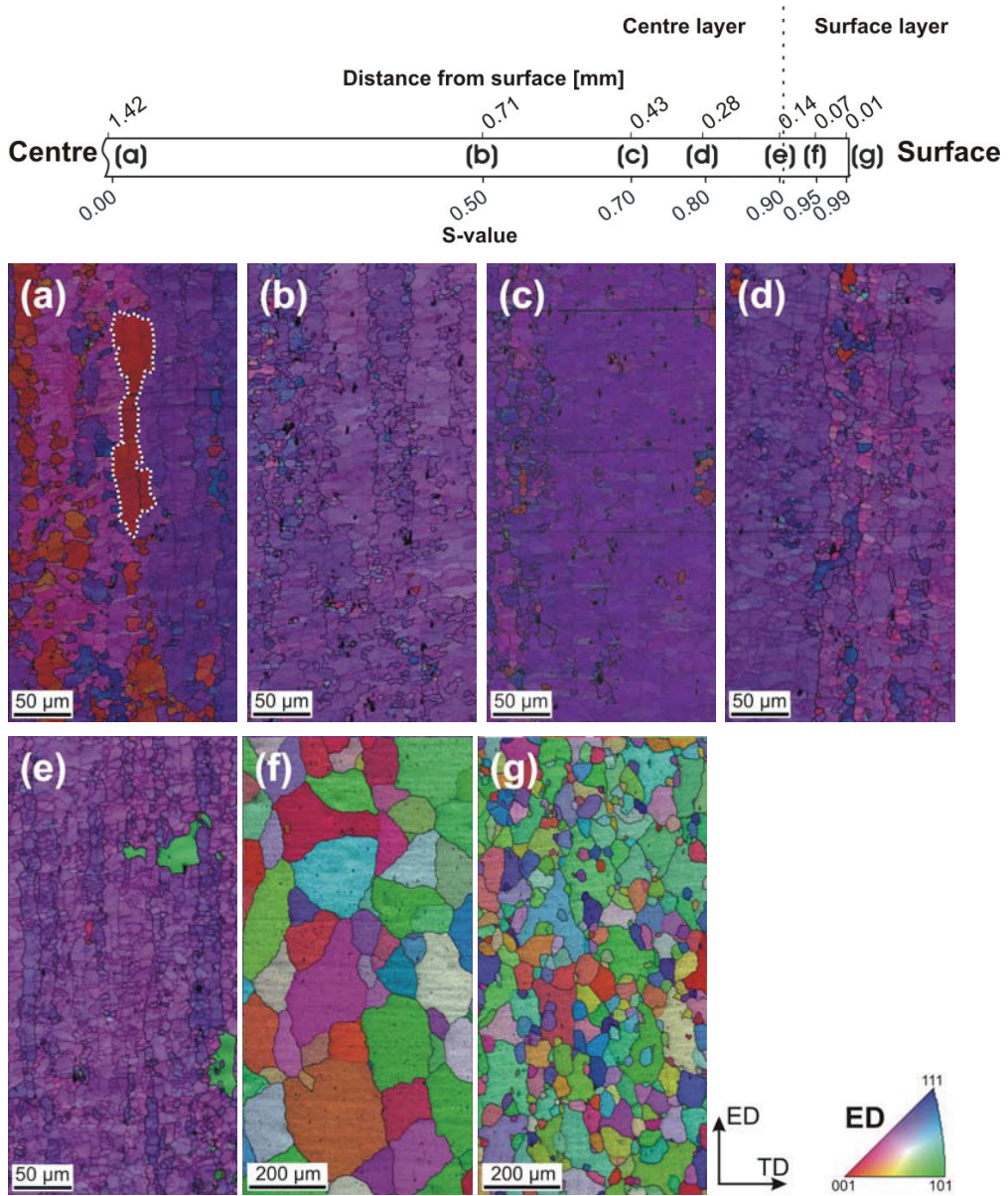


Figure 5.9 – IPF map overlaid the image quality of the EBSD patterns at different positions through the profile thickness of AA6082. The orientation data is acquired at different magnifications with 0.4 μm and 2.0 μm step size within the centre (a-e) and surface (f-g) layer respectively. The contour from one of the Cube bands in the centre position is highlighted with a dotted line.

Experimental results – Part A

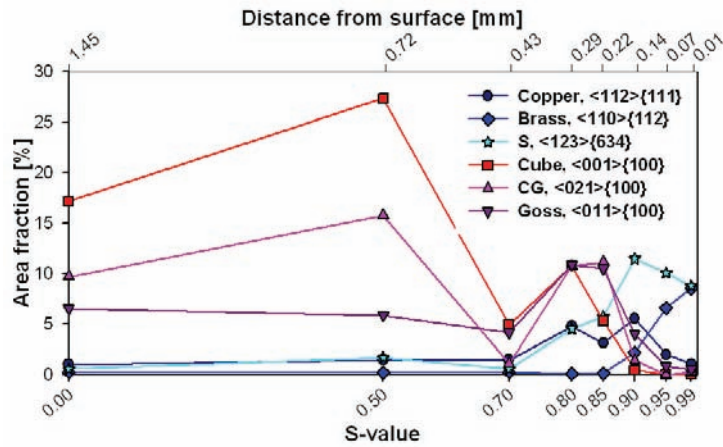


Figure 5.8 – Area fractions of the different texture components at different positions through the thickness of AA6063.

AA6082

The AA6082 has a fibrous microstructure with a recrystallized surface layer, hence the microstructure has evident through-thickness variations as already indicated in conjunction with Figure 5.3. The microstructure consists primarily of two pronounced different layers, i.e. a large centre layer with a deformed microstructure and a recrystallized surface layer with some microstructural variations (Figure 5.9).

Throughout the more or less homogeneous centre layer the grain and sub-grain sizes seem to be independent of the position within the layer. However, the fraction of Cube bands increases toward the centre position. The inverse pole figure map from the centre position (Figure 5.9 (a)) shows a large fraction of grains with Cube orientation aligned along the extrusion direction (Cube bands).

The surface layer, on the other hand, has a microstructure similar to the microstructure observed in the surface layer of AA6063 (Figure 5.6). From the IPF maps presented in Figure 5.9, the size of the recrystallized surface layer is calculated to be approximately 120µm. The green grains in Figure 5.9 (e) are recrystallized grains surrounded by a deformed microstructure. Hence these grains belong to the recrystallized surface layer. The image quality (the quality of the EBSD pattern) provides additional information

Experimental results – Part A

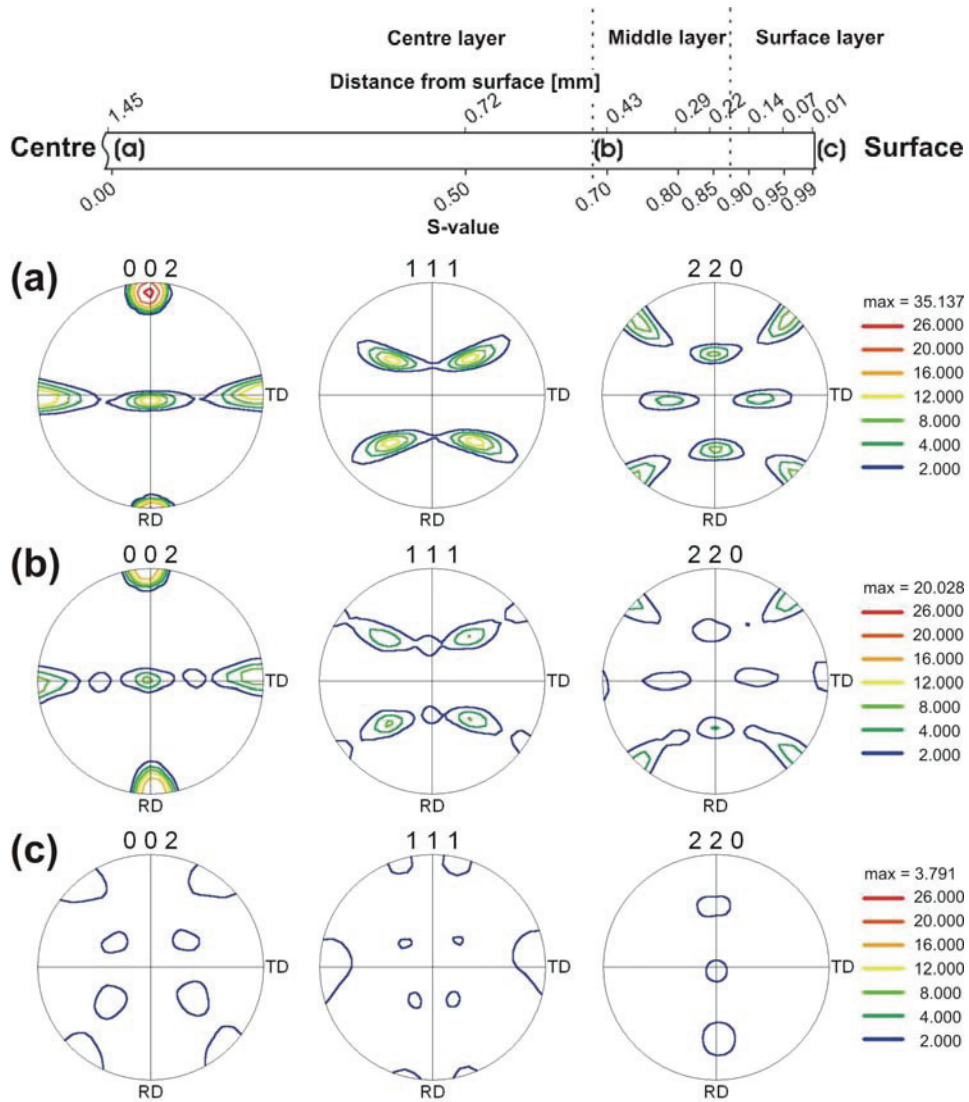


Figure 5.7 – Calculated pole figures based on crystallographic orientation data from different positions through the profile thickness of AA6063. The corresponding positions are shown in the sketch at the top.

Experimental results – Part A

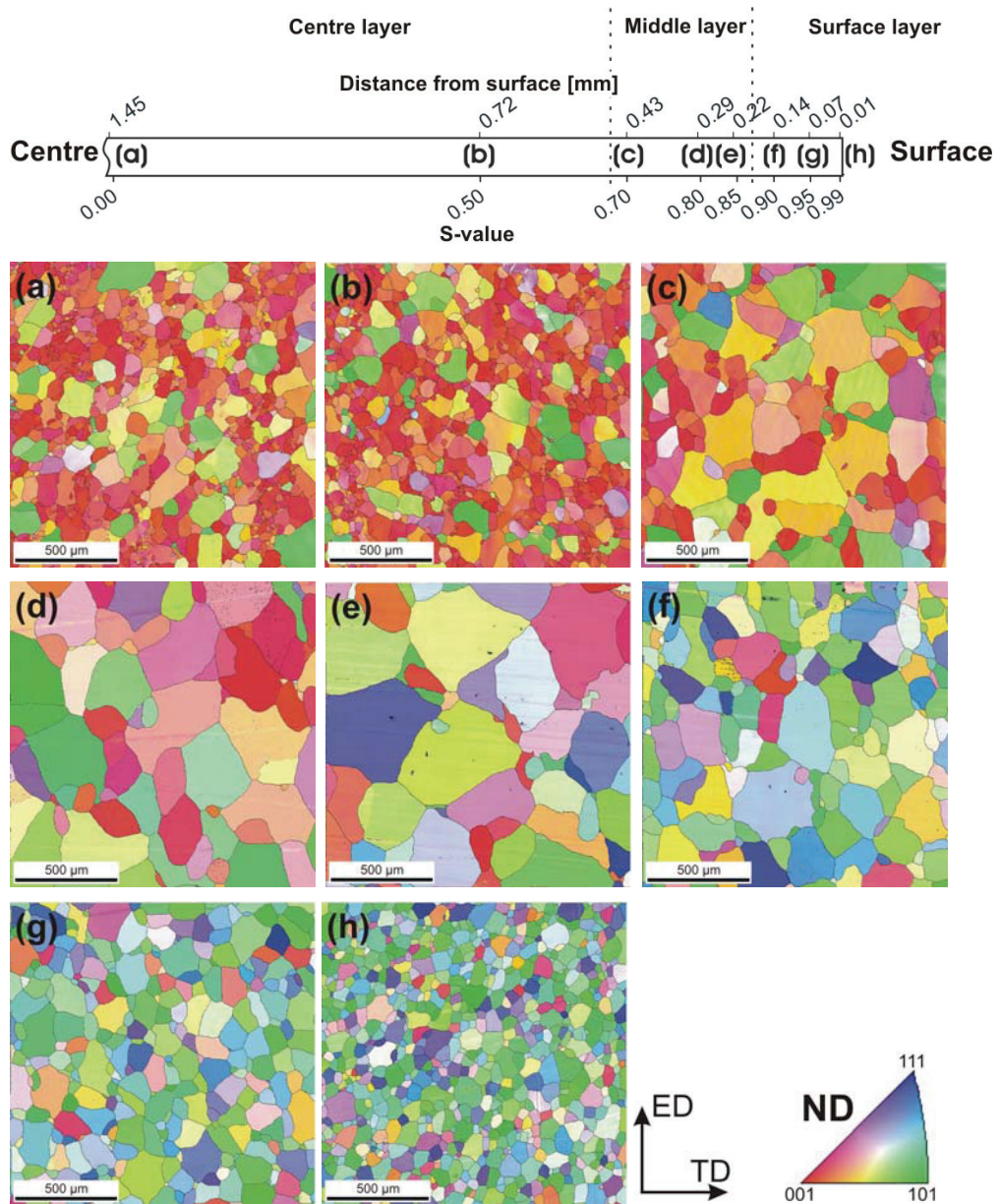


Figure 5.6 – IPF map acquired with a step size of 2μm at different positions through the profile thickness of AA6063. The corresponding positions are shown in the sketch at the top.

Experimental results – Part A

5.2. The table also shows that the standard deviation of the grain size measurement is large for all positions investigated, indicating a very heterogeneous microstructure.

Table 5.2 – Measured grain size and standard deviations (Std.) at investigated positions through the profile thickness of AA6063. 5° is used as the minimum misorientation angle for the grain size calculations.

Position	Grain size ED [μm]	Std. ED [μm]	Grain size TD [μm]	Std. TD [μm]
S = 0.00	64	30	55	34
S = 0.50	66	31	56	33
S = 0.70	119	86	104	79
S = 0.80	173	98	159	93
S = 0.85	202	144	198	140
S = 0.90	131	69	103	53
S = 0.95	90	57	82	47
S = 0.99	58	29	51	18

The IPF maps presented in Figure 5.6 give a first indication of an evident texture gradient through the profile thickness. The colours of the IPF maps change dramatically from the centre toward the surface, thus the texture of the material changes. The crystallographic texture can be divided into the same set of layers as used for the microstructure. The centre layer has a strong Cube texture somewhat rotated around the ED (Figure 5.7 (a)). The Cube texture sharpens towards the middle layer where the texture first split into two separate texture components (Cube and Goss) (Figure 5.7 (b)) before it rotates further around the ED, producing a zone circumscribing the equator plane. The texture also becomes more random at the profile surface (Figure 5.7 (c)) with evident traces of texture components typically associated with shear deformation, as shown in Figure 5.8. This leads to a decrease in the maximum texture intensity towards the surface, i.e. the profile has a maximum intensity of 35.1 at S=0.00 and 3.8 at S=0.99 (see Figure 5.7). The area fractions of all the relevant texture components from the different positions through the thickness are given in Figure 5.8. In Appendix C, calculated pole-figures based on orientation data from all positions investigated are included.

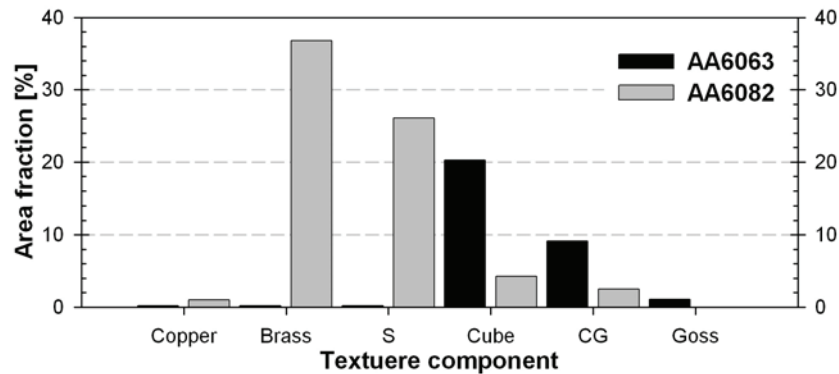


Figure 5.5 – Measured area fraction of the most important texture components through the thickness in the half-width position of the profile. Texture components were defined within 10° from the ideal orientations. Note that the Goss component of AA6082 is absent.

5.1.3 Through-thickness variations

Extruded profiles are expected to have through-thickness variations due to the inhomogeneous deformation taking place through the die during extrusion. The deformation mode at the profile surface ($S=1.0$) is close to perfect shear while the deformation in the centre region of the profile ($S=0.0$) is controlled by plane compression. Strong temperature and deformation mode gradients across the thickness during processing give rise to large textural and microstructural variations. The extent of these through-thickness variations is alloy dependent as will be presented in more detail in the following sections.

AA6063

This profile has a fully recrystallized microstructure but the thickness can be divided into three separate layers based on differences in the microstructure (Figure 5.6). The microstructure consists of equiaxed grains with a grain size of approximately $50\mu\text{m}$ in the centre layer of the profile ($S=0.00 - S=0.70$). In the middle layer ($S=0.70 - S=0.85$) the grain size increases rapidly and the grains become somewhat elongated in the ED. Further toward the surface the grain size decreases and becomes more equiaxed, ending up with a grain size of approximately $40\mu\text{m}$ at $S=0.99$. The measured grain sizes at all investigated positions based on 5° boundary misorientation angle are presented in Table

Experimental results – Part A

texture dominated by the Cube component as presented by pole figures in Figure 5.4. The calculated orientation distribution functions (ODF) are given in Appendix B. Figure 5.5, which presents the area fraction of the most common texture components, shows that the texture also has a relatively large volume fraction of the CG component. Hence, the Cube component is somewhat rotated around the ED towards the CG and Goss component as indicated in Figure 5.4. A material with a perfect cube texture will have symmetrical crystallographic orientations both in the ED and the TD. However, the crystallographic texture of this material is not fully symmetrical since the texture is rotated around the ED, which gives rise to a characteristic fibre along the Φ -axis of the $\varphi_2=0^\circ$ section of the ODF (Appendix B). Figure 5.4 also presents the crystallographic texture of the fibrous AA6082 which possesses a typical deformation texture. Here, the area fraction of the typical recrystallization components (Cube, CG and Goss) is very low. However, the area fraction of the more typical deformation components like Brass and S is quite pronounced. Neither Brass nor S are $0^\circ/90^\circ$ -symmetric, something which means that AA6082 possesses less $0^\circ/90^\circ$ -symmetry than the AA6063 (Figure 5.5).

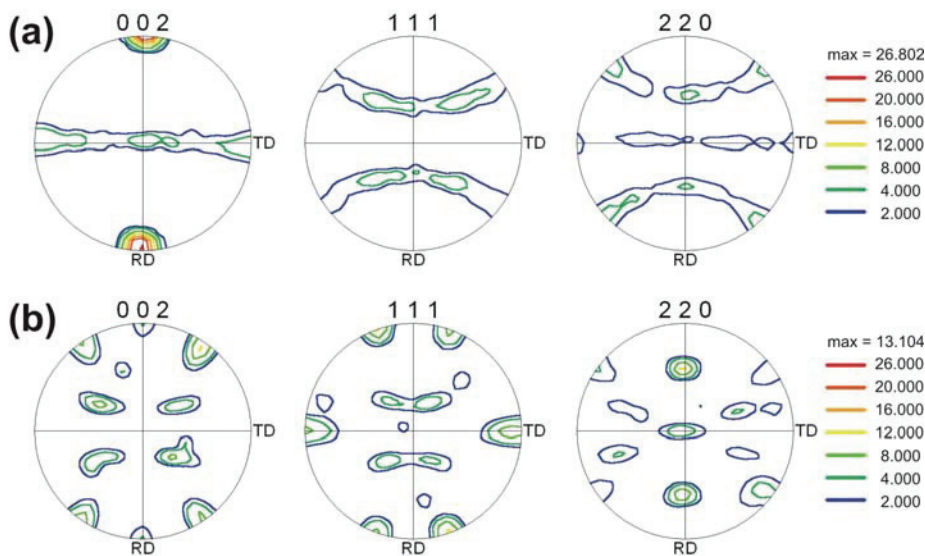


Figure 5.4 – Measured 002, 111 and 220 pole figures representing the initial global texture. (a) AA6063 and (b) AA6082.

Experimental results – Part A

Table 5.1 – Average grain size of both alloys measured by EBSD in conjunction with the linear intercept method by use of different boundary misorientation angles.

Alloy	Boundary misorientation angle	Grain size ED [μm]	Grain size ND [μm]
AA6063	5°	90	63
AA6063	10°	116	83
AA6063	15°	173	98
AA6082	15°	13	4

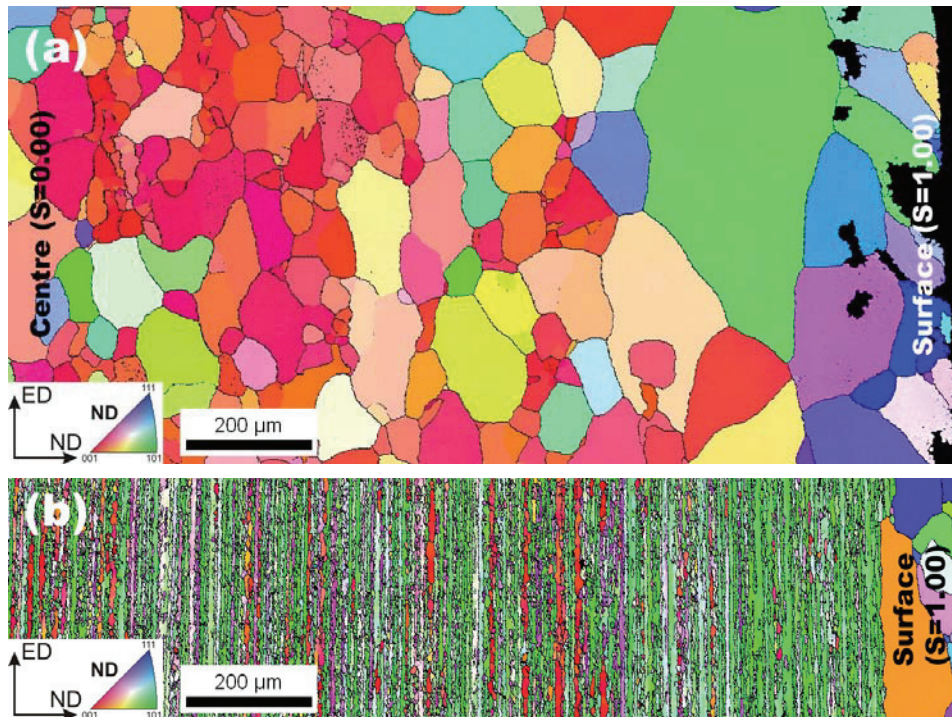


Figure 5.3 – IPF map of the variations in microstructure from the centre to the surface of the investigated profiles. The left hand side represents the centre position while the right hand side represents the surface position of the profile. (a) AA6063 and (b) AA6082.

5.1.2 Crystallographic texture

Evident microstructural variations, like the one observed for the investigated materials, often also give rise to variations in crystallographic texture. The crystallographic texture of AA6063 is very typical for materials with a recrystallized microstructure, i.e. a strong

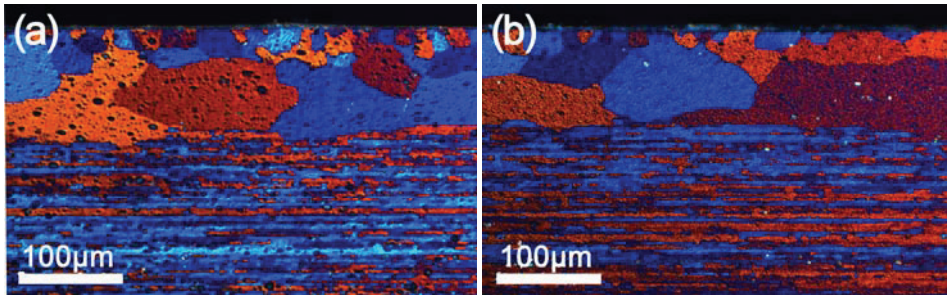


Figure 5.2 – Light optical micrograph of the microstructure close to the surface in the longitudinal transverse (ED-ND) plane of AA6082. (a) Prior to solution heat-treatment. (b) After solution heat-treatment.

The average grain sizes in both the ED and the ND of the two alloys have been measured by use of the linear intercept method and are shown in Table 5.1. The grain sizes are dependent on the minimum misorientation angles selected for the measurements. The measured grain size of AA6063 increases by a factor of 2 when the boundary misorientation angle is increased from 5° to 15° .

It is beyond doubt that the microstructure of AA6063 is fully recrystallized. Hence, the observed changes in grain size as a function of the boundary misorientation angle can not be related to any deformation substructure. The prominent increase in grain size is therefore most likely an intrinsic behaviour of all materials with a strong recrystallized texture, especially materials possessing a rotated recrystallization texture like the investigated AA6063 (see section 5.1.2 for details). Several grains in a material with such a strong texture have close to identical crystallographic orientations. When the number of grains with almost identical orientations is high, it is reasonable to assume that the microstructure will consist of neighbouring grains with close to identical orientation, i.e. the microstructure will consist of grain boundaries with low misorientation angles. For the same reason the measured grain size will be very dependent upon the selected boundary misorientation angle.

Experimental results – Part A

part of AA6082 is much more homogeneous than the corresponding part of AA6063. The through-thickness variations observed in these two alloys will be presented in more detail in section 5.1.3.

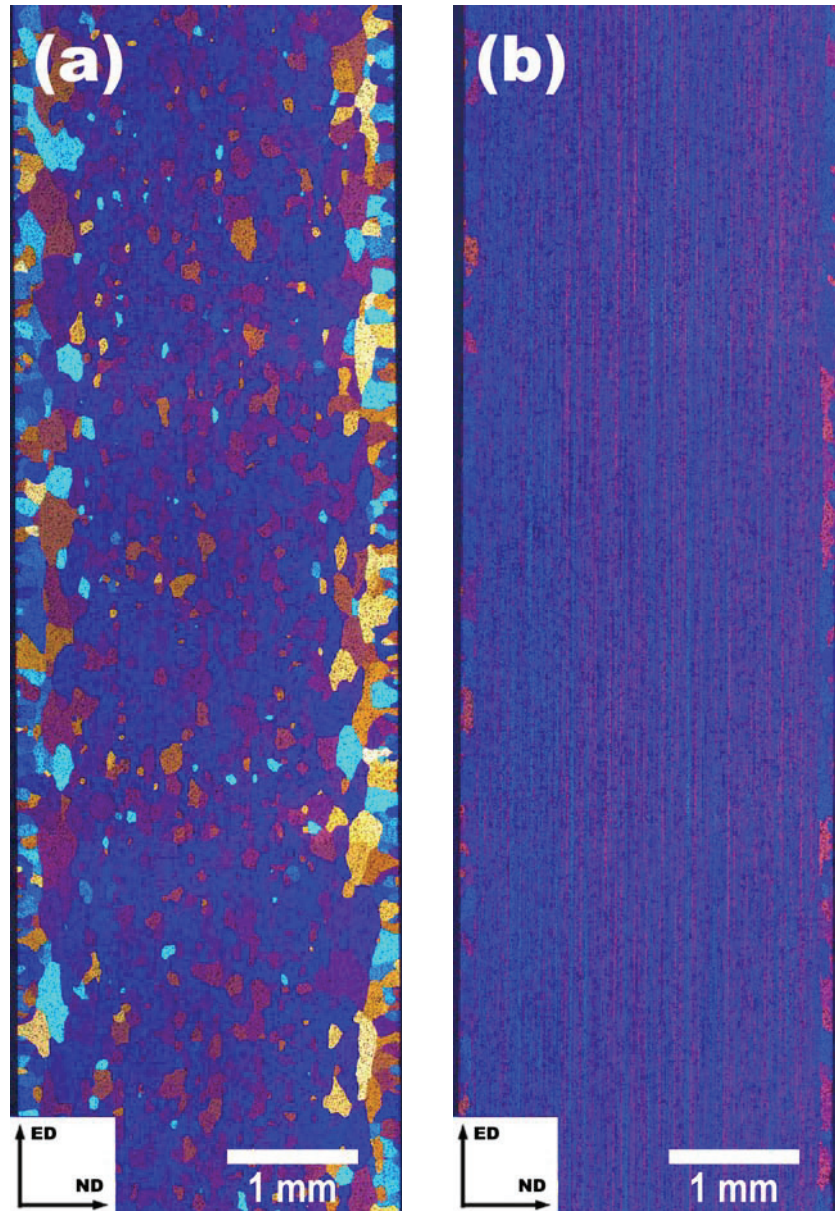


Figure 5.1 – Light optical micrograph of the microstructure in the longitudinal transverse (ED-ND) plane. (a) AA6063 and (b) AA6082.

Part A: Characterisation of materials – Effects of heat-treatment, texture and through-thickness variations

Information about the microstructural and mechanical properties is important in order to understand the mechanical behaviour of a material. The two extruded aluminium profiles investigated in this work are therefore given a thorough characterisation. The effect of heat-treatment on mechanical properties is included, since alteration in mechanical properties is very important in regard to industrial forming operations.

5.1 Characterisation of as-received materials

The properties of the two extruded profiles investigated are determined by the alloy composition and the extrusion process. Extrusion is a non-homogeneous deformation process which gives rise to variations over the profile cross-section. The through-thickness variations in the microstructure have been characterised by applying EBSD investigations at different positions through the thickness.

5.1.1 Microstructure

The microstructure of the two profiles is very different in spite of both being Al-Mg-Si-type alloys. The AA6063 has a fully recrystallized microstructure consisting of relatively equiaxed grains as shown by the light optical micrograph of the longitudinal transverse (ED-ND) plane in Figure 5.1 (a). The corresponding inverse pole figure (IPF) map of the same plane is shown in Figure 5.3(a) and it is clear that the profile possesses an evident through-thickness gradient, especially close to the profile surface. The AA6082 on the other hand, has a fibrous microstructure with a recrystallized surface layer as shown in Figure 5.1 (b) and Figure 5.2. The recrystallized surface layer is approximately 120 μ m thick, giving rise to an even more evident through-thickness texture gradient as shown in Figure 5.3 (b). The figures also show that the size of the recrystallized surface layer is close to constant along the extrusion direction (ED) (Figure 5.1 (b)), and neither is the microstructure affected by the solution heat-treatment (Figure 5.2). However, the fibrous

5 Experimental results

As mentioned above, the main objective of this work has been to investigate and explain the mechanical anisotropy observed in extruded profiles. State-of-the-art experimental techniques have been developed and used in order to investigate the mechanisms taking place in extruded profiles during deformation. Experiments are performed on several length scales, facilitating a better understanding of plastic deformation processes operating during subsequent forming operations. The acquired knowledge can also be used to improve shape tolerances of forward extruded profiles in the future.

The experimental results are organised in two separate parts based on the techniques used and the mechanisms investigated. Part A is titled “Characterisation of materials – Effects of heat-treatment, texture and through-thickness variations”. The basic properties of the selected materials are thoroughly investigated in this part but also the effect of heat-treatment (artificial ageing) on the observed mechanical anisotropy is characterised in great detail. The second part presents the in-situ deformation investigations performed in the SEM, using a new technique developed and implemented during this work: “SEM in-situ investigations of plasticity – Slip activity, grain rotation and texture evolution”. This part contains calculations of slip activity and how this depends on crystallographic texture. Also, crystallographic rotations taking place during deformation are investigated in detail. Local strain distribution during in-situ deformation has been characterised using digital speckle correlation analysis (DSCA).

4.4 Local strain measurements

The local strain measurements were based on the digital speckle correlation analysis (DSCA) technique (see section 2.6.1 for more details). The commercial software 7XD, developed at INSA – Annecy in France has been used to perform strain measurements of in-situ tensile specimens based on secondary electron (SE) micrographs acquired in the SEM. This technique uses a fixed grid (gold grid) or a random speckle on the specimen surface to correlate the different positions in consecutive micrographs. Further, the strain calculations are related to a micrograph acquired prior to deformation. The two most important parameters for these calculations are the grid size and the binned pattern size. These parameters were selected such that the size of the virtual grid was equivalent to the gold grid produced on the specimen surface (see section 4.1.2 for details regarding preparation of the gold grid). The local strain measurements performed in the SEM with a gauge length of approximately $10\mu\text{m}$ were proven to be equivalent to strain measurements from ordinary simple tension experiments using conventional extensometers.

Experimental techniques

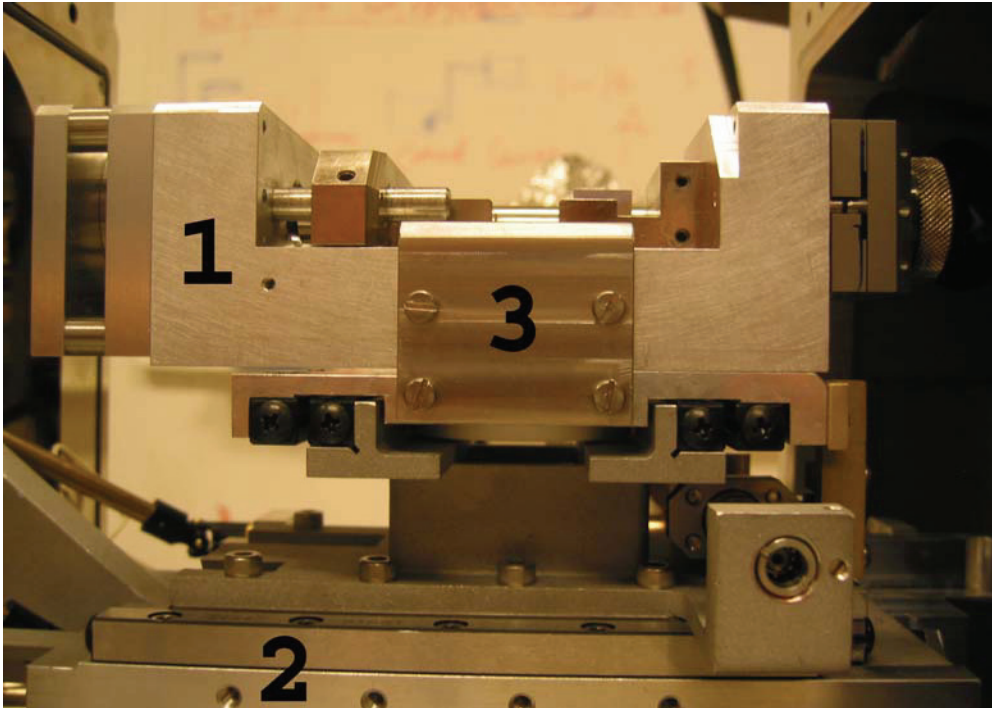


Figure 4.10 – Deformation unit (1) mounted on top of the modified Hitachi S3500-N stage (2) by a simple fixing bracket (3).

Experimental techniques

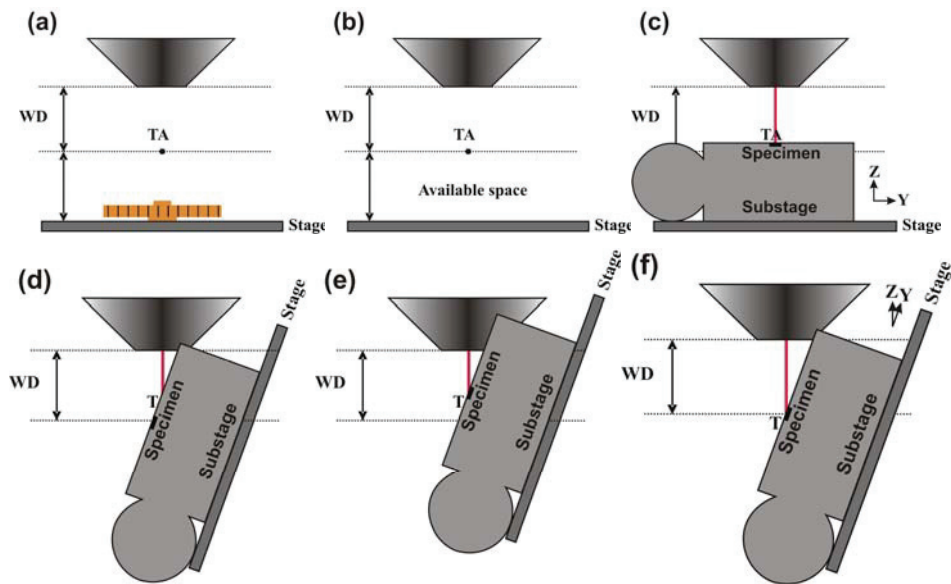


Figure 4.8 – Schematic illustration of the deformation unit inside the Hitachi S3500-N chamber. WD and TA are the optimal working distance for EBSD investigations and the position of tilt axis respectively. The deformation unit must be placed in the available space between the TA and the stage surface. (a) Prior to any modifications (b) After removal of rotation unit (c) Deformation unit placed inside the SEM chamber. The specimen surface is higher than the TA. (d) Stage tilted 70° for EBSD investigation. The specimen surface is rotated away from the electron beam. (e) Stage movement perpendicular to the TA in order to reposition the specimen under the electron beam. (f) Optimal working distance for EBSD investigations are achieved by moving the stage in the Z-direction.

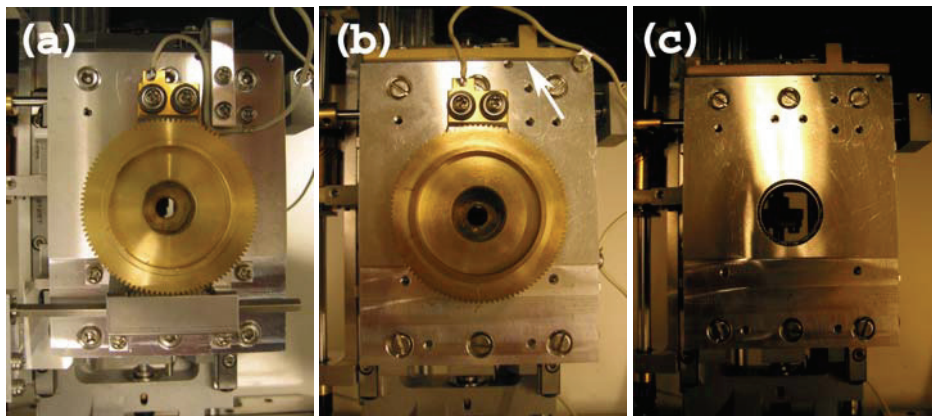


Figure 4.9 – Modifications of the Hitachi S3500-N stage. (a) Prior to any modifications. (b) Permanent redesign of the Y-direction movement bracket. The bracket is indicated by a white arrow. (c) Temporary removed rotation unit in order to allow mounting of deformation unit.

Experimental techniques

plane of the Hitachi S3500-N. Figure 4.8 presents a schematic illustration of the difficulties related to this limitation. The free distance between the substage and the TA (tilt axis) was far too small (Figure 4.8 (a)), which made some modifications of the stage necessary. The bracket performing the Y-direction movement was permanently modified and the rotation unit had to be removed temporarily as shown in Figure 4.9. However, the available space was too small even after these modifications (Figure 4.8 (b)), and the specimen surface was not at eucentric height (Figure 4.8 (c)). Consequently, the specimen surface would therefore move out of the electron beam when tilted 70° (Figure 4.8 (d)) and this had to be compensated by moving the stage perpendicular to the TA (Figure 4.8 (e)). Movement perpendicular to the TA reduced the working distance significantly and the specimen surface was no longer at the optimal working distance for EBSD investigations. The stage had therefore to be moved in the Z-direction in order to reach this optimal working distance (Figure 4.8 (f)). The tilt axis was fixed to the stage, therefore it would also move when the Z-direction position is changed. The machine was mounted to the stage by a simple bracket as shown in Figure 4.10. Non-eucentric specimen mounting introduced much more complicated testing operations and the probability of making fatal errors increased dramatically. In spite of these problems, no damage took place during this experimental work. It was also feared that the large weight of the deformation unit could lead to mechanical vibrations or drift but neither this became any problem at the magnifications used. Also the Hitachi S4300-SE has been modified such that the deformation unit can be mounted into this microscope (see appendix A for details).

Experimental techniques

simply replaced by a compression unit. The compression unit required rectangular specimens with maximum dimensions of $3 \times 3 \times 5 \text{ mm}^3$. Neither compression nor simple tension experiments at elevated temperatures have been performed in this work. It is also worth noticing the large weight (1.6kg) of the deformation unit when it is set up for both straining and heating. For further details concerning the heating-stage, please refer to Appendix A.

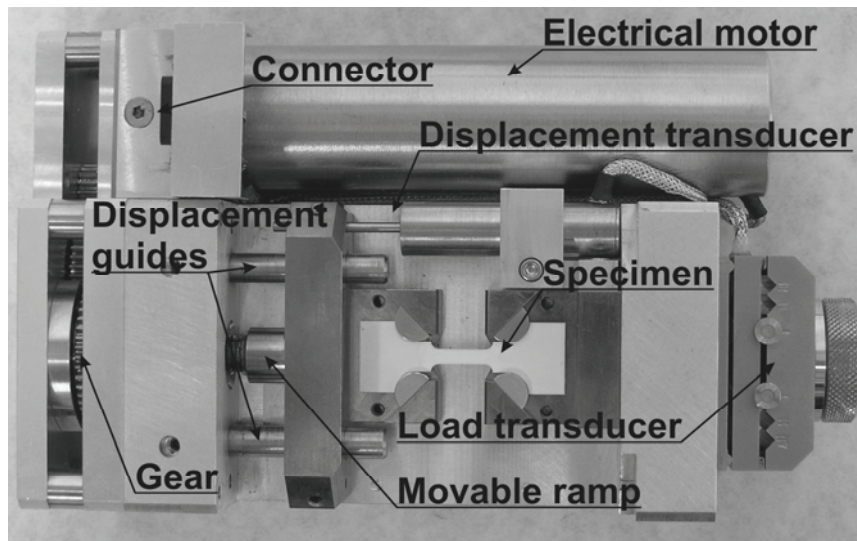


Figure 4.7 – Deformation unit for use in the SEM. Important components are labelled.

ii) The SEM (Hitachi S3500-N)

The conventional Hitachi S3500-N has been the SEM of choice for the in-situ experiments, mainly because this microscope was believed to be more user-friendly with regard to specimen exchange time. The spatial resolution of this instrument was not comparable with the resolution obtained by a field emission SEM. However, this has not been a limiting factor.

There were several potential problems connected to placing a substage inside the chamber of a SEM. The problems that arose during installation in the Hitachi S3500-N will be described in the following. It was desirable to have the specimen surface in the eucentric height (parallel to the tilt axis) since this eases the SEM operations. The height of the deformation unit made it impossible to place the specimen surface in the eucentric

i) Deformation unit

A central part of the in-situ system is the deformation unit. This unit is simply a small tensile machine which can be placed inside the chamber of a SEM (substage). The space available inside a SEM is normally very limited so the tensile machine has a very compact design. The deformation unit implemented to this in-situ system was originally developed at the CNRS – PMTM laboratory at University Paris 13, France (Chiron et al. 1996) and further modified at the Norwegian University of Science and Technology. All the in-situ experiments presented in this work were performed with this deformation unit.

The substage design is very compact ($15.5 \times 9.5 \times 4.5 \text{ cm}^3$) as shown in Figure 4.7. The unit was controlled by external software connected to the substage by a 15pin mini D-sub connector. Deformation took place by simple tension with one fixed and one movable ramp. The movable ramp was screw-driven by an electrical step motor and the strain rate was adapted by the gear. The deformation behaviour could be monitored by the stress vs. strain curves obtained during deformation. The longitudinal strains were calculated based on the stroke movement measured by a LVDT (Linear Variable Differential Transformer) displacements transducer while the deformation force was measured by the load transducer.

Due to the special design, it was possible to tilt the substage 70° without interfering with the objective lens of the SEM. Thus, this in-situ unit was designed for simultaneous deformation and EBSD-mapping. The deformation unit requires specimens with a rectangular cross section and specimen heads specially adapted for the machine as shown in Figure 4.2. Semi-circled alignment parts at both ends forced the specimen to be aligned with the tensile direction during loading. It was important to perform an accurate specimen alignment with regard to the global reference system in order to obtain accurate uniaxial deformation.

This deformation unit could also be combined with a heating unit which allows in-situ simple tension investigations at elevated temperatures. The furnace is simply clamped underneath the parallel part of the specimen and heats the sample locally. The substage could also be used to perform compression experiments. The semi-circled parts are there

Experimental techniques

i) In-plane investigations

The in-plane specimens were 1mm thick and were sampled from the centre position in the normal direction (ND), i.e. with specimen geometry as shown in Figure 4.2. Simple tension deformation was performed with a constant stroke rate, giving rise to an initial macroscopic strain rate of $1.1 \times 10^{-4} \text{ s}^{-1}$. The specimens were typically deformed in steps corresponding to $\sim 2.0\%$ nominal strain and SE micrographs were acquired between every step. The specimen was horizontal both during deformation and SE imaging. EBSD investigations were typically performed between every third step (i.e. every $\sim 6.0\%$ nominal strain). The same area was investigated throughout the deformation process allowing the deformation behaviour for a given number of grains to be studied in great detail. The global texture measurements and the detailed investigations of the microstructure consisted of more than 3000 and ~ 40 grains respectively. Microstructural investigations were also performed on specimens with an artificial gold grid.

ii) Through-thickness investigations

In general, the through-thickness investigations were performed in the same way as the in-plane ones. However, the specimen geometry was somewhat more complicated (Figure 4.5) and the specimen width corresponded to the profile thickness ($\sim 3\text{mm}$). The through-thickness variations were investigated by selecting the area of interest equal to the half width ($\sim 1500\mu\text{m}$) of the specimen. Hence, the profile thickness was investigated from the centre ($S=0.00$) to the surface ($S=1.00$). It was not possible to cover the area of interest by using only one micrograph at the desired magnification, hence the SE micrograph consisted of four micrographs stitched together in an image processing software.

4.3.3 Optimisation of in-situ systems

The optimisation of the in-situ system has been one of the most important experimental tasks in this work. It has been mostly motivated by the need for a better understanding of the deformation behaviour. The quality of the results obtained with an in-situ system depends on the in-situ unit and the SEM capabilities. The interaction between these two components was also of primary importance. The following section presents the in-situ system developed during this work.

Experimental techniques

It was essential for a global texture measurement to represent the distribution of all possible crystallographic orientations. This was in general obtained by selecting orientations from a large area of the specimen. Large spatial resolution was redundant since the spread in orientation within the individual grains was normally neglectable. The step size was adapted to give only one measurement per grain. However, it was selected equal to the minimum grain size when the material had a very heterogeneous microstructure. The global texture measurements consisted of more than 25.000 orientations due to the large area investigated. A large number of orientations gave a very accurate description of the materials orientation distribution. Engler (2004) stated that the orientation distribution of a specimen can normally be described with only 500 randomly selected orientations. This statement was tested by extracting different numbers of orientations randomly from the global texture measurements, and it was shown that the reduction in the number of mapped orientations only give minor changes. Hence, the scan size used in this work is strongly exaggerated.

4.3.2 In-situ deformation investigations

In-situ deformation investigations in SEM facilitate studies of the deformation behaviour locally. This is a relatively new technique that could be used to study several important metallurgical phenomena. In the present work the tensile deformation process was interrupted in order to perform the surface investigations (SE imaging and EBSD mapping). After each mapping sequence the deformation was continued, and so forth. Hence, these investigations were not fully in-situ but rather “semi-in-situ”.

Two different types of in-situ deformation investigations on the fully recrystallized AA6063 have been performed. In-plane (ED-TD plane) investigations have been used to study the global texture evolution, and more detailed investigations of grain rotations and surface slip-trace development have been performed in-plane. Through-thickness investigations were the second type of in-situ deformation studies performed, i.e. deformation variations over the thickness in a material with a very strong texture gradient.

Experimental techniques

Table 4.2 – Normal software setup for EBSD investigations used in the present work. Camera binning is a clocking scheme used to combine the charge collected by several adjacent CCD pixels. This increases both the sensitivity and the acquisition speed of the camera at the expense of resolution. Theta step size describes the resolution of the Hough transform. *Specimens taken from the recrystallized surface area are tested with the same setup as AA6063.

Parameter	AA6063		AA6082*	
	Microstructure	Texture	Microstructure	Texture
Camera binning	8x8	8x8	4x4	4x4
Step size [μm]	2	10-15	0.4	10
Scan size [μm^2]	1500x1500	3000x3000	200x400	1500x3000
Pixel shape	Hexagonal	Hexagonal	Hexagonal	Hexagonal
Binned pattern size	96	96	140	120
Theta step size:	2°	1°	1°	1°

Table 4.3 – Typical SEM setup for EBSD investigations used in this work.

Parameter	Value
Acc. voltage	20 kV
Tilt angle	70°
Probe current	2.0-2.5 nA
Working distance	20mm

The information generated from an EBSD investigation was very dependent on the number of indexed points within the individual grains. It was desirable to have only one orientation per grain for global texture measurement, while more than 1000 orientations were typically necessary to perform detailed studies of the orientation gradients through a grain. The number of measurements within the individual grains could be controlled by choosing an appropriate step size. Hence, the step size selected for microstructure investigations of AA6063 and AA6082 is $2\mu\text{m}$ and $0.4\mu\text{m}$ respectively. A typical EBSD measurement used to study the microstructure evolution and the development of orientation gradients in deformed aluminium consisted of ~ 70000 orientations distributed among ~ 50 grains.

Experimental techniques

A most critical quality of EBSD software is to calculate the crystallographic orientation accurately and within a short period of time. How easily the orientation data can be post-treated and presented is another important quality. EBSD software from the three most well known suppliers (HKL Channel 5, Oxford Inca and Edax TSL OIM3.5) were all available at the Electron Microscopy laboratory at the Department of Materials Science and Engineering, NTNU. All three were compared with regard to both data acquisition and post-processing. It was concluded, based on an overall evaluation, that the Edax TSL OIM3.5 software and its successors OIM4.X were best suited for this type of work.

This software had a control panel with several available acquisition options, making it easy to optimise the EBSD acquisition parameters for reliable results. However, EBSD acquisition was both material and preparation dependent, so it was almost impossible to give any universal solution for the testing parameters. The testing conditions selected would also affect the testing parameters. For example, the parameters selected for a detailed investigation of the orientation gradient within a deformed grain differs significantly from the parameters used for global texture measurements. Table 4.2 presents the typical software setup for the different types of EBSD investigations. The SEM parameters, on the other hand, were more independent and were normally kept constant for all types of EBSD investigations. A typical microscope setup used for these investigations is given in Table 4.3.

Experimental techniques

fine-scaled microstructure material due to its improved resolution. It is also worth noticing that the Schottky emitter has an extremely stable beam current, which was very convenient for EBSD investigations. The following sections will be used to present the experimental techniques involving scanning electron microscopy and the modification made to the SEM in order to allow in-situ deformation investigations will also be presented.

4.3.1 Electron backscatter diffraction (EBSD)

The electron backscatter diffraction technique has been used to obtain information about the micro and macro texture of the materials investigated. The microstructure and its evolution during deformation have also been determined based on experiments performed with this technique. Important properties of the materials investigated could be determined by use of the crystallographic information obtained by EBSD. EBSD was therefore a very important experimental technique for material characterisation.

The main components of an operating EBSD system is the SEM, the EBSD-detector including a camera that acquires the diffraction patterns and the software that calculates the crystallographic orientation based on these patterns. It is also important to remember that the software should also be able to post-treat the crystallographic orientation information acquired.

The most important properties of the SEM were the beam current and stability. A stable beam current was essential since variations reduce the accuracy of the EBSD measurements. Both microscopes used in this work have a satisfying beam current stability and were very well suited for EBSD investigations.

An important feature of the applied EBSD-detector was the pattern acquisition speed. The camera used was a Nordif digital CD200 EBSD detector with a maximum acquisition speed of 43fps (frames per second). This speed was satisfying for the experiments performed, but it is of course desirable to increase the acquisition speed even further in order to perform fully in-situ investigations with shorter step sizes. This can be obtained when the next generation Nordif EBSD-detectors with acquisition speeds more than 500fps become available.

4.2 Tensile testing

The tensile testing experiments in this work were performed on two different length scales. The macroscopic results were acquired by use of an ordinary testing machine while a very compact in-situ testing machine was used to investigate the microscopic behaviour in a SEM. Section 4.3.3 gives a detailed description of the simple tension experiments performed in the SEM.

Investigations of the macroscopic behaviour were performed for all the material conditions investigated in this work (see Table 3.3). The tensile specimens were sampled from the extruded profile 0° (parallel to ED), 45° and 90° (parallel to TD) with respect to the extrusion direction (ED). A minimum of three parallels were tested in each direction in order to verify the experimental results. Simple tension experiments were performed in an MTS 880 servo-hydraulic testing machine at a constant ramp rate corresponding to an initial strain rate of $1.1 \times 10^{-3} \text{ s}^{-1}$. The tensile specimens had a width of 12.7mm and a parallel length of 75 mm as shown in Figure 4.2. The transversal and longitudinal strains were measured by a MTS transversal (MTS 632.23F-20) extensometer and a MTS 50mm longitudinal (MTS 632.25F-20) extensometer respectively.

Tensile testing of thin specimens taken from three different positions through the profile thickness was also performed in the same way as described above. Notice that the thickness of these specimens was only 0.3mm, making transversal strain measurements more difficult due to problems with the gripping mechanisms of the extensometer.

4.3 Scanning Electron Microscopy (SEM)

Scanning electron microscopy has been by far the most important tool utilised in this work. The SEM has been used both for metallographic characterisation of the starting material and as a platform for the detailed in-situ deformation behaviour experiments. Two different scanning electron microscopes were used. The first was a very user-friendly conventional tungsten filament SEM with low-vacuum capabilities (Hitachi S3500-N). This microscope was used for the in-situ investigations and characterisation of the recrystallized material. The second microscope was a high resolution field emission SEM (Hitachi S4300-SE) which was used for characterisation of the fibrous

Experimental techniques

sputtered onto the produced grid and then a 20nm thick Au-layer was evaporated on top of the base layer. This gave a continuous layer of gold covering the entire surface of the specimen as shown in Figure 4.6 (d). The remaining PMMA was finally dissolved and removed by cleaning the specimen with ethyl acetate in an ultrasonic bath for 15 minutes, also removing the gold deposit on top of the PMMA. The gold deposit on the specimen surface would not be affected by this cleaning procedure, and the electro polished surface reappeared with an evident gold grid that could be used for strain analysis during investigations in the SEM (Figure 4.6 (e)).

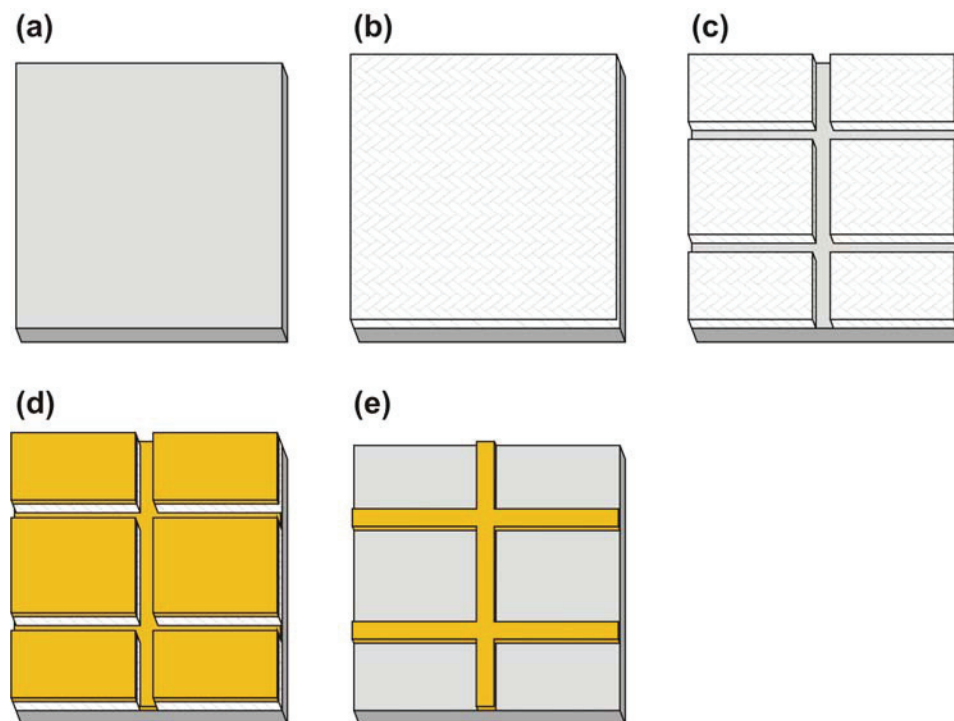


Figure 4.6 – Chronological illustration of the surface grid production procedure. (a) Electro polished specimen surface. (b) Specimen surface with continuous plastic film overlaid. (c) Plastic film with a grid after electron beam exposure. (d) Specimen with gold both in the grid and on the surface of the remaining film. (e) Specimen with gold grid after removal of the remaining film.

4.1.2 Metallographic preparation and surface grids

The sampled specimens developed a heavily deformed surface layer during machining which had to be removed prior to investigations in the light optical microscope or in the SEM. This was obtained by mechanical grinding to ASTM mesh 2400 and subsequent mechanical polishing with 3 and 1 μm diamond paste, followed by “shock” electro-polishing in Struers electrolyte A2 for 4 seconds at 30V and 10°C. The specimens investigated in the light optical microscope were anodized in a 5% HBF₄ aqueous solution (Bakers reagent) (Petzow 1976) for ~2 minutes at 20V and 18°C in order to reveal the grain structure under polarised light.

The undeformed and smooth surface obtained after electro-polishing was necessary for EBSD investigations. However, random features in the specimen surface are absent. Hence, an artificial random speckle had to be created in order to allow EBSD investigations in combination with local strain measurements, using the DSCA technique described later in section 4.4. It was very difficult to produce a sufficiently fine random speckle and a compromise had to be made. In this work an artificial gold grid was produced on the specimen surface. The gold grids were produced in the CNRS – PMTM laboratory at University Paris 13 with a quadratic grid size of 10x10 μm^2 and a grid line width of ~1 μm .

Figure 4.6 presents a schematic illustration of the procedures utilised to produce the gold grid. First, a thin film (~0.4 μm thick) of PMMA (Polymethylmetacrylate) was deposited onto the electro polished surface by spin coating (Figure 4.6 (b)). The specimen was then annealed for 30 minutes at 130°C in order to remove the residual stresses from the spin coating. The grid was produced by exposing the polymer film to the electron beam of a SEM. Movement of the electron beam was controlled by external software and the electron beam broke the polymers down to monomers, which could easily be removed by cleaning the specimen in a solution consisting of 25% ethyl methyl ketone and 75% Propanol-2. The grid became visible in the PMMA film after removal of the monomers (Figure 4.6 (c)). However, this grid could not be investigated in the SEM, so a thin layer of gold was deposited on top of the grid produced in the SEM. The deposition procedure was divided in two operations in order to optimise the adhesiveness between the electro polished surface and the evaporated gold layer. First, a 1nm-thick base Au-layer was

Experimental techniques

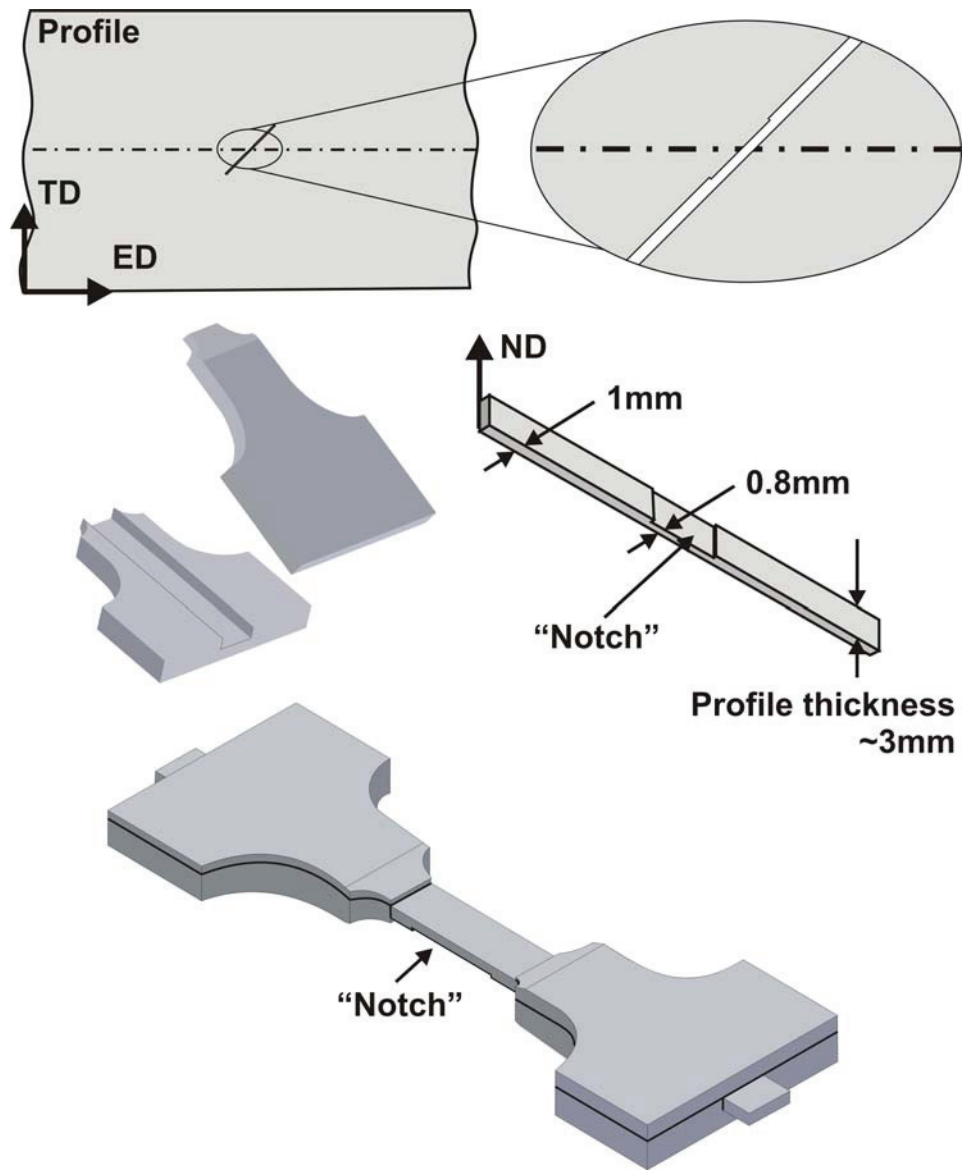


Figure 4.5 – Specimen (45° direction) for investigation of through-thickness deformation in SEM. The gauge length piece is machined from the profile and the width of this part corresponds to the profile thickness. The small “notch” in the gauge length is produced in order to concentrate the plastic deformation. Prefabricated specimen heads are finally glued to the parallel part and the through-thickness deformation can be investigated in the SEM.

Experimental techniques

It was most convenient to study the surface of the gauge length during SEM simple tension deformation. The gauge width of these specimens was 3 mm while the total width of the gripping section was 14 mm (see Figure 4.2 (bottom)). Due to the geometrical limitations set by the SEM chamber, it was not possible to study the through-thickness deformation in the TD plane during in-situ SEM deformation. However, by doing some radical modifications of the specimen geometry, through-thickness investigations were made possible (i.e. see the illustration in Figure 4.5). The gauge length of the specimen was machined as described above and the width of this part corresponds to the profile thickness. In addition, a short 0.8mm thick “notch” was introduced (see Figure 4.5). During straining, the plastic deformation was localised to this area due to 20% reduction of the cross-section. The specimen heads were prefabricated in a material with higher strength in order to avoid plastic deformation of the specimen heads during testing. The prefabricated heads were mounted onto the gauge length piece with two-component epoxy glue. The final specimen assembly is shown in Figure 4.5. However, it is worth noticing that the glued connection will shear off if the “notch” in the parallel part was omitted. Without the “notch”, the full length of the gauge length piece deforms plastically, hence the contraction in width and thickness will weaken the glued connection and the glue would fail.

Experimental techniques

The through-thickness texture variations were investigated by testing specimens sampled from different positions through the thickness. In order to avoid any through width variations, also these specimens were taken close to the centre line (see Figure 4.1). The position along the thickness direction (normal direction) were denoted by an S-value which starts with S=1.0 at the profile surface and ends with S=0.0 in the centre of the profile. Figure 4.4 presents a schematic illustration of the S-value notation used for the different positions. The AA6063 and AA6082 were tested at eight and seven different positions through the thickness, respectively. Table 4.1 summarises the distance beneath the surface for all positions investigated.

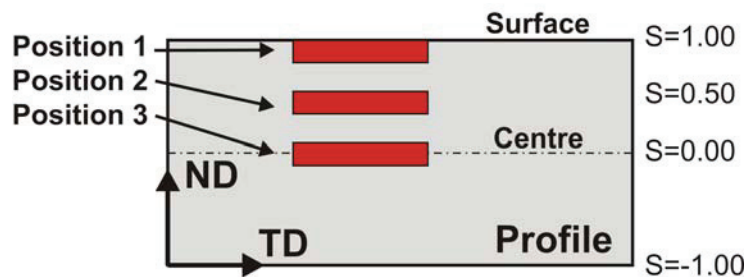


Figure 4.4 – Schematic illustration of the notation used for representing the different positions through the profile thickness.

Table 4.1 – Distances beneath the surface [mm] and corresponding S-notations applied for the different through-thickness positions.

Alloy	S=0.00	S=0.50	S=0.70	S=0.80	S=0.85	S=0.90	S=0.95	S=0.99
AA6063	1.45	0.72	0.43	0.29	0.22	0.14	0.07	0.01
AA6082	1.42	0.71	0.43	0.29	-	0.14	0.07	0.01

The specimens prepared for in-situ testing in the SEM were given a special geometry (Figure 4.2 (bottom)) and a thickness of 1.0 mm. All these specimens were in addition to ordinary machining given some additional metallographic preparation. This is required in order to obtain satisfying EBSD patterns and high quality SE micrographs. It was necessary to remove the heavily deformed surface layer developed during machining. The procedures applied to achieve the required specimen quality will be described in the following paragraph.

Experimental techniques

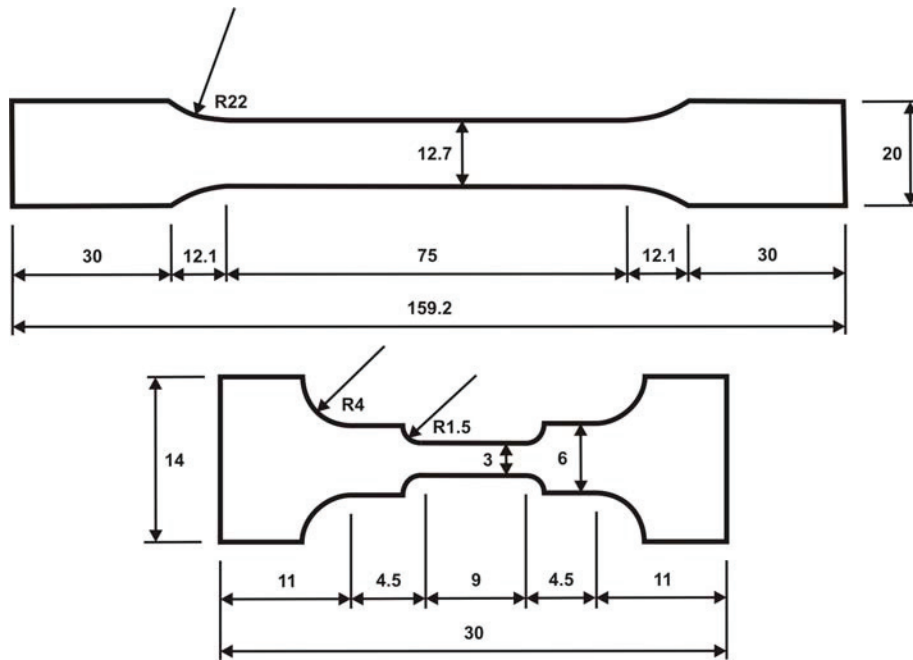


Figure 4.2 – Geometry for standard full-size (top) and in-situ SEM specimens (bottom) for simple tension testing. All dimensions in [mm]. The thickness of the full-size specimens was either 0.3 mm or full profile thickness (3.0 mm), while the typical SEM specimens had a thickness of ~1.0 mm.

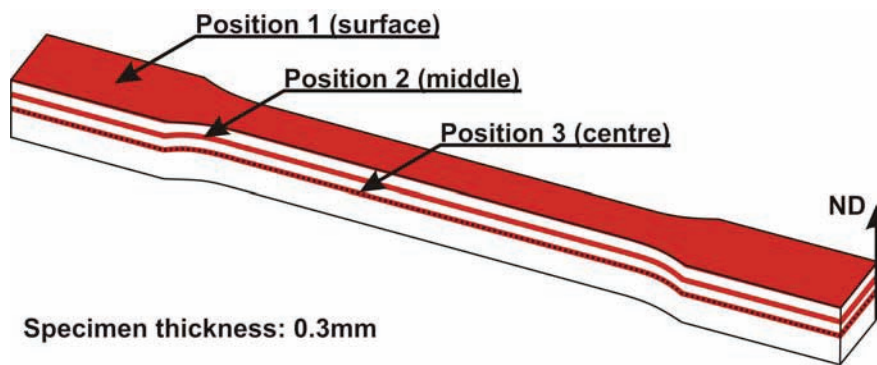


Figure 4.3 – Schematic illustration of simple tension specimens taken from different positions through the profile thickness. Here, ND=profile normal direction.

Experimental techniques

tension specimens were sampled such that the centre specimen position always intersects the centre line of the profile. This figure also indicates that an exception was made for specimens taken parallel to ED. This was done in order to reduce the consumption of material. It was assumed that three parallel specimens could be produced without being influenced by the through width variations. All the simple tension specimens were sampled according to the procedures described above.

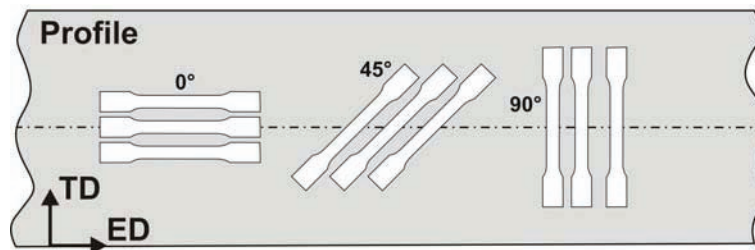


Figure 4.1 – Sampling positions of simple tension specimens where TD and ED are the profile transversal and longitudinal (extrusion) directions.

The full thickness tensile specimens were machined from the extruded profile by using an ordinary CNC cutting machine. The surface was not machined away in order to maintain the true full thickness of the material. The applied specimen geometry of full thickness specimens is shown in Figure 4.2. Sub-size specimens having the same in-plane geometry and 0.3 mm in thickness were sampled from three different positions through the profile thickness. The three positions were labelled Position 1, 2 and 3 and are taken from the centre, middle and surface part of the profile thickness respectively. Figure 4.3 and Figure 4.4 present the thickness direction position of the three sub-size specimens investigated. Investigations on sub-size simple tension specimens were only preformed in material condition T1.

4 Experimental techniques

A good and comprehensive understanding of the applied experimental techniques is a key element in utilizing the results obtained in this work. For this reason, this chapter will be used to describe the experimental techniques. The background for the selected testing parameters will also be commented.

4.1 Specimen sampling and preparation

Specimen sampling from extruded profiles is critical due to expected through profile variations. Hence, small changes in the sampling position could strongly affect the testing results. Also specimen preparation is of great importance, especially for EBSD investigations, since even minor changes in specimen preparation procedure can lead to significant alteration of the results. The following sections give a detailed description of the specimen sampling procedures and preparation techniques used during this work.

4.1.1 Specimen sampling

Since extruded profiles are believed to be subjected to variations both through the cross-section and along the extrusion direction (ED), it is necessary to use strict sampling procedures in order not to introduce uncertainties.

The profiles investigated were cut into 2-meter-long parts and labelled by Hydro Aluminium AS. However, this labelling did not include any information about the position along the total length, making it impossible to determine any relationship between the different parts and the press cycle. This introduced some uncertainties with regard to possibilities for variations along the profile length but these were neglected in the present work.

It is known that extruded profiles, especially very flat profiles, can develop some variations over the width (Fjeldly 1999). Those investigated in this work had a cross-section (thickness x width) of 3x205 mm², hence it was reasonable to assume that they possess such variations. The variations were avoided by sampling all specimens from the centre width position of the profile as shown in Figure 4.1. Consequently, the simple

Materials and material processing

texture from extrusion, i.e. the cold rolled profiles developed a weak deformation texture. A consecutive annealing heat-treatment at 520°C for 10 minutes resulted in a fully recrystallized microstructure with a close to random crystallographic texture. The material was stored at room temperature for more than 1000 hours in order to reduce the effect of Mg in supersaturated solid solution.

Materials and material processing

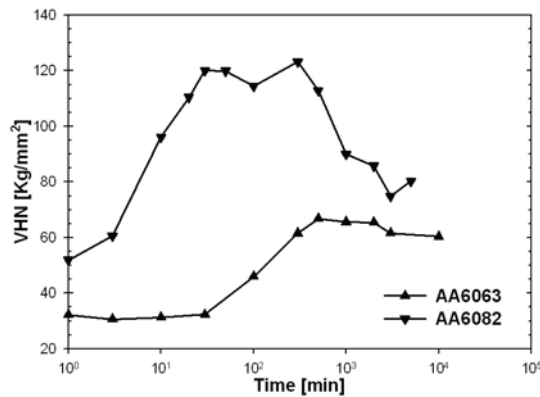


Figure 3.2 – Hardening curves for artificial ageing at 185°C, after solution heat-treatment at 540°C for 20 minutes.

Table 3.3 – Description of the material conditions investigated.

Material Condition	Description
W, 10min	Solution-heat-treated and tested 10 min. after water quenching
T4, 3h	Solution-heat-treated and naturally aged for 3 hours prior to testing
T4, 24h	Solution-heat-treated and naturally aged for 24 hours prior to testing
T4, >1kh	Annealed and naturally aged more than 1000 hours prior to testing
T6	Solution-heat-treated and artificially aged at 185°C to peak strength prior to testing
T7	Solution-heat-treated and artificially aged at 185°C to the over aged condition prior to testing
T1	Naturally aged for more than 2 years after extrusion

3.2.3 Additional processing

Both alloys investigated have a strong crystallographic texture. It was therefore necessary to perform additional investigations on material almost without texture to obtain a more complete understanding of the slip system activation during simple tension. Some additional processing was therefore performed to reduce the texture of the extruded AA6063 profile. The profile was first cross-rolled (50% reduction) at room temperature in a laboratory rolling mill. Cross-rolling reduces the crystallographic

Table 3.2 – Press conditions for the extruded aluminium profiles.

Alloy	Billet temp.	Container temp.	Ram speed	Profile temp. front
AA6063 ^a	460°C	440°C	14-16 mm/sec.	515-523°C
AA6082 ^b	515°C	440°C	15-16 mm/sec.	520-543°C

Alloy	Profile temp. middle	Profile temp. end	Temp. after spray cooling
AA6063 ^a	511-528°C	505-517°C	~360°C
AA6082 ^b	518-532°C	503-524°C	~360°C

^a Pettersen and Furu (2001a)^b Pettersen and Furu (2001b)

3.2.2 Heat-treatments

Several different heat-treatments were applied to both alloys in order to produce a wide range of material conditions. The solution heat-treatment was performed in an air circulating furnace at 540°C for 20 minutes followed by water quenching, while the artificial age-hardening was performed in an ordinary oil bath at 185°C. The material was stored at room temperature for 10 minutes between the solution heat-treatment and the artificial age-hardening. The ageing behaviour at 185°C was explored in order to determine the ageing times necessary to obtain the peak aged (T6) and over aged (T7) material. This was done by measuring the Vickers hardness after various ageing times and subsequent water quenching. The obtained ageing curves are shown in Figure 3.2. These measurements were performed using a 5 kg load, loading time 15 seconds and a loading speed of 150 $\mu\text{m/s}$. Based on the ageing curve acquired, the T6 condition was expected to be reached at 700 and 250 minutes while ageing times 10,000 and 5000 minutes were necessary to reach the T7 condition for the AA6063 and AA6082 respectively. Specimens were also stored at room temperature for different amounts of time in order to produce naturally aged material conditions. Table 3.3 presents the notations used together with a description of all material conditions investigated herein.

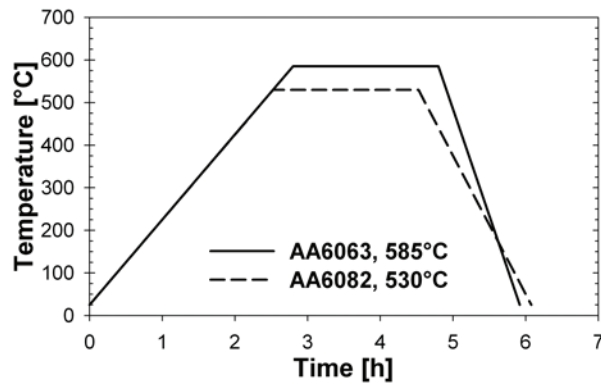


Figure 3.1 – Approximate homogenisation treatments of billets prior to extrusion.

3.2 Material processing

All processing from refining and casting to completion of the final product affects the material properties. It is therefore important to have detailed understanding of the processing taking place prior to the investigations performed in this work.

3.2.1 Extrusion

Billets with a diameter of 203 mm were extruded into flat profiles with a cross section of $3 \times 205 \text{ mm}^2$ by Hydro Aluminium AS. The extrusion process was performed at a reduction ratio of 53 and a ram speed of approximately 15 mm/sec. Immediately after the outlet of the extrusion die, the profiles were cooled with maximum water spray-cooling, followed by forced air-cooling. The press conditions are summed up in Table 3.2. The profiles were stored at room temperature for more than two years prior to further processing and the profiles were therefore received in the naturally stabilised condition, T1.

3 Materials and material processing

This chapter presents the materials investigated as well as the material processing prior and during the present investigations.

3.1 Materials

This work has focused on commercial aluminium alloys representing high volume production in the extrusion industry. Two different precipitation hardening alloys from the Al-Mg-Si system have been investigated (Table 3.1). The two alloys are AA6063 which is a low strength 6xxx series alloy and AA6082 which is a typical high strength alloy. Both alloys were DC-cast and homogenised (see Figure 3.1) by Hydro Aluminium, Sunndal prior to any processing. AA6082 contains somewhat more magnesium and silicon giving rise to higher strength but, more importantly it also contains some manganese (0.54 wt%). Al-Mg-Si alloys with 0.5-0.7 wt% Mn will precipitate small Mn-dispersoids of the $MnAl_6$ -type at temperatures lower than 705°C. These dispersoids will prevent recrystallization during hot deformation (Petzow and Effenberg 1993). As a consequence, AA6063 becomes fully recrystallized while AA6082 develops a fibrous microstructure with a recrystallized surface layer after extrusion. Flat extruded profiles with a cross section of 3 x 205 mm² were received from Hydro Aluminium AS. Previously, these profiles have been characterised and investigated within the VIRFORM project (van der Winden et al., 2002), hence the properties of these materials have already been reported extensively, e.g. Engler (2002), Ryen (2003) and Pedersen et al. (2004). All details regarding these alloys and processing of the investigated profiles are given in Pettersen and Furu (2001a and 2001b).

Table 3.1 – Chemical composition of the two investigated alloys.

Alloy	Wt% Mg	Wt% Si	Wt% Mn	Wt% Fe	Wt% Cu
AA6063	0.46	0.44	0.03	0.19	0.006
AA6082	0.67	1.04	0.54	0.20	0.003

Theoretical background

(Bjerkaas et al. 2006). This indicates that the EBSD technique is actually able to capture the bulk behaviour during deformation

Theoretical background

Comparison between different techniques

X-ray diffraction (XRD) has since the introduction of crystallographic texture been the reference technique for measuring texture of polycrystalline materials. The crystallographic texture obtained with XRD and EBSD has been compared several times since the introduction of EBSD in the early nineties (Hjelen 1990). Generally, it has been shown that the measured crystallographic texture is independent of the measuring technique utilised (Bjerkaas and Sjølstad 2003, Saito et al. 2004). However, when the grain size exceeds a certain value (typically 50-100 μm), XRD can no longer provide statistically significant data. For very coarse grained materials (>1mm) and for heterogeneous materials such as welded joints, EBSD can still be used thanks to stage motion in the SEM. In EBSD, the orientation distribution function (ODF) is then directly calculated from the individual orientations by taking one point per grain or by taking all data points and weighting orientation data with the respective area fraction of grains (Gourgues-Lorenzon 2007). One must however, keep in mind that EBSD is a surface analysis technique.

When bulk (high energy x-ray diffraction) is compared to surface (EBSD by use of SEM) investigations, it is clear that bulk studies provide the most reliable results. However, the cost and complexity of this method makes EBSD/SEM the favourable alternative when it comes to studying crystallographic rotations of individual grains of a polycrystalline material. Further, the spatial resolution of 3DXRD is coarser (about a few μm) than that of EBSD but the angular resolution is high ($\sim 0.05^\circ$) (Gourgues-Lorenzon 2007).

As already mentioned above, there is some controversy regarding the results obtained from in-situ EBSD measurements. The EBSD technique has some considerable limitations since it only obtain information from the surface region of the specimen. It can therefore easily be claimed that the technique is insufficient since the acquired results are not representative for bulk deformation of the material. Hence, the results only provide a description of the surface behaviour. The works performed by the Risø group has shown that the rotation paths observed with bulk deformation are consistent with the rotation paths observed by performing in-situ EBSD investigations in the SEM

Theoretical background

Surface investigations during in-situ deformation

The deformation mechanisms operating at the sample surface can be studied by investigating the sample surface during deformation. Placing a deformation unit inside the chamber of a scanning electron microscope (SEM) allows this type of investigations. Rémi Chiron and his group at the CNRS – PMTM laboratory in Paris have been pioneers when it comes to in-situ deformation in the SEM (Chiron et al. 1996, Delaire et al. 2000). Other groups have also performed detailed investigations of the deformation mechanisms by use of this method in combination with EBSD-investigations. The impressive works by Zhang and Tong (2004) and Han et al. (2003), which have studied the microstructure and crystallographic rotation evolution respectively, are such examples. Also the group at McMaster University in Canada have started to utilise this method in order to obtain a better understanding of deformation mechanisms operating during forming of aluminium (Kang et al. 2005, Kang et al. 2006).

Bulk investigations during in-situ deformation

Bulk investigations are the most advanced method for studying deformation mechanisms. The method is based on diffraction with focused hard x-rays. Consequently, synchrotron radiation facilities are necessary in order to utilise this method. The “Metal Structures in Four Dimensions”-group at the Risø National Laboratory in Denmark should have credit for bringing this work forward, and they have developed methods that make it possible to follow the deformation of individual grains within the bulk material (see e.g. Margulies et al. 2001, Nielsen et al. 2001 and Poulsen et al. 2003). 3D X-ray diffraction (3DXRD) has been widely used both to study rotations taking place during deformation and recrystallization during annealing. By applying this method, it has been possible to study the crystallographic rotation and by that the deformation mechanisms in great detail (Winther et al. 2004, Winther 2005). The method has also been used by other groups (see e.g. Forbød et al. 2007), but the technique is far from being readily available.

Theoretical background

2.7.5 Available in-situ techniques

The introduction of sophisticated in-situ techniques has inaugurated a new era within material science. These new techniques have made it possible to study deformation mechanisms, annealing behaviour (see e.g. Ferry 1998, Juul Jensen 2005 and Lens et al. 2005) and phase transformations (see e.g. Gourgues-Lorenzon (2007) for a comprehensive review) in a way that were completely unrealistic only a couple of decades ago. In general, these techniques can be utilised for all the topics listed above. However, this section will focus on techniques most frequently used to study deformation mechanisms. Deformation mechanisms can basically be studied by use of three principally different methods:

- Normal characterisation and investigations of pre-deformed samples
- Surface investigations during in-situ deformation
- Bulk investigations during in-situ deformation

Normal characterisation and investigations of pre-deformed samples

Investigations of pre-deformed samples are in many regards the least sophisticated and most “old-fashioned” method, but still very useful to study deformation mechanisms. The PhD-works by Sørensen (1997), Iveland (2000) and Ryen (2003) acquired information of the operating deformation mechanisms by use of this method.

The researchers at the Risø National Laboratory in Denmark have performed several detailed investigations on dislocation boundary formation and the dislocation structure of the material by studying pre-deformed samples in the transmission electron microscope (TEM) (see e.g. Wert et al. 1997, Wert 2002, Wert and Huang 2003, Winther 2004 and Li et al. 2006). The drawback with this method is that it is impossible to investigate the same area several times. Hence, the evolution of individual grains during deformation can not be studied.

Theoretical background

precipitates have to be by-passed by the moving dislocations. Further, this means that a transition between localised and more homogeneous deformation will be dependent on the particle size as indicated in Figure 2.26. As indicated by the figure, dislocations tend to move along well-defined paths (the path of the first dislocations passing through the grain upon early stages of plastic deformation) when the precipitates are shearable (localised deformation). Several explanations have been proposed for this behaviour. Hornbogen and Gahr (1975) suggested that the localisation was related to local softening of the slip plane due to a decrease in precipitate strength. More recent investigations (e.g. see Poole et al. 2005) indicate that this matter is much more complicated and the observed localisation could possibly be more like an intrinsic property of aluminium alloys. In other words, when a dislocation source is activated, this source tends to stay active and will therefore suppress competing dislocation sources. On the other hand, when the dislocations have to overcome the precipitates by by-passing, they try to avoid any interaction with the precipitates, i.e. the slip distribution is more homogeneously distributed when the precipitate size is larger than d_c .

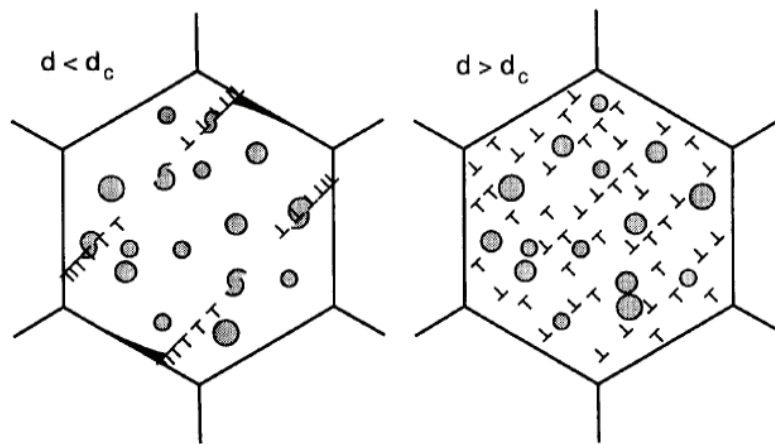


Figure 2.26 – Consequences of d_c on strain localisation. Shearable particles leading to strain localisation (left) and non-shearable particles leading to more distributed deformation (right) (Hornbogen and Starke 1992).

Theoretical background

authors showed that the investigated material possesses a strong angular dependency of the plastic strain ratio in supersaturated solid solution. They reported that the anisotropy disappeared after artificial ageing to the peak-aged condition (T6) and reappeared after ageing to the substantially over-aged condition (T7), as shown in Figure 2.25.

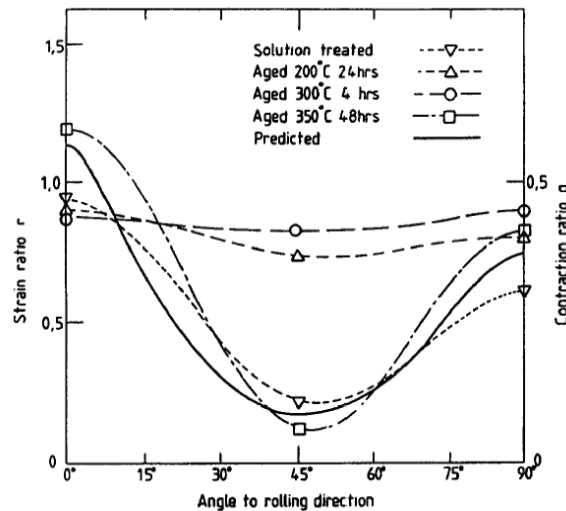


Figure 2.25 – Variation in r -value with test direction in Al-4%Cu in solution treated and artificially aged conditions compared with predictions of texture analysis (Bate et al. 1981).

It has been performed several interesting studies of how the plastic behaviour of a material has been altered due to the introduction of precipitates (see e.g. Hornbogen and Gahr 1975, Barlat and Vasudevan 1991, Hornbogen and Starke 1992, Sehitoglu et al. 2005 and Poole et al. 2005). A common observation is that precipitates alter the coarseness of slip taking place during deformation. During investigations in crystal plasticity, it has been reported that heterogeneous slip is favoured by low stacking fault energy, alloying elements in solid solution, shearable precipitates, when few slip systems are operating and with large grain sizes. Fine slip on the other hand, is favoured by bypassed particles, many operating slip systems and small grain sizes (Hornbogen and Gahr 1975).

Furthermore, the precipitate diameter (d) increases during ageing (see e.g. Hornbogen and Gahr 1975). It has been suggested that the transition from shearable to non-shearable precipitates takes place when the precipitates reach a critical diameter (d_c). Then

Theoretical background

have all studied the development of secondary slip traces during simple tension of polycrystalline materials and they have shown that the grains deform by multiple slip at very low strains (4% deformation) and close to 50% of the grains investigated develop additional slip traces locally.

Also crystallographic rotations during deformation and how these rotations are related to the deformation mechanisms have been studied to a large extent by these techniques. It has become possible to follow the rotation paths of individual orientations, hence given more insight into how slip enforces crystallographic rotation (see e.g. Han et al. 2004).

Even though it is commonly agreed that the mechanical anisotropy, and by that the forming behaviour, to a large extent is controlled the crystallographic texture (Althoff 1971), the understanding of mechanical anisotropy is still an important topic within material science. The distribution of solute elements and precipitates (Barlat and Liu 1998) and the microstructure (Winther et al. 1997) has also been known to alter the anisotropy. The section below will present earlier work on how age-hardening affect the mechanical anisotropy.

2.7.4 Age-hardening

Age-hardening (particle strengthening) has been studied in great detail after the phenomena was first discovered by Wilm in the beginning of last century (1911). At that time, it was impossible to understand the underlying physical processes. However, the introduction of dislocations (Orowan 1934, Polanyi 1934, Taylor 1934) together with new and more advanced experimental techniques (high-resolution transmission electron microscopy (TEM)) has made it possible to study and explain the observed particle strengthening mechanisms. It has been shown that the particles act as obstacles to the dislocations movement (slip) and thus reduce their mobility. These obstacles can be overcome in two basically different ways, either by shearing or by bypassing (Nembach 1997). The latter mechanism has been suggested by Orowan (1948) and was subsequently named after him (the Orowan mechanism).

In the work of Bate et al. (1981), they studied changes in plastic anisotropy accompanying precipitation from a supersaturated solid solution of an Al-4%Cu. These

Theoretical background

It is worth noticing that the majority of these investigations have been focusing on explaining the texture evolution that take place during plastic deformation, while only a modest fraction of these works have been devoted to how the forming behaviour is affected by thickness variations. The PhD work of Xiao-Hu Zeng (1995), titled “Anisotropy of Plastic and Elastic Deformation of Al-Li Alloys”, is one of few works totally devoted to the correlation of the plastic properties and the texture gradients. Zeng studied the crystallographic texture changes through the thickness of some rolled sheets. He found from texture-based calculations, that the texture gradient had a strong effect on the shape of the yield loci and the forming limit diagram (FLD) (Zeng et al. 1994, Zeng and Barlat 1994).

2.7.3 Deformation mechanisms

The work of Xiao-Hu Zeng among others was based on the assumption that the yield loci shape was determined by the deformation mechanisms operating locally. Hence, different deformation mechanisms were dominating at different positions through the thickness. For the last decades, the selection of different deformation mechanisms has been a very important topic of research. Computer modelling has tried to implement these mechanisms by developing more advanced crystal plasticity models. The new GIA and ALAMEL models are examples of such more sophisticated models (Van Houtte et al. 2005).

Slip traces have been used for decades in order to study the plastic deformation of crystals. For example, in the middle of the last century the different stages (stage 1-3) of hardening were extensively investigated by use of slip traces (see e.g. Diehl 1955 and Cahn 1950). Detailed investigations of slip traces and how these develop during deformation have also been used to reveal information about the slip planes activated and how the deformation structure develops during deformation (Honeycombe 1984, Sørensen 1997).

This information has been combined with information about the crystallographic orientations and used to predict the number of slip systems activated for individual crystallographic orientations (see e.g. Delaire et al. 2000, Nibur and Bahr 2003, Choi et al. 2004). Delaire et al. (2000), Zhang and Tong (2004) and Henning and Vehoff (2005)

2.7.2 Mechanical anisotropy and forming behaviour

Mathematical models utilising crystal plasticity theory and phenomenological models of elastoplasticity have also be used to predict the effect of mechanical anisotropy on formability (see e.g. Lademo et al. 1999, Lademo et al. 2002, Lademo et al. 2005 and Fjeldbo et al. 2005). Forming limit diagrams (FLD) has been computed and compared to experimental results, showing that this technique is able to predict the forming limit of various materials.

Forming of extruded aluminium profiles is important for several industrial applications. Extruded profiles are often found to possess mechanical anisotropy, which has to be fully understood in order to make use of the competitive advantage of utilising these profiles formed to complex shapes. For this reason, it has also been performed several detailed experimental studies of anisotropy in extruded profiles at the Norwegian University of Science and Technology (see e.g. Søreng 1997, Iveland 2000 and Ryen 2003).

Further, it is known that aluminium processed by either extrusion or rolling often possesses through-thickness variations (see e.g. Engler et al. 2000 and Turner et al. 2002). This is especially true for commercial Al-Li based alloys that normally develop strong through-thickness texture gradients (Peters et al. 1986, Bowen 1988, Engler and Lücke 1991). The heterogeneous processing conditions taking place during rolling is assumed to give rise to the gradients observed in rolled sheets. During rolling, the deformation of sheet ingots changes from shear influenced at the surface to plane compression along the centreline. Also the amount of deformation varies quite significantly through the sheet thickness. It is expected that the variation in deformation, coupled with the recrystallization that sometimes occurs during heat-treatment, produce an evident gradient in crystallographic texture through the sheet thickness. The processing taking place during extrusion is normally much more heterogeneous than the processing conditions observed during rolling (Valberg and Malvik 1994). Hence, it is therefore concluded that also extruded products can develop strong through-thickness variations (Przystupa et al. 1994), especially for profiles subjected to large reduction during extrusion (see e.g. Aukrust et al. 1996, Aukrust et al. 1997, Søreng 1997, Pettersen 1999, Fjeldly 1999 and Iveland 2000).

Theoretical background

2.7.1 Crystal plasticity

Crystal plasticity has been one of the main topics for this work, as it also has for a impressive number of other studies throughout the last century. As already mentioned in Chapter 2.2, crystal plasticity is the bases for the improved knowledge concerning mechanical properties such as anisotropy and forming behaviour.

A better understanding of the deformation mechanisms taking place during deformation stimulated the research of understanding mechanical anisotropy. Experiments performed on single crystals made it possible to study directional dependency in great detail. The early works of e.g. Ewing and Rosenhain (1900) and Schmid and Boas (1935) provided a thorough understanding of the mechanical anisotropy of single crystals. This understanding of anisotropy was based on crystal symmetry. The classical polycrystalline plasticity models are based on this knowledge coupled with the information from the crystallographic texture (Sachs 1928, Taylor 1938, Bishop and Hill 1951). A more detailed description of these models was given in Chapter 2.2.

At the end of last century, crystal plasticity models were combined with finite element (FE) simulations in order to predict material properties after deformation, e.g. texture evolution during forming. Aukrust et al. (1994) simulated the texture development during extrusion of a profile comparable to the profiles investigated in this work by use of the Taylor model integrated into a FE-model. By using this technique, Aukrust et al. (1994) were able to predict the texture variations often observed through the thickness of an extruded profile. These investigations were part of a significant research project initiated by Hydro Aluminium in order to obtain a better understanding of crystal plasticity and how it could be used to understand the mechanical properties after processing (see e.g. Bauger 1994, Aukrust and Vatne 1994, Irgens et al. 1995 and Aukrust et al. 1997).

The knowledge acquired by coupling crystal plasticity and FE-simulations made it possible to better understand the deformation mechanisms operating during deformation. Hence, this knowledge were of great industrial importance and resulted into several great works within the topic “through-process–modelling” (see e.g. Marthinsen et al. 2002, Furu et al. 2004 and Neumann et al. 2005).

Theoretical background

and is always square, while the second is in a subpixel position in the deformed micrograph and is a quadrilateral.

When the displacement fields are determined by the correlation technique, these can be used to calculate the local planar strain distribution in the material.

The theoretical background for the DSCA technique presented in this section is based on the work performed by Vacher et al. (1997), thus a more comprehensive review of the DSCA technique may be found in this work.

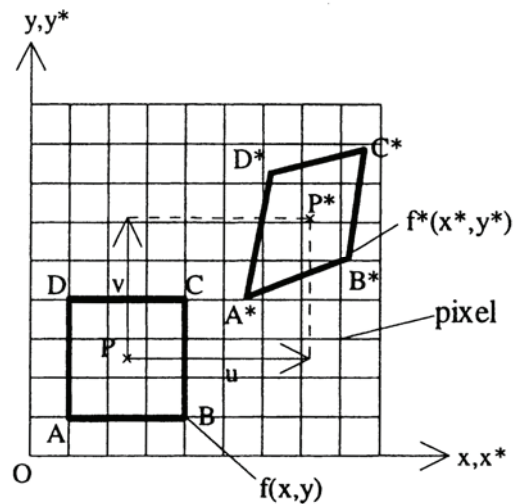


Figure 2.24 – Displacement field $u(x, y)$ and $v(x, y)$ between an initial and a deformed micrograph (Vacher et al. 1997).

2.7 Earlier work – State-of-the-art

So far, Chapter 2 has only given the general theoretical background for the characterisation and plasticity discussed and the experimental techniques applied. The remaining of this chapter will be used to review the state-of-the-art among earlier works within the topics treated in this thesis. The chapter will also include a review of available in-situ techniques as well as an evaluation of their strength and weaknesses.

Theoretical background

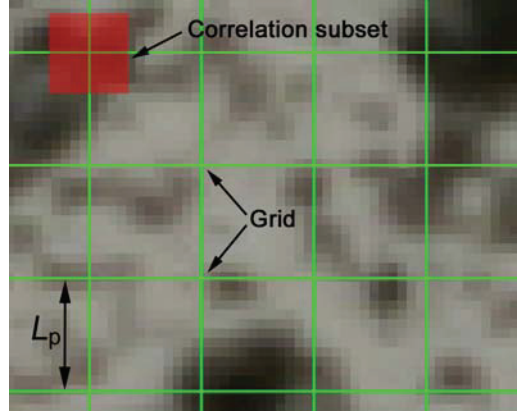


Figure 2.23 – Illustration of the correlation subset and the grid elements on a digital image.

The initial grey level of the micrograph/frame is represented by the discrete function $f(x, y)$ which on the deformed micrograph/frame $f^*(x^*, y^*)$, becomes (Vacher et al. 1997):

$$f^*(x^*, y^*) = f^*[x + u(x, y), y + v(x, y)] \quad (22)$$

with $u(x, y)$ and $v(x, y)$ being the displacement fields for one given grid element as shown in Figure 2.24. These displacement fields are obtained for every grid element by using the correlation method between an initial image grid element and its successor in the deformed micrograph. The calculations are based on the comparison between a subset of the initial image and its counterpart in the deformed image by computing the correlation coefficient (Vacher et al. 1997):

$$\text{Cor} = 1 - \frac{\int_{\Delta S} f(x, y) f^*(x^*, y^*) dx dy}{\sqrt{\int_{\Delta S} f(x, y)^2 dx dy \int_{\Delta S} f^*(x^*, y^*)^2 dx dy}} \quad (23)$$

where ΔS is the area of the concerned correlation pattern on the initial image. For a perfect correlation, $f(x, y) = f^*(x^*, y^*) \Rightarrow \text{Cor} = 0$ and for an imperfect correlation, $0 > \text{Cor} > 1$. The correlation coefficient is used as an indicator of the similarity degree between the two subsets. The first subset is centred on a pixel of the initial micrograph

Theoretical background

and micro-meter scales (Doumalin et al. 1999, Knauss et al. 2003). In the following section, the theory behind DSCA will be presented in some more detail.

2.6.1 Digital Speckle Correlation Analysis

This strain measurement technique was initially developed by Mguil-Touchal et al. (1997). The principle of the method consists in comparing two digital images of a same object surface with a random surface appearance. The first micrograph is acquired prior to deformation while the second is acquired after deformation (tensile test, shearing test, etc.). When the original specimen surface does not have a random appearance, this must be obtained artificially. For ordinary simple tension specimens where the meso/macro properties are investigated, this can be obtained by some simple black and white spray paints. However, when the strains at the grain level should be investigated, more advanced techniques must be applied. A gold grid deposit on the sample surface is an example of such a technique, and section 4.1.2 describes the production of a gold grid with a grid size of $10\mu\text{m}$ in more detail.

The technique compares the acquired images using a grey level correlation coefficient. In other words, points from the initial image will be found on the final image with a precision lower than a camera pixel.

The image in which the strain is to be analysed is divided into a certain number of grid elements with sides L_p (Figure 2.23), user defined by a given number of pixels. Around each of the four points of a grid element, a square analysis zone or subset is defined by another given number of pixels.

Theoretical background

The two different definitions of the strains give close to identical results up to a strain of ~ 0.1 but after this point the average linear strain (e) gives much higher results than the true strain.

The change in length during simple tension deformation is normally obtained by using a high accuracy strain-gauge extensometer. However, there are several disadvantages of using extensometers to measure the displacement during deformation. First of all, strain-gauge extensometers provide only a one-dimensional measure of the strain, i.e. two extensometers have to be applied in order to simultaneously measure both the longitudinal and transversal strains. Note that calculations of the plastic strain ratio are based on both strains as shown in section 2.4.1. More important, strain-gauge extensometers only represent the average behaviour of the material in the measurement area, i.e. between the legs of the extensometer. Therefore, the extensometer measure is only valid when the material behaviour is homogeneous within the measurement area. This is especially a problem in materials with very heterogeneous deformation behaviour (Al-Mg-Si and Al-Zn-Mg alloys due to the Portevin-Le Châtelier effect, etc.). Local strain investigations (meso and micro scale) are also very difficult using strain-gauge extensometers.

Over the last two decades new non-contact measurements techniques have appeared. Mostly based on optics, their principles rely on either beam light/sample interaction, i.e. interpretation of interference fringes (see e.g. Tu et al. 1997 and Steinchen et al. 1998) or on correlation techniques, i.e. tracking the motion of geometric grids (see e.g. Chu et al. 1985 and Mguil-Touchal et al. 1997). The two techniques can also be combined as shown by He et al. 2002, Laraba-Abbes et al. 2003 and Zhang et al. 2003.

The accuracy of the former technique is in the order of a few wave-lengths (typically 0.2-0.3 μm). However, they are limited to small displacement gradients i.e. small strains. The latter technique, on the other hand, is less accurate but does not have any limitations with respect to strain. Among those techniques, digital speckle correlation analysis (DSCA) has become widely used. It only requires the surface of the specimen to have a random speckle and pictures of that surface at different instants during deformation. Applications are common at both the macro (Wattrisse et al. 2001, Dumoulin et al. 2003)

Theoretical background

material is almost exhausted. At this stage the material becomes unstable with respect to shear, and shear banding becomes an alternative macroscopic slip mode which accommodates strain accumulation during stage IV hardening. The microstructure inside the bands consists of cells/subgrains that are elongated in the band direction, which appears to be sharply misoriented (10-40°) with respect to the surroundings (Hatherly 1978). The material within the heterogeneity is softer than the surrounding matrix, the bands are non-crystallographic and macroscopic, and are often found with an orientation relationship of 35-38° to the deforming plane (Roven and Nes 1984). Shear bands can extend over distances of several grains or even through the whole specimen. Shear banding in aluminium alloys is often associated with the addition of magnesium, and the shear bands are frequently observed as failure mechanism in quenched Al-Zn-Mg alloys (Chung et al. 1977, King et al. 1982, Søreng 1997, Fjeldly et al. 2001). For a more comprehensive description of shear banding in aluminium alloys see e.g. Humphreys and Hatherly (1996).

2.6 Strain measurements

The strain introduced to a material during deformation (typically simple tension deformation) is often easily characterised by the average linear strain (e), which is defined as the ratio of change in length (ΔL) to the original length (L_0).

$$e = \frac{\Delta L}{L_0} = \frac{L - L_0}{L_0} \quad (20)$$

This definition of strain is satisfactory for elastic strains where ΔL is very small. However, in plastic deformation the strains are frequently large, and the gauge length changes considerably. Ludwik (1909) first proposed the definition of true or natural strain (ε) which obviates this difficulty. In this definition of strain the change in length is referred to as the instantaneous gauge length, rather than the original gauge length (Dieter 1988).

$$\varepsilon = \int_{L_0}^L \frac{dL}{L} = \ln \frac{L}{L_0} = \ln(e+1) \quad (21)$$

Theoretical background

$$\alpha_{theo(i)} = \arccos(S_{z(i)}) \quad \text{and} \quad \beta_{theo(j)} = \arctan\left(\frac{-m_{x(j)}}{m_{y(j)}}\right) \quad (19)$$

where the suffixes i and j represent the inspected slip direction and slip plane respectively.

2.5.2 Transition and kink bands

Microstructural heterogeneities like transition and kink bands may appear at higher strains. Transition bands are defined as bands separating different parts of a grain which has split and rotated away from each other during deformation (Hu 1962). These bands develop when neighbouring volumes of a grain deform on different slip systems and rotate toward different crystallographic orientations. In many cases deformation bands occur with approximately parallel sides and involve a double orientation change A to C and the C to A (i.e. Humphreys and Hatherly 1996). A deformation band of this special type will be called a kink band following the nomenclature of Orowan (1942). Figure 2.22 presents an illustration of both transition and kink bands within a grain.

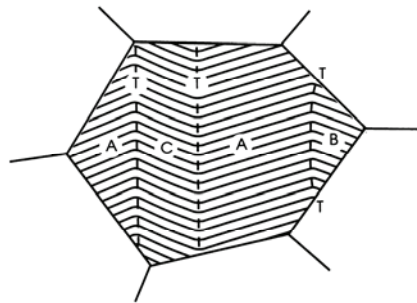


Figure 2.22 – Schematic illustration of transition bands (A-B) and kink bands (A-C-A) (Humphreys and Hatherly 1996).

2.5.3 Shear banding

At high strains (cold rolled material) a new mode of deformation occurs and a new microstructural heterogeneity appears. Shear bands were described in detail by Adcock (1922) but were largely forgotten until the work of Brown (1972). Shear bands are bands of highly strained material formed as a result of strain instability occurring after large deformations. This phenomenon occurs when the dislocation storage capacity of the

Theoretical background

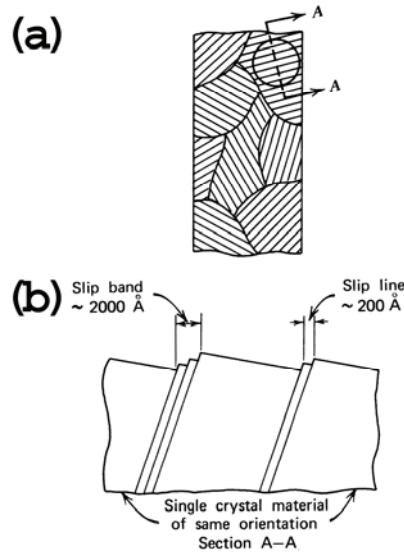


Figure 2.21 – (a) Illustration of grain structure revealed by slip traces. (b) Slip plane intersection with specimen surface due to crystallographic slip (Verhoeven 1975).

The observed slip plane traces are often characterised by the in-plane angle β_{obs} (the angle between the observed slip traces and the DD). The slip direction (\mathbf{s}) and slip plane normal vector (\mathbf{m}) of the 12 potential slip systems for all individual grains are expressed in the specimen axis system as:

$$\mathbf{s} = \mathbf{G}^{-1}\mathbf{s}_0, \quad \mathbf{m} = \mathbf{G}^{-1}\mathbf{m}_0, \quad \mathbf{G} = \mathbf{g}\mathbf{g}' \quad (18)$$

where \mathbf{s}_0 and \mathbf{m}_0 are the slip direction and slip plane normal vectors in the crystallographic frame respectively, \mathbf{g} is the orientation matrix of a grain defining the position of the crystallographic axes with respect to the specimen axis system (Schwartz et al. 2000), and \mathbf{g}' is the rotation from the specimen to the crystallographic system.

Further, the \mathbf{s} and \mathbf{m} vectors from the EBSD results are used to calculate the theoretical angle β_{theo} for the four $\{111\}$ -planes. Another parameter calculated from the same results, is the theoretical out-of-plane angle α_{theo} between the slip direction and the specimen surface normal. This parameter is important because slip planes with a low α_{theo} will not produce visible slip traces since the out-of-plane movement can not be detected. The parameters α_{theo} and β_{theo} were computed according to

Theoretical background

accuracy of these calculations is dependent on the accuracy of the plasticity model applied.

2.5 Microstructural evolution

The microstructure of a material exposed to plastic deformation will clearly be altered. The generation and migration of dislocations, and the subsequent interaction, storage and recovery of the dislocations are fundamental to evolution of the deformation structure (see e.g. Dieter 1988 and Humphreys and Hatherly 1996). Clear changes in microstructure are evident first at high strains, but some small changes are detectable already at initial plastic deformation much less than 1% plastic strain.

2.5.1 Slip traces

The polished surface of a metal crystal deformed plastically will become covered with one or more sets of parallel fine lines called slip traces, bands or lines. The early work of Ewing and Rosenhain (1900) showed that there were steps in the surface resulting from microscopic shear movements along well-defined crystallographic planes, i.e. surface relief due to slip caused by the plastic deformation on the individual slip planes. Figure 2.21 presents an illustration of the grain structure covered with slip traces. The figure also shows that the deformation of each grain is accomplished by small blocks of the crystal sliding past each other along parallel sets of planes. The slip does not occur on just one plane but are localised to small regions of parallel planes.

Theoretical background

plastic strain ratio is normally given as the r -value or Lankford coefficient. For a tensile test this parameter is defined as

$$r = \frac{\varepsilon_w}{\varepsilon_t} \quad (17)$$

where ε_w is the width or transversal strain and ε_t is the thickness strain. Hence the r -value gives a relation between the contractions in the transverse and normal direction. In the case of $r=1$, the contractions are equal in the two directions and the formability is good. However, if the r -value is small, the thickness contraction is large and the material has a high susceptibility for failure. This happens because the material rapidly goes into a state of plane strain and instability occurs (Marciniak and Duncan 1992).

A classical example of anisotropy and formability is the deep-drawing operation of a cup from a textured sheet. Firstly, as the strength varies with direction, a variation in the resistance towards flow will result in an orientation dependence of the elongation. This appears as “ears” on the top of the cup, since a weak direction will have a low flow resistance with an ear as the result. Secondly, a variation in r -value around the cup circle will give different thinning of the cup wall. Normally, these are undesired effects, as they limit the formability, give varying properties and increase the amount of scrap. However, the mechanical anisotropy can also give beneficial results if taken into account during design and production, e.g. by placing the strong directions at critical positions in the final product.

2.4.2 Texture-based calculations

The mechanical properties and their directional dependency can be approximated based on the crystallographic texture acquired from the EBSD measurements. The Schmid value of all tensile directions can be calculated directly from the crystal orientation of the individual grain and the deformation direction (DD). Further, the Taylor factor in the different directions can be calculated from the different polycrystalline plasticity models like the Taylor and Self-Consistent models. These models can also be used to calculate the theoretical r -values of the material. However, it is important to remember that the

Theoretical background

2.4 Anisotropy and formability

The formability of a material defines its ability to withstand plastic deformation without failure. The ability to be formed into various geometrical shapes is one of the most important properties of metals and alloys. However, the formability will be strongly dependent on the orientation of the sheet or profile in the forming process. Hence, a good understanding of the directionality of properties may be used to improve and optimise forming operations.

An isotropic material has equal mechanical properties in all directions. Most metals used for practical applications exhibit a directional dependency of the mechanical properties. The tensile properties (yield strength, ductility, r -value etc.) is often observed to vary with the principal direction of deformation, hence relative to the rolling or extrusion direction. This phenomenon is referred to as mechanical anisotropy, and is treated in more detail in the following.

2.4.1 Mechanical anisotropy

Several factors are responsible for the mechanical anisotropy observed in metals and alloys. The most important factor is probably the texture or crystallographic anisotropy. However, also grain shape, precipitates and dislocation structures may influence the mechanical properties (see e.g. Bate et al. 1981, Chung et al. 2000 and Ekstrom et al. 2002).

While a single crystal is highly anisotropic, an aggregate of completely differently orientated grains might be almost isotropic. This relates to the variation in strength of different orientations, which for a tensile test is given by the Schmid value (m) for each individual grain. In a polycrystalline material with crystallographic texture a large number of the individual grains have approximately the same orientation, causing anisotropy.

Mechanical properties like yield strength, ultimate tensile strength, uniform strain and plastic strain ratio are of special interest for manufacturers and other material consumers. The strength parameters are closely connected to the Taylor and Schmid factors. The

Theoretical background

Table 2.3 – Ideal deformation and recrystallization texture components observed in FCC metals.

Texture component	Miller indices	Euler angles		
	$\{hkl\}\langle uvh \rangle$	φ_1	Φ	φ_2
Deformation				
Copper, Cu	$\{112\}\langle 111 \rangle$	90°	35°	45°
S	$\{123\}\langle 634 \rangle$	59°	37°	63°
Brass, B	$\{011\}\langle 211 \rangle$	35°	45°	$0/90^\circ$
Goss, G	$\{110\}\langle 001 \rangle$	0°	45°	$0/90^\circ$
Recrystallization				
Cube, C	$\{100\}\langle 001 \rangle$	0°	0°	$0/90^\circ$
CG	$\{520\}\langle 001 \rangle$	0°	22.5°	$0/90^\circ$
Goss, G	$\{110\}\langle 001 \rangle$	0°	45°	$0/90^\circ$
ND-rotated Cube	$\{001\}\langle 110 \rangle$	45°	0°	$0/90^\circ$
P	$\{011\}\langle 122 \rangle$	65°	45°	0°
R	$\{124\}\langle 211 \rangle$	57°	29°	63°

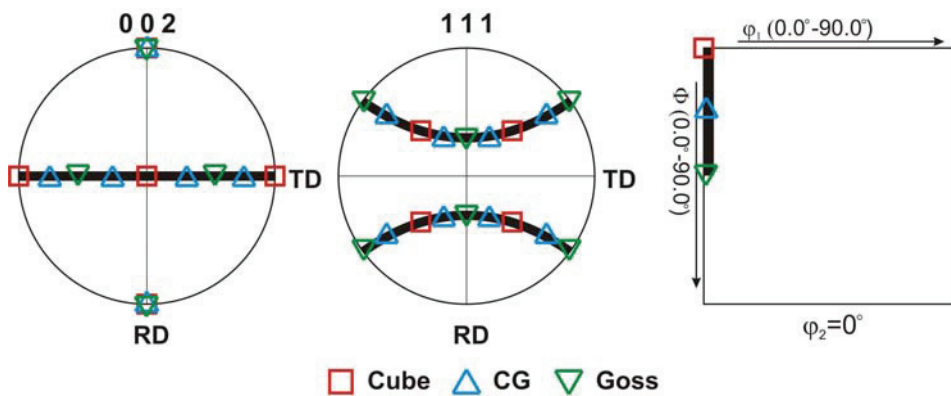


Figure 2.20 – Location of the ideal recrystallization texture components frequently observed in extruded aluminium profiles presented in the 002 and 111 pole figures as well as the $\varphi_2=0^\circ$ section of the ODF.

Theoretical background

component is often the most dominating of these components. This orientation has [100] directions aligned with the principle sample axes (extrusion direction (ED), transversal direction (TD) and normal direction (ND)). The recrystallization texture observed in extruded aluminium profiles is often best described as a continuous fibre extending from the Cube (C) orientation to the Goss (G) orientation. This texture is frequently referred to as the ED rotated Cube texture. Figure 2.20 presents a schematic representation of this fibre in the pole figure as well as the $\varphi_2=0$ section of the ODF. This figure also includes an additional texture component introduced to get a better description of the fibre. The CG component is the Cube orientation rotated 22.5° around the ED, i.e. the CG component is oriented halfway between the Cube and Goss orientations.

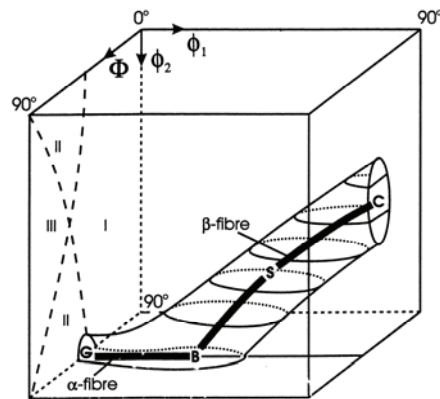


Figure 2.19 - Schematic representation of the FCC rolling texture in the first subspace of the three dimensional Euler angle space. The representation of ideal texture components: Copper (here C), S, Brass (B) and Goss (G) are also indicated (Hirsch and Lüke 1988).

Theoretical background

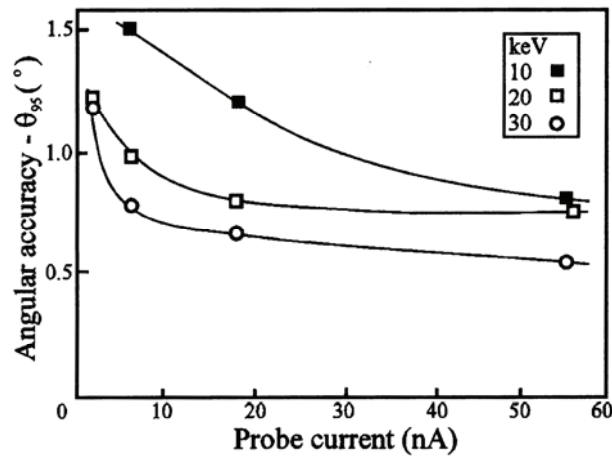


Figure 2.18 – The effect of probe current on the angular accuracy in the FE SEM for single grains in a large-grained aluminium sample (Humphreys and Brough 1999).

2.3.5 Texture components in FCC materials

Deformation texture in FCC metals and alloys are determined primarily by the deformation mode/modes and the stacking fault energy of the material. It is customary to refer to the deformation texture in materials with high stacking fault energy, like aluminium, as “pure metal textures” to distinguish them from the “alloy type textures” characteristic of materials with low stacking fault energy. The “pure metal textures” are often described by a set of four ideal texture components as shown in Table 2.3. However, the observed deformation texture is not satisfactorily described by these ideal components, but more accurately by representing the texture as a continuous tube or fibre of orientations which runs from the Brass through the S to the Copper orientation. By convention the axis of this tube is called the β -fibre and deformation textures are often only presented in the form of orientation densities along this fibre (e.g. Hirsch and Lüke 1988). A second fibre, the α -fibre, is also often used to describe the texture. This fibre extends from the Goss orientation to the Brass orientation (Humphreys and Hatherly 1996). Figure 2.19 presents a schematic representation of the α - and β -fibre.

The observed textures after recrystallization are completely different from the deformation textures. However, the recrystallization texture is strongly dependent upon the deformation texture prior to annealing. Also the recrystallization texture can be described by a set of several ideal texture components as shown in Table 2.3. The Cube

Theoretical background

20kV found the spatial resolution in Al to be approximately 30nm (Humphreys et al. 1999).

The acquired EBSP is achieved from a volume very close to the sample surface since these electrons have lost very little energy. Hence, the size of the interaction volume depends upon the tilt angle (typical 70°), sample material and the energy of the primary electrons. Few experimental studies have been conducted to measure the depth resolution of EBSD, but it is thought to be quite small and of the order of 10-100 nm (Goldstein et al. 2003).

The absolute angular resolution of a crystallite is typically obtained with an accuracy of $\sim 2^\circ$, depending on the sample alignment and EBSD operating conditions (e.g. Humphreys 1999). However, the accuracy in determining the relative orientation between adjacent data points is of greater importance when studying orientation gradients and low angle grain boundaries. This accuracy is related to the precision in which the orientations of data points within the same crystallite can be determined. It would be expected that all the orientations are identical if diffraction patterns are obtained from a single grain within a large-grained polycrystal. However, if the crystallographic orientation is calculated based on several EBSP acquired from a single crystal or the interior of a large grain, small orientation deviations will be observed. This “orientation noise” is mainly a result of the accuracy in the pattern-solving algorithm and are beyond the direct control of the microscopist. However, it has been shown that the angular resolution is affected by the microscope operating-conditions (see e.g. Krieger Lassen 1996 and Humphreys and Brough 1999), and this effect has been measured for a FE SEM as shown in Figure 2.18. The angular resolution obtained with a FE SEM and satisfying operating conditions on aluminium are found to be in the range of $0.6-1.0^\circ$ (Humphreys 2001).

Theoretical background

The high tilt angle increases the backscatter yield as shown in Figure 2.17 where the energy distribution from samples perpendicular and tilted 70° with respect to the electron beam are compared. This is advantageous because the increased signal improves the ability to collect EBSP. It is also important to notice that most of the backscattered electrons in the tilted sample have close to initial electron beam energy. The crystallographic information in the EBSPs is produced by the electrons that have lost very little (the high energy peak) while the remainder of the distribution contribute to the overall background intensity (noise) of the EBSP (Goldstein et al. 2003).

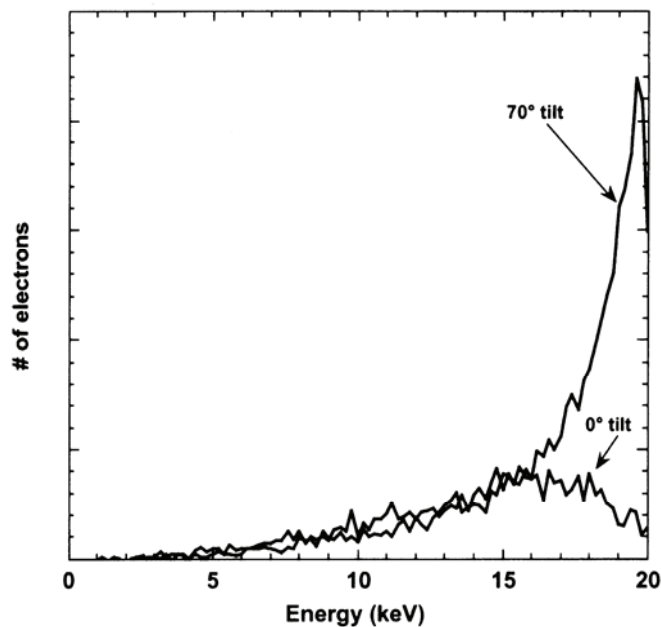


Figure 2.17 – Comparison of energy distribution from a sample perpendicular to and tilted 70° with respect to the electron beam at 20kV acceleration voltage (Goldstein et al. 2003).

Monte Carlo electron trajectory simulations have shown that the resolution of EBSD is related directly to the electron probe size. Hence, it is apparent that higher spatial resolution can be obtained from SEM instruments with field emission (FE) electron guns due to the smaller beam size, provided sufficient beam current is available. The spatial resolution is also a function of the acceleration voltage and the atomic number of the sample (Humphreys et al. 1999). Higher acceleration voltage and lower atomic number will degrade the spatial resolution. One study using an FE electron source operated at

Theoretical background

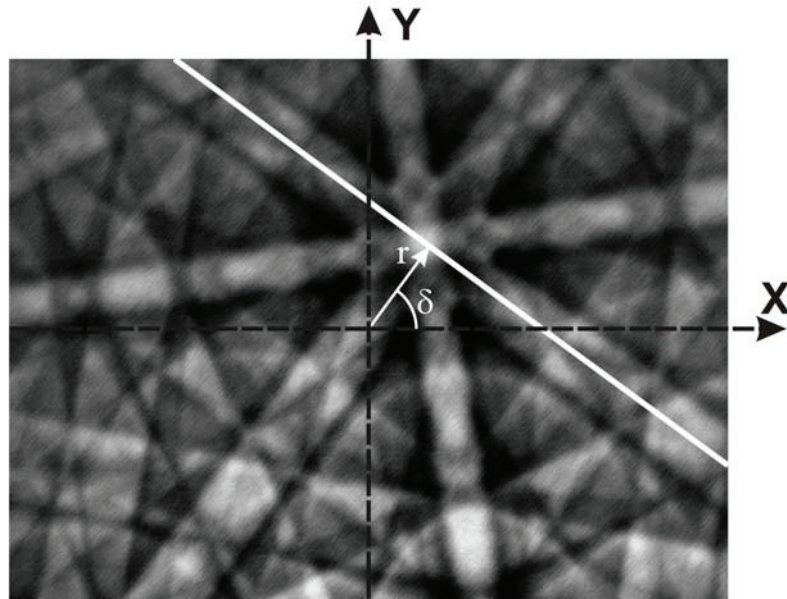


Figure 2.16 – A typical EBSP from a material with FCC structure. Each of the Kikuchi lines can be represented by the two parameters r and δ , where r is the shortest distance from the line to the origin of the x-y coordinate system and δ is the rotation of its normal vector.

The EBSP gives the crystallographic orientation of a position (pixel) on the specimen surface given by the position of the stationary electron beam. When the orientation of the given position is determined, the beam moves to a new position where a new EBSP is generated. The process is repeated several times until the entire area of interest is analysed. The distance on the specimen surface between succeeding positions are commonly referred to as the step size. The image acquisition and calculation of the crystallographic orientations are fully automated and combining state-of-the-art hardware with high tech EBSD software makes it possible to index up to 43 frames/sec (Nordif 2005).

The spatial resolution of EBSD measurements are strongly influenced by the tilt angle, working distance and acceleration voltage. Large sample tilt results in an asymmetric spatial resolution. The optimal resolution is obtained parallel to tilt axis. For a tilt angle of 70° , the resolution perpendicular to the tilt axis is roughly three times the resolution parallel to the tilt axis.

Theoretical background

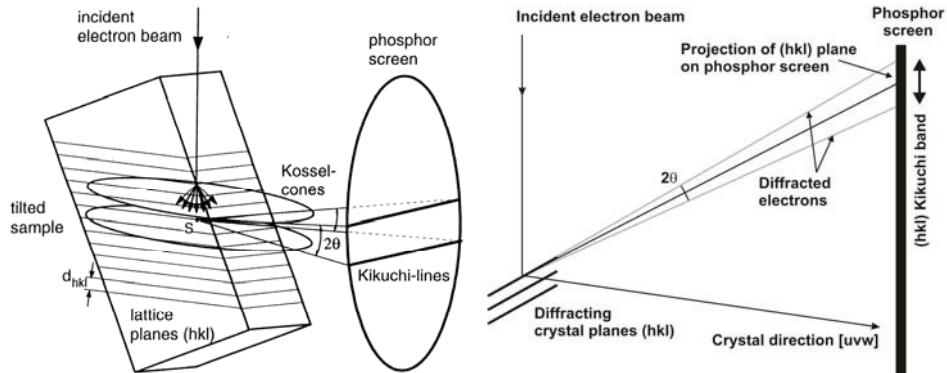


Figure 2.15 – Schematic illustration of the formation of one set of Kikuchi lines from diffraction of the electron beam with one family of lattice planes. Left 3D-view (Randle and Engler 2000) and right 2D-view.

The phosphor screen converts the electrons to light, which makes it possible to acquire the EBSP by a low-light-level CCD camera (Hjelen et al. 1993). The locations of the Kikuchi lines are identified by performing a Hough transformation of the digital images (Krieger Lassen et al. 1992). The Hough transformation

$$r = x \cdot \cos \delta + y \cdot \sin \delta \quad (16)$$

makes it possible to describe the Kikuchi lines by their distance r from the origin and the rotation δ of its normal vector as illustrated in Figure 2.16. The position of the pixel transformed from the EBSP is given by the x and y values. The Kikuchi lines are transformed to spots in the (δ, r) space (Hough transformation space) and the positions of the peaks can be determined by standard peak findings techniques. The positions of the spots correspond to the diffracting planes in the sample, and the crystal orientation can be identified when a sufficient number of planes are determined (Krieger Lassen et al. 1992).

Theoretical background

Cizek et al. 1996, Tong et al. 1997, Tatschl and Kolednik 2003, Poulsen et al. 2003 and Han et al. 2003). For the last couple of years there has been major progress in this type of work at NTNU.

The EBSD technique can also be used for identification of micrometer or submicrometer crystalline phases through determination of the characteristic crystallographic parameters such as crystal plane spacing, angles between planes, and crystal symmetry elements (Schwartz et al. 2000). This is especially important for characterisation of geological materials (see e.g. Moen et al. 2004 and Leinum et al. 2004).

2.3.4 EBSD measurements

EBSD patterns are obtained in the SEM by illuminating a highly tilted specimen with a stationary electron beam. The electrons will be subjected to scattering in all directions when the electron beam enters a crystalline sample. Some of the electrons will have an angle of incidence with the different atomic planes that fulfils the Bragg law:

$$\lambda = 2d_{hkl} \cdot \sin \theta_B \quad (15)$$

where θ_B is the Bragg angle, λ is the electron wavelength and d_{hkl} is the interplanar spacing for the crystal plane with the Miller indices (hkl). The electrons that fulfil the Bragg law will be elastically scattered and will result in two cones as illustrated in Figure 2.15. The two diffraction cones are positioned symmetrically around the diffracting crystal plane and separated by twice the Bragg angle ($2\theta_B$). The two cones will be recorded on a two-dimensional phosphor screen as hyperbolas. However, since diffraction of the electrons through the Bragg angle is occurring in all directions, the locus of the diffracted radiation is the surface of a cone which extends about the normal of the reflecting atomic planes with half apex angle $90 - \theta_B$. Hence, the hyperbolas appear as two almost straight parallel lines on the phosphor screen. These lines are the backscattered Kikuchi lines, and each pair of these lines corresponds to the diffraction from a particular crystal plane which produces an electron backscattered pattern (EBSP) as shown in Figure 2.16. The Kikuchi lines are used to determine the crystallographic orientation of the material volume generating the EBSP. The formation of the EBSP is described in great detail by e.g. Reimer (1998) and Wells (1999).

Theoretical background

the main focus at NTNU. This work was initiated by Hjelen (1990) and has since then been continued by several PhD works at NTNU. Skjervold (1993) used the technique to investigate the orientation gradient evolution in grains during deformation. This was the first attempt to investigate the microstructure evolution during deformation. In more recent times investigations of deformation behaviour and microstructure evolution of large strains have become possible. The deformation and softening behaviour of heavily cold rolled AA3xxx series alloys have been investigated by Sjølstad (2003) and Tangen (2004). They used the technique to study both the deformation structure and the recrystallized microstructure after annealing. The average grain size and the grain size distribution were also determined by use of EBSD techniques (Tangen et al. 2002). Material processed by severe plastic deformation (SPD) develops very small grain sizes ($\sim 4\mu\text{m}$) (Iwahashi et al. 1997), and are therefore very difficult to characterise by EBSD. Also this problem has been overcome by using field emission scanning electron microscopes with improved spatial resolution (Tangen et al. 2003). Aluminium alloys deformed by Equal channel angular pressing (ECAP) has been characterised by Werenskiold (2004), and the EBSD technique made it possible to perform a detailed study of the deformation mechanisms operating in the ECAP process. At NTNU there has also been considerable interest given to characterisation of the microstructure and through-thickness variations of extruded aluminium profiles, and EBSD has also been used for this purpose (see e.g. Ryen 2003, Fjeldbo et al. 2005 and Hallem 2005). The state-of-the-art EBSD work performed at NTNU has led to a continuous improvement of this powerful technique.

In-situ EBSD applications have been a new field of great interest for the last few years. Also here, the SEM laboratory at NTNU has been a pioneer with regard to development and application of new experimental techniques. The work by Kobberrød et al. (1998) was the initiation of in-situ EBSD investigations in SEM. Kobberrød et al. performed heating experiments where they studied the grain boundary migration in aluminium. Subsequent heating experiments combined with EBSD investigations have been performed to study the recrystallization behaviour of aluminium alloys (see e.g. Tangen et al. 2001, Karlsen et al. 2004 and Korsnes et al. 2004). In the last decade, some in-situ deformation investigations have been performed in order to study the rotation and deformation behaviour of the individual grains within a polycrystalline material (see e.g.

Theoretical background

volume element of the sample. If the totality of all volume elements in the sample which possess the orientation $d\mathbf{g}$ is denoted dV , and the total sample volume is denoted V , then an orientation distribution function can be defined by (Bunge 1983):

$$\frac{dV}{V} = f(\mathbf{g})d\mathbf{g} \quad (14)$$

This is the orientation distribution of the volume and $f(\mathbf{g})$ the orientation distribution function which is a description of the crystallographic texture of the material. A material without any crystallographic texture has $f(\mathbf{g})=1$. The crystallographic texture of a material is often presented by an orientation distribution function (ODF) plot but also different kinds of pole figures are widely used to represent the texture. The orientation distribution function of a material can, for example, be calculated from the EBSD measurements obtained in the SEM.

2.3.3 Electron backscatter diffraction (EBSD)

Electron backscatter diffraction (EBSD) has become a common technique used in the characterisation of polycrystalline materials. EBSD in the scanning electron microscope (SEM) is a technique that can provide a vast amount of information about crystalline materials. Orientation imaging mapping (OIM) performed on a grain-by-grain basis provides information about the crystallographic orientation of the individual grains in a material (microtexture) and the relation of these orientations to significant microstructural features (Randle and Engler 2000). Since the very beginning of this technique has the Norwegian University of Science and Technology been a pioneer within EBSD (Hjelen 1990). In fact, the 3rd commercial EBSD system available was in 1985 installed at SINTEF/Norwegian Institute of Technology (NTH) by David Dingley (1984), another pioneer within EBSD. (NTH is now known as the Norwegian University of Science and Technology, NTNU.) In the very beginning EBSD measurements were used to manually determine the crystallographic orientation of individual grains. Hjelen et al. (1991) used this technique to study the origin of recrystallization textures in aluminium. The technique has since then been used as a powerful tool within both the metallurgical and geological communities. The crystallographic aspects of plastic deformation together with the recrystallization behaviour of aluminium alloys have been

Theoretical background

to K_A (the red orientation in Figure 2.14) and then rotating the variable coordinate system until it reaches the orientation \mathbf{g} (the green orientation in Figure 2.14). First, the crystal is rotated about the ND-axis through the angle φ_1 . Then it is rotated about the new RD'-axis through the angle Φ . Finally the variable frame is again rotated about the new ND''-axis (001) through the angle φ_2 . The definition of the Euler angles is presented in Figure 2.14. This representation is often referred to as Bunge notation:

$$\mathbf{g} = \{\varphi_1, \Phi, \varphi_2\} \quad (13)$$

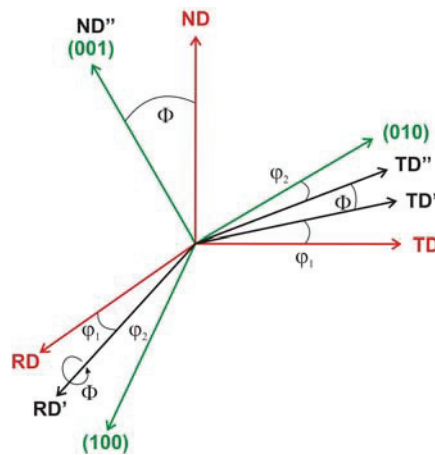


Figure 2.14 – Definition of the Euler angles by use of the Bunge notation (after Engler 2004).

2.3.2 Orientation distribution

In polycrystalline materials, crystallites of different shape, size and orientation are generally present. It can thus also occur that regions of different orientation are not separated from each other by clearly defined grain boundaries. On the contrary, continuous orientation changes are often observed through the microstructure. Variations within the specimen make it necessary to specify the orientation \mathbf{g} of each position through the specimen volume in order to completely describe the crystal orientation of a polycrystalline material. Such a representation of the crystal orientation is very complicated, and its mathematical treatment so advanced that it is not practically applicable. However, a good approximation is obtained by considering only the orientations and not the position coordinates of the individual crystallites within a

2.3.1 Orientation of individual crystallites

The texture of a polycrystalline material is often defined as the orientation distribution function (ODF) of all the crystallites. A sample coordinate system K_A is defined in order to describe the orientation of the individual crystallites. In the same way, each crystallite is given a crystal coordinate system K_B , and the rotation \mathbf{g} (crystallographic orientation) which is specified with respect to the sample-fixed coordinate system K_A .

$$K_B = \mathbf{g} \cdot K_A \quad (11)$$

The crystal coordinate system may conveniently be adapted to crystal symmetry, e.g. the cubic axes [100], [010], [001] of the unit cell. Also the sample coordinate system will usually be adapted to sample symmetry, e.g. RD (ED in extruded profiles), TD, ND in sheet metals as shown in Figure 2.12.

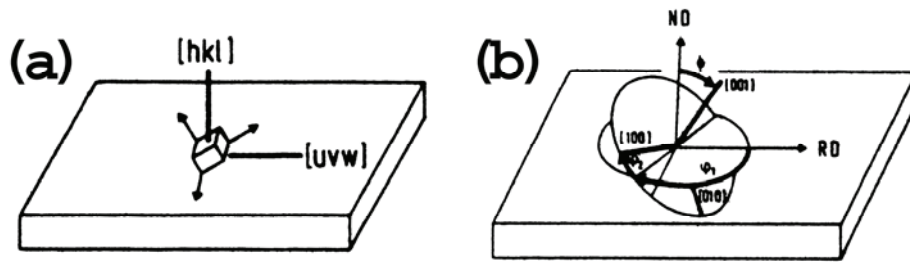


Figure 2.13 – Two representations of the orientation \mathbf{g} (a) Miller indices (hkl)[uvw] (b) Euler angles $\{\varphi_1, \Phi, \varphi_2\}$ (Bunge 1983)

The two most common ways to represent the orientation \mathbf{g} which describes the crystallographic orientation of the individual crystallites are Miller indices and Euler angles as shown in Figure 2.13. The Miller indices represent the orientation given by the plane (hkl) parallel to the rolling plane (extrusion plane in extruded profiles) and the direction [uvw] parallel to the rolling (extrusion) direction:

$$\mathbf{g} = (hkl)[uvw] \quad (12)$$

Euler angles are by far the most widely used representation of crystallographic orientations. Here the orientation is described by a set of three dependent Euler angles. The Euler angles are obtained by initially putting the crystal coordinate system parallel

Theoretical background

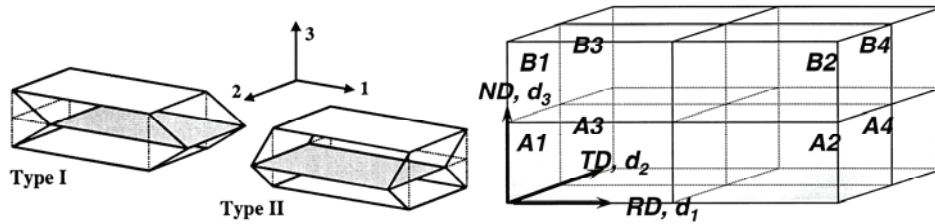


Figure 2.11 – Schematic illustration of the two most common types of grain clusters in the LAMEL model (left, Van Houtte et al. 2005) as well as the grain cluster arrangement used for the eight grains in the GIA model (right, Crumbach et al. 2004).

2.3 Texture

Most polycrystalline materials contain grains with crystallographic orientations that are not randomly distributed but instead are clustered to some degree around a particular orientation or set of orientations. Materials in which the grains are oriented non-randomly are said to have a preferred orientation or texture. The mechanical and thermal history of a specimen determines the nature of the texture that is developed. This section is concerned with the basic features of texture and texture measurements. Texture development in aluminium alloys and the effect of crystallographic texture are also treated to some extent.

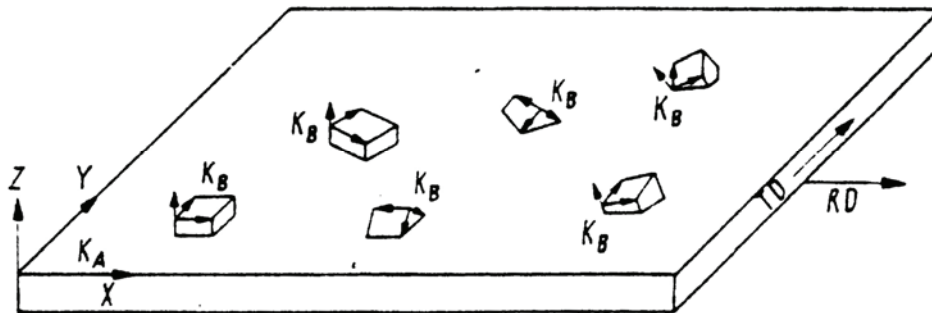


Figure 2.12 – The sample fixed coordinate system K_A and the crystal fixed coordinate system K_B in a sheet (Bunge 1983).

Theoretical background

each individual grain; it is only required that the average deformation of all grains belonging to a cluster is equal to the macroscopic deformation. The Taylor condition is then maintained at the boundary of the cluster. It is clear that this boundary is artificial, since in a real microstructure this boundary usually does not have a different character than the grain boundaries inside the cluster. It is also clear that the choice of N , the number of grains in the cluster, size and shape of the cluster are very important. It is possible to obtain a FC Taylor model ($N=1$), Sachs model ($N=\text{very large}$) and anything in between. The most widely known multi-grain models are the LAMEL model (Van Houtte et al. 2002) and its new “brother”, the advanced LAMEL (ALMAEL) model (Van Houtte et al. 2005) both with $N=2$, together with the Grain Inter-Action (GIA) model (Crumbach et al. 2001 and Engler et al. 2005) having $N=8$. Figure 2.11 presents an illustration of the two most common types of grain clusters in the LAMEL model as well as the grain cluster arrangement used in the GIA model. It is much more complicated to investigate the selection of activated slip systems for these more advanced models. The number of activated slip systems in the individual grains is dynamic and depends on the orientations’ composition within the cluster. It is therefore difficult to determine the number of activated slip systems for the individual grains (orientations) and it is reasonable to assume that the number of activated slip systems for one orientation can vary from one to five.

It should be noted that LAMEL and ALAMEL model simulations do not need significantly more calculation time than a standard FC Taylor calculation. The GIA model does need more time, but not so much as the CPFEM model (Van Houtte et al. 2005).

It has been shown that these new and more advanced polycrystalline plasticity models give far better predictions of deformation texture than the more standard models presented above (see e.g. Li and Van Houtte 2002 and Van Houtte et al. 2005).

Theoretical background

models try to obtain better average stresses and strains than the Taylor and the Sachs models. The self-consistent models may be regarded as generalised RC models, in which the relaxation is determined on the basis of a mathematical model for the interaction between a grain and its surroundings. The latter is then treated as a homogenous medium. Self-consistent models are much more complicated than the Taylor models (relaxed or not). A more comprehensive review of the self-consistent model may be found in e.g. Lebensohn and Tomé (1993).

2.2.7 Advanced polycrystalline plasticity models

Neither of the models presented above provide satisfying deformation texture predictions, especially not if quantitative methods are used for the comparison with experimental results. One reason could be that the local interaction between grains is insufficiently taken into account. Therefore, some new and more advanced plasticity models have been proposed. The Crystal Plasticity Finite Element Method (CPFEM) model (Kalidindi et al. 1992, Bate 1999, Mika and Dawson 1999) is a more recent plasticity model. The CPFEM model is based on finite element mesh placed over the microstructure (each element represents a single grain, or part of a single grain), and the crystallographic texture is represented by statistical distribution of orientations representing a few thousand grains. The orientations are chosen such that they offer a suitable representation of a macroscopic RVE, i.e. a volume element large enough to have the average properties of the polycrystalline material. This means that both lattice orientations, locations of grains with given orientations, grain shapes and sizes and orientation of grain boundaries are all chosen at random from a real microstructure in a representative way. Usually all this is done in a rather rudimentary way and much progress can still be made in this field, for example by incorporating topological data obtained by using orientation imaging microscopy. However, the CPFEM model requires two orders of magnitude more calculation time than other advanced polycrystalline plasticity models. Therefore, this model is practically impossible to use for industrial forming simulations (Van Houtte et al. 2005).

However, newer polycrystalline plasticity models which are much faster than the CPFEM models but still reach a comparable quantitative accuracy have been developed. In these so-called “multi-grain” models, the Taylor condition is no longer enforced on

Theoretical background

It has been argued that the Taylor FC model is too strict and the results could have been improved by somewhat “relaxing” the geometrical constraints. The idea of relaxation was conceived approximately 20 years ago (see e.g. Honneff and Mecking 1981, Kocks and Chandra 1982 and Van Houtte 1982) and was based on the observation that grains tend to become flattened and elongated during rolling. The misfit caused by a difference between for example l_{13} and L_{13} could perhaps be tolerated, and such a relaxation is the basis behind the relaxed constraint (RC) Taylor model. Relaxation of the longitudinal shear (l_{13}) is often referred to as the “lath” type Taylor RC model. Four slip systems would be active according to this model. The “pancake” type model also adopts this relaxation, but this model also relaxes the transverse shear (l_{23}), hence only three slip systems will be activated. Figure 2.10 presents a schematic illustration of the relaxation in the lath and pancake type Taylor RC model.

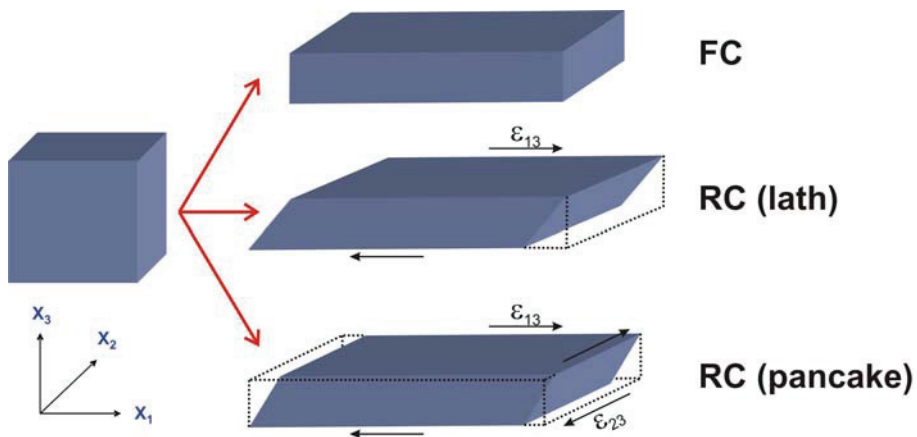


Figure 2.10 – Schematic illustration of the full constraint (FC) and the relaxation in the lath and pancake type relaxed constraint (RC) Taylor models.

2.2.6 The Self-Consistent model

In the Taylor model, the strain compatibility is achieved at the expense of the stress continuity and equilibrium at the grain boundaries. In the Sachs model, on the other hand, the stress continuity and equilibrium are chosen over the strain compatibility. Neither of these models gives a satisfying description of the material during deformation. However, it is possible to satisfy both strain compatibility and stress equilibrium for simplified grain shapes by employing a self-consistent model. These

Theoretical background

$$\dot{W} = \sum_{s=1}^{12} \tau_c^s \cdot |\dot{\gamma}^s| = \min \quad (9)$$

where τ_c^s is the critical resolved shear stress on slip system s .

A slip system is activated when the shear stress, τ^s reaches the critical value, τ_c^s . This requirement gives a stress relation when considering the active slip systems:

$$\frac{1}{2} \sum_{s=1}^{12} (b_i^s n_j^s + b_j^s n_i^s) \sigma'_{ij} = \tau_c^s \quad (10)$$

from which the deviatoric stress, σ'_{ij} in each grain can be obtained. However, no unique solution is obtained for the stress when the critical resolved shear stress is set to be identical in all slip systems (common assumption for FCC materials). The equation will give several equal solutions of five non-zero $\dot{\gamma}^s$ -values all giving a \dot{W} minimum (five activated slip systems). This problem is often referred to as the Taylor ambiguity, and there exist several different methods of solving this ambiguity. The simplest method is to simply pick one of the solutions by random.

For this approach even to be viable, each of the individual crystals must be able to accommodate an arbitrary deformation, requiring five independent slip systems. While the Taylor assumption is reasonable for materials comprising crystals with many slip systems of comparable strength, using the model in other situations can lead to prediction of excessively high stresses, incorrect texture components, or both (Wenk and Van Houtte 2004).

The Taylor FC model offers a solution for the strain rates and stresses in every grain of a multigrain used during a simulation. If, considering such a solution for a grain with a particular lattice orientation, it can hardly be interpreted as the stress occurring in a grain of a real polycrystal with the same lattice orientation. Indeed a real grain has boundaries with other grains, each with particular lattice orientations. As a result, the solution offered by the FC model will not achieve stress equilibrium at these grain boundaries (Van Houtte et al. 2005).

Theoretical background

In this equation; $\dot{\Omega}_{ij}^L$ is the spin of the crystal lattice, $\dot{\gamma}^s$ is the shear slip rate of slip system s , b_i^s is the slip direction of slip system s , and n_j^s is the normal of the slip plane of this slip system. The kinematical equation is based on the assumption that the macroscopic velocity gradient tensor L_{ij} is known and equal to the microscopic velocity gradient:

$$L_{ij} = l_{ij} \quad (6)$$

The macroscopic velocity gradient for simple tension deformation is given by:

$$L_{ij} = \begin{bmatrix} 1 & 0 & 0 \\ 0 & -\frac{r}{1+r} & 0 \\ 0 & 0 & -\frac{r}{1+r} \end{bmatrix} \cdot \dot{\epsilon} \quad (7)$$

where $\dot{\epsilon}$ is the strain rate and r is the r -value or Lankford coefficient ($r = \frac{\epsilon_w}{\epsilon_t}$). Further,

the kinematical equation also states that the slip rates, $\dot{\gamma}^s$ of all slip systems must be calculated and the combination of all slip processes active at a given moment determines what happens to the crystal. Hence, the symmetric part of l_{ij} becomes the strain rate tensor:

$$d_{ij} = \frac{1}{2} \sum_{s=1}^{12} (b_i^s n_j^s + b_j^s n_i^s) \dot{\gamma}^s \quad (8)$$

This equation gives a set of five independent equations with twelve unknown $\dot{\gamma}^s$. Hence, an additional set of requirements is needed in order to solve the equation.

The energetic assumption of Taylor fulfils this requirement. This assumption suggests that the slip systems are chosen so that the internally dissipated friction work per unit time \dot{W} is minimised:

Theoretical background

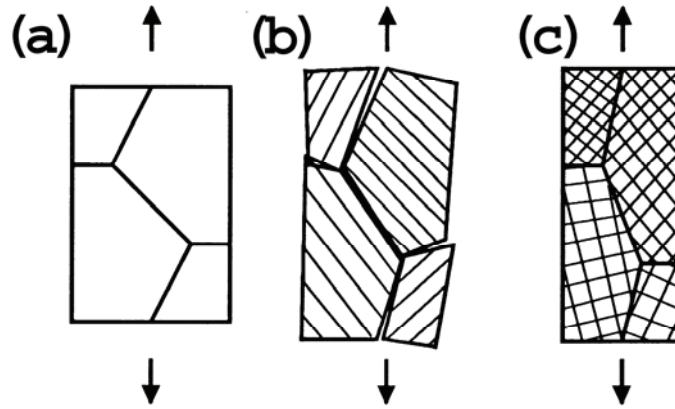


Figure 2.9 – Tension of a polycrystal (a) Before plastic deformation. (b) Large plastic deformation according to the Sachs model (single slip). (c) Large plastic deformation according to the Taylor model (polyslip) (Gambin 2001).

2.2.5 The Taylor model

The Taylor model (Taylor 1938) states that the plastic strain of all crystallites within a polycrystal is the same and hence equal to the macroscopic plastic strain. The idea behind the Taylor model can also be formulated as follows: The neighbourhood of a grain embedded in a polycrystalline material introduces very strong constraints on the individual grains; it must have exactly the same strain as its surroundings; no misfit strains are allowed. The elastic strains are also neglected. The original version of the Taylor model is normally referred to as the Full Constraint (FC) Taylor model, as it maximises the influence of the geometrical constraints (Van Houtte et al. 2005).

In order to develop this model, Taylor made use of a local constitutive law based on crystal plasticity which establishes the relation between the local stress, strain and rigid body rotation inside a RVE (representative volume element). The local constitutive law consists of a kinematical equation and an energetic assumption.

The kinematical equation relates the microscopic velocity gradient l_{ij} which describes the local deformation (per unit time) with the slip rates of all active slip systems:

$$l_{ij} = \dot{\Omega}_{ij}^L + \sum_{s=1}^{12} b_i^s n_j^s \dot{\gamma}^s \quad (5)$$

Theoretical background

2.2.4 The Sachs model

The oldest plasticity model is the one proposed by Sachs in 1928 and later proposed by Cox and Sopwith (1937) and Kochendörfer and Swanson (1960) in a slightly different form. Sachs assumed that each grain only deforms by one activated slip system, namely that with the highest resolved shear stress. He further assumed that a polycrystal is an aggregate of independently deforming single crystals, and the principle axes of stress are the same in all grains of a homogeneously stressed polycrystal. Hence, the Sachs model is based on the Schmid value of each crystallite. Please notice, according to the Sachs model, single slip in a grain leads to a misfit of its shape with respect to the surroundings. It would lead to large interaction stresses between grains and it would quickly lead to material separation at the grain boundaries. This is schematically illustrated in Figure 2.9.

However, the arguments used in favour of the Sachs model are nevertheless based on metallographic observations. A single set of slip traces is often observed on the surface of deformed polycrystalline materials, except near grain boundaries (see e.g. Zankl 1963, Schwink 1965 and Schwink and Vorbrugg 1967). There are a number of objections to such observations (Kocks 1970). Firstly, the surface grains are not under the full constraint of the compatibility conditions caused by the interaction of grains across grain boundaries. Secondly, one observed slip trace can correspond to several independent slip systems. Thirdly, even under the condition of several slip systems activated, it is rarely expected that an equal amount of slip on all activated slip systems occurs. In general, it seems that the Sachs model is quite satisfactory at the very beginning of plastic yielding of crystal aggregates. However, for higher plastic strains, the Taylor model is assumed to give a better description of reality.

Theoretical background

1. Small single-crystalline volume elements (Figure 2.8 a) which are characterised by their crystallographic orientation \mathbf{g} and the rotation $\Delta\mathbf{g}$ after a small deformation step.
2. Big polycrystalline volume elements (Figure 2.8 b) which are characterised by their orientation distribution function $f(\mathbf{g})$, i.e. the texture, and the texture change $\Delta f(\mathbf{g})$ after a small deformation step. In this latter case, the total texture change $\Delta f(\mathbf{g})$ may be divided into two parts:
 - i. An average rotation $\Delta\bar{\mathbf{g}}$ as indicated by the big circular arrow in Figure 2.8 (b). This part can be interpreted qualitatively as the rotation of some common reference axis system characteristic of the whole volume element (b).
 - ii. A "spreading" of the individual crystal orientations away from this common (rotated) reference system indicated by the small individual arrows in volume element (b).

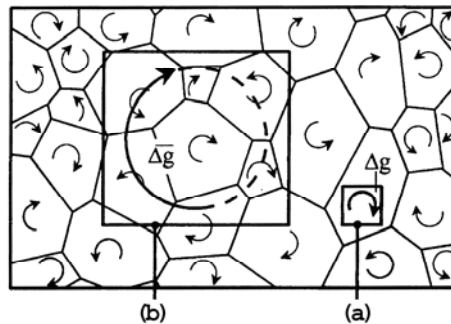


Figure 2.8 – Schematic illustration of lattice rotation in a polycrystalline material. (a) Small single-crystalline volume element with unique lattice rotation ($\Delta\mathbf{g}$). (b) Large polycrystalline volume element with individual rotations ($\Delta\mathbf{g}$) and the average rotation ($\Delta\bar{\mathbf{g}}$) (Bunge and Nielsen 1997).

Crystal rotations can be modelled using different assumptions for the individual single crystalline volume elements (Figure 2.8 a) as well as for the interaction of the differently oriented crystallites (inside the volume element of Figure 2.8 b). The basis of some classical crystal plasticity models will be presented in the following.

Theoretical background

Plastic deformation of single crystals often proceeds by slip in only one slip system as illustrated in Figure 2.7. However, in polycrystalline material (Figure 2.8) each crystallite is surrounded by its neighbours. This requires continuity of plastic deformation across the grain boundaries. The enforced shape change introduces usually slip (and thus rotation) on several slip systems simultaneously. Therefore, the lattice rotations in the polycrystalline metal are not uniform within each individual grain. The orientation rotation behaviour of each grain during deformation is not easy to interpret. It has been found that the rotations of the crystallites show a very broad spread, which may be attributed to the individual environment of each crystallite. However, the average rotation paths of the grains are usually quite well described by the Taylor model (see e.g. Bunge and Fuchs 1969, Han et al. 2003 and Winther et al. 2004). This means that grains having an initial orientation with a $[100]$ or $[111]$ parallel to the deformation direction (DD) are relatively stable during deformation, while grains having a $[110]$ parallel to the DD tend to rotate towards a more stable orientation.

It has also been shown that different parts of a crystallite may rotate in different directions such that they become distinguishable crystallites themselves (see e.g. Wert 2002). In this sense a polycrystalline material is composed of crystallites, each of which has its particular crystal orientation \mathbf{g} and each of which rotates in its own way as is illustrated schematically in Figure 2.8. The rotations lead to texture changes, i.e. the development of deformation textures. This process has been studied in great detail (see e.g. Dillamore and Roberts 1965). Texture changes resulting from plastic deformation are often accompanied by changes of the plastic properties. Hence, the orientation changes of the crystallites must be taken into account in any comprehensive theory of polycrystal plasticity. This can be done particularly on two different length scales (Bunge and Nielsen 1997):

Theoretical background

direction) to the crystal lattice, one point can be found in the standard triangle that represents the loading axis. Therefore the loading axis during deformation can be traced by a series of points in this triangle as shown in the same figure. After a rotation from D to point 2, the specimen has become orientated so that two slip systems have the same maximum Schmid value. Normally at this point, deformation proceeds on both slip systems simultaneously to produce duplex or multiple slip. The additional slip system is often referred to as the conjugate slip system. The duplex slip causes further movement of the specimen axis along the $[001]-[\bar{1}11]$ boundary toward the $[\bar{1}12]$ pole which is the mid way between the two operative slip directions. When the stress axis reaches this orientation, it is assumed that this orientation is maintained until localised necking take place, followed by fracture.

If the movement of individual dislocations are omitted, slip on a slip system can be modelled by homogeneous shear (\mathbf{F}^P) as illustrated in Figure 2.7. The shape change occurring during shear of the considered volume element is generally accompanied by a rigid rotation (\mathbf{F}^*). This rotation changes the orientation of the crystal axes whereas slip (by itself) does not. In fact both slip and rotation take place simultaneously ($\mathbf{F} = \mathbf{F}^* \cdot \mathbf{F}^P$), hence the volume element changes its shape and rotates at the same time as shown in Figure 2.7 (Kahn and Huang 1995).

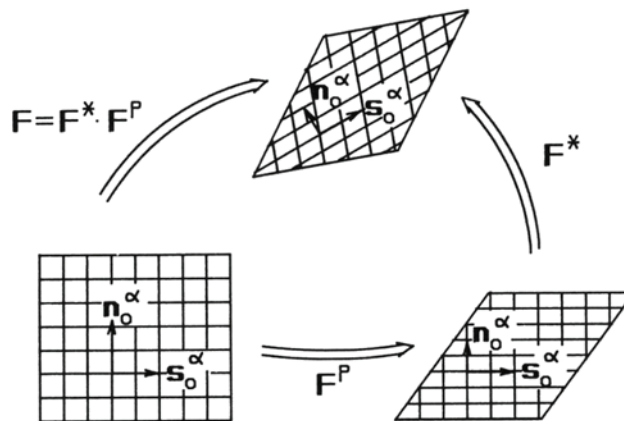


Figure 2.7 – Illustration of the kinematics of single-crystal deformation. The mutually perpendicular grids represent the crystal lattice. \mathbf{s}_0^α and \mathbf{n}_0^α are the initial unit vector in the slip direction and the initial unit normal vector to the slip plane of the α slip system, respectively (Kahn and Huang 1995).

Theoretical background

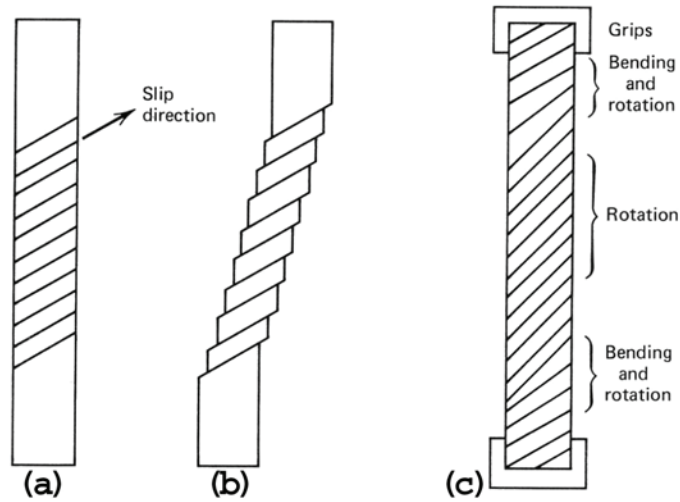


Figure 2.5 – Physical changes in a single crystal deformed in a tensile machine. (a) Undeformed single crystal. (b) Deformed single crystal without friction in the lateral direction. (c) The lateral movement accomplished by simple rotation of the lattice in the centre and combined rotation and bending near the grips (Verhoeven 1975).

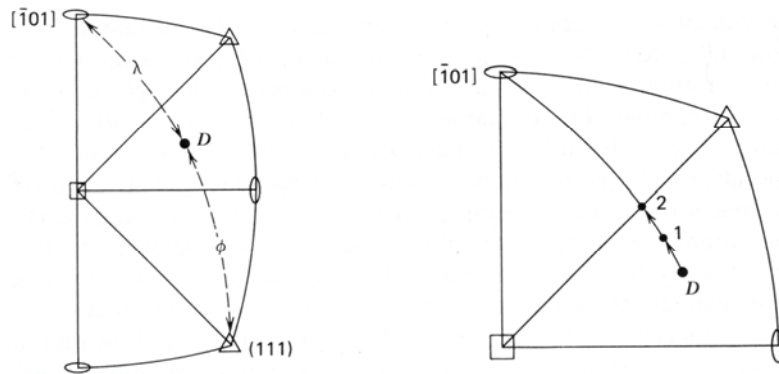


Figure 2.6 – Representation on a stereographic projection of a deformation induced crystal rotation (Verhoeven 1975).

The slip direction of a single crystal with initial orientation D will during large tensile plastic deformation rotate toward the tensile axis so that $\lambda < \lambda_0$, where λ_0 and λ are the initial and current angle between the tensile axis and slip direction respectively. This rotation can be represented by moving the point D toward the $[\bar{1}01]$ direction along the great circle through D and $[\bar{1}01]$ as shown in Figure 2.6. At any instant of the deformation, using the current relative orientation of the loading axis (deformation

Theoretical background

Schmid values of several slip systems are equivalent, and these crystallites are assumed to have more than one operative slip system (Figure 2.4).

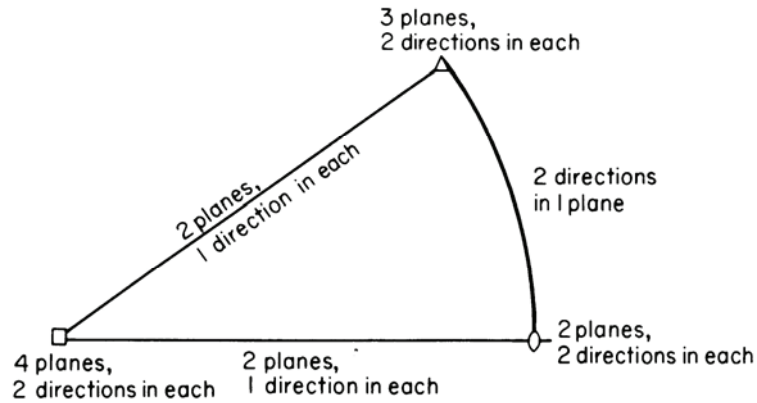


Figure 2.4 – Number of equivalent slip systems at special orientations in the inverse pole figure. The squares, triangles and circles indicate eight, six and four equivalent slip systems respectively (Honeycombe 1984).

2.2.3 Rotation of the crystal lattice

A very important phenomenon in plastic deformation is that the crystal lattice will rotate relative to a fixed coordinate frame (e.g. the tensile machine and the loading axis which are fixed to the ground) during significant plastic deformations. To illustrate lattice rotation, simple tension of a single crystal will be presented as shown in Figure 2.5. If the grips of the tensile machine could move freely without friction in the lateral direction, the specimen would deform as shown in Figure 2.5 (b). However, the tensile grips allow no lateral movement of the specimen ends. As a consequence, the lack of motion in the lateral direction must be accomplished by a simple rotation of the lattice, i.e. the slip direction s would rotate toward the tensile axis. Close to the grips some additional bending and appurtenant distortion has to be included in order to obey the constraint enforced from the fixed grips.

Theoretical background

where \mathbf{n}^s is the slip plane normal and the \mathbf{s}^s is the unit vector in the Burgers vector (slip) direction of slip system s .

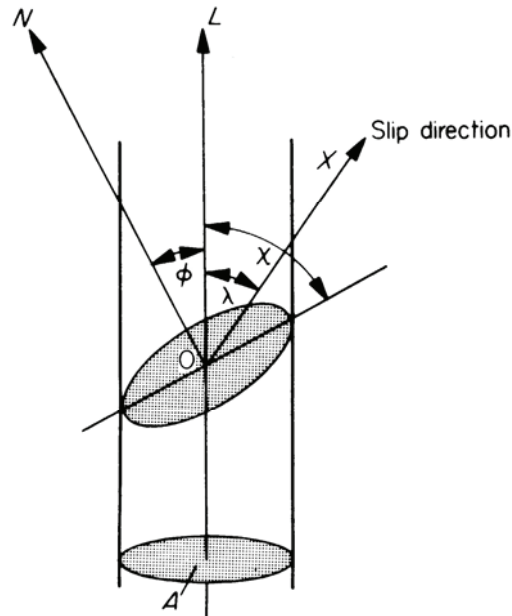


Figure 2.3 – Schematic illustration of the resolved shear stress on a slip system during simple tension deformation (Honeycombe 1984).

It is also worth noticing that in some special circumstances the equation above will become zero. τ becomes zero if the tension axis is normal to the slip plane ($\lambda=90^\circ$), or if the tension axis is parallel to the slip plane ($\chi=0^\circ$). Deformation by slip will not be expected in these two extreme orientations. The reason is that the shear stress in the slip direction would be zero. On the other hand, the maximum shear stress is obtained when $m=0.5$, that is when ϕ and λ are both 45° , hence $\tau_{\max}=0.5\sigma_t$. Here, it is evident that single crystals will give rise to a plastically anisotropic behaviour due to a discrete distribution of slip systems.

Furthermore, the Schmid value of the individual slip systems is controlled by the orientation of the crystallite in relation to the tensile stress. The primary slip systems (highest Schmid value) of the different standard stereographic triangles are included in the standard stereographic projection presented in Figure 2.2. For some orientations, the

Theoretical background

described by continuum mechanics (see e.g. Liu et al. 1997 and Wilkinson et al. 1997) even though the material deforms by slip, which clearly is a non-continuous deformation process (Verhoeven 1975 and Honeycombe 1984).

2.2.2 Schmid's law – geometry of slip

Slip will occur upon the $\{111\}$ planes when a single crystal of an FCC metal is deformed in tension. The force causing slip is not the tensile force but rather the decomposed shear force in one of the $\{111\}$ planes along one of the slip directions. Hence, the tensile force must be decomposed into the individual slip systems. This was first postulated by Schmid in 1924, where he states that yield would begin on a slip system when the resolved shear stress on this system reached a critical value, independent of the axial tensile stress and other normal stresses on the lattice plane. This statement is now commonly referred to as Schmid's law.

Consider a crystal of cross-sectional area A having a tensile load L imposed giving a tensile stress σ_t . Figure 2.3 shows this crystal and its slip plane in which OX is the slip direction and λ is the angle between the axis and the slip direction. The tensile axis makes an angle χ with the slip plane, so that the area of the slip plane is $A/\sin\chi$. Therefore, the tensile stress on the slip plane is

$$\frac{L}{A} \sin \chi = \sigma_t \sin \chi \quad (2)$$

and the shear stress on the slip plane resolved in the slip direction is

$$\tau = \sigma_t \sin \chi \cdot \cos \lambda = \sigma_t \cos \phi \cdot \cos \lambda = \sigma_t \cdot m \quad (3)$$

where ϕ is the angle between the tension axis and the normal ON of the slip plane, and σ_t is the tensile stress (Honeycombe 1984). The geometrical part of this equation is often referred to as the Schmid value, m . The general Schmid tensor of the slip system s is computed in the crystal coordinate system using

$$m_{ij}^s = \frac{1}{2} (s_i^s n_j^s + s_j^s n_i^s) \quad (4)$$

Theoretical background

Theoretically, any of the 12 different $\{111\}\langle 110\rangle$ slip systems can be activated during deformation but the strain is often distributed among a limited number of these slip systems. The required number of slip systems activated has been discussed heavily since the introduction of the well known Sachs (Sachs 1928) and Taylor (Taylor 1938) models in the first half of last century. The process of slip activation during deformation is still under debate and the arguments for selection of slip systems will most likely be debated for a long time.

Moreover, from a crystal plasticity point of view, the probability for slip is the same for all slip systems with equal Schmid value. This means that activation of slip system A2 (Schmid and Boas notation) on a given A-plane within a particular grain means that the same slip system also should be activated on all other parallel A-planes within that grain. The slip (deformation) should in other words be homogeneously distributed among all A2 slip systems in that particular grain. However, this is normally not the case for aluminium alloys, and the slip tends to localise to small regions separated by regions without or very limited plastic deformation (see e.g. Honeycombe 1984 and Yau and Wagoner 1993). It is this localisation of slip which makes the slip traces visible at the specimen surface, i.e. the traces are an area with localised deformation. The reason for this localisation is not fully understood, but it is believed that the origin lies within the material itself. The condition for initiating localised deformation after any amount of pre-straining is usually related to a situation taking place in the material where the next increment of strain-induced hardening is cancelled out by an accompanying strain-induced softening. Then further straining tends to concentrate in the locations where resistance to continued deformation is first lost, i.e. the deformation is localised to a limited number of slip planes (Backofen 1972, Sørensen 1997). As a consequence, the microstructure often develop slip traces when the dislocations move along activated slip planes and intersect the specimen surface. Hence, the activation of slip plane, and by that the activation of slip systems, can be investigated by studying the appearance of the slip traces.

Predictions of the mechanical properties, i.e. how the material deforms, is often performed by computerised modelling in order to simulate the production of new components. The deformation behaviour is for simplicity often with satisfying results

Theoretical background

a notation used to distinguish the twelve possible slip systems in an individual crystal as shown in Figure 2.2. The notation is based on a letter A-D which defines the slip plane and a number 1-6 which defines the slip direction. Table 2.2 presents the twelve possible slip systems based on the Schmid and Boas notation.

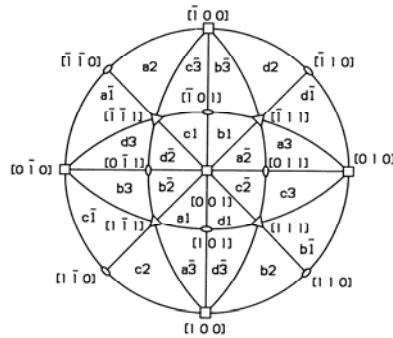


Figure 2.2 – Standard [001] stereographic projection of FCC crystals (Kahn and Huang 1995).

Table 2.2 – Schmid and Boas notation for slip systems in FCC crystals (Schmid and Boas 1935).

Slip System	Slip plane	Slip direction
A2	$(\bar{1}11)$	$[0\bar{1}1]$
A3	$(\bar{1}11)$	$[101]$
A6	$(\bar{1}11)$	$[110]$
B2	(111)	$[0\bar{1}1]$
B4	(111)	$[\bar{1}01]$
B5	(111)	$[1\bar{1}0]$
C1	$(\bar{1}\bar{1}1)$	$[011]$
C3	$(\bar{1}\bar{1}1)$	$[101]$
C5	$(\bar{1}\bar{1}1)$	$[1\bar{1}0]$
D1	$(1\bar{1}1)$	$[011]$
D4	$(1\bar{1}1)$	$[\bar{1}01]$
D6	$(1\bar{1}1)$	$[110]$

Theoretical background

general, grain boundary sliding and diffusional creep become significant only at high temperatures but they must also be considered at very low strain rates. Twinning, on the other hand generally becomes operative at low temperatures in materials having HCP structure. However, twinning in aluminium has been observed but then at very low temperatures or very high strains (see e.g. Gray III 1988 and Werenskiold 2004). Slip is by far the most important deformation mechanism in aluminium and only this mechanism will be treated in the following.

The slip mechanism has been described by Verhoeven (1975) as the parallel movement of two adjacent regions relative to each other across some plane (or planes). The early work of Ewin and Rosenheim (1900) showed that slip takes place along well-defined crystallographic planes. Such crystallographic planes are referred to as the slip plane, while the direction of shear in the plane is called a slip direction. The combination of a slip plane and a direction in that plane is referred to as a slip system. The slip planes in FCC metals are usually those with the closest atomic packing, while the slip direction is always the closest packed direction in the slip plane. Figure 2.1 presents the atomic arrangement of the closest packed planes in a FCC metal.

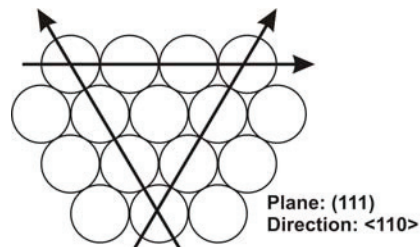


Figure 2.1 – The atomic arrangement in the plane with closest atomic packing in aluminium. The three closest packed directions are also indicated.

The FCC metals deform primarily on the close-packed octahedral {111} planes in the <110> close packed directions. In special cases non-octahedral slip in aluminium alloys has been observed on both the {110} and the {100} planes (see e.g. Perocheau and Driver 2002). However, for all practical considerations only octahedral slip is activated during deformation of aluminium at room temperature. A crystallite consists of four different {111} planes and each plane has three equivalent closest packed directions as indicated in Figure 2.1. Hence, face-centred cubic metals have a total of twelve possible slip systems which can take part in the deformation. Schmid and Boas (1935) developed

Theoretical background

Table 2.1 – IADS (International Alloy Designation System) for wrought aluminium alloys. (X) indicates that only a fraction of the AA8xxx alloys are heat-treatable (AAUS 1970).

Alloy system	Heat-treatable	Description
AA1xxx	-	Commercially pure Al (>99% Al)
AA2xxx	X	Al-Cu and Al-Cu-Li
AA3xxx	-	Al-Mn
AA5xxx	-	Al-Mg
AA6xxx	X	Al-Mg-Si
AA7xxx	X	Al-Mg-Zn
AA8xxx	(X)	Al-Li, Sn, Zr, B, Fe or Cr

2.2 Polycrystalline plasticity theory

The primary task of a polycrystalline plasticity theory is to formulate the relations between the macromechanical behaviour of the polycrystal and the fundamental mechanisms of single crystal deformation. Several objectives can be achieved from investigations concerned with polycrystalline plasticity. First, it allows for identification of the believed micro mechanisms that are responsible for observed macroscopic phenomena. Secondly, the increased understanding on the fundamental level may in turn provide a basis for improved predictions of the macroscopic plastic deformation.

2.2.1 Basic plasticity

The mechanical properties of a material may be represented by a stress-strain diagram. If the applied stress is less than the elastic limit, the deformation is said to be elastic. The material deforms plastically if the stress level is equal to or greater than the yield stress, and any stress level above the yield stress is referred to as the flow stress. Hence, elastic deformation is completely recoverable while plastic deformation is not recoverable upon release of stress. Only the plasticity theory is presented in this section since just the plastic part of the deformation is treated in this work.

Plastic deformation of metals can take place by use of four primary mechanisms (Verhoeven 1975): slip, twinning, grain boundary sliding and diffusional creep. In

Theoretical background

2.1.2 Heat-treatable aluminium alloys

The heat-treatable aluminium alloys achieve their strength mainly from precipitates, and belong to the AA2xxx, AA6xxx and AA7xxx alloy systems (see Table 2.1) (AAUS 1970). These alloys are usually first solution-heat-treated, i.e. heated into the single-phase area of the phase diagram where alloying elements are dissolved in solid solution. A rapid quench freezes the atoms in a supersaturated solid solution (ssss) from where the precipitation sequence starts (Martin 1968). Alloys investigated in the solution-heat-treated condition are often denoted the “W-condition” (ISO 2004). As an example, the precipitation sequence in the AA6xxx system is generally given by:



Precipitation after solution heat-treatment can take place at room temperature (natural age-hardening), in which the stabilised material condition is referred to as the “T4-condition” (ISO 2004). However, artificial age-hardening are normally used in order to achieve a more stabilised material with as high strength as possible. Following the above sequence from left to right, the size of the precipitates increases and the coherency between the matrix and the precipitates is gradually lost. The maximum strength (T6-condition) generally occurs when there is a mixture of coherent and semi-coherent precipitates. Over-ageing to the T7-condition produces stable incoherent particles which results in a lower strengthening effect (Martin 1968). Material cooled from the fabrication temperature (natural solution heat-treatment) and then naturally aged is referred to as the T1-condition (ISO 2004). For a more comprehensive review of heat-treatable aluminium alloys see e.g. Polmear (2004).

2 Theoretical background

The main objective of this theoretical part is to give a summary of previous work done concerning room temperature plastic deformation behaviour in face-centred cubic (FCC) materials. A good understanding of crystal plasticity and the mathematical models used to describe crystal plasticity is of prime importance in order to provide a physical basis for microstructure- and alloy design. On the other hand, experimental observations are critical to the developers of plasticity modelling and for understanding the real phenomena taking place in nature. Hence, a two-fold understanding is a key factor in reaching the main objectives of this investigation. Further, this part summarises the main findings reported in the literature concerning in-situ deformation and electron backscatter diffraction (EBSD) observations on aluminium alloys. The theoretical background for the most important experimental techniques applied is also given in this chapter.

2.1 Aluminium alloys

Aluminium is an important material for the transportation industry due to its low density, high specific strength and competitive crash performance (Hirsch 2004). Also, the ability to easily recycle aluminium alloys is very advantageous from an environmentally point of view (Hirsch 2004). The properties of aluminium have made this material become an even more important material for the future. Wrought aluminium alloys are divided in two groups based on their age-hardenability.

2.1.1 Non-heat-treatable aluminium alloys

Non-heat-treatable aluminium alloys constitute a class of alloys that owe their strength mainly to elements in solid solution. However, also some types of particles will give rise to additional strength increase, mostly due to Orowan hardening (Orowan 1948, Verhoeven 1975). A heat-treatment will generally not produce any strengthening precipitates as in the heat-treatable alloys. The alloy systems belonging to this class are the AA1xxx, AA3xxx, AA5xxx and the AA8xxx alloy systems. A description of the different alloying systems and their main alloying elements are given in Table 2.1.

Introduction

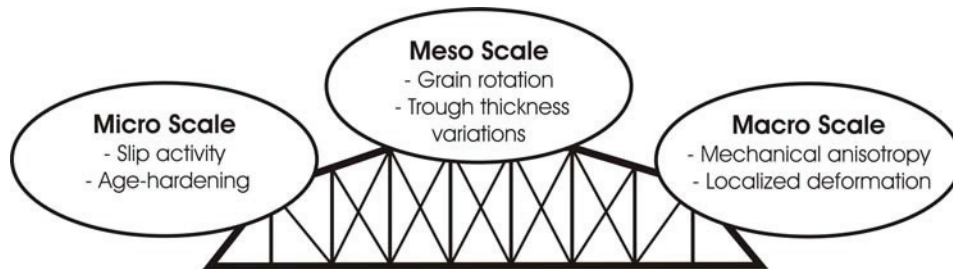


Figure 1.1 – Illustration presenting the different features operating at different length scales that have to be fully understood in order to comprehend how to improve the shape tolerances of extruded profiles with a factor 10.

In this work, special attention has been paid to the effect of heterogeneities in slip activation on the macroscopic mechanical anisotropy. This has been obtained by initially performing a detailed characterisation of two extruded Al-Mg-Si profiles. Further, in-situ EBSD investigations have been applied to better understand the macroscopic properties.

1 Introduction

Modern production processes demands a high degree of automation involving tight geometrical tolerances of the various components. The new requirements on profile shape control are the most critical and come from various product areas like the heat transfer business, general extrusion and, of course, production for the automotive industry. The most prominent example is from the automotive industry. Future requirements from down stream processing of profiles challenges the extrusion industry, since extruded profiles often have strong microstructure- and texture gradients through the thickness which clearly affect the mechanical properties.

The strategy of Hydro Aluminium is to be world leading within aluminium extrusion. The “FREMAT – Understanding and Controlling Variations in Extrusion of Aluminium” research program was initiated by Hydro Aluminium in close collaboration with the Norwegian Research Council in order to attain such a position. The very challenging vision of this project is to improve shape tolerances on extruded products by a factor of ~10. To fulfil this vision, it is essential to understand, quantify and control effects from material flow balance, development of residual stresses, microstructural evolution and thermo-mechanical coupling of die and extruded material on a completely new level of accuracy.

This work is part of the “Microstructure and shape” subproject that addresses metallurgical effects and microstructural evolution. The primary objective is directed towards obtaining an improved understanding of the operating deformation mechanisms, and by that obtaining a better understanding of how shape tolerances, i.e. mechanical anisotropy can be controlled. This can only be obtained if the connections between the different deformation mechanisms operating on all length scales are fully understood. Figure 1.1 illustrates the importance of studying individual mechanisms in order to find the net effect.

6.3.5	STRAIN HETEROGENEITIES	215
6.3.6	HARD VS. SOFT ORIENTATIONS	218
6.3.7	EFFECTS OF NEAREST NEIGHBOURS	220
6.4	IMPACT AND RELEVANCE TO SHAPE OF EXTRUSIONS	222
6.5	IN-SITU DEFORMATION IN THE SEM – STATUS AND CHALLENGES	224
6.5.1	IN-SITU DEFORMATION UNIT	224
6.5.2	CHALLENGES (RELATED TO IN-SITU DEFORMATION IN THE SEM)	225
6.5.3	FOCUSED ION BEAM (FIB)	226
7	<u>CONCLUSION</u>	<u>228</u>
	<u>REFERENCES</u>	<u>230</u>
	<u>APPENDIX A – HEATING UNIT</u>	<u>239</u>
	<u>APPENDIX B – CALCULATED ODFS</u>	<u>241</u>
	<u>APPENDIX C – THROUGH-THICKNESS VARIATIONS</u>	<u>242</u>
	<u>APPENDIX D – EFFECT OF AGE-HARDENING</u>	<u>246</u>
	<u>APPENDIX E – THROUGH-SPECIMEN-THICKNESS-CURVATURES</u>	<u>249</u>

5.5.2	ROTATION PATHS – RANDOM TEXTURED MATERIAL	126
5.5.3	AMOUNT OF ROTATION	129
5.5.4	ORIENTATION GRADIENTS	132
5.6	PLASTICITY	134
5.6.1	SLIP TRACE EVOLUTION	134
5.6.2	SLIP SYSTEM ACTIVITY	146
5.7	LOCAL STRAIN DISTRIBUTION	153
5.7.1	MICRO SCALE	154
5.7.2	MESO SCALE	159
6	DISCUSSION	166
<hr/>		
6.1	MECHANICAL ANISOTROPY	166
6.1.1	CRYSTALLOGRAPHIC TEXTURE	166
6.1.2	TEXTURE VS. MECHANICAL OBSERVATIONS (MAINLY AA6063)	170
6.2	OBSERVATIONS AND TAYLOR ANALYSES REGARDING THROUGH-THICKNESS VARIATIONS	177
6.2.1	TAYLOR ANALYSES	177
6.2.2	EVALUATION OF THE VOCE-TYPE MODEL	180
6.2.3	EXPERIMENTAL EFFECTS	183
6.2.4	FINAL COMMENTS ON THE VOCE-TYPE MODELLING	186
6.2.5	INTERNAL STRESSES	187
6.2.6	PLASTIC STRAIN RATIOS	188
6.2.7	FINAL COMMENTS ON PROFILE THICKNESS STRAIN DISTRIBUTION	194
6.3	DEFORMATION MECHANISMS AND CRYSTAL PLASTICITY	195
6.3.1	THE NATURE OF SLIP TRACES	195
6.3.2	CRYSTALLOGRAPHIC ROTATIONS DURING DEFORMATION	201
6.3.3	SELECTION OF SLIP SYSTEMS	207
6.3.4	ACTIVATION OF SLIP SYSTEMS – EXPERIMENTAL OBSERVATIONS VS. TEXTURE-BASED CALCULATIONS	211

4.1.2	METALLOGRAPHIC PREPARATION AND SURFACE GRIDS	67
4.2	TENSILE TESTING	69
4.3	SCANNING ELECTRON MICROSCOPY (SEM)	69
4.3.1	ELECTRON BACKSCATTER DIFFRACTION (EBSD)	70
4.3.2	IN-SITU DEFORMATION INVESTIGATIONS	73
4.3.3	OPTIMISATION OF IN-SITU SYSTEMS	74
4.4	LOCAL STRAIN MEASUREMENTS	80
5	<u>EXPERIMENTAL RESULTS</u>	<u>81</u>
<u>PART A: CHARACTERISATION OF MATERIALS – EFFECTS OF HEAT-TREATMENT, TEXTURE AND THROUGH-THICKNESS VARIATIONS</u>		<u>82</u>
5.1	CHARACTERISATION OF AS-RECEIVED MATERIALS	82
5.1.1	MICROSTRUCTURE	82
5.1.2	CRYSTALLOGRAPHIC TEXTURE	85
5.1.3	THROUGH-THICKNESS VARIATIONS	87
5.2	MECHANICAL PROPERTIES AND ANISOTROPY	95
5.2.1	MECHANICAL PROPERTIES	95
5.2.2	FURTHER DETAILS REGARDING AGE-HARDENING EFFECTS	102
5.2.3	AGE-HARDENING VS. ANISOTROPY AND SHAPE	111
<u>PART B: SEM IN-SITU INVESTIGATIONS OF PLASTICITY – SLIP ACTIVITY, GRAIN ROTATION AND TEXTURE EVOLUTION</u>		<u>114</u>
5.3	INITIAL INVESTIGATIONS	114
5.4	GLOBAL TEXTURE EVOLUTION WITH INCREASING STRAIN	116
5.5	GRAIN ROTATION WITH INCREASING STRAIN	122
5.5.1	ROTATION PATHS – HEAVILY TEXTURED MATERIAL	122

2.3.4	EBSD MEASUREMENTS	28
2.3.5	TEXTURE COMPONENTS IN FCC MATERIALS	33
2.4	ANISOTROPY AND FORMABILITY	36
2.4.1	MECHANICAL ANISOTROPY	36
2.4.2	TEXTURE-BASED CALCULATIONS	37
2.5	MICROSTRUCTURAL EVOLUTION	38
2.5.1	SLIP TRACES	38
2.5.2	TRANSITION AND KINK BANDS	40
2.5.3	SHEAR BANDING	40
2.6	STRAIN MEASUREMENTS	41
2.6.1	DIGITAL SPECKLE CORRELATION ANALYSIS	43
2.7	EARLIER WORK – STATE-OF-THE-ART	45
2.7.1	CRYSTAL PLASTICITY	46
2.7.2	MECHANICAL ANISOTROPY AND FORMING BEHAVIOUR	47
2.7.3	DEFORMATION MECHANISMS	48
2.7.4	AGE-HARDENING	49
2.7.5	AVAILABLE IN-SITU TECHNIQUES	52
3	<u>MATERIALS AND MATERIAL PROCESSING</u>	56
3.1	MATERIALS	56
3.2	MATERIAL PROCESSING	57
3.2.1	EXTRUSION	57
3.2.2	HEAT-TREATMENTS	58
3.2.3	ADDITIONAL PROCESSING	59
4	<u>EXPERIMENTAL TECHNIQUES</u>	61
4.1	SPECIMEN SAMPLING AND PREPARATION	61
4.1.1	SPECIMEN SAMPLING	61

Table of contents

PREFACE	I
ABSTRACT	III
ACKNOWLEDGMENTS AND CONTRIBUTIONS	V
TABLE OF CONTENTS	VII
1 INTRODUCTION	1
2 THEORETICAL BACKGROUND	3
2.1 ALUMINIUM ALLOYS	3
2.1.1 NON-HEAT-TREATABLE ALUMINIUM ALLOYS	3
2.1.2 HEAT-TREATABLE ALUMINIUM ALLOYS	4
2.2 POLYCRYSTALLINE PLASTICITY THEORY	5
2.2.1 BASIC PLASTICITY	5
2.2.2 SCHMID'S LAW – GEOMETRY OF SLIP	9
2.2.3 ROTATION OF THE CRYSTAL LATTICE	11
2.2.4 THE SACHS MODEL	16
2.2.5 THE TAYLOR MODEL	17
2.2.6 THE SELF-CONSISTENT MODEL	20
2.2.7 ADVANCED POLYCRYSTALLINE PLASTICITY MODELS	21
2.3 TEXTURE	23
2.3.1 ORIENTATION OF INDIVIDUAL CRYSTALLITES	24
2.3.2 ORIENTATION DISTRIBUTION	25
2.3.3 ELECTRON BACKSCATTER DIFFRACTION (EBSD)	26

Acknowledgments and contributions

The Norwegian Research Council and Hydro Aluminium are gratefully acknowledged for the founding through the FREMAT project. Hydro Aluminium is further acknowledged for giving me the opportunity to gain industrial experience through several internships at different facilities. Special thanks to my supervisors, Professor Hans Jørgen Roven and Professor Jarle Hjelen. They have fully supplemented each other, and their encouragement and enthusiasm has stimulated me to complete this work. I would also like to give a special thanks to Dr. Trond Furu for his motivating interest.

My good friend Dr. Stéphane Dumoulin is gratefully acknowledged for his involvement in strain measurements, mathematical and continuum mechanical calculations. This work could not have been completed without his help. The thorough introduction to in-situ deformation in the SEM provided by Rémi Chiron at the CNRS – PMTM laboratory in Paris has been crucial for this work and is very well acknowledged. I would also like to acknowledge all my colleagues in the department, in particular Dr. Stian Tangen, Dr. Knut Sjølstad, Dr. Jens Christofer Werenskiold, Dr. Bjørn Holmedal, Dr. Håkon Hallem, Mr. Tomas Erlie, Mr. Przemyslaw Szczygiel and Mr. Anders Lilleby, who all assisted me both professionally and socially during this work.

Further, I have been fortunate to supervise three master degree students during my PhD work. I would like to thank Mr. Snorre Kjørstad Fjeldbo, Mrs. Randi Mørkrid and Mr. Peter Bråten for their thorough work performed during their master works.

I would like to acknowledge my colleagues at the scanning electron microscopy laboratory, not only for providing high performance equipment and knowledge that allows state-of-the-art research within this field, but also for the close friendship during my time at NTNU. Also my current colleagues at Hydro Aluminium Holmestrand should be acknowledged for their support this last year.

Finally, I would like to thank the two most important women in my life, my fiancée Margrethe and my new-born daughter Oda, that both have been extremely patient during my time as a PhD-student.

align the DD to one of the above directions. Also the rotation of individual grains seemed to have a strong relationship to the actual activation of slip systems.

The mechanical anisotropy and shape tolerances could be explained in terms of crystallographic texture, i.e. variations in the actual activation of slip. As a result, the macroscopic properties (e.g. mechanical anisotropy) were to a large extent controlled by the mechanisms operating at the microscopic length scale. A full understanding of the operating mechanisms should therefore involve exact information from all length scales.

Abstract

A comprehensive characterisation and study of plasticity in two extruded Al-Mg-Si profiles has been carried out. The primary objective of the experimental work has been directed towards obtaining an improved understanding of the operating deformation mechanisms and mechanical anisotropy observed on all length scales during plastic deformation. In-situ deformation in the SEM combined with EBSD investigations has been an important tool in order to obtain this objective. The experimental results have been divided into two separate parts. Part A covers the characterisation and mechanical anisotropy investigations, while Part B covers the more detailed in-situ investigations.

Two alloys, one with a recrystallized microstructure and the other with a non-recrystallized (fibrous) microstructure, have been subjected to a detailed characterisation concerned with mechanical anisotropy, through-thickness variations and effects of various heat-treatments. The experimental investigations showed that both alloys possess highly anisotropic properties. The effects of temper designation, directional dependency and position through the thickness were studied.

The in-situ deformation studies gave new insights into the fundamental reasons for the observed mechanical anisotropy and the related deformation mechanisms. Detailed investigations of the slip traces in combination with calculated Schmid value distributions provided information on potential slip activity for the various slip systems. It was found that the number of slip systems activated was very heterogeneous and this number can even vary from region to region within one individual grain. In other words, the strain distribution seemed very heterogeneous. Further, the actual number of activated slip systems was in general less than predicted by the widely used Taylor model. Consequently, if the accuracy of texture-based calculations should be improved, more advanced models like the GIA (Grain Inter-Action) and the LAMEL models should be applied.

It was also found that crystallographic orientations having a [100] or a [111] parallel to the deformation direction (DD) were more stable during simple tension deformation. Moreover, crystallographic orientations not having this configuration rotated in order to

Preface

The experimental research presented in this thesis has been carried out at the Norwegian University of Science and Technology (NTNU), Department of Materials Science and Engineering in the period from August 2002 to March 2006. The thesis reached its final form by end of June 2007.

The work was part of the project FREMAT, sub-project “Microstructure and Shape” and has been financed by the Norwegian Research Council and Hydro Aluminium AS. It has allowed the author to work within both development of new experimental techniques and detailed crystal plasticity of extruded Al-Mg-Si profiles, something that certainly has been appreciated. Hopefully, this work will result in new insight into crystal plasticity, but also initiation of new works within the field of in-situ EBSD.

The close collaboration with Hydro Aluminium AS allowed for introducing the author to various in-depth aspects related to aluminium extrusion technology. This in turn, has opened up for a better understanding of current industrial challenges and hopefully improved the relevance and quality of the work presented herein.

NTNU

Norwegian University of Science and Technology

Thesis for the degree philosophiae doctor

Faculty of Natural Sciences and Technology
Department of Materials Science and Engineering

© Hans Bjerkaas

ISBN 978-82-471-3375-0 (printed version)
ISBN 978-82-471-3389-7 (electronic version)
ISSN 1503-8181

Doctoral theses at NTNU, 2007:154

IMT-Report 2007:94

Printed by NTNU-trykk

Hans Bjerkaas

Characterisation and Plasticity in Extruded Al-Mg-Si Profiles engaging In-situ EBSD

Thesis for the degree philosophiae doctor

Trondheim, June 2007

Norwegian University of Science and Technology
Faculty of Natural Sciences and Technology
Department of Materials Science and Engineering

